Complexity

Frontiers in Data-Driven Methods for Understanding, Prediction, and Control of Complex Systems

Lead Guest Editor: Murari Andrea
Guest Editors: Jesus Vega, Gonzalo Farias, Teddy Craciunescu, and Michela Gelfusa

Frontiers in Data-Driven Methods for Understanding, Prediction, and Control of Complex Systems

Complexity

Frontiers in Data-Driven Methods for Understanding, Prediction, and Control of Complex Systems

Lead Guest Editor: Murari Andrea
Guest Editors: Jesus Vega, Gonzalo Farias, Teddy Craciunescu, and Michela Gelfusa

Contents

Contents

Hindawi
Complexity
Volume 2020, Article ID 8923197, 20 pages
https://doi.org/10.1155/2020/8923197

Research Article

Multiobjective Genetic Programming Can Improve the Explanatory Capabilities of Mechanism-Based Models of Social Systems

Tuong M. Vu,[1] **Charlotte Buckley**,[2] **Hao Bai**,[2] **Alexandra Nielsen**,[3] **Charlotte Probst**,[4] **Alan Brennan**,[1] **Paul Shuper**,[4] **Mark Strong**,[1] **and Robin C. Purshouse**[2]

[1]*School of Health and Related Research, University of Sheffield, Sheffield, UK*
[2]*Automatic Control and Systems Engineering, University of Sheffield, Sheffield, UK*
[3]*Alcohol Research Group, Public Health Institute, Emeryville, CA, USA*
[4]*Institute for Mental Health Policy Research, Centre for Addiction and Mental Health, Toronto, Canada*

Correspondence should be addressed to Tuong M. Vu; t.vu@sheffield.ac.uk

Received 13 September 2019; Revised 28 February 2020; Accepted 28 March 2020; Published 5 June 2020

Guest Editor: Murari Andrea

The generative approach to social science, in which agent-based simulations (or other complex systems models) are executed to reproduce a known social phenomenon, is an important tool for realist explanation. However, a generative model, when suitably calibrated and validated using empirical data, represents just one viable candidate set of entities and mechanisms. The model only partially addresses the needs of an abductive reasoning process—specifically it does not provide insight into other viable sets of entities or mechanisms nor suggests which of these are fundamentally constitutive for the phenomenon to exist. In this paper, we propose a new model discovery framework that more fully captures the needs of realist explanation. The framework exploits the implicit ontology of an existing human-built generative model to propose and test a plurality of new candidate model structures. Genetic programming is used to automate this search process. A multiobjective approach is used, which enables multiple perspectives on the value of any particular generative model—such as goodness of fit, parsimony, and interpretability—to be represented simultaneously. We demonstrate this new framework using a complex systems modeling case study of change and stasis in societal alcohol use patterns in the US over the period 1980–2010. The framework is successful in identifying three competing explanations of these alcohol use patterns, using novel integrations of social role theory not previously considered by the human modeler. Practitioners in complex systems modeling should use model discovery to improve the explanatory utility of the generative approach to realist social science.

1. Introduction

Agent-based simulation (ABS) is a well-established tool for understanding complex systems using the generative social science approach. The goal of generative social science is to explain and understand a social phenomenon as the result of actions of autonomous entities acting according to causal mechanisms or rules as encoded in an agent-based model [1]. If a modeler encodes a model that produces a known empirical pattern, the so-called "generative test" is met, and the postulated mechanisms form a candidate explanation for the phenomenon. Many social phenomena may be explained by a multiplicity of theories, each of which could pass the generative test when encoded as an ABS, leaving us to wonder which theory is correct; how can theories be combined; and what is missing from our theories? Here, we propose a novel method of discovering new models and extending the explanatory capabilities of theory-driven generative models using multiobjective genetic programming—a process of knowledge discovery. Elements of a generative theory or several generative theories are codified in a common grammar, evolved through genetic

programming, evaluated for empirical fit, complexity, and interpretability, and interpreted by subject matter experts to bring new insight to the social phenomenon.

In this paper, we set out the following aims: (1) to explain the role of complex systems models for realist explanation; (2) to define the structural calibration method: a retroductive model discovery framework; (3) to demonstrate the application of the model discovery framework to a specific mechanism-based social systems model; and (4) to discuss the implications of computer aided model discovery in light of the case study results.

2. Methods

2.1. The Role of Abductive Reasoning in Mechanism-Based Explanation. The context for our methods is the generative [1] or mechanism-based [2] approach to the study of complex social systems. In this approach, we assume that any concrete phenomenon (which may be empirically observable to a greater or lesser degree) emerges from the dynamic interplay of *real* entities and mechanisms that exist independently of our ability to detect them [3]. In this context, the role of complex systems modeling is principally explanatory, in helping to gain insights into theorised entities and mechanisms by representing them in a dynamic simulation model.

Abductive reasoning plays a key role in mechanism-based explanations and can be conceived of in two parts [4]:

(i) Redescription: situating the concrete phenomenon as a case which emerges from the hypothesized interacting components (i.e., entities and mechanisms) of one or more theories.

(ii) Retroduction: identifying which of the components in the redescription are fundamentally constitutive to the emergence of the phenomenon (i.e., entities and mechanisms whose inexistence would preclude the phenomenon).

The development of a complex systems model by a human modeler is principally a redescription activity—the modeler uses existing theory (and potentially develops new theory) to construct a set of equations and rules that, when executed as a simulation, produce emergent outcomes that are in some sense comparable to the phenomenon under investigation. As part of the model building process, the modeler defines—either explicitly or implicitly—an ontology of real entities, the agents of agent-based simulations, and mechanisms, the rules that determine action and interaction.

The generative approach commits the modeler to at least a limited form of retroduction—the simulation, as redescription, is scrutinised for its ability to reproduce the concrete phenomenon, in so far as the latter is observable in empirical data. The simulation parameters often have to be manipulated in order to achieve good similarity; in the computational modeling community, this process is known as *calibration* [5] and is commonly identified as belonging to best practice programs for analytical sociological research [6]. If a simulation can be calibrated successfully, then the redescription it encodes is said to pass the *generative sufficiency* test—it remains a candidate explanation for the phenomenon [1]. However as a retroductive process, the generative approach, when applied to a single simulation model, has two fundamental shortcomings: (1) it does not allow the entities and mechanisms to be accepted as fundamentally constitutive since to do so would be to commit the fallacy of affirming the consequent; (2) neither does it allow the entities and mechanisms to be rejected as fundamentally constitutive, only that their present configuration or representation in the simulation model is nonconstitutive.

Together, these limitations form the basis for many of the concerns about complex systems modeling raised within the sociological community (see, for example, [7]). We argue that the limitations arise from the focus of the modeling on a single redescription, i.e., a single ABS. To improve our explanatory capability, we need to increase the number of redescriptions considered within the overall modeling process, i.e., by building multiple ABS that either interpret a single theory in different ways or represent multiple different theories or both. By subjecting a plurality of redescriptions to retroduction, we can seek to identify commonalities in the theory components that survive the generative sufficiency test; we can also seek to increase the robustness of the test outcome to potential issues with the configuration or representation of a theory within the simulation. Within the context of model calibration activities, this concept is operationalized as interrogating model structure (i.e., the selection and configuration of entities and mechanisms) in addition to model parameters—we call this *structural calibration*. Perhaps surprisingly, given its key role in the abductive reasoning process, the complex systems modeling community has yet to pay significant attention to the issue of structural calibration. Below we review the handful of existing works on this topic.

2.2. Existing Works on Structural Calibration of Simulation Models. A very small literature exists on the structural calibration (described variously as "theory discovery" [8], "model discovery" [9], and "inverse generative social science" [10]) of mechanism-based models, all of which use evolutionary computing (EC) methods to steer the search for good model structures. In the earliest known study, Smith [11] used a genetic algorithm to identify simplified representations of behavior that could reproduce the observed social assortativity of birds. Later, with a focus on reproducing observed human crowd dynamics, Zhong et al. [12] used gene expression programming to identify the structure of a reward function representing individual decision making in a "sense-think-act" framework. Gunaratne and Garibay [8] used genetic programming to revise agents' farm selection rules for the "Artificial Anasazi" model, in order to more accurately reproduce the archeological population demography of Long House Valley, Arizona. Most interestingly, again within the context of the Artificial Anasazi, the same authors then used genetic programming to identify components for Epstein's Agent_Zero model of human

behavior as the basis of farm selection decisions [9]. Finally, in work that forms a prelude to the present study, Vu et al. [10] used multiobjective genetic programming to identify alternative situational mechanisms for a social norms model of alcohol use, aimed at both improved representation of observed drinking patterns in the US over a 15-year period and theoretical interpretability (operationalized as the number of terms in the situational mechanism).

There exist a number of issues and limitations with these early techniques. While the studies have demonstrated success at improving the goodness of fit to empirical data, they have all been limited in scale—focusing on specific aspects of larger models. Further, the studies focusing on human behavior have also struggled with the issue of theoretical meaningfulness of the structures that have been identified. While minimizing or constraining the number of terms in the candidate behavioral rules is clearly helpful at improving interpretability, it is often the case that the new structures remain challenging to interpret in terms of the original theory, with this crucial activity deferred to future work.

2.3. Proposed Approach to Structural Calibration. Here, we describe a new framework for structural calibration and position it explicitly as a tool for realist explanation that can be used alongside more traditional approaches within the realist tradition [3]. Our approach is grounded in the recognition that the human modeler uses a creative process of redescription that results in the construction of an ontology for entities and mechanisms that may be implicated in the generation of a complex phenomenon. The starting point for our framework is this ontology. We exploit the ontology to (a) construct new candidate redescriptions (i.e., simulation model structures) that can be realized via the ontology; (b) test the candidate redescriptions in terms of their explanatory value, where "value" can be a plurality of considerations, such as empirical goodness of fit, structural parsimony, interpretability, and theoretical credibility.

The ontology developed by the modeler can be considered as a set of basic building blocks of entities and mechanisms. While we could, as humans, use the building blocks to construct an exhaustive set of possible alternative simulation model structures (by assembling the building blocks in different ways), even a relatively small set of building blocks can result in a very large number of alternatives that cannot be practically explored by hand. An alternative is to use machine learning approaches, where we make intelligent use of computational resources to automatically search through the space of possible model structures. In the vein of the existing literature, we regard the family of evolutionary computing approaches known as *genetic programming* (GP) as a highly promising workhorse for structural calibration [13]. Multiobjective genetic programming is particularly beneficial because it allows researchers to evaluate candidate model structures according to a set of explicitly stated considerations of explanatory value [14]. In our present framework, we concentrate on two aspects of value: (i) the ability of the model structure, with suitably calibrated parameters, to reproduce the phenomenon so far as we understand it from our beliefs and empirical data; (ii) the meaningful interpretability of the model structure in terms of theory.

2.4. Generating Candidate Model Structures: Grammar-Based Genetic Programming. Evolutionary computing is a field that applies the principles of natural evolution in computing. In EC, a population of candidates is evolved over many generations based on a fitness function. A typical process starts with a random population of candidates. The candidates with high fitness are then probabilistically chosen to breed and produce the candidates for the next generation. Two common genetic operators for breeding are crossover (combining random parts from two selected candidates) and mutation (altering a random part of a selected candidate). Genetic programming applies this idea of evolution for computer programs [13, 15].

The basic genetic operators (i.e., crossover and mutation) are entirely random and can result in the construction of illegal programs (e.g., that breach requirements for legal expressions or type restrictions of the programming language). For this reason alone, it is often appropriate to constrain the structure of programs in advance of the evolutionary process. An approach to enforcing particular structures is using a grammar [16]. GP approaches that use a grammar to express constraints are called grammar-based genetic programming (GGP). For example, the expression $f(x, y) = x * x + y$ is one of many possible specific structures that could be generated with the following grammar:

$$\begin{aligned} \text{E} &::= \text{var} \mid (\text{E op E}), \\ \text{op} &::= + \mid - \mid *, \\ \text{var} &::= \text{x} \mid \text{y} \mid \text{z}. \end{aligned} \tag{1}$$

Each line in the grammar is a production rule. The elements on the left-hand-side can be rewritten and are called nonterminal symbols. On the other hand, elements that cannot be rewritten are terminals. The first production rule is an expression (E) which can equal either a variable (var) or a combination of two expressions (E) by an operator (op). The second rule allows three operators: plus, minus, and multiply. The last production rule specifies three variables: x, y, and z.

Each structure produced by the grammar is represented by a tree. The tree representation allows researchers to measure the structural complexity of models by counting the number of nodes (terminal and nonterminal symbols) in the tree. Even the simple expression $f(x, y) = x * x + y$, shown in Figure 1, has a node count of 15. Crossover is operationalized by cutting a branch of the tree and replacing it with a branch from another tree. Mutation is operationalized by replacing a node with a randomly generated tree.

2.5. Description of the Model Discovery Process. This section describes the proposed model discovery process, depicted by the flowchart of Figure 2. The process is a variant of a recent approach described by Vu et al. [10]. There are three roles in

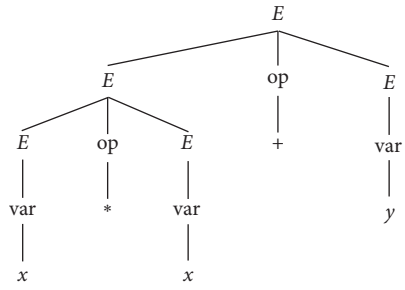

Figure 1: An example tree of an expression $f(x, y) = x * x + y$.

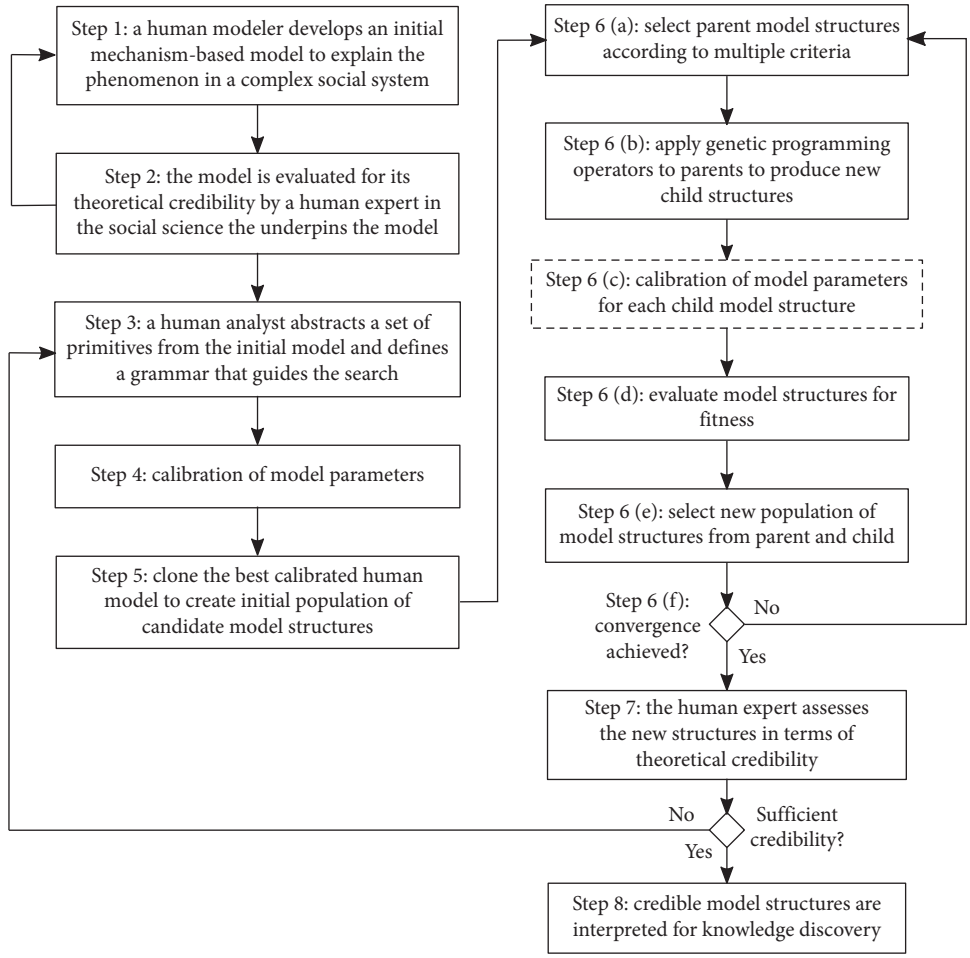

Figure 2: Model discovery framework. The dashed rectangle is the process that is not implemented in the present paper.

the model discovery process: modeler, analyst, and domain expert. The modeler designs, implements, and tests agent-based models. The analyst analyses the model structure and abstracts a set of basic building blocks of entities and mechanisms. The domain expert possesses the knowledge and understanding about the social science that underpins the model and can assess the model's theoretical credibility.

In Step 1 of the model discovery process, a human modeler develops a mechanism-based model to explain the phenomenon in a complex social system (the baseline model). This redescription process is undertaken by the modeler based on existing knowledge captured in social theories. In Step 2, the model is evaluated for its theoretical credibility by a human expert in the social theories that underpin the model (i.e., a domain expert). Redevelopment of the model may occur following this step (representing a return to Step 1). Once the human expert is satisfied with the baseline model, in Step 3, a human analyst abstracts a set of primitives, i.e., "building blocks," from the model. These sets of primitives are the entities and mechanisms to be exposed and modified in the evolutionary step (Step 6). In addition, a grammar is defined to guide the search. Since the grammar is

a set of production rules for combining the primitives, the analyst can enforce certain structures based on the modeler's knowledge of the system; noncredible operations can be prohibited. In Step 4, the model parameters are calibrated using the baseline model structure against the empirical calibration targets. In Step 5, the model built by human modeler, along with the best calibrated parameters, is cloned to fill the initial population of model structures.

Step 6 is the heart of the evolutionary approach. Parent structures are selected from the population of model structures (Step 6(a)). After applying the genetic operators (crossover and mutation), new child structures are generated (Step 6(b)). Ideally, the parameters of the new child structures are recalibrated to see if the model error can be minimized further (Step 6(c)). However, such a nested approach to calibration is very computationally intensive, and so we necessarily omitted this step due to limits on the available computing resources. Instead, we allowed the GP to select constants from not only a general set of constants but also values of calibrated parameters generated at Step 4. Next (in Step 6(d)), the new structures are evaluated for their fitness (such as model error compared to empirical data). After evaluation, the new population is selected based on the objectives (Step 6(e)). These evolutionary steps are performed until convergence is achieved or when a maximum number of iterations is reached (Step 6(f)).

In Step 7, through deliberative discussion with the analyst and the modeler, the domain expert assesses the set of new structures with the highest fitness values in terms of theoretical credibility. If the new structures lack sufficient credibility, the domain expert, the modeler, and the analyst return to Step 3 to discuss changes to the grammar to improve the meaningfulness of the operations that can be selected by the evolutionary algorithm. Further iterations of Steps 3 to 7 are carried out until credible structures are generated or resources are exhausted. In Step 8, credible model structures are interpreted for knowledge discovery purposes, promoting discussion about the underlying social theories used in the model and, potentially, further theory development or empirical data gathering.

3. Application

We applied the new framework to a specific mechanism-based social systems model. Here, we interpreted the causal mechanisms derived from *social role theory* as drivers of alcohol consumption to build a complex systems model of population-level alcohol use patterns in the US since the 1980s (Figure 3). Social role theory is a collective term used to describe a diverse range of mechanism-based explanations for individual and collective behaviors and practices from the fields of social psychology, sociology, and anthropology [17]. Particular conceptualizations of role theory have been used within the alcohol research community to explain observed trends in alcohol use—specifically relating to the interplay between alcohol use and positional roles such as parent, partner, and paid employee [18]. Our aim in this application is to test the extent to which credible conceptualizations of role theory can reproduce historical trends in population alcohol use (as measured via survey data).

In this application, different roles in the model discovery process were undertaken by different authors. The modeler role was principally undertaken by HB, AB, and RCP. The analyst role was undertaken by CB and TMV. The domain expert was PS.

3.1. Social Roles as a Mechanism-Based Explanation of Alcohol Use: The Human-Built Model as It Relates to Role Theory. The concept of *role strain* is central to many of the studies relating positional roles to alcohol use. Biddle [17] defines role strain as the "experience of stress associated with positions or expected role." Role strain is hypothesized to arise through a number of pathways where alcohol can act as cause, consequence, or both. Alcohol can be used by individuals as a means of coping with role strain arising from role overload (holding a role set that is too complex), role deprivation (lacking roles that provide meaning to life), or role incongruence (holding roles which are nonnormative with respect to status or identity) [19, 20]. Alcohol use can also induce or exacerbate role strain, where use is incompatible with the demands of performing the role [21]. In the model, role strain is the arithmetic mean of role incongruence and role overload (equation (1) in Table 1). Role overload (equation (2) is determined by the roles an agent holds, their levels of involvement in these roles, and four calibrated parameters representing the effect of holding each role on experiencing role overload. Role incongruence (equation (3)) is the arithmetic mean of the difference between each role holding status and the prevalence of that role in society (i.e., the percentage of people holding that role).

In the mechanism known as *role selection*, individuals may act (consciously or otherwise) to prevent or reduce role strain by avoiding or escaping from roles that are incompatible with their existing alcohol use [21]. This mechanism is implemented by adjusting the probability of transitioning between roles based on the heavy drinking status of the agent (where heavy drinking is defined as having consumed 5+ standard drinks in the previous month) (equations (4) and (5)). In a contrasting *role socialisation* mechanism, individuals gradually adopt and internalize drinking practices that are compatible with the roles they hold [21–23]. A difference in drinking disposition is calculated when individuals gain or lose roles (equations (6) and (7)). The new disposition to drink (equation (8)) is a function of this difference in disposition and a modifier (equation (9)), calculated using the number of days the new role has been held and the speed of socialisation.

Knibbe et al. [18] suggested that the set of positional roles held by an individual can affect the ability of that person to participate in drinking situations, depending on the extent to which drinking is integrated into the structure of everyday life within society. In this sense, social roles act as mechanisms that regulate the daily *opportunities* for using alcohol. Individuals in the model have a different opportunity to drink outside and inside the home, which depends on the roles they hold. The opportunity to drink out and in are each

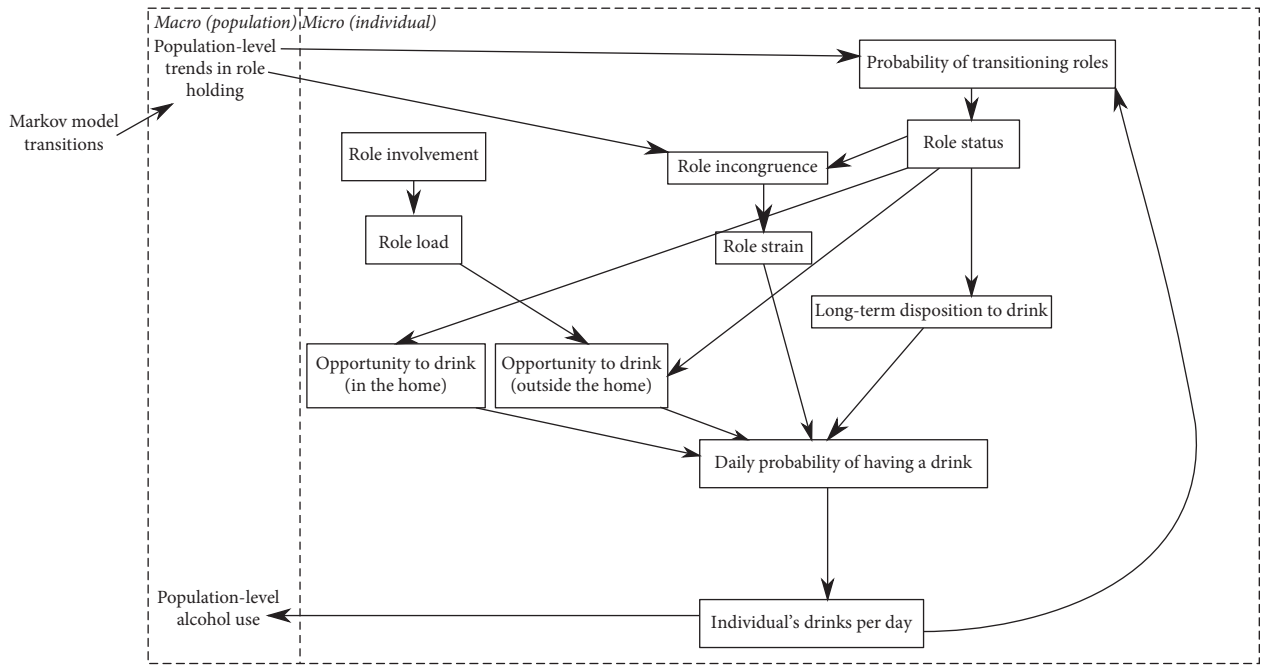

Figure 3: Schematic of roles model.

calculated as a log odds (equations (10) and (11)) and then converted to probabilities (equations (12) and (13)). The log odds for drinking outside the home are based on an agent's role load, employment status, and two calibrated parameters to describe the unknown effect sizes of these factors on opportunity to drink out. Role load and a combination of marital and parenthood status determine the log odds of drinking opportunity inside the home. Again, this equation contains parameters describing the unknown effect of these factors on the opportunity to drink in.

The conditional probability of agent i consuming a jth drink (equations (14) and (15)) is governed by each agent's long-term disposition to drink, their probability of drinking in and outside the home, and role strain.

3.2. Data

3.2.1. Model Initialization. To initialize the models, data from the National Survey on Drug Use and Health (NSDUH) 1979–2010 [24], Panel Study of Income Dynamics (PSID) 1979–2010 [25], and the US Census 1980–2010 [26] were used. A microsynthesis [27] was generated for a demographically representative population of 1000 individuals aged 12–80 in the USA, 1980. The model was initialized with these 1000 agents on the first day of 1980. The sociodemographic attributes of agents were initialized from the microsynthesis: age, sex, ethnicity, employment status, marital status, and parenthood status. Additionally, the microsynthesis initialized agents with alcohol use attributes: a 12-month drinking status, usual number of drinking days per month, usual quantity of drinks per month, and number of days where more than five drinks are consumed per month.

3.2.2. Simulation. During each simulated year, individuals enter the model as new 12-year-old adolescents and new migrants. Individuals also leave the model due to death and outward migration. Total counts of new migrants to enter in each year were estimated using the American Community Survey 1980–2010 [28] and were microsynthesised to data from the nearest NSDUH year to give a representative migrant population with corresponding baseline drinking behavior. Mortality rates for the microsimulation were derived from the Center for Disease Control and Prevention (CDC) all cause mortality data for the US between 1979–1998 [29] and 1999–2010 [30].

Transition probabilities for moving between each of the eight unique combinations of social roles variables (marriage, employment, and parenthood) are applied annually during the simulation. These probabilities were derived from multistate Markov models fitted to marriage, parenting, and employment trends from a representative US study, the Panel Study of Income Dynamics 1979–2000 [25].

At initialization, each agent is allocated a vector which represents their long-term disposition to drink. These are initialized from the mean and standard deviation of their drinking frequency and quantity at baseline.

3.2.3. Calibration Targets. Calibration targets for alcohol use were derived from empirical data from NSDUH for the years 1979–2010. Four alcohol use targets per year were used for calibration: (1) prevalence—the proportion of individuals reporting consuming an alcoholic beverage during the previous year; (2) frequency—among drinkers, the average number of drinking days per month; (3) quantity—among drinkers, the average grams of alcohol consumed per day;

Table 1: Equations in the human-built model.

No.	Concept	Model equation	Description
1	Role strain	$\text{RoleStrain}_i[k] = (\text{RoleLoad}_i[k] + \text{RoleIncongruence}_i[k])/2$	Role strain is the overall stress an individual experiences as a result of the social roles they hold.
2	Role load	$\text{RoleLoad}_i[k] = \boldsymbol{\beta_1} * \text{ParentStatus}_i[k] * \mathbf{ParentInvolvement_i} + \boldsymbol{\beta_2} * \text{MaritalStatus}_i[k] * \mathbf{MaritalInvolvement_i} + \boldsymbol{\beta_3} * \text{EmploymentStatus}_i[k] * \mathbf{EmploymentInvolvement_i} + \boldsymbol{\beta_4} * (1 - \text{MaritalStatus}_i[k]) * \text{ParentStatus}_i[k] * \mathbf{ParentInvolvement_i}$	Role load is the stress that results from needing to perform a role. Role status is either 0 (not having a role) or 1 (having a role). Role involvement represents how much a person is involved in a role, if they hold it (between 0 and 1, from no involvement to full involvement). There are four terms: one term for each of the three roles (having a role and more involvement in that role increases the stress) and a term for additional stress when an individual is a single parent (holding the role without the support of another parent).
3	Role incongruence	$\text{RoleIncongruence}_i[k] = (\text{ParentStatus}_i[k] - \text{sParentExpectancy}_{sex,age}[k] + \text{MaritalStatus}_i[k] - \text{sMaritalExpectancy}_{sex,age}[k] + \text{EmploymentStatus}_i[k] - \text{sEmploymentExpectancy}_{sex,age}[k])/3$	Role incongruence is the stress that results from holding a role that deviates from societal expectations for an individual's identity (encoded as a sex-age category). It is the average of the differences for each role between the current status and the corresponding societal expectancy (prevalence of that role in the society is between 0 and 1).
4	Role transition update for gaining roles	Heavy drinkers: (i) $\text{TP}_i[k] = \text{sTP}_{sex,age}[k-1] * (1 + \boldsymbol{\beta_{12}})$ Non heavy drinkers: (i) $\text{TP}_i[k] = \text{sTP}_{sex,age}[k-1] * (1 - \text{AnnualHeavyDrinkingPrevalence}[k-1] * (1 + \boldsymbol{\beta_{12}}))/(1 - \text{AnnualHeavyDrinkingPrevalence}[k-1])$	To account for role selection, individual role transitions over the lifecourse are calculated by modifying the societal transition rates according to whether or not the individual is a heavy drinker (equations (4) and (5)). Heavy drinking makes it less likely for an individual to gain roles. Heavy drinking makes it more likely for an individual to lose roles. AnnualHeavyDrinkingPrevalence represents the population prevalence of heavy drinking in the model (between 0 and 1).
5	Role transition update for losing roles	Heavy drinkers: (i) $\text{TP}_i[k] = \text{sTP}_{sex,age}[k-1] * (1 + \boldsymbol{\beta_{13}})$ Non heavy drinkers: (i) $\text{TP}_i[k] = \text{sTP}_{sex,age}[k-1] * (1 - \text{AnnualHeavyDrinkingPrevalence}[k-1] * (1 + \boldsymbol{\beta_{13}}))/(1 - \text{AnnualHeavyDrinkingPrevalence}[k-1])$	

Table 1: Continued.

No.	Concept	Model equation	Description
6	Difference in disposition to drink due to gaining roles	$\text{DispositionDifference}_{i,j}[k] = \text{Disposition}_{i,j}[k] * (1 + \boldsymbol{\beta_{10}}) - \text{Disposition}_{i,j}[k]$	To account for role socialisation, the disposition to drink is gradually reduced the longer an individual holds a role and is gradually increased if an individual loses a role. The full disposition effect to apply is calculated using equations (6) and (7). The proportion of that effect to apply after a particular number of days of socialisation is calculated using the logistic function in equation (9). This modifier is then applied to scale the full disposition effect using equation (8) and calculate the overall disposition at time k. Socialisation effects accrue over one year following a role transition.
7	Difference in disposition to drink due to losing roles	$\text{DispositionDifference}_{i,j}[k] = \text{Disposition}_{i,j}[k] * (1 + \boldsymbol{\beta_{11}}) - \text{Disposition}_{i,j}[k]$	
8	New disposition to drink (after role socialisation)	$\text{Disposition}_{i,j}[k] = \text{Disposition}_{i,j}[k-1] + \text{DispositionDifference}_{i,j}[k] * \text{modifier}_i[k]$	
9	Modifier for socialisation mechanisms	$\text{modifier}_i[k] = \hat{e}((\text{DaysofSocialisation}_i[k] - \textbf{sSocialisationSpeed})/365)/(1 + \hat{e}((\text{DaysofSocialisation}_i[k] - \textbf{sSocialisationSpeed})/365))$	
10	Opportunity to drink out	$\text{logOddsOppOut}_i[k] = \log(\boldsymbol{\beta_5} * (1 - \boldsymbol{\beta_6} * \text{RoleLoad}_i[k] + \boldsymbol{\beta_7} * \text{EmploymentStatus}_i[k]))$	Equations (10) and (11) describe the log odds for the opportunities to drink outside and inside the home, with reference to having no opportunity to drink. β_5 is the baseline opportunity. Role load acts to reduce both opportunities. Individuals have more opportunity to drink outside the home if employed and more opportunity to drink inside the home when holding marital or parenting roles. Equations (12) and (13) operationalize the logit model that derives the probabilities of drinking outside and inside the home on any given day from the log odds of equations (10) and (11) (for three mutually exclusive scenarios: drinking in, drinking out, and not drinking)
11	Opportunity to drink in	$\text{logOddsOppIn}_i[k] = \log(\boldsymbol{\beta_5} * (1 - \boldsymbol{\beta_8} * \text{RoleLoad}_i[k] + \boldsymbol{\beta_9} * (\text{MaritalStatus}_i[k] + \text{ParentStatus}_i[k])))$	
12	Probability of having an opportunity to drink out	$\text{probOppOut}_i[k] = \hat{e}(\text{logOddsOppOut}_i[k])/((\hat{e}(\text{logOddsOppIn}_i[k]) + \hat{e}(\text{logOddsOppOut}_i[k]) + 1))$	
13	Probability of having an opportunity to drink in	$\text{probOppIn}_i[k] = \hat{e}\ (\text{logOddsOppIn}_i[k])/((\hat{e}(\text{logOddsOppIn}_i[k]) + \hat{e}\ (\text{logOddsOppOut}_i[k]) + 1))$	
14	Probability of drinking first drink ($j = 0$)	$\text{ProbabilityDrink}_{i,0}[k] = \text{Disposition}_i[k] * (\text{ProbOppOut}_i[k] + \text{ProbOppIn}_i[k]) * (1 + \boldsymbol{\beta_{14}} * \text{RoleStrain}_i[k])$	The daily drinking probability is modeled as the long-term drinking disposition, mediated by drinking opportunities and role strain. We differentiate between drinking frequency (first drink in an occasion) and quantity (next drink, given that an occasion has begun).
15	Probability of drinking next drink ($j > 0$)	$\text{ProbabilityDrink}_{i,j}[k] = \text{Disposition}_i[k] * (\text{ProbOppOut}_i[k] + \text{ProbOppIn}_i[k]) * (1 + \boldsymbol{\beta_{15}} * \text{RoleStrain}_i[k])$	

The concepts in the concept column are from the schematic in Figure 3. These equations contain unobserved parameters (highlighted in bold) which modify the effects of social role mechanisms. These are given values following model calibration (Section 3.3) which searches for the set of parameters which best fit historically observed trends in alcohol use over time. The agents in the model, indexed by i, represent individual drinkers; their behavior is a decision to consume the jth drink in a drinking occasion. The model also includes two dynamic structural entities: expectancies for holding roles at a given point in the lifecourse and average transition probabilities (TPs) between roles. For clarity, all structural entities carry the prefix s. The discrete time unit (representing each day) in the simulation is k.

and (4) heavy episodic drinking—among drinkers, the average number of occasions where 5+ drinks were consumed, per month. The targets are split by subgroup, with four subgroups defined by the number of roles held (0–3 roles). We chose to categorize by the number of roles ($n = 4$) instead of the combination of roles ($n = 8$) for two reasons: firstly, this is an indicator commonly used in the social roles literature [19]; secondly, the eight role decomposition is too great for the standard error of the targets to be informative from a calibration perspective. In summary, there are 16 targets (4 alcohol use targets by 4 different number of roles) for each year between 1979 and 2010.

3.2.4. Implementation. The model was implemented in C++ using the RepastHPC 2.2.0 toolkit [31]. The model is run forward in time for 20 years for calibration (1980–1999) and 10 years for validation (2000–2009). Each model tick represents one day in the simulation. On each day of the simulation, the probability of drinking is calculated for each agent. Once per year in the simulation, transition probabilities for role transitions are applied and role expectancies are updated.

3.3. Parameter Calibration. The model contains 31 parameters for calibration, which are highlighted in bold text in Table 1. For this paper, a Latin hypercube space-filling design was employed to sample 5,000 parameter sets from the joint prior distribution using the lhs package in *R* [32]. The Latin hypercube was optimized by maximizing the minimum distance between samples [33]. These parameter sets are evaluated using an error metric that compares the simulated results against the calibration targets.

$$\text{error} = \frac{1}{\text{NM}} \sum_{n=1}^{N} \sum_{m=1}^{M} \frac{\left| y_m^*[n] - y_m[n] \right|}{\sqrt{\left(s_m[n]\right)^2 + \left(d_m\right)^2}}, \tag{2}$$

where N is the number of observations, M is the number of outputs, $y_m^*[n]$ is the simulated data for output m at time n, $y_m[n]$ is the mean of empirical target data for output m at time n, $s_m[n]$ is the standard error of the empirical target data for output m at time n, and $(d_m)^2$ is the variance of the model discrepancy for output m, which is 10% of the possible range for each output. Model discrepancy captures the fact that model is not a perfect representation of reality.

As described in Section 3.2.3, there are 16 targets (prevalence, frequency, quantity, and heavy episodic drinking, each split by the number of roles held, 0–3), and thus M is 16. N is different for each output because some years are missing in the empirical data. The parameterization that provided the minimum error in equation (2) was selected as the result of the calibration process. The human-built model along with the best parameterization was selected as the reference model for the structural calibration process.

3.4. Grammar-Based Genetic Programming: Design and Implementation. This section describes a GGP system designed to perform the model discovery process. For the grammar that guided the GP process, the popular context-free grammar was used. The full grammar written in Backus–Naur form [34] is available in Figure 4. Considering the representation of the GGP candidates, each candidate is represented by a tree that is generated following the production rules of the grammar. Each GGP candidate (a program <*p*>) contains 9 expressions for the 9 role-related terms used in the roles model: role selection mechanism, role socialisation mechanism, role load, role incongruence, role strain, log-odds-out modifier, log-odds-in modifier, first-drink disposition, and next-drink disposition. Several groups of variables, along with constants and calibrated parameters, were defined. Each can be formed only by a defined combination of variables, operators, and constants. Some role-related terms use the same expression because they have the same structure and the same constraints, e.g., `probFirstDrink` and `probNextDrink` both use expression <*e*5>. This grammar provides a hierarchical structure that can capture the layers of role-related concepts in the reference model.

For the initialization of the GGP, we decided to start with an initial population filled with the same structure. The structure used as the starting point is the reference model, i.e., the structure designed by human modelers with the best fitted parameterization. Additionally, a multiobjective GGP was employed to simultaneously minimize both model error and complexity. These two objectives address the two aspects of value we discussed in Section 2.3: (i) the ability of the model to reproduce the phenomenon so far as we understand it from our beliefs and empirical data; (ii) the meaningful interpretability in terms of theory.

The first objective, model error, is captured by comparing the simulated data from the model with the empirical data from the real world. The model error is described in equation (2) (Section 3.3). The second objective, complexity, is a proxy for interpretability and parsimony. Minimizing the complexity during model discovery also constrains the model discovery process from discovering too complex structures that overfit the empirical data and are not interpretable by domain experts. The complexity is defined by the number of nodes in the GGP candidate, with a special case that node ON is counted as 2 in contrast to node OFF being counted as 1. The drawback when using complexity as a proxy is that it does not guarantee meaningful interpretability, i.e., low complexity can also result in meaningless model structures. Therefore, at the end of every iteration of the model discovery process, we worked with the domain expert to verify the interpretability of all structures in terms of theoretical meaningfulness. We asked the expert to classify model structures using a crisp binary definition of credible or noncredible. While the judgment was holistic, the classification process was a deliberative discussion between the expert, the modeler, and the analyst. This discussion was recorded and used subsequently to produce a set of qualitative criteria for judging model credibility.

For the selection process, the popular NSGA-II optimizer [35] was used to develop an even representation of the Pareto front that shows the trade-off between model error and complexity. During the evaluation, the corresponding expressions in the simulation's source code were edited based on a candidate structure; then the simulation was recompiled and run in order to collect the simulated results for calculating the model error.

The described GGP system was implemented using the PonyGE2 toolkit [34] and set up with the following parameters:

(i) 500 GGP candidates per generation

(ii) Initialization: 500 copies of the reference structure

(iii) GP operators: 75% subtree crossover and 25% subtree mutation

(iv) Maximum tree depth: 17

```
<p> ::= RoleSelectionMech=<e0>; RoleSocialisationMech=<e0>; RoleLoad=<e1>;
RoleIncongruence=<e2>; RoleStrain=<e3>; OutMod=<e4>; InMod=<e4>;
probFirstDrink=<e5>; probNextDrink=<e5>;



# Variables
<v0> ::= MaritalStatus | ParentStatus | EmploymentStatus
<v1> ::= InvolvedxMarital | InvolvedxParent | InvolvedxEmployment
<v2> ::= DiffExpectancyMarital | DiffExpectancyParent |
DiffExpectancyEmployment
<v3> ::= RoleLoad | RoleIncongruence
<v4> ::= RoleStrain | ProbOppIn | ProbOppOut | Disposition



# Toggle for mechanisms
<e0> ::= ON | OFF

# Role load
<e1> ::= (<e1>+<e1>) | (<e1>-<e1>) | (<e1>*<e1>) | (<c>*<e1>) | (<c>+<e1>) |
(1-<e1>) | (<e1>-<c>) | <v1> | <v0>

# Role incongruence
<e2> ::= (<e2>+<e2>) | (<e2>-<e2>) | (<e2>*<e2>) | (<c>*<e2>) | (<c>+<e2>) |
(1-<e2>) | (<e2>-<c>) | <v2> | (<v0>*<e2>) | ((1-<v0>)*<e2>)

# Role strain
<e3> ::= (<e3>+<e3>) | (<e3>-<e3>) | (<e3>*<e3>) | (<c>*<e3>) | (<c>+<e3>) |
(1-<e3>) | (<e3>-<c>) | <v3>

# Modifiers for logOddsOppOut/In
<e4> ::= (<e4>+<e4>) | (<e4>-<e4>) | (<e4>*<e4>) | (<c>*<e4>) | (<c>+<e4>) |
(1-<e4>) | (<e4>-<c>) | <v0> | RoleLoad

# Daily drinking probability (first and next drink)
<e5> ::= (<e5>+<e5>) | (<e5>-<e5>) | (<e5>*<e5>) | (<c>*<e5>) | (<c>+<e5>) |
(1-<e5>) | (<e5>-<c>) | <v4>



# Constants and calibrated parameters
<c> ::= 0 | 1 | 2 | 3 | 4 | 5 | 6 | 7 | 8 | 9 |
        0.1 | 0.2 | 0.3 | 0.4 | 0.5 | 0.6 | 0.7 | 0.8 | 0.9 |
        10 | 100 | 0.01 | 0.001 | 0.333 | 0.25 |
        0.179 | 0.038 | 0.128 | 60.952 |
        0.253 | 11.187 | 23.786 | 2.010 |
        1.104 | 9.100
```

Figure 4: Context-free grammar. Variables have the same name as in Table 1 but, for improved clarity, without the indexing notation. Shorthand notation is defined for the multiplication of role involvement and role status (e.g., `InvolvedxMarital` = `MaritalInvolvement` ∗ `MaritalStatus`) and for the difference between the role status and role expectancy (e.g., `DiffExpectancyMarital` = `MaritalStatus` − `sMaritalExpectancy`).

(v) 2 objectives (goodness of fit and complexity) with NSGA-II replacement and selection operators

The GGP process was run on an Intel i9 9980XE processor with 36 cores. The source code of the simulation with the best calibrated parameters (RepastHPC) and the GGP system (PonyGE2) is available at bitbucket.org/r01cascade/roles_ggp_complexity and is licensed under the GNU General Public License version 3.

4. Results

4.1. GGP Results and the Pareto Front. In the case study, three iterations of the model discovery process were

required to produce any structures that the domain expert deemed as credible. Modifications were made to the grammar between each iteration in an attempt to improve the effectiveness of the discovery process. This was an open-ended trial and error iterative process involving the modeler and the analyst. We stopped the process once credible structures had been discovered. The evolution of the grammar is documented in the Supplementary Material A. The final grammar is shown in Figure 4.

In the final iteration of the process, both model error and model complexity objectives reduced over generations and converged at the 20th generation, after which no change to the Pareto front was observed. Figure 5 shows the final population of 14 nondominated structures and also includes the reference structure for comparison. These models are indexed by their complexity, e.g., model 24 is the model on the Pareto front with complexity 24. All the structures discovered by the GGP are less complex than the reference structure. Six of them are worse than the reference model in terms of model error, while the remaining eight offer improved fit over the calibration window.

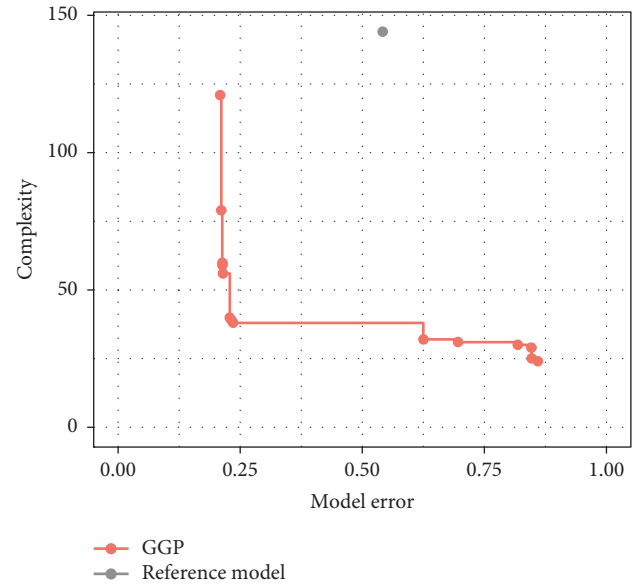

Figure 5: GGP structures on the Pareto front versus the reference structure (model error is the error when compared the simulated results against calibration targets; complexity is measured as the number of nodes in the tree of a GGP candidate).

4.2. Theoretical Credibility of the Discovered Models. We worked with a domain specialist to examine the nondominated model structures generated by the GGP in terms of their theoretical credibility and coherency with respect to social role theory. Table 2 compares the structures of the reference model and selected GGP models. In Table 2, elements not affecting agent drinking (`probFirstDrink` and `probNextDrink` variables, equations (14) and (15)) are highlighted in italic.

Through analysis of the deliberative discussions held between the expert, analyst, and modeler, it was possible to generate three qualitative criteria that enable a consistent assessment of credibility for this example case study. In what follows, we provide a narrative discussion of credibility across the Pareto front in Figure 5. However, a complete documentation of all GGP models and corresponding justifications of credibility is also included in the Supplementary Material B. The three identified criteria for theoretical credibility are as follows:

(1) At least one of the theory constructs must be implicated in the model dynamics. In a mechanism-based model of alcohol use, the mechanisms need to be used to generate drinking behavior. For models based on role theory, this means that the models must use at least one of the core theory constructs of role strain, role load, role incongruence, or opportunity. For example, in the absence of a role socialisation process, using solely a variable that describes drinking history (`Disposition`) does not generate a credible mechanism-based model in terms of role theory.

(2) The theory constructs must be used to represent mechanisms, rather than being proxies for black-box variable-centric explanation. In some of the identified models, we observed that theory constructs could be replaced directly by observable sociodemographic properties of the agents. These cases indicate that the mechanism-based explanation is being avoided in favor of a black-box variable-centric "determinants" approach to understanding drinking behaviors that is more conventional in the literature [36]. For example, in a mechanism-based model, marital status should not directly define opportunity, where opportunity then directly determines disposition to drink.

(3) The model equations that describe the mechanisms must be compatible with the causal logic and evidence base for the theory. In a mechanism-based model, some of the encoded causal relationships between core theory constructs are only meaningful when constrained in terms of direction, sign, and/or magnitude. For example, role load must either not affect or cause a decrease in opportunity to drink—it is inconceivable, in role theory terms, that role load could cause an increase in opportunity (since load implies time use by agents that cannot be combined with drinking).

Focusing now on the Pareto front, the model with lowest complexity on the front (on the far right of Figure 5) is model 24—this model includes a single term for each production rule, with both role selection and role socialisation processes switched off (Table 3). When parsed, all but two of the production rules are inactive—`probFirstDrink` and `probNextDrink`—with both set to the term `Disposition`. This term represents the initial dispositions to drink endowed to the agents based on observed drinking patterns in NSDUH data, so essentially model 24 encodes the

Table 2: Structures of the discussed models (structures of the reference model, model 24, model 25, and model 29).

Name	The reference model	Model 24	Model 25	Model 29
RoleSelectionMech	ON	OFF	ON	OFF
RoleSocialisationMech	ON	OFF	OFF	OFF
RoleLoad	0.180 ∗ InvolvedxMarital + 0.039 ∗ InvolvedxParent + 0.128 ∗ InvolvedxEmployment + 60.952 ∗ (1 − MaritalStatus) ∗ InvolvedxParent	*InvolvedxEmployment*	*InvolvedxEmployment*	InvolvedxMarital
RoleIncongruence	0.333 ∗ DiffExpectancyMarital + 0.333 ∗ ∗ DiffExpectancyParent + 0.333 ∗ DiffExpectancyEmployment	*DiffExpectancyMarital*	*DiffExpectancyMarital*	DiffExpectancyMarital
RoleStrain	0.5 ∗ RoleLoad + 0.5 ∗ RoleIncongruence	*RoleLoad*	*RoleLoad*	RoleIncongruence
OutMod	OutMod = (1 − 0.25357 ∗ RoleLoad) + 11.18756 ∗ EmploymentStatus	*RoleLoad*	*RoleLoad*	EmploymentStatus
InMod	InMod = (1 − 23.786 ∗ RoleLoad) + 2.010 ∗ (MaritalStatus + ParentStatus)	*RoleLoad*	*RoleLoad*	RoleLoad
probFirstDrink	(ProbOppIn + ProbOppOut) ∗ disposition ∗ (1 + 1.104 ∗ RoleStrain)	Disposition	Disposition	Disposition ∗ ProbOppIn
probNextDrink	(ProbOppIn + ProbOppOut) ∗ Disposition ∗ (1 + 9.100 ∗ RoleStrain)	Disposition	Disposition	Disposition

Elements not affecting agent drinking are highlighted in italic.

Table 3: Structures of the discussed models (structures of model 38, model 59, and model 79).

Name	Model 38	Model 59	Model 79
RoleSelectionMech	ON	ON	OFF
RoleSocialisationMech	OFF	ON	OFF
RoleLoad	InvolvedxMarital	*InvolvedxMarital*	InvolvedxEmployment
RoleIncongruence	*1 – DiffExpectancyEmployment*	*0.333 ∗ DiffExpectancyMarital + 0.333 ∗ DiffExpectancyParent + 0.333 ∗ DiffExpectancyEmployment*	DiffExpectancyEmployment
RoleStrain	*RoleIncongruence*	*RoleIncongruence*	7 ∗ RoleIncongruence + RoleLoad
OutMod	RoleLoad	MaritalStatus	1 – 10 ∗ RoleLoad
InMod	EmploymentStatus	ParentStatus	1 – ParentStatus ∗ RoleLoad
probFirstDrink	(LifetimeDisposition ^2) ∗ (4 + ProbOppIn)	(LifetimeDisposition ^2) ∗ (4 + ProbOppIn)	Disposition ∗ (0.9 ∗ Disposition + ProbOppIn) ∗ (1.104 ∗ RoleStrain + 0.8)
probNextDrink	Disposition	Disposition	1.25 ∗ Disposition^2 ∗ (RoleStrain + 1)

Elements not affecting agent drinking are highlighted in italic.

heuristic "past behavior predicts future behavior" with no aspect of role theory present. This heuristic is clearly sufficient to reproduce target data at the start of the simulation but the fit to targets becomes progressively poor over time.

As we begin to traverse the Pareto front in the direction of increasing complexity (from right to left in Figure 5), elements relating to role theory begin to be introduced into the production rules; however, these elements do not necessarily survive the parsing process. For example, model 25 switches on role selection, but—as with model 24—no components relating to roles are present in the final `probFirstDrink` and `probNextDrink` production rules. We can conclude that the very small improvement observed for model 25 in comparison to model 24 is due to low level stochasticity in the simulation.

In the next model, model 29, role selection and socialisation processes are switched off but production rule `probFirstDrink` is now set to `Disposition` $*$ `ProbOppIn`, i.e., the probability of engaging in a drinking occasion is scaled by the probability of having the opportunity to drink at home, while the number of drinks consumed in such an occasion continues to follow the heuristic "past behavior predicts future behavior." Following the production rules upward, we identify that, as a result of the log-odds structure that is preserved in all models, `ProbOppIn` is increased by role load (`RoleLoad`) and decreased by holding an employment role (`EmploymentStatus`). Meanwhile, role load is defined as level of involvement in a held marital role (`InvolvedxMarital`). From the perspective of role theory, this model is interpretable but not credible: (i) since only `ProbOppIn` is included, but the possibility of `ProbOppOut` = 0 across all agents is not credible, `ProbOppIn` is interpreted as simply a surrogate for any kind of drinking opportunity; (ii) opportunity is seen to increase as a result of role load, which is not credible, since opportunity should decrease with role load, and is seen to decrease as a result of being employed, which is also not credible because, outside of role load considerations (for which employment is not present in the model), being employed should provide increased opportunities for drinking (e.g., due to income or exposure to social drinking situations). Model 29 also offers little improvement in model error compared to the overall "past behavior predicts future behavior." Overall, it is very clear that this model is found wanting.

Continuing to traverse the Pareto front from right to left, we find that the first model to offer a credible interpretation in terms of role theory is model 38. This model also offers a substantial improvement over the less complex "past behavior predicts future behavior" model in terms of model error. In model 38, the frequency of drinking occasions (`probFirstDrink`) is increased by the probability of an at-home drinking opportunity (where, as for model 29, this should be interpreted as a surrogate for any kind of drinking opportunity). Some attempts by the GGP at parameter calibration are also seen here, with nonlinear scaling of `Disposition`. Opportunity is increased by holding an employment role and decreased by role load (the latter defined as level of involvement in a marital role). Despite reservations about the limited extent of the definition of role load, this opportunity mechanism appears plausible. Role holding is also influenced by drinking behavior in this model, since role selection is switched on—feedback is therefore in action and we can claim at this point that the GGP has discovered a true dynamical model that involves roles.

The second model that can be regarded as credible in terms of role theory is model 59—this model suggests that experiencing role strain increases the likelihood of a drinking occasion (due to the `RoleStrain` multiplier on `Disposition` in the prob`FirstDrink` production rule). Role strain is defined purely as role incongruence, where the latter concept is preserved intact from the reference model (i.e., role incongruence is the average deviation of an agent's role holding from normative roles). Both role selection and socialisation are also active in this model, but no opportunity mechanisms are present.

The third model offering credibility in terms of role theory is model 79. In the model, role strain increases both frequency of drinking occasions and per-occasion quantity (via positive modifiers on `probFirstDrink` and `probNextDrink`, respectively). Role strain arises as a weighted combination of role load and role incongruence, where load arises from high levels of involvement in an employment role and incongruence arises through nonnormative employment status (e.g., being working age unemployed). Opportunity also influences drinking frequency (via the `PropOppIn` shift in the `probFirstDrink` production rule)—again, to be credible, `PropOppIn` must be interpreted as a general opportunity, rather than having any locational context. Opportunity is reduced through the interaction of role load with parenting (via the `InMod` production rule) and also reduced by role load in isolation (via `OutMod`). In this model, neither role selection nor socialisation is active.

4.3. Calibrated Goodness of Fit. The reference model has an error of 0.54 against the time series of targets used for calibration (covering the period 1980–2000). The time series plot for the reference model is shown by the pink line in Figure 6. Fit to drinking prevalence is good, except for the one-role subgroup. Fit to frequency, quantity, and heavy episodic drinking is generally poor, particularly for the zero-role subgroup. Models lying on the Pareto front represent a range of errors, including both better and worse than the reference model. The credible models are quite considerably better, as seen from the time series plots in Figure 6. The issue with drinking prevalence in the one-role subgroup and issues with frequency and quantity are largely eliminated—with remaining problems largely confined to underestimation of heavy episodic drinking in the three-roles group.

It should be noted that the goodness of fit of the reference model is weak in comparison to other models. This issue could have been caused by either an inadequate parameter calibration process or fundamental inability of the structures initially designed by the modeler to capture the target dynamics. To seek an improvement in the goodness of fit of the reference model, we could have run a more extensive parameter calibration or undertaken handcrafting of

Figure 6: Time series of 16 outputs of the reference model, 3 credible GGP models, and the empirical target data (mean target data ± 95% confidence interval). The horizontal axis is the simulated *years* and each graph has a dashed vertical line that separates 20 calibration years and 10 validation years. The vertical axis is the value for each target with different units for *prevalence* (of current drinking in the past 12 months), *frequency* (average number of drinking days in the past 30 days among current drinkers), *quantity* (average grams of pure alcohol consumed per day among current drinkers in the past 30 days), and *heavy episodic drinking* (average number of days where 5+ drinks were consumed in the past 30 days among current drinkers).

the structure. However, we decided the calibrated model was adequate for the GGP process to work with and intentionally did not try to improve the goodness of fit further. It is clear here, from a model development lifecycle perspective, that the boundary between the reference model and the GGP can be blurred.

4.4. Validated Goodness of Fit. Target time series data used for validation covers the period 2000–2010.This period covers an increase in drinking prevalence, frequency, and heavy episodic consumption that contrasts with the gentle declines seen over the calibration window. All three theoretically credible models exhibit a substantial relative decline in performance over the validation period (see Table 4). The calibration and validation errors are inversely correlated, suggestive of overfitting to noise in the calibration targets. However, the decline in even the lowest complexity credible model (model 38) suggests that the retroduction fundamentally lacks generalizability to an adjacent temporal period, i.e., the real entities and mechanisms identified are invalid or incomplete. Looking in more detail at the validation issues, models 38 and 59 generate continuing declines in drinking for two-role and three-role groups that are trending in the opposite direction in the empirical data. The models also generate a collapse in heavy episodic drinking among the three-role subgroup that is not supported by the data. The most complex of the credible models—model 79—does capture the trend reversal (if slightly lagged) for most two-role and three-role outcomes but underestimates frequency and quantity for the no-role group.

Table 4: Goodness-of-fit errors for the reference model and the three credible GP models.

Model	Calibration error	Validation error
The reference model	0.542	0.750
Model 38	0.236	0.340
Model 59	0.214	0.390
Model 79	0.211	0.444

5. Discussion

5.1. Model Discovery Case Study Findings

5.1.1. Insights into Mechanisms. Our model discovery framework offers three alternative perspectives (corresponding to three credible models 38, 59, and 79) that all offer a substantially better fit to the calibration window data compared to the reference model. In perspective (i), the retroducted mechanisms influencing alcohol use are opportunity and role selection; roles affect drinking frequency only, but not quantity. The relevant roles are employment (which drives opportunity) and being strongly involved in a marital role (which reduces opportunity via the role load it creates). Role strain is not important nor is role socialisation. Perspective (ii) suggests that role strain drives increased drinking frequency but not quantity. Role strain is due to holding nonnormative roles, with all three roles implicated. Both role selection and socialisation are important, but drinking opportunity is not important. Finally in perspective (iii), role strain drives both increased frequency and increased quantity. Opportunity drives frequency only. Role selection and socialisation are not important. Parenting and employment are implicated for role strain, but marriage is not. A universal caveat on these perspectives, which were driven by data over 1980–2000, is that validation issues were identified over the period 2000–2010.

5.1.2. How Do These Retroducted Insights Compare to Empirical Findings? In the first perspective (i), holding an employment role increases opportunity to drink, while high levels of involvement in a marital role reduces opportunity to drink, with no other role-based pathways activated. These retroducted mechanisms are both supported by empirical research. Using data from a large birth cohort in the UK, Staff et al. [37] demonstrated that the employment role in isolation was associated with increased alcohol consumption, and both marital and parental roles were associated with a decrease in consumption. Further, the authors suggested that these effects may be caused by differences in opportunities to drink associated with the marital role, for example, by reducing the number of occasions an individual will engage in socialising which could impact alcohol use. This potential mechanism is reflected in perspective (i), whereby an individual has less opportunity to drink and therefore less frequent drinking occasions if they are married (and highly involved in their marital role). This is also supported by Bachman's analysis [22], which found that the association between the marital role and reductions in alcohol consumption was strongly moderated by reductions in evenings out and increased disapproval for use.

In perspective (ii), role incongruence is suggested to be a driver of role strain, which influences the frequency of drinking. This is supported by Biddle [17] who suggests that individuals can experience role strain due to experiencing roles outside the normative timings, for example, transitioning into a parent role as an unmarried teenager. Role strain as a driver of alcohol use has also been empirically observed [19], which suggests that individuals may use alcohol to cope with stress. Additionally in perspective (ii), both role socialisation and selection mechanisms are active. The importance of role socialisation mechanisms as a driver of alcohol use is supported by Lee et al. [23] who found that heavy drinking occasions were reduced after individuals had become married. Additionally, Bachman [22] conducted a review of the literature linking marriage and alcohol use and suggested that the majority of studies find socialisation effects for the marriage role, i.e., gaining the marriage role leads to reductions in alcohol use. The involvement of role selection mechanisms in alcohol use behavior is also supported by the wider literature on role theory and alcohol use. Specifically, Lee et al. [38] provided evidence for role selection mechanisms, finding that earlier alcohol misuse reduces the likelihood of transitioning into social roles. This could be interpreted in a role selection context—if an individual is a heavy drinker, they are less likely to transition into a role which would be incompatible with their drinking.

An increase in alcohol consumption due to role strain is also implicated as a mechanism in perspective (iii). Here, role strain arises due to a combination of role load and role incongruence, which are determined by high levels of involvement in an employment role or a nonnormative employment status, respectively. Role strain as a driver of both alcohol consumption frequency and quantity is supported by Cooper [39], who found in a study of adolescents in the US that drinking as a means of coping (with role strain or otherwise) was associated with heavier drinking patterns. Additionally, in this model, having an opportunity to drink affects frequency of alcohol consumption and is reduced if the parenting role is held. This is supported by Kuntsche and colleagues [19] who found that in a large study of westernised countries, holding a greater number of roles, including parenthood, was associated with a reduction in alcohol consumption, via a decrease in opportunities to drink.

5.2. Benefits of the Framework.

Our approach represents a novel and promising technique for knowledge discovery which is able to generate models with theoretically interpretable mechanisms and can fit historical patterns of data in complex dynamic representations of social systems. The model discovery framework offers a substantial improvement compared to the reference model, in terms of both lowered complexity for interpretability and improved fit to historically observed alcohol consumption trends. However, it is important that in the last step, domain experts are involved to interpret the options generated by the model.

Our technique can therefore provide new approaches for developing theories to explain complex social systems.

A further advantage of this approach is that it is both theory and data-driven. We use formalised theories of behavior and several large empirical datasets to inform both the initial settings of the model (agent population characteristics) and the phenomenon to be explained—population-level alcohol use is derived from a large nationally representative survey.

This method is also very flexible. Firstly, the grammar can be easily modified to redefine search directions, introduce new building blocks, restrict or relax constraints, or introduce different ways to combine the building blocks. This can be done within the grammar without changing the whole model discovery process. Additionally, although we present a case study modeling alcohol consumption, the framework could also be utilized to explain and understand a variety of complex models of social systems. Our method is easily adapted to look at alternative theories of behavior and even to search across multiple theories to give novel combinations which provide a better explanation of empirical data trends.

5.3. Limitations. One limitation of this approach is that the GGP works with the primitives and the grammar that the modeler provides it with. It is therefore possible that theoretically meaningful and adequately explanatory models could be missed because the modeler does not allow for it. In our case study, deliberative discussions during GGP identified that the concept of opportunity encapsulated both time and money resources, which are impacted differently by role theory mechanisms; including these aspects explicitly might arguably have improved the model's explanatory capability. Model discovery is an iterative, problem-specific process. To design the primitives, modelers have to decide which elements in their models are interesting and relevant to their research questions. The level of abstraction is also important: lower levels of abstraction usually have more elements and possible combinations. As for the grammar design, good practices can be found in the work of Nicolau and Agapitos [40].

Additionally, not all aspects of the model were exposed to the GGP process; for example, socialisation and selection mechanisms could be either switched on or off, but the equations could not be modified. If socialisation is switched on, the new disposition to drink is always determined by the same calculation; however, exposing this to the GGP could offer alternative candidate mechanisms for the effects of transitioning roles on underlying desire to drink. This would also allow us to investigate in future model iterations whether socialisation effects vary for different roles, as suggested by Bachman et al. [22].

The GGP method can produce complicated models in terms of theories, which require interpreting by a domain expert. In this paper, out of 14 nondominated structures discovered in the final iteration of the GGP, three were deemed to be theoretically meaningful. For a more efficient search, it would be beneficial if either the grammar allows only meaningful structures or the model discovery process can enforce the theoretical meaningfulness in other ways (such as during the crossover and mutation operators). However, the prior encoding of meaning is very challenging to achieve and there is also a risk of missing novel ideas due to overconstraining the search. Further, we stopped the discovery process once a small number of credible models had been identified. If we had continued to refine the grammar, further credible models may have been identified—including models that offered reduced complexity or increased goodness of fit over those existing models. In the context of retroduction, such models may have offered greater insight into the relationship between social roles and alcohol use. At present, it remains unclear what a good yield of interpretable theories would be from a model discovery process.

We identified three qualitative criteria for model credibility. These criteria arose from deliberative discussions in relation to the role theory case study and, as such, their generalizability remains untested. We worked with only a single domain expert, but multiple experts may have offered different criteria or interpreted the same criteria differently. While we enforced a crisp binary categorization of model credibility in the search process, given the qualitative nature of the criteria, it may be more appropriate to adopt multinomial and/or fuzzy measures of credibility in future work.

Lastly, our implementation of the proposed discovery process skipped the recalibration stage for parameters of the newly discovered structures (Step 6(c)) due to computational limitations. We addressed this issue by allowing calibrated constants as primitives, but this approach is not as rich as a full calibration for each new structure. This problem is actually present in many GP works, especially with computationally expensive programs. The potential solution is leveraging surrogate models to approximate the fitness evaluation in GP [41, 42].

5.4. Implications for Complex Systems Modeling Practice. Retroduction—teasing out the complex interaction of real entities and mechanisms that brings about a concrete phenomenon—is challenging. Complex systems models (CSMs) that attempt this are often charged with being arbitrary and/or absolutist in their conceptions of reality. Structural calibration avoids this by looking across a wide multiplicity of models that retain the base elements of mechanism-based theory. Complex systems modelers, who use formal models to help explain concrete phenomena, should use structural calibration as part of their standard modeling practices, in the same way that data-driven modelers, who use formal models to explain variance in patterns of data, consider term selection.

However, automated structural calibration is a major enterprise. It requires complex systems modelers to (i) think more about ontology—what are the base elements of theory that are candidates for inclusion in any model? and (ii) formally describe entities and mechanisms in a consistent way that allows them to be recombined together in meaningful ways. To help, we have developed an open-source

model discovery framework for CSM developers that forces an ontological focus and provides an underlying formal language that is amenable to automatic structural calibration.

This work and the underlying model discovery process contribute to the needs for standards and modeling practices in the ABS community. Collins et al. [43] pointed out that as ABS matures, with many simulation software tools (like Netlogo [44] and Repast Symphony [45]), potential standards and protocols will be needed and proposed. For example, Grimm et al. [46] designed the ODD (Overview, Design concepts, and Details) protocol as a generic and structured template to describe agent-based models for better communication and replicability. Another example is the UML (Unified Modeling Language) to develop and document agent-based models [47–49]. There are also many discussions and proposals about different aspects of the ABS development process. A recently proposed software architecture [50], namely MBSSM (Mechanism-Based Social System Modelling), is designed based on a middle-range theory approach to express individual social theory mechanisms in a unified way. Following this line of thought, our model discovery process can be addressed as a protocol concerned with structural uncertainty. It is common to decide on a model structure and then calibrate the parameters within the model to capture parameter uncertainty. Our work takes this further and addresses the between-model uncertainty of structural assumptions. More importantly, we demonstrated the feasibility of automated model structure discovery by embracing both theory and empirical data. Exploring different model structures is not only valuable for theory testing but also can contribute to theory exploration.

6. Conclusion

Here, we have presented a novel method which utilizes genetic programming techniques to discover new and adapted behavioral theories from models of complex social systems. Using a case study of a social role theory to inform mechanism-based model of population-level alcohol use, we have demonstrated that our approach can find new, theoretically meaningful and interpretable mechanisms which drive population alcohol use in a complex systems model. It would take a human modeler an infeasible amount of time to manually construct a multiplicity of different variations of the mechanisms. The GP method assists in efficient screening of mechanism variants. This screening process can be important, since different realizations of a mechanism can produce qualitatively different model outputs [51]. The novel models generated by the GP method offer a better fit to alcohol consumption data than a reference model, which was constructed by a human modeler representing one possible interpretation of the mechanisms of role theory. Our approach is flexible and can be easily extended to complex systems models that are seeking to explain other social phenomena. Our method also offers novel directions for future knowledge discovery and social theory development, based on the fusion of data-driven and theory-driven methods.

A key part of realist explanation is comparison and integration across multiple theories [4]. While our existing example is limited to the building blocks defined in social role theory, there is no reason why building blocks relating to other theories cannot be defined. However, integration of these wider building blocks, such that they can be exploited by machine learning, will require a common language for expression of the theories. We see middle-range theory [52] and its realization in the so-called Coleman Boat [53], or other micro-macro schemes, as a potentially useful template for formal descriptions of theory and their translation, via a model discovery framework, into integrated simulation models. Future work will aim to incorporate additional theories and to generate novel combinations of multiple theories.

Data Availability

The data used to support the findings of this study are included within the article.

Conflicts of Interest

The authors declare that there are no conflicts of interest regarding the publication of this paper.

Authors' Contributions

TMV designed the primitives and implemented the model discovery process. AB, CB, and RCP designed the roles model, which was implemented by HB. CB implemented the microsimulation. AN and CP contributed to mechanism development. TMV, AB, MS, and RCP designed the model discovery process. PS aided in the interpretation of the findings. RCP led the research and its conceptual underpinnings. TMV, CB, RCP, MS, and AN wrote the paper.

Acknowledgments

The authors would like to thank Jack E. Hutton for preliminary work on structural calibration for the roles models which he conducted in his MEng dissertation and thank the whole CASCADE team for their input to wider discussions in generating the research reported in this paper. RCP would also like to thank the organizers and participants of the Economic and Social Research Council seminar series "Complexity and Method in the Social Sciences: An Interdisciplinary Approach" (2014–2017), which stimulated the thinking developed in this paper. Research reported in this publication was supported by the National Institute on Alcohol Abuse and Alcoholism of the National Institutes of Health (award no. R01AA024443). This research was conducted as part of the Calibrated Agent Simulations for Combined Analysis of Drinking Etiologies (CASCADE) project.

Supplementary Materials

Supplementary Material A—the evolution of the grammar contains three iterations of the grammar with change logs. Supplementary Material B—the structures on the Pareto front and corresponding theoretical credibility. (*Supplementary Materials*)

References

[1] J. M. Epstein, "Agent-based computational models and generative social science," *Complexity*, vol. 4, no. 5, pp. 41–60, 1999.

[2] P. Hedstrom, "Dissecting the social: on the principles of analytical sociology," vol. 34, 2005.

[3] T. Lawson, *Economics and Reality*, Routledge, Abingdon, UK, 1997.

[4] B. Danermark, M. Ekström, L. Jakobsen, and J. Ch. Karlsson, *Explaining Society: Critical Realism in the Social Sciences*, Routledge, Abingdon, UK, 2002.

[5] R. Boero and F. Squazzoni, "Does empirical embeddedness matter? Methodological issues on agent-based models for analytical social science," *Journal of Artificial Societies and Social Simulation*, vol. 8, 2005.

[6] F. J. León-Medina, "Analytical sociology and agent-based modeling: is generative sufficiency sufficient?" *Sociological Theory*, vol. 35, no. 3, pp. 157–178, 2017.

[7] D. Byrne and G. Callaghan, *Complexity Theory and the Social Sciences: The State of the Art*, Routledge, Abingdon, UK, 2013.

[8] C. Gunaratne and I. Garibay, "Alternate social theory discovery using genetic programming: towards better understanding the artificial anasazi," in *Proceedings of the GECCO 2017 Genetic and Evolutionary Computation Conference*, ACM Press, Berlin, Germany, pp. 115–122, 2017.

[9] C. Gunaratne and I. Garibay, "Evolutionary model discovery of factors for farm selection by the artificial anasazi," in *Proceedings of the International Conference Computer Science and Engineering*, p. 27, ACM, New York, NY, USA, 2017.

[10] T. M. Vu, C. Probst, J. M. Epstein, A. Brennan, M. Strong, and R. C. Purshouse, "Toward inverse generative social science using multi-objective genetic programming," in *Proceedings of the GECCO 2019 Genetic and Evolutionary Computation Conference*, Association for Computing Machinery, Prague, Czech Republic, pp. 1356–1363, 2019.

[11] V. A. Smith, "Evolving an agent-based model to probe behavioral rules in flocks of cowbirds," *ALIFE*, vol. 2008, pp. 561–568, 2008.

[12] J. Zhong, L. Luo, W. Cai, and M. Lees, "Automatic rule identification for agent-based crowd models through gene expression programming," *AAMAS*, vol. 2014, pp. 1125–1132, 2014.

[13] R. Poli, W. B. Langdon, N. F. McPhee, and J. R. Koza, *A Field Guide to Genetic Programming*, Lulu Press, Morrisville, NC, USA, 2008.

[14] K. Rodriguez-Vazquez, C. M. Fonseca, and P. J. Fleming, "Identifying the structure of nonlinear dynamic systems using multiobjective genetic programming," *IEEE Transactions on Systems, Man, and Cybernetics-Part A: Systems and Humans*, vol. 34, no. 4, pp. 531–545, 2004.

[15] J. R. Koza, *Genetic Programming: On the Programming of Computers by Means of Natural Selection*, MIT Press, Cambridge, MA, USA, 1992.

[16] R. I. McKay, N. X. Hoai, P. A. Whigham, Y. Shan, and M. O'Neill, "Grammar-based genetic programming: a survey," *Genetic Programming and Evolvable Machines*, vol. 11, no. 3–4, pp. 365–396, 2010.

[17] B. J. Biddle, *Role Theory: Expectations, Identities, and Behaviors*, Academic Press, Cambridge, MA, USA, 1979.

[18] R. A. Knibbe, M. J. Drop, and A. Muytjens, "Correlates of stages in the progression from everyday drinking to problem drinking," *Social Science & Medicine*, vol. 24, no. 5, pp. 463–473, 1987.

[19] S. Kuntsche, R. A. Knibbe, and G. Gmel, "Social roles and alcohol consumption: a study of 10 industrialised countries," *Social Science & Medicine*, vol. 68, no. 7, pp. 1263–1270, 2009.

[20] R. W. Wilsnack and R. Cheloha, "Women's roles and problem drinking across the lifespan," *Social Problems*, vol. 34, no. 3, pp. 231–248, 1987.

[21] K. Yamaguchi and D. B. Kandel, "On the resolution of role incompatibility: a life event history analysis of family roles and marijuana use," *American Journal of Sociology*, vol. 90, no. 6, pp. 1284–1325, 1985.

[22] J. G. Bachman, P. M. O'Malley, J. E. Schulenberg, L. D. Johnston, A. L. Bryant, and A. C. Merline, *The Decline of Substance Use in Young Adulthood: Changes in Social Activities, Roles, and Beliefs*, Lawrence Erlbaum Associates Publishers, Mahwah, NJ, USA, 2002.

[23] M. R. Lee, L. Chassin, and D. MacKinnon, "The effect of marriage on young adult heavy drinking and its mediators: results from two methods of adjusting for selection into marriage," *Psychology of Addictive Behaviors*, vol. 24, no. 4, pp. 712–718, 2010.

[24] U.S. Department of Health and Human Services, *Substance Abuse and Mental Health Services Administration, Center for Behavioral Health Statistics and Quality*, National Survey on Drug Use and Health (NSDUH), New York, NY, USA, 1979.

[25] University of Michigan, *Survey Research Center, Panel Study of Income Dynamics (PSID): Main Interview*, University of Michigan, Ann Arbo, MI, USA, 2018.

[26] S. Manson, J. Schroeder, D. Van Riper, and S. Ruggles, *IPUMS National Historical Geographic Information System: Version 14.0 [Database]*, IPUMS, Minneapolis, MN, USA, 2019.

[27] R. Lovelace and M. Dumont, *Spatial Microsimulation with R*, Chapman and Hall/CRC, New York, NY, USA, 2016.

[28] S. Ruggles, S. Flood, R. Goeken et al., *IPUMS USA: Version 9.0 [dataset]*, IPUMS, Minneapolis, MN, USA, 2019.

[29] Centers for Disease Control and Prevention, National Center for Health Statistics, "Compressed mortality file, 1979–1998. CDC WONDER online database, compiled from compressed mortality file CMF 1968–1988, series 20, no. 2A, 2000 and CMF 1989–1998, series 20, no. 2E," 2003.

[30] Centers for Disease Control and Prevention, National Center for Health Statistics, "Underlying cause of death, 1999–2017 on CDC WONDER online database, released december, 2018. Data are from the multiple cause of death files, 1999–2017, as compiled from data provided by the 57 vital statistics jurisdictions through the vital statistics cooperative program," 1999.

[31] N. Collier and M. North, "Parallel agent-based simulation with repast for high performance computing," *Simulation*, vol. 89, no. 10, pp. 1215–1235, 2013.

[32] R. Carnell, "Lhs R package: latin hypercube samples," 2019.

[33] M. Stein, "Large sample properties of simulations using Latin hypercube sampling," *Technometrics*, vol. 29, no. 2, pp. 143–151, 1987.

[34] M. Fenton, J. McDermott, D. Fagan, S. Forstenlechner, M. O'Neill, and E. Hemberg, "Pony GE2: grammatical evolution in python," *Genetic and Evolutionary Computation Conference*, vol. 17, 2017.

[35] K. Deb, A. Pratap, S. Agarwal, and T. Meyarivan, "A fast and elitist multiobjective genetic algorithm: NSGA-II," *IEEE Transactions on Evolutionary Computation*, vol. 6, no. 2, pp. 182–197, 2002.

[36] L. Gell, G. Bühringer, J. McLeod et al., *What Determines Harm from Addictive Substances and Behaviours?*, Oxford University Press, Oxford, UK, 2016.

[37] J. Staff, K. M. Greene, J. L. Maggs, and I. Schoon, "Family transitions and changes in drinking from adolescence through mid-life," *Addiction*, vol. 109, no. 2, pp. 227–236, 2014.

[38] M. R. Lee, L. Chassin, and D. P. MacKinnon, "Role transitions and young adult maturing out of heavy drinking: evidence for larger effects of marriage among more severe premarriage problem drinkers," *Alcoholism: Clinical and Experimental Research*, vol. 39, no. 6, pp. 1064–1074, 2015.

[39] M. L. Cooper, "Motivations for alcohol use among adolescents: development and validation of a four-factor model," *Psychological Assessment*, vol. 6, no. 2, pp. 117–128, 1994.

[40] M. Nicolau and A. Agapitos, "Understanding grammatical evolution: grammar design," in *Handbook of Grammatical Evolution*, C. Ryan, M. O'Neill, and J. Collins, Eds., pp. 23–53, Springer International Publishing, Berlin, Germany, 2018.

[41] T. Hildebrandt and J. Branke, "On using surrogates with genetic programming," *Evolutionary Computation*, vol. 23, no. 3, pp. 343–367, 2015.

[42] M. Zaefferer, J. Stork, O. Flasch, and T. Bartz-Beielstein, "Linear combination of distance measures for surrogate models in genetic programming," in *Parallel Problem Solving from Nature–PPSN XV*, A. Auger, C. M. Fonseca, N. Lourenço, P. Machado, L. Paquete, and D. Whitley, Eds., pp. 220–231, Springer International Publishing, Berlin, Germany, 2018.

[43] A. Collins, M. Petty, D. Vernon-Bido, and S. Sherfey, "A call to arms: standards for agent-based modeling and simulation," *Journal of Artificial Societies and Social Simulation Index*, vol. 18, p. 12, 2015.

[44] U. Wilnesky, *NetLogo, Center of Connected Learning and Computer-Based Modeling*, Norwestern University, Evanston, IL, USA, 1999.

[45] M. J. North, N. T. Collier, J. Ozik et al., "Complex adaptive systems modeling with repast simphony, complex adapt," *System Model*, vol. 1, p. 3, 2013.

[46] V. Grimm, U. Berger, D. L. DeAngelis, J. G. Polhill, J. Giske, and S. F. Railsback, "The ODD protocol: a review and first update," *Ecological Modelling*, vol. 221, no. 23, pp. 2760–2768, 2010.

[47] B. Bauer, J. P. Müller, and J. Odell, "Agent uml: a formalism for specifying multiagent software systems," *International Journal of Software Engineering and Knowledge Engineering*, vol. 11, no. 03, pp. 207–230, 2001.

[48] H. Bersini, "UML for ABM," *Journal of Artificial Societies and Social Simulation Index*, vol. 15, p. 9, 2011.

[49] T. M. Vu, C. Wagner, and P.-O. Siebers, "ABOOMS: overcoming the hurdles of continuous-time public goods games with a simulation-based approach," *Journal of Artificial Societies and Social Simulation Index*, vol. 22, p. 7, 2019.

[50] T. M. Vu, C. Probst, A. Nielsen et al., "A software architecture for mechanism-based social systems modelling in agent-based simulation models," *Journal of Artificial Societies and Social Simulation*, vol. 23, p. 1, 2020.

[51] H. Muelder and T. Filatova, "One theory - many formalizations: testing different code implementations of the theory of planned behaviour in energy agent-based models," *Journal of Artificial Societies and Social Simulation Index*, vol. 21, p. 5, 2018.

[52] R. K. Merton, *On Theoretical Sociology*, Free Press, New York, NY, USA, 1967.

[53] J. S. Coleman, "Social theory, social research, and a theory of action," *American Journal of Sociology*, vol. 91, no. 6, pp. 1309–1335, 1986.

Hindawi
Complexity
Volume 2020, Article ID 7348281, 14 pages
https://doi.org/10.1155/2020/7348281

Research Article

Linkboost: A Link Prediction Algorithm to Solve the Problem of Network Vulnerability in Cases Involving Incomplete Information

Chengfeng Jia,[1] **Jie Ma**,[1,2,3] **Qi Liu**,[1] **Yu Zhang**,[4] **and Hua Han**[5]

[1]*School of Navigation, Wuhan University of Technology, Wuhan 430063, China*
[2]*Hubei Inland Shipping Technology Key Laboratory, Wuhan 430063, China*
[3]*National Engineering Research Center for Water Transportation Safety, Wuhan 430063, China*
[4]*School of Logistics Engineering, Wuhan University of Technology, Wuhan 430063, China*
[5]*School of Science, Wuhan University of Technology, Wuhan 430070, China*

Correspondence should be addressed to Jie Ma; majie@whut.edu.cn

Received 14 September 2019; Revised 1 January 2020; Accepted 8 February 2020; Published 8 April 2020

Guest Editor: Gonzalo Farias

The vulnerability of network information systems has attracted considerable research attention in various domains including financial networks, transportation networks, and infrastructure systems. To comprehensively investigate the network vulnerability, well-designed attack strategies are necessary. However, it is difficult to formulate a global attack strategy as the complete information of the network is usually unavailable. To overcome this limitation, this paper proposes a novel prediction algorithm named Linkboost, which, by predicting the hidden edges of the network, can complement the seemingly missing but potentially existing connections of the network with limited information. The key aspect of this algorithm is that it can deal with the imbalanced class distribution present in the network data. The proposed approach was tested on several types of networks, and the experimental results indicated that the proposed algorithm can successfully enhance the destruction rate of the network even with incomplete information. Furthermore, when the proportion of the missing information is relatively small, the proposed attack strategy relying on the high degree nodes performs even better than that with complete information. This finding suggests that the nodes important to the network structure and connectivity can be more easily identified by the links added by Linkboost. Therefore, the use of Linkboost can provide useful insight into the operation guidance and design of a more effective attack strategy.

1. Introduction

With the development of big data, the management of intensive knowledge in a complex network represents a key technique that can dramatically change the way we perceive the world. Most real-world networks, such as traffic, social, or biological networks, are complex and inevitably undergo network failures [1]. To solve this problem, the critical nodes, the removal of which may lead to network collapse, must be determined. Therefore, the vulnerability or robustness of complex networks, especially in terms of the failure of critical nodes, has attracted considerable attention in the past few years [2].

The most fundamental network vulnerability approach mainly relies on removing some crucial nodes and their corresponding edges in the network and calculating the retention of the largest giant component of the network [3]. From the mathematical point of view, it is desirable to find a strategy to remove the important nodes, to ensure that the structure of the network can be destroyed at the lowest cost. To protect such critical nodes, the connectivity of the network should be preserved as much as possible. If complete information regarding the network is available, the network vulnerability can be evaluated in a relatively easy manner, and several methods are available to determine the nodes that critically influence the network vulnerability. Holme et al. [4] proposed a node attacking strategy based on the rank of degree, and a residual network was used to calculate the size of the largest giant component of the network. The

results indicated that the high degree nodes can be usually considered as the most important nodes influencing the network vulnerability. Chen et al. [5] used the method of the so-called "equal graph partitioning degree" to identify the key nodes. In particular, they divided a network into two clusters with an arbitrary size ratio and determined the key nodes that connected these clusters. It was observed that the attack on these key nodes could rapidly disintegrate the entire network. Hu et al. [6] used the dynamic Bayesian network to predict the best attack order on the nodes and found that attacking a small number of key nodes could lead to a rapid collapse of the complete network.

However, all the abovementioned approaches assumed the network to be panoramic; in other words, it was considered that all the connections in the network are known in advance. In real life, it is difficult to obtain such perfect data. For instance, in a terrorist relationship network, only knowing part of the terrorist information is not sufficient to uncover the organizational structure and the mutual relationship contained in the network [7]. Another example is the biological virus network, in which although the molecular composition can be learned through chemical analysis, the comprehensive connections between the molecules are difficult to determine [8]. Thus, the network connections that we can observe are often partial and incomplete. Although all the information regarding the nodes can be obtained from the network topology, some latent connections exist that cannot be discovered directly, similar to that in the situations shown in Figure 1. For such networks with incomplete information, the vulnerability cannot be directly investigated by using the topology of the network, as performed in traditional methods.

The research on network vulnerability with incomplete information is generally divided into two categories. The first category involves studies employing statistical methods such as the random walk to find several hidden key nodes [9]. The second category involves studies that use a recently popular technology, namely, the link prediction technology to find the hidden edges from incomplete network connections. In this case, once the network has been complemented, the traditional attack strategies can be employed to study the vulnerability.

Despite the considerable research effort pertaining to link prediction, the current state-of-the-art algorithms mostly do not consider the imbalanced distribution of the network data [10]. In general, in a real network, the nodes are paired and the number of paired nodes with edges is considerable smaller than that of the nodes without edges. From the view of supervised learning, the number of connected node pairs is not sufficient to enable learning owing to the lack of sampling, resulting in low prediction accuracy. In the network, because the learning algorithm is biased toward the nonconnected pair samples, it is more difficult to predict the connections between the nodes with small degrees. However, such hard-to-recall edges are critical to perform a network vulnerability analysis, as they may represent the pivot connecting the largest giant component [4], and the nodes with a larger betweenness tend to have a smaller degree value [5]. Therefore, the presence of an uneven data class distribution is a considerable challenge for realizing link prediction, although such imbalanced data is actually crucial to realize a network attack with incomplete information.

To solve the problem of the data class imbalance, SMOTE [11] and other data generation algorithms can be used to generate a new data of a minority class to balance the class distribution. However, the use of these methods may change the original distribution of the data, thereby reducing the overall prediction accuracy. In contrast from the approach of changing the original distribution of data, this work focused on the minority class samples obtained by changing the sampling weight of the raw data. The most representative and effective algorithm involving sampling weights is the AdaBoost algorithm [12], which, as a data-driven algorithm, can adaptively change the technique of data sampling on the basis of the classification results in the latest iteration. However, because this algorithm cannot deal with the imbalanced data, it is difficult to achieve a high accuracy in link prediction. To overcome this limitation, this paper proposes a novel link prediction algorithm, Linkboost, which can improve the AdaBoost algorithm by increasing the sampling weight of the minority samples in an adaptive manner.

The main contributions of this work can be summarized as follows:

(i) The proposed Linkboost improves the AdaBoost algorithm by adaptively updating the sampling weight, which is advantageous in dealing with the imbalanced class distribution of the network data. The weight updating rule lays more emphasis on the cost of misclassifying the minority class samples than the corresponding cost for the majority class samples. Specifically, this rule increases the sampling weights of the wrongly classified samples in the minority class more aggressively and decreases the weights of the correctly classified samples more conservatively. Furthermore, the convergence of the Linkboost is demonstrated by analyzing the upper bound of the loss function.

(ii) When Linkboost is applied for link prediction, the edges that need to be added are supposed to be closely related to the latent connections. Consequently, we quantify the degree of the network incompleteness and the magnitude of the additional link information. These two key factors can facilitate the development of better attack strategies as the optimum magnitude of the additional information can be specified accordingly in terms of the degrees of network incompleteness.

(iii) In many real-world information networks, owing to privacy or legal restrictions, implicit connections exist in the network, which make it difficult to evaluate the importance of the nodes that are not explicitly connected. Linkboost can determine these implicit edges, thereby providing useful insight for the operation guidance and design of a more effective attack strategy regardless of whether the network is completely observed.

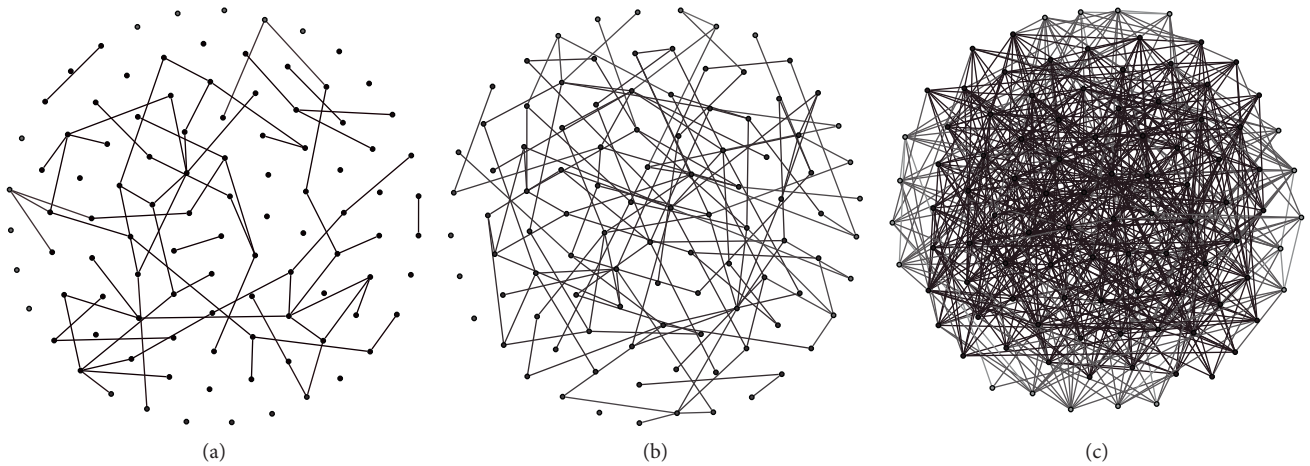

Figure 1: Network with different proportions of missing information: (a) more missing information, (b) less missing information, and (c) full information.

2. Literature Review

In most of the early works regarding network vulnerability, it was assumed that the complete information of the network structure can be obtained. With complete information, the nodes that are important to the network vulnerability can be identified by employing various available node importance measures. However, in real life, the complete knowledge of the network structure is not always available. For such cases, some researchers employed partial information to identify the most important nodes to perform network crash analyses. Gallos et al. [13] first studied the stability of scale-free networks by using different attack strategies when the edges were partially hidden in the network; they reported that the optimal node attack strategy has a strong correlation with the degree of the nodes. Wu et al. [14] recognized that the global index (such as the median, shortest distance, and commute time) of the network is unstable when only a few edges are missing, which leads to the deviation of the selection of the key nodes. In this regard, the researchers proposed a hybrid index based on the local information combined with the maximum connected graph and verified the stability of the mixed indicator. Liu and Li [15] applied this concept for the protection of power networks, in which the distribution of the local roads and power capacity information of the power station are available, while a part of the connections remains unknown.

All the abovementioned studies identified the important nodes according to the observed topology of the network. However, because these nodes are recognized using incomplete information, the identification of these "important nodes" is not always correct. Therefore, it is of significance to develop an optimum attack strategy for such incomplete networks. Consequently, in this study, we develop a link prediction algorithm to examine the vulnerability of complex networks with incomplete information by restoring the missing information of the network. Subsequently, the widely used high degree strategy [16] is applied to perform the attack.

In recent years, link prediction has become a hotspot branch in the field of complex networks. In most of the recent studies, link prediction was performed to estimate the likelihood of the existence of a link between the node pairs in the network. Similarly, in our work, one of the link prediction algorithms is used to recover parts of the missing links before the attack, and the targets are later identified based on the predicted network. Among the existing link prediction algorithms, machine-learning algorithms, which treat link prediction as a binary classification problem, are widely used in large-scale networks [17, 18]. To determine whether the node pairs have connected edges, the node pairs are divided into positive and negative examples, which represent the connected and unconnected pairs, respectively. However, in a real network, the node pairs connected to other pairs are considerably fewer than the node pairs with no connections. For instance, of all Facebook users, considerably fewer pairs of users follow each other than those that do not. The large-scale authorship network is another such example. In most cases, papers and studies are published under the name of a single author, and co-authorship only exists in a few cases (because a balanced network requires each author in the network to engage in co-authorship with half of the authors in the network). In the classification problem, the classification result will be biased if the contribution of the negative sample is ignored, and the optimization goal is simply the minimization of the classification error [19]. More importantly, such an imbalance considerably influences the network vulnerability because the node pairs with high degree nodes are more easily detected, whereas the pairs with low degree nodes tend to be ignored more frequently. These low degree nodes are likely to be crucial nodes [4], the failure of which may lead to the collapse of the largest connected subcomponent [20]. To overcome this limitation, this paper proposes a new link prediction algorithm to solve the imbalance problem.

3. Proposed Algorithm

3.1. Network Vulnerability and Class Imbalance. A network can be represented as a simple undirected graph $G = (V, E)$, where V is the set of nodes and E is the set of links. Let $N = |$

$V|$ and $W = |E|$ be the numbers of nodes and links, respectively. k_i denotes the degree of the node v_i, which equals the number of links connected to node. We assume that all the nodes are known, but the partial link information is missing. The network can be observed as G_O. It is assumed that the missing link information is predicted using the link prediction algorithm, and the predicted network is G_P.

We identify the crucial nodes from the predicted network G_P, and then use these nodes to attack the complete network G. Once a node is attacked, its attached edges are removed simultaneously. $\widehat{V} \subseteq V$ denotes the set of nodes that are attacked (important nodes), and $\widehat{E} \subseteq E$ denotes the set of removed links. Thus, the network obtained after the node attacks is $\widehat{G} = (V - \widehat{V}, E - \widehat{E})$. We define the disintegration ratio $S = |\widehat{V}|/N\,(S \in [0, 1])$ as the vulnerability evaluation index of the node attacks. In this study, the high degree strategy [16] is employed, in which the nodes are selected to be attacked according to their degree ranks (i.e., high degree nodes are attacked first).

Figure 2 shows the difference in the direct attack and attack after link prediction. We assume that three links are hidden, which are marked as red edges in Figure 2(a), and the observed network G_O is as shown in Figure 2(b). In this case, V_b is the largest degree node (degree = 3) that can be observed. According to the high degree strategy, V_b is attacked first. When V_b is removed, the residual network is as shown in Figure 2(c). At this point, the disintegration ratio $S = |\widehat{V}|/N = 4/7$. In contrast from the direct attack, the proposed method involves adding a possible edge by using the link prediction algorithm on the basis of the incomplete network G_O, which generates the repaired network G_P, as shown in Figure 2(d). Next, we use the high degree strategy from G_P to attack the network. The largest degree node is V_e, which has a degree of four. After attacking node V_e, the residual network is as shown in Figure 2(e), and the disintegration ratio $S = |\widehat{V}|/N = 3/7$. This finding shows that the attack strategy is more effective after the network is repaired using the link prediction algorithm.

Figure 2 indicates that the use of a suitable link prediction algorithm is the core of the abovementioned network attack strategy. Such algorithms aim at estimating the likelihood of the existence of a link between two nodes based on the observed network structure and the attributes of the nodes. Given that $G = \langle V, E\rangle$, all the nodes are assumed to be known, and the partial link information is considered missing. We define $\alpha = |E_M|/W$, $\alpha \in [0, 1]$ as the proportion of the missing links. In general link prediction research, the hidden edges are randomly selected. E_O and E_M denote the sets of the observed links and missing links, respectively. Clearly, $E_O \cup E_M = E$. Therefore, the observed network can be represented as $G_O = (V, E_O)$. Let $E_U = V \times V$ represent the universal set containing all $N(N-1)/2$ possible links. The task of link prediction is to reveal the set of missing links E_M via link prediction. G_P represents the improved network involving the additional predicted links E_P. $\beta = |E_P|/|E_O|$ is defined as the magnitude of the additional link information.

In the existing research, many scholars demonstrated that the use of machine-learning algorithms could achieve a high accuracy in link prediction. From the perspective of machine-learning algorithms, the link prediction problem can be regarded as a binary classification problem. If $u \in V$, $v \in V$, and $(u, v) \in E_O$, the pair of nodes (u, v) can be considered a positive example if a link exists between u and v. In contrast, if the pair of nodes is a negative example, no edge is present between u and v. In a real network, the number of connected nodes in the network is considerably smaller than the number of node pairs without an edge, which means $|E| \ll |E_U - E|$. In the field of machine learning, this condition represents an imbalanced classification problem. Because the goal of most machine algorithms is to minimize the overall sample prediction error, the prediction results may be biased if we ignore the imbalanced distribution of the classes. For a given network, the misclassification of minority class samples means that the hidden edges are not correctly recognized. In particular, when the degree of a node is extremely small, the link prediction algorithm tends to predict that the node has no connection to other nodes. However, in the study of the network vulnerability, some nodes connecting the subnetwork may have only a few connected edges, and these may represent the minority class samples. If this part of the node pairs is not correctly predicted, the wrong attack strategy will be formulated. Therefore, this work focuses on the design of the link prediction algorithm for the class imbalance problem, aiming to restore the network as much as possible to develop the optimal attack strategy.

3.2. Linkboost Link Prediction. The link prediction problem, as one of the most significant link analysis and mining tasks, has been used to restore complete networks according to partially observed information. The link prediction algorithm has been applied in the social, biological, and bioinformatics domains to help better analyze and understand the structural topology and evolution mechanism of a network. In this study, we propose a novel link prediction algorithm, Linkboost, which improves the AdaBoost algorithm by increasing the sampling weight of the minority samples in an adaptive manner. The proposed algorithm is expected to solve the problem of imbalanced data distribution in the network and improve the accuracy of link prediction.

The link prediction framework of Linkboost is shown in Figure 3. First, the static indicators (such as the degree) of the network and similarity indicators (such as the common neighbor) of the node networks are used to extract the feature of the node pairs in the network. Next, the Linkboost algorithm is used to improve the classification accuracy of the minority class by performing resampling with preference. Finally, the network vulnerability is examined using high degree attack strategies by considering the proportion of the missing link α and the magnitude of the additional link β.

In the existing link prediction research, many network structural features have been used to describe the topology characteristics of the network. Based on the past literature [21, 22] and considering the global characteristics of real network nodes, we add two kinds of features based on the distance and random walk:

(1) Node-based features: node degree and high-order degree

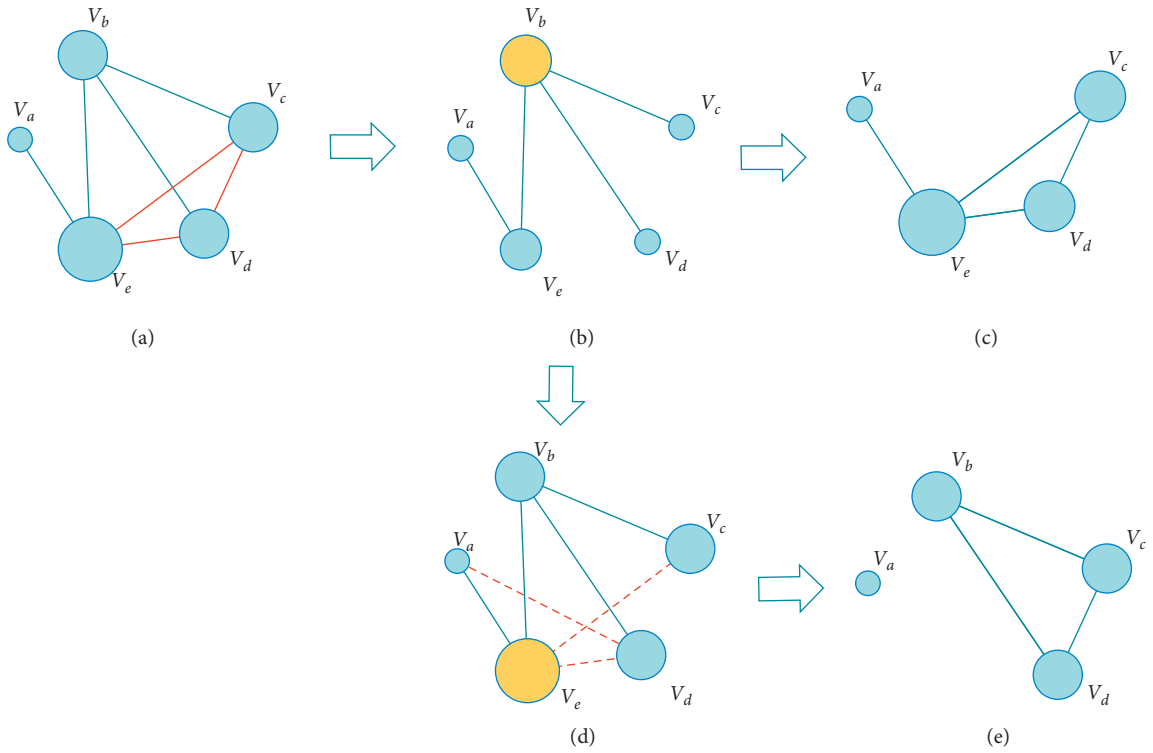

Figure 2: Comparison between the residual networks for a direct attack and attack after link prediction. (a) Complete network G. (b) Incomplete network G_O with three hidden edges. (c) Residual network after node V_b, which is the highest degree node in the incomplete network G_O, is attacked. (d) Predicted network G_P with three predicted links added (red dotted lines). (e) Residual network after node V_e, which is the highest degree node in the predicted network G_P, is attacked.

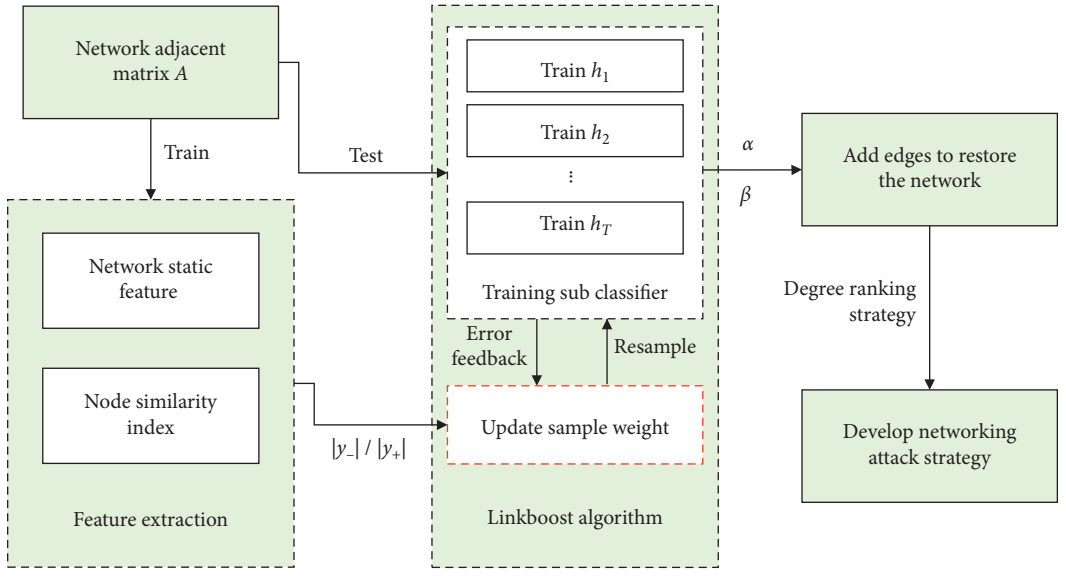

Figure 3: Overview of the Linkboost framework.

(2) Features based on common neighbors: number of common neighbors, Jaccard index, AA index, Katz index, and Salton index

(3) Features based on distance: shortest path and partial region path

(4) Features based on random walks: PageRank [23] and SimRank [22]

After completing the feature extraction of the network, these features are fed into the Linkboost algorithm. The pseudocode of the Linkboost algorithm is presented as Algorithm 1.

Input: Network missing adjacency matrix A
Output: Final strong hypothesis $H(x) = \sum_{t=1}^{T} \alpha_t h_t(x)$, connection score R_1, nonconnection score R_2.
(1) Extract features and tag, $S = \{(x_1, y_1), \ldots, (x_m, y_m)\}$, $x_i \in X$, $y_i \in \{-1, +1\}$. Here x_i is the feature of the network node pair, y_i is the label of the node pair, indicating whether there is an edge exists. $M = |E_O|$, $N = |E_U - E_O|$.
(2) Initialize the weight distribution of the training data. $D_1 = (w_{11}, w_{12}, \ldots, w_{1|A|})$, where $w_{1,i} = (1/2M)$, if $y_i = 1$; $w_{1,i} = (1/2N)$, if $y_i = -1$.
(3) *For* t in T iterations
(4) Resample S according to D_t
(5) Find h_t: $\arg\min(\varepsilon_j) = \sum_{i=1}^{m} [y \neq h_j(x_i)]$, where$h_j \in H$.
(6) *If* $\varepsilon_i < 1/2$
(7) *Continue*
(8) *else*
(9) save h_t, calculate $\alpha_t = 1/2 * \log(1 - \varepsilon_t/\varepsilon_t)$,
(10) update$D_{t+1} = (w_{t+1,1}, w_{t+1,2}, \ldots, w_{t+1,|A|})$ and $Z_t = \sum_j^{|A|} w_{t+1,j}$
(11) *If* $y_i = 1$, $w_{t+1,j} = 1/2M$;
(12) *If* $y_i = -1$,$w_{t+1,j} = (w_{t,i}/Z_t)\exp(-\alpha_m y_i h_t(x_i))$, $\quad i = 1, 2, \ldots, |A|$
(13) *End If*
(14) *End For*
(15) Predict connection of the network using $H(x) = \sum_{t=1}^{T} \alpha_t h_t(x)$, obtain R_1 and R_2

Algorithm 1: Process flow of the Linkboost link prediction algorithm.

As mentioned previously, in the proposed algorithm, the sampling mode is changed so that each iteration of the sampling focuses not only on the misclassified samples but also on the minority class samples. Specifically, in the initialization step, the weight of the positive examples (which also belong to the minority class) is defined as $w_{1i}^{+} = 1/(2M)$, where M is the number of edges. The weight of the negative examples (which also belong to the majority class) is defined as $w_{1i}^{-} = 1/(2N)$, where N is the number of nodes pairs without a connection. In most real-world networks, $M \ll N$ and $w_{1,i}^{+} \gg w_{1,i}^{-}$; therefore, the positive sample is easier to be sampled. In the process of iteration, the update mode is also affected by the class label. For a positive sample, the weight of the next sample is the same as $1/2M$, so as to assign a higher probability of being sampled. For a negative sample, the weights are updated based on whether they are classified correctly. In negative cases, the misclassified node pairs have a higher probability of being sampled in the next iteration. If the negative sample$y_i = -1$ is classified correctly, $h_t(x_i) = -1$. Consequently, $-\alpha_m y_i h_t(x_i) < 0$ and $w_{t+1} < w_t$. This means that if the negative samples are classified correctly, the probability of being sampled in the next iteration is decreased. If the prediction is wrong, the probability of being sampled in the next round increases. However, because of the limitation of the normalization factor Z_t, the expectation of the sampling weight of the negative samples is smaller than that of the positive samples $E(w^{+}) > E(w^{-})$. This means that the model pays more attention to the recall of the positive samples while focusing on learning the samples that are easily misclassified. This improved sampling method can help recognize more node pairs with connected edges.

As the proposed approach modified the calculation method of the initial and iterative weights of the traditional AdaBoost algorithm, the convergence of this algorithm must be demonstrated by considering the upper bound of the loss function. For the overall sample, the loss function is

$$\frac{1}{M+N}\sum_{i=1}^{M+N}[H(x_i) \neq y_i] \quad \text{if } H(x_i) \neq y_i,$$
$$[H(x_i) \neq y_i] = 1; \quad \text{if } H(x_i) = y_i, [H(x_i) \neq y_i] = 0. \tag{1}$$

Theorem 1. $1/(M+N)\sum_{i=1}^{M+N}[H(x_i) \neq y_i] \leq (1/(M+N))\sum_i \exp(-y_i H(x_i)) = \prod_T (Z_i - 1/2)$.

Proof. If $H(x_i) \neq y_i$, $-y_i H(x_i) < 0$. So, $\exp(-y_i H(x_i)) \geq 1$, the left inequality is proofed:

$$w_{t+1,i} = \begin{cases} 1/2M, & \text{if } y_i = 1, \\ (w_{t,i}/Z_t)\exp(-\alpha_t y_i H_t(x_i)), & \text{if } y_i = -1, \end{cases}$$

$$Z_t = \sum_{i=1}^{M+N} w_{t,i}$$

$$= M\sum_{i=1}^{M}\frac{1}{2M} + \sum_{i=M+1}^{M+n}\left(\frac{w_{t,i}}{Z_t}\right)\exp(-\alpha_t y_i H_t(x_i))$$

$$= \frac{1}{2} + \sum_{i=M+1}^{M+n}\left(\frac{w_{t,i}}{Z_t}\right)\exp(-\alpha_t y_i H_t(x_i)),$$

$$\frac{1}{M+N}\sum_i \exp(-y_i H(x_i))$$

$$= \frac{1}{M+N}\sum_i \exp\left(-\sum_{i=1}^{M+N}\alpha_t y_i H_t(x_i)\right)$$

$$
\begin{aligned}
&= w_{1,i} \sum_i \exp\left(- \sum_{i=1}^{M+N} \alpha_t y_i H_t(x_i) \right) \\
&= w_{1,i} \prod_1^{M+N} \exp\left(-\alpha_t y_i H_t(x_i)\right) \\
&= \left(Z_1 - \frac{1}{2}\right) \sum_i w_{2,i} \prod_2^{M+N} \exp\left(-\alpha_t y_i H_t(x_i)\right) \\
&= \left(Z_1 - \frac{1}{2}\right)\left(Z_2 - \frac{1}{2}\right) \sum_i w_{3,i} \prod_3^{M+N} \exp\left(-\alpha_t y_i H_t(x_i)\right) \\
&= \left(Z_1 - \frac{1}{2}\right)\left(Z_2 - \frac{1}{2}\right) \ldots Z_{T-1} \sum_i w_{T,i} \exp\left(-\alpha_T y_i H_T(x_i)\right) \\
&= \prod_1^T \left(Z_t - \frac{1}{2}\right).
\end{aligned} \tag{2}
$$

Theorem 1 indicates that although the algorithm assigns more importance to the classification accuracy of the minority class samples, the loss function of the overall sample is still convergent. Therefore, when using the Linkboost algorithm, the node pairs with the connected edges have a high recall rate, which provides a good basis for the development of the attack strategy. □

4. Experiment and Results Analysis

4.1. Proportion of the Missing Links and Magnitude of the Additional Link Information. Linkboost predicts a network from an incomplete network; however, two problems remain. (1) The degree of incompleteness for a network, that is, the missing link proportion in the network must be defined. (2) Although the Linkboost algorithm can be used to determine the classification scores R_1 and R_2, where $R_1 + R_2 = 1$, the threshold to separate the two classes must still be determined. In the network, the number of edges predicted to be added must be determined. To address these two problems, we define two parameters α and β:

$$
\begin{aligned}
\alpha &= \frac{E_M}{E}, \\
\beta &= \frac{E_P}{E_O}.
\end{aligned} \tag{3}
$$

Here, α represents the proportion of the edges that are missed among all the edges. A smaller α means that a larger number of positive samples can be learned using the learning algorithm. β represents the ratio of the additional link information obtained using Linkboost.

4.2. Experimental Data and Evaluation Metrics. To experimentally validate the effectiveness of the algorithm and analyze the sensitivity of the parameters α and β in different networks, four real large-scale networks were employed, including ArXiv hep-th, Cora citation, Facebook, and Skitter. ArXiv hep-th [24] is the network of publications in ArXiv's High Energy Physics, Theory (hep-th) section. The directed links that connect the publications are citations. In the Cora network [25], the nodes represent scientific papers, and the edge between two nodes indicates the existence of co-authorship. The Facebook network [26] describes a network in which a part of Facebook users follow each other. The Skitter network [24] is the undirected network of autonomous systems on the Internet connected to each other, as obtained from the Skitter project. Table 1 presents a clear representation of the imbalance of the network data and the impact of the network topology attributes on the network vulnerability.

The evaluation index used in this study is divided into two parts: one to evaluate the accuracy of the Linkboost algorithm in the link prediction task, and the other to evaluate the vulnerability of the network with different α and β values. In machine learning, the area under the curve (AUC) approach is generally used to evaluate the accuracy of classification for data with an imbalanced class distribution. The AUC index is more accurate than other predictive accuracy indicators such as the accuracy, recall, and precision.

After using the link prediction algorithm, the network is predicted with the added edges. Owing to the implementation of the effective high degree strategy, the network begins to collapse. To measure the vulnerability of the network after the attack, Xiao et al. [27] considered the largest component size during all possible baleful attacks and presented an evaluation metric $S(n)$:

$$
\begin{aligned}
S(n) &= \frac{V_S}{V}, \\
f &= \frac{n}{V}, \quad \text{when } S(n) = 0,
\end{aligned} \tag{4}
$$

where V is the number of nodes in a complex network, V_S is the largest component fraction after attacking$n$ nodes, and $S(n)$ reflects the degree of network destruction. A smaller $S(n)$ corresponds to a larger amount of network destroyed. The zero point (which refers to the point of complete collapse of the network) of $S(n)$ is denoted by the disintegration evaluation metric f, which represents the proportion of nodes that needs to be attacked.

4.3. Comparative Algorithm Theory. The Linkboost algorithm proposed in this paper mainly targets at the data with imbalanced class distribution, such as complex network node pairs. In order to study the accuracy and applicability of this algorithm, other existing algorithms are used for comparison.

AUC-logistic regression [28]: for training sets, $T = \{(i, j, z) \mid (i, j) \in E, (i, z) \notin E\}$. The optimization goals of the learning algorithm are

$$
\varphi_{\text{AUC–Logistic}} = \sum_{(i,j,z)\in T} \ell\left(x_i^T M x_j - x_i^T M x_Z\right), \tag{5}
$$

Table 1: Topology index of the four networks.

Network	$\|V\|$	$\|E\|$	$\langle k \rangle$	Cluster coefficient	Assortativity
ArXiv hep-th	27,770	352,807	25.41	0.12	−0.03
Cora network	23,166	91,500	7.90	0.12	−0.05
Facebook	46,952	876,993	37.35	0.09	0.22
Skitter	1,696,415	11,095,298	13.08	0.53	−0.08

where M is the feature matrix and $x_i$is the ith row of the adjacent matrix.

K-means undersampled [29]: in this algorithm, K-means algorithm is used to find the cluster center, and the data around the cluster center are undersampled. By reducing the majority of class samples, the positive and negative class distribution is balanced.

Entropy algorithm [30]: the algorithm proves the applicability of crossentropy to the distributed unbalanced data and uses the sorting of crossentropy to find the hidden edge:

$$\min_{M} L(M) = \lambda \Omega(M) + \sum_{q \in V} \varphi\left(S^{R}(M), R^{q}\right), \tag{6}$$

where $S^{q}(M)$ represents the independence between vectors in the feature matrix M, Ω represents the regularized parameters to prevent overfitting of the learning algorithm, P is crossentropy, and the function ϕ is

$$\varphi(S, R) = -\sum_{i=1}^{N-1} P_R(i) \log\left(P_s(i)\right). \tag{7}$$

RankSVM [31]: the training set $T = \{(i, j, z) \mid (i, j) \in E, (i, z) \notin E\}$. The optimization goals of the learning algorithm are

$$\varphi_{\mathrm{SVM}} = \sum_{(i,j,z) \in T} \max\left(0, 1 + x_i^T M x_z - x_i^T M x_j\right), \tag{8}$$

where M is the adjacent matrix and x_i is the ith row of the connection matrix.

Because the Linkboost algorithm is an improvement of the AdaBoost algorithm, we compare it with the original AdaBoost algorithm to demonstrate that the proposed technique is more suitable for the classification of imbalanced data.

4.4. Analysis of Experimental Results. Table 2 presents the performance of each algorithm on the AUC index. In general, the Linkboost algorithm achieves high prediction accuracy.

the prediction is completed, it is necessary to set the threshold to identify the number of edges added to the observed network E_O so that the high degree attack strategy can be developed on the basis of the network $E_O + E_P$. In the analysis described herein, we use different α and β to observe the change in the network vulnerability index f and determine the optimal edge addition proportion $\beta*$, which makes the network most prone to collapse. Specifically, we perform testing on the ArXiv hep-th network, as shown in Figure 4.

As shown in Figure 4, the red dashed lines represent the proportion of the attacking nodes when the network totally collapses with complete information. The blue lines represent the proportion of the attacking nodes when the network totally collapses with the additional predicted information. Figure 4(a) illustrates a unique phenomenon involving 10% covered edges. After different proportions β of edges are added through link prediction, the network crashes faster than in the case of an attack with complete information. This finding is in contrast to an intuitive sense that decisions made with incomplete information should be less accurate than those made with complete information.

To further evaluate this unexpected phenomenon, we examined the vulnerability index f of the network under different parameter combinations (α, β), and the results are shown in Figure 5. It can be seen that when the network has a few missing edges, adding the edges appropriately can accelerate the network collapse. When β is more than a certain threshold, the efficiency of the network disintegration roughly increases as β increases. The thresholds differ from each other as the missing link proportion α changes.

To illustrate the influence of α on the network vulnerability, we control the ratio of α and change the attack node proportion. Four scenarios are considered: (1) $\alpha = 0.1$; (2) $\alpha = 0.2$; (3) $\alpha = 0.5$; and (4)$\alpha = 0.7$, where $\beta = \beta*$. By adopting the high degree node attacking strategy, the vulnerability of the original networks is calculated after each attack. Subsequently, the network vulnerability evaluation metric is calculated. Figure 6 shows the simulation results for the four scenarios in the route views network, which has relatively few nodes (6747 nodes) for convenient calculation. It can be seen that when $\alpha = 0.1, 0.2, 0.5$, the attack strategy after link prediction is more effective than a direct attack (marked as green areas). In particular, when $\alpha = 0.1$, the high degree attack strategy after link prediction outperforms the degree attack strategy with complete information.

To examine whether this phenomenon is also applicable to other networks, we performed research considered four large networks. A total of 10% of the edges in the network were hidden randomly, yielding $\alpha = 0.1$. Next, we observed the change in the vulnerability index f under different β. According to Figure 7, in the ArXiv hep-th, Cora citation, and Skitter network, the high degree attack strategy based on the repaired network is better than that with complete information. However, in the Facebook network, regardless of the number of links added, the high degree attack strategy under complete information is always the optimal choice.

This phenomenon can be explained as follows. For many real-world information networks, owing to privacy or legal restrictions, the problem of data sparsity exists in the

Table 2: Comparison of link prediction results.

AUC	AUC-logistic	K-means undersampled	Entropy	RankSVM	Adaboost	Linkboost
ArXiv hep-th	0.9098	0.6502	0.8239	0.8412	0.7715	**0.9122**
Cora citation	0.9397	0.7201	0.9066	0.8239	0.8024	**0.9401**
Facebook	0.8510	0.7701	0.7923	0.6248	0.8122	**0.8517**
Skitter	0.8760	0.7245	0.7966	0.8539	0.8038	**0.8839**

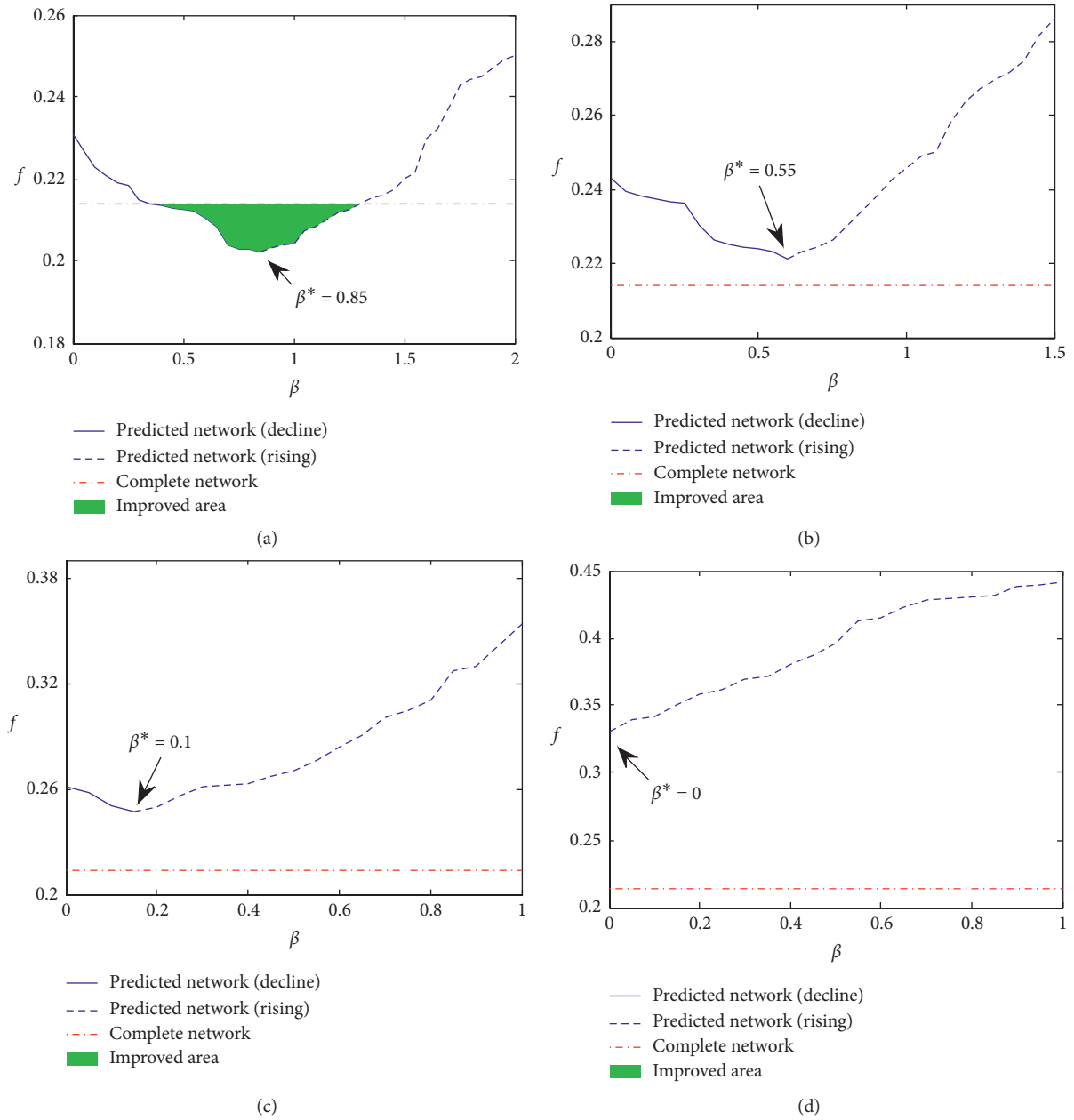

Figure 4: Disintegration evaluation metric as a function of the additional link information ratio with regard to the complete and predicted networks. (a) $\alpha = 0.1$. (b) $\alpha = 0.3$. (c) $\alpha = 0.5$. (d) $\alpha = 0.7$.

network structure [32]. In other words, implicit connections exist in the network, which makes it difficult to evaluate the importance of the nodes that are not explicitly connected [33]. Consequently, Linkboost is designed to clarify the implicit structure as much as possible, which provides valuable guidance for the design of a more effective attack strategy.

To verify this aspect, we repeated the previous test on a complete network. In contrast from the last experiment, the role of link prediction was not to reveal the edges selected to

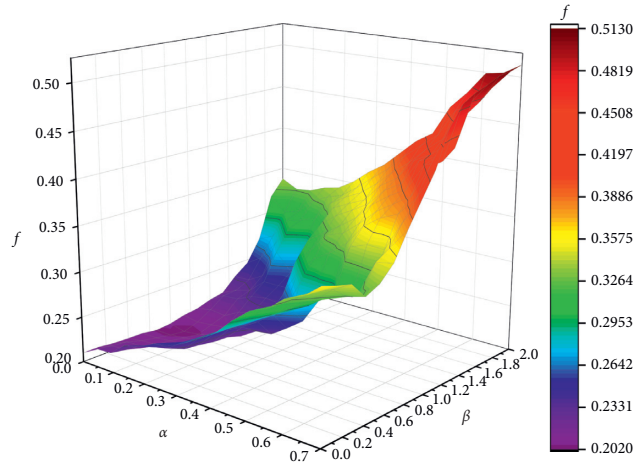

Figure 5: Disintegration evaluation metric f as a function of the proportion of missing links and ratio of the additional link information.

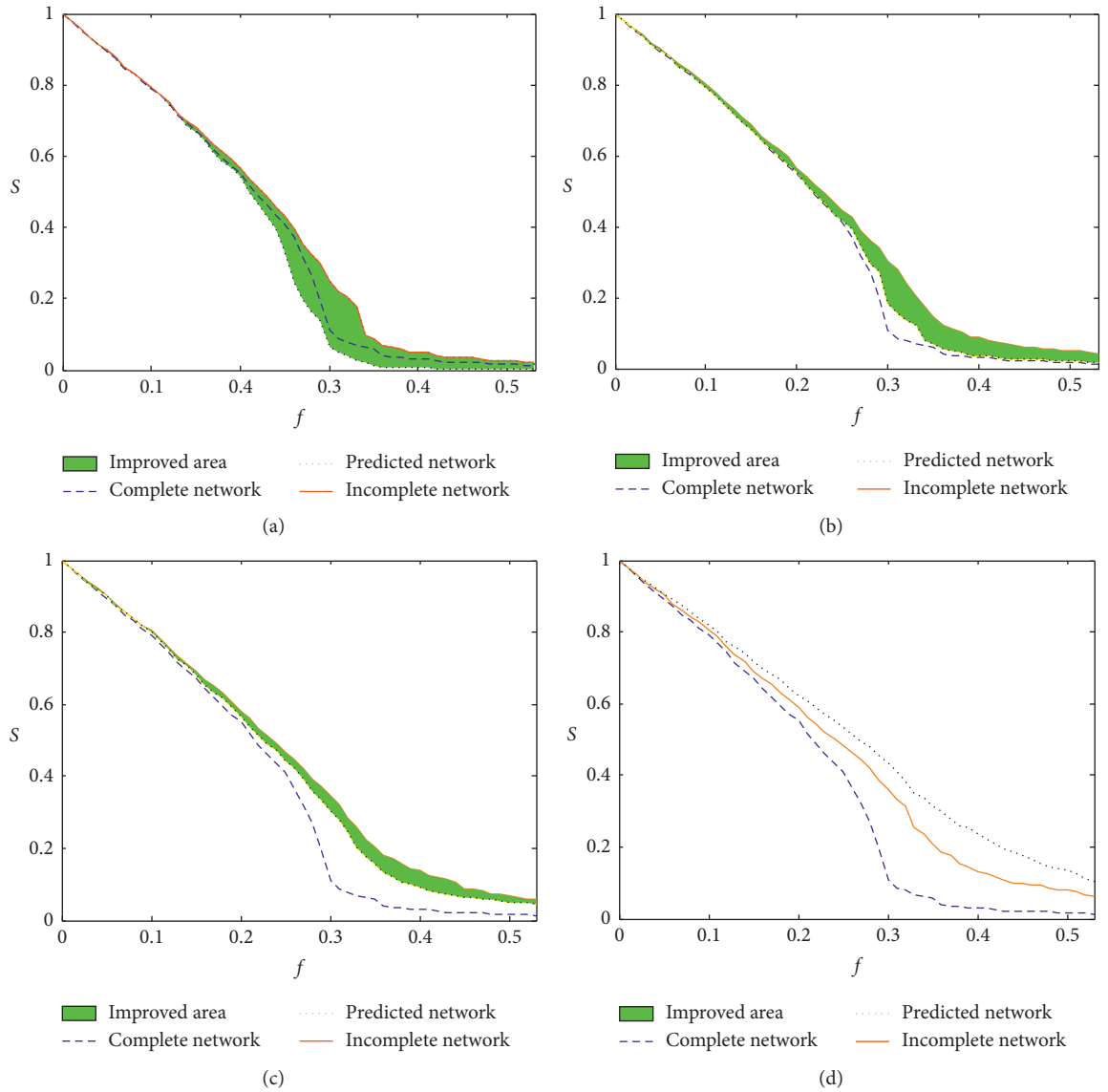

Figure 6: Size of the giant component versus the proportion of attacked nodes with regard to the incomplete, complete, and predicted networks. (a) $\alpha = 0.1$. (b) $\alpha = 0.3$. (c) $\alpha = 0.5$. (d) $\alpha = 0.7$.

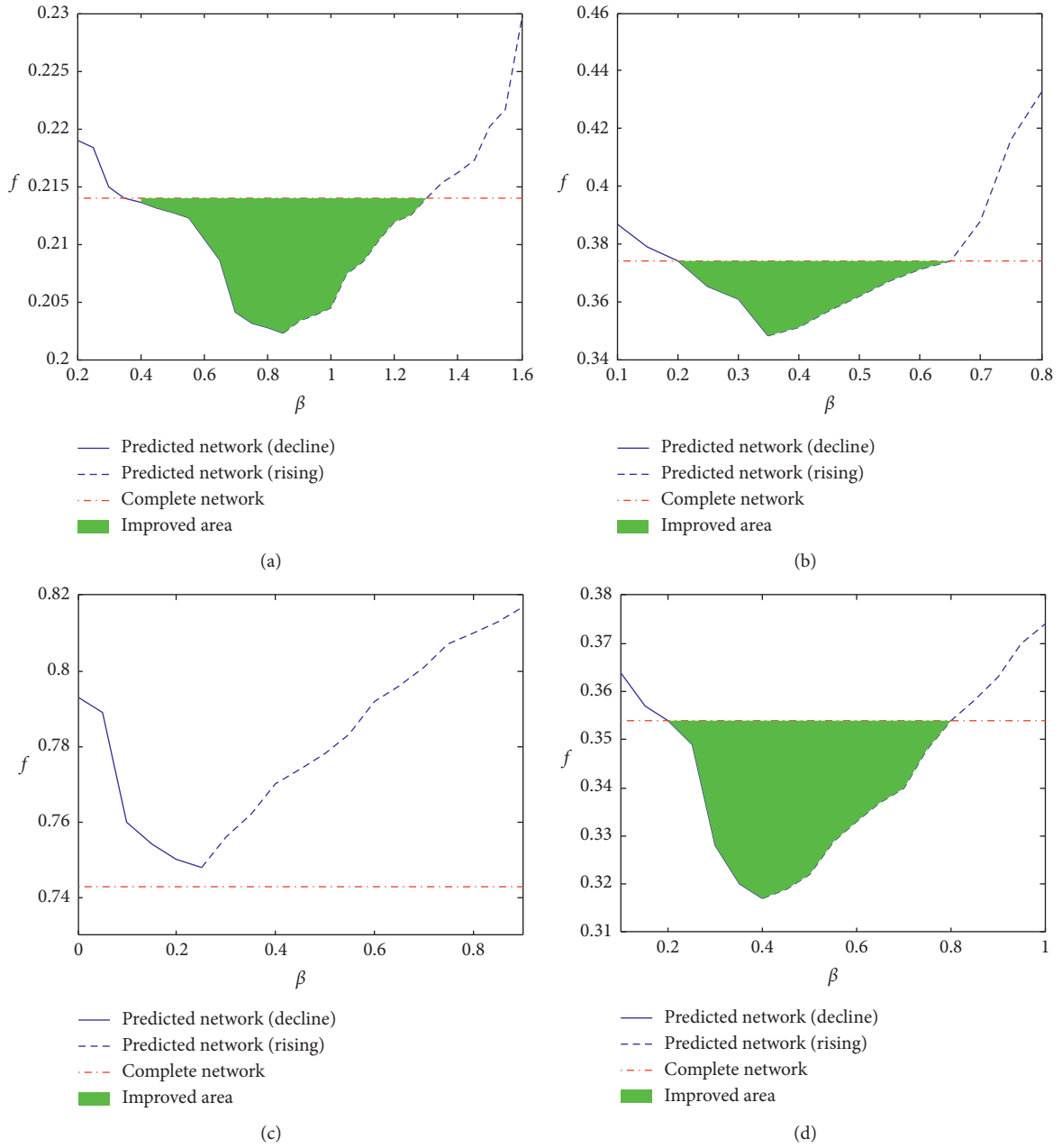

FIGURE 7: Disintegration evaluation metric as a function of the ratio of additional link information in four real networks when the proportion of the missing links is small ($\alpha = 0.1$). (a) ArXiv hep-th network. (b) Cora citation network. (c) Facebook network. (d) Skitter network.

be hidden but to add implicit edges to assist in formulating attack strategies. Consequently, we set $\alpha = 0$ and varied β. Similar to the last experiment, the high degree node attacking strategy was adopted, and f was calculated after each attack.

Figure 8 shows that the attack strategy after link prediction still outperforms the direct attack even in a complete network. The exception to this rule is the Facebook network, in which after $\beta > 0$, f increases with the increase in β, as shown in Figure 8(c). In a sense, this example illustrates that Linkboost does not provide effective guidance for the attack strategy of the Facebook network. This exception can be explained by the network topologies listed in Table 1. In contrast to that of other three networks, the assortativity index of the Facebook network is positive (0.22), indicating that the high degree nodes tend to connect with other large degree nodes in the network. Furthermore, this trend indicates that the implicit edge in the network may exist in the node pairs with a high degree. However, Linkboost prioritizes the classification accuracy of the minority samples, which makes it difficult to predict the connection between the large degree nodes. This aspect explains why Linkboost cannot effectively develop an effective attack strategy on a network with positive assortativity, such as the Facebook network.

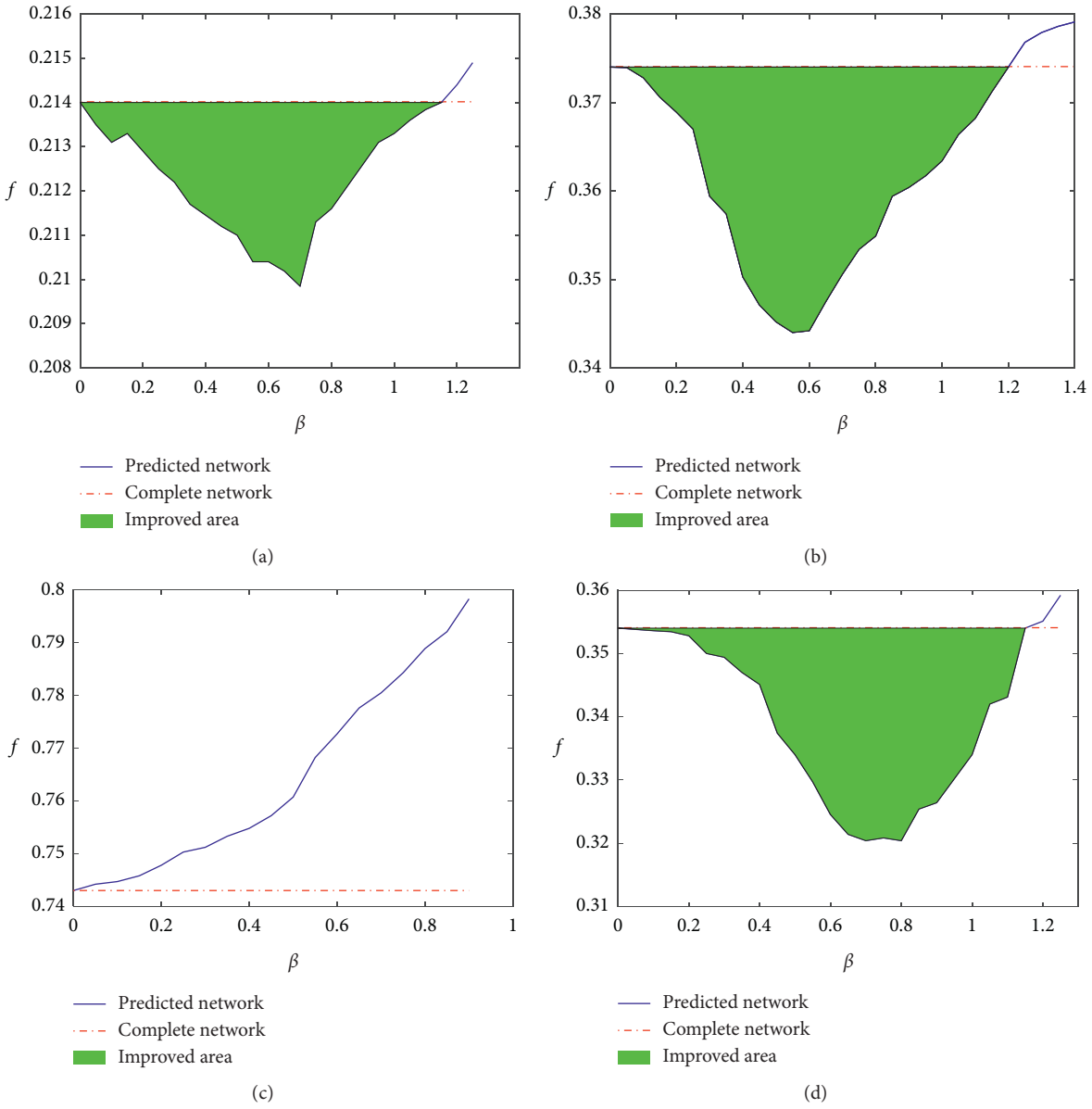

FIGURE 8: Disintegration evaluation metric as a function of the ratio of additional link information in four real networks with no missing links ($\alpha = 0$). Linkboost is applied on these four complete networks to reveal the implicit links to help design a more effective attack strategy. (a) ArXiv hep-th network. (b) Cora citation network. (c) Facebook network. (d) Skitter network.

5. Conclusions

This paper proposes a novel link prediction algorithm Linkboost, considering the imbalanced class distribution of network data. This method is conducive to the development of an attack strategy when the complete information of network cannot be obtained directly. The algorithm can be applied to different real networks, and it can help discover valuable linking information to conduct a network vulnerability investigation. To solve the problem of classification with imbalanced data, Linkboost changes the manner of updating the sampling weight adaptively when constructing the subclassifiers. The convergence of the algorithm was demonstrated by analyzing the upper bound of the loss function. Finally, we verified the effectiveness of the algorithm using four actual networks with different parameters. Linkboost achieved the best performance compared to that of other imbalanced classification algorithms. When using the complemented network, the developed attack strategy is more effective in accelerating the network collapse, which is more advantageous than a direct attack. Consequently, the proposed algorithm provides more sophisticated insights into incomplete information and helps restore the information of the network, which facilitates the identification of crucial nodes for network survivability.

Data Availability

The network data and part of codes used to support the findings of this study have been deposited in the Github (https://github.com/jisokjisok/link_prediction_dissertation/tree/master/get_data/network_data).

Conflicts of Interest

The authors declare that they have no conflicts of interest.

Acknowledgments

This research was supported by the National Natural Science Foundation of China under Grant nos. 51679182 and 71874132.

References

[1] X. Fu, H. Yao, and Y. Yang, "Exploring the invulnerability of wireless sensor networks against cascading failures," *Information Sciences*, vol. 491, pp. 289–305, 2019.

[2] D. Chao, Y. Hong, J. Du, X. Peng, Z. Wang, and J. Zhao, "Cascading failure in interconnected weighted networks based on the state of link," *International Journal of Modern Physics C*, vol. 28, no. 3, pp. 1703–1705, 2017.

[3] R. Jacob, K. P. Harikrishnan, R. Misra, and G. Ambika, "Measure for degree heterogeneity in complex networks and its application to recurrence network analysis," *Royal Society Open Science*, vol. 4, no. 1, p. 160757, 2017.

[4] P. Holme, B. J. Kim, C. N. Yoon et al., "Attack vulnerability of complex networks," *Physical Review E Statistical Nonlinear & Soft Matter Physics*, vol. 65, no. 2, Article ID 056109, 2002.

[5] Y. Chen, G. Paul, S. Havlin et al., "Finding a better immunization strategy," *Physical Review Letters*, vol. 101, no. 5, Article ID 058701, 2008.

[6] X. Hu, G. Wang, and R. Ma, "Complex network vulnerability based on dynamic Bayesian network," *Fire Control and Command Control*, vol. 41, no. 3, pp. 29–35, 2017.

[7] C. C. Yang, N. Liu, and M. Sageman, "Analyzing the terrorist social networks with visualization tools," *Intelligence and Security Informatics*, vol. 3975, pp. 331–342, 2006.

[8] Z. Pei, Y. Zhou, N. A. Chen, L. Liu, and Q. Wang, "Critical public opinion location and intelligence theme clustering strategy-based biological virus event detection and tracking model," *International Journal of Wireless and Mobile Computing*, vol. 9, no. 2, pp. 192–198, 2015.

[9] X. Tian and C. Zhang, "Survivability model of equipment support network based on incomplete information," *Systems Engineering-Theory & Practice*, vol. 37, no. 3, pp. 790–798, 2017.

[10] R. Lichtnwalter and N. V. Chawla, "Link prediction: fair and effective evaluation," in *Proceedings of the 2012 IEEE/ACM International Conference on Advances in Social Networks Analysis and Mining*, Istanbul, Turkey, August 2012.

[11] J. J. Carbajal-Hernández, L. P. Sánchez-Fernández, I. Hernández-Bautista, J. D. J. Medel-Juárez, and L. A. Sánchez-Pérez, "Classification of unbalance and misalignment in induction motors using orbital analysis and associative memories," *Neurocomputing*, vol. 175, pp. 838–850, 2016.

[12] B. Schölkopf, J. Platt, and T. Hofmann, "AdaBoost is consistent," *Journal of Machine Learning Research*, vol. 8, no. 2, pp. 105–112, 2007.

[13] L. K. Gallos, P. Argyrakis, A. Bunde, R. Cohen, and S. Havlin, "Tolerance of scale-free networks: from friendly to intentional attack strategies," *Physica A: Statistical Mechanics and Its Applications*, vol. 344, no. 3-4, pp. 504–509, 2004.

[14] J. Wu, H. Z. Deng, Y. J. Tan, and D. Z. Zhu, "Vulnerability of complex networks under intentional attack with incomplete information," *Journal of Physics A: Mathematical and Theoretical*, vol. 40, no. 11, pp. 2665–2671, 2007.

[15] X. Liu and Z. Li, "Local load redistribution attacks in power systems with incomplete network information," *IEEE Transactions on Smart Grid*, vol. 5, no. 4, pp. 1665–1676, 2014.

[16] C. Hong, X. B. Cao, W. B. Du et al., "The effect of attack cost on network robustness," *Physica Scripta*, vol. 87, no. 5, Article ID 055801, 2013.

[17] B. Moradabadi and M. R. Meybodi, "Link prediction based on temporal similarity metrics using continuous action set learning automata," *Physica A: Statistical Mechanics and Its Applications*, vol. 460, pp. 361–373, 2016.

[18] Y. Yang, R. N. Lichtenwalter, and N. V. Chawla, "Evaluating link prediction methods," *Knowledge and Information Systems*, vol. 45, no. 3, pp. 751–782, 2015.

[19] M. Pavlov and R. Ichise, "Finding experts by link prediction in co-authorship networks," in *Proceedings of the International Conference on Finding Experts on the Web with Semantics. CEUR-WS.Org*, pp. 42–55, Busan, Korea, November 2007.

[20] H. Wang, J. Huang, X. Xu, and Y. Xiao, "Damage attack on complex networks," *Physica A: Statistical Mechanics and Its Applications*, vol. 408, no. 408, pp. 134–148, 2014.

[21] S. Brin and L. Page, "The anatomy of a large-scale hypertextual web search engine," in *Proceedings of the International Conference on World Wide Web*, Elsevier Science Publishers B. V., Brisbane, Australia, pp. 107–117, April 1998.

[22] J. Widom, "SimRank:a measure of structural-context similarity," in *Proceedings of the Eighth ACM SIGKDD International Conference on knowledge Discovery and Data Mining. ACM*, pp. 538–543, Edmonton, Canada, July 2002.

[23] A. N. Langville and C. D. Meyer, "Google's pagerank and beyond," *Mathematical Intelligencer*, vol. 30, no. 1, pp. 68-69, 2011.

[24] J. Leskovec, J. Kleinberg, and C. Faloutsos, "Graph evolution: densification and shrinking diameters," *ACM Trans. Knowledge Discovery from Data*, vol. 1, no. 1, pp. 1–40, 2007.

[25] L. Subelj and M. Bajec, "Model of complex networks based on citation dynamics," in *Proceedings of the 22nd International Conference on World Wide Web-WWW'13 Companion*, pp. 527–530, Rio de Janeiro, Brazil, May 2013.

[26] B. Viswanath, A. Mislove, M. Cha, P. Krishna, and Gummadi, "On the evolution of user interaction incomplete facebook," in *Proc. Workshop on Online Social Networks*, pp. 37–42, 2009.

[27] Y.-D. Xiao, S.-Y. Lao, L.-l. Hou, and L. Bai, "Mitigation of malicious attacks on network observation," *International Journal of Modern Physics C*, vol. 26, no. 10, Article ID 1550108, 2015.

[28] A. K. Menon and C. Elkan, "Link prediction via matrix factorization," in *Proceedings of the European Conference on Machine Learning and Knowledge Discovery in Databases*, pp. 437–452, Springer-Verlag, Athens, Greece, September 2011.

[29] N. S. Kumar, K. N. Rao, A. Govardhan, K. S. Reddy, and A. M. Mahmood, "Undersampled *K*-means approach for handling imbalanced distributed data," *Progress in Artificial Intelligence*, vol. 3, no. 1, pp. 29–38, 2014.

[30] B. Li, S. Chaudhuri, and A. Tewari, "Handling class imbalance in link prediction using learning to rank techniques," 2016, https://arxiv.org/abs/1511.04383.

[31] M. Yazdani, R. Collobert, and A. Popescubelis, "Learning to rank on network data," *International Journal of Information Management*, vol. 6, no. 3, pp. 187-188, 2017.

[32] Z. Daokun, Y. Jie, Z. Xingquan et al., "Network representation learning: a survey," *IEEE Transactions on Big Data*, vol. 6, no. 1, pp. 3–28, 2018.

[33] M. Li, R. Zheng, H. Zhang et al., "Effective identification of essential proteins based on prior knowledge, network topology and gene expressions," *Methods*, vol. 67, no. 3, 2014.

Hindawi
Complexity
Volume 2020, Article ID 4825767, 10 pages
https://doi.org/10.1155/2020/4825767

Research Article

Convolutional Neural Network for Seizure Detection of Nocturnal Frontal Lobe Epilepsy

Fabio Pisano,[1] **Giuliana Sias**,[1] **Alessandra Fanni**,[1] **Barbara Cannas**,[1] **António Dourado**,[2] **Barbara Pisano**,[1] **and Cesar A. Teixeira**[2]

[1]*Department of Electrical and Electronic Engineering, University of Cagliari, Cagliari 09123, Italy*
[2]*Univ Coimbra, CISUC-Center for Informatics and Systems of the University of Coimbra, Department of Informatics Engineering, Coimbra, Portugal*

Correspondence should be addressed to Fabio Pisano; fabio.pisano@diee.unica.it

Received 9 September 2019; Accepted 22 February 2020; Published 31 March 2020

Guest Editor: Murari Andrea

The Nocturnal Frontal Lobe Epilepsy (NFLE) is a form of epilepsy in which seizures occur predominantly during sleep. In other forms of epilepsy, the commonly used clinical approach mainly involves manual inspection of encephalography (EEG) signals, a laborious and time-consuming process which often requires the contribution of more than one experienced neurologist. In the last decades, numerous approaches to automate this detection have been proposed and, more recently, machine learning has shown very promising performance. In this paper, an original Convolutional Neural Network (CNN) architecture is proposed to develop patient-specific seizure detection models for three patients affected by NFLE. The performances, in terms of accuracy, sensitivity, and specificity, exceed by several percentage points those in the most recent literature. The capability of the patient-specific models has been also tested to compare the obtained seizure onset times with those provided by the neurologists, with encouraging results. Moreover, the same CNN architecture has been used to develop a cross-patient seizure detection system, resorting to the transfer-learning paradigm. Starting from a patient-specific model, few data from a new patient are enough to customize his model. This contribution aims to alleviate the task of neurologists, who may have a robust indication to corroborate their clinical conclusions.

1. Introduction

Nocturnal frontal lobe epilepsy (NFLE) is a rare form of epilepsy, typically inherited, which affects both sexes from 1 to 60 years, and is associated with cognitive decline. Crises are characterized by frequent and brief hypermotor sleep seizures, which may range from a simple awakening from sleep to more focused motor movements, with dystonic and tonic postures, grimaces, screams or groans, episodic nocturnal wanderings, and stereotyped agitated somnambulism, among others [1, 2]. In this paper, the problem of detecting NFLE seizures, using Electroencephalographic (EEG) signals as inputs to an original Convolutional Neural Network (CNN) prediction model, is addressed.

The use of EEG signals is corroborated by most of the literature on epileptic seizure detection, which considers indeed the EEG the gold standard to analyse the electrical activity of the brain [3].

In the literature, there is a wide range of proposals for the identification of general epileptic seizures [4–13], mostly based on the machine-learning approach, which support the doctors in the time-consuming manual labelling [4]. However, very few contributions specifically dealing with NFLE are present, and they reach lower performance indices. In [14], a detection system for NFLE seizures has been proposed, which is based on accelerometer signals, obtaining a value of sensitivity of 91.67% and specificity of 84.19% on three pediatric patients. The accelerometers were already proposed in [15, 16] to detect epileptic seizures with pros and cons; even if they are more comfortable to wear, they can only reveal seizures associated to motor activity. Moreover, high false-positive rates are often possible due to motion

artifacts that cannot be readily distinguished from convulsions. In [17], a machine-learning technique has been proposed to classify NFLE seizures and nonseizures using the C4/A1 EEG channel (according to the International 10–20 System [18]), which is one of the monopolar derivations currently used for the conventional sleep staging and arousal scoring [19], obtaining a value of specificity of 82.4%. In [20], the Self-Organizing Maps (SOMs) are used to develop patient-specific seizure detection systems for NFLE. The proposed method allows the construction of maps that contain important information on the current brain state, showing the potential of the map to correctly cluster data from seizure and nonseizure patterns. In addition, it also suggests the use of SOMs for early crisis detection by projecting the EEG trace onto it. Following the trajectory of this projection on the map, it is possible to activate an alarm depending on the composition of the cluster where the current EEG sample is projected. The method has been tested on nine patients obtaining a mean value of sensitivity equal to 80.5% and a mean value of specificity equal to 90.2%.

Despite these quite good results, the cited literature shows that the feature engineering phase is crucial for the success of the machine-learning predictive models and the identification of proper seizure indicators is a preliminary due diligence. In fact, it highly influences the performance of the classifier and it is often conditioned to a specific knowledge and competencies on the pathophysiology under study. Moreover, extracting features is usually carried out by hand and it is very time consuming, requiring a high number of scenarios simulations in order to choose the best combination of features. To avoid this challenging phase, in the present paper, CNNs have been used. In fact, CNNs are able to automatically learn relevant low-dimensional features from high-dimensional data by successively applying convolutional and downsampling operations.

CNNs, which belong to the so-called deep neural networks [21–23], are now affirming themselves for the automated detection of epileptic seizures from EEG signals. In [24], Acharya et al. proposed a one-dimensional (1-D) CNN with 13 layers: 5 convolutional layers, 5 max-pooling layers, and 3 fully connected layers. The CNN has been trained to classify EEG epochs in three classes: normal, preictal, and seizure. Using 100 single channel EEG traces of five patients from the Bonn EEG database [25], an accuracy of 88.67%, a sensitivity of 95%, and a specificity of 90% are obtained with a ten-fold crossvalidation. Even if the results are promising, comparison with the literature on the same database revealed that the proposed detection system could be improved provided that more EEG data are available. In [26], Ullah et al. proposed an ensemble of pyramidal 1-D CNNs (P-1D-CNN) to solve the same three classes' detection problem addressed in [24] on the same University of Bonn database. Each P-1D-CNN has three convolutional layers and two fully connected layers. Several simulations have been performed to select the best model parameters. In order to overcome the lack of data, already highlighted in [24], two data augmentation schemes have been introduced. A majority voting strategy has been adopted to fuse the decisions of the ensemble of CNNs, reaching an average accuracy of 96.1%. In [27], the authors exploited the attitude of the CNNs to process images, rather than 0-D temporal sequences. For this purpose, the raw EEG multichannels data have been firstly filtered, then segmented using a prefixed time window, and finally converted into a series of EEG-plot images. The proposed CNN, which is based on the VGG-16 architecture of [28], has been trained to classify each image into seizure or nonseizure class. The results, presented in terms of median true positive rate labelling by seconds is 74%, which the authors claimed to be higher than that of commercially available seizure detection software. In [29], each single-channel EEG signal is converted into a 2D plot and the plots corresponding to 22 different EEG channels are combined in 3D images depending on the mutual correlation of the intensities between the electrodes. Then, using 3D kernels, a 3D CNN, with 4 convolutional layers, 3 max pooling layers, and 2 fully connected layers, has been built to detect interictal, preictal, and ictal stages in 13 epileptic patients. An accuracy of 90%, a sensitivity of 88.9%, and a specificity of 93.8% is obtained using a ten-fold cross-validation procedure.

As shown in the cited references, training CNN models requires a huge amount of EEG records manually labelled by skilled neurologists, which may be a tedious and time-consuming task. Hence, as highlighted by most of the authors, the major issues limiting the performance of these deep-learning seizure detection methods are the amount of training data, which may not be enough, and the feature space of seizures, which may vary significantly across different patient EEG recordings and even for the same patient. To overcome these limitations, in the present paper, a transfer-learning strategy, which can significantly reduce the quantity of data needed for training, is adopted. A survey on the transfer learning is reported in [30], where it is defined as "the ability of a system to recognize and apply knowledge and skills learned in previous tasks to novel tasks." Transfer learning proved to be particularly useful in training deep neural networks that can share some lower layers of a network previously trained with data from other tasks, while the upper layers are retrained and fine-tuned using task-dependent data [31]. Transfer-learning techniques are still largely unexplored although they seem to have a great potential to overcome the issue of lack of data available for epileptic seizure detection.

In the present paper, the CNNs have been firstly used to build patient-specific seizure detection systems for three patients affected by NFLE. The detection problem has been modelled as a seizure and nonseizure classification problem, obtaining performances that overcome those of other methods presented in [20] for the same patients. The patient-specific CNN model has been used also to find the seizure onset, limiting the time-consuming manual labelling for doctors. Then, a transfer-learning technique has been adopted, allowing to fine tune one of the CNN models, trained with data from one patient, to obtain a detection predictor for a different patient. The results obtained in the present work indicate that even just a seizure is enough to customize the CNN to the new patient.

The rest of this paper is organized as follows. The database used, the data augmentation schema, and CNN model architecture are discussed in Section 2. Section 3 presents and discusses the results obtained by the patient-specific and the cross-patient detection systems. Section 4 concludes the findings of the study.

2. Materials and Methods

A combination of deep learning and transfer learning has been used to build patient-specific and cross-patient seizure detection systems. The detection problem has been formalized as a two-class classification problem, where the two classes correspond to seizure (SZ) or nonseizure (NS) states during the sleep and has been approached by training Convolutional Neural Network models with long-term EEG recordings including epileptic seizures.

2.1. Dataset. Data for this study comes from two epilepsy centers: Unidade de Monitorização em Epilepsia e Sono do Centro Hospitalar e Universitário de Coimbra, Portugal, Epilepsiezentrum, Universitätsklinikum Freiburg, Germany, on behalf of the EPILEPSIAE project [32]. The data concern three patients affected by nocturnal seizures located in the frontal lobe (NFLE). The same patients have been considered also in [20], and the subject numbers refer to those in Table 1 of [20]. The relevant information on the patients enrolled in this study is summarized in Table 1.

The initial and final time of a seizure (SZ) have been identified based on the agreement between at least two expert neurologists. For the nonseizure recordings, no information is available about the patient sleeping or awake state. As in [20], also in the present study, it has been hypothesized that the patients were sleeping in the ten minutes preceding a seizure and these ten minutes are considered to characterize a nonseizure state (NS).

The dataset includes eleven scalp EEG channels, placed according to the International 10–20 System [33] with a sampling rate of 256 Hz. According to the neurologists' suggestions, the eleven selected channels, coloured in blue in Figure 1, are those more suitable for the NFLE seizure detection: three central channels (C3, C4, and Cz), two frontal channels (F3 and F4), two frontal-polar channels (Fp1 and Fp2), two parietal channels (P3 and P4), and two occipital channels (O1 and O2). All the channels are unipolar derivations with a common reference electrode.

2.2. EEG Segmentation and Data Augmentation. Data, coming from the continuous 11 recordings, each one corresponding to an EEG channel, have been segmented using an overlapping sliding window of 5 seconds. In this way, each time window, or *segment*, has 1280 data points in the 11D space. The data segmentation allows to increase the number of training samples, which is mandatory, especially in deep learning [26, 29]. For the training of the network, the data from seizures were segmented with an overlap with the previous window of 0.1484 s, 0.5508 s, 1 s, for patient #5, patient #6, and patient #9, respectively. The overlap times during seizures for the three patients have been differently chosen in order to reduce the class unbalance due to different total seizure times (see Table 1). As the mean seizure time is about 10% of the nonseizure recordings, the length of the nonseizure segments is still equal to 5 seconds without overlapping, whereas, for the seizure segments, the overlap time has been dynamically set to produce a balanced number of segments within the two classes. This operation can produce windows with very similar data, so with few novelties for the CNN training; however, in our opinion, it seems to be the most effective way to balance the classes while maintaining a high quantity of data for deep learning. During testing, a sliding window of 5 s with an overlap of 1 second, for all patients and both phases (seizure/nonseizure), has been used.

In order to improve the quality of the raw EEG signals, a preprocessing step has been performed. After discarding the windows with missing data, a standard thresholding of potential values has been performed. Here, data have been labelled as artifacts if the absolute value of any data point in the trial exceeded a fixed threshold. This method is currently the most widely used artifact detection method in the EEG community. It is most effective for detecting gross eye blinks or eye movement artifacts. Since even a small number of these extreme values can lead to inaccurate results, the segments including these extreme values have been discarded. Furthermore, filtering has been a necessary step due to the presence of 50 Hz line noise and DC offset (removal of the 0 Hz). Thus, a Notch filter at 50 Hz with bandwidth 1 Hz has been applied to remove 50 Hz line noise, and the average value of each electrode along the preseizure phase has been removed as DC offset. The cleaned dataset for each patient has been then partitioned, in order to randomly assign the different seizures to the training, validation, and test sets.

2.3. CNN Architecture. For the development of the CNN architecture, the deep residual network (ResNet) structure [34] has been adapted for the problem of seizure detection. The CNN architecture is shown in Figure 2.

A first convolutional unit (CU_0), made up of three layers, transforms the input image of size 1280×11 into a 4-channels image of size 320×11. The responsible of the size reduction is the convolutional layer, having filters of size 5×1 and stride 4×1. A max pooling layer (MP), with pool size 5×1 and stride 4×1, follows the first convolutional unit, reducing again the image dimension to a 4-channel image of size 80×11. A second convolutional unit (CU_1) made up of seven layers filters the 4-channel image of size 80×11 by means of a residual connection. Two following convolutional units (CU_2 and CU_3), each one made up of nine layers, filter out the 4-channel image of size 80×11 by means of a residual connection, reducing the image dimension first to a 16-channel image of size 20×11 and then to a 64-channel image of size 5×11. An average pooling layer (AP), with pool size 5×1, reduces the image dimension to a 64-channel image of size 1×11, producing a set of 704 features. Finally, a fully connected layer (FC) processes the 704 features, output

Table 1: Patients from European epilepsy database.

Patient	Sex	# of SZ	SZ time (mean) (s)	Total SZ time (s)	Total record time (s)	Epilepsy center
Pat #5	M	5	38.00	190.00	3190.00	Coimbra
Pat #6	F	8	89.66	717.29	5517.29	Freiburg
Pat #9	M	15	84.38	1265.75	10265.75	Freiburg

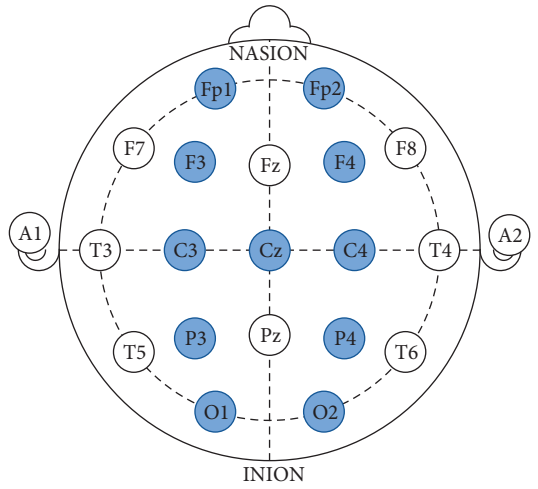

Figure 1: The International 10–20 System [33] with the 11 selected channels (in blue).

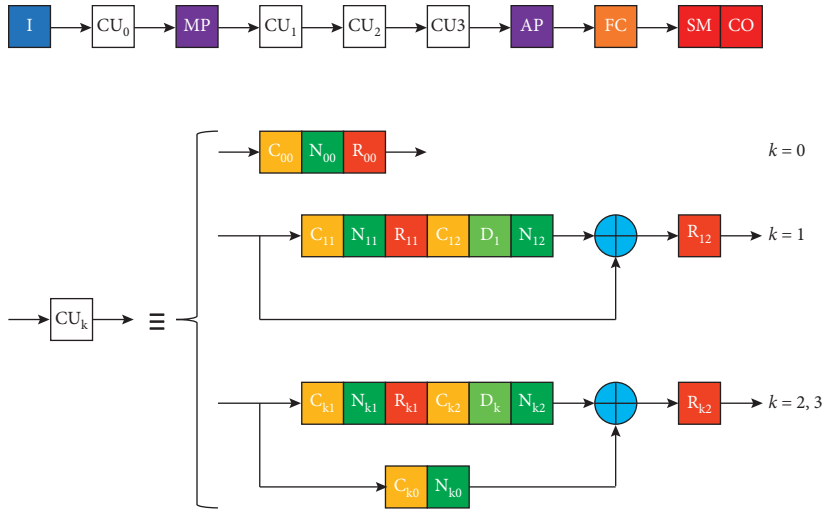

Figure 2: CNN architecture, where I is the image input layer; CU_k is the k^{th} convolutional unit; MP and AP are the max pooling and average pooling layers, respectively; FC is the fully connected layer; and SM and CO are the SoftMax and classification output layer, respectively. In the k^{th} convolutional unit, C_{kj}, N_{kj}, R_{kj}, and D_k are the j^{th} convolutional layer, the j^{th} batch normalization layer, the j^{th} ReLu layer, and the dropout layer, respectively.

of the average pooling layer, and feeds a SoftMax layer (SM) for classification (CO).

In this architecture, each channel of the input image is filtered separately, obtaining a set of 64 features per electrode. Features coming from different electrodes are combined in the fully connected layer, i.e., only after the convolutional units, for classification.

Dropout layers with dropout probability of 20% have been included inside CU_1, CU_2, and CU_3 convolutional units in order to reduce overfitting on the training set and improve generalization. The algorithm used to train the network is the stochastic gradient descent with momentum [35].

3. Results and Discussion

The performance of the deep models has been evaluated using some metrics employed in most of the literature on epilepsy and, in general, in classification by machine learning, such as Accuracy, Specificity, Sensitivity, and Gmean:

$$\text{Accuracy (AC)} = \frac{\text{TP} + \text{TN}}{\text{TP} + \text{TN} + \text{FP} + \text{FN}},$$
$$\text{Specificity (SP)} = \frac{\text{TN}}{\text{TN} + \text{FP}},$$
$$\text{Sensitivity (SS)} = \frac{\text{TP}}{\text{TP} + \text{FN}},$$
$$\text{Gmean} = \sqrt{\text{Specificity} \times \text{Sensitivity}}, \quad (1)$$

where TP (True Positives) are the seizure patterns (SZ) correctly classified, TN (True Negatives) are the nonseizure patterns (NS) correctly classified, FP (False Positives) are the nonseizure patterns classified as seizure patterns, and FN (False Negatives) are the seizure patterns classified as nonseizure patterns.

3.1. Patient-Specific Seizure Detection. Firstly, patient-specific seizure detection systems have been developed for each of the three patients. Table 2 reports the number of seizures and the number of segments used for training, validating, and testing. MATLAB R2018b deep-learning library has been used to develop the CNN models. To train the models an Intel® Core™ i7 CPU with 16 GB memory has been used, with the help of a Nvidia GeForce GTX 960M with 4 GB memory.

As an example, Figure 3 shows the performance for patient #9, in terms of accuracy on training, validation, and test sets, against training epochs. The training procedure continues epoch after epoch only if the validation performance increases with respect to the previous epoch. If not, the training is interrupted. This very strong constraint helps avoiding overfitting on the training set, which would occur if the usual crossvalidation procedure is adopted, due to the big size of the network. As shown in Figure 3, for patient #9, the training has been stopped at the 8^{th} epoch since no better performance has been obtained on the validation set. The training time of the patient-specific models range from approximately 1 hour to 5 hours depending on the seizures in the training and validation sets.

Table 3 reports the performance in terms of Accuracy, Specificity, and Sensitivity for the three patients.

Values greater than 94% have been achieved for all the performance indices of all the patients with mean values higher than 93%, except for sensitivity related to patient #9 which is equal to 83.94%. From Table 3, it can be seen that patient #6 presents very high values for all the indices, reaching even 100% of specificity. Patient #5 still has quite high-performance values, even if it is less than the previous case, due to relatively low value of specificity, whereas patient #9 presents an opposite behaviour with a high value of specificity and the lowest value of sensitivity, showing that EEG features vary from one patient to the other.

For each patient, the obtained results, in terms of geometric mean of specificity and sensitivity (Gmean), have been compared with those in [20], where SOM and SVM have been used as classifiers. This last method is widely used in epileptic seizure detection systems [4, 36]. The results reported in Table 4 show that CNN improves the performance of both the methods by several percentage points.

These patient-specific models can be used to support the neurologists in the time-consuming identification of the seizure onset time. In particular, during the evolution of the EEG recordings, the condition derived from the CNN model is used to trigger the alarm (i.e., the seizure onset) when the sliding window is classified as SZ for at least d consecutive seconds. The assertion time d has been optimized on the same set used to train the model. As an example, Table 5 reports the difference Δt in seconds between the alarm time given by the algorithm (t_{alarm}) and the seizure onset time provided by the neurologists (t_{SZ}) for the EEG recordings of the patient #9. As it can be noted, in 87% of cases, the alarm time differs from the seizure onset time by less than 10 s. In the other two cases, this difference is at most 17 s. Figure 4 reports the cumulative alarm time

Table 2: Dataset composition for training, validation, and test.

Patient	# of SZ	# of SZ train	# of SZ valid	# of SZ test	# of segment train	# of segment valid	# of segment test
Pat #5	5	3	1	1	1205	421	645
Pat #6	8	4	2	2	1193	710	1319
Pat #9	15	7	3	5	1009	486	3313

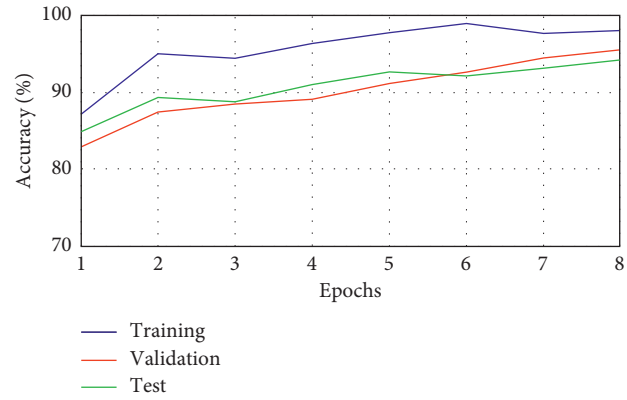

Figure 3: Accuracy on training, validation, and test set for patient #9 against training epochs.

Table 3: Test performance (%) of the patient-specific models.

Patient	Pat #5	Pat #6	Pat #9	Mean values
Accuracy	94.42	99.77	94.99	96.39
Specificity	94.12	100	96.32	96.81
Sensitivity	98.00	97.67	83.94	93.20

Table 4: Comparison of Gmean (%) with some state-of-the-art techniques.

Method	SOM	SVM	CNN
Pat #5	86.02	87.05	96.04
Pat #6	90.57	89.84	98.83
Pat #9	82.92	82.13	89.92

Table 5: Difference Δt (s) between the alarm time given by CNN and the seizure onset time provided by the neurologists for the three patients.

SZ #	1	2	3	4	5	6	7	8	9	10	11	12	13	14	15
Δt (s)	−4	−2	17	−3	−7	14	1	−3	10	0	5	−3	−1	−5	0

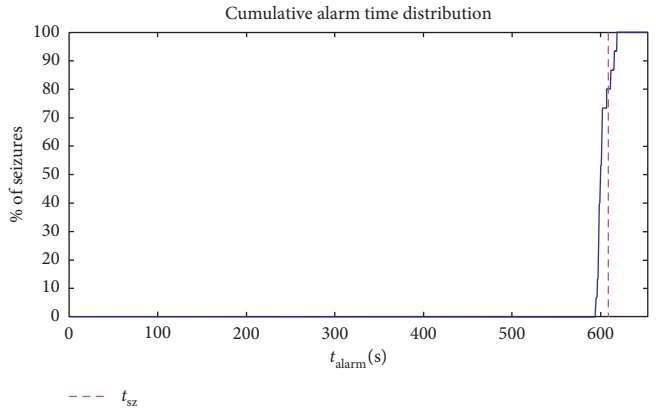

Figure 4: Cumulative alarm time distribution for patient #9. The dashed vertical line refers to the seizure onset time provided by the neurologists.

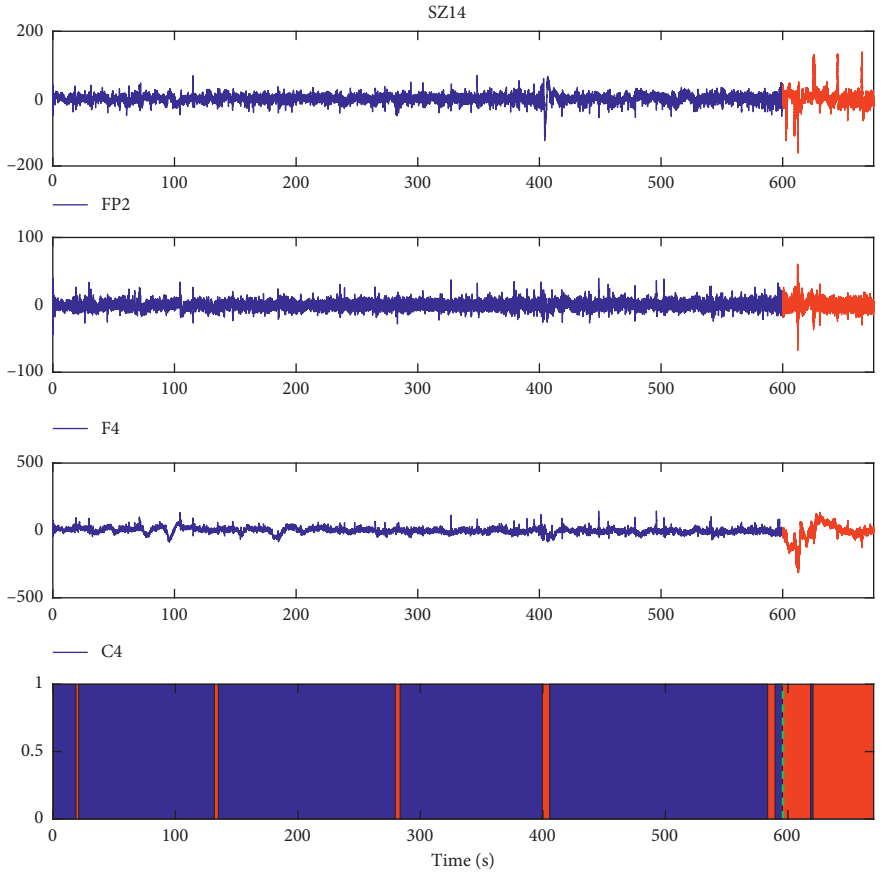

Figure 5: Example of the test seizure #14 of patient #9. Top three plots: raw signals of the channels FP2, F4, and C4 coloured on the basis of the NS and SZ state; bottom plot: bar graph of the answer of the CNN model, where a blue bar represents a pattern classified as NS, whereas a red bar characterizes a SZ pattern. The green vertical dashed line identifies the onset seizure time given by the CNN (t_{alarm}).

Table 6: Test Performance (%) of the cross-patient seizure detection system of patient #5.

	SZ #1	SZ #2	SZ #3	SZ #4	SZ #5
Accuracy	41.57	93.47	90.97	91.44	98.32
Specificity	28.03	85.92	95.70	85.56	98.22
Sensitivity	100	100	81.69	97.47	100
Gmean	52.94	92.69	88.42	91.32	99.11

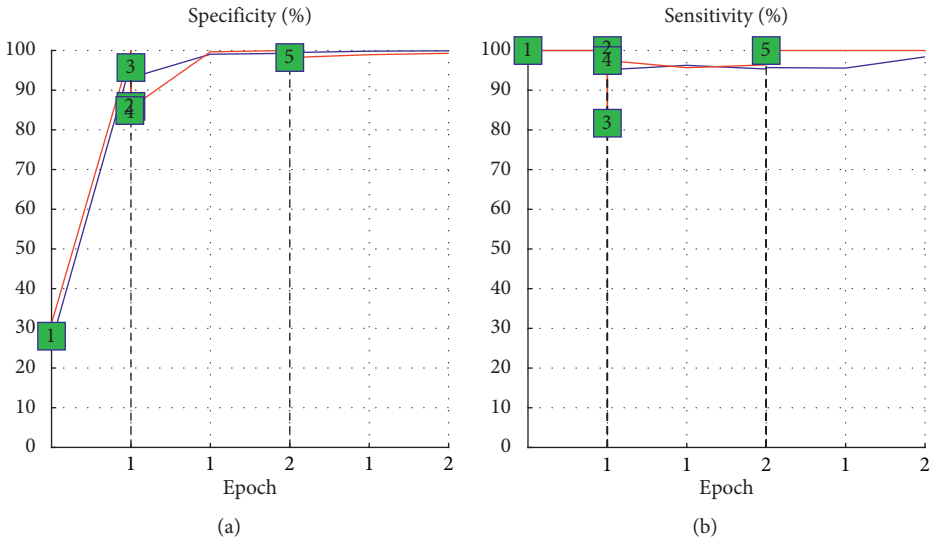

Figure 6: Results of the cross-patient seizure detection procedure in terms of Specificity (a) and Sensitivity (b), starting from the seizure detection model of patient #9 and fine-tuning it for patient #5. Figure shows the trend of Specificity and Sensitivity during the temporal occurrence of the 5 seizures of patient #5. Blue line: trend on the training set; red line: trend on the validation set; green squares: results on the test set.

distribution for patient #9. In the same figure, the seizure onset time provided by the neurologists is reported. Note that, because in each EEG recordings the first 10 minutes correspond to nonseizure states (NS), t_{SZ} is always equal to 600 s.

Figure 5 shows, as an example, the testing seizure #14 of patient #9 and the preceding 10 min. The three top plots in Figure 5 report the raw signals of the channels FP2, F4, and C4, which have been colored in blue for the NS state and in red for the SZ state. The bottom plot in Figure 5 shows a bar graph where each bar, corresponding to one second, is colored depending on the answer of the CNN: a blue bar represents a pattern classified as NS, whereas a red bar characterizes a SZ pattern. By comparing the bars with the raw signals during the temporal evolution of the EEG recording a very good correspondence is found.

These results, showing a good performance of the CNN, are obtained from models that have been trained using a number of seizures. However, in case of a new patient, instead of collecting a sufficient number of seizures to customize a new patient-specific model from scratch (which sometimes is difficult) transfer-learning capabilities can be used. Starting from a model already trained for other patients, it may be retrained with new seizures of the new patient, obtaining a cross-patient seizure detection system with transfer learning among the patients.

3.2. Transfer Learning for Cross-Patient Seizure Detection. Transfer learning is a technique consisting of pretraining a model on one set of data and then fine-tuning it on another. In this case, the deep cross-patient transfer learning framework is applied to classify EEG data of a patient using the CNN trained with the EEG of another subject. In particular, starting from a patient-specific CNN model, its weights are used as the initial values for a second phase of training using seizures of another patient. This could provide many advantages when few seizures are available.

As an example, the patient-specific CNN model of patient #9 (CNN9) has been assumed as the starting model. This choice has been done because on one hand patient #9 has the highest number of seizures and on the other its model achieves the lowest performance in terms of Gmean.

Table 6 shows the results of the cross-patient seizure detection procedure applied to detect the seizures of patient #5 starting from the network pretrained on patient #9; Figure 6 reports the trends of Sensitivity and Specificity during the temporal occurrence of the five seizures of patient #5, for the training set (blue line) and for the validation set (red line). The green squares in the same figure represent the performance obtained on the test seizures.

Starting from the CNN9 model, the first of the five seizures of patient #5 are used as a test case. As expected, the performance is quite low because the model has not been yet customized to the new patient. In particular, the CNN9

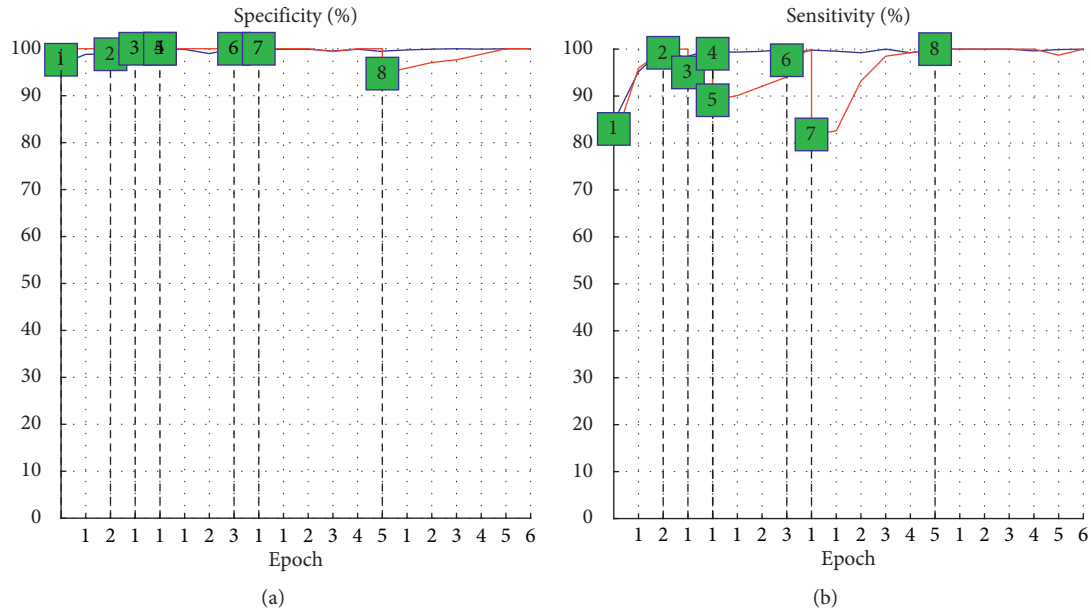

Figure 7: Results of the cross-patient seizure detection procedure in terms of Specificity (a) and Sensitivity (b), starting from the seizure detection model of patient #9: trend of Specificity and Sensitivity during the temporal occurrence of the 8 seizures of the patient #6. Blue line: trend on the training set; red line: trend on the validation set; green squares: results on the test set.

Table 7: Steps of the cross-patient seizure detection process for patient #5.

	Training SZ	Validation SZ	Test SZ	# Epochs	CPU time (s)
Step 0	—	—	1	0	0
Step 1	1	1	2	1	14
Step 2	1	2	3	0	454
Step 3	1, 2	3	4	0	960
Step 4	1, 2, 3	4	5	2	1528

Table 8: Test Performance (%) of the cross-patient seizure detection system on patient #6.

	SZ #1	SZ #2	SZ #3	SZ #4	SZ #5	SZ #6	SZ #7	SZ #8
Accuracy	88.53	99.26	97.75	99.63	95.94	98.82	92.07	96.37
Specificity	97.65	98.82	100	100	100	100	100	94.71
Sensitivity	83.22	100	95.04	99.01	89.11	97.63	81.82	100
Gmean	90.14	99.41	97.49	99.50	94.40	98.81	90.45	97.32

model performs a low specificity (about 28%), whereas the value of sensitivity is very high (100%). This suggests refining the starting model by using patient-specific information.

Hence, in the next step, two-thirds of the EEG segments of the first seizure have been used as the training set and the other one-third as validation set, whereas the performance of the customized model has been tested on the second seizure, showing an improvement of specificity that increases to 85.92%, while sensitivity is not degraded. In the subsequent steps, the last seizure has been used to test the model customized on the preceding seizures. As it can be noted, during the testing of the subsequent seizures, Specificity and Sensitivity values fluctuate keeping always above 80% and providing an ever high Gmean value up to the value of about 99% in the last tested seizure.

For each step of the procedure, Table 7 reports a summary of the cross-patient seizure detection process: the seizures used for training, validation, and test, the number of epochs performed during the training, and the total CPU time in seconds. If the number of epochs is zero, it means that, during the training, no network configuration has been found that improves the prediction accuracy on the validation step. Note that the process took less than 30 minutes to fine-tuning the model with each new data pattern.

Table 8 and Figure 7 reports the same results of Table 6 and Figure 6 but referring to patient #6, starting again from the CNN9 model.

In this case, the cross-patient seizure detection system performs very well since the first seizure, especially concerning the specificity, which always takes values above about 95%.

This fluctuating trend, especially concerning the sensitivity, demonstrates the diversity of seizures not only among patients but also within the same patient, which challenges all classifiers, whatever deep they may be.

Table 9: Steps of the cross-patient seizure detection process for patient #6.

	Training SZ	Validation SZ	Test SZ	# Epochs	CPU time (s)
Step 0	—	—	1	0	0
Step 1	1	1	2	2	17
Step 2	1	2	3	1	12
Step 3	1, 2	3	4	1	622
Step 4	1, 2, 3	4	5	0	817
Step 5	1, 2, 3, 4	5	6	3	1206
Step 6	1, 2, 3, 4, 5	6	7	1	32
Step 7	1, 2, 3, 4, 5, 6	7	8	5	415

In Table 9, the transfer-learning process from CNN9 to patient #6 is shown, with the same information reported in Table 7. Also, in this case, retraining the CNN9 with a new seizure takes no more than 20 minutes.

4. Conclusions

A CNN architecture has been deployed, by adapting the ResNet structure to the problem of seizure detection from EEG traces in nocturnal frontal lobe epilepsy (NFLE). The adjustment in the architecture consisted mainly in using 1D filters in the convolutional layers, to filter separately the information coming from different electrodes, and including dropout layers to reduce overfitting on the training set and improve generalization. An advantage of the deep-learning approach is that the complex and time-consuming feature engineering step is not required. Moreover, the developed patient-specific detection systems have demonstrated to be superior to those in the literature towards all the performance indexes, with accuracy above 94% for all the considered patients. In our knowledge, this is the first application of deep learning to NFLE seizure detection. Moreover, using the potentiality of the transfer learning, the lack of an extensive EEG database has been overcome and the possibility to develop a cross-patient seizure detection system has been demonstrated. Indeed, a patient-dependent system can be fine-tuned to a new patient with few data and limited computational effort.

Data Availability

Data were recorded on behalf of the EPILEPSIAE project.

Consent

Prior to admission, all patients were informed about the study and each one gave informed consent.

Conflicts of Interest

The authors confirm that there are no known conflicts of interest associated with this publication and there has been no significant financial support for this work that could have influenced its outcome.

Acknowledgments

The authors would like to acknowledge EU FP 7 Project EPILEPSIAE Grant 211713. This work was supported by the Open Access Publishing Fund of the University of Cagliari, with the funding of the Regione Autonoma della Sardegna–L.R. n. 7/2007.

References

[1] F. Provini, G. Plazzi, P. Tinuper, S. Vandi, E. Lugaresi, and P. Montagna, "Nocturnal frontal lobe epilepsy: a clinical and polygraphic overview of 100 consecutive cases," *Brain*, vol. 122, no. 6, pp. 1017–1031, 1999.

[2] P. Ryvlin, S. Rheims, and G. Risse, "Nocturnal frontal lobe epilepsy," *Epilepsia*, vol. 47, no. 2, pp. 83–86, 2006.

[3] F. Rosenow, K. M. Kleim, and H. M. Hamer, "Non-invasive EEG evaluation in epilepsy diagnosis," *Expert Rev Neurother. Expert Review of Neurotherapeutics*, vol. 15, no. 4, 2015.

[4] U. R. Acharya, S. Vinitha Sree, G. Swapna, R. J. Martis, and J. S. Suri, "Automated EEG analysis of epilepsy: a review," *Knowledge-Based Systems*, vol. 45, pp. 147–165, 2013.

[5] O. Faust, U. R. Acharya, H. Adeli, and A. Adeli, "Wavelet-based EEG processing for computer-aided seizure detection and epilepsy diagnosis," *Seizure*, vol. 26, pp. 56–64, 2015.

[6] D. Chen, S. Wan, J. Xiang, and F. S. Bao, "A high-performance seizure detection algorithm based on Discrete Wavelet Transform (DWT) and EEG," *Plos One*, vol. 12, no. 3, Article ID e0173138, 2017.

[7] M. Bandarabadi, C. A. Teixeira, F. Sales, and A. Dourado, "Wepilet, optimal orthogonal wavelets for epileptic seizure prediction with one single surface channel," *IEEE Engineering in Medicine and Biology Society*, vol. 2011, pp. 7059–7062, 2011.

[8] M. Zabihi, S. Kiranyaz, A. B. Rad, A. K. Katsaggelos, M. Gabbouj, and T. Ince, "Analysis of high-dimensional phase space via poincaré section for patient-specific seizure detection," *IEEE Transactions on Neural Systems and Rehabilitation Engineering*, vol. 24, no. 3, pp. 386–398, 2016.

[9] U. R. Acharya, H. Fujita, V. K. Sudarshan, S. Bhat, and J. E. W. Koh, "Application of entropies for automated diagnosis of epilepsy using EEG signals: a review," *Knowledge-Based Systems*, vol. 88, pp. 85–96, 2015.

[10] L. Wang, W. Xue, Y. Li et al., "Automatic epileptic seizure detection in EEG signals using multi-domain feature extraction and nonlinear analysis," *Entropy*, vol. 19, no. 6, p. 222, 2017.

[11] Y. Park, L. Luo, K. K. Parhi, and T. Netoff, "Seizure prediction with spectral power of EEG using cost-sensitive support vector machines," *Epilepsia*, vol. 52, no. 10, pp. 1761–1770, 2011.

[12] A. Kavitha and V. Krishnaveni, "A novel automatic stepwise signal processing based computer aided diagnosis system for epilepsy-seizure detection and classification for EEG," *Biomedical Research*, vol. 10, 2016.

[13] P. Swami, T. K. Gandhi, B. K. Panigrahi, M. Tripathi, and S. Anand, "A novel robust diagnostic model to detect seizures in electroencephalography," *Expert Systems with Applications*, vol. 56, pp. 116–130, 2016.

[14] K. Cuppens, L. Lagae, B. Ceulemans, S. Van Huffel, and B. Vanrumste, "Detection of nocturnal frontal lobe seizures in pediatric patients by means of accelerometers: a first study," in *Proceedings of the 31st Annual International Conference of the IEEE EMBS*, Minneapolis, MA, USA, September 2009.

[15] T. M. E. Nijsen, J. B. A. M. Arends, P. A. M. Griep, and P. J. M. Cluitmans, "The potential value of three-dimensional accelerometry for detection of motor seizures in severe epilepsy," *Epilepsy & Behavior*, vol. 7, no. 1, pp. 74–84, 2005.

[16] T. M. E. Nijsen, R. M. Aarts, P. J. M. Cluitmans, and P. A. M. Griep, "Time-frequency analysis of accelerometry data for detection of myoclonic seizures," *IEEE Transactions on Information Technology in Biomedicine*, vol. 14, no. 5, pp. 1197–1203, 2010.

[17] B. Pisano, B. Cannas, G. Milioli et al., "Autosomal dominant nocturnal frontal lobe epilepsy seizure characterization through wavelet transform of EEG records and self organizing maps," in *Proceedings of the 2016 IEEE 26th International Workshop on Machine Learning for Signal Processing (MLSP)*, pp. 1–6, Vietri sul Mare, Italy, September 2016.

[18] H. H. Jasper, "Report of the committee on methods of clinical examination in electroencephalography," *Electroencephalography and Clinical Neurophysiology*, vol. 10, no. 2, pp. 370–375, 1958.

[19] M. Bonnet, "EEG arousals: scoring rules and examples," *Sleep*, vol. 15, no. 2, pp. 173–184, 1992.

[20] B. Pisano, C. A. Teixeira, A. Dourado, and A. Fanni, "Application of Self Organizing Map to Identify Nocturnal Epileptic Seizures," *Neural Computing and Applications*, vol. 10, 2019.

[21] G. Litjens, T. Kooi, B. E. Bejnordi et al., "A survey on deep learning in medical image analysis," *Medical Image Analysis*, vol. 42, pp. 60–88, 2017.

[22] S. Pouyanfar, "A survey on deep learning: algorithms, techniques, and applications," *ACM Computing Surveys*, vol. 51, no. 5, pp. 92–36, 2018.

[23] M. Z. Alom, "A State-of-the-Art Survey on Deep Learning Theory and Architectures," *Electronics*, vol. 8, 2019.

[24] U. R. Acharya, S. L. Oh, Y. Hagiwara, J. H. Tan, and H. Adeli, "Deep convolutional neural network for the automated detection and diagnosis of seizure using EEG signals," *Computers in Biology and Medicine*, vol. 100, pp. 270–278, 2018.

[25] University of Bonn, *Bonn Epilepsiae Data Base*, University of Bonn, Bonn, Germany, 2019.

[26] I. Ullah, M. Hussain, E.-U.-H. Qazi, and H. Aboalsamh, "An automated system for epilepsy detection using EEG brain signals based on deep learning approach," *Expert Systems With Applications*, vol. 107, pp. 61–71, 2018.

[27] A. Emami, N. Kunii, T. Matsuo, T. Shinozaki, K. Kawai, and H. Takahashi, "Seizure detection by convolutional neural network-based analysis of scalp electroencephalography plot images," *NeuroImage: Clinical*, vol. 22, Article ID 101684, 2019.

[28] K. Simonyan and A. Zisserman, "Very deep convolutional networks for large-scale image recognition," in *Proceedings of the ICLR 2015, International Conference on Learning Representations*, pp. 1–14, San Diego, CA, USA, May 2015.

[29] X. Wei, L. Zhou, Z.. : Chen, L. Zhang, and Y. Zhou, "Automatic seizure detection using three dimensional CNN based on multi-channel EEG," *BMC Medical Informatics and Decision Making*, vol. 18, no. 5, p. 111, 2018.

[30] S. J. Pan and Q. Yang, "A survey on transfer learning," *IEEE Transactions on Knowledge and Data Engineering*, vol. 22, no. 10, pp. 1345–1359, 2010.

[31] I. Goodfellow, Y. Bengio, and A. Courville, *Deep Learning (15.2 Transfer Learning and Domain Adaptation)*, MIT Press, Cambridge, MA, USA, 2016.

[32] J. Klatt, H. Feldwisch-Drentrup, M. Ihle et al., "The EPILEPSIAE database: an extensive electroencephalography database of epilepsy patients," *Epilepsia*, vol. 53, no. 9, pp. 1669–1676, 2012.

[33] K. He, "American Electroencephalographic Society guidelines for standard electrode position nomenclature," *Journal of Clinical Neurophysiology*, vol. 8, no. 2, pp. 200–202, 1991.

[34] K. He, X. Zhang, S. Ren, and J. Sun, "Deep residual learning for image recognition," in *Proceedings of the IEEE Conference on Computer Vision and Pattern Recognition (CVPR)*, pp. 770–778, Las Vegas, NV, USA, 2016.

[35] N. Qian, "On the momentum term in gradient descent learning algorithms," *Neural Networks*, vol. 12, no. 1, pp. 145–151, 1999.

[36] T. N. Alotaiby, S. A. Alshebeili, T. Alshawi, I. Ahmad, and F. E. A. El-Samie, "EEG seizure detection and prediction algorithms: a survey," *EURASIP Journal on Advances in Signal Processing*, vol. 2014, no. 1, p. 183, 2014.

Hindawi
Complexity
Volume 2020, Article ID 4253540, 7 pages
https://doi.org/10.1155/2020/4253540

Research Article

Application of Causal Inference Analysis Economic Growth on Labor Production from Foreign Direct Investment

Po Sheng Ko,[1] Kuo Chih Lu,[2] Cheng Chung Wu,[3] and Tiantong Yuan[4]

[1]*Department of Public Finance and Taxation, National Kaohsiung University of Science and Technology, Kaohsiung, Taiwan*
[2]*Department of International Business, National Kaohsiung University of Science and Technology, Kaohsiung, Taiwan*
[3]*Department of Finance, Suqian College, Suqian, Jiangsu, China*
[4]*Department of Business Administration, Krirk University, Bangkok, Thailand*

Correspondence should be addressed to Cheng Chung Wu; wu_0110@yahoo.com.tw

Received 5 September 2019; Revised 7 February 2020; Accepted 15 February 2020; Published 16 March 2020

Guest Editor: Murari Andrea

In recent four decades, policy reform has integrated China's economy into global. Since 1981, foreign direct investment (FDI) has been gradually flowing into the Yangtze River Delta region. As a result, this region has enjoyed strong economic strength based on abundant human resources and convenient transportation network. Shanghai, the key city, has become one of the major cites attracting FDI; meanwhile, FDI also has had a tremendous impact on Shanghai's economic development, including employment. To sum up, Shanghai has been chosen as the research object in this paper. This research is organized by four parts: firstly, a theoretical analysis of employment effects of FDI is presented; secondly, after combining the actual utilization of FDI and employment in Shanghai, an empirical analysis of the effects of FDI on employment quantity and employment quality is carried out by data and regression models; thirdly, this research found FDI has exerted a negative influence on employment quantity in Shanghai; moreover, FDI also has shown a positive impact on the employment quality; and finally, the paper has proposed some suggestions to FDI's utility in the future.

1. Introduction

In the last decade, China has grown rapidly because of FDI and replaced the United States as the world's largest recipient of FDI in 2002. Shanghai is the metropolitan area of the Yangtze River Delta and has exceptional conditions to attract foreign investment. Therefore, Shanghai has turned into a major recipient of FDI in China. The massive FDI inflows had many significant effects on Shanghai with many aspects, and the change of local employment is one of the major effects. This research selects Shanghai as the research subject and focuses on studying the effects of FDI on the change of local employment, such as employment quantity, employment distribution, and employment quality as three sectors of the economy.

The primary sector involves the retrieval and production of raw materials, such as corn, coal, wood, and iron. The secondary sector involves the transformation of raw or intermediate materials into goods, such as manufacturing steel into cars or textiles into clothing. The tertiary sector involves supplying of services to consumers and businesses, such as baby-sitting, cinema, and banking. In fact, all three sectors are affected by FDI; however, some sectors are affected significantly while others are not.

The effects of FDI on the employment distribution in the three sectors will vary because of different scope of influence from FDI in each sector. Compared with other sectors, the impact from FDI on the primary sector is not significant. The secondary sector always plays the leading role in China national economy, and FDI weighs heavily in this sector. Therefore, FDI has a more significant influence on employment in this sector. Foreign companies increase their direct investment into the tertiary sector, which causes the labor demand increase in the service industry. Therefore, FDI surely has a greater scope of influence on employment quantity in the tertiary sector.

FDI has two effects that are direct generation effect and indirect generation effect. Direct generation effect creates job opportunities in the home country through subsidiaries or operation bases, while indirect generation effect means the job opportunities increase in host countries through other approaches and spillover effect.

Most of the time, FDI has a direct positive effect on the number employed in the foreign companies and indirect positive or negative effect on total employment quantity in Shanghai since the total employment demand is an inverted U curve along with the FDI amount [1]. For example, in recent years, both the number of employees in foreign companies and total employment had an obvious rising trend; however, researchers still cannot assert the FDI has a full positive effect for total employment since some other reasons may also cause the total employment to rise, FDI just one of many reasons.

Furthermore, FDI normally requires a high-quality job that offers high salary with high requirement and high work efficiency; however, if the work amount does not change, high work efficiency will signify lesser labor demand. Crowding-out effect would also appear when an international company enters the market through "merger" or "acquisition," a reasonable downsizing of employee amount occurs cutting down employment as the result.

In addition, FDI has both positive and negative effects on employment quality. Foreign companies often offer better wages, benefit packages, and working environment, as well as quality training. Meanwhile, more foreign enterprises discriminate against the host country's social security system for their employees.

According to Ko et al. [2], a theoretical analysis applied on how FDI affects the employment is presented. Secondly, an empirical analysis of FDI effects on employment's quantity, employment's distribution, and employment's quality is carried out by collecting relevant data and establishing regression models, with combining the actual utilization of FDI and employment in Shanghai. This study finds that although FDI does exert a positive influence on the quantity of employment in Shanghai's tertiary industry, FDI is not conducive to primary and secondary industries. In addition, FDI has shown positive and negative impacts on the quality of employment [1]. Besides, the paper will propose some suggestions in order to enhance the positive effects of FDI on employment. Finally, the researchers will propose two regression models to test the actual effect of FDI on employment, which are as follows: Model A is used to test the FDI's effect on total employment, and then, Model B has added W/P variable to test the FDI's effect for employment quality. Moreover, employment distribution in three sectors is analyzed by second-hand statistic data.

2. Review of the Literature

FDI refers to "Foreign Direct Investment," also known as "Direct International Investment," which means investors participate in the entity's production and operation and exercise substantial control over management. The yield relies on the condition of the entity's operation and exhibits high variability. Most of the scholars suggest that the employment effects caused by FDI in the host countries are mainly on three aspects: employment quantity, employment distribution, and employment quality. The authors are interested in finding the impacts of FDI inflow on employment quantity, employment distribution, and employment quality by analysis effects of FDI in three economic sectors.

2.1. Effects on Employment Quantity. Tang [3] believes that FDI causes both positive and negative effects on the employment quantity. For example, FDI will increase job opportunities, which is a positive employment-generation effect; meanwhile, the international enterprises' entering will cause crowding-out effect, a negative employment-generation effect that results in reducing existing employees.

FDI will create considerable job opportunities and boost employment. Generally, direct generation effect means the FDI creates job opportunities and increases employment directly in the host country. When an international company enters with "Greenfield Investment," it will bring net capital into the host country, the international company will establish subsidiaries or an operation base there, and then newly-founded companies will recruit local people and increase employment in the host country.

Indirect generation effect means the job opportunities in host countries are increased with other approaches such as expatriate and work permit. Generally, the FDI will form an "enterprise-correlation effect" by increasing the job opportunities in local companies which associate with the intercountry companies. Entering of the FDI's companies will drive the operation of the local companies. When the demand of the foreign companies is equal to the output of domestic companies, the demand of the products will rise, and then the local companies' scale of production will be expanded. The labor demand of domestic companies will have a surplus due to the shortage of employees, and then the domestic companies will have to recruit new employees in order to increase productivity; therefore, new job opportunities will be generated indirectly.

Moreover, FDI increases the employment quantity indirectly by the "spillover effect." Foreign companies introduce new technologies and new types of industry into the host countries. Meanwhile, it will accelerate the development of the latest high-tech industry in the host countries and increase employment in multifarious industries. Therefore, numerous job opportunities will be generated indirectly. In addition, the FDI inflow brings capital which will rapidly spur productivity like the effect of economy of scale. As a result, the host countries' factors of production will be properly dispensed, and the not-utilized factors will be able to be utilized. The dominant resources can be employed efficiently to escalate new productivity and generate more new job opportunities. However, crowding-out effect also appears when an international company enters through "merger" or "acquisition"; as a result, a "reasonable" downsizing will occur, crowding-out employees and cutting down employment. Moreover, the international companies usually have stricter criteria concerning employees' working

skills than the local firms do. Therefore, it is a common phenomenon that local employees are laid off as a result of not meeting the skill requirements of the foreign companies. In addition, the foreign companies are more capital-intensive, so the operation mode should crowd out some employment in labor-intensive local companies. Entering of FDI will fuel the competition of the local market and eliminate the lamed companies, thereby causing a considerable level of unemployment and reducing job opportunities.

2.2. Effect on Employment Distribution. From an industrial perspective, the effects of FDI on the employment distribution in the three sectors will vary because of the different influence extent of FDI on three economic sectors. Compared with other sectors, the impact from FDI on the primary sector is not significant. The primary sector is mainly agriculture/farming and is usually run by units as "family," so it does not require additional employees. Furthermore, the agricultural industry is vital to national well-being and the people's livelihood, so the authorities will usually impose more restrictions on foreign entities wishing to engage in this field. As a result, foreign companies will make relatively low investment in this sector. In addition, related technologies are currently advancing at blinding speed. Since the agricultural industry also applies modern methods to production, this will lead to less demand on the labor force. Consequently, the FDI certainly will not have any remarkable impact on the primary sector.

In China, the secondary sector, mainly manufacturing, always plays the leading role in the national economy, and FDI weighs heavily in this sector. Therefore, FDI has a more significant influence on employment in this sector. In the contemporary society, after material demands have been fulfilled, the demand for incorporeal service and spiritual satisfaction is boosting, which leads to the tertiary sector blossoming. Accordingly, foreign companies' direct investment into the tertiary sector will keep increasing. The service industry of labor demand is large so that FDI will surely have a greater scale of influence on employment in the tertiary sector.

2.3. Effects on Employment Quality. FDI has both positive and negative effects on employment quality. In the positive aspect, Cui and Li [4] suggest that FDI can contribute to the improvement of employment quality in the host countries. Foreign companies often offer better wages, benefit packages, and working environment; they also introduce new know-how and technologies to the employees in the host countries. Most of the foreign companies put a lot of effort into quality training and enhancing workers' skills so that, after being recruited, employees have the opportunity to get training to improve various abilities. Meanwhile, the employees' quality and skills will be cultured and improved due to a superior working environment.

The negative effects usually appear in regard to the foreign companies' negligence of employees in host countries. More and more foreign enterprises discriminate against the host country's social security system for the employees that mainly happens in small-sized foreign companies, which manifests as some or all employees are unable to obtain basic social security services. In order to reduce the cost, some foreign companies even provide very undesirable and poor working conditions with no security assurance, which raises considerable safety concerns about the working environment. In conclusion, the analysis on the quantity, distribution, and quality reveals that FDI has both positive and negative effects on local employment. The following sections present analysis on FDI's specific effects on the three aspects through empirical analysis.

3. FDI in Shanghai

The FDI started to flow into China in 1979 but did not reach the Yangtze River Delta region until 1986, despite a few years during which actual FDI inflow dropped, but the trend of foreign investment in actual use went up by year, and employment grew in Shanghai between 1986 and 2015 constantly. In fact, this study adopted the statistics data from 1981 to 2015.

Cao [5] had explored how Shanghai dealt with FDI along with the situation of employment, and the results indicated the FDI flows in Shanghai can be divided into four stages. The beginning stage was from 1986 to 1991. In this period, China's open policy focused on the southern regions like the Pearl River Delta region, which included Shenzhen, Zhuhai, Shantou, and Xiamen.

Chen and Wu [6] pointed out that China's FDI is mainly concentrated in coastal areas, attracting a large number of migrant workers from the mainland. This kind of population migration related to FDI may have an impact on China's inland urbanization. However, there is little research on this issue. This paper aims to study the regional impact of FDI on China's inland urbanization. The research had found that FDI has a negative interregional impact on inland urbanization in average. However, the impact of FDI from different trade patterns in coastal and inland areas on China's inland urbanization is different.

In this stage, a large number of foreign companies were set up in Pearl River Delta, but Shanghai just had scarce FDI in actual use; meanwhile, the employment experienced no apparent fluctuation. Basically, total employment was maintained at 8 million approximately.

Skyrocketing stage was from 1992 to 1997. During this period, FDI flows into Shanghai which actually reached a climax. The FDI in actual use in Shanghai was US$1.3 billion in 1992, and the total FDI amount exceeded US$2.3 billion in 1993; FDI has reached US$3.2 billion in 1994, US$4.7 billion in 1996, and US$4.8 billion in 1997. Meanwhile, total employment remained at a relatively stable state. The total employment in Shanghai was 8.069 million people in 1992 and reached to 8.5 million in 1997.

In 1997, the financial crisis spread rapidly to most Asian countries so that FDI in actual use showed a negative growth in Shanghai. The growth rate was −24.3% in 1998 and −16.4% in 1999. As a result, total employment also had negative growth rate in this phase, while the total

employment reduced 1.3% in 1998 and lost 2.9% in 1999 statistically. Finally, experts called the following short and unusual period "Adjustment and Shrinking stage" between 1998 and 1999.

Next stage was from 2000 to 2008, called "Sustained Growth stage." During this period, FDI in actual use surged, US$3.16 billion in 2000, US$4.392 billion in 2001, and over US$5 billion in 2002, and had reached to US$10 billion in 2008. At the same time, the number of total employment in Shanghai had reached to 10.53 million people.

3.1. FDI Inflow to Three Sectors in Shanghai. Based on results of former research studies, FDI has mainly pooled in the tertiary sector, followed by the secondary, and was least in the primary sector. For example, the actual FDI inflow to the tertiary sector in Shanghai was US$6.8 billion in 2008, which was 67.8% of the total actual FDI inflow for the entire year. In the mean period, it was US$3.2 billion for the secondary sector, which was 32.09% of the total, while the primary sector gained US$13 million from FDI, which was a paltry 0.13% of the total. This ratio is still stable until the latest statistic in 2015. It is pretty clear that the tertiary sector had attracted more foreign capital than the secondary and primary sector; in other words, the extent of FDI effects on the tertiary industry is several times larger than the secondary and primary sector.

In fact, the primary sector always remained at the lowest level. For example, FDI amount is US$6 million in this sector in 2000, the secondary sector received US$1.59 billion FDI in 1999, meanwhile, the tertiary sector took US$1.54 billion. A greatest disparity happened in 2002 when the secondary sector gained US$3.13 billion FDI, the tertiary sector merely acquired US$1.88 billion, and the gap was US$1.25 billion. Nevertheless, the FDI flows to the tertiary sector surpassed that to the secondary in 2003 and received the highest amount of FDI by comparing the other two sectors. The trend of FDI flows to the secondary sector kept descending since 2004; it was US$3.587 billion in 2004, and the FDI amount was cut down to US$2.597 billion in 2007. Meanwhile, the FDI amount was ascending in the tertiary sector, and the FDI amount had increased from US$3.337 billion in 2003 to US$6.835 billion in 2008.

3.2. Employment Quantity. Based on the panel data of 262 cities in China with a range from 2004 to 2012, by using the GMM model of the dynamic panel system and regression technology of instrumental variables, this paper provides empirical research of the impact of FDI on China's urbanization [7]. This research has found that FDI has played a significant positive role in China's urbanization development. However, the positive role of FDI on urbanization development varies from region to region. Foreign direct investment has a positive effect on the urbanization of coastal areas but has little or no significant effect on the urbanization of inland areas. The analyzed results indicate that the factors such as economic structure, economic development level, fixed asset investment level, and urban population scale are important determinants of China's urbanization other than FDI solely.

China Second National Economic Census indicates that the number of employees hired by foreign companies was 1.1337 million people in Shanghai in 2008, that is, 10.76% of the total employment, which means 10.5324 million people. In other words, out of every 100 employees, 10.5 worked for foreign companies. In 2016, employees hired by foreign companies numbered over 2 million and over 20% of the total employment.

China Second National Economic Census also indicates that, between 1999 and 2008 except for 2008, the number of foreign companies was increasing in Shanghai yearly, and the employment in 2007 was 1.2378 million. In percentage terms, the employment in foreign companies in Shanghai was 0.568 million people during 1999, which was 6.24% of the total employment in 1999, 8.08% in 2001, 10.04% in 2003, 10.41% in 2005, and 13.62% in 2007. Although the financial crisis in the second half of 2007 impacted employment in Shanghai, the employment in foreign companies shows an escalation trend yearly. Employees hired by the foreign companies were cut to 1.1138 million people in 2008, and the percentage dropped to 10.58%. However, employment in foreign enterprises increased in overall level, and the percentage compared with the total employment climbed steadily.

The analysis shows that the FDI in actual use in Shanghai kept growing every year and both total employment and employment in foreign companies were also increasing. With regard to the three sectors of the economy, FDI flooded into the tertiary sector, followed by the secondary, and the primary got the least. This research finds that FDI certainly affects the amount of employment and the employment distribution in the three sectors of the economy. The next section presents an empirical analysis on the effects to employment caused by FDI in Shanghai by establishing relevant regression models.

3.3. Employment Distribution. Employment showed an obvious disparity among the three sectors in Shanghai. Before the 21st century, employment was clustered in the secondary sector, but employment in the tertiary sector exceeded that of the secondary to become the major hiring industry since 2000.

In regard to the total employment in the three sectors, employment in the primary sector was 2.24 million people in 1979 and then was reduced to 0.49 million in 2008. The proportion shrank from 31.55% to 4.69%, a drop of 26.86 percentage points (pp) within 30 years. The trend implies that the structure of a society moves towards industrialization and urbanization when a massive amount of surplus agricultural labor transfers to the secondary and tertiary sectors.

The proportion of employment in the secondary sector was expanding in Shanghai between 1979 and 1990; in percentage form, it was 46.43% in 1979 and reached 59.30% in 1990. It showed a decreasing trend starting from 1991. The employment proportion in the secondary sector shrank

from 59.04% in 1991 to 40.27% in 2008. The manufacturing industry was no longer an "accumulator" to increase employment. However, employment in the tertiary sector kept expanding in Shanghai. The employment in the tertiary sector increased from 21.59% in 1978 to 72.64% in 2013. Moreover, the employment in the tertiary sector has exceeded than that in the secondary sector since 2000.

3.4. Employment Quality. Based on the research of Chen and Wu [6], the FDI and exports had significant effects on China's urbanization. By analyzing the data of 262 prefecture level cities in China from 2004 to 2013, with the method of generalized moment model of the dynamic panel system of instrumental variable regression, the research finds that FDI and exports play positive roles in China's urbanization significantly. However, the impact of FDI and exports on urbanization varies from region to region. FDI has a positive and significant impact on the urbanization of coastal areas but has no impact on the urbanization of inland areas. Export has a positive and significant impact on the urbanization of coastal and inland areas, but the impact of coastal areas is much greater than that of inland areas. The results indicate that attracting more FDI and promoting exports will contribute to China's urbanization, especially in the inland areas.

The employment quality includes the working environment, wages, and benefits, as well as the ability improvements. Based on former research results, researchers recognized FDI inflow has had significant effects on the employment quality in Shanghai, but the effects, also, are both positive and negative.

In general, FDI accelerates the improvement of the minimum wages, employee benefits, and the development of individual's ability. Firstly, foreign companies always provide higher salary and better working environment than local employers. According to "Shanghai Statistical Yearbook," wages in foreign companies are often higher than the ones in the state-owned or the public sectors.

Table 1 reveals that the average wages in foreign companies were higher than those in the state-owned enterprises and the public sector between 1999 and 2006. The wages in the foreign companies compared with the state-owned and public sectors were 1.13 times and 2.67 times greater, respectively.

International corporations usually provide very competitive packages, which included pension, medical, work injury, unemployment, maternal insurances, and house funds, as well as a career development plan and more stable future clearly. At the same time, international corporations' policies focus on personal skills and improving quality of work so that the foreign companies usually provide newly hired employees with vocational training. For example, Unilever's subsidiary in Shanghai lays stress on strengthening employees' international competitiveness particularly. Unilever in Shanghai has a comprehensive system for aiding employees' improvement and individual's future development. There is a division which seeks in-house talents and future leaders in Unilever and assists the employees to obtain global perspectives through working, training courses, and international relocation. In Unilever, all employees are open minded and ready for challenging tasks and improvement of themselves.

In addition, foreign companies usually find relevant R&D departments locally when entering a foreign market. The introduction of R&D departments always helps to enhance employees' personal abilities. According to the statistics, there are 257 foreign companies of "Fortune" top 500 enterprises settled in Shanghai with 1,884 investment projects and 45 R&D centers until 2006. The R&D and technical centers of foreign companies enable local engineers to obtain the latest know-how, which will improve human resources in Shanghai and build up their own talent pools. Additionally, FDI also has indirect effects on improving the quality of employment in Shanghai. Competition between foreign and local companies stimulates the local companies to improve their management and methods of production. As a result, the productivity of the local companies will increase, and job training will be strengthened, which will indirectly improve the employment quality in Shanghai.

On the contrary, FDI also has a negative effect on the employment quality in Shanghai, such as stability. For example, numerous foreign companies were shut down due to the financial crisis in 2007, and countless employees were laid off. According to the Shanghai Statistic Bureau, the employees hired by foreign companies numbered 1.2378 million in 2007, and the number was cut to 1.1138 million in 2008, which indicates the foreign companies cut redundant workers for cost-down reasons when encountering crises. However, other figures show that the total employment in Shanghai was 9.0908 million people in 2007 and 10.53 million in 2008, which signified growth of 1.44 million in total labor so that total employment in Shanghai was increasing instead of falling during the financial crisis. In fact, the employment growth occurred in the local companies' recruitment plan. From this perspective, employment in local companies is more stable than in foreign subsidiaries. The trend of employment in foreign companies is to have shorter term contracts when an enterprise faces falling profit. It will lay off workers without any hesitation, and as the workers have insufficient job security, this leads to employment instability.

4. Model and Results

4.1. Model and Variables. Most of the relevant studies suggest that the introduction of FDI will have a direct effect on the employment in the foreign companies so that this research chose the "actual FDI inflow in Shanghai" as the independent variable, while chose the "amount of employment in foreign companies" as the dependent variable to establish the following model:

$$\ln Q_t = \beta_0 + \beta_1 \ln \mathrm{FDI}_{t-1} + \varepsilon_t, \quad \text{(Model A)} \tag{1}$$

$$\ln Q_t = \beta_0 + \beta_1 \ln \mathrm{FDI}_{t-1} + \beta_2 \ln \frac{W}{P_{t-1}} + \varepsilon_t. \quad \text{(Model B)} \tag{2}$$

Table 1: Relevant information on the average wages in different kinds of enterprises.

	1999	2000	2001	2002	2003	2004	2005	2006
Foreign companies	19,728	21,158	25,572	26,365	29,106	29,282	35,709	40,683
State-own enterprises	16,852	18,865	21,961	24,719	28,406	31,287	36,077	36,010
Public sector	11,127	12,020	13,693	14,851	16,973	19,986	22,486	15,209

Source: Shanghai Statistical Yearbook 2000–2007 and China Financial Statistical Yearbook.

Table 2: Descriptive statistics variables.

	N	Minimum	Maximum	Mean	Std. deviation	Skewness	Kurtosis
lnFDI	35	5.70	14.43	11.8465.	2.47904	−1.181	0.452
lnWP	35	2.14	6.97	4.6308	1.63621	−0.148	−1.451
lnQ	35	4.55	4.60	4.5774	0.01605	0.327	−1.368

Table 3: Results of Model A and Model B.

Variables/estimation	Model A	Model B
ln FDI_{t-1}	0.006* (0.001)	0.007* (0.001)
ln W/P_{t-1}	—	0.001* (0.002)
C	4.644* (0.007)	4.627* (0.006)
Adjusted R^2	0.756	0.850
F statistics	106.168***	97.082*
Observation	35	35

Note: the numbers in parentheses are standard errors. *The estimated coefficients are statistically significant at 1%.

In Model A, "Q" stands for the "amount of employment in foreign companies in Shanghai," and "FDI" stands for the "actual FDI inflow in Shanghai." "ε_t" stands for random error, which reflects the uncertainties between "Q" (refers to the amount of employment in foreign companies) and "FDI" (refers to the actual FDI inflow).

In Model B, "Q" stands for the "amount of employment in foreign companies in Shanghai," and "FDI" stands for the "actual FDI inflow in Shanghai" that are the same as Model A. Besides, "W" stands for nominal wage (refers to the rate of pay employees are compensated) and "P" stands for Consumer Price Index, where "W/P" is defined as the real wage (which is the nominal wage adjusted for inflation) in the proposed Model B and "ε_t" stands for random error that reflects the uncertainties between "Q" and "FDI."

Table 2 shows descriptive statistics of explanatory variables. The above analysis shows that the coefficient of determination R^2 is 0.756 in Model A and 0.850 in Model B, which indicate both equations of Model A and Model B are fitting good. The degree of freedom is 35, and the critical number coefficient is greater than F value = 0.05, which displays a significant linear relationship and shows the explanatory variable and response variable are at high levels in regard to the interpretation. According to the insight of t-value, the critical number is t which shows the FDI has a significant effect on the gross employment in Shanghai, under the condition that the significance level was present at 5%.

4.2. Empirical Results. In the empirical stage, researchers adopted the data from 1981 to 2015 in China National Bureau of Statistics as the sample to deal with the question of "When the discrepancy of the relative figures is huge, will it seriously impact the regression results?" Therefore, the currency of FDI value was converted from US$100 million to RMB ¥ 100 million for the regression analysis. "Q" refers to the "amount of employment in foreign companies in Shanghai," while takes "per 10 thousand people" as the unit. The results from GLS regression analysis are listed in Table 3.

The coefficients of determinations of both equations show goodness of fit. Therefore, Model A indicates that lnFDI has an obvious negative effect with total employment. In fact, though FDI has created a large number of new jobs, it still squeezed numerous existing jobs. As a result, new jobs are less than squeezed, which answered why the empirical result is negative.

In Model B, the authors add variable lnW/P in the calculation process, and after lnW/P has been put in, the prior variables lnFDI had no significant relationship with total employment since lnFDI and lnW/P are highly correlated. The newly added variable W/P has made the equation repetition explanation. At the same time, lnFDI in Model B is not as important as it was in Model A. As a result, FDI created many high-end jobs, and these jobs have promoted the whole employment quality; however, high-end positions openings have replaced a large number of existing low-end positions.

5. Conclusion and Suggestion

Based on empirical analysis on the effects of FDI in Shanghai, the conclusions and suggestion regarding the quantity, distribution, and quality of employment are as follows.

The regression analysis on the relationship between FDI and the quantity of employment in Shanghai indicates that FDI will reduce the total employment. Even though a large number of employees are hired by foreign companies, it created still small than squeezed. Because efficient positions will take over inefficient jobs previously, that is why, FDI has a negative relationship with employment quantity. On the contrary, FDI has an obvious promotion about employment quality because high-end jobs have also squeezed the existing low-end jobs, thus promotion for the whole employment quality.

From previous analysis, if Shanghai has a high unemployment rate in the future, more FDI flow will make this situation more seriously; on the contrary, if Shanghai with an obvious labor shortage in the future, more FDI flow will ease this problem, which also further promote the employment quality.

Researchers also suggest that Shanghai should attract more FDI inflow by utilizing its exceptional location, abundant labor force, and enormous economic capabilities in order to enable foreign companies to expand and create more high-end job opportunities. In this stage, the types of FDI in Shanghai are mainly joint venture, wholly-owned, and associated enterprise. Therefore, Shanghai can innovate its own way of exploiting the FDI and develop more channels for increasing the inflow. Shanghai's government could encourage the local private companies to have more interactions with foreign companies and use these platforms for local companies to learn from foreign companies. Meanwhile, the local private sector can also learn the methods of internationalizing, such as fund raising in the international financial market, joint venture, or incorporation with foreign companies. Furthermore, Shanghai should improve its mechanisms of labor market operation to encourage the flow of various professionals among different organizations, taking full advantage of the FDI. Eventually, Shanghai should keep the economy growing at stable rates, while creating more high-end job opportunities.

Data Availability

The FDI data used to support the findings of this study are available from the corresponding author upon request.

Conflicts of Interest

The authors declare that they have no conflicts of interest.

References

[1] F. Paukert, "Income distribution at different levels of development: a survey of evidence," *International Labour Review*, vol. 108, no. 97, 1973.

[2] P. S. Ko, C. C. Wu, Y. S. Mai, and Z. R. Xu, "A study of three sectors employment effects resulting from foreign direct investment-empirical analysis on the data from Shanghai," *International Journal of Business Administration and Management Research*, vol. 4, no. 2, pp. 19–24, 2018.

[3] Y. Tang, "How FDI affects the employment in China," Market Weekly, Theory Study, 2008.

[4] X. Cui and Z. Li, *Empirical Analysis on the Economic Effects by FDI in China*, World Economic Forum, Geneva, Switzerland, 2003.

[5] H. Cao, *Analysis on FDI in China by Stage*, The Modernization of Emporia, Emporia, KS, USA, 2009.

[6] C. Chen and Y. Wu, "Interregional impact of foreign direct investment on China's inland urbanization," *The Singapore Economic Review*, vol. 64, no. 4, pp. 997–1017, 2019.

[7] Y. Wu and C. Chen, "The impact of foreign direct investment on urbanization in China," *Journal of the Asia Pacific Economy*, vol. 21, no. 3, pp. 339–356, 2016.

Hindawi
Complexity
Volume 2020, Article ID 4281219, 15 pages
https://doi.org/10.1155/2020/4281219

WILEY | Hindawi

Research Article

Forecasting-Aided Monitoring for the Distribution System State Estimation

S. Carcangiu, A. Fanni, P. A. Pegoraro, G. Sias, and S. Sulis

DIEE, University of Cagliari, Via Marengo 2, 09123 Cagliari, Italy

Correspondence should be addressed to G. Sias; giuliana.sias@diee.unica.it

Received 13 September 2019; Revised 13 December 2019; Accepted 11 January 2020; Published 28 February 2020

Guest Editor: Gonzalo Farias

In this paper, an innovative approach based on an artificial neural network (ANN) load forecasting model to improve the distribution system state estimation accuracy is proposed. High-quality pseudomeasurements are produced by a neural model fed with both exogenous and historical load information and applied in a realistic measurement scenario. Aggregated active and reactive powers of small or medium enterprises and residential loads are simultaneously predicted by a one-step ahead forecast. The correlation between the forecasted real and reactive power errors is duly kept into account in the definition of the estimator together with the uncertainty of the overall measurement chain. The beneficial effects of the ANN-based pseudomeasurements on the quality of the state estimation are demonstrated by simulations carried out on a small medium-voltage distribution grid.

1. Introduction

Power systems are rapidly evolving, and, correspondingly, control and management systems need information on the actual operating conditions of the grids, in order to manage them effectively. This information can be obtained in several ways and concerns different types of data, but, in any case, the proper operation of the systems is strictly connected to an accurate knowledge of the operating conditions of the grid [1]. Knowledge on possible operating conditions of the network can be obtained by means of load flow and power flow methods (see, for example, [2–4]), which are used, for instance, starting from nominal data in the planning stage or to find optimal configuration during contingencies. Other methods, suitable to know the state of the network, in terms of node voltages and/or branch currents, at run time starting from available measurements can be based on state estimation (SE) techniques. SE methods applied to the electrical power systems date back to the 1970s, when Fred Schweppe proposed the use of SE for achieving an accurate picture of the operating conditions of transmission networks [5]. The conventional state estimators assume the monitoring system to be overdetermined by having redundant measurements, thus ensuring the system observability, which is crucial for the state estimator to work. Unlike transmission systems, the number of real-time measurements in distribution systems (DSs) is usually limited. Despite the recent vast deployment of smart meters (SMs), the monitoring systems of DSs are still underdetermined; moreover, possible metering or communication problems causing missing/delayed data contribute to real-time measurements scarcity. For DSs, SE is not feasible unless the so-called pseudomeasurements are introduced in order to ensure the observability of the system and to perform, thus, the so-called distribution system state estimation (DSSE). In reviews [6, 7], it is possible to find the context of research activity on DSSE techniques. In the following, the focus will be on the definition of pseudomeasurements for DSSE. Typically, pseudomeasurements are indirect or derived measurements used to describe load/generator power absorption/generation. It is worth recalling that loads in electric DS have highly different location, size, and typology, and distributed generation can be highly variable. Thus, an accurate idea of the behaviour of the overall load configuration is challenging and can be essential for an effective DSSE [8]. In order to allow DSSE to function properly, pseudomeasurements from load estimates and short-term load forecasts can be used [9, 10]. In recent times, research has been carried out on the application of machine

learning techniques both for load estimation and load forecasting problems.

Traditional load power estimation can be performed from typical load profiles of each user type. Assuming the demand at each hour is equal to the demand at the same hour of the previous equivalent day is a common choice. The load profiles can be considered as derived estimates of the customer load behaviour with high variance. Consequently, the quality of the state estimates obtained with this approach is generally poor. To improve the accuracy of load power consumption estimation in [11], a neural network approach is proposed to realign the average load profiles with the real power flow measurements available at the network substation. In particular, for each bus, two feed-forward artificial neural networks (ANNs) are trained, the first one associates real active power flow measurements with active power injections, whereas the second one relates real reactive power flow measurements with reactive power injections.

In the literature, algorithms based on Multiple Linear Regression (MLR) analysis [10] and machine learning techniques [12] have been proposed for load forecasting.

Load forecasting is a difficult task as the time evolution of the loads is complex and exhibits several levels of seasonality; the load at a given hour can be correlated not only with the load at the previous hour but also with the loads at the same hour on the previous day and with the same day in the previous week. Moreover, many important exogenous variables can be considered, especially weather-related variables. In this context, ANNs with their inherent capability to infer a function from data represent an efficient solution for load modelling more than linear models. Generating pseudomeasurements using ANNs for load forecasting has been demonstrated to be a viable solution especially for local-level load modelling [12]. In [13], a closed-loop estimator is proposed for a medium-voltage DS, where a machine learning function provides pseudomeasurements to DSSE. The output of the estimator is then fed back to the machine learning function, which allows the estimation when measurement data are missing. For each medium-voltage (MV) node, two feed-forward ANNs are trained to independently forecast nodal active and reactive power. Load time series and indices categorizing the load time series according to the load patterns are used as ANN inputs. The ANNs are retrained over time whenever a new load time series of an MV node is available. In [14], a SE tool with closed flow between the estimator and the machine learning function is proposed as in [13]. In [14], a feed-forward ANN is trained to forecast active power value one step ahead with three types of inputs: historical load information and weather-related and time-related variables. Once the predictive model has been developed, its performance is monitored continuously in order to detect the deterioration over the medium-to-long term (i.e., weeks to months) and retrain it accordingly.

Among all the proposed machine learning methods, multilayer perceptron (MLP) neural networks demonstrated to perform better than others for load forecasting [11, 15]. In particular, in [15], five machine learning methods, i.e., MLP, Support Vector Machines, Radial Basis Functions, Decision trees, and Gaussian Process, have been compared to forecast the active power charges for the next 100 hours. The comparison has been made using three measures of accuracy (MAPE—Mean Absolute Percentage Error; MAE—Mean Absolute Error; and RMSE—Root Mean Squared Error) showing that the MLP is the most robust among the others.

In this context, this paper proposes an MLP load forecasting model for generating simultaneously high-quality active and reactive power pseudomeasurements for an effective branch-current-based DSSE (BC-DSSE). The estimator uses all the available information suitably considering uncertainty sources and correlations. In particular, appropriate weights are introduced to take into account the SM and forecast uncertainties. A realistic measurement scenario composed of few real measurements, SMs, load forecasts, and suitable pseudomeasurements is assumed. In particular, a feed-forward ANN is trained to predict one step ahead the power demands at each MV node. Exogenous variables have been used as predictive model inputs together with historical load information. A closed-loop information, flowing from the ANN outputs to the inputs, has been created to allow the BC-DSSE even though SM measurements are not available at the MV node for the last 24 hours.

The approach proposed in this paper is validated by means of simulation performed on a grid derived from a portion of a distribution network [16], which is a simplified version of an 18-bus UK radial feeder.

2. Distribution System State Estimation

DSSE is the key routine to obtain a picture of the network status at a given time instant. The system is locally considered under steady-state conditions, and the underlying measurement model can be described as follows:

$$\underline{z} = \underline{h}(\underline{x}) + \underline{\epsilon}, \tag{1}$$

where $\underline{z}$ is the vector of available measurements $z_1, \ldots, z_M$; $\underline{x}$ is the vector including all the variables that uniquely define the state of the network; and $\underline{h}(\cdot)$ represents all the measurement functions (generally nonlinear) linking the reference measured values to the state of the system. Vector $\underline{\epsilon}$ includes all the measurement errors and is considered a zero-mean random vector. The state $\underline{x}$ can have different formulations (the so-called voltage state or current state, either in polar or rectangular coordinates), which are equivalent from a theoretical perspective but can lead to advantages in the implementation of DSSE solution routines. Hereafter, the following state $\underline{x}$ is considered (see the BC-DSSE algorithm in [17]):

$$\underline{x} = \left[V_s \;\; I_1^r \;\; \cdots \;\; I_{N_{br}}^r \;\; I_1^x \;\; \cdots \;\; I_{N_{br}}^x \right], \tag{2}$$

where V_s is the voltage magnitude at a node of the network, which is chosen as the reference (e.g., the slack node), while I_k^r and I_k^x are the real and imaginary parts of $k-$th branch current, with the branch index ranging from 1 to the number of branches N_{br}. This branch-current formulation allows

linearizing some of the measurement functions and thus simplifying the estimation process.

From (1), it is clear that, to estimate the network state, it is necessary to manipulate the information coming from measurements in $\underline{z}$, also taking into account the characteristics of the measurement errors. As mentioned above, in DSs, it is hard to have a widespread installation of measurement devices and thus the availability of real-time measurements is typically limited. The measurement vector $\underline{z}$ can thus be divided as follows:

$$\underline{z} = \begin{bmatrix} \underline{z}_{\text{real-time}} \\ \underline{z}_{\text{pseudo}} \end{bmatrix}, \tag{3}$$

where $\underline{z}_{\text{real-time}}$ includes the M_r real-time measurements, which can be voltage magnitude, current magnitude, and active or reactive power measurements as far as conventional measurements are concerned. Vector $\underline{z}_{\text{pseudo}}$ represents information that can be derived from other sources (pseudomeasurements), mainly historical information on active and reactive power consumption or generation. Every load or aggregated load of the network is thus analysed to define its average power absorption or injection. Pseudomeasurements are necessary to allow system observability in this context, but their accuracy is usually very low.

The most widespread technique to perform DSSE is represented by the Weighted Least Squares (WLS) approach, which aims at finding the state that minimizes the following objective function:

$$\hat{\underline{x}} = \text{argmin}_{\underline{x}} \left(\underline{z} - \underline{h}(\underline{x})\right)^T \cdot \underline{\underline{W}} \cdot \left(\underline{z} - \underline{h}(\underline{x})\right), \tag{4}$$

which is the sum of the weighted squared residuals. Matrix $\underline{\underline{W}}$ represents the weighting matrix that allows penalizing or favouring each residual in a different way depending on the accuracy of the corresponding measurement or pseudomeasurement. $\underline{\underline{W}}$ is usually chosen as the inverse of the variance-covariance matrix of the measurements $\underline{\underline{\Sigma}}_{\underline{z}}$ so that all measurements are weighted differently depending on their uncertainty (corresponding to a maximum likelihood estimation in case of normally distributed measurements), which is typically block-diagonal, since measurements performed by different devices can be considered uncorrelated.

The minimization in equation (4) is typically obtained by an iterative Newton solution of the following system of normal equations (considering the generic iteration i) [9]:

$$\underline{\underline{G}}_i \Delta\hat{\underline{x}}_i = \underline{\underline{H}}_i^T \underline{\underline{W}}\, r_i = \underline{\underline{H}}_i^T \underline{\underline{W}} \left(\underline{z} - \underline{h}\left(\hat{\underline{x}}_i\right)\right), \tag{5}$$

where $\Delta\hat{\underline{x}}_i = \hat{\underline{x}}_{i+1} - \hat{\underline{x}}_i$ is the estimated state variation and $\underline{\underline{H}}_i = \mathrm{d}\,\underline{h}/\mathrm{d}\underline{x}^T|_{\hat{\underline{x}}_i}$ is the Jacobian of the measurement functions in $\underline{h}$ with respect to the state variables computed at the previously estimated state. The so-called gain matrix $\underline{\underline{G}}_i$ can be written as

$$\underline{\underline{G}}_i = \underline{\underline{H}}_i^T \underline{\underline{W}}\, \underline{\underline{H}}_i, \tag{6}$$

and it is constant when measurement functions are linear or can be linearized (see [17] for examples and details).

Pseudomeasurements are employed similarly to other measurements but are usually associated with very large uncertainties (e.g., derived from historical variability of loads), which result in small contributions to the objective function in equation (4). Focusing on active power, a typical approach is to consider the following quantities for an unmonitored network node j:

$$\begin{aligned} z_{P_j} &= \frac{1}{|\Gamma|} \sum_{n \in \Gamma} P_j(nT_s), \\ \sigma^2_{z_{P_j}} &= \frac{\sum_{n \in \Gamma} \left(P_j(nT_s) - z_{P_j}\right)^2}{K}, \end{aligned} \tag{7}$$

where z_{P_j} and $\sigma_{z_{P_j}}$ indicate the active power pseudomeasurement and its standard deviation, respectively, $P_j(nT_s)$ is the active power injected (the injection convention is used for both absorbed and generated power) into node j, and T_s defines the time resolution of the available information (historical data). The set Γ includes the considered time instant indices (with n indicating the generic time instant) for all the available power samples, and $K = |\Gamma| - 1$ is its cardinality decreased by one to obtain the classical unbiased variance estimator. The higher the variability of the load/generator, the larger the corresponding variance, which is inversely proportional to the weight $w_{z_{P_j}}$ associated with the pseudomeasurement. A typical variation range of the power drawn by a load is over 50% of its nominal value, so it is easy to see that pseudomeasurements, while guaranteeing observability, are often of little help in improving the estimation accuracy.

In this context, SMs, and, in particular, those of 2nd generation, can play a significant role in enhancing pseudomeasurement definition. New SMs can provide voltage magnitude and active and reactive power measurements, with a much faster reporting rate than before. Italian authority for electric energy, for instance, gives and continuously updates directives on the functionalities for new-generation SMs, which include, among others, a 2 s measurement interval for "instantaneous" power measurements [18]. These measurements might be, in the future, directly acquired and integrated into estimation algorithms, but due to the huge number of installed SMs (above 30 million in Italy), it would be difficult to directly manage them in real-time and investment costs for communication and computation could easily become overwhelming.

For this reason, it is much more likely that SM measurements are used in an indirect and delayed way. The approach proposed in this paper is to collect active and reactive power measurements from SMs and exploit them to forecast the power consumption at a given time with anticipation compatible with the timing and data collection requirements. To this purpose, load forecasting Artificial Neural Network (ANN) models have been trained for different types of loads and/or aggregation of loads, as detailed in the following section. In fact, SM measurements from large customers or from a set of users connected to a given node (for instance, in a medium-voltage network) can be gathered from the field one day or few hours ahead the time instant of BC-DSSE execution and aggregated, so that they can serve as inputs in the neural load forecasting process.

As previously mentioned, once the forecast power consumption or generation of a given node is obtained, it can be included in $\underline{z}$ as an enhanced pseudomeasurement and it is thus important to associate the correct covariance matrix to the new forecast quantities, thus allowing a correct weighting of the corresponding residual in the WLS procedure, according to equation (4).

Focusing on a generic bus j, the forecast procedure gives two predicted quantities P_j^F and Q_j^F, which are the active and reactive power injections, respectively. The following covariance matrix is thus needed:

$$\underline{\underline{\Sigma}}_{\underline{z}_{PQ_j}} = \begin{bmatrix} \sigma^2_{z_{P_j}} & \sigma_{z_{P_j} z_{Q_j}} \\ \sigma_{z_{P_j} z_{Q_j}} & \sigma^2_{z_{Q_j}} \end{bmatrix}, \tag{8}$$

where $\sigma^2_{z_{P_j}}$ and $\sigma^2_{z_{Q_j}}$ are the variances of new pseudomeasurements z_{P_j} and z_{Q_j}, while $\sigma_{z_{P_j} z_{Q_j}} = \rho_{PQ_j} \sigma_{z_{P_j}} \sigma_{z_{Q_j}}$ is the covariance between the pseudomeasurement errors of the two forecast powers and ρ_{PQ_j} is the corresponding correlation coefficient. It is interesting to notice that, while in conventional DSSE approaches, the active and reactive powers pseudomeasurements are usually considered as uncorrelated, in the proposed approach, further information is taken into account and the correlation arising in the simultaneous estimation of P_j and Q_j can be easily included in the estimator by using the submatrix $\underline{\underline{W}}_{\underline{z}_{PQ_j}} = \underline{\underline{\Sigma}}^{-1}_{\underline{z}_{PQ_j}}$ in the overall weighting matrix.

Another important aspect, which is usually overlooked in the literature, is the modelling of the SM uncertainty. The proposed load forecasting is designed to obtain an estimation of the measured P_j and Q_j at a given time instant nT_s from previous available measurements, but this means that the computed power values can be considered only as approximations of the measured values (reference values are obviously unknown in practical conditions and real-time operation). The SM measurement chain is an additional source of uncertainty that affects the values considered in equation (8). As an example, the calibration process of SM devices cannot be perfect and compensate for all the systematic errors in all the operating conditions.

For this reason, in the following, the definition of the weights is discussed in detail in the presence of both forecast and SM errors. Focusing on z_{P_j} and z_{Q_j}, it is possible to distinguish the two zero-mean error contributions as follows:

$$z_{P_j} = P_j^F = P_j^{\text{ref}} + e_{P_j} = P_j^{\text{ref}} + e^F_{P_j} + e^{\text{SM}}_{P_j}, \tag{9}$$

$$z_{Q_j} = Q_j^F = Q_j^{\text{ref}} + e_{Q_j} = Q_j^{\text{ref}} + e^F_{Q_j} + e^{\text{SM}}_{Q_j}, \tag{10}$$

where P_j^{ref} and Q_j^{ref} are the ideal reference values of active and reactive power, $e^F_{P_j}$ and $e^F_{Q_j}$ are the corresponding forecast errors, and $e^{\text{SM}}_{P_j}$ and $e^{\text{SM}}_{Q_j}$ are the errors associated with the aggregated SM outputs. In the following, in the absence of further information, all the errors of the SMs associated with loads or generators grouped under the jth node are considered independent. Similarly, the active and reactive power measurement errors are assumed uncorrelated.

Given the relative standard uncertainty α^{SM} of the generic SM (as derived from the SM datasheets and assumed as common to all SMs, without loss of generality), the relative standard uncertainty associated with $e^{\text{SM}}_{P_j}$ becomes

$$u_{e^{\text{SM}}_{P_j}} = \alpha^{\text{SM}} \frac{\sqrt{\sum_{i \in \Lambda_j} \left(P_i^{\text{SM}}\right)^2}}{\sum_{i \in \Lambda_j} P_i^{\text{SM}}}, \tag{11}$$

where P_i^{SM} is the measured active power of load i, which belongs to the set Λ_j of the loads downstream the MV node j. Since the lack of knowledge in SM behaviour can be considered as independent from the prediction errors, the overall variance of the measurement z_{P_j} can be expressed as follows:

$$\begin{aligned} \sigma^2_{z_{P_j}} &= \sigma^2_{e_{P_j}} = \sigma^2_{e^F_{P_j}} + \sigma^2_{e^{\text{SM}}_{P_j}} = \sigma^2_{e^F_{P_j}} + u^2_{e^{\text{SM}}_{P_j}} P_j^2 = \sigma^2_{e^F_{P_j}} \\ &\quad + u^2_{e^{\text{SM}}_{P_j}} \left(\sum_{i \in \Lambda_j} P_i^{\text{SM}} \right)^2. \end{aligned} \tag{12}$$

Similar expressions are valid for the reactive power while the correlation coefficient ρ_{PQ_j}, under the above assumptions, becomes as follows:

$$\rho_{PQ_j} = \frac{\sigma_{z_{P_j} z_{Q_j}}}{\sigma_{z_{P_j}} \sigma_{z_{Q_j}}} = \frac{\sigma_{e^F_{P_j} e^F_{Q_j}}}{\sigma_{z_{P_j}} \sigma_{z_{Q_j}}} = \frac{\rho^F_{PQ_j}}{\sqrt{1 + \left(\sigma^2_{e^{\text{SM}}_{P_j}} / \sigma^2_{e^F_{P_j}} \right)} \sqrt{1 + \left(\sigma^2_{e^{\text{SM}}_{Q_j}} / \sigma^2_{e^F_{Q_j}} \right)}}, \tag{13}$$

where $\rho^F_{PQ_j}$ is the correlation coefficient of the active and reactive power forecast errors.

The way these values are computed in practice is explained in the following section, where information available at each step is discussed. The above equations allow the computation of the elements of $\underline{\underline{\Sigma}}_{\underline{z}_{PQ_j}}$ (see equation (8)) and thus, the definition of the weights for BC-DSSE that reflect appropriately the actual uncertainty in the proposed pseudomeasurement model.

3. Load Forecasting Neural Network Model

A Multilayer Perceptron (MLP) ANN with one hidden layer is used to forecast the load demand one step ahead (roughly speaking "$t + 1$ prediction," where the actual time step depends on the chosen ANN model in terms of input and output variables), where the time interval for prediction update is assumed equal to half an hour. In particular, residential and Small and Medium Enterprises (SMEs) loads have been considered in this paper. An MLP has been trained for each single or aggregated load. It has to be noted that, while for the residential loads, only the active power has been forecasted, as in the majority of the literature, for the SME loads, the corresponding reactive power is also considered in the proposed model. Figure 1 shows the structure of the MLP neural network for a SME.

The relationship between input and output patterns is described by the following algebraic equations system:

$$\begin{cases} \text{input layer} & \underline{\underline{W}}_1 \cdot \underline{v} + \underline{b}_1 = \underline{y}, \\ \text{hidden layer} & \underline{h_l} = f\left(\underline{y}\right), \\ \text{output layer} & \underline{\underline{W}}_2 \cdot \underline{h_l} + \underline{b}_2 = \underline{o}, \end{cases} \tag{14}$$

where $\underline{v}$ is the input vector, which contains variables related to the time instant t:

(i) Two weather variables at the time instant t: temperature, measured in °C, and humidity, in percentage;

(ii) Three time-related variables: these consist of a label corresponding to the hour of the day $[1, 2, \ldots, 12]$, a label for the day of the week $[1, 2, \ldots, 7]$, and a label {1/0}, where 1 indicates a working day and 0 indicates a nonworking day;

(iii) Four historical demand variables, which have a strong correlation with the recorded demand profile (active power for residential loads, whereas both active and reactive powers for SMEs): the demand at the previous hour, the demand at the same hour of the previous day, the demand at the same hour of the previous week, and the 24-hour average power evaluated considering all the recorded values in the previous day. As the considered time step is half an hour, the variables at the previous one hour, one day, and one week correspond to 2 steps, 48 steps, and 336 steps back.

The output $\underline{o}$ of the network consists in the one-step ahead forecast load demand.

At time instant nT_s that corresponds to the current time tag of DSSE computation update, information on active and/or reactive powers of node j is needed. In the proposed solution, if the ANN forecast model is available for node j, powers P_j and/or Q_j are obtained, thanks to the performed prediction. In this case, the instant indicated as "$t+1$" in the forecast model description (see Figure 1) corresponds to the current time instant nT_s. For ease of presentation, a perfect match has been here adopted between T_s and the time interval of prediction update (half-hour step for both prediction and estimation updates), but other solutions at different rates are also possible following a similar scheme. As mentioned above, an ANN model is built for all the loads of interest and its outputs (load predicted powers) are fed into the DSSE algorithm at the following time step, with the procedure described in the previous section.

$\underline{\underline{W}}_1$ is the weight matrix of the input layer, $\underline{b}_1$ is the bias vector of the input layer, $\underline{y}$ is the input of the hidden layer, $\underline{h_l}$ is the output of the hidden layer, $f(\cdot)$ is the hidden neuron (logistic) activation function, $\underline{\underline{W}}_2$ is the weight matrix of the output layer, and $\underline{b}_2$ is the bias vector of the output layer.

The Levenberg–Marquardt algorithm [19], which combines the gradient descent method and the Gauss–Newton method, has been used for the MLP training. The hyperbolic tangent sigmoid transfer function is used in the hidden layer. The inputs and outputs are normalized in the range $[-1, 1]$ before being used to train the ANN to balance the importance of input variables.

In the following, the case study and the database used to train and test the forecasting models are described.

4. Case Study

To evaluate the performance of the proposed approach, several tests have been carried out on a single-phase 18-bus network derived from a UK network (Figure 2) [20]. Connected to the 33 kV at bus 1, the network has a common rated bus voltage level at 11 kV. This network is used since it is adopted for other studies in the literature and gives a realistic load scenario for a MV network. On this topology, both industrial and residential loads have been considered as explained in detail in the next section. There is no loss of generality in considering loads information (SM measurements) coming from the database described in the next section, since individual loads are aggregated to replicate a load scenario that is compatible with nominal data of the considered network in [20]. Main assumptions and test results are also reported and discussed in the following.

4.1. Database for the Load Forecasting. To train and test the neural networks used to perform the load forecasting, data related to the active power consumption, available from the Commission for Energy Regulation (CER) [21], have been used. This database is anonym, and it consists of recorded half-hourly SM energy consumption from 6445 customers that participated in the "Electricity Smart Metering Customer Behavior Trials" [22]. The data are collected over a period of 18 months (from July 14, 2009, to December 31, 2010), at various distribution network locations in Ireland. The customer types are classified as residential (4225), SME (485), and others (1735). The present paper focuses on residential (the largest group in the available database) and SME customers who completed the trial. The SME customers are grouped into four subsectors: entertainment (including hotels, restaurants, sporting facilities, and public houses), industrial manufacturing, offices, and retail premises.

After removing the consumers having missing data, a database of 3423 residential and 287 SME consumers has been obtained. For SME loads, the reactive power profiles have been obtained starting from a real power factor (PF) profile recorded on a typical industrial site. In particular, the recorded PF profile has been propagated on the whole observation period. No reactive power was taken into account for residential loads.

Analyzing residential and SME data, a significant difference between the two consumer types can be observed. Figure 3 shows the power consumption (P, where the node index is dropped in the following when unnecessary, for the sake of simplicity) of four residential loads, randomly selected from the database. As can be noted, the energy consumption of each household is low, not regular, and very different in two consecutive working days as it depends on the lifestyle of its residents. On the contrary, the SME loads

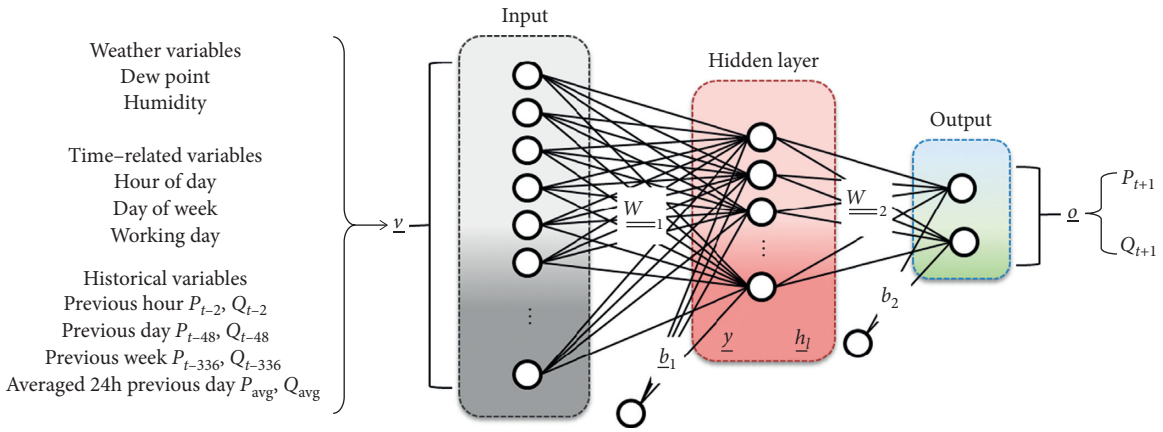

Figure 1: Structure of the active (P) and reactive (Q) power one-step ahead forecasting neural network model for SMEs (the structure of the neural network for residential loads considers only active power both in the input and the output layers).

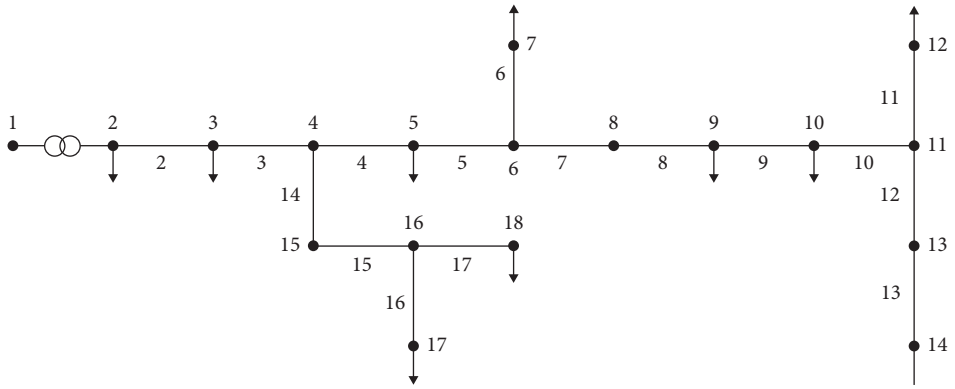

Figure 2: 18-node test network.

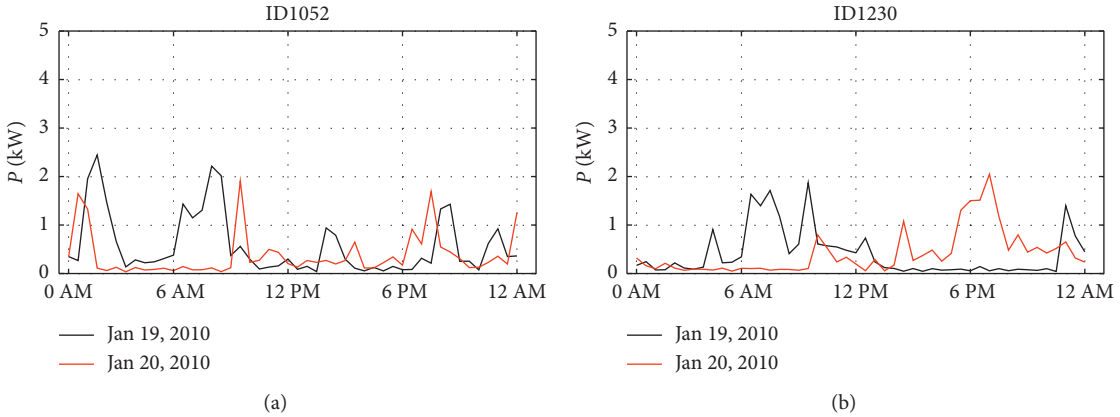

Figure 3: Continued.

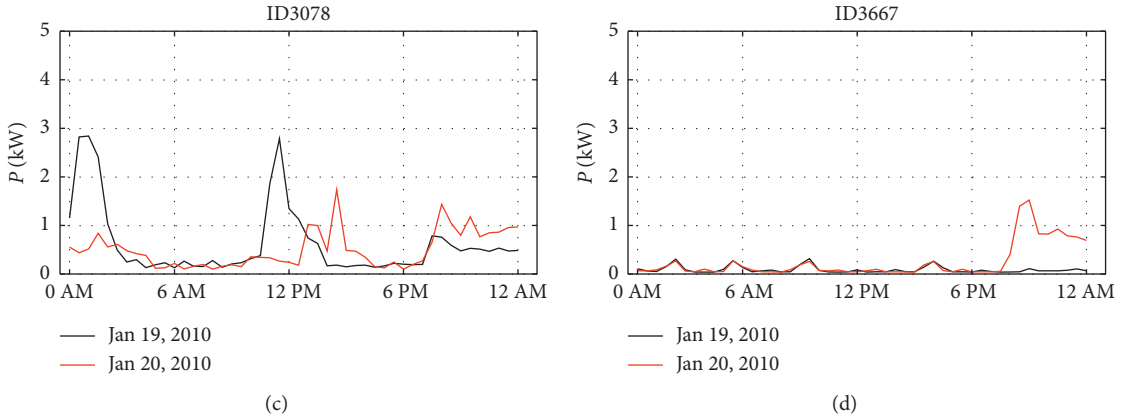

Figure 3: Power consumption of four residential loads in two consecutive working days.

(Figure 4) appear typically high and mostly regular due to the regular activity during the working hours and working days. Therefore, a different load forecasting performance for these two subsets is expected.

Since the objective of this paper is an effective state estimation of a DS, different equivalent MV loads have been created aggregating loads from the database with the aim to obtain power levels compatible with those of the considered grid (Figure 2). The load aggregation has been performed simply summing together the readings of several SMs. In particular, three different SME loads (sme_1, sme_2, and sme_3) are obtained by aggregating 21, 26, and 46 individual SMEs data, respectively. Moreover, two different residential loads (res_1 and res_2) are obtained by aggregating, respectively, the energy consumption of 523 and 537 residential loads randomly chosen. In Table 1, the ranges of the active power of the aggregate loads are reported.

Figure 5 shows the power consumption of one aggregated residential (res_1) and one aggregated SME (sme_3) load in the same two consecutive days considered in Figures 3 and 4. As expected, the aggregation makes the load profile more predictable. In fact, especially in the case of residential loads (Figure 5(a)), the agregate load is more periodic and smoother than individual ones. This is because the aggregation operation permits to remove the high-frequency impulses corresponding to random events in the individual curve, alleviating and smoothing the randomness. Regarding the aggregated SME load (Figure 5(b)), its periodicity is more evident because the individual SME loads are already more periodic than individual residential loads.

The demand profiles depend not only on historical load evolution but also on exogenous variables, such as season and weather-related variables. Therefore, weather data, collected from the Irish Meteorological Service [23], have been added to the database. Among the weather variables, in this paper, the temperature (in °C) and the humidity (in percentage) have been chosen as neural model inputs. This is because when the value of the temperature varies, the power system demand also varies. Furthermore, the humidity plays a relevant role in driving electricity demand during the warm months. In fact, the temperature above certain values is intensified by high humidity [24]. As the aggregation has been performed by selecting individual loads located in different Irish areas, the simple averages of the temperature and the humidity percentage measured by several weather stations located in the central area of Ireland are used to represent the corresponding weather variables.

To highlight the dependence of the load energy consumption on the weather data, Figure 6 reports the daily energy consumption of res_1 and sme_3 and the average daily temperature trend over the same period. As can be noted, both residential and SME aggregated loads show a time pattern dependent on the temperature, with a stronger dependence for the residential load. Obviously, the dependence of the load energy consumption on the temperature data, even if prevailing, is not the only one. In fact, the drastic reduction in the consumption of SME loads and the increase in the residential one at the end of December 2009 are mainly related to the Christmas-New Year period rather than the temperature. In this paper, the dependence of the load energy consumption to the weather data is demonstrated by evaluating how the performance of the forecasting model is affected when the weather variables are excluded from the inputs of the model. The results are shown in the following section. Other weather variables, such as precipitation and wind speed, were analyzed, but it was found that, in this case, they do not have a significant impact on the energy demand.

As Figure 6 highlights, the considered energy consumption time series shows strong regularity, and a spectrum analysis revealed a prevalent daily periodicity, but at the same time, it is decidedly nonlinear. This complex data behavior can be captured by a MLP, which owns the ability to construct a larger set of nonlinear input/output mapping, by combining an appropriate number of nonlinear activation functions. Therefore, in this case study, a simple MLP, with a suitable structure, can be enough to build a performing forecasting model avoiding the overfitting of the training data.

4.2. Performance of the Load Forecasting Models. A neural load forecasting model has been designed for each aggregated load characterized by the range reported in Table 1. In order

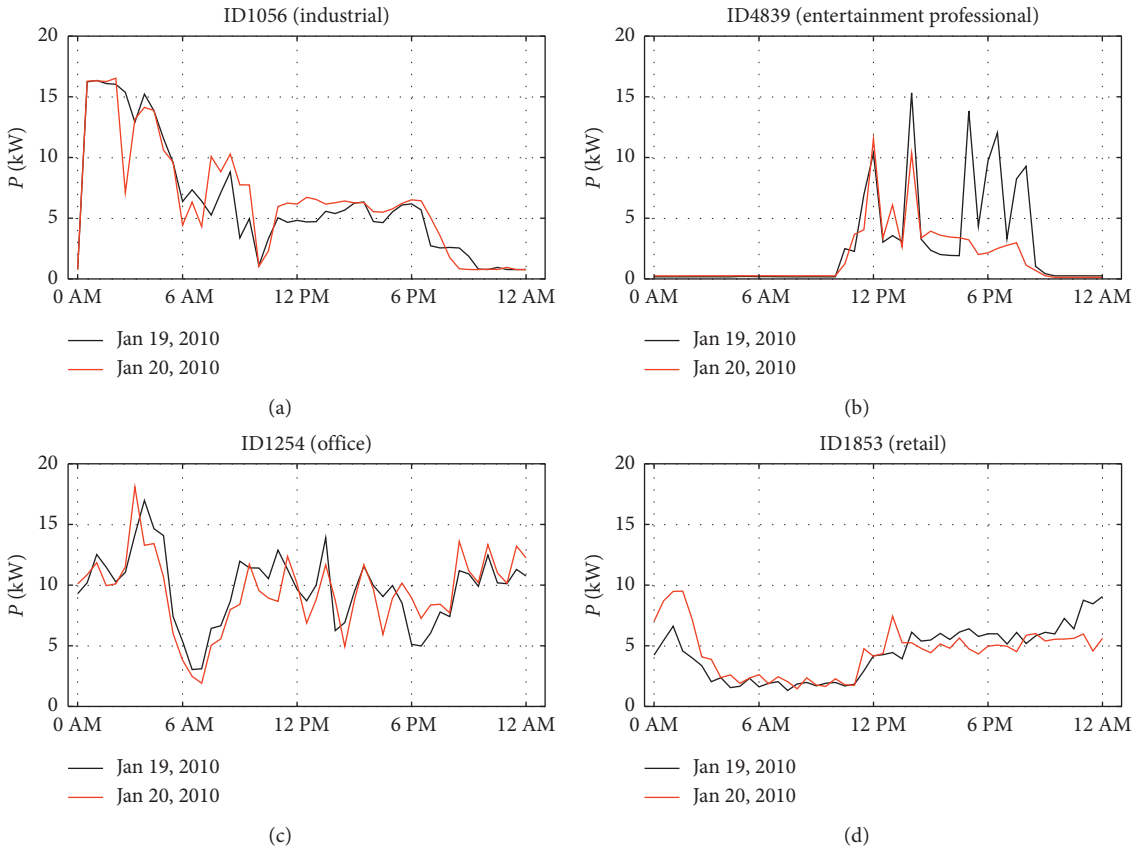

Figure 4: Power consumption of four SME loads in two consecutive working days.

Table 1: Range of active power P of the aggregate loads.

	sme_1	sme_2	sme_3	res_1	res_2
Min (kW)	67.70	101.64	192.32	69.68	73.05
Max (kW)	420.55	537.83	907.10	639.99	663.22

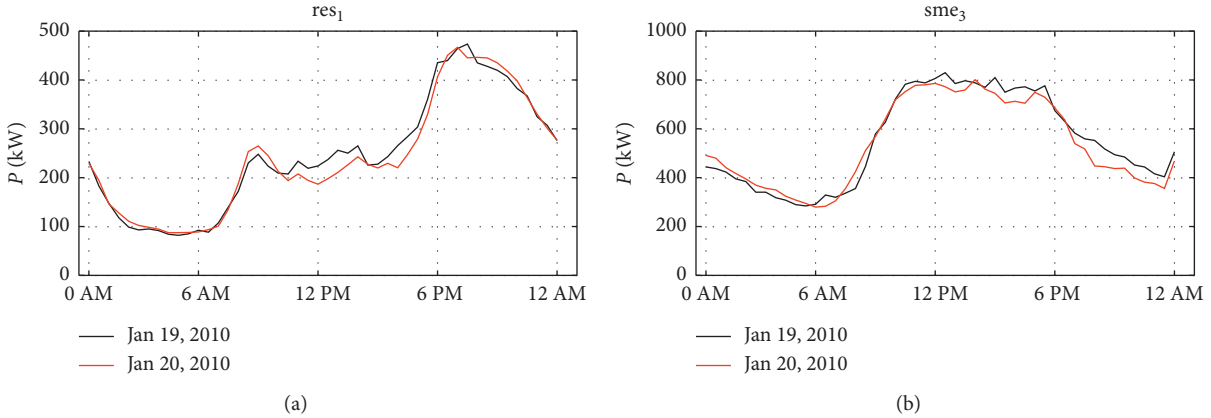

Figure 5: Aggregation of residential (a) and SME (b) loads.

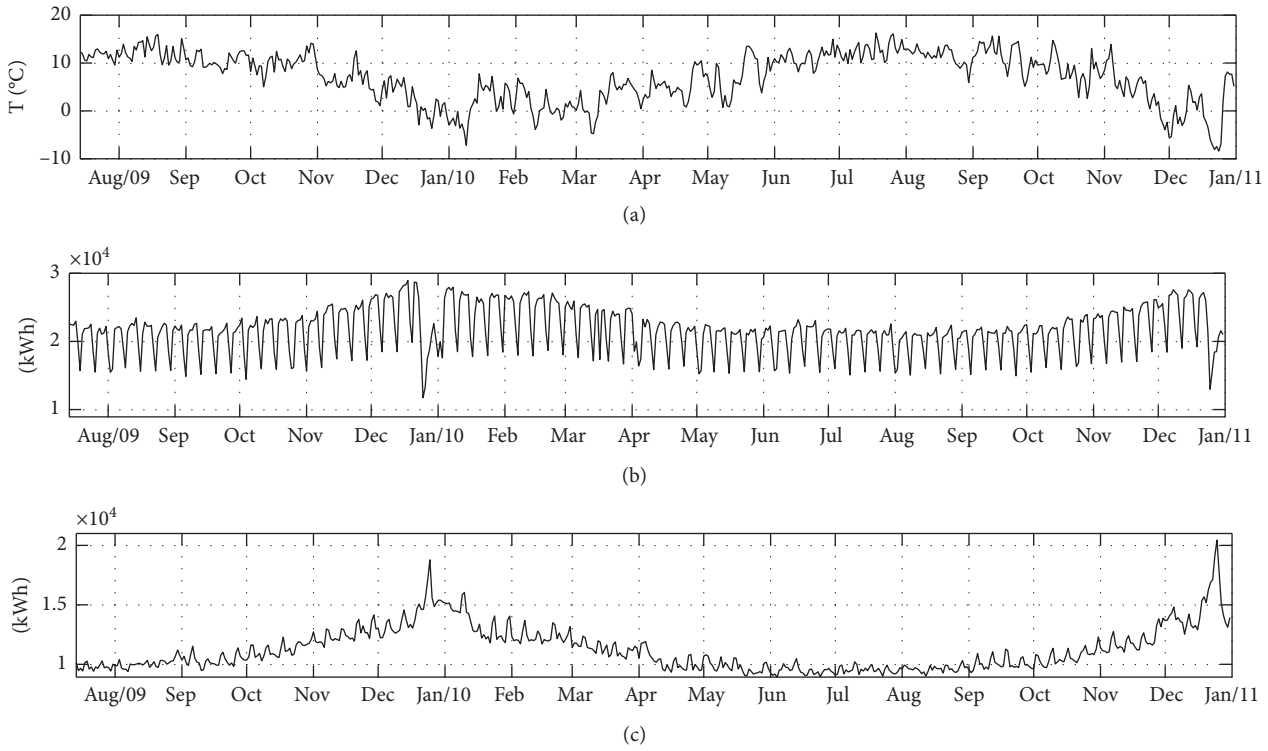

Figure 6: Residential and SME aggregate daily energy consumption compared with the average daily temperature trend. (a) Average daily temperature. (b) sme_3 daily energy consumption. (c) res_1 daily energy consumption.

to optimize the load forecasting network architecture, a trial-and-error approach has been performed to choose the appropriate number of hidden layer nodes, which consists in progressively growing the number of nodes, and selecting the network that minimizes the prediction error on the validation set. This optimization procedure resulted in 20 neurons for all the five networks (associated with loads in Table 1). Therefore, the best MLP architecture consists of an input layer with one neuron for each input variable (thus 9 or 13, for residential or SME, respectively), one hidden layer with 20 neurons, and an output layer with one neuron for each output variable (1 or 2 for residential or SME, respectively). Thus, the dimensions of the weight matrices and bias vectors in equation (14) result in 20×9 for $\underline{\underline{W}}_1$, 20×1 for $\underline{b}_1$, 1×20 for $\underline{\underline{W}}_2$, and 1×1 for $\underline{b}_2$ in case of residential loads. In case of SME loads, $\underline{\underline{W}}_1$ and $\underline{b}_1$ are 20×13 and 20×1, respectively, whereas $\underline{\underline{W}}_2$ and $\underline{b}_2$ are 2×20 and 2×1, respectively.

The time series of each load profile is composed of 25728 half-hourly active and reactive (when considered) power values, from August 1, 2009, to December 31, 2010, while the July 2009 data were not used as only the recordings of fifteen days were available. The MLP training has been performed using the data of the first 12 months. The validation has been performed using the following 2 months (from August 1, 2010, to September 30, 2010). The last 3 months (from October 1, 2010, to December 31, 2010) have been used to test the trained neural model.

Since the forecasting accuracy depends both on the quality and quantity of the historical data used to train the predictor, a greater amount of data, for example, an extra year would certainly improve the prediction performance.

Note that a realistic assumption about the monitoring architecture could be that data from SMs are actually available after 24 hours. However, the proposed solution can also work with data collected one hour before (that could represent a future-proof scenario). Thus, during the training of the neural model, this information, both for active and reactive powers, has been included among inputs, because it is always available in the offline phase. In the online test phase, the corresponding inputs have been replaced by the values forecasted by the neural predictor at the previous steps. The outputs of the predictor are then fed back to the input layer creating a closed-loop information flow. This allows the state estimation even when measurement data are missing.

To evaluate the performance of the predictive models, the MAE, the MAPE, and the Root Mean Square Percentage Error (RMSPE), defined as in the following, have been used:

$$\begin{aligned} \text{MAE} &= \frac{1}{n}\sum_{i=0}^{n}\left|o_i - \widehat{o}_i\right|, \\ \text{MAPE} &= \frac{100}{n}\sum_{i=0}^{n}\left|\frac{o_i - \widehat{o}_i}{o_i}\right|, \\ \text{RMSPE} &= 100\sqrt{\frac{1}{n}\sum_{i=0}^{n}\left|\frac{o_i - \widehat{o}_i}{o_i}\right|^2}, \end{aligned} \tag{15}$$

where o_i is the actual load value, which can thus represent either the active power P or the reactive power Q of the considered load (respectively, P_j and Q_j when referring to

the network nodes as in the DSSE section above); $\hat{o}_i$ is the corresponding predicted load value; and n is the number of training or testing samples. The smaller the values of MAE, MAPE, and RMSPE are, the better the forecasting performance is.

Figure 7 shows (in the top) the actual (black line) and the predicted (red line) active power load time series and (in the bottom) the corresponding differences between predicted and actual load powers for a month (October) of the test set related to sme_1. Figure 8 reports the same time series for res_1. As can be noted, the trends of the two loads are efficiently modeled by the neural predictors.

Figures 9 and 10 report the behavior of the actual and predicted real power load time series (top) and the corresponding prediction error (bottom), for the sme_1 and res_1 respectively, during the first test week. The MAPE for the forecasted active power in this time window results in 4.7% for the sme_1 and 4.8% for res_1. Moreover, the validity of the zero-mean hypothesis has been verified for errors of both active and reactive power prediction.

In Table 2 and in Table 3, the training and test performances, obtained for the SME and residential aggregate loads, are reported, respectively.

It can be noted that, as expected, the performance deteriorates in the test phase. The SME loads show that the error percentages of the active and reactive power are very similar. The correlation coefficients between the real and reactive power errors are then evaluated to be used in the following, for the state estimation.

The results on the test set show that the proposed predictive model is able to forecast simultaneously both active and reactive powers (when required) with limited errors, starting from both exogenous and historical measurements. Moreover, it overcomes the problem of limited or time-delayed historical measurement availability throughout a closed loop information flow, which replaces the missing data with values forecasted by the predictor itself at the previous step.

The influence of the input variables on the load energy consumption can be evaluated through the performance of the forecasting model. In fact, the performance of the neural network model is expected to deteriorate when an effective variable is excluded from the inputs. In this paper, since aggregated loads show a time pattern dependent on the temperature, highlighted in Figure 6, the dependence of the load energy consumption on the weather data has been assessed. Removing the weather variables, the RMSPE on the test set increases by about 2%, for both active and reactive powers for SME costumers, and by about 1% for the residential ones (which are significant variations with respect to the results reported in Tables 2 and 3).

5. Performance of the Distribution Systems State Estimation

To assess the estimator performance, several simulations have been carried out starting from a measurement scenario that is realistic for a distribution grid. Two measurement points have been assumed on the network: on bus 1, with a magnitude voltage measurement and an active and reactive power flow measurement; on bus 4, with a magnitude voltage measurement. SMs have been considered providing data fully available the day after the measurements. An accuracy equal to 1% for the magnitude of the voltage and equal to 3% for the power flows and SM measurements have been assumed.

A Monte Carlo approach has been applied in order to obtain statistically sound results, and the following assumptions are made:

(i) Number of Monte Carlo trials, $N_{\text{MC}} = 1000$

(ii) A maximum deviation of 50% with respect to the nominal values for the active and reactive powers drawn by the loads (uniform distribution)

(iii) Measurement errors uniformly distributed

The SME loads sme_1, sme_2, and sme_3 have been connected to buses 17, 14, and 7, respectively (and thus are described by the couples $P_{17} - Q_{17}$, $P_{14} - Q_{14}$, and $P_7 - Q_7$), while residential loads res_1 and res_2 have been associated with buses 3 and 12 (and thus associated with P_3 and P_{12}). As for these loads, the last 1000 values of the test set have been considered, which correspond to a temporal interval of about 21 days. For each instant, a different operating condition of the network is thus considered by using such values for SME and residential loads and extracting the reference values applying the SM uncertainty. For all the other loads, active and reactive powers are extracted from nominal values according to the above assumption. Then, all reference values are computed from these load conditions by means of load flow calculation. Finally, measurements are also extracted from their random distribution and used as inputs to the BC-DSSE.

To assess the performance of the estimator, two different formulations and configurations of the BC-DSSE that correspond to different computation and management of the pseudomeasurements have been adopted. The first one, which uses the proposed estimator, exploits the predictions of the loads coming from the corresponding neural load forecasting models. This case is indicated as "*Prediction*" in Figures 11–13 reporting DSSE results in the following.

As mentioned in the previous section, the forecast active and reactive powers of SME loads (P_j^F and Q_j^F, with $j \in \{7, 14, 17\}$) have been used for each instant together with the forecast active power of residential loads (P_j^F with $j \in \{3, 12\}$).

To build the weighting matrix, besides the real-time measurement weights, submatrices concerning forecast loads must be included (see equations (9) and (10)) in the BC-DSSE. According to equation (12) (and its counterpart for reactive power), the variance of the pseudomeasurement is computed by using the RMSPE of the training set for the forecast errors and the datasheet information for the SMs. Since the SM measurements are not available in real time, the relative uncertainty of the aggregated power is evaluated for each time instant as the relative uncertainty of the day before at the same hour and it is

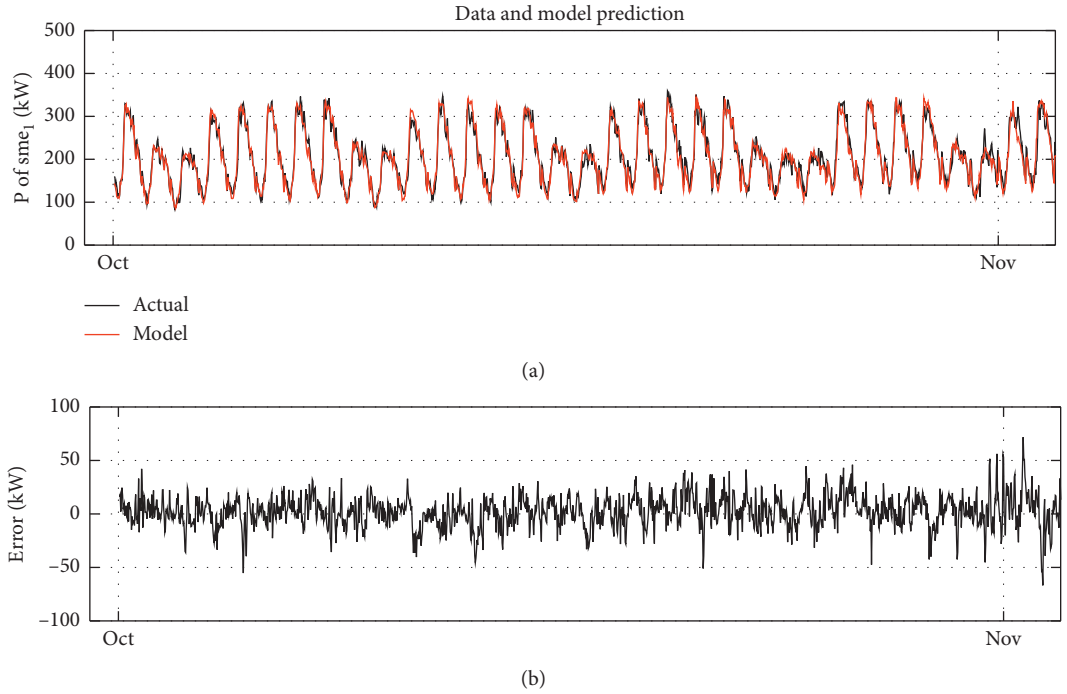

FIGURE 7: Test set behavior related to sme$_1$: (a) the red curve represents the predicted real power values and black curve represents the actual one; (b) the differences between predicted and actual load powers.

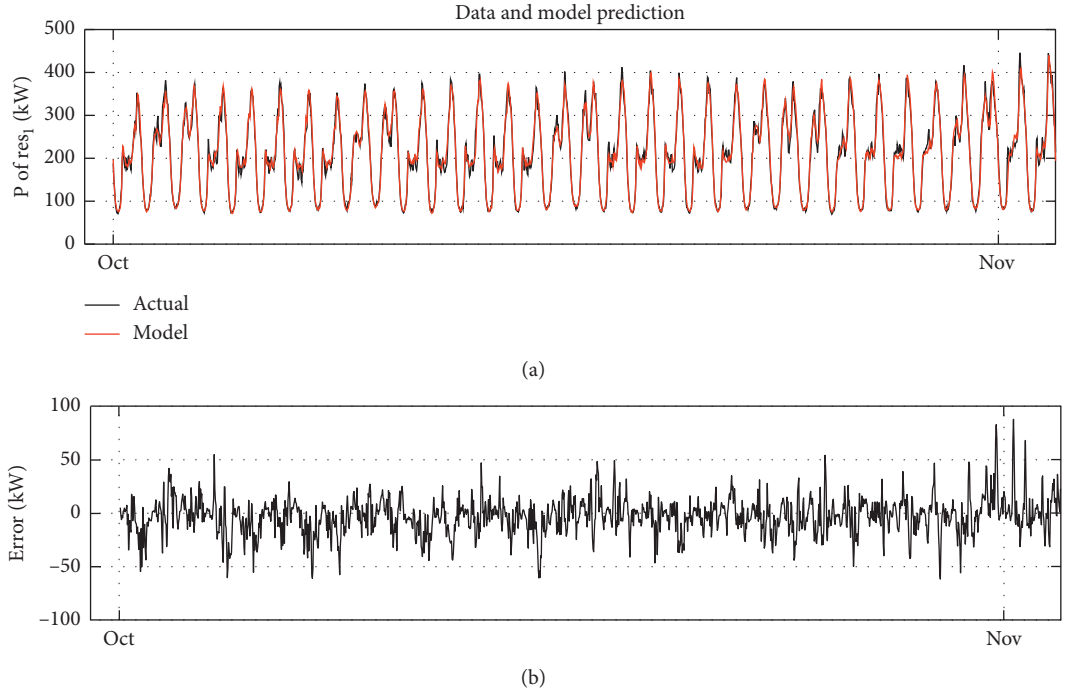

FIGURE 8: Test set behavior related to res$_1$: (a) the red curve represents the predicted real power values and black curve represents the actual one; (b) the differences between predicted and actual load powers.

associated with the aggregated forecast powers at the current instant. The above procedure has been applied for all the estimations. It is interesting to notice that, with this model, RMSPE can also be updated at fixed intervals by considering the measurements and forecast data obtained in the meanwhile.

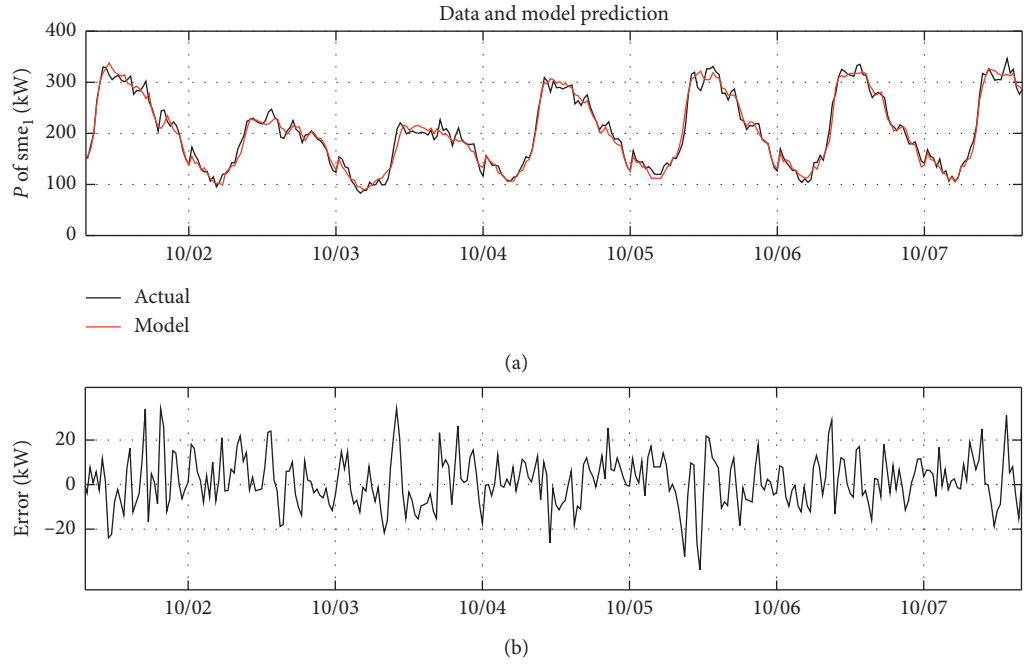

Figure 9: Detail of the first test week related to sme_1; (a) the red curve represents the forecasted real power values, and the black curve represents the actual one; (b) the corresponding error in kW.

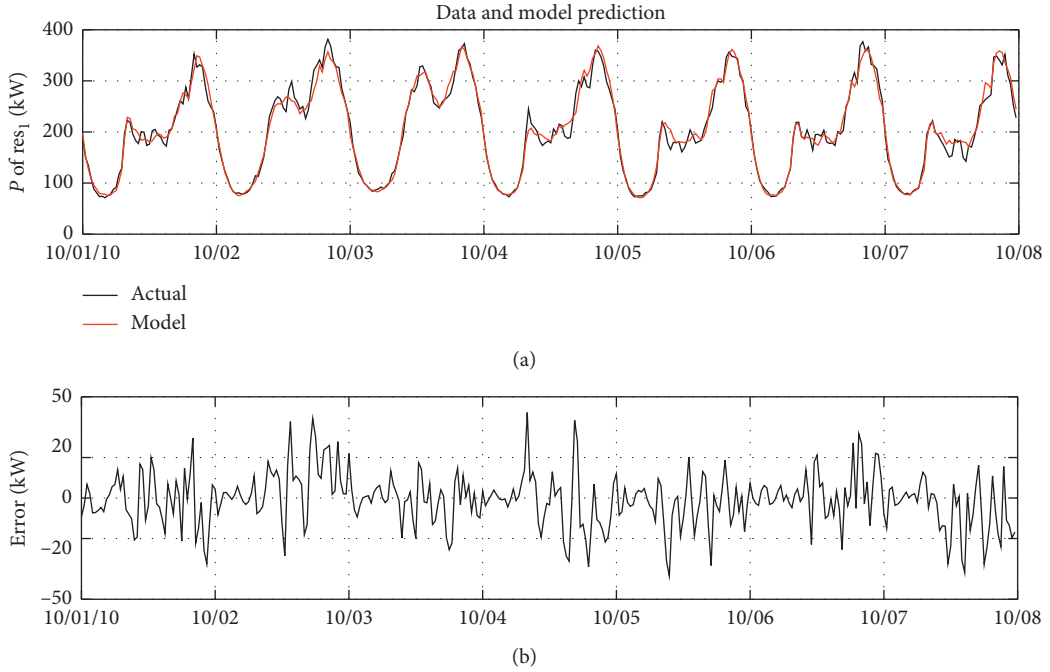

Figure 10: Detail of the first test week related to res_1: (a) the red curve represents the forecasted real power values, and the black curve represents the actual one; (b) the corresponding error in kW.

The second formulation corresponds to the classical BC-DSSE where no forecasting is considered, and pseudomeasurements of nodes 3, 7, 12, 14, and 17 are directly computed from the available measurement data. In particular, the measured power values collected the day before at the same hour are used as pseudomeasurements. This estimator thus does not apply predictions (and is referred to as "*No prediction*" algorithm) and is considered as a benchmark for the proposed method in the same network scenarios.

Table 2: Performance of the neural load forecasting models for the SME aggregated loads (training and test).

Aggregate load	Active power (P)						Reactive power (Q)					
	MAE (kW)		MAPE (%)		RMSPE (%)		MAE ($k$var)		MAPE (%)		RMSPE (%)	
	Train	Test	Train	Test	Train	Test	Train	Test	Train	Test	Train	Test
sme_1	11.2	15.2	5.5	7.4	7.5	12.0	2.1	2.8	5.5	7.4	7.5	11.9
sme_2	11.7	15.5	5.2	7.5	7.0	10.8	2.2	3.3	5.2	7.5	7.0	10.8
sme_3	17.4	26.9	4.1	6.2	5.4	9.1	3.3	5.1	4.1	6.2	5.4	9.0

Table 3: Performance of the neural load forecasting models for the residential aggregated loads (training and test).

Load	Active power (P)					
	MAE (kW)		MAPE (%)		RMSPE (%)	
	Train	Test	Train	Test	Train	Test
res_1	10.7	16.9	4.9	7.6	6.7	10.5
res_2	12.0	19.3	5.1	8.1	6.7	11.0

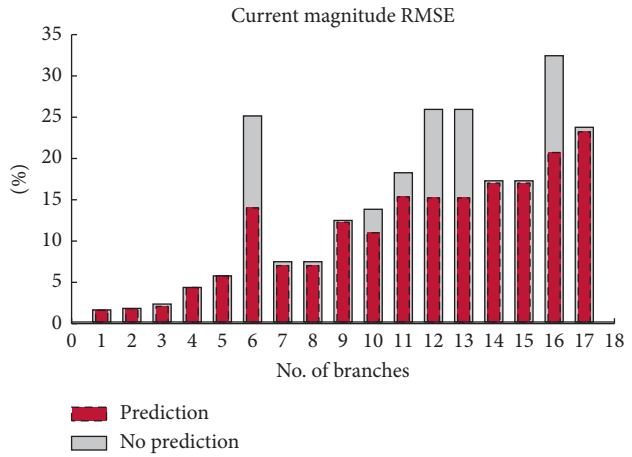

Figure 11: Current magnitude RMSEs obtained with and without the ANN-based prediction.

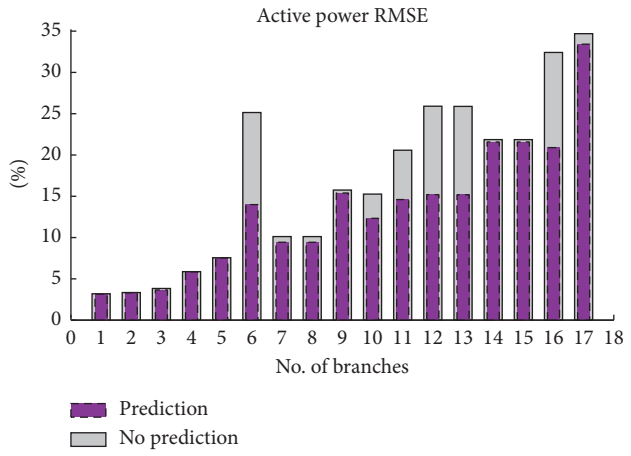

Figure 12: Active power RMSEs obtained with and without the ANN-based prediction.

Once the state variables (branch currents) are estimated along with derived quantities (e.g., voltages and power flows), a comparison of the results obtained with the two methods is performed in terms of percent root mean square errors (RMSEs) of the estimations (i.e., the square root of the mean of the squared differences between the estimated quantities and the corresponding reference values). RMSE results of the branch-current magnitude estimations are presented in Figure 11. The bar plot in red (dash line) shows the results obtained considering the prediction of the loads, while the bar plot in grey (the same holds for the Figures 12 and 13) presents the results obtained considering the above-described pseudomeasurements. A reduction close to 12% (meaning that the error is about halved) has been obtained as a best case on branch 6, where the largest forecast load sme_3 is connected, and an average reduction of more than 3% is also obtained. It is clear that the reductions in the estimation errors are more evident close to the position of the forecast loads. Branches 12 and 13 clearly show the same accuracy results, since node 13 is a zero-injection node. The same holds for the pairs 7-8 and 14-15.

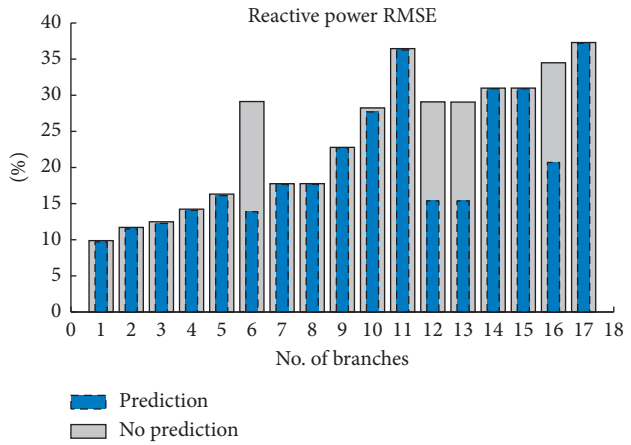

Figure 13: Reactive power RMSEs obtained with and without the ANN-based prediction.

Figure 12 shows the results obtained in terms of percent RMSE of the active power flow estimations for all the network branches. The bar plot in violet (dash line) shows

the results obtained considering the prediction. The considerations that can be drawn by these results are similar to those obtained for the branch currents: estimation improvements are more evident for the branches that are close to larger predicted loads. The error reduction is also more effective when lateral branches or leaves of the network are considered. In this case, the proposed algorithm brings a maximum reduction about 11.5% (error reduction of about 44%). Moreover, an average reduction of more than 3.3% is obtained.

As for reactive power estimations, it is possible to see in Figure 13 that the estimations are mainly affected by the prediction of the industrial loads locally, since the reactive power forecast is also available for them. A reduction of the percent RMSEs larger than 13% is obtained at branches 12, 13, and 16, while it is larger than 15% (the estimation error is more than halved in this case) for branch 6.

The test result highlights how the distribution state estimation performance significantly improves, introducing as pseudo-measurements the active and reactive power forecasted by the neural predictors instead of the power consumptions measured at the same hour of the day before. The improvements are more evident for branches close to larger loads.

6. Conclusions

Neural network load forecasting models demonstrated to produce reliable input information for a distribution state estimator, overcoming the problem of limited and time-delayed SM measurements or temporary failure in the communication system. In order to improve the accuracy of the state estimation, different requirements have been fulfilled: (i) the neural models are able to forecast simultaneously both active and reactive powers with limited errors, starting from both exogenous and historical measurements; (ii) the correlation between the forecasted real and reactive power errors has been determined, which results in significant information for the state estimation algorithm; (iii) a closed loop information flow allows the load forecasting, and hence, the state estimation, even when real measurement data are missing by replacing them with forecasted values; (iv) to build effectively the weighting matrix, needed to solve the state estimation algorithm, the variance of the pseudomeasurements can be updated at fixed intervals by considering the measurements and forecast data obtained in the meanwhile.

The test results show that introducing pseudomeasurements forecasted by the neural predictors significantly improves the DSSE and, more importantly, the improvements are more evident for the branches that are close to larger predicted loads almost halving the percent RMSEs of power and current estimations.

In summary, the proposed approach can be used for the state estimation of medium-voltage distribution networks that are either underdetermined, due to limited real-time measurements, or overdetermined but with delayed measurements from SMs.

Data Availability

The data used to support the findings of this study are available from the corresponding author upon request.

Conflicts of Interest

The authors declare that they have no conflicts of interest.

Acknowledgments

This research work has been supported by "Fondazione di Sardegna" within the research project "SUM^{2} GRIDS—Solutions by mUltidisciplinary approach for intelligent Monitoring and Management of power distribution GRIDS"—Triennal Agreement between Fondazione di Sardegna and Sardinian Universities, Regione Sardegna—L.R. 7/2007 year 2017–DGR 28/21, 17.05.2015. The article charge of this work was supported by the Open Access Publishing Fund of the University of Cagliari, with the funding of the Regione Autonoma della Sardegna L.R. n. 7/2007.

References

[1] C. Muscas, M. Pau, P. A. Pegoraro, and S. Sulis, "Smart electric energy measurements in power distribution grids," *IEEE Instrumentation & Measurement Magazine*, vol. 18, no. 1, pp. 17–21, 2015.

[2] R. Madani, S. Sojoudi, and J. Lavaei, "Convex relaxation for optimal power flow problem: mesh networks," *IEEE Transactions on Power Systems*, vol. 30, no. 1, pp. 199–211, 2015.

[3] S. Bolognani and S. Zampieri, "On the existence and linear approximation of the power flow solution in power distribution networks," *IEEE Transactions on Power Systems*, vol. 31, no. 1, pp. 163–172, 2016.

[4] A. Adel Mohamed and B. Venkatesh, "Rectangular branch-based load flow," *IET Generation, Transmission & Distribution*, vol. 13, no. 22, pp. 5151–5159, 2019.

[5] F. Schweppe, "Power system static-state estimation, Part III: implementation," *IEEE Transactions on Power Apparatus and Systems*, vol. 89, no. 1, pp. 130–135, 1970.

[6] K. Dehghanpour, Z. Wang, J. Wang, Y. Yuan, and F. Bu, "A survey on state estimation techniques and challenges in smart distribution systems," *IEEE Transactions on Smart Grid*, vol. 10, no. 2, pp. 2312–2322, 2019.

[7] A. Primadianto and C.-N. Lu, "A review on distribution system state estimation," *IEEE Transactions on Power Systems*, vol. 32, no. 5, pp. 3875–3883, 2017.

[8] D. Della Giustina, M. Pau, P. A. Pegoraro, F. Ponci, and S. Sulis, "Electrical distribution system state estimation: measurement issues and challenges," *IEEE Instrumentation & Measurement Magazine*, vol. 17, no. 6, pp. 36–42, 2014.

[9] A. Abur and A. Gomez-Exposito, *Power System State Estimation: Theory and Implementation*, Marcel Dekker, New York, NY, USA, 2004.

[10] G. Gross and F. D. Galiana, "Short-term load forecasting," *Proceedings of the IEEE*, vol. 75, no. 12, pp. 1558–1573, Dec. 1987.

[11] E. Manitsas, R. Singh, B. C. Pal, and G. Strbac, "Distribution system state estimation using an artificial neural network approach for pseudo measurement modelling," *IEEE Transactions on Power Systems*, vol. 27, no. 4, pp. 1888–1896, 2013.

[12] H. S. Hippert, C. E. Pedreira, and R. C. Souza, "Neural networks for short-term load forecasting: a review and evaluation," *IEEE Transactions on Power Systems*, vol. 16, no. 1, pp. 44–55, 2001.

[13] J. Wu, Y. He, and N. Jenkins, "A robust state estimator for medium voltage distribution networks," *IEEE Transactions on Power Systems*, vol. 28, no. 2, pp. 1008–1016, 2013.

[14] B. P. Hayes, J. K. Gruber, and M. Prodanovic, "A closed-loop state estimation tool for MV network monitoring and operation," *IEEE Transactions on Smart Grid*, vol. 6, no. 4, pp. 2116–2125, 2015.

[15] A. El khantach, M. Hamlich, and N. E. Belbounaguia, "Short-term load forecasting using machine learning and periodicity decomposition," *AIMS Energy*, vol. 7, no. 3, pp. 382–394, 2019.

[16] A. R. Ahmadi and T. C. Green, "Optimal power flow for autonomous regional active network management system," in *Proceedings of the 2009 IEEE Power & Energy Society General Meeting*, pp. 1–7, Calgary, Canada, July 2009.

[17] M. Pau, P. A. Pegoraro, and S. Sulis, "Efficient branch-current-based distribution system state estimation including synchronized measurements," *IEEE Transactions on Instrumentation and Measurement*, vol. 62, no. 9, pp. 2419–2429, Sept. 2013.

[18] ARERA, *Sistemi di smart metering di seconda generazione per la misura di energia elettrica in Bassa tensione*, ARERA, Milan, Italy, 2019.

[19] J. Principe, N. R. Euliano, and W. Lefebvre, *Neural and Adaptive Systems*, John Wiley & Sons, Inc., Hoboken, NY, USA, 2000.

[20] M. Pau, P. A. Pegoraro, and S. Sulis, "WLS distribution system state estimator based on voltages or branch-currents: accuracy and performance comparison," in *Proceedings of the 2013 IEEE International Instrumentation and Measurement Technology Conference (I2MTC)*, pp. 493–498, Minneapolis, MN, USA, May 2013.

[21] Commission for Energy Regulation (CER), "CER smart metering project—electricity customer behaviour trial, 2009–201," in *Irish Social Science Data Archive: Belfield, Irland*, Commission for Energy Regulation (CER), Dublin, Ireland, 1st edition, 2012, http://www.ucd.ie/issda/CER-electricity.

[22] Electricity smart metering customer behaviour trials findings report," Tech. Rep. CER11080a, Commission for Energy Regulation, Dublin, Ireland, 2011.

[23] Met Eireann (Irish Meteorological Service), http://www.met.ie.

[24] J. Xie, Y. Chen, T. Hong, and T. D. Laing, "Relative humidity for load forecasting models," *IEEE Transactions on Smart Grid*, vol. 9, no. 1, pp. 191–198, 2018.

Hindawi
Complexity
Volume 2020, Article ID 5902698, 15 pages
https://doi.org/10.1155/2020/5902698

Research Article

Optimal Control Strategies of HFMD in Wenzhou, China

Zuqin Ding,[1] Yong Li,[2] Yongli Cai,[1] Yueping Dong,[3] and Weiming Wang[1]

[1]*School of Mathematical Science, Huaiyin Normal University, Huaian 223300, China*
[2]*School of Information and Mathematics, Yangtze University, Jingzhou 434023, China*
[3]*School of Mathematics and Statistics, Central China Normal University, Wuhan 430079, China*

Correspondence should be addressed to Weiming Wang; weimingwang2003@163.com

Received 19 August 2019; Revised 18 November 2019; Accepted 10 January 2020; Published 24 February 2020

Guest Editor: Murari Andrea

In this paper, we investigate the dynamics and optimal control strategies of a modified hand, foot, and mouth disease (HFMD) model incorporating the EV-A71 vaccination in Wenzhou, China, analytically and numerically. We define the basic reproduction number $\mathcal{R}_0$ and show that it can be used to determine whether HFMD becomes extinct or not. Based on the monthly reported HFMD cases in Wenzhou for 76 months, we estimate the parameters in the dynamic model by using the method of minimum chi-square fitting, conduct the sensitivity analysis to investigate the influence of each uncertain parameter on $\mathcal{R}_0$ with the methods of Latin hypercube sampling and partial rank correlation coefficient, and find that the EV-A71 vaccination does not lead to the extinction of HFMD, but slightly reduces the incidence of HFMD. In order to control the spread of HFMD in Wenzhou, we need to increase the rate of EV-A71 vaccination, decrease the contact rates, and shorten the course of disease.

1. Introduction

Hand, foot, and mouth disease is a common infectious disorder caused by various enteroviruses, and enterovirus 71 (EV71) and Coxsackievirus A16 (CV-A16) are the most commonly reported [1–3]. HFMD predominantly affects children younger than 5 years old, and most patients exhibit a self-limiting illness that typically includes fever, skin eruptions on the hands and feet, and vesicles in the mouth [1, 2, 4]. Also, it is a highly contagious disease with a latency period of 2–7 d. More often than not, the patients will recover over 7 to 10 d [5, 6].

There are no specific treatment drugs and vaccine available for HFMD, but three inactivated monovalent EV-A71 vaccinations have been licensed in mainland China, all of which have demonstrated high efficacy (90.0%–97.4%) against EV-A71-associated HFMD in infants and young children. However, these vaccinations do not offer protection against HFMD caused by the CV-A16 serotype or others [2, 7, 8].

In recent years, many dynamical HFMD models have been revealed as a powerful tool to analyze the spread and control of HFMD qualitatively and quantitatively [9–15]. Ma et al. [15] and Li et al. [16, 17] pointed out that numerous subclinical cases (adults) who carry HFMD virus but have no symptoms play an important role, leading to the recurrent outbreaks of HFMD. Wang et al. [18, 19] considered asymptomatic infectious individuals and contaminated environments contribute substantially to new HFMD infections. Chadsuthi and Wichapeng [20] had investigated HFMD transmission dynamics in Bangkok, Thailand, and concluded that the direct transmission from asymptomatic individuals and indirect transmission via free-living viruses are important factors to new HFMD infections.

Particularly, Zhu et al. [5] established an SEIQRS epidemic model with periodic transmission rate to investigate the spread of seasonal HFMD in Wenzhou and found that HFMD becomes an endemic disease in Wenzhou, and for controlling the spread of HFMD, it is beneficial to increase the quarantined rate or decrease the treatment cycle. In [6], the authors presented a spatial-temporal ARMA model and found that HFMD had positive spatial autocorrelation and the incidence seasonal peak was between May and July. Zhou et al. [21] investigated the epidemiological feature of HFMD in Wenzhou. Dai et al. [22] had shown that the school opening and meteorological factors were primarily

responsible for annual multiple-peak pattern of the outbreaks of HFMD in Wenzhou.

But, to our knowledge, the research on the effects of the EV-A71 vaccination on the spread of HFMD in Wenzhou seems rare.

Thanks to the insightful work of Li et al. [16, 17], in this paper, we will focus on the optimal control strategies of HFMD in Wenzhou incorporating the EV-A71 vaccination. The rest of this article is organized as follows: In Section 2, we introduce the data of HFMD in Wenzhou and build a HFMD model with periodic transmission rate. In Section 3, we present the simulation results of the monitor data of Wenzhou from January 2012 to April 2018 and give the sensitivity analysis of the basic reproduction number and the optimal control strategies. In Section 4, we conclude the epidemiological significance of the results.

2. Materials and Dynamic Model

2.1. Data Source. Wenzhou is a prefecture-level city in southeastern Zhejiang province in the People's Republic of China. It is surrounded by Yandang mountains, the East China Sea, and 436 islands, while its lowlands are almost entirely along its East China Sea coast, which is nearly 355 kilometres (221 miles) long. Most of Wenzhou's area is mountainous as almost 76 percent of its 11,784 square kilometre (4,550 square miles) surface area is classified as mountains and hills. The 2010 China National Census registered 9.122 million residents in the Wenzhou area [21]. The prefecture-level city of Wenzhou currently administers four districts (Lucheng, Longwan, Ouhai, and Dongtou), two county-level cities (Rui'an and Yueqing), and five counties (Yongjia, Wencheng, Pingyang, Taishun, and Cangnan) (see Figure 1).

Since Wenzhou has a humid subtropical climate zone with an annual average 18.08°C (or 64.5°F), it is of particular public health significance to update molecular epidemiology of HFMD in Wenzhou [5]. HFMD data are obtained mainly from epidemiologic bulletins published by the Wenzhou Center for Disease Control and Prevention from January 2012 to April 2018 (76 months), including basic demographic characteristics of HFMD cases and daily incident cases [23]. Because Dongtou District is composed of 168 islands and the number of HFMD patients is relatively small, we only simulate the data of HFMD in Wenzhou and 10 districts' county-level cities or counties under its jurisdiction, except Dongtou District. According to the obtained records, there are 197,821 HFMD cases.

2.2. Dynamic Model of HFMD. Suppose that the whole population $N(t)$ is divided into six compartments at time t: susceptible with vaccination $S_1(t)$, susceptible without vaccination $S_2(t)$, exposed $E(t)$, clinical infectious $I(t)$, subclinical infectious $L(t)$, and recovered $R(t)$. Obviously, $N(t) = S_1(t) + S_2(t) + E(t) + I(t) + L(t) + R(t)$. Similar to the models in [5, 16, 17, 22], we can establish the following flowchart of compartments of HFMD (see Figure 2):

In addition, the corresponding transmission model of HFMD in Wenzhou is as follows:

$$\begin{cases} \dfrac{dS_1}{dt} = \Lambda_1 - \dfrac{\sigma\beta_1(t)S_1 I}{N} - \dfrac{\sigma\beta_2(t)S_1 L}{N} + \gamma_1 R - \mu S_1, \\ \dfrac{dS_2}{dt} = \Lambda_2 - \dfrac{\beta_1(t)S_2 I}{N} - \dfrac{\beta_2(t)S_2 L}{N} + \gamma_2 R - \mu S_2, \\ \dfrac{dE}{dt} = \dfrac{\sigma\beta_1(t)S_1 I}{N} + \dfrac{\sigma\beta_2(t)S_1 L}{N} + \dfrac{\beta_1(t)S_2 I}{N} + \dfrac{\beta_2(t)S_2 L}{N} - (\alpha+\mu)E, \\ \dfrac{dI}{dt} = \rho\alpha E - (\delta_1+\mu)I, \\ \dfrac{dL}{dt} = (1-\rho)\alpha E - (\delta_2+\mu)L, \\ \dfrac{dR}{dt} = \delta_1 I + \delta_2 L - (\gamma_1+\gamma_2+\mu)R. \end{cases} \tag{1}$$

All parameters in model (1) are positive, and the interpretations of them are as follows:

(i) μ: natural death rate
(ii) α: rate of progression to the infectious
(iii) δ_1 and δ_2: recovery rates of the infectious
(iv) γ_1 and γ_2: immune loss rates
(v) Λ_1 and Λ_2: recruitment rates
(vi) ρ: rate of HFMD inpatients
(vii) σ: the reduction in risk of infection due to EV71
(viii) $\beta_1(t)$ and $\beta_2(t)$: rates of disease transmission

It is worthy to note that, in model (1), the periodic transmission rates between S_1, S_2, I, and L are employed. This is indeed a well-established way of introducing seasonality into epidemic models and applied widely [24–27]. The transmission rate between S_1, S_2, and I is taken as

$$\beta_1(t) := a_1 + \left(1 + b_1 \sin\left(\frac{\pi t}{T + c_1}\right)\right), \tag{2}$$

and the transmission rate between S_1, S_2, and L is taken as

$$\beta_2(t) := a_2 + \left(1 + b_2 \sin\left(\frac{\pi t}{T + c_2}\right)\right), \tag{3}$$

where a_1, b_1, c_1, a_2, b_2, and c_2 are positive constants, a_1 and a_2 are the baseline contact rates, and b_1 and b_2 are the magnitudes of forcing, which can be determined by the minimum chi-square fitting [16, 28] in Section 2.3.

Since the EV-A71 vaccination was given in Wenzhou from October 2016 (the 59th month), we assume that the coefficient of reduction in exposure due to vaccination is σ_0 and a piecewise function is employed to represent σ as the following:

Figure 1: The specific geography location of Wenzhou city, including 10 districts' county-level cities/counties [6].

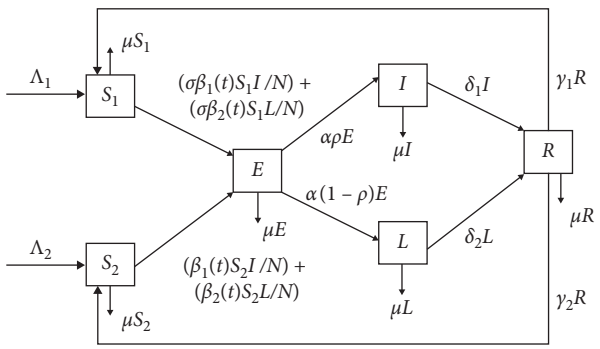

Figure 2: Flowchart of compartments of the HFMD model.

$$\sigma = \begin{cases} 1, & 1 \le t \le 58, \\ \sigma_0, & 59 \le t \le 76. \end{cases} \tag{4}$$

It is easy to obtain that model (1) always has a disease-free equilibrium $P^0 = (S_1^0, S_2^0, 0, 0, 0, 0)$, where $S_1^0 = \Lambda_1/\mu$ and $S_2^0 = \Lambda_2/\mu$. From model (1), we have

$$\frac{dN}{dt} = \Lambda_1 + \Lambda_2 - \mu N. \tag{5}$$

Therefore, the biologically feasible region for model (1) is

$$\Omega = \left\{ (S_1, S_2, E, I, L, R) \in \mathbb{R}_+^6 \mid 0 < S_1 + S_2 + E + I + L + R \le \frac{\Lambda_1 + \Lambda_2}{\mu} \right\}. \tag{6}$$

Easy to prove that region Ω is positively invariant with respect to system (1).

The basic reproduction number $\mathscr{R}_0$, defined as the average number of secondary infections generated by a single infected individual introduced into a completely susceptible population [29–33], is one of the important quantities in epidemiology. For model (1), following the method in [30], we can obtain $\mathscr{R}_0$ as follows:

$$\mathscr{R}_0 := \left(\frac{\widetilde{\beta}_1 S_1^0}{S_1^0 + S_2^0} + \frac{\widehat{\beta}_1 S_2^0}{S_1^0 + S_2^0} \right) \frac{\rho\alpha}{(\alpha+\mu)(\delta_1+\mu)} + \left(\frac{\widetilde{\beta}_2 S_1^0}{S_1^0 + S_2^0} + \frac{\widehat{\beta}_2 S_2^0}{S_1^0 + S_2^0} \right) \frac{(1-\rho)\alpha}{(\alpha+\mu)(\delta_2+\mu)}, \tag{7}$$

where

$$\widetilde{\beta}_1 = \frac{1}{76}\left(\int_1^{58} \beta_1(t)dt + \sigma_0 \int_{59}^{76} \beta_1(t)dt \right),$$

$$\widetilde{\beta}_2 = \frac{1}{76}\left(\int_1^{58} \beta_2(t)dt + \sigma_0 \int_{59}^{76} \beta_2(t)dt \right),$$

$$\widehat{\beta}_1 = \frac{1}{76} \int_1^{76} \beta_1(t)dt, \tag{8}$$

$$\widehat{\beta}_2 = \frac{1}{76} \int_1^{76} \beta_2(t)dt.$$

Similar to that in [5], we can obtain the threshold dynamics of model (1) as follows.

Theorem 1. *If $\mathcal{R}_0 < 1$, the disease-free equilibrium $P^0 = (S_1^0, S_2^0, 0, 0, 0, 0)$ of model (1) is globally asymptotically stable, while if $\mathcal{R}_0 > 1$, model (1) has at least one positive periodic solution which is uniformly persistent and P^0 is unstable.*

The proof of Theorem 1 is similar to that of Theorems 4 and 7 in [5], and we omit it here.

2.3. Parameter Estimation and Numerical Simulations. In this section, we will estimate all the parameters and initial conditions of model (1). On the basis of the biological significance of parameters, we set the upper and lower bounds of each parameter. According to the data of the sixth census, the average life expectancy of the Chinese people is 76.34 years in 2015 [34]; hence, we take the natural death rate as $\mu = 1/(76.34 \times 12) = 1.0916 \times 10^{-2}$. According to the statistics data released by Wenzhou Municipal Bureau of Statistics [35], from 2012 to 2018, the permanent population of Wenzhou is about 9 million. Specifically, the most populous cities, Rui'an and Yueqing are about 1.4 million people every year and the cities with the smallest population (Wencheng and Taishun) are about 0.2 million people every year.

From statistics data of HFMD in Wenzhou, we can only obtain the initial value of $I(0)$ directly (see for details Tables 1 and 2). Obviously, we cannot obtain other initial values of $S_1(0)$, $S_2(0)$, $E(0)$, $L(0)$, and $R(0)$. In this situation, we can take the whole population as the susceptible and assume that the upper and lower limits of the two types of the susceptible ($S_1(0)$ and $S_2(0)$) as 10^6 and 10^4 for all regions and we can obtain the values of $S_1(0)$ and $S_2(0)$ with the help of MATLAB by using the following "multiple starting points" optimization algorithm. Also, the initial values of $E(0)$, $L(0)$, and $R(0)$ can also be obtained in MATLAB, whose results are shown in Tables 1 and 2.

Next, we will describe the specific simulation method. Hence, we need to estimate the other 16 parameters and 5 initial values through calculating the minimum sum of chi-square [16, 28]:

$$J(\theta) = \sum_{i=1}^{76} \frac{\left(T(t_i) - \hat{T}(t_i)\right)^2}{\hat{T}(t_i)}, \tag{9}$$

where $T(t_i)(i = 1, 2, \ldots, 76)$ shows the real value each month and $\hat{T}(t_i)(i = 1, 2, \ldots, 76)$ shows the estimated value each month.

In order to find the optimal parameters, we choose the fminsearch function in the optimization toolbox of the software MATLAB and we try to avoid the occurrence of local optimal solutions by using the following "multiple starting points" optimization algorithm [36, 37]:

(i) *Step 1*. Parametric hypothesis: set a reasonable range of each parameter and initial condition of model (1) to be estimated;

(ii) *Step 2*. Evaluating simulation results: random values in the range of the first step are taken as the initial values of the first simulation. Judging whether the simulation results converge or not, the objective function value (sum of chi-square) is calculated;

(iii) *Step 3*. Repetitive simulation: if the simulation results are not convergent, the sum of chi-square values is quite different from that of the previous simulation. Take the simulation result as a new starting value and simulate it again;

(iv) *Step 4*. Getting a set of optimal solutions: repeat Steps 2 and 3 until the simulation results converge, and the sum of chi-square values does not change significantly;

(v) *Step 5*. Getting multiple sets of optimal values: randomly change the starting value of the simulation and repeat Steps 2, 3, and 4. Then, we can get multiple sets of optimal parameters;

(vi) *Step 6*. Hypothesis test: in order to screen out the results which conform to the hypothesis test, we can give the original hypothesis and alternative hypothesis, which can be seen in literatures [16, 28], and select the significant level as 0.05, $\chi^2_{0.05}(54) = 72.153$. For this reason, if the chi-square value is less than this value (see Tables 1 and 2), it is considered that the original hypothesis is not rejected;

(vii) *Step 7*. Screening out the most reasonable and optimal parameters: through the sixth step, we get several sets of optimal parameter values, further calculate the basic reproduction number, discuss the actual meaning of each parameter, and remove the unreasonable values.

Using the algorithm above, we can estimate the parameters and initial values of model (1) (see Tables 1 and 2), and the medians and arithmetic means of them are shown in Table 3 in Appendix. The range of the latent period $1/\alpha$ is 1.0 d to 6.2 d, and the median value of it is about 1.7 d. The range of the course of treatment for clinical infectious $1/\delta_1$ is about 2.9 − 10.0 *d*, and the median value is about 5.4 d. The range of the course of treatment for clinical infectious $1/\delta_2$ is about 2.0 − 9.5 *d*, and the median value is about 2.8 d. With these parameters, we can numerically solve model (1) to fit the monthly reported HFMD cases, and the numerical results of the relations between the fitted data with the real data of Wenzhou are shown in Figure 3.

In addition, Li et al. [6] found that the distribution of HFMD in Wenzhou is heterogeneous at county level and Ouhai municipal district is the most severe region, followed by Lucheng, Longwan, and Ruian. For the sake of learning of HFMD dynamics in Wenzhou, we show the numerical results of 10 districts' county-level cities or counties in Figure 4.

The simulation results (see Figures 3 and 4 and Tables 1–3) can basically describe the prevalence of HFMD in Wenzhou. Considering the vaccination again, it is true that the epidemic situation can be simulated to decline after October 2016. The pattern of HFMD dynamics is similar among the 10 districts' county-level cities. Two peaks appear in Spring and Autumn each year in all 10 districts (see

Table 1: Parameters and their values.

Range of parameter	Wenzhou	Lucheng	Longwan	Ouhai	Rui'an
$\alpha \in [0, 30]$	30.0000	14.7784	20.6481	6.1205	6.2197
$\delta_1 \in [3, 15]$	4.4101	5.4885	3.8918	5.7724	10.3272
$\delta_2 \in [3, 15]$	7.0402	12.1971	11.2610	11.0008	7.0558
$\gamma_1 \in [0, 10]$	0.0112	5.2515	0.2798	3.3819	0.2913
$\gamma_2 \in [0, 10]$	4.2300	9.8776	9.9723	9.5839	9.9936
$\Lambda_1 \in [0, 100]$	0.0001	29.5983	8.01×10^{-5}	16.7320	6.31×10^{-6}
$\Lambda_2 \in [0, 100]$	0.0002	29.3058	0.0106	7.6879	32.9412
$\rho \in [0, 0.5]$	0.1610	0.1670	0.1346	0.1747	0.3090
$\sigma_0 \in [0, 0.5]$	0.7473	0.9262	0.1146	0.9438	0.8278
$T \in [6, 18]$	6.1037	6.1231	6.0470	6.1428	6.0046
$a_1 \in [0, 30]$	23.897	29.9995	25.6717	30.0000	29.5449
$a_2 \in [0, 30]$	6.17×10^{-8}	0.1291	0.0753	0.1256	0.0002
$b_1 \in [-1, 1]$	0.9604	0.7050	0.9110	0.9135	0.5348
$b_2 \in [-1, 1]$	0.7911	1.0000	0.9997	1.0000	0.7523
$c_1 \in [0, 1]$	0.0532	0.1160	0.0012	0.1665	0.0670
$c_2 \in [0, 1]$	0.2992	0.1284	0.1507	0.0464	1.09×10^{-6}
$\widetilde{\beta}_1$	23.1928	30.1031	21.0575	30.2313	28.9888
$\widetilde{\beta}_2$	0.9568	1.1290	0.8659	1.1262	0.9792
$\widehat{\beta}_1$	24.9188	31.0146	26.6997	31.0177	30.5655
$\widehat{\beta}_2$	1.0223	1.1508	1.1093	1.1423	1.0281
$S_1(0) \in [10^4, 10^6]$	863190	130216	83540	109356	335684
$S_2(0) \in [10^4, 10^6]$	995989	107109	999996	119795	10^6
$E(0) \in [0, 10^5]$	13	564	104	1378	0
$I(0)$	1091	89	38	39	215
$L(0) \in [0, 10^5]$	1	0	0	3319	12051
$R(0) \in [0, 10^6]$	458	6818	10241	4259	0
χ^2	—	35.3842	0.8659	25.2958	17.7474
$\mathscr{R}_0$	1.0015	1.0042	1.0034	1.0030	1.0116

Table 2: Parameters and their values.

Range of parameters	Yongjia	Yueqing	Wencheng	Pingyang	Taishun	Cangnan
$\alpha \in [0, 30]$	4.9592	29.9046	27.7359	27.8485	29.0212	15.0574
$\delta_1 \in [3, 15]$	8.1110	4.3826	4.2318	5.3634	3.0259	5.9019
$\delta_2 \in [3, 15]$	3.2000	14.9895	13.2424	12.2123	14.4614	7.9358
$\gamma_1 \in [0, 10]$	3.85×10^{-5}	0.2154	2.83×10^{-6}	2.0229	0.0225	5.34×10^{-6}
$\gamma_2 \in [0, 10]$	7.4057	9.9999	8.3133	8.6110	8.3528	9.9993
$\Lambda_1 \in [0, 100]$	0.0006	6.82×10^{-5}	2.35×10^{-5}	9.6393	3.40×10^{-6}	69.2267
$\Lambda_2 \in [0, 100]$	0.0217	0.0524	41.3280	99.9888	0.0513	33.7068
$\rho \in [0, 0.5]$	0.2402	0.1970	0.1599	0.1665	0.1222	0.1718
$\sigma_0 \in [0, 0.5]$	0.5428	0.4965	0.9104	0.9950	0.8878	0.9862
$T \in [6, 18]$	6.0000	6.0755	6.0239	6.0679	6.2586	6.0357
$a_1 \in [0, 30]$	25.2706	20.1875	23.6496	29.3384	22.3592	29.9524
$a_2 \in [0, 30]$	0.0004	0.1394	0.1961	0.1180	0.0064	0.1250
$b_1 \in [-1, 1]$	0.6885	0.9267	0.4246	0.9999	0.5025	0.9516
$b_2 \in [-1, 1]$	0.4533	0.9998	0.6541	0.5145	0.8819	0.8654
$c_1 \in [0, 1]$	0.1425	0.0667	0.1098	0.0940	0.1448	6.86×10^{-7}
$c_2 \in [0, 1]$	0.2421	0.1338	0.1972	0.1625	0.0776	0.1284
$\widetilde{\beta}_1$	23.2590	18.5501	23.8494	29.9458	22.4753	30.4902
$\widetilde{\beta}_2$	0.8983	1.0254	1.1848	1.1235	0.9842	1.1453
$\widehat{\beta}_1$	26.2984	21.2133	24.6651	30.3681	23.3613	30.9833
$\widehat{\beta}_2$	1.0194	1.1687	1.2211	1.1341	1.0095	1.1556
$S_1(0) \in [10^4, 10^6]$	25732	205161	144028	78907	269882	99081
$S_2(0) \in [10^4, 10^6]$	971958	223628	183048	136866	10^6	108336
$E(0) \in [0, 10^5]$	28	148	117	925	89	831
$I(0)$	93	228	19	204	18	132
$L(0) \in [0, 10^5]$	3450	0	1	1	0	860
$R(0) \in [0, 10^6]$	1875	7037	5352	26	7589	3708
χ^2	4.8267	49.6591	1.1284	31.9636	0.0831	22.7046
$\mathscr{R}_0$	1.0124	1.0128	1.0059	1.0163	1.0004	1.0089

Table 3: The medians and arithmetic means of the parameters.

Parameter	Median	Arithmetic mean	Source
$\alpha \in [0, 30]$	18.2294	25.3815	Estimate
$\delta_1 \in [3, 15]$	5.6497	5.4260	Estimate
$\delta_2 \in [3, 15]$	10.7556	12.2047	Estimate
$\gamma_1 \in [0, 10]$	1.1465	0.2856	Estimate
$\gamma_2 \in [0, 10]$	9.2109	9.7308	Estimate
$\Lambda_1 \in [0, 100]$	12.5196	0.0003	Estimate
$\Lambda_2 \in [0, 100]$	24.5073	18.4969	Estimate
$\rho \in [0, 0.5]$	0.1843	0.1733	Estimate
$\sigma_0 \in [0, 0.5]$	0.7631	0.8991	Estimate
$T \in [6, 18]$	6.0779	6.0575	Estimate
$\widetilde{\beta}_1$	25.8951	26.4191	Calculate
$\widetilde{\beta}_2$	1.0462	1.0745	Calculate
$\widehat{\beta}_1$	27.6188	28.5339	Calculate
$\widehat{\beta}_2$	1.1139	1.1382	Calculate
$\mathscr{R}_0$	1.0079	1.0103	Calculate

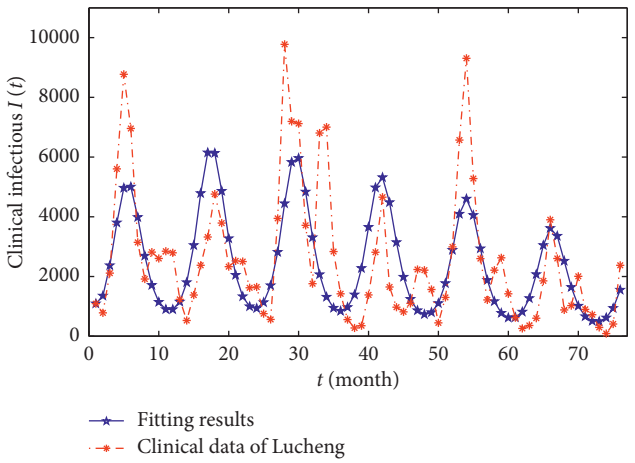

Figure 3: The reported data vs. the numerical solution of the HFMD model (1) in Wenzhou.

Figure 4), which is also consistent with the case of Wenzhou (see Figure 3). The estimation of $\mathscr{R}_0$ is little bit larger than 1 (see Tables 1 and 2). Also, $\mathscr{R}_0$ is calculated by the integral average of periodic function (see Tables 1 and 2). In Wenzhou city, $\overline{\mathscr{R}_0} = 1.0064 > 1$. In addition, from Table 3, we can find that, except Λ_1 and γ_1, the medians of other parameters are similar to the arithmetic mean, which means that the incidence of HFMD in Wenzhou is basically the same as the epidemic regularity.

2.4. Sensitivity Analysis. From Theorem 1, we know that the basic reproduction number $\mathscr{R}_0$ can be used to govern whether HFMD goes into extinction or not. It should be noted that there are 11 undetermined parameters in $\mathscr{R}_0$, each with different mean value and variance (see Table 3 in Appendix), which means that it is tedious and extremely complex to study the effects of these parameters on the HFMD dynamics. In order to detect the underlying factors more simply, a better idea is to do the sensitivity analysis of different categories of parameters [22].

Parametric sensitivity analysis is generally divided into two types: deterministic sensitivity analysis and uncertainty sensitivity analysis [38]. The former generally calculates the partial derivatives of the basic reproduction number with respect to each parameter, while the latter generally assumes that each parameter conforms to a certain prior distribution (e.g., uniform and standard normal distribution).

In order to identify the sensitivity of different parameters to $\mathscr{R}_0$, we used Latin hypercube sampling (LHS) and partial rank correlation coefficient (PRCC) [39] to detect the influence of each uncertain parameter on $\mathscr{R}_0$. The sample size is chosen as $n = 2000$. All 11 parameters in the expression of $\mathscr{R}_0$ are used as input values, $\mathscr{R}_0$ as the output value, and the significance level is taken as 0.01. Suppose that all the input parameters are standard normal distributions, and the estimated expectations are shown in Tables 1 and 2.

The numerical results of the partial rank correlation coefficient of $\mathscr{R}_0$ are shown in Table 4, and its bar chart is shown in Figure 5. The larger the PRCC in absolute value, the more important the parameters in responding to the change of new HFMD cases. Hence, we can conclude that parameters α, ρ, $\widetilde{\beta}_1$, $\widetilde{\beta}_2$, $\widehat{\beta}_1$, and $\widehat{\beta}_2$ have positive impacts on $\mathscr{R}_0$; conversely, δ_1, δ_2, γ_1, γ_2, and σ_0 have negative impacts. Also, the most sensitive parameter for $\mathscr{R}_0$ is ρ, followed by δ_1, $\widehat{\beta}_2$, $\widehat{\beta}_1$, $\widetilde{\beta}_1$, δ_2, and $\widetilde{\beta}_2$. These may provide potential guidance for HFMD prevention and control in strategy formulation.

3. Optimal Control Strategies

Optimal control theory deals with the problem of finding a control law for a given system such that a certain optimality criterion is achieved [16, 40, 41]. Based on the results of sensitivity analysis, we choose $\beta_1(t)$, $\beta_2(t)$, δ_1, and δ_2 as controlled parameters. Considering the actual situation of HFMD epidemic in Wenzhou and the approximate medical expenditure of Wenzhou residents, we design the optimal control strategies:

(i) Decreasing the transmission rates: assume that the associated force of transmission rates, $\beta_1(t)$ and $\beta_2(t)$, are reduced by $u_1(t)$ and $u_2(t)$, respectively. Also, $1 - u_1(t)$ and $1 - u_2(t)$ measure the precaution effort such as window ventilation, attention to disinfection, regular exercise, and HFMD prevention and control knowledge education.

(ii) Increasing the recovery rates: assume that the recovery rates (δ_1 and δ_2) are increased by $u_3(t)$ and $u_4(t)$, respectively. Also, $1 + u_3(t)$ and $1 + u_4(t)$ measure the efficiency of treatment to achieve early recovery for the clinical infectious $I(t)$ and the efficiency increasing children's immunity (i.e., more fruits, vegetables, and regular exercise) for the subclinical infectious, respectively.

Taking into account the assumptions above, model (1) incorporating four control measures is governed by the following differential equations:

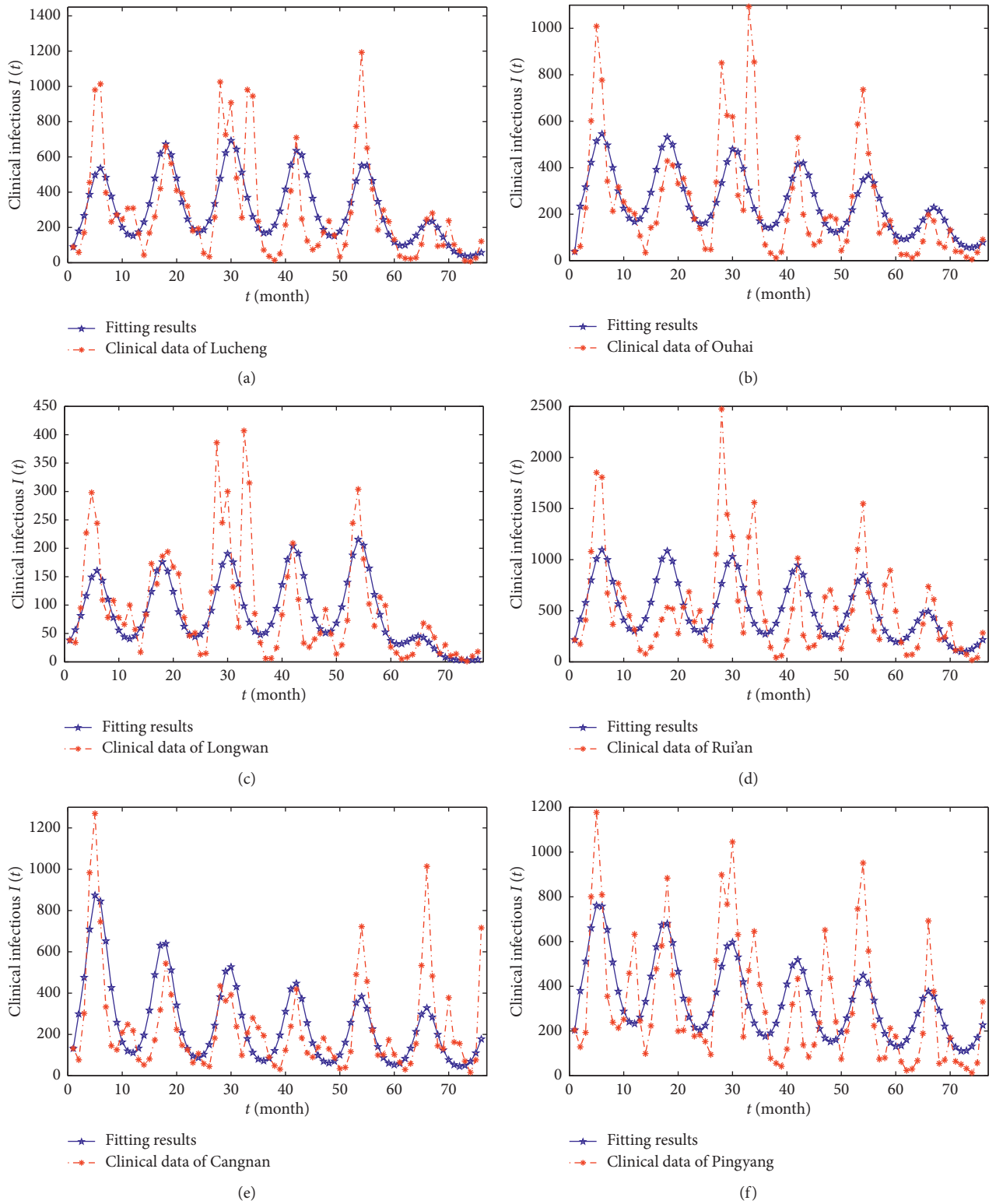

Figure 4: Continued.

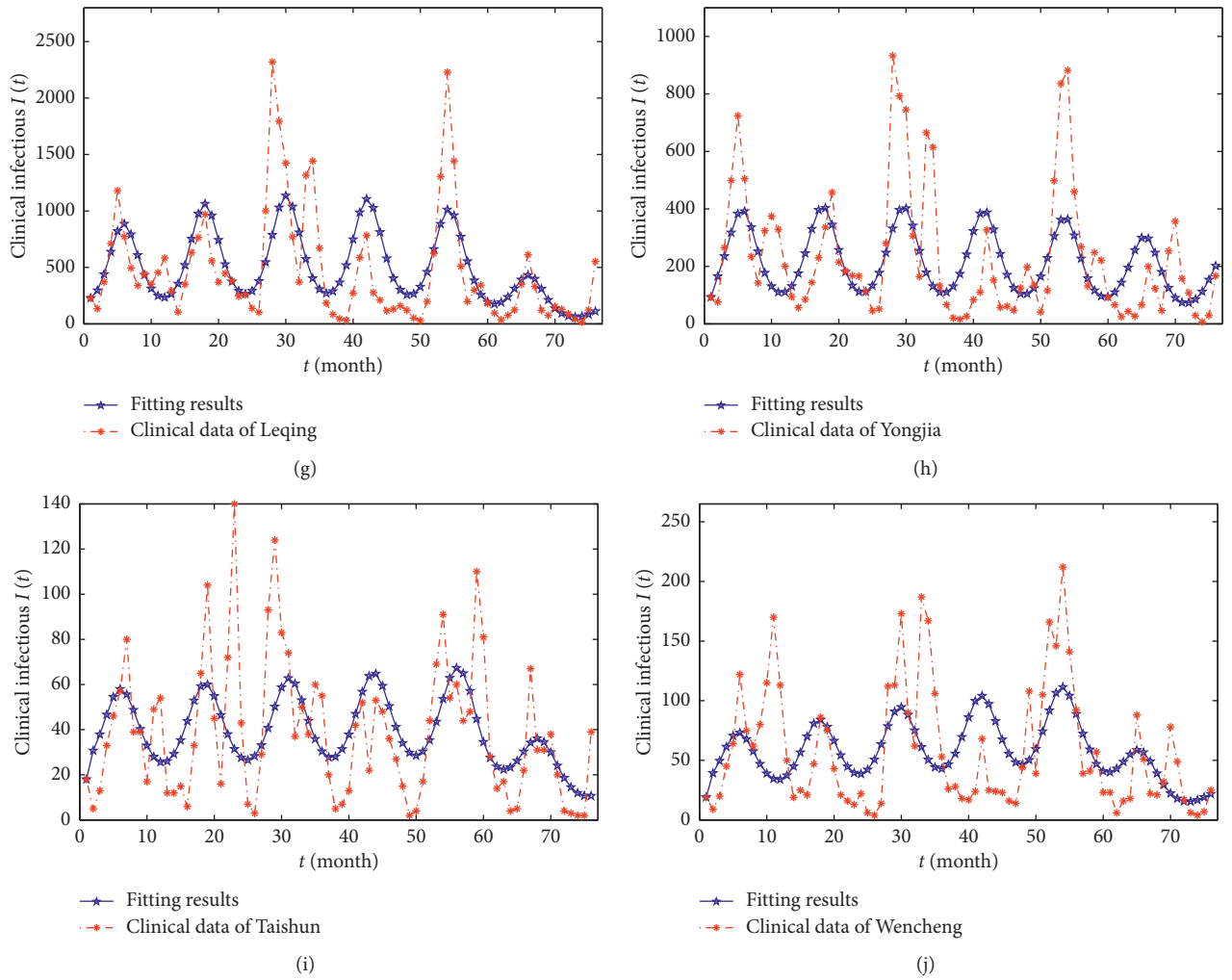

FIGURE 4: The reported data vs. the numerical solution of the HFMD model (1) in (a) Lucheng, (b) Ouhai, (c) Longwan, (d) Rui'an, (e) Cangnan, (f) Pingyang, (g) Yueqing, (h) Yongjia, (i) Taishun, and (j) Wencheng.

$$
\begin{cases}
\dfrac{dS_1}{dt} = \Lambda_1 - \dfrac{\sigma\beta_1(t)(1-u_1)S_1 I}{N} - \dfrac{\sigma\beta_2(t)(1-u_2)S_1 L}{N} + \gamma_1 R - \mu S_1, \\
\dfrac{dS_2}{dt} = \Lambda_2 - \dfrac{\beta_1(t)(1-u_1)S_2 I}{N} - \dfrac{\sigma\beta_2(t)(1-u_2)S_2 L}{N} + \gamma_1 R - \mu S_2, \\
\dfrac{dE}{dt} = \dfrac{\sigma\beta_1(t)(1-u_1)S_1 I}{N} + \dfrac{\sigma\beta_2(t)(1-u_2)S_1 L}{N} + \dfrac{\beta_1(t)(1-u_1)S_2 I}{N} + \dfrac{\sigma\beta_2(t)(1-u_2)S_2 L}{N} - (\alpha+\mu)E, \\
\dfrac{dI}{dt} = \rho\alpha E - (\delta_1(1+u_3)+\mu)I, \\
\dfrac{dL}{dt} = (1-\rho)\alpha E - (\delta_2(1+u_4)+\mu)L, \\
\dfrac{dR}{dt} = (\delta_1(1+u_3)+\mu)I + (\delta_2(1+u_4)+\mu)L - (\gamma_1+\gamma_2+\mu)R,
\end{cases}
\tag{10}
$$

Table 4: PRCC values for $\mathscr{R}_0$.

Input parameter	PRCC	P value
α	0.039809769392456	0.075818905660133
δ_1	−0.845417442920200	0
δ_2	−0.233470793181710	0
γ_1	−0.013915647248970	0.534988619354773
γ_2	−0.013936543241846	0.534375545613689
ρ	0.992295606945784	0
σ_0	−0.036960654931174	0.099286931216591
$\tilde{\beta}_1$	0.468625053788954	0
$\tilde{\beta}_2$	0.169141046318725	0.000000000000031
$\hat{\beta}_1$	0.657754383903920	0
$\hat{\beta}_2$	0.677554835647717	0

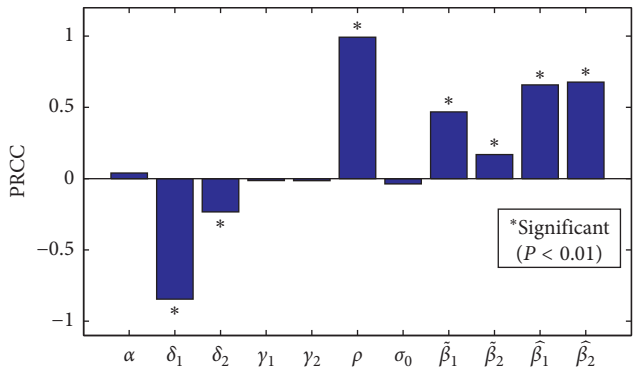

Figure 5: The values of PRCC on the outcome of $\mathscr{R}_0$. All parameter values are derived from Wenzhou city in Table 2.

with appropriate initial conditions.

For the optimal control problem of system (10), we consider the control variables $u(t) = (u_1, u_2, u_3, u_4) \in U$ relative to the state variables S_1, S_2, E, I, L, and R where control variables are bounded and measured with

$$U = \{(u_1, u_2, u_3, u_4) \mid u_i \in L[0,1], 0 \le u_i \le 1, \quad t \in [0,T],\ (i = 1,2,3,4)\}, \tag{11}$$

where T represents a given control period. Define the objective function:

$$J(u_1, u_2, u_3, u_4) = \int_0^T \left(A_1 I + A_2 L + \sum_{i=1}^{4} \frac{1}{2} B_i u_i^2 \right) \mathrm{d}t, \tag{12}$$

where A_i $(i = 1, 2)$ represent the weight constants of the clinical infectious and subclinical infectious individuals, respectively, B_i $(i = 1, 2, 3, 4)$ are weight constants for transmission rates, and $\beta_1(t)$ and $\beta_2(t)$ are recovery rates of infectious δ_1 and δ_2, respectively.

The main focus is to minimize the number of the exposed, the clinical infectious and the subclinical infectious, and the costs required to control HFMD by using possible minimal control variables u_i $(i = 1, 2, 3, 4)$. Hence, we need to find $(u_1^*, u_2^*, u_3^*, u_4^*)$ such that

$$J(u_1^*, u_2^*, u_3^*, u_4^*) = \min_U J(u_1, u_2, u_3, u_4), \tag{13}$$

subject to system (10).

In order to find an optimal solution, we first present the Lagrangian and Hamiltonian for the optimal control problems. Also, the Lagrangian of the problem is

$$\mathscr{L}(I, L, u_1, u_2, u_3, u_4) = A_1 I + A_2 L + \sum_{i=1}^{4} \frac{1}{2} B_i u_i^2. \tag{14}$$

We need to find the minimal value of the Lagrangian, so we define the Hamiltonian $\mathscr{H}$ for the control problem as

$$\mathscr{H} = \mathscr{L}(I, L, u_1, u_2, u_3, u_4) + \lambda_1 \frac{\mathrm{d}S_1}{\mathrm{d}t} + \lambda_2 \frac{\mathrm{d}S_2}{\mathrm{d}t} + \lambda_3 \frac{\mathrm{d}E}{\mathrm{d}t} + \lambda_4 \frac{\mathrm{d}I}{\mathrm{d}t} + \lambda_5 \frac{\mathrm{d}L}{\mathrm{d}t} + \lambda_6 \frac{\mathrm{d}R}{\mathrm{d}t}, \tag{15}$$

where λ_i $(i = 1, 2, \ldots, 6)$ are the adjoint functions to be determined suitably. We apply Pontryagin's maximum principle [42]. If (x, u) is an optimal solution of the optimal control problem, then there exists a nontrivial vector function $\lambda = (\lambda_1, \lambda_2, \lambda_3, \lambda_4, \lambda_5, \lambda_6)$ satisfying the following inequalities:

$$\frac{\mathrm{d}x}{\mathrm{d}t} = \frac{\partial \mathscr{H}(t, x, u, \lambda)}{\partial \lambda}, \tag{16}$$

$$0 = \frac{\partial \mathscr{H}(t, x, u, \lambda)}{\partial u}, \tag{17}$$

$$\frac{\mathrm{d}\lambda}{\mathrm{d}t} = -\frac{\partial \mathscr{H}(t, x, u, \lambda)}{\partial x}. \tag{18}$$

Now, we apply the necessary conditions to the Hamiltonian $\mathscr{H}$.

Theorem 2. *For problems (10)–(13) with fixed initial conditions $S_1(0)$, $S_2(0)$, $E(0)$, $I(0)$, $L(0)$, and $R(0)$ and a fixed final time T, there exist adjoint functions λ_i $(i = 1, 2, \ldots, 6)$ such that*

$$\begin{cases} \dfrac{d\lambda_1}{dt} = (\lambda_1 - \lambda_3)(f_1 + f_2) + (\lambda_3 - \lambda_2)(f_3 + f_4) + \lambda_1\mu, \\ \dfrac{d\lambda_2}{dt} = (\lambda_3 - \lambda_1)(f_5 + f_6) + (\lambda_2 - \lambda_3)(f_7 + f_8) + \lambda_2\mu, \\ \dfrac{d\lambda_3}{dt} = (\lambda_3 - \lambda_1)(f_5 + f_6) + (\lambda_3 - \lambda_2)(f_3 + f_4) + \lambda_3(\alpha + \mu) - \lambda_4\rho\alpha - \lambda_5(1 - \rho)\alpha, \\ \dfrac{d\lambda_4}{dt} = -A_1 + (\lambda_1 - \lambda_3)(f_9 - f_6) + (\lambda_2 - \lambda_3)(f_{10} - f_4) + \lambda_4(\delta_1(1 + u_3) + \mu) - \lambda_6\delta_1(1 + u_3), \\ \dfrac{d\lambda_5}{dt} = -A_2 + (\lambda_3 - \lambda_1)(f_5 - f_{11}) + (\lambda_3 - \lambda_2)(f_3 - f_{12}) + \lambda_5(\delta_2(1 + u_4) + \mu) - \lambda_6\delta_2(1 + u_4), \\ \dfrac{d\lambda_6}{dt} = (\lambda_3 - \lambda_1)(f_5 + f_6) + (\lambda_3 - \lambda_2)(f_3 + f_4) + \lambda_6(\gamma_1 + \gamma_2 + \mu), \end{cases} \tag{19}$$

where

$$\begin{aligned} f_1 &= \frac{\sigma\beta_1(t)(1 - u_1)I(N - S_1)}{N^2}, \\ f_2 &= \frac{\sigma\beta_2(t)(1 - u_2)L(N - S_1)}{N^2}, \\ f_3 &= \frac{\beta_1(t)(1 - u_1)S_2 I}{N^2}, \\ f_4 &= \frac{\beta_2(t)(1 - u_2)S_2 L}{N^2}, \\ f_5 &= \frac{\sigma\beta_1(t)(1 - u_1)S_1 I}{N^2}, \\ f_6 &= \frac{\sigma\beta_2(t)(1 - u_2)S_1 L}{N^2}, \\ f_7 &= \frac{\beta_1(t)(1 - u_1)I(N - S_2)}{N^2}, \\ f_8 &= \frac{\beta_2(t)(1 - u_2)L(N - S_2)}{N^2}, \\ f_9 &= \frac{\sigma\beta_1(t)(1 - u_1)S_1(N - I)}{N^2}, \\ f_{10} &= \frac{\beta_1(t)(1 - u_1)S_2(N - I)}{N^2}, \\ f_{11} &= \frac{\sigma\beta_2(t)(1 - u_2)S_1(N - L)}{N^2}, \\ f_{12} &= \frac{\beta_2(t)(1 - u_2)S_2(N - L)}{N^2}, \end{aligned} \tag{20}$$

with transversality conditions (boundary conditions)

$$\lambda_i(T) = 0, i = 1, 2, \ldots, 6. \tag{21}$$

Furthermore, u_i^* $(i = 1, 2, 3, 4)$ *are represented by*

$$\begin{aligned} u_1^* &= \max\left\{\min\left\{1, \frac{(\lambda_3 - \lambda_1)\sigma\beta_1(t)S_1^* I^* + (\lambda_3 - \lambda_2)\beta_1(t)S_2^* I^*}{B_1 N^*}\right\}, 0\right\}, \\ u_2^* &= \max\left\{\min\left\{1, \frac{(\lambda_3 - \lambda_1)\sigma\beta_2(t)S_1^* L^* + (\lambda_3 - \lambda_2)\beta_2(t)S_2^* L^*}{B_2 N^*}\right\}, 0\right\}, \\ u_3^* &= \max\left\{\min\left\{1, \frac{(\lambda_4 - \lambda_6)\delta_1 I^*}{B_3}\right\}, 0\right\}, \\ u_4^* &= \max\left\{\min\left\{1, \frac{(\lambda_5 - \lambda_6)\delta_2 L^*}{B_4}\right\}, 0\right\}. \end{aligned} \tag{22}$$

Proof. To determine the adjoint equations and the transversality conditions, we use Hamiltonian (15). Setting $S_1(t) = S_1^*(t)$, $S_2(t) = S_2^*(t)$, $E(t) = E^*(t)$, $I(t) = I^*(t)$, $L(t) = L^*(t)$, and $R(t) = R^*(t)$ and differentiating Hamiltonian (15) with respect to S_1, S_2, E, I, L, and R, respectively, we can obtain (19). Solving the equations $\partial\mathscr{H}/\partial u_i = 0$, $i = 1, 2, 3$, on the interior of the control set and using the optimality conditions and the property of the control space U, we can derive (22). □

Theorem 3. *Problems (10)–(13) with given initial conditions* $S_1(0)$, $S_2(0)$, $E(0)$, $I(0)$, $L(0)$, *and* $R(0)$ *are fixed final time* T, *which admits a unique optimal solution* $(S_1^*, S_2^*, E^*, I^*, L^*, R^*)$ *associated to an optimal control set* $(u_1^*, u_2^*, u_3^*, u_4^*)$ *on* $[0, T]$.

Proof. The existence of an optimal solution $(S_1^*, S_2^*, E^*, I^*, L^*, R^*)$ associated with an optimal control $(u_1^*, u_2^*, u_3^*, u_4^*)$ comes from the convexity of the integrand of the cost functional J with respect to the controls (u_1, u_2, u_3, u_4) and

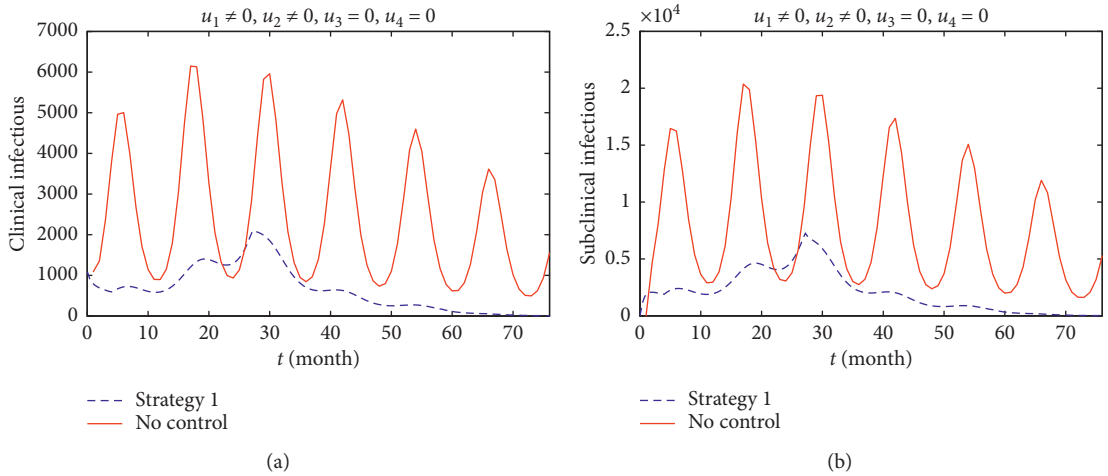

Figure 6: The time-series plots of I (a) and L (b) without (red line) and with (blue line) control Strategy 1.

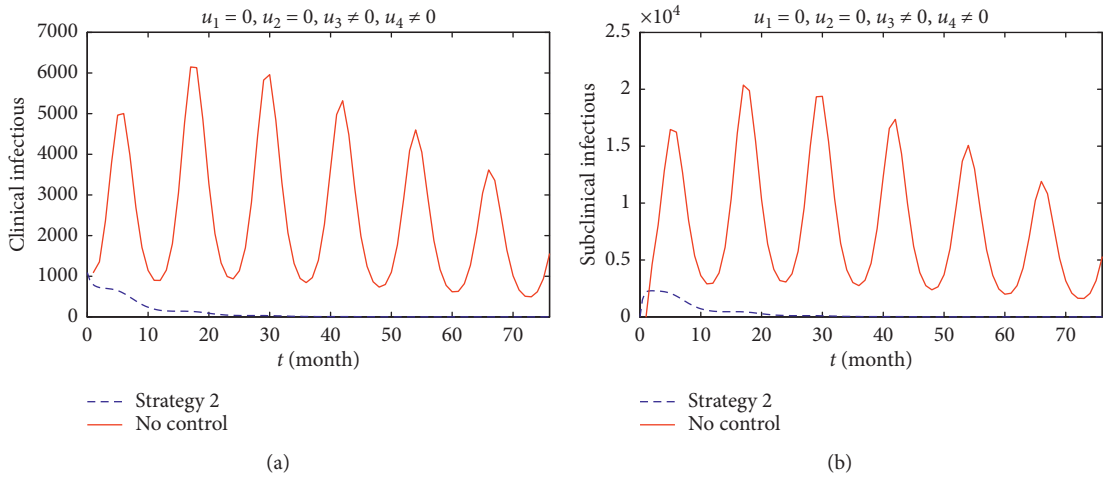

Figure 7: The time-series plots of I (a) and L (b) without (red line) and with (blue line) control Strategy 2.

the Lipschitz property of the state system with respect to state variables S_1, S_2, E, I, L, and R (see [43, 44]). For small final time T, the optimal control is given by (22) that is unique by the analysis above. Because the problems (10)–(13) are autonomous, uniqueness is valid for any time T and not only for small time T. □

The optimal control set predicted by Theorems 2 and 3 represents the optimal intervention strategy, given the cost constraints, and can be found by the application of celebrated Pontryagin's maximum principle [42] and appropriate numerical methods [45].

To find out the optimal control and the state system numerically, we use the approximate algorithm for obtaining the optimal control based on the forward-backward sweep scheme which is proposed in [46]. In order to speed up the convergence, we use the convex combination as follows.

Update u_i by entering the new adjoint variables $\lambda_i, i = 1, 2, \ldots, 6$, into formula (22). They are not stored as the control variables u_i, but as temporary vectors $\overline{u}_i$. The control variables u_i are set as the convex combination of the last iteration of u_i, namely, $oldu_i$, and the temporary vectors $\overline{u}_i$. That is,

$$u_i = c^k \overline{u}_i + \left(1 - c^k\right) oldu_i, \tag{23}$$

where k is the current iteration and $c \in (0, 1)$. Here, we adopt $c = 0.2$.

The control period T is 76 months, and the initial condition and parameters come from Wenzhou city in Table 2. The weight constant values in the objective functional are $A_1 = 0.4$, $A_2 = 0.1$, $B_1 = 0.4$, $B_2 = 0.4$, $B_3 = 0.1$, and $B_4 = 0.1$. The numerical settings of $A_i\,(i = 1, 2)$ indicate that we hope the number of the clinical infectious will decrease more than the subclinical infectious. Also, the specific cost of each

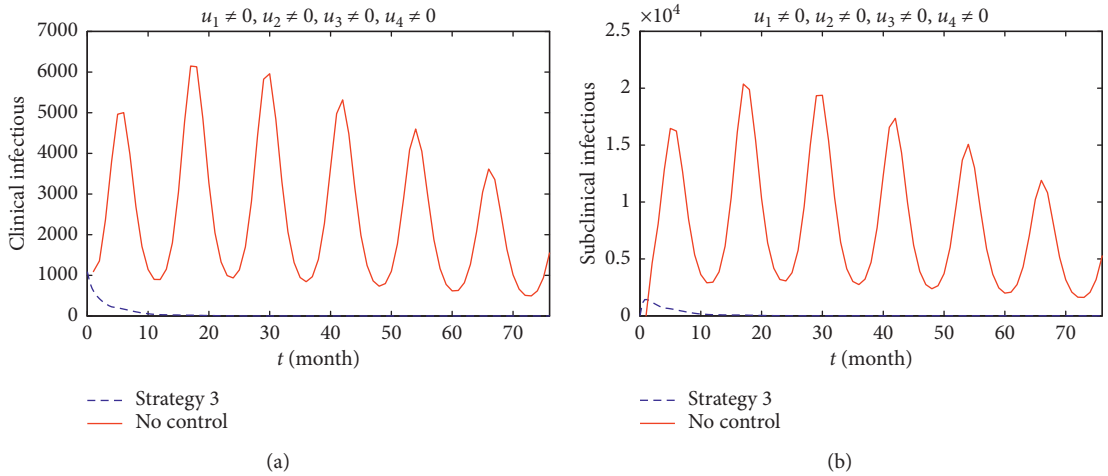

Figure 8: The time-series plots of I (a) and L (b) without (red line) and with (blue line) control Strategy 3.

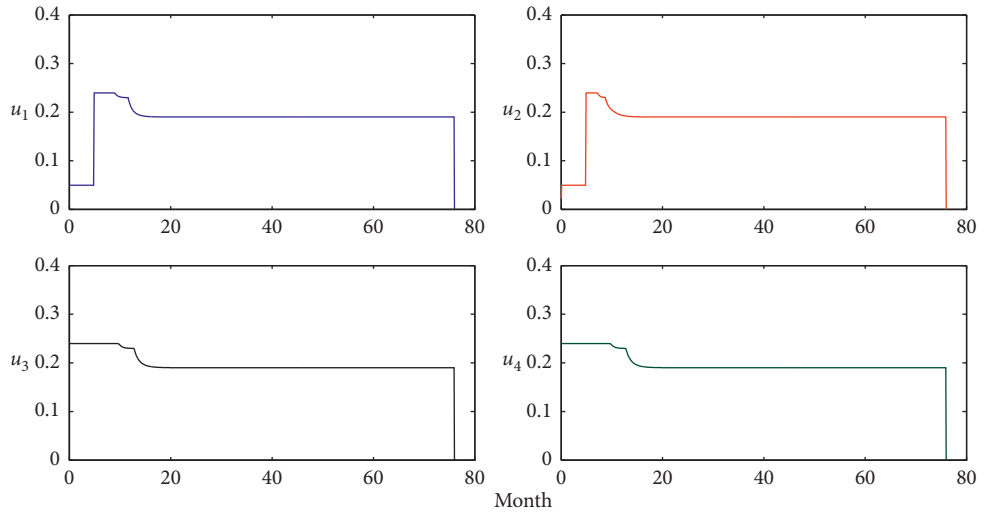

Figure 9: The optimal control variables $u_i, i = 1, 2, 3, 4$, of Strategy 3.

control measure is represented by the numerical values of B_i $(i = 1, 2, 3, 4)$.

We next consider three control schemes:

(i) *Strategy 1*. Only considering to reduce contact rates $\beta_1(t)$ and $\beta_2(t)$, the epidemic situation will be controlled in the 67th month (see Figure 6), which shows that hand washing and disinfection and so on can control HFMD;

(ii) *Strategy 2*. Only considering to increase the recovery rate δ_1 and δ_2, the epidemic situation will be controlled in the 22nd month (see Figure 7), which indicates that active treatment will lead to faster recovery;

(iii) *Strategy 3*. Considering both to reduce the contact rate $\beta_1(t)$ and $\beta_2(t)$ and increase the recovery rate δ_1 and δ_2, HFMD will be controlled in the 10th month (see Figure 8), which indicates that the optimal control strategy proposed by model (10) is effective. The time-varying optimal control parameters u_1, u_2, u_3, and u_4 of Strategy 3 are shown in Figure 9.

4. Concluding Remarks

In this paper, we investigate the dynamics of a modified HFMD model (1) with the periodic transmission rate in Wenzhou, China. The value of this study lies in two aspects:

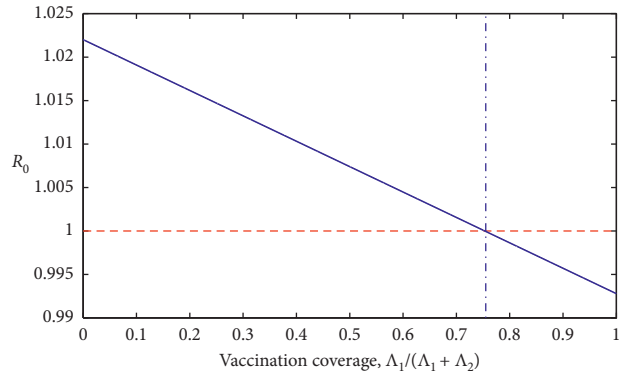

FIGURE 10: The relation between the rate of vaccination with $\mathscr{R}_0$.

mathematically, we define the reproduction number $\mathscr{R}_0$ and show that it can be used to govern the stochastic dynamics of the HFMD model (1): if $\mathscr{R}_0 < 1$, the system has a unique stable disease-free equilibrium which means the extinction of HFMD; if $\mathscr{R}_0 > 1$, it has an endemic equilibrium which leads to the persistence of HFMD (see Theorem 1). In addition, we establish the optimal control strategies (see Theorem 3) of system (10) corresponding to model (1). Epidemiologically, we show that the cost of EV-A71 vaccination affects the dynamics of the model in the following aspects:

(i) The EV-A71 vaccination cannot lead to the extinction of HFMD in Wenzhou: from the fitting charts 3 and 4, the use of vaccination indeed slightly decline in HFMD patients, but from the sensitivity analysis of the basic reproduction number $\mathscr{R}_0$, the cost of vaccination cannot lead to the extinction of HFMD and HFMD will periodically break out in Wenzhou. In fact, the vaccination is only useful to HFMD patients caused by EV-A71, and useless to HFMD patients caused by CX-A16 and others. In addition, according to the median of recruitment rate (see Table 4), one can obtain that $\overline{\Lambda}_1/\overline{\Lambda}_1 + \overline{\Lambda}_2 = 33.81\%$, which shows that about 33.81% of newborns are vaccinated in Wenzhou. The reason of low rate of vaccination may be that EV-A71 vaccination is not included in the medical insurance plan in China. Also, the EV-A71 vaccination can reduce the incidence of HFMD slightly, so increasing the rate of EV-A71 vaccination will benefit the control of HFMD spread in Wenzhou. See Figure 10 for more details.

(ii) The effect of ρ: the rate of HFMD inpatients ρ is the most sensitive parameter, which reflects that subclinical patients are the most important cause of persistent outbreaks of HFMD. This coincides with the existing literature [15–17].

(iii) The control strategy: we investigate the HFMD dynamics with three types of control schemes: (1) to reduce the contact rates $\beta_1(t)$ and $\beta_2(t)$ (see Figure 6); (2) to increase the recovery rates δ_1 and δ_2 (see Figure 7); (3) to reduce $\beta_1(t)$ and $\beta_2(t)$ and increase δ_1 and δ_2 (see Figure 8) and find that strategy (3) is the optimal policy. That is, in order to control the spread of HFMD, we need to pay attention to the personal hygiene to reduce the contact of the infectious persons and contaminative objects (β_1 and β_2), and increasing the active treatment and immune-boosting to shorten the course of infection will help to control the epidemic of HFMD.

It should be noted that, in the numerical results in Figure 3, there are errors between the simulations and actual HFMD cases; the maximum difference between them is about 5000. In fact, model (1) is based on some assumptions and we only consider the key factors of the spread of HFMD (see Figure 2) and neglect the influences of other factors such as sudden meteorological, temperature, and humidity. Ignoring these factors can make errors of the fitting results. However, if we consider more factors in modeling, we cannot obtain any analytical results (such as Theorem 1) about model (1). On the other hand, in the present paper, we adopt two simple periodic functions (2) and (3) as the transmission rates, which are the main factor of simulation results. Also, if we choose more complex periodic functions, we will add more parameters in model (1) and we cannot obtain the main results of optimal control strategies in Theorems 2 and 3. These are the main causes to bring about the maximum difference between simulated and actual HFMD cases that is about 5000. But, from Figure 3, we can know that except several months, other months fit well and we can learn about the trend of the spread of HFMD in Wenzhou.

In future research, we will take the interference of other factors, such as randomness and intervention strategies, to obtain more practical rules of the transmission of HFMD.

Data Availability

The data used to support the findings of this study are available from the corresponding author upon request.

Conflicts of Interest

The authors declare that there are no conflicts of interest regarding the publication of this paper.

Acknowledgments

This research was supported by the National Natural Science Foundation of China (Grant nos. 61672013, 11601179, and 61772017) and Huaian Key Laboratory for Infectious Diseases Control and Prevention (HAP201704).

References

[1] W. Xing, Q. Liao, C. Viboud et al., "Hand, foot, and mouth disease in China, 2008–12: an epidemiological study," *The Lancet Infectious diseases*, vol. 14, no. 4, pp. 308–318, 2014.

[2] S. Takahashi, Q. Liao, T. Boeche et al., "Hand, foot, and mouth disease in China: modeling epidemic dynamics of enterovirus serotypes and implications for vaccination," *PLoS Medicine*, vol. 13, no. 2, Article ID e1001958, 2016.

[3] S. Takahashi, C. Metcalf, Y. Arima et al., "Epidemic dynamics, interactions and predictability of enteroviruses associated with hand, foot and mouth disease in Japan," *Journal of The Royal Society Interface*, vol. 15, no. 146, Article ID 20180507, 2018.

[4] Hand, Foot, and Mouth Disease (HFMD), https://www.cdc.gov/hand-foot-mouth/index.html.

[5] Y. Zhu, B. Xu, X. Lian, W. Lin, Z. Zhou, and W. M. Wang, "A hand-foot-and-mouth disease model with periodic transmission rate in Wenzhou, China," *Abstract and Applied Analysis*, vol. 2014, Article ID 234509, 11 pages, 2014.

[6] J. Li, Y. Fu, A. Xu, Z. Zhou, and W. M. Wang, "A spatial-temporal ARMA model of the incidence of hand, foot, and mouth disease in Wenzhou, China," *Abstract and Applied Analysis*, vol. 2014, Article ID 238724, 2014.

[7] R. Li, L. Liu, Z. Mo et al., "An inactivated enterovirus 71 vaccine in healthy children," *The New England Journal of Medicine*, vol. 370, no. 9, pp. 829–837, 2014.

[8] S. Yu, Q. Liao, Y. Zhou et al., "Population based hospitalization burden of laboratory-confirmed hand, foot and mouth disease caused by multiple enterovirus serotypes in Southern China," *PLoS One*, vol. 13, no. 12, Article ID e0203792, 2018.

[9] B. Kim, H. Ki, S. Park, E. Cho, and B. Chun, "Effect of climatic factors on hand, foot, and mouth disease in South Korea, 2010–2013," *PLoS One*, vol. 11, no. 6, Article ID e0157500, 2016.

[10] W. Koh, T. Bogich, K. Siegel, J. Jin, E. Chong et al., "The epidemiology of hand, foot and mouth disease in asia," *The Pediatric Infectious Disease Journal*, vol. 35, no. 10, pp. e285–e300, 2016.

[11] Z. Du, L. Xu, W. Zhang et al., "Predicting the hand, foot, and mouth disease incidence using search engine query data and climate variables: an ecological study in Guangdong, China," *BMJ Open*, vol. 7, no. 10, Article ID e016263, 2017.

[12] S. Coates, M. Davis, and L. Andersen, "Temperature and humidity affect the incidence of hand, foot, and mouth disease: a systematic review of the literature—a report from the international society of dermatology climate change committee," *International Journal of Dermatology*, vol. 58, no. 4, pp. 388–399, 2019.

[13] L. Wang, Y. Li, and L. Pang, "Dynamics analysis of an epidemiological model with media impact and two delays," *Mathematical Problems in Engineering*, vol. 2016, Article ID 1598932, 9 pages, 2016.

[14] J. Liu, "Threshold dynamics for a HFMD epidemic model with periodic transmission rate," *Nonlinear Dynamics*, vol. 64, no. 1-2, pp. 89–95, 2011.

[15] Y. Ma, M. Liu, Q. Hou, and J. Zhao, "Modeling seasonal HFMD with the recessive infection in Shandong, China," *Mathematical Biosciences and Engineering*, vol. 10, no. 4, pp. 1159–1171, 2013.

[16] Y. Li, L. Wang, L. Pang et al., "The data fitting and optimal control of a hand, foot and mouth disease (HFMD) model with stage structure," *Applied Mathematics and Computation*, vol. 276, pp. 61–74, 2016.

[17] Y. Li, M. Huang, and L. Peng, "A multi-group model for estimating the transmission rate of hand, foot and mouth disease in mainland China," *Mathematical Biosciences and Engineering*, vol. 16, no. 4, pp. 2305–2321, 2019.

[18] J. Wang, Y. Xiao, and R. A. Cheke, "Modelling the effects of contaminated environments on HFMD infections in mainland China," *Biosystems*, vol. 140, pp. 1–7, 2016.

[19] J. Wang, Y. Xiao, and Z. Peng, "Modelling seasonal HFMD infections with the effects of contaminated environments in mainland China," *Applied Mathematics and Computation*, vol. 274, pp. 615–627, 2016.

[20] S. Chadsuthi and S. Wichapeng, "The modelling of hand, foot, and mouth disease in contaminated environments in Bangkok, Thailand," *Computational and Mathematical Methods in Medicine*, vol. 2018, Article ID 5168931, 8 pages, 2018.

[21] Z. Zhou, Y. Xu, C. Hu et al., "Epidemiological features of hand, foot and mouth disease during the period of 2008–14 in Wenzhou, China," *Journal of Tropical Pediatrics*, vol. 63, pp. 182–188, 2016.

[22] C. Dai, Z. Wang, W. Wang, Y. Li, and K. Wang, "Epidemics and underlying factors of multiple-peak pattern on hand, foot and mouth disease in Wenzhou, China," *Mathematical Biosciences and Engineering*, vol. 16, no. 4, pp. 2168–2188, 2019.

[23] Wenzhou Center for Disease Control and Prevention, http://www.wzcdc.org.cn/.

[24] J. Ma and Z. Ma, "Epidemic threshold conditions for seasonally forced SEIR models," *Mathematical Biosciences and Engineering*, vol. 3, no. 1, pp. 161–172, 2006.

[25] I. A. Moneim and D. Grennhalgh, "Use of a periodic vaccination strategy to control the spread of epidemics with seasonally varying contact rate," *Mathematical Biosciences and Engineering*, vol. 2, no. 3, pp. 591–611, 2005.

[26] L. J. White, J. N. Mandl, M. G. M. Gomes, A. T. Bodley-Tickell, P. A. Gane, and P. Perez-Brena, "Understanding the transmission dynamics of respiratory syncytial virus using multiple time series and nested models," *Mathematical Biosciences*, vol. 209, no. 1, pp. 222–239, 2007.

[27] J. Zhang, Z. Jin, G. Sun, and S. Ruan, "Modeling seasonal rabies epidemics in China," *Bulletin of Mathematical Biology*, vol. 74, no. 5, pp. 1226–1251, 2012.

[28] X. Zhang, Y. Zhao, and A. U. Neumann, "Partial immunity and vaccination for influenza," *Journal of Computational Biology*, vol. 17, no. 12, pp. 1689–1696, 2010.

[29] P. V. D. Driessche and J. Watmough, "Reproduction numbers and sub-threshold endemic equilibria for compartmental models of disease transmission," *Mathematical Biosciences*, vol. 180, no. 1-2, pp. 29–48, 2002.

[30] W. D. Wang and X. Q. Zhao, "Threshold dynamics for compartmental epidemic models in periodic environments," *Journal of Dynamics and Differential Equations*, vol. 20, no. 3, pp. 699–717, 2008.

[31] W. Wang, X. Gao, Y. Cai, H. Shi, and S. Fu, "Turing patterns in a diffusive epidemic model with saturated infection force," *Journal of the Franklin Institute*, vol. 355, no. 15, pp. 7226–7245, 2018.

[32] Y. Cai, X. Lian, Z. Peng, and W. M. Wang, "Spatiotemporal transmission dynamics for influenza disease in a heterogenous environment," *Nonlinear Analysis: Real World Applications*, vol. 46, pp. 178–194, 2019.

[33] Y. Cai, Z. Ding, B. Yang, Z. Peng, and W. M. Wang, "Transmission dynamics of Zika virus with spatial structure—a case study in Rio de Janeiro, Brazil," *Physica A: Statistical Mechanics and its Applications*, vol. 514, pp. 729–740, 2019.

[34] The Website of National Bureau of Statistics of China (in Chinese), http://www.stats.gov.cn/.

[35] Wenzhou Bureau of Statistics: Bulletin of Main Population Data of Wenzhou City, http://wztjj.wenzhou.gov.cn/.

[36] Y. Yang, H. Zhu, Z. Bi et al., "Smart-MSP: a self-adaptive multiple starting point optimization approach for analog circuit synthesis," *IEEE Transactions on Computer-Aided Design of Integrated Circuits and Systems*, vol. 37, no. 3, pp. 531–544, 2018.

[37] H. Kim, R. T. Haftka, W. H. Mason et al., "Probabilistic modeling of errors from structural optimization based on multiple starting points," *Optimization and Engineering*, vol. 3, no. 4, pp. 415–430, 2002.

[38] M. Samsuzzoha, M. Singh, and D. Lucy, "Uncertainty and sensitivity analysis of the basic reproduction number of a vaccinated epidemic model of influenza," *Applied Mathematical Modelling*, vol. 37, no. 3, pp. 903–915, 2013.

[39] S. Marino, I. B. Hogue, and C. J. Ray, "A methodology for performing global uncertainty and sensitivity analysis in systems biology," *Journal of Theoretical Biology*, vol. 254, no. 1, pp. 178–196, 2008.

[40] J. Karrakchou, M. Rachik, and S. Gourari, "Optimal control and infectiology: application to an HIV/AIDS model," *Applied Mathematics and Computation*, vol. 177, no. 2, pp. 807–818, 2006.

[41] K. S. Lee and A. A. Lashari, "Stability analysis and optimal control of pine wilt disease with horizontal transmission in vector population," *Applied Mathematics and Computation*, vol. 226, pp. 793–804, 2014.

[42] L. S. Pontryagin, V. G. Boltyanskii, R. V. Gamkrelidze et al., *The Mathematical Theory of Optimal Processes*, Wiley, New York, USA, 1962.

[43] W. H. Fleming and R. W. Rishel, *Deterministic and Stochastic Optimal Control*, Springer-Verlog, New York, USA, 1975.

[44] L. Cesari, *Optimization-Theory and Applications*, Springer-Verlog, New York, USA, 1983.

[45] H. S. Rodrigues, M. T. T. Monteiro, and D. F. M. Torres, "Optimal control and numerical software: an overview," in *Systems Theory: Perspectives, Applications and Developments*, pp. 93–110, Nova Science, New York, USA, 2014.

[46] S. Lenhart and J. T. Workman, *Optimal Control Applied to Biological Models*, Chapman & Hall/CRC, London, UK, 2007.

Hindawi
Complexity
Volume 2020, Article ID 8206245, 14 pages
https://doi.org/10.1155/2020/8206245

Research Article

Hybridized Extreme Learning Machine Model with Salp Swarm Algorithm: A Novel Predictive Model for Hydrological Application

Zaher Mundher Yaseen,[1] **Hossam Faris**,[2] **and Nadhir Al-Ansari**[3]

[1]*Sustainable Developments in Civil Engineering Research Group, Faculty of Civil Engineering, Ton Duc Thang University, Ho Chi Minh City, Vietnam*
[2]*King Abdullah II School for Information Technology, The University of Jordan, Amman, Jordan*
[3]*Civil, Environmental and Natural Resources Engineering, Lulea University of Technology, 97187 Lulea, Sweden*

Correspondence should be addressed to Zaher Mundher Yaseen; yaseen@tdtu.edu.vn

Received 8 August 2019; Accepted 16 January 2020; Published 21 February 2020

Guest Editor: Jesus Vega

The capability of the extreme learning machine (ELM) model in modeling stochastic, nonlinear, and complex hydrological engineering problems has been proven remarkably. The classical ELM training algorithm is based on a nontuned and random procedure that might not be efficient in convergence of excellent performance or possible entrapment in the local minima problem. This current study investigates the integration of a newly explored metaheuristic algorithm (i.e., Salp Swarm Algorithm (SSA)) with the ELM model to forecast monthly river flow. Twenty years of river flow data time series of the Tigris river at the Baghdad station, Iraq, is used as a case study. Different input combinations are applied for constructing the predictive models based on antecedent values. The results are evaluated based on several statistical measures and graphical presentations. The river flow forecast accuracy of SSA-ELM outperformed the classical ELM and other artificial intelligence (AI) models. Over the testing phase, the proposed SSA-ELM model yielded a satisfactory enhancement in the level accuracies (8.4 and 13.1 percentage of augmentation for RMSE and MAE, respectively) against the classical ELM model. In summary, the study ascertains that the SSA-ELM model is a qualified data-intelligent model for monthly river flow prediction at the Tigris river, Iraq.

1. Introduction

Due to the wide range of space and time variabilities, river flow modeling has been a critical problem in water management and hydrology [1]. The operation of many water resources system rule curves needs monthly river flow forecasts [2]. Various methods capable of forecasting river flow under different conditions with different levels of accuracy have been proposed, considerably evolving within the past decades from the simple linear equations to the complex and complicated ones. Researchers have considered various river flow forecasting methods such as the conceptual (HEC-HMS and HBV) [3–5], stochastic (AR-autoregressive and ARMA-autoregressive moving average) [6], and the physical-based (SWAT) models [7, 8].

The complex relationship between rainfall and river flow variables and the lack of sufficient hydrological data of watersheds have made data-driven models such as artificial intelligence more suitable for river flow forecasting compared to the process-based models [9]. Currently, a single method which can be employed generally for all types of basins and systems is yet to be developed. Hydrologists have currently been building reliable forecasting methods by exploiting the available and new scientific techniques such as hybrid intelligence models. The ability of hybrid AI models in addressing the associated nonlinearity and non-stationarity problems has attracted great attention in different domains [10, 11]. Likewise, this explains their wide applications in modeling the river flow in particular [12, 13] and hydrological processes in general [14].

Studies have demonstrated a wide range of forecasting accuracies using AI models with the geographic topographies of the test sites despite their success in other fields [15–18]. The development of a model that will be used to forecast in any environmental condition is an aspect yet to be explored. Researchers in water resources management engineering should be motivated by the assertion: does the integration of an optimization algorithm with AI models as hybrid intelligent models boost their predictive model accuracies? Hydrologists and intelligence system modelers, in an attempt to address the raised issue, have faced the challenge of properly selecting the input combinations known to rule the predictable accuracy of an objective predictive model for model development [19].

The literature stated a very massive implementation of the AI models for river flow modeling. These models are artificial neural network, genetic programming, fuzzy logic methods, support vector machine models, M5 tree models, complementary AI models coupled with data time series preprocessing techniques, and hybrid model [14]. Most recently, a new version of the ANN model called extreme learning machine was developed by the authors in [20], as a robust predictive model. The employment of ELM in the field of hydrology and particularly in river flow modeling demonstrated a very promising and enhancement in the modeling process [14].

The first attempt of modeling river flow using ELM was established in [21]. The authors developed an ELM model to capture the associated nonlinearity of the seasonal river inflow of the Brazilian Hydropower. Their Finding evidenced the potential of the proposed model and emphasised several hydrological investigations later on. Li and Cheng [22]studied the capacity of ELM to module the monthly scale reservoir inflow in China. The ELM model provided an accurate result in comparison with several other well-established AI models. An improved ELM model is developed in a new version called online sequential extreme learning machine (OS-ELM) for multiple river flow scales prediction in Canada [22]. The same OS-ELM model was developed for flood events forecasting for hourly river flow monitoring [23]. The findings of the improved ELM model demonstrated a noticeable prediction performance. In another attempt, Yaseen et al. developed an ELM model to forecast the monthly scale river flow located in semiarid environment in Iraq. The proposed model revealed good capability to mimic the monthly river flow trend. Later on, several studies approved the potential of the ELM in the field of hydrology processes [13, 24–29]. Based on the reported literature of the extreme learning machine modeling and its version improvement in hydrological problems over a very short period, the authors' attention is mainly to modify this robust predictive model and attempt to enhance its predictability skills.

Despite the noticeable promising implementation of the ELM model in wide range of hydrology applications, it still suffers limitations and drawbacks. First, the random assignment of the input weights and biases can negatively affect the generalization capability of the network [30]. In addition, ELM needs larger number of hidden neurons which results in more complex models [31]. Hence, the main motivation of the current research is to propose a new training optimization for the ELM model to solve the aforementioned problems and improve the predictability performance of the ELM model.

In this research, a new optimization algorithm called Salp Swarm Algorithm is proposed and hybridized with the ELM model for optimizing the input weights and hidden biases of the network. SSA is a modern nature-inspired algorithm proposed in [32]. SSA has shown an impressive performance in optimizing various complex and challenging engineering problems. Based on these facts, the motivation of exploring the capabilities of this optimizer is endeavoured and the authors work to improve the performance of the classical ELM model for the surface hydrology application. For this reason, a real case of semiarid environment of the Tigris river in Iraq is investigated which is an extension for the published work [33].

This research is organized as following. A brief introductory of the proposed methodology is given in Section 2. The description of the investigated case study is described in Section 3. The proposed ELM model based on the SSA optimizers is introduced and discussed in detail in Section 4. The experiments and results are given and discussed in Section 5. Finally, the conclusions and findings of this work are summarized in Section 6.

2. Preliminaries

2.1. Salp Swarm Algorithm. SSA is a recent nature-inspired algorithm which mimics the swarming behaviour of sea creatures called salps [32]. Salps have barrel-shaped gelatinous bodies, and they move around by pumping water through their body from one side to the other. Salps exist as colonies and move together as chains. In SSA, the movement behaviour is mathematically modelled for solving optimization problems. The models suppose that there are two main types of salps: leaders and followers. The leaders are the salps that lead the chain in the front direction, while the followers follow their leaders synchronously and in harmony as shown in Figure 1.

Like all swarm intelligent algorithms, SSA starts by randomly initializing a swarm of N salps. Each salp is represented by one-dimensional vector of n elements, while the swarm is represented as a two-dimensional matrix x. The algorithm also refers to the target of the swarm as a food source F. The movement of the leader chain x_j^1 is modelled as given in the following formula:

$$x_j^1 = \begin{cases} F_j + c_1\left(\left(\mathrm{ub}_j - \mathrm{lb}_j\right)c_2 + \mathrm{lb}_j\right), & c_3 \geq 0.5, \\ F_j + c_1\left(\left(\mathrm{ub}_j - \mathrm{lb}_j\right)c_2 + \mathrm{lb}_j\right), & c_3 < 0.5, \end{cases} \tag{1}$$

where j is the dimension of the position to be updated, F_j is the jth element of the food source position, ub_j and lb_j are the upper and lower bounds of the jth element, c_2 and c_3 are the random numbers drawn from the interval [0, 1], and c_1 is the dynamic variable that changes its value over the course of iterations according to the following formula:

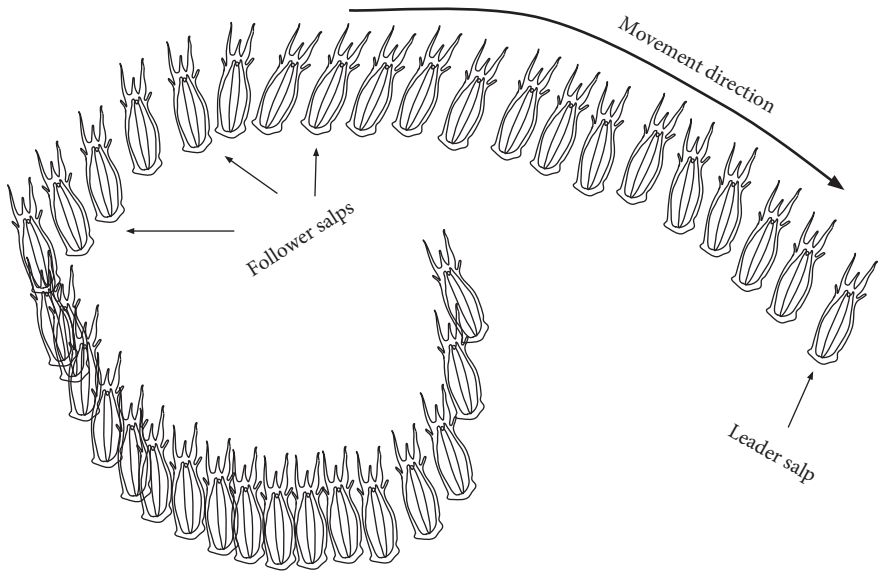

Figure 1: Leaders and followers of salps chain movement.

$$c_1 = 2e^{-(4l/L)^2}, \tag{2}$$

in which l represents the current iteration and L is a predefined number of maximum iterations. Note that c_1 is a very important variable in the SSA process which controls the balance between the exploration and exploitation processes of the optimization algorithm. The followers update their position accordingly as

$$x_j^i = 0.5\left(x_j^i - x_j^{i-1}\right), \tag{3}$$

where x_j^i is the ith element of the jth position and $i \geq 2$. The procedure of the SSA algorithm is presented in Figure 2.

2.2. Extreme Learning Machines. Artificial neural networks (ANN) have been used as a universal approximator to deal with complex problems in a wide spectrum of different domains. One of these common problems is classification and regression problems. For ANN to be able to predict the value of the output variable, it needs to be trained based on a set of examples using a learning algorithm. One of the recent and successful variants of ANNs is ELM. ELM is a learning framework for single hidden layer feedforward neural networks (SLFN) introduced recently in [20]. The main merit of the ELM model is the learning process convergence speed that emphasizes the capability over the classical gradient decent approach for training the SLFN [34]. In addition, the nonrequirement for algorithm tuning parameters is similar to the back-propagation algorithm. The ELM model requires no human interactive for tuning [35]. Further, ELM does not require an iterative process to tune the SLFN parameters. Instead, it randomly modifies the input weights and the hidden biases and then it governs the output weights systematically using the potential of the Moore–Penrose (MP) generalized inverse method. An illustration of the SLFN-based ELM is shown in Figure 3.

Pseudocode of the SSA algorithm.

```
Initialize a swarm of slaps x_i(i = 1, 2, ..., n)
While (Termination condition is not met) do
    Calculate the fitness of each salp in the swarm
    Set F as the position of best salp
    Update c_1 by equation (2)
    for (each salp (x_i)) do
        if (i == 1) then
            Update the leader's position using equation (1)
        else
            Update the follower's position using equation (3)
        end if
    end for
    Check and return salps if they go beyond upper and
lower bounds
end while
Return F
```

Figure 2: Salp Swarm Algorithm procedure.

The output of SLFN is trained using a dataset with N distinct examples denoted as (x_i, t_i), $i = 1, 2, \ldots, N$, where x_i is the input vector and t_i is the output vector. The activation function $g(.)$ and k hidden neurons is

$$f_i = \sum_{j=1}^{k} \beta_j g\left(w_j x_i + b_j\right), \quad j = 1, 2, \ldots, N, \tag{4}$$

where w_j denotes the weight vector that links the input nodes to the jth hidden node, b_j signifies the bias value of the jth hidden node, and β_j are the values of the output weights that connect the jth hidden node with the output nodes [36]. Formula (4) is written compactly as

$$O = H \times \beta, \tag{5}$$

where H is the output matrix of the hidden layer. ELM assigns the weights and the biases randomly without the need to take into consideration the input data. ELM determines the output weights by solving equation (5) using

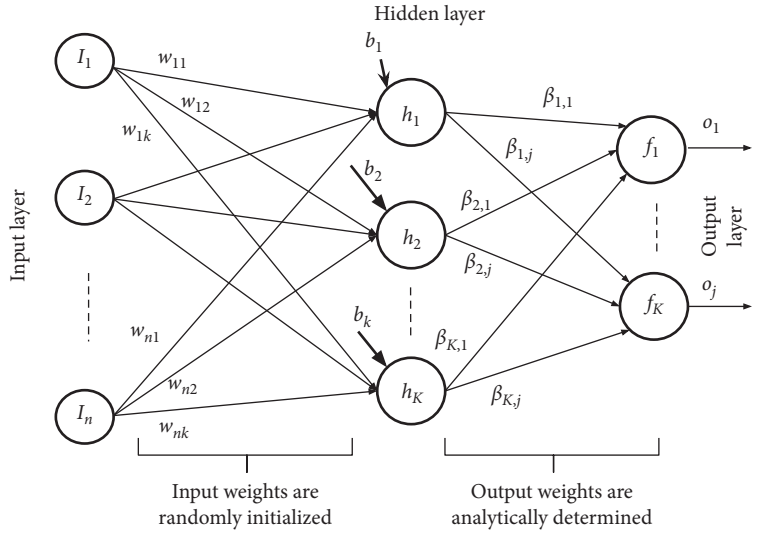

Figure 3: The architecture of the single hidden layer ELM model.

MP generalized inverse. The output weights can be determined by ELM using the following formula:

$$\widehat{\beta} = H^{\dagger} \times T. \tag{6}$$

The process of the ELM predictive model is presented in Figure 4.

3. Case Study and Site Description

In this study, the Tigris river which is located in the Iraq region is selected for examining the proposed hybrid predictive model. The total length of the river is around 1718 km. The river originates from Turkey and flows toward Iraq in the southern part. Most of the river basin (about 85 percentage) is located in Iraq with an approximate catchment area of 253000 km^2. Tigris and Euphrates rivers are presenting the chief freshwater resources in Iraq, providing water for multiple usages such as domestic, agricultural, industrial uses, and several other usages. The region environment of the river has a semiarid climate, with the Tigris basin having a climatic range from semihumid in the headwaters to the north to semiarid in the area close to where it met with the Euphrates river in the southern part of the region. The average precipitation in the basin per year is between 400 and 600 mm, even though the annual precipitation values in the upper and lower parts have been registered as 800 and 150 mm, respectively. Due to the high precipitation rates in the Zagros Mountains in the east of the Tigris basin, it has a significantly higher mean precipitation of approximately 300 mm/year compared to the Euphrates basin [37]. Precipitation mainly occurs in the basins around November and April, while January to March witness snowfall in the mountains. The climatic conditions in the lowlands of Iraq and Syria (semiarid to arid) usually facilitate a considerable loss of water to evapotranspiration in the Mesopotamian region. The Tigris basin has an air temperature of about −35°C during the winter in the Armenian Highlands and about 40°C on the Jezira plateau during the

ELM algorithm for training SLFN.

Input: $L = \{(x_i, t_i) \mid x_i \in R^n, t_i \in R^m, i = 1, 2, ..., N\}$
//Training dataset L consists of a set of N training samples and their associated output values.
$g(x)$: activation function.
$\tilde{N}$: Number of hidden nodes
Output: Output weight $\widehat{\beta}$
(1) procedure ELM(L, N, $g(.)$)
(2) Initialize weights w_i and biases b_i randomly [−1, 1], $i = 1, 2, ..., \tilde{N}$.
▷ w_i is the vector of weights that connect the hidden node i to all input nodes.
▷ b_i is the bias value of the hidden node i
(3) Calculate the hidden layer output matrix H

$$H = \begin{bmatrix} g(w_1.x_1 + b_1) \dots g(w_{\tilde{N}}.x_1 + b_{\tilde{N}}) \\ \vdots \qquad\qquad \vdots \\ g(w_1.x_N + b_1) \dots g(w_{\tilde{N}}.x_N + b_{\tilde{N}}) \end{bmatrix}$$

(4) Find output weight $\widehat{\beta}$ using MP generalized inverse

$$\widehat{\beta} = H^{\dagger}T$$

$$\widehat{\beta} = (H^T H)^{-1} H^T T$$

(5) return $\widehat{\beta}$ ▷ The output weights
(6) end procedure

Figure 4: The extreme learning machine model learning procedure.

summer [38]. Baghdad, the capital city of Iraq, has an average rainfall of about 216 mm, with rainfall usually experienced from December to February. At the capital, the Tigris river mean river flow is 235 m^3·s^{-1}. The maximum weather temperature experienced around is 45°C during the summer and about 10°C during the winters [39, 40].

For the modeling establishment, the monthly river flow scale is used to build the predictive model measured at the Baghdad station (see Figure 5). The historical river flow database is gathered from the USGS Data Series 540 [41]. The statistical description of the utilized dataset is tabulated in Table 1. The area of the drainage site is 134, 000 km^2, which is

Figure 5: The case study location: Baghdad metrological station, Tigris river, Iraq.

Table 1: Descriptive statistics for the mean monthly river flow for the Tigris river at Baghdad (Iraq) (1991–2010) [33].

Partition	Time period	No. records	Q ($m^3 \cdot s^{-1}$)				
			Mean	St. dev.	Median	Minimum	Maximum
Training	Jun. 1991–Dec. 2007	187	780.099	379.712	674.700	298.100	2651.000
Testing	Jan. 2007–Dec. 2010	48	489.879	136.746	445.900	331.400	936.400
Complete	Jun. 1991–Dec. 2010	235	720.820	363.469	636.900	298.100	2651.000

coordinated between the Latitude of 33°24′34″N and a Longitude of 44°20′32″E. Over the past two decades, a noticeable negative river flow deterioration was observed for the Tigris river. This deterioration is associated with several causes such as diplomatic issues or climate change. Hence, the necessity of providing an accurate and reliable data-intelligence model for this river system is highly recommended.

4. Proposed SSA-ELM Forecasting Model

There are two basic points that should be determined before applying any evolutionary or swarm-based algorithm to optimize any problem which are the representations of the solution and the choice of the cost function. These two points are addressed for the proposed SSA-ELM model as follows:

(i) In order to handle an optimization problem using a metaheuristic algorithm, the solution of the problem should be represented properly in the algorithm. That is, the way that the solution is encoded as an individual. In the proposed SSA-ELM model, each individual represents a potential solution as a real vector I, where I consists of two parts: inputs weights and hidden biases as given in equation (10). All elements of I are generated in [−1, 1]:

$$I = [W_{11}, W_{12}, \ldots, W_{nk} b_1, \ldots b_k]. \quad (7)$$

(ii) In all metaheuristic algorithms, a cost function is utilized to assess the quality of the generated solutions over the course of iterations. In this work, the root mean squared error (RMSE) is selected as the cost function which is the most commonly used cost function in evolutionary extreme learning algorithms. RMSE can be measured as given in equation (8). The goal of the algorithm is to find the ELM model that has the minimum value of RMSE:

$$\text{RMSE} = \sqrt{\frac{\sum_{j=1}^{N} \left\| \sum_{j=1}^{K} \beta_j g\left(w_j x_i + b_j\right) - t_i \right\|}{m \times N}}. \quad (8)$$

The procedure of the proposed SSA-ELM algorithms can be described as follows:

First, the algorithm starts by generating randomly a predefined number N of particles. Each of the particles represents a candidate ELM network as explained previously.

Then, the fitness of each particle is calculated using the following steps:

(i) Assign the values of the input weights and hidden biases that a given particle carries to a network structure.

(ii) Calculate the output weights of the ELM network using the PM method based on the training part of the dataset.

(iii) Calculate the RMSE as given in equation (8) based on the validation part of the dataset.

After performing the fitness evaluation step, the particles are sorted according to their fitness values. The best L particles that generate ELM networks with lowest RMSE values are nominated as leaders. The rest of the particles in the swarm are considered as followers. The description of the proposed predictive algorithm is displayed in Figure 6.

The positions of the leaders and followers are updated according to equations ((1) and (3)), respectively. The evaluation and update steps are repeated until a predefined number of iterations is reached.

The training procedure of the proposed model is established using correlated lags computed via the correlations statistical approach (i.e., autocorrelation and partial autocorrelation functions) to detect appropriate input attributes to the targeted attribute (see Figure 7). This process is accomplished in harmony with major researches of the literature [42, 43]. Based on the visualization of the correlation statistic, five lags time of river flow historical information (attributes variables) influence the one-step ahead river flow modeling. Hence, a combination of five scenarios model (M1, M2, ..., M5) architecture is constructed as follows:

$$\begin{aligned}
&\text{Model 1} \quad \text{M1: } Q_{(t)} = fQ_{(t-1)},\\
&\text{Model 2} \quad \text{M1: } Q_{(t)} = fQ_{(t-1)}, Q_{(t-2)},\\
&\text{Model 3} \quad \text{M1: } Q_{(t)} = fQ_{(t-1)}, Q_{(t-2)}, Q_{(t-3)},\\
&\text{Model 4} \quad \text{M1: } Q_{(t)} = fQ_{(t-1)}, Q_{(t-2)}, Q_{(t-3)}, Q_{(t-4)},\\
&\text{Model 5} \quad \text{M1: } Q_{(t)} = fQ_{(t-1)}, Q_{(t-2)}, Q_{(t-3)}, Q_{(t-4)}, Q_{(t-5)},
\end{aligned} \tag{9}$$

where $Q_{(t)}$ is the target river flow step "one month ahead" and $Q_{(t-1)}$, ..., $Q_{(t-5)}$ are the lag times up to five months previously. Here, five input combinations are constructed for the prediction matrix of the SSA-ELM and ELM predictive models.

5. Application Results and Analysis

Over the past couple decades, massive attention has been focused on hydrological time series modeling, particularly for river flow process. This is owing to the need of an accurate and reliable intelligent model that can be implemented in real practice. Several machine learning approaches have been proposed to forecast and simulate the river flow time series. As a matter of fact, the assumption of the hydrological time series is originated by stochasticity, nonlinearity, and redundancy. Also, the underlying mechanisms of river flow generation are mostly different from low-, medium-, and high-flow periods. In other words, the extreme events of flows rely upon the outburst of heavy storm of rainfall events. Hence, developing a new data-intelligent model characterized by sophistication to forecast all kind of flow patterns satisfactory is still under process mission for the hydrology engineers. In this research, the application of forecasting the monthly river flow (semiarid environment) using the hybrid SSA-ELM model is presented. Indeed, using a univariate modeling is more challenging for the hydrologist as it is fulfilled for the benefit of the catchment that lacks the metrological information.

The perdition skills for the conducted modeling were carried out using two types of performance indicators including the goodness (e.g., (r) and (WI)) and the absolute error measures (e.g., (RMSE) and (MAE)). The mathematical description of these performance indicators is

$$r = \frac{\sum_{i=1}^{i=N}\left[\left(S_i^{\text{obs}} - \overline{S^{\text{obs}}}\right)\cdot\left(S_i^{\text{pred}} - \overline{S^{\text{pred}}}\right)\right]}{\sqrt{\sum_{i=1}^{i=N}\left(S_i^{\text{obs}} - \overline{S^{\text{obs}}}\right)^2}\cdot\sqrt{\sum_{i=1}^{i=N}\left(S_i^{\text{pred}} - \overline{S^{\text{pred}}}\right)}},$$

$$\text{where } -1 \le r - 1$$

$$\text{WI} = 1 - \left[\frac{\sum_{i=1}^{i=N}\left(S_i^{\text{obs}} - S_i^{\text{pred}}\right)^2}{\sum_{i=1}^{i=N}\left(\left|S_i^{pred} - \overline{S^{obs}}\right| + \left|S_i^{obs} - \overline{S^{obs}}\right|\right)^2}\right], \tag{10}$$

$$\text{RMSE} = \sqrt{\frac{1}{N}\sum_{i=1}^{i=N}\left(S_i^{\text{obs}} - S_i^{\text{pred}}\right)^2},$$

$$\text{MAE} = \frac{1}{N}\sum_{i=1}^{i=N}\left|S_i^{\text{obs}} - S_i^{\text{pred}}\right|,$$

where S_i^{obs} and S_i^{pred} are the observed and forecasted values of river flow, $\overline{S^{\text{obs}}}$ and $\overline{S^{\text{pred}}}$ are the mean values of river flow, and N is the number of the observations of the testing phase.

For SSA, the size of the population is set to 50 while the number of iterations is set to 1000. These values were recommended and showed superior results when applied for solving complex optimization problems in [32]. For ELM, the common sigmoid function activation function is used [44]. However, the number of hidden nodes was systematically determined by experimenting different numbers starting from 2 hidden nodes up to 10 with a step of 2 nodes each time.

Table 2 tabulates the efficiency results of the hybrid SSA-ELM model achieved based on the testing data for each input combination attribute. The results are validated against the published results of ELM, support vector regression (SVR), and generalized regression neural network (GRNN) which were conducted in [33], on the same case study. In addition, Table 2 also lists the results of random forests (RF) implemented in Weka the popular suite of machine learning software [45].

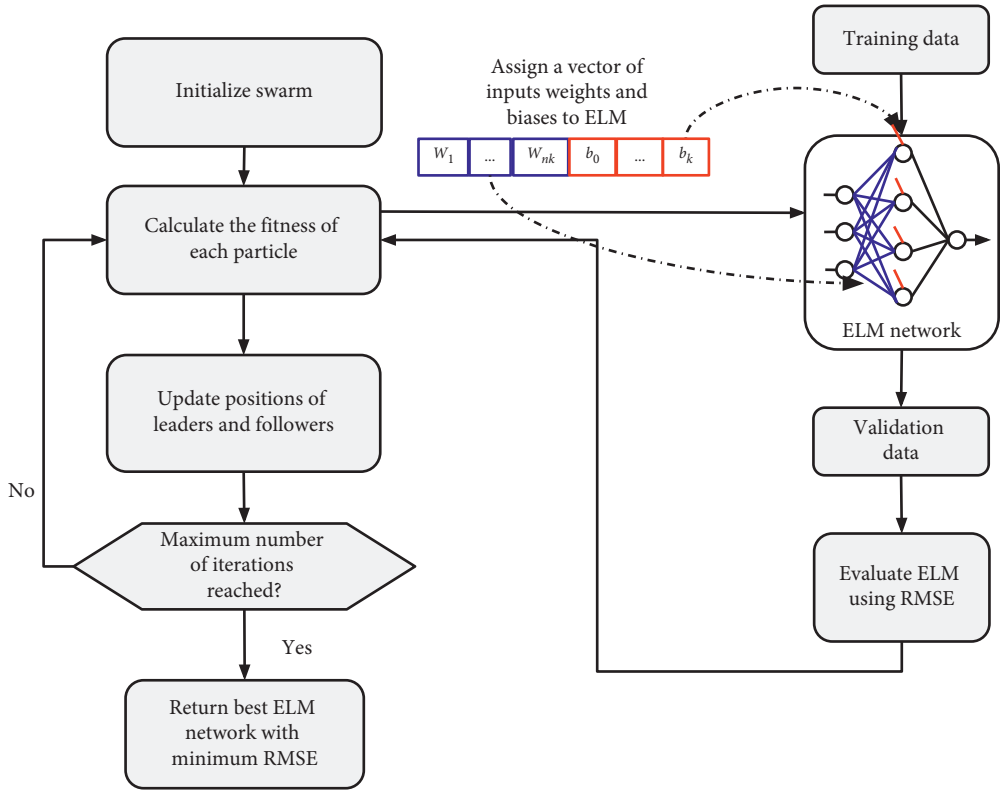

Figure 6: Description of the proposed SSA-ELM algorithm.

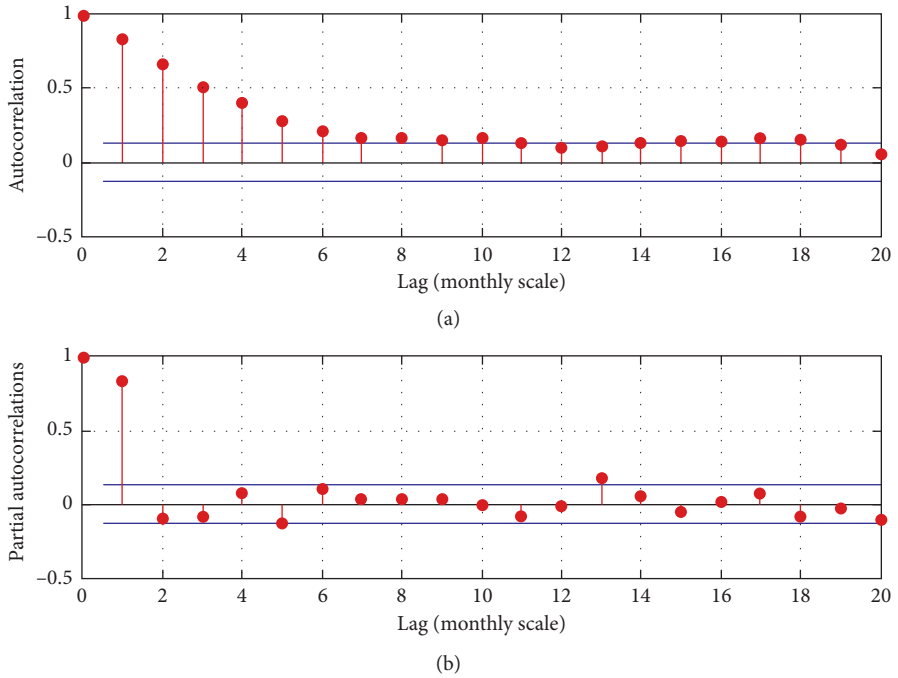

Figure 7: The statistical correlation process function of the investigated monthly scale river flow.

Indeed, the motivation of the current study is to improve the performance of the nontuned predictive model ELM through complementing with an evolutionary nature-inspired novel optimization algorithm (i.e., SSA). Based on the investigated results, an excellent performance in terms of lower RMSE and MAE values and higher r and WI values, respectively, when forecasting the present river flow data, was observed. The results exhibited a noticeable

Table 2: Performance evaluation for ELM and SSA-ELM, SVR, GRNN, and RF models.

Input combinations	Models	r	WI	RMSE ($m^3 \cdot s^{-1}$)	MAE ($m^3 \cdot s^{-1}$)
M1	SSA-ELM	0.812	0.861	80.592	66.203
	ELM	0.81	0.82	98.272	87.012
	SVR	0.761	0.802	106.749	90.905
	GRNN	0.658	0.689	127.818	113.698
	RF	0.372	0.531	189.778	131.966
M2	SSA-ELM	0.809	0.850	80.516	62.185
	ELM	0.817	0.834	95.571	83.899
	SVR	0.715	0.769	111.228	95.14
	GRNN	0.468	0.54	125.187	103.551
	RF	0.373	0.549	175.765	142.347
M3	SSA-ELM	0.784	0.812	86.868	62.185
	ELM	0.815	0.814	104.307	92.544
	SVR	0.741	0.776	118.02	101.85
	GRNN	0.496	0.54	125.187	103.551
	RF	0.037	0.33	280.85	225.27
M4	SSA-ELM	0.800	0.855	87.84	69.069
	ELM	0.803	0.826	98.432	85.117
	SVR	0.728	0.769	119.539	106.585
	GRNN	0.346	0.507	133.522	114.063
	RF	0.127	0.39	1246.48	196.745
M5	SSA-ELM	0.801	0.856	87.659	67.886
	ELM	0.799	0.853	87.906	71.544
	SVR	0.715	0.768	124.155	108.367
	GRNN	0.248	0.416	135.35	112.606
	RF	0.222	0.0001	668.76	657.031

enhancement in the prediction skills using the proposed SSA-ELM model in comparison with the benchmark ELM-based model. The improved performance with SSA-ELM attributed to the robustness of the novel evolutionary optimization method SSA linked to the ELM model. This robustness may have contributed to the internal function parameter optimization for each input combination.

The Taylor diagram is another modern graphical presentation to diagnose the predictability of the modeling through visualizing the errors from the benchmark observed record. This diagram graphically summarizes the model's efficiency in approximating the accuracy to the observed data. The Taylor diagram of the hybrid SSA-ELM and classical ELM is illustrated in Figure 8. The position of each model appeared on the diagram measures the accuracy of that model in accordance to the observed river flow. Based on the diagram presentation, the SSA-ELM model has a higher value of correlation compared to the ELM model. The SSA-ELM model approximated well with observed and located nearer to the actual record. The RMSE between the predicted and observed river flow was denoted as proportional to the distance to the point of the observation. The standard deviation of the predictive model is proportional to the radial distance from the origin.

For detailed inspection for the performance of the SSA-ELM model over the benchmark ELM model, Figure 9 presents the relative error (RE) distribution indicator in the form of boxplot. Based on the generated graph, the hybrid SSA-ELM performed an acceptable improvement with average RE between −10 and + 10% and over 80% of the testing period. The maximum RE magnitude recorded on the overestimation is +35%, whereas the underestimation aspect is recorded as −25%. This is much different from the classical ELM that exceeded the −40% in the underestimation aspect.

Scatter plots for the ELM and SSA-ELM models are presented in Figures 10 and 11, respectively. The graphical presentation followed the determination coefficient values as it is the square value. The proposed hybrid model was performed closer to the ideal line between the observed and forecasted values.

It is an excellent fashion of evaluating the current research results by comparing with modern established researches with the regards of hybrid evolutionary nature-inspired algorithms integrated with AI-predictive models. Most recently, the applications of metaheuristic techniques have shown an extensive and noticeable optimization methods for AI predictive models. This is owing to the main advantages such as flexibility, give an optimal solution, and free from gradient decent drawbacks [32]. In the last five years, there are various successful attempts on hybridizing the AI models with evolutionary optimization algorithms in the field of hydrology. For instance, a combination between the adaptive neurofuzzy system (ANFIS) model with the firefly algorithm (FFA) was conducted for modeling the roller length of the hydraulic jump [46]. An integration of the classical multilayer perceptron with FFA for pan evaporation process is given in [47]. River flow forecasting for tropical environment was established using the ANFIS-FFA model [48]. On the same region of the case study implemented in this research, the water quality index prediction model was developed based on the hybridization of the support vector machine model

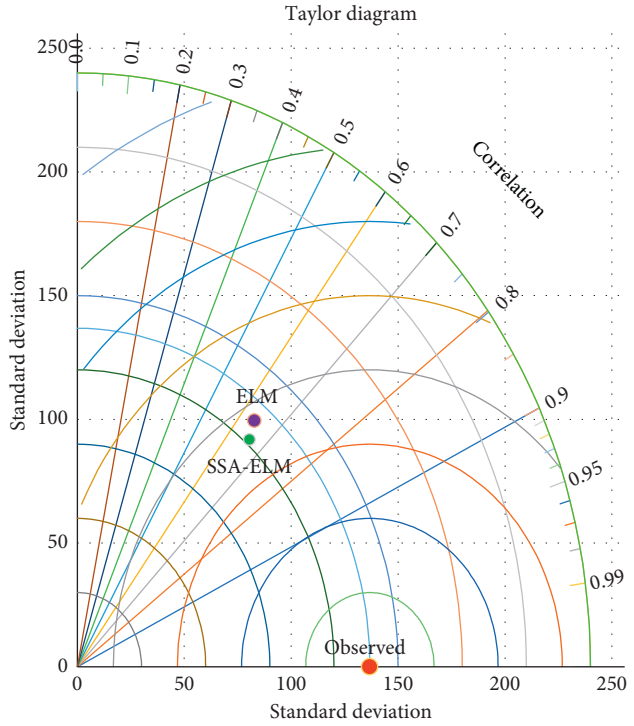

Figure 8: Taylor diagram graphical presentation for the ELM and SSA-ELM predictive models.

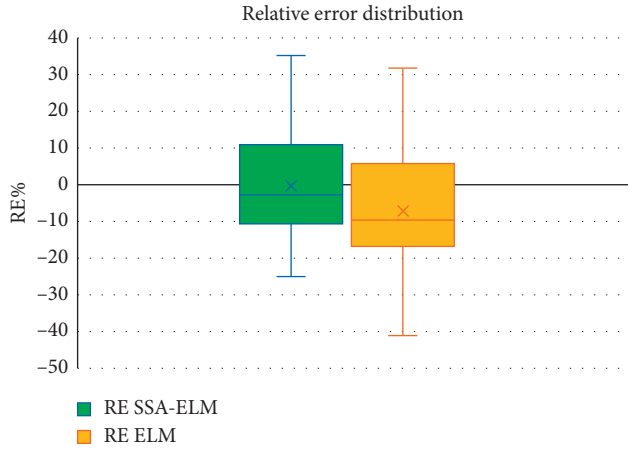

Figure 9: Relative error distribution percentage of SSA-ELM and ELM models.

with the firefly algorithm [49]. All the examples exhibited earlier on the hybrid models demonstrated an excellent performance over the AI-based models. It is evidenced that the present study was performed in harmony with a new era of the hybrid intelligent models in the field of surface hydrology.

For the best knowledge of the practical implementation, the proposed hybrid intelligence SSA-ELM model has the possibility of the online learning potential. As reported in Figure 12, the scheme demonstrated the capacity of the online forecasting system in which there is a possibility to be practiced as a flooding warning system. The online forecasting system starts by obtaining the metrological information (e.g., river flow velocity (V), cross section area (A), and river discharge (Q)) using sensors device. The data information was transferred via cricket wireless and digitized into a comma separated value (CSV) format in which it is readable by any software environment. At this stage, the learning process based on the historical records is conducted using the SSA-ELM predictive model. The outcome of the predictive model was subjected to a specific range of river flow threshold values. If the prediction value is within the threshold, the loop of the learning process is repeated using the new recalled historical information. Otherwise, if the prediction is out of the threshold range, a notification of the alarm system is integrated (global system for mobile communications) that can

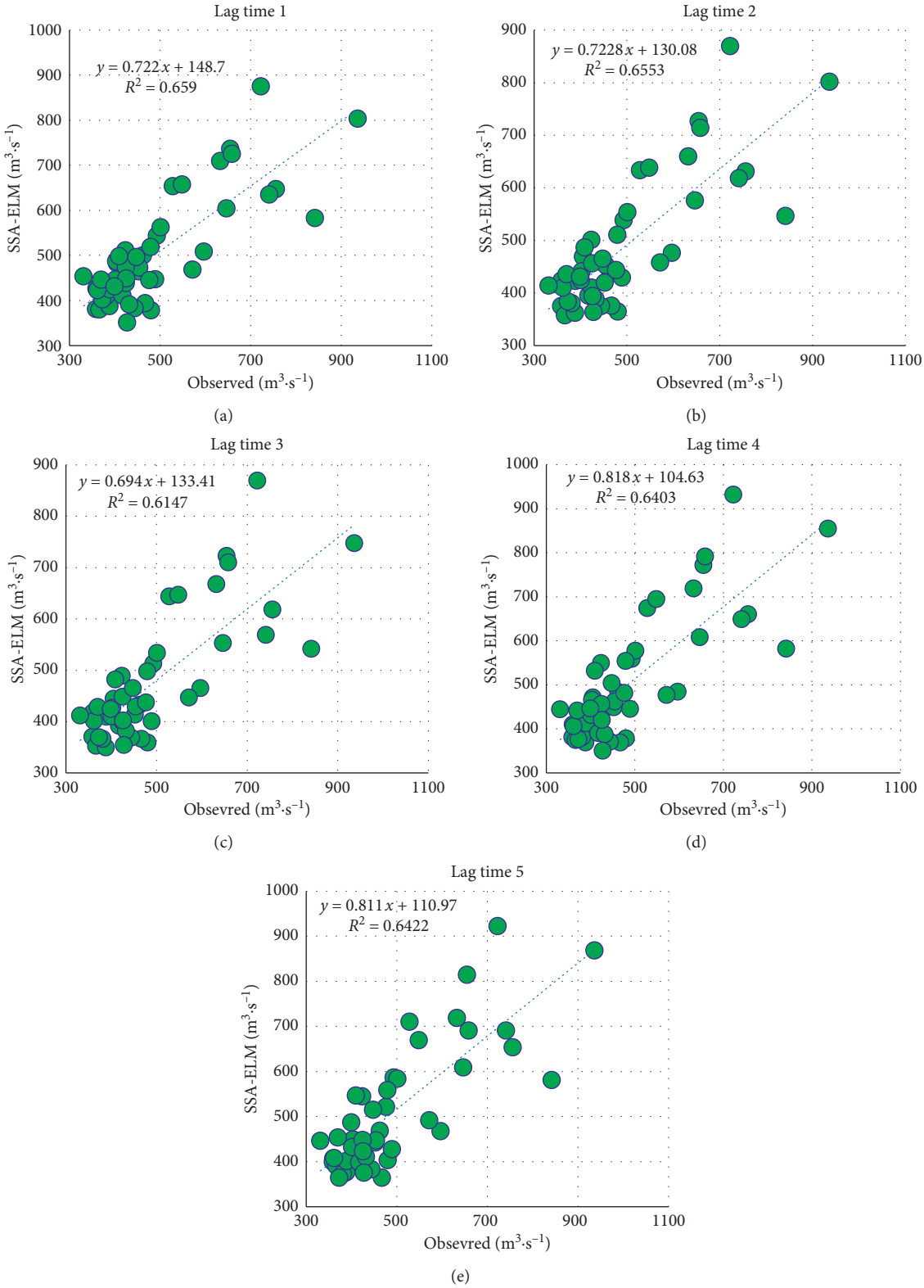

Figure 10: Scatter plot variation between the observed and forecasted river flow using the SSA-ELM model and for the five input combinations.

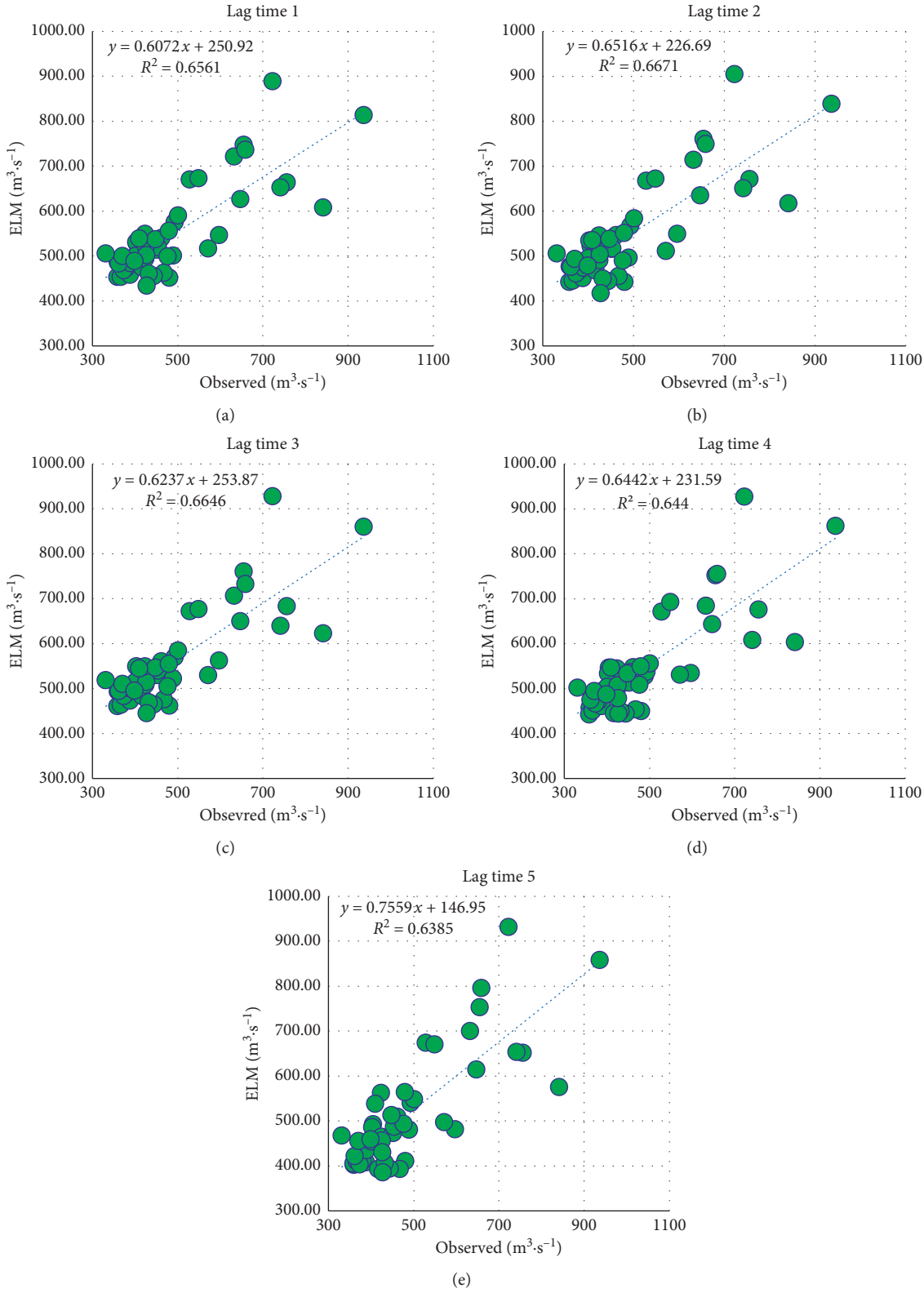

Figure 11: Scatter plot variation between the observed and forecasted river flow using the ELM model and for the five input combinations.

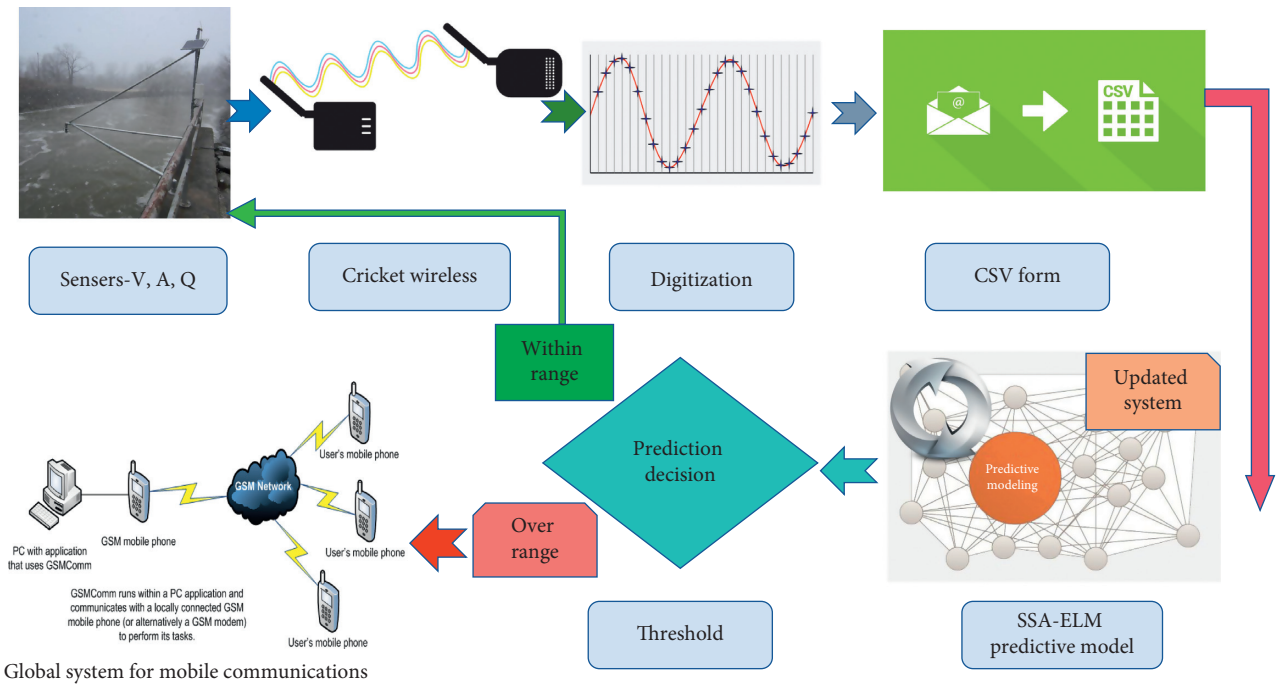

Figure 12: A proposition for online forecasting system based on the proposed methodology.

deliver a message of alarm to the nearby civilian for preparing an emergency evacuation. This merit can contribute remarkably to the water resources engineering, river management, and monitoring perspective.

6. Conclusions

In this research, a novel hybrid intelligent predictive model was developed to be implemented on a regression hydrological problem (i.e., river flow forecasting). A new nature-inspired optimization algorithm called Salp Swarm Algorithm was integrated with the modern AI model (i.e., ELM model) to build a robust intelligent predictive model. The basic concept of the introduced SSA is inspired from the swarming behaviour of the salp chain. The developed SSA-ELM model was applied for monthly time scale river flow data located in semiarid environment in the Iraq region. Twenty years over the period (1991–2010) was used to design the training and testing phases following the published research [33]. Several input combination attributes were investigated in accordance with the most correlated lag times. The hybrid SSA-ELM model exhibited an excellent level of accuracies in comparison with the ELM-based model. In numerical evaluation, the SSA-ELM model demonstrated an acceptable level of augmentation with regards to the absolute metrics (8.4 and 13.1% for RMSE and MAE, respectively). On the other aspect, the results verified that the lag time as an input attribute is very significant on the modeling performance of the predictive model. In conclusion, the developed model outcomes enthuse for proposing an online forecasting system that can be applied as a real-time monitoring river engineering practice. For future work, further research can be conducted based on investigating the efficiency of the proposed model by incorporating several hydrological processes such as rainfall, humidity, wind speed, and others in modeling the target output river flow [50]. In addition, inspecting longer data span of historical data information is highly recommended to be devoted as it is a limitation of the current research. On the algorithmic level, the proposed model can be extended in a way that other parameters in the ELM network can be optimized and such parameters include the number of hidden nodes in the hidden layer, the transfer functions, and the activation functions [51–53].

Data Availability

The data used to support the findings of this study are available from the corresponding author upon request.

Conflicts of Interest

The authors have no conflicts of interest to declare.

References

[1] J. Patskoski and A. Sankarasubramanian, "Reducing uncertainty in stochastic streamflow generation and reservoir sizing by combining observed, reconstructed and projected streamflow," *Stochastic Environmental Research and Risk Assessment*, vol. 32, no. 4, pp. 1065–1083, 2018.

[2] F. Fathian, A. Fakheri-Fard, T. Ouarda, Y. Dinpashoh, and S. S. M. Nadoushani, "Multiple streamflow time series modeling using VAR–MGARCH approach," *Stochastic Environmental Research and Risk Assessment*, vol. 32, no. 2, pp. 407–425, 2019.

[3] M. Azmat, M. Choi, T.-W. Kim, and U. W. Liaqat, "Hydrological modeling to simulate streamflow under changing climate in a scarcely gauged cryosphere catchment," *Environmental Earth Sciences*, vol. 75, no. 3, pp. 1–16, 2016.

[4] K. Stahl, R. D. Moore, J. M. Shea, D. Hutchinson, and A. J. Cannon, "Coupled modelling of glacier and streamflow response to future climate scenarios," *Water Resources Research*, vol. 44, 2008.

[5] A. K. Verma, M. K. Jha, and R. K. Mahana, "Evaluation of HEC-HMS and WEPP for simulating watershed runoff using remote sensing and geographical information system," *Paddy and Water Environment*, vol. 8, no. 2, pp. 131–144, 2010.

[6] R. Modarres and S. S. Eslamian, "Streamflow time series modeling of Zayandehrud River," *Iranian Journal of Science and Technology, Transaction B: Engineering*, vol. 30, pp. 567–570, 2006.

[7] I. Masih, S. Maskey, S. Uhlenbrook, and V. Smakhtin, "Assessing the impact of areal precipitation input on streamflow simulations using the SWAT Model1," *JAWRA Journal of the American Water Resources Association*, vol. 47, no. 1, pp. 179–195, 2011.

[8] K. Rahman, C. Maringanti, M. Beniston, F. Widmer, K. Abbaspour, and A. Lehmann, "Streamflow modeling in a highly managed mountainous glacier watershed using SWAT: the upper Rhone River watershed case in Switzerland," *Water Resources Management*, vol. 27, no. 2, pp. 323–339, 2013.

[9] Z. M. Yaseen, A. El-shafie, O. Jaafar, H. A. Afan, and K. N. Sayl, "Artificial intelligence based models for stream-flow forecasting: 2000–2015," *Journal of Hydrology*, vol. 530, pp. 829–844, 2015.

[10] W. Hu, L. Yan, K. Liu, and H. Wang, "A short-term traffic flow forecasting method based on the hybrid PSO-SVR," *Neural Processing Letters*, vol. 43, no. 1, pp. 155–172, 2016.

[11] Z. M. Yaseen, O. Kisi, and V. Demir, "Enhancing long-term streamflow forecasting and predicting using periodicity data component: application of artificial intelligence," *Water Resources Management*, vol. 30, no. 12, pp. 4125–4151, 2016.

[12] A. Danandeh Mehr, E. Kahya, F. Bagheri, and E. Deliktas, "Successive-station monthly streamflow prediction using neuro-wavelet technique," *Earth Science Informatics*, vol. 7, no. 4, pp. 217–229, 2013.

[13] R. C. Deo and M. Şahin, "An extreme learning machine model for the simulation of monthly mean streamflow water level in eastern Queensland," *Environmental Monitoring and Assessment*, vol. 188, no. 2, 2016.

[14] Z. M. Yaseen, S. O. Sulaiman, R. C. Deo, and K.-W. Chau, "An enhanced extreme learning machine model for river flow forecasting: state-of-the-art, practical applications in water resource engineering area and future research direction," *Journal of Hydrology*, vol. 569, pp. 387–408, 2019.

[15] H. Jiang and Y. Dong, "A novel model based on square root elastic net and artificial neural network for forecasting global solar radiation," *Complexity*, vol. 2018, Article ID 8135193, 19 pages, 2018.

[16] B. B. Sahoo, R. Jha, A. Singh, and D. Kumar, "Application of support vector regression for modeling low flow time series," *KSCE Journal of Civil Engineering*, vol. 23, no. 2, pp. 923–934, 2019.

[17] A. Mohanta, K. Patra, and B. Sahoo, "Anticipate Manning's coefficient in meandering compound channels," *Hydrology*, vol. 5, no. 3, p. 47, 2018.

[18] B. B. Sahoo, R. Jha, A. Singh, and D. Kumar, "Long short-term memory (LSTM) recurrent neural network for low-flow hydrological time series forecasting," *Acta Geophysica*, vol. 67, no. 5, pp. 1471–1481, 2019.

[19] J. L. Salmeron, M. B. Correia, and P. R. Palos-Sanchez, "Complexity in forecasting and predictive models," *Complexity*, vol. 2019, Article ID 8160659, 3 pages, 2019.

[20] G.-B. Huang, Q.-Y. Zhu, and C.-K. Siew, "Extreme learning machine: theory and applications," *Neurocomputing*, vol. 70, no. 1–3, pp. 489–501, 2006.

[21] H. Siqueira, L. Boccato, R. Attux, and C. Lyra, "Unorganized machines for seasonal streamflow series forecasting," *International Journal of Neural Systems*, vol. 24, no. 3, Article ID 1430009, 2014.

[22] A. R. Lima, A. J. Cannon, and W. W. Hsieh, "Forecasting daily streamflow using online sequential extreme learning machines," *Journal of Hydrology*, vol. 537, pp. 431–443, 2016.

[23] B. Yadav, S. Ch, S. Mathur, and J. Adamowski, "Discharge forecasting using an online sequential extreme learning machine (OS-ELM) model: a case study in Neckar River, Germany," *Measurement*, vol. 92, pp. 433–445, 2016.

[24] M. Rezaie-Balf and O. Kisi, "New formulation for forecasting streamflow: evolutionary polynomial regression vs. extreme learning machine," *Hydrology Research*, vol. 49, no. 3, pp. 939–953, 2017.

[25] Z. M. Yaseen, M. F. Allawi, A. A. Yousif, O. Jaafar, F. M. Hamzah, and A. El-Shafie, "Non-tuned machine learning approach for hydrological time series forecasting," *Neural Computing and Applications*, vol. 30, no. 5, pp. 1479–1491, 2018.

[26] A. R. Lima, A. J. Cannon, and W. W. Hsieh, "Nonlinear regression in environmental sciences using extreme learning machines: a comparative evaluation," *Environmental Modelling & Software*, vol. 73, pp. 175–188, 2015.

[27] S. Heddam and O. Kisi, "Extreme learning machines: a new approach for modeling dissolved oxygen (DO) concentration with and without water quality variables as predictors," *Environmental Science and Pollution Research*, vol. 24, no. 20, pp. 16702–16724, 2017.

[28] S. Heddam, "Use of optimally pruned extreme learning machine (OP-ELM) in forecasting dissolved oxygen concentration (DO) several hours in advance: a case study from the Lamath River, Oregon, USA," *Environmental Processes*, vol. 3, no. 4, pp. 909–937, 2016.

[29] Z. M. Yaseen, S. M. Awadh, A. Sharafati, and S. Shahid, "Complementary data-intelligence model for river flow simulation," *Journal of Hydrology*, vol. 567, pp. 180–190, 2018.

[30] P. Mohapatra, K. Nath Das, and S. Roy, "A modified competitive swarm optimizer for large scale optimization problems," *Applied Soft Computing*, vol. 59, pp. 340–362, 2017.

[31] M. T. Hagan and M. B. Menhaj, "Training feedforward networks with the Marquardt algorithm," *IEEE Transactions on Neural Networks*, vol. 5, no. 6, pp. 989–993, 1994.

[32] S. Mirjalili, A. H. Gandomi, S. Z. Mirjalili, S. Saremi, H. Faris, and S. M. Mirjalili, "Salp swarm algorithm: a bio-inspired optimizer for engineering design problems," *Advances in Engineering Software*, vol. 114, pp. 163–191, 2017.

[33] Z. M. Yaseen, O. Jaafar, R. C. Deo et al., "Stream-flow forecasting using extreme learning machines: a case study in a semi-arid region in Iraq," *Journal of Hydrology*, vol. 542, pp. 603–614, 2016.

[34] G. Huang, G.-B. Huang, S. Song, and K. You, "Trends in extreme learning machines: a review," *Neural Networks*, vol. 61, pp. 32–48, 2015.

[35] H. Sanikhani, R. C. Deo, Z. M. Yaseen, O. Eray, and O. Kisi, "Non-tuned data intelligent model for soil temperature estimation: a new approach," *Geoderma*, vol. 330, pp. 52–64, 2018.

[36] M. Eshtay, H. Faris, and N. Obeid, "Improving extreme learning machine by competitive swarm optimization and its

application for medical diagnosis problems," *Expert Systems with Applications*, vol. 104, pp. 134–152, 2018.

[37] N. Al-ansari, M. Abdellatif, M. Ezeelden, S. S. Ali, and S. Knutsson, "Climate change and future long-term trends of rainfall at north-east of Iraq," *Journal of Civil Engineering and Architecture*, vol. 8, no. 6, pp. 790–805, 2014.

[38] D. Bozkurt, O. Sen, and S. Hagemann, "Projected river discharge in the Euphrates-Tigris basin from a hydrological discharge model forced with RCM and GCM outputs," *Climate Research*, vol. 62, no. 2, pp. 131–147, 2015.

[39] N. Al-Ansari, A. A. Ali, and S. Knutsson, "Present conditions and future challenges of water resources problems in Iraq," *Journal of Water Resource and Protection*, vol. 6, no. 12, pp. 1066–1098, 2014.

[40] S. A. Salman, S. Shahid, T. Ismail, N. B. A. Rahman, X. Wang, and E.-S. Chung, "Unidirectional trends in daily rainfall extremes of Iraq," *Theoretical and Applied Climatology*, vol. 134, no. 3-4, pp. 1165–1177, 2018.

[41] D. K. Saleh, *Stream Gage Descriptions and Streamflow Statistics for Sites in the Tigris River and Euphrates River Basins, Iraq*, US Department of the Interior, US Geological Survey, Reston, VA, USA, 2010.

[42] K. P. Sudheer, A. K. Gosain, D. Mohana Rangan, and S. M. Saheb, "Modelling evaporation using an artificial neural network algorithm," *Hydrological Processes*, vol. 16, no. 16, pp. 3189–3202, 2002.

[43] Ö. Kisi, "Multi-layer perceptrons with Levenberg-Marquardt training algorithm for suspended sediment concentration prediction and estimation," *Hydrological Sciences Journal*, vol. 49, pp. 1025–1040, 2004.

[44] A. A. H. Alwanas, A. A. Al-Musawi, S. Q. Salih, H. Tao, M. Ali, and Z. M. Yaseen, "Load-carrying capacity and mode failure simulation of beam-column joint connection: application of self-tuning machine learning model," *Engineering Structures*, vol. 194, pp. 220–229, 2019.

[45] M. Hall, E. Frank, G. Holmes, B. Pfahringer, P. Reutemann, and I. H. Witten, "The WEKA data mining software," *ACM SIGKDD Explorations Newsletter*, vol. 11, no. 1, p. 10, 2009.

[46] H. Azimi, H. Bonakdari, I. Ebtehaj, and D. G. Michelson, "A combined adaptive neuro-fuzzy inference system-firefly algorithm model for predicting the roller length of a hydraulic jump on a rough channel bed," *Neural Computing and Applications*, vol. 29, no. 6, pp. 249–258, 2016.

[47] M. A. Ghorbani, R. C. Deo, V. Karimi, Z. M. Yaseen, and O. Terzi, "Implementation of a hybrid MLP-FFA model for water level prediction of Lake Egirdir, Turkey," *Stochastic Environmental Research and Risk Assessment*, vol. 32, no. 6, pp. 1683–1697, 2017.

[48] Z. M. Yaseen, I. Ebtehaj, H. Bonakdari et al., "Novel approach for streamflow forecasting using a hybrid ANFIS-FFA model," *Journal of Hydrology*, vol. 554, pp. 263–276, 2017.

[49] J. Li, H. Ali, A. Samer, S. Hasan et al., "Hybrid soft computing approach for determining water quality indicator: Euphrates River," *Neural Computing and Applications*, vol. 31, no. 3, pp. 827–837, 2017.

[50] L. Diop, A. Bodian, K. Djaman et al., "The influence of climatic inputs on stream-flow pattern forecasting: case study of Upper Senegal River," *Environmental Earth Sciences*, vol. 77, no. 5, p. 182, 2018.

[51] S. Q. Salih and A. A. Alsewari, "Solving large-scale problems using multi-swarm particle swarm approach," *International Journal of Engineering & Technology*, vol. 7, no. 3, pp. 1725–1729, 2018.

[52] S. Q. Salih and A. A. Alsewari, "A new algorithm for normal and large-scale optimization problems: nomadic people optimizer," *Neural Computing and Applications*pp. 1–28, 2019, In press.

[53] H. A. Abdulwahab, A. Noraziah, A. A. Alsewari, and S. Q. Salih, "An enhanced version of black hole algorithm via levy flight for optimization and data clustering problems," *IEEE Access*, vol. 7, pp. 142085–142096, 2019.

Hindawi
Complexity
Volume 2020, Article ID 7132349, 23 pages
https://doi.org/10.1155/2020/7132349

WILEY | Hindawi

Research Article

A Unified Approach for the Identification of Wiener, Hammerstein, and Wiener–Hammerstein Models by Using WH-EA and Multistep Signals

J. Zambrano,[1] **J. Sanchis**,[2] **J. M. Herrero**,[2] **and M. Martínez**[2]

[1]*Universidad Politécnica Salesiana, Cuenca, Ecuador*
[2]*Instituto Universitario de Automática e Informática Industrial, Universitat Politécnica de Valéncia, Valéncia, Spain*

Correspondence should be addressed to J. Zambrano; jzambranoa@ups.edu.ec

Received 1 July 2019; Revised 3 January 2020; Accepted 11 January 2020; Published 21 February 2020

Academic Editor: Marcelo Messias

Wiener, Hammerstein, and Wiener–Hammerstein structures are useful for modelling dynamic systems that exhibit a static type nonlinearity. Many methods to identify these systems can be found in the literature; however, choosing a method requires prior knowledge about the location of the static nonlinearity. In addition, existing methods are rigid and exclusive for a single structure. This paper presents a unified approach for the identification of Wiener, Hammerstein, and Wiener–Hammerstein models. This approach is based on the use of multistep excitation signals and WH-EA (an evolutionary algorithm for Wiener–Hammerstein system identification). The use of multistep signals will take advantage of certain properties of the algorithm, allowing it to be used as it is to identify the three types of structures without the need for the user to know a priori the process structure. In addition, since not all processes can be excited with Gaussian signals, the best linear approximation (BLA) will not be required. Performance of the proposed method is analysed using three numerical simulation examples and a real thermal process. Results show that the proposed approach is useful for identifying Wiener, Hammerstein, and Wiener–Hammerstein models, without requiring prior information on the type of structure to be identified.

1. Introduction

Block-oriented models are a class of nonlinear model consisting of an interaction of linear-time invariant (LTI) dynamic subsystems and nonlinear (NL) static elements [1, 2]. This interaction between basic blocks is not restricted to serial connections, and blocks can be used more than once. Therefore, block-oriented models comprise a series of structures that can be useful when modelling dynamic systems affected by memoryless nonlinearities. An overview of the most common block-oriented model structures can be found in [3]. The simplest structures within this class of model are the Wiener (LTI-NL) and Hammerstein (NL-LTI) models. Generalisations of these basic models lead to more complex structures known as Wiener–Hammerstein (LTI-NL-LTI) and Hammerstein–Wiener (NL-LTI-NL) models.

Static nonlinearities are very common in real systems, and for this reason, block-oriented models have great potential within the identification of nonlinear systems. This class of models has been successfully used in practice including biological processes [4–6]; chemical processes [7–9]; electronic systems [10, 11]; and others [12, 13]. Motivation for block-oriented models includes the identification of systems, and many reports of control applications using these types of models can be found in the literature [14–18].

In the context of block-oriented models, LTI subsystems are typically represented by pulse transfer models, impulse response models, and state space models, while nonlinearity blocks are usually parameterized with polynomials, piece wise functions, splines, neural networks, basis functions, and wavelets, among others. When LTI subsystems and NL blocks are represented with one of these forms, the model is parametric. However, block-oriented models can also be

represented in a nonparametric form [19] or in a combined way [20]. This paper is concerned with parametric block-oriented models based on serial connections with a single nonlinear block, i.e., Wiener, Hammerstein, and Wiener–Hammerstein models. The latter structure provides higher modelling capabilities than Wiener and Hammerstein; however, its identification scenario is more complex due to the presence of two LTI blocks.

Knowledge of linear dynamics is a good starting point for identifying block-oriented models [3]. In this context, the *Best Linear Approximation* (BLA) of a nonlinear system is preferred [21–24]. The BLA can greatly simplify the identification problem in Wiener and Hammerstein models. In both cases, once linear dynamics are obtained, static nonlinearity can be obtained by solving an optimisation problem that is linear in the parameters. However, a more efficient estimate of Wiener and Hammerstein models may require a whole parameter refitting using nonlinear optimisation. Several identification algorithms for Wiener and Hammerstein models have been developed in the literature, and the works of Giri and Bai [2] and dos Santos et al. [25] show a good selection of algorithms.

In the case of Wiener–Hammerstein models, identification is not so easy since the BLA must be divided to establish the dynamics of both LTI blocks. Several methods to split the BLA can be found in the literature [26–33]. After the front and back dynamics of a Wiener–Hammerstein model have been classified, a fine-tuning of model parameters must be made to achieve an efficient estimate. Usually, considerable user interaction is demanded—at least two procedures are required from the BLA. In addition, the final model estimated greatly depends on these previous stages (a poor division of the BLA will obviously lead to a poor estimate). To minimise these drawbacks, a new methodology called WH-EA (evolutionary algorithm for Wiener–Hammerstein system identification) was introduced in [34]. This algorithm enables estimating all the parameters of a Wiener–Hammerstein model with a single procedure from the BLA. With WH-EA, a good estimate does not depend on intermediate procedures since the evolutionary algorithm looks for the best BLA partition, while the locations of the poles and zeros are fine-tuned and nonlinearity is captured simultaneously.

Although state-of-the-art methods for BLA splitting offer their own advantages and disadvantages, they make the identification of Wiener–Hammerstein models a subjective task with an acceptable degree of maturity. However, from a practical point of view, obtaining the BLA can be a complex and sometimes unfeasible task. On one side, multiple realisations—each with a large amount of data—may be required to obtain the BLA. In real processes with slow dynamics, experiments for obtaining the BLA would require too much time, so it would be impractical. On the other hand, excitation signals used to obtain the BLA must belong to the Riemann equivalence class of asymptotically normally distributed excitation signals [35]. The most common signals of this type are the Gaussian noise sequences and random-phased multisines [22, 36] and not all real processes can be excited with this kind of inputs.

Beyond problems derived from BLA attainment, several methods for Wiener, Hammerstein, and Wiener–Hammerstein model identification can be found in the literature [3]. Almost all have in common that they use the BLA as a starting point—although this has not been used much for Wiener and Hammerstein models. Although the three model structures are differentiated by how the dynamics are distributed around static nonlinearity, to date, there is no method to identify any of the three models without distinction. Existing methods have been developed independently and exclusively for a single structure. That is, one for identifying Wiener cannot be used to identify Hammerstein models and vice versa. If there is uncertainty about the location of the dynamics and the static nonlinearity, the user would be obliged to make separate estimates of Wiener, Hammerstein, and Wiener–Hammerstein using three different identification methods. After this tedious task, the performance of the models obtained should be compared to select the appropriate one.

At first glance, it would seem that existing Wiener–Hammerstein identification methods could easily overcome this drawback, since the Wiener and Hammerstein models are specific cases of the Wiener–Hammerstein structure where the dynamics have been distributed to only one side of the static nonlinearity. However, this situation must be handled carefully. Existing methods to identify Wiener–Hammerstein models address the problem of identification as an optimisation problem. In that case, to achieve a good convergence, it is necessary to define appropriately the range where the static nonlinearity will be captured. Since static nonlinearity is located in different positions with respect to the dynamics, the nonlinearity bounds are different for the three types of structures. Note that it is not the same to capture the static nonlinearity before or after a dynamic block given that the domain and codomain of the nonlinear function will change notably. Defining a very small search space will result in the nonlinearity not being properly captured. On the other hand, a search space too broad will cause a slow convergence, or worse, the algorithm could get stuck at a local minimum. Therefore, without beforehand information on the process structure, the search space of static nonlinearity could be defined incorrectly.

Difficulties in estimating the BLA in practical applications and the need to know, prior to the selection of an identification method, if static nonlinearity is in front, behind, or in the middle of the dynamics have been the principal motivations to present this work. The aim is to create a unified approach to estimate Wiener, Hammerstein, and Wiener–Hammerstein models without the need for the user to know a priori the structure of the process under test. This unified approach is based on the use of WH-EA without any modification. However, for WH-EA can identify any of the three structures without distinction, an effective and common search space for static nonlinearity is stated. This search space will be useful for any possible structure without the need for their dimensions to change as WH-EA distributes the dynamics. It must be taken into account that it is

not an oversized search space, rather it is a search space with optimal dimensions to capture static nonlinearity regardless of the distribution of the dynamics.

In the case of Wiener, Hammerstein, and Wiener–Hammerstein models, a search space for static nonlinearity can be defined using information from the input and output dataset used during the identification procedure. However, when an arbitrary excitation signal (e.g., a Gaussian signal) is applied, the process structure must be known to define an effective search space. Since this work assumes that the process structure is unknown, from the input and output dataset a common search space useful for the three structures will be defined. As it will be seen in Section 2.4, this common search space will be possible as long as the applied excitation signal leads the output of the process to steady state and for this reason, multistep signals will be used. In addition, multistep excitation will enable an effective exploration of different process operation zones highlighting existing nonlinearities (not possible if Gaussian signals are used to excite the process). Note that Gaussian signals are useful for capturing the dynamic behavior of a system, however, these types of signals are not suitable for highlighting static non-linearites - as in the case of saturations.

Since this approach will not use Gaussian-type signals, an initial linear model obtained using standard linear identification methods can be used instead of the BLA. In noisy environments and under the effect of nonlinearity, the initial linear model will be a biased version of the real process dynamics. As it will be shown, the potentiality of WH-EA is exploited to refine the location of the poles and zeros of this initial model while they are distributed around nonlinear block (which is also captured simultaneously).

Unlike other proposals where a single type of model is addressed, this paper presents a new approach that allows the identification of any of the three types of block-oriented models indistinctly without any beforehand information about the type of structure. This approach is useful for identifying nonlinear systems, where it is known a priori that the system is affected by a static nonlinearity but its location with respect to dynamics is unknown. From the core idea of this paper, other derived novelties are highlighted below:

(i) In this proposal, the BLA is not used. This is a significant advantage since the estimation of the BLA can be impractical in many real applications due to the execution time required to excite the process under test.

(ii) This approach uses multistep excitation signals. This type of signals allows nonlinearities to emerge better. This is very useful since nonlinear estimation starts from dynamics already known.

(iii) Thanks to the normalisation of the dynamics and the use of multistep signals a common search space for the three types of models can be stated. This search space is not dependent on any parameter provided by the user, such as it was the case of the Ω parameter in [34].

(iv) The estimation is done in continuous time, which gives the user a clearer view of the process behaviour under test.

The rest of this paper is organised as follows. Section 2 presents the identification framework that has been divided into five parts. First, the structure of the Wiener, Hammerstein, and Wiener–Hammerstein models and their mathematical formulation are described. The initial linear model estimation and selection of its structure is then addressed, followed by the optimisation problem statement. The search space for static nonlinearity is then analysed for these three types of models when creating a common search space. Finally, several aspects related to multistep inputs, such as excitation signals, are presented. Section 3 presents an abstract of WH-EA including codification of the individuals, its genetic operators, and details of how the algorithm works. To end, in Section 4, the presented methodology is applied to three numerical examples and a real application (a thermal process). Finally, concluding remarks are presented in Section 5.

2. Identification Framework

2.1. Structure of Nonlinear Models and Problem Formulation. All the three block-oriented models treated in this work have a single nonlinear element. In the case of the Wiener–Hammerstein models, two LTI blocks $G_w(s, \boldsymbol{\rho}_w)$ and $G_h(s, \boldsymbol{\rho}_h)$ surround the nonlinear element $f(v(t), \boldsymbol{\rho}_{nl})$. Wiener and Hammerstein models are specific cases of Wiener–Hammerstein models when one of the linear blocks lacks dynamics. If dynamics are present only at the input linear block, the resulting model is known as a Wiener model. When dynamics are present only at the output block, the resulting model is known as a Hammerstein model.

In this paper, the block-model structure of the process to be identified is unknown, so the most general form is considered as a starting point for the problem formulation. Let us represent Wiener, Hammerstein, and Wiener–Hammerstein models by

$$y(t, \boldsymbol{\rho}) = G_h(s, \boldsymbol{\rho}_h) f\left(G_w(s, \boldsymbol{\rho}_w) u(t), \boldsymbol{\rho}_{nl}\right), \tag{1}$$

$$\boldsymbol{\rho} = \left[\boldsymbol{\rho}_w, \boldsymbol{\rho}_{nl}, \boldsymbol{\rho}_h\right], \tag{2}$$

where $u(t)$ and $y(t)$ are the model input and output, respectively, and vectors $\boldsymbol{\rho}_w$ and $\boldsymbol{\rho}_h$ contain the parameters of the dynamic blocks, while $\boldsymbol{\rho}_{nl}$ contains the parameters of static nonlinearity.

Notice that equations (1) and (2) correspond to the formulation of Wiener–Hammerstein models or generic case. In the case of Wiener models, vector $\boldsymbol{\rho}_h$ does not exist and $G_h = 1$, whereas in the case of Hammerstein models, vector $\boldsymbol{\rho}_w$ does not exist and $G_w = 1$.

This paper establishes a common framework for the identification of Wiener, Hammerstein, and Wiener–Hammerstein models that is only possible under certain constraints that are detailed in Section 2.4. For all three cases, the identification problem starts from (1) and is addressed as a classification problem. The evolutionary

algorithm will determine if there are dynamics distributed between the two blocks or if the dynamics are present just in one of them.

For the two LTI blocks to be parameterized, both LTI subsystems are represented in the continuous time domain as rational transfer functions in factorised form (zero-pole-gain):

$$G_w(s) = K_w \frac{\prod_{i=1}^{n_b}\left(s + z_{w_i}\right)/\left(z_{w_i}\right)}{\prod_{i=1}^{n_a}\left(s + p_{w_i}\right)/\left(p_{w_i}\right)}, \tag{3}$$

$$G_h(s) = K_h \frac{\prod_{i=1}^{n_d}\left(s + z_{h_i}\right)/\left(z_{h_i}\right)}{\prod_{i=1}^{n_c}\left(s + p_{h_i}\right)/\left(p_{h_i}\right)}, \tag{4}$$

where $-p_{w_i}$ with $i = 1, \ldots, n_a$ and $-z_{w_i}$ with $i = 1, \ldots, n_b$ represent front LTI poles and zeros, respectively. In a similar way, $-p_{h_i}$ with $i = 1, \ldots, n_c$ and $-z_{h_i}$ with $i = 1, \ldots, n_d$ represent poles and zeros of the back LTI one. Static gains of each linear block are represented by K_w and K_h, while s is the complex Laplace variable. Considering this, let us define vectors $\boldsymbol{\rho}_w$ and $\boldsymbol{\rho}_h$ as

$$\boldsymbol{\rho}_w = \left[K_w, z_{w_1}, z_{w_2}, \ldots, z_{w_{nb}}, p_{w_1}, p_{w_2}, \ldots, p_{w_{na}}\right], \tag{5}$$

$$\boldsymbol{\rho}_h = \left[K_h, z_{h_1}, z_{h_2}, \ldots, z_{h_{nd}}, p_{h_1}, p_{h_2}, \ldots, p_{h_{nc}}\right]. \tag{6}$$

Notice that poles and zeros in (3) and (4) are not restricted to be real, since $-p_{w_i}$, $-p_{h_i}$, $-z_{w_i}$, and $-z_{h_i}$ can also represent complex poles or zeros, respectively.

Static nonlinearity can also be represented in different ways. In this case, piecewise functions are used as WH-EA uses them:

$$w(t) = f\left(v(t), \boldsymbol{\rho}_{nl}\right), \tag{7}$$

where $v(t)$ is the input signal to the nonlinear block, while $\boldsymbol{\rho}_{nl}$ contains the abscissas and ordinates which define the breakpoint locations of the piecewise function. Notice that for a Wiener system, $y(t) = w(t)$, while for a Hammerstein system, $v(t) = u(t)$.

The problem formulation is completed by the following assumptions:

A1. The model to be identified corresponds to a Wiener, Hammerstein, or Wiener–Hammerstein system, where the structure is unknown but the general dynamics must be known.

A2. There is no cancellation of poles and zeros and the location of the poles is consistent with a stable system.

A3. The system under test will be identified from an input/output dataset, where the input excitation signal $u(t)$ is a multistep signal (see Section 2.5 for more details), while the measured output $y(t)$ may be corrupted by stationary additive noise $n(t)$:

$$y(t) = y_0(t) + n(t). \tag{8}$$

2.2. Initial Linear Model. In our context of Wiener–Hammerstein models, obtaining a perfect linear dynamic model in the presence of noise and nonlinearities is not an easy task; however, gathering an overview of system dynamics can be a good starting point. The BLA is an option that has been used generally in the estimation of Wiener–Hammerstein models. From a theoretical point of view, the fastest and most robust method to find the BLA hides the effect of noise and nonlinearities, and so the dynamics can be captured with great precision [22]. However, from a practical point of view, obtaining the BLA is not always possible or may require the use of multiple realisations, especially when the robust method is used.

In practical applications, the BLA can present a lack of accuracy, once its poles/zeros have been distributed and the nonlinearity captured, and refinement of the dynamics is always possible to improve model preciseness. In this work, it is assumed that the initial linear model is not perfect but it can be fine-tuned during estimation. The initial model can be obtained as usual from the response to a step signal. The process under test can be excited with a small amplitude step avoiding excitation of the nonlinearity. Due to its static nature, any process operating point can be selected to inject the step signal. Estimated models in different operation zones will give similar dynamics but with different static gains (it is advisable to avoid zones near operation limits since the nonlinearity can be stronger due to saturation phenomena).

The purpose of this paper is not to discuss methods for linear system identification. For a direct estimation in continuous time and to obtain models with better precision, *simple refined instrumental variable method for continuous-time models* (SRIVC) has been used [37, 38], available in the CONtinuous-Time System IDentification (CONTSID) toolbox for Matlab [39–41].

Since that initial linear model estimation is based on a step response, it is assumed that a small amount of data will be used. For this reason, the *Modified minimum Description Length* (MDL) criterion has been used to select the best linear structure [42]:

$$\mathrm{MDL} = \frac{V(\boldsymbol{\rho}\mathbf{l}, \mathbf{Z})}{N_L} e^{p_c\left(n_{\rho l}, N_L\right)}, \tag{9}$$

where $\boldsymbol{\rho}\mathbf{l}$ are the estimated model parameters, $\mathbf{Z}$ is a two-dimensional vector containing the input/output data, $n_{\rho l}$ is the number of parameters in the estimated model, N_L represents the amount of data used for estimation, $V(\boldsymbol{\rho}\mathbf{l}, \mathbf{Z})$ is the quadratic-like cost function depending on the difference between measurements and model (ϵ), computed using (10), and $p_c(n_{\rho l}, N_L)$ is the term known as the corrected penalty and is computed using (11).

$$V(\boldsymbol{\rho}\mathbf{l}, \mathbf{Z}) = \left(\frac{1}{2}\right)\epsilon^T \epsilon, \tag{10}$$

$$p_c\left(n_{\rho l}, N_L\right) = \frac{\ln\left(N_L\right)\left(n_{\rho l} + 1\right)}{N_L - n_{\rho l} - 2}. \tag{11}$$

2.3. Optimisation Problem Statement. From the initial linear model and an input/output dataset $\{u(t), yr(t)\}_{t=1}^{N}$, WH-EA

is used to find the best set of parameters that represent the nonlinear model. The procedure includes the refinement of the initial linear model, the characterisation of static nonlinearity, and the pole/zero distribution of the initial linear model around the static nonlinearity. The best set of parameters is assigned to a model of Wiener, Hammerstein, or Wiener–Hammerstein. For this purpose, the identification problem is stated as an optimisation problem based on a prediction-error method and the mean absolute error criterion (notice that any other criterion could be used in the proposed method, such quadratic or maximum error criteria):

$$\varepsilon_{\mathrm{NL}}(t, \boldsymbol{\rho}) = yr(t) - y(t, \boldsymbol{\rho}), \tag{12}$$

$$J(\boldsymbol{\rho}) = \frac{1}{N} \sum_{t=1}^{N} \mathrm{abs}\left(\varepsilon_{\mathrm{NL}}(t, \boldsymbol{\rho})\right). \tag{13}$$

The solution of the optimisation problem is written as

$$\widehat{\boldsymbol{\rho}} = \arg\min_{\boldsymbol{\rho}} J(\boldsymbol{\rho}), \tag{14}$$

where $\widehat{\boldsymbol{\rho}}$ contains the best set of parameters to represent the nonlinear model.

2.4. Search Space for Static Nonlinearity. In the present approach, the problem of identifying Wiener, Hammerstein, and Wiener–Hammerstein models is addressed as an optimisation problem that is solved with WH-EA. For the algorithm to converge successfully and the best model to be estimated, it is necessary to define a suitable search space for static nonlinearity. The minimum and maximum values of the input and output signals of the nonlinear block give a clear idea of the domain and codomain of the static nonlinearity; therefore, from this information, it is possible to define its search space. However, it is necessary to point out that the minimum and maximum values of the input signal to the nonlinear block depend on the excitation signal used and the location of the nonlinearity around the dynamics of the process, while the minimum and maximum values of the output signal depend on the input signal to the block and the nonlinearity itself. This can be clearly seen in Figure 1, where a Gaussian signal has been used to excite three models containing the same dynamics and the same static nonlinearity. These models differ only in the distribution of the dynamic that has intentionally been handled to give rise to the three structures that are addressed in this paper.

In the case of Wiener and Wiener–Hammerstein models, the limits that define the horizontal search space of the nonlinear static function are affected by the static gain and the dynamics of the linear input block. Since the linear blocks of these two models are different, the limits are also different. For example, for the Wiener–Hammerstein model defined in Figure 1, the limits that horizontally define the search space for static nonlinearity are −1.68 and 1.85, while for the Wiener model, the limits are −1.10 and 1.12. In the case of the Hammerstein model, these limits could be obtained directly from the minimum and maximum values of the excitation signal (−2.38 and 2.43). It is evident that the limits that horizontally define the search space are different for the three types of models. This difference is also reflected in the vertical limits—even though the three models have the same static nonlinearity. The fact that there are different search spaces makes it necessary to know a priori the process structure under test in order to define an adequate search space. If it is not possible to know the process structure, an oversized search space could be defined; however, this will surely complicate the convergence of any search algorithm.

This section shows how to create a unified search space for the three types of models. This search space is independent of the distribution of the dynamics, so the search algorithm will not be restricted to estimating a certain structure. In other words, thanks to the creation of this unified search space, WH-EA will be able to estimate Wiener, Hammerstein, and Wiener–Hammerstein models without the need for the user to specify a priori the process structure.

For a better understanding, prior to explaining how to create a unified search space, in the first instance, it is shown how to determine the search space of the three types of models assuming an arbitrary excitation signal (e.g., a Gaussian signal). For all three cases, it is assumed that the intermediate signals are not measurable and the dynamic blocks are nonreversible, and therefore the only way to determine the search space is by using information from the input and output data and from the initial linear model.

Let us assume, for the three cases of analysis, that the input signal $u(t)$ is bounded by a maximum value $u_{\max}$ and a minimum value $u_{\min}$ with a mean value of u_{mean}. In the same way, the output $y(t)$ is bounded by a maximum value $y_{\max}$ and a minimum value $y_{\min}$, and it has a mean y_{mean}.

2.4.1. Search Space in Wiener–Hammerstein Models. In a Wiener–Hammerstein model, the excitation signal $u(t)$ enters the first LTI block ($G_w(s)$). This block will produce an output $v(t)$ with mean v_{mean}, bounded by a maximum value $v_{\max}$ and minimum value $v_{\min}$. The relationship between minimum and maximum values of signals $u(t)$ and $v(t)$ is determined by

$$v_{\min} = \Omega * u_{\min}, \tag{15}$$

$$v_{\max} = \Omega * u_{\max}, \tag{16}$$

where Ω is a scaling factor depending on the block $G_w(s)$. Without loss of generality, the static gain of $G_w(s)$ can be normalised to one, since the real gain can be absorbed by static nonlinearity. Under this normalisation, it can be assumed that there will be no offset between input and output signals since $G_w(s)$ is an LTI subsystem; therefore, $v_{\mathrm{mean}} = u_{\mathrm{mean}}$. The same can be applied to the output block $G_h(s)$; therefore, $w_{\mathrm{mean}} = y_{\mathrm{mean}}$, where w_{mean} is the mean of the signal $w(t)$.

The search space for static nonlinearity in a Wiener–Hammerstein model will be horizontally bounded by $v_{\min}$ and $v_{\max}$. To compute these parameters, $u_{\min}$ and $u_{\max}$ can be obtained directly from the input signal $u(t)$, whereas Ω would be a user-defined parameter. Selection of this parameter will be addressed later in this same section.

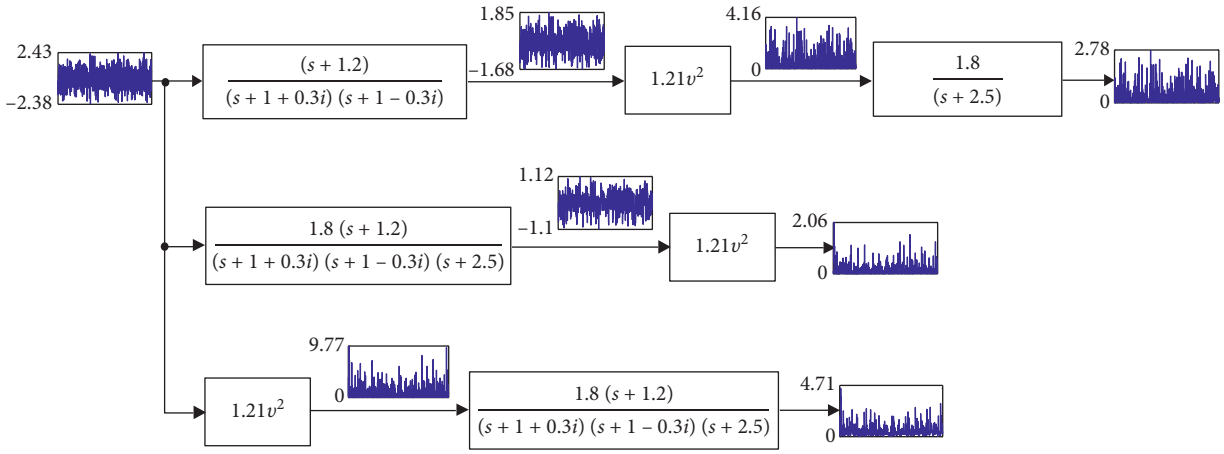

FIGURE 1: Example of search space limits for static nonlinearity in Wiener, Hammerstein, and Wiener–Hammerstein models when they are excited with a Gaussian signal.

Search space for nonlinearity is vertically delimited by $w_{\min}$ and $w_{\max}$ corresponding to the minimum and maximum values of signal $w(t)$. The linear dynamic model complements the information required to find this values. The static gain of this model corresponds to the slope of the straight line (K_{NL}) passing through the point $(v_{\text{mean}}, w_{\text{mean}})$ and the extreme points $(v_{\min}, w_{\min})$ and $(v_{\max}, w_{\max})$. Therefore, $w_{\min}$ and $w_{\max}$ can be found using (17) and (18) (it should be noted that if the linear dynamic model has negative static gain, the search space for static nonlinearity would be delimited by the coordinate pair $(v_{\min}, w_{\max})$ and $(v_{\max}, w_{\min})$). The search space for the static nonlinearity of a Wiener–Hammerstein model is illustrated in Figure 2.

$$w_{\min} = y_{\text{mean}} + K_{\text{NL}}\left(\Omega u_{\min} - u_{\text{mean}}\right), \tag{17}$$

$$w_{\max} = y_{\text{mean}} + K_{\text{NL}}\left(\Omega u_{\max} - u_{\text{mean}}\right). \tag{18}$$

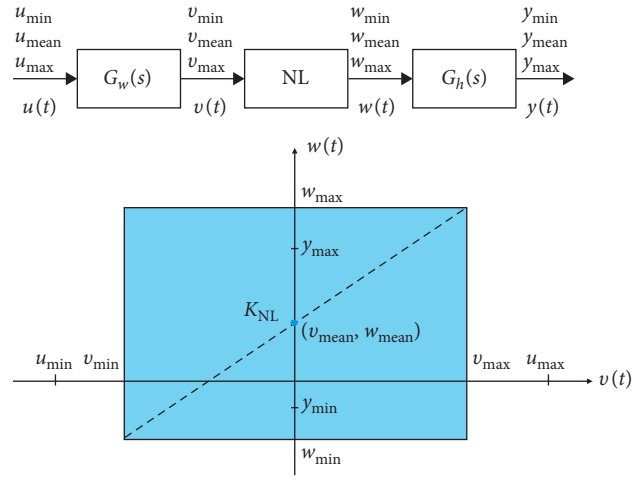

FIGURE 2: Search space for nonlinear static function in a Wiener–Hammerstein model.

2.4.2. Search Space in Wiener Models. In this case, the input signal $u(t)$ produces an output $v(t)$ and nonlinearity search space is horizontally bounded by $(v_{\min}, v_{\max})$, whereas vertical bounds will be given by $y_{\min}$ and $y_{\max}$.

It is well known that the identification of Wiener models is not as complex as the identification of Wiener–Hammerstein models. In a Wiener identification, once the linear block is known, the signal $v(t)$ can be obtained directly; therefore, to define the search space for static nonlinearity, it would not be necessary to use (15) and (16). However, estimation of the intermediate variable $v(t)$ can be useful when dealing with Wiener models. This approach assumes that the distribution of the dynamics around nonlinearity is unknown; therefore, it is not possible to estimate $v(t)$, rather it is necessary to establish a search space for nonlinearity that is common for all three structures.

To define the horizontal bounds of the search space of a Wiener model, without loss of generality, we could follow the same guidelines that were followed for Wiener–Hammerstein models, that is, values of $v_{\min}$ and $v_{\max}$ can be determined with (15) and (16), considering the scaling factor Ω. The static nonlinearity search space for a Wiener model is shown in Figure 3. The extremes of the search space give rise to the straight line whose slope K_{NL} must match the static gain of the initial linear dynamic model.

2.4.3. Search Space in Hammerstein Models. In a Hammerstein model, the input signal $u(t)$ enters the nonlinear block; therefore, $u_{\min}$ and $u_{\max}$ horizontally define the search space for static nonlinearity, while vertical bounds are defined by $w_{\min}$ and $w_{\max}$. To estimate the intermediate variable $w(t)$, the dynamic block needs to be invertible, which is impossible from a practical point of view. Furthermore, our approach assumes that pole/zero distribution around nonlinearity is unknown; therefore, for the sake of establishing a common search space for the three structures, $w_{\min}$ and $w_{\max}$ can be determined following the same procedure that was used for Wiener–Hammerstein models. The search space for the static nonlinearity of a Hammerstein model is illustrated in Figure 4.

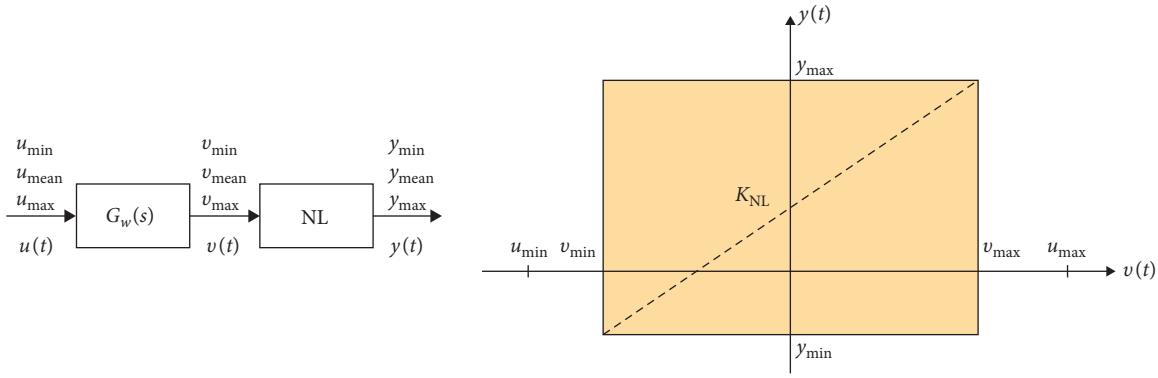

Figure 3: Search space for nonlinear static function in a Wiener model.

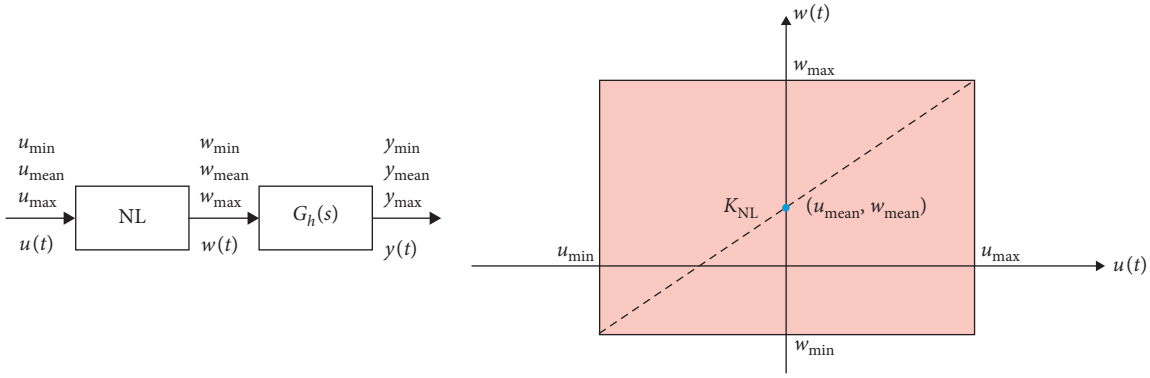

Figure 4: Search space for nonlinear static function in a Hammerstein model.

2.4.4. A Common Search Space Definition for Wiener, Hammerstein, and Wiener–Hammerstein Models. According to previous sections, when an arbitrary signal $u(t)$ excites the system (for example, a Gaussian signal), horizontal and vertical limits that define the search space for static nonlinearity are different for the three types of models. This fact implies that the identification algorithm should change the search space over which the nonlinearity is captured at the same time that distributes the dynamics. To solve this drawback, a common and fixed search space for the three types of structures will be defined. To achieve a common search space, it is necessary that both horizontal and vertical limits of the search space for each model are the same. Therefore, it is necessary that in the Wiener and Wiener–Hammerstein models, when an excitation signal $u(t)$ is applied, the dynamics and static gain of the $G_w(s)$ block cause an output signal $v(t)$ whose minimum and maximum values are equal to the minimum and maximum values of $u(t)$, respectively. That is, $v_{min} = u_{min}$ and $v_{max} = u_{max}$.

With the static gain of $G_w(s)$ normalised to one, the amplitude of the signal $v(t)$ will only be affected by the dynamics present in this linear block. The effect of the dynamics present $G_w(s)$ on $v(t)$ is represented by the Ω factor. According to (15) and (16), so that $v_{min} = u_{min}$ and $v_{max} = u_{max}$, Ω must be one. However, Ω cannot take any value without taking into account the input signal. For example, if a Gaussian signal is used to excite the system, the output of $G_w(s)$ will be modified in amplitude and the corresponding minimum and maximum values of $u(t)$ and $v(t)$ will be different. However, if an input causes the output of $G_w(s)$ in a Wiener or Wiener–Hammerstein model to reach steady state, both amplitudes will be coincident since $G_w(s)$ has unity gain.

Similarly, vertical bounds must be coincident to achieve a common search space for the three types of models. For this to occur, amplitudes of $w(t)$ and $y(t)$ must be equal. If $u(t)$ brings to $y(t)$ at steady state, normalising the static gain of $G_h(s)$ to 1 would mean that vertical bounds coincide for the three cases. A good option to obtain the output of a dynamic system at steady state is to apply step inputs with sufficient duration. Figure 5 shows how the horizontal and vertical limits that give rise to the search space of static nonlinearity are the same for the three types of models. The models used are the same as in Figure 1; the difference is that the static gains of the dynamic blocks in Figure 5 have been normalised to 1. A multistep signal has been used to excite the three models. The step duration ensures that the response of the three models reaches steady state at each step change. As can be seen, the limits that define horizontally the search space of the three models are 0 and 4.68. One great advantage of having a unified search space is that these limits can be obtained directly from the minimum and maximum values of the input signal. Similarly, the limits that vertically define the search space are the same for the three models (0 and 26.5). These limits can be obtained directly from the minimum and maximum values of the output signal.

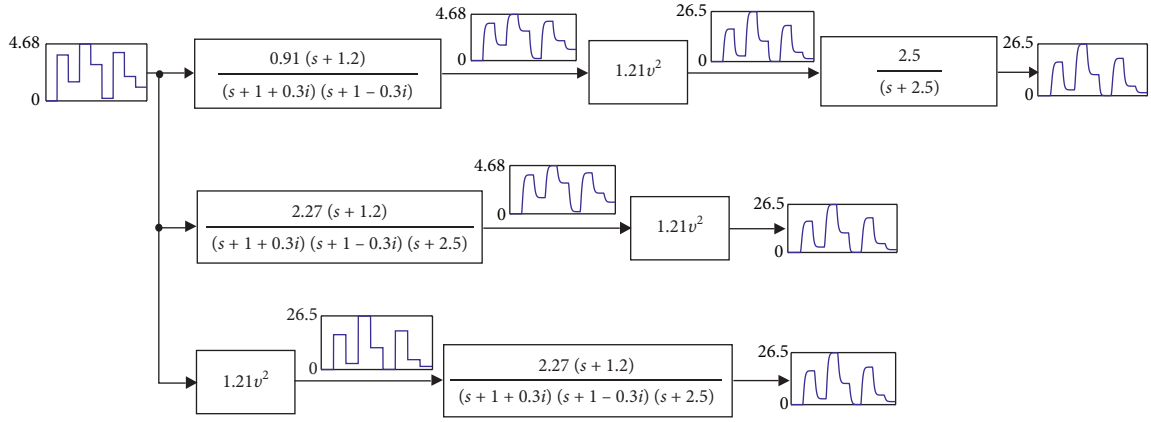

Figure 5: Example of search space limits for static nonlinearity in Wiener, Hammerstein, and Wiener–Hammerstein models when they are excited with a multistep signal.

A good option to obtain the output of a dynamic system at steady state is to apply step inputs of sufficient duration. In Section 2.5 more details on how to design this signal will be given.

With the above discussion, the common search space for the three types of models can be constructed directly from input $u(t)$ and output $y(t)$ measurements. If the gain of the initial linear model is positive, the search space will be defined by coordinates $(u_{\min}, y_{\min})$ and $(u_{\max}, y_{\max})$, while if it is negative, the search space will be defined by $(u_{\min}, y_{\max})$ and $(u_{\max}, y_{\min})$.

2.5. The Multistep Signal. Previous sections state that the process under test must be excited with an input based on steps. Step duration must be long enough for the process to reach steady state. Since it is intended to capture a nonlinearity that is present throughout the entire process operating range, it will be necessary to design a multistep signal with different amplitudes.

For this aim, three important aspects must be considered: step duration; number and amplitude of steps; and the minimum difference between two consecutive steps. All the steps of the excitation signal can have a fixed duration, based on the process dynamics under test. This duration can be easily established based on the initial tests in which the initial linear model was obtained.

A very small amount of data could mean that nonlinearity is not captured correctly and the dynamics will not be distributed properly. A large amount of data would lead to a satisfactory estimate, but could demand an important computational cost. How much data need to be used for identification of a nonlinear model deserves debate, and a vast majority of nonlinear model identification methods require a large volume of input and output data.

Calculating the static nonlinearity with precision will lead to a good dynamic classification. Therefore, an effective exploration of the entire process operating range will be required, and step amplitudes must change within input limits by varying randomly, and the number of changes will depend on the desired precision. Furthermore, the minimum difference between two consecutive steps should also be considered when designing the multistep signal. Amplitude changes of the steps will give rise to transitory stages, which contain information to classify the dynamics. If they are very small, these transitory intervals will not contain substantial information for the classification. A suitable scenario to classify the dynamics is achieved when the nonlinearity is visible. Therefore, amplitude changes of the steps must be large to highlight nonlinearity.

Figure 6 reflects this fact through a numerical simulation example. Four operating points of the system are explored for two scenarios (large/small step input changes) where the same static nonlinearity and the same dynamic have been considered. The nonlinearity consists of a cubic function $(1/64x^3)$, while the dynamic is formed with three poles $(-2.4;\ -1.5 + 0.856i;\ -1.5 - 0.856i)$ and a real zero (-1.56). For each case, three simulations were executed corresponding to Wiener, Hammerstein, and Wiener–Hammerstein models and dynamic blocks were normalised with unit static gain (for the Wiener–Hammerstein model, the zero and the complex poles were placed before the nonlinearity, while the remaining pole was placed afterwards).

In Figure 6(b), no difference between the responses can be seen when the excitation signal has small amplitude changes. Conversely, Figure 6(a) shows a marked difference between responses when the excitation signal has larger amplitude changes. Table 1 shows the differences between responses as mean absolute error (MAE) and reveals the advantage of using excitation signals with large amplitude changes. This means that the identification algorithm has more information to distinguish if the dynamics are in front, behind, or distributed on both sides of the nonlinearity. Notice how low MAE_{ss} values imply no significant difference between the structures formed as the algorithm cannot split the dynamics properly.

Multistep signals are ideal to highlight the nonlinearities of a process; however, this type of signal has some limitations that must be evaluated by the user prior to the estimation of a process. A multistep signal is enabled to excite the dominant dynamics of a process. In contrast, a well-designed Gaussian signal or equivalent is enabled to excite all the oscillatory

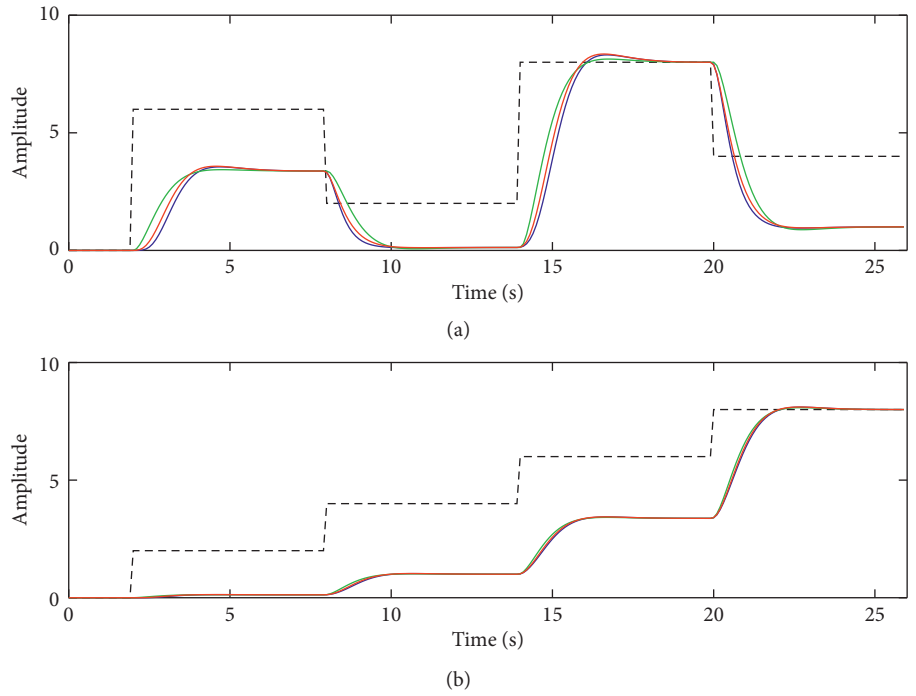

Figure 6: Responses of Wiener (blue), Hammerstein (green), and Wiener–Hammerstein (red) models when they are excited with a multistep signal (dashed) with large (a) and small (b) amplitude changes.

Table 1: Model comparison calculated as MAE when they are excited with large amplitude changes (MAE_{ls}) or low ones (MAE_{ss}).

Model comparison	MAE_{ls}	MAE_{ss}
Wiener-Hammerstein	0.2396	0.0342
Wiener-Wiener-Hammerstein	0.0895	0.0126
Hammerstein-Wiener-Hammerstein	0.1653	0.0235

modes of a process. The persistence of the Gaussian signal enables capturing all the dynamics; however, from a practical point of view, there are two important aspects that must be considered. Precision is not the only criterion to consider for the selection of a model; it is also necessary to consider its complexity. For example, for practical control applications, a model with an excessive number of poles and zeros is not always necessary, and in many cases, only the dominant dynamic is required. On the other hand, to excite all the oscillating modes of a process, the Gaussian signal must be of a long duration. For this reason, its use is impractical in real processes with relatively slow dynamics. Table 2 shows a comparison of the characteristics of a Gaussian signal and a multistep signal.

The issues of using Gaussian signals in processes with slow dynamics are further aggravated when the BLA is required, as its estimation may require multiple realisations. The proposed unified approach, besides enabling estimation of Wiener, Hammerstein, and Wiener–Hammerstein models without a priori information from the user, provides a practical alternative to estimate processes where the BLA estimation is not possible, either because they are slow dynamically, or they are not enabled to handle Gaussian signals.

Table 2: Comparison of characteristics between a multistep signal and a Gaussian signal.

Features	Multistep signal	Gaussian signal
Frequency content.	Low.	High.
Applicability on real processes.	Highly applicable.	It is not always possible.
Information on static nonlinearity.	High information content.	Lower information content, especially if the nonlinearities are at the extremes of the process operation range.
Information on the dynamics.	Less information content. Ideal to estimate the dominant dynamics of a process.	High content if the signal is well designed. Ideal to estimate all the dynamics of a process.
Complexity.	Easy design.	Not so simple to design. The bandwidth must be selected carefully.
Duration.	Do not need to be so extensive.	Must be extensive to excite all the oscillatory modes of a process.

3. WH-EA Abstract

WH-EA is an elitist evolutionary algorithm inspired by biological evolution over generations. It is based on a population of NP individuals who evolve through the

generations and compete with each other for their survival. This section presents the main components of the algorithm; nonetheless, complete information can be found in [34].

3.1. Structure of Individuals and Genetic Operators. Each individual contains coded information ($\boldsymbol{\theta}_i^g = [\mathbf{P}_i^g, \mathbf{B}_i^g, \mathbf{C}_i^g]$) representing a possible solution for the optimisation problem. It is comprised of three genetic portions: location of poles and zeros ($\mathbf{P}_i^g$); location of the breakpoints ($\mathbf{B}_i^g$) to capture the static nonlinearity; and the classification of poles and zeros ($\mathbf{C}_i^g$). The algorithm contains customised mutation and crossover operations, performed on each piece of genetic information. Figure 7 shows the structure of an individual and the genetic operations that apply to each part. The subscript i identifies an individual in the population, while the superscript g indicates the current generation.

Location of poles and zeros for each individual is encoded in a single vector. Its elements $zr_1, \ldots, zr_{nr}$ and $pr_1, \ldots, pr_{mr}$ contain the location of real poles and zeros, respectively. Real and imaginary parts of complex zeros are coded in $zc_1, \ldots, zc_{nc}$ and $zi_1, \ldots, zi_{nc}$, while complex poles are coded in $pc_1, \ldots, pc_{mc}(x)$ and $pi_1, \ldots, pi_{mc}$, respectively. Values of mr, nr, mc, and nc depend on the initial linear model and indicate the number of real poles and zeros as well as the number of pairs of complex conjugate poles and zeros, respectively.

Figure 8 depicts the correspondence that exists between an encoded individual and the resulting nonlinear model. In the example, an initial linear model of four zeros and six poles has been considered, while to capture the static nonlinearity, four points have been assigned. From the initial linear model, $nc = 1$ and $nr = 2$ since there is a pair of complex zeros and two real zeros. In the same way, $mc = 1$ and $mr = 4$ since there is a pair of complex poles and four real poles. The binary code contained in $\mathbf{C}_i^g$ indicates how the poles and zeros of the initial linear model are distributed around the static nonlinearity.

3.1.1. Pole-Zero Locations. Since the initial linear model is not perfect, the location of the poles and zeros must be refined with new estimates around the known values. To explore new locations in the S-plane, two genetic operations are carried out. In both operations, an offspring is created from all the genetic information of his parent except in one gene. The modified gene is formed depending on the selected genetic operation. These operations work as follows:

(i) *Mutation M.1.* The modified gene is determined by a random number with Gaussian distribution ($N_{zp}(0, \sigma^2(g))$) that is generated within the corresponding search space. The search space is defined by the user specifically for each gene. The standard deviation to generate the random number is variable throughout the generations. This deviation decreases from σ^2_{ini} to σ^2_{end} as the algorithm evolves. This enables controlling the aggressiveness of the mutations, that is, in the final generations, the mutations will be more subtle to achieve a fine-tuning of the parameters. Initial and final values of the standard deviation are defined by the user and are expressed as a percentage ratio of the search space of each gene.

(ii) *Crossover C.1.* The modified gene is formed by crossing genetic information between the father and the best individual in the population. Crossing is determined by an average between the values of the corresponding genes.

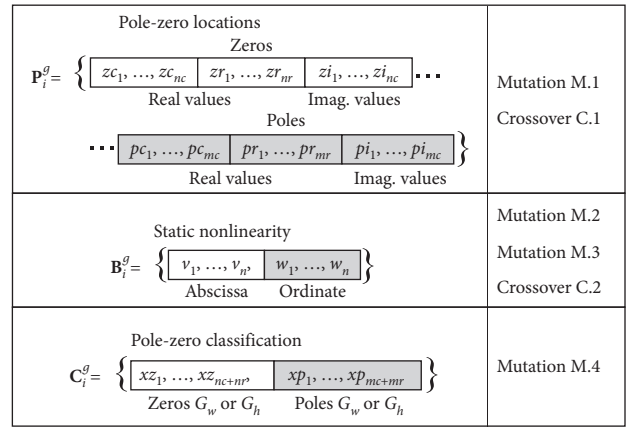

FIGURE 7: Structure of an individual and genetic operations performed on each piece of genetic information.

The refit of locations of poles and zeros is carried out within a search space defined by the user. This search space must be bounded around each pole or each zero based on a minimum and maximum value. For example, a real pole at -0.5 with bounds of ± 0.1 may move between -0.4 and -0.6. Bound selection depends on how close the pole or zero is in relation to the imaginary axis. The poles and zeros closest to the origin are more dominant than those that are further away; therefore, they are more sensitive to changes. Since only fine-tuning is performed at the location of the poles and zeros, smaller dimensions have been selected for the poles most attached to the origin, while the farthest poles have greater freedom of movement since they are less sensitive.

There is no recipe for precisely defining these bounds; however, it should be taken into account that large bounds will allow a better exploration but at the cost of the algorithm converging more slowly.

3.1.2. Static Nonlinearity. Information regarding static nonlinearity is also encoded in a single vector. This information contains the abscissas $(v_1, \ldots, v_n)$ and ordinates $(w_1, \ldots, w_n)$ of the breakpoints that define the piecewise linear function. The user-defined parameter n indicates the number of breaking points used to capture the static nonlinearity.

To capture nonlinearity with great precision, two mutations plus one crossover are executed on this portion of genetic information. In both mutations, an offspring is created from all the genetic information of his parent except in two genes. These two modified genes correspond to an abscissa and its corresponding ordinate that describe the breaking point position. On the other hand, the crossover

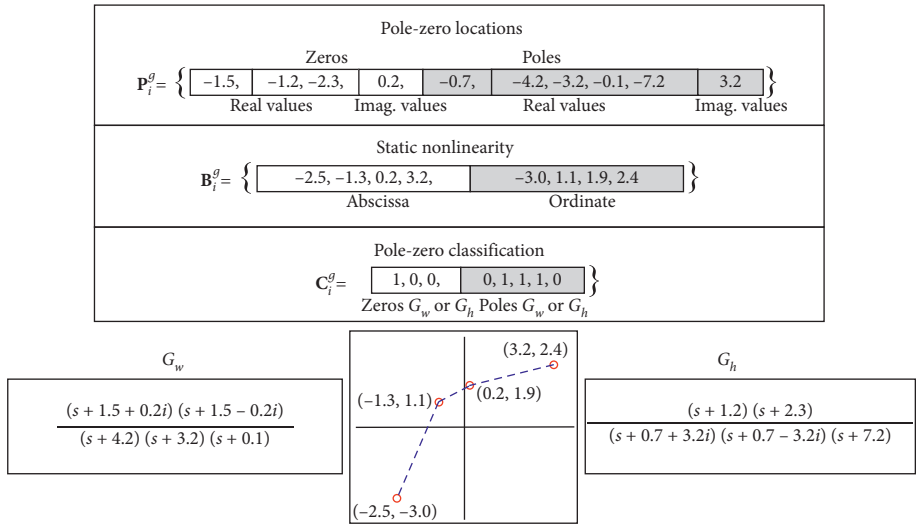

Figure 8: Example of an encoded individual and the resulting nonlinear model.

operation generates an offspring taking all the genetic information of his parent except in one gene. The modified gene corresponds to the ordinate of a breaking point. The three genetic operations applied to this portion of genetic information work as follows:

(i) *Mutation M.2.* The two genes that correspond to the coordinates of a breaking point change randomly. For this, two random numbers $((N_v(0, \sigma^2(g))$ and $N_w(0, \sigma^2(g)))$ with Gaussian distribution are generated within the corresponding search space. To avoid overlapping points, the search space for the genes corresponding to the abscissa is determined by the position of the neighbouring points. The search space for ordinates is the same for all points and corresponds to the codomain of the nonlinear function that is determined as indicated in Section 2.4. To control the aggressiveness of the mutations, standard deviations for generating random numbers are variable throughout the generations as in Mutation M.1. The initial and final values of both standard deviations are user-defined parameters that are also expressed as a percentage ratio of the search space of each gene.

(ii) *Mutation M.3.* This mutation allows concentrating as many points as possible in places where there are curvatures. The gene corresponding to the abscissa is modified in such a way that the points can jump between them. The new value of the abscissa is calculated as the midpoint between the two breakpoints that form the segment over which the point will jump. This segment is determined randomly. On the other hand, the gene corresponding to the ordinates is modified using a quadratic interpolation and information of the points near the location where the jump occurred. Quadratic interpolation will cause a smooth transition of a point when it jumps from one segment to another.

(iii) *Crossover C.2.* The modified gene corresponding to the ordinate of a point is formed by crossing genetic information between the father and the best individual in the population. Crossing is determined by an average between the values of the corresponding genes.

Parameter α indicates how close the break points can be located. This parameter is considered in the aforementioned genetic operations to prevent break points from overlapping. This is an important situation to consider since interpolation methods require that there are no break points with equal values on the abscissa axis; however, α must be small enough to allow break points to join in the curvatures.

The ratio between the horizontal size of the search space and the number of break points $((V_{\max} - V_{\min})/n)$ gives an idea of how small α should be. If α would take the value of this ratio, a uniform horizontal distribution of the break points along the search space would be achieved; however, what is required is that the points be grouped into the curvatures. In this sense, α must take a lower value than this ratio. In any case, it should be taken into account that it is better to select a small α value because if the break points are not required to be so close together, the corresponding genetic operations will be responsible for separating them, while if a large α value is selected and the break points require grouping, the algorithm will not be able to do so and precision will be lost in capturing static nonlinearity.

3.1.3. Pole-Zero Classification. This portion of genetic information contains binary coded information that enables the distribution of the dynamics. The binary codification will indicate whether the identified system is a Wiener, Hammerstein, or Wiener–Hammerstein structure. In this last case, the code will also indicate how the poles and zeros have been distributed between the two LTI subsystems. The first part of the binary vector $(xz_1, \ldots, xz_{nc+nr})$ is used for zero classifications, while the second part $(xp_1, \ldots, xp_{mc+mr})$ is used for pole classifications.

Pole and zero classifications are based on a correspondence between $\mathbf{P}_i^g$ and $\mathbf{C}_i^g$. When an element of $\mathbf{C}_i^g$ is equal to 1, the corresponding pole or zero of $\mathbf{P}_i^g$ will be located in the LTI subsystem prior to nonlinearity, whereas if it takes the value of 0, it will be located in the LTI subsystem that follows the nonlinearity. The genetic operation applied to this information portion works as follows:

(i) *Mutation M.4*. To test different dynamic structures as the algorithm evolves, this genetic operation randomly modifies all the genes, i.e., each time the mutation M.4 is required, a new binary code is generated. This code is generated considering that the resulting linear subsystems cannot be improper; in addition, in case there is a dynamic distribution, the sum of the zeros and the sum of the poles between the two subsystems must be equal to the number of zeros and poles of the initial linear model, respectively.

3.2. Algorithm Description. WH-EA is based on three stages: initialization of the population; offspring generation; and population update. From an initial population of NP individuals, the algorithm evolves based on the mutation and crossover operators described in Section 3.1. In each generation, there will be an individual with the best fitness ($\boldsymbol{\theta}_{\text{best}}^g$). When the algorithm obtains the last generation (MaxGen), the individual with the best fitness will be the solution to the optimisation problem. Algorithm 1 shows a pseudocode of WH-EA, while a detail of the three algorithm stages is indicated below.

3.2.1. Initialisation of the Population. In this stage, NP individuals with the genetic structure of Figure 7 are generated. The first individual of the population is built as follows:

(i) Poles and zeros of the initial linear model give rise to the genetic information portion corresponding to pole-zero locations ($\mathbf{P}_1^0$).

(ii) The n points used to capture the nonlinear function are distributed uniformly along the diagonal formed within the search space of the static nonlinearity (see Section 2.4 for more details). Distribution of these points gives rise to the genetic information portion of the static nonlinearity ($\mathbf{B}_1^0$).

(iii) A random binary code is generated to fill the genetic information portion corresponding to the classification of poles and zeros ($\mathbf{C}_1^0$).

Once the first individual has been structured, mutations M.1, M.2, and M.4 are applied successively on this individual to give rise to the new individuals that will occupy a place in the initial population.

3.2.2. Offspring Generation. In each generation g, an individual ($r_1 \in [1, \text{NP}]$) of the population is selected randomly. The selected individual is known as a parent ($\boldsymbol{\theta}_{r_1}^g = [\mathbf{P}_{r_1}^g, \mathbf{B}_{r_1}^g, \mathbf{C}_{r_1}^g]$), since it will give rise to an offspring who will inherit a large part of its genetic information. An offspring will differ to a lesser or greater extent from its parent depending on the genetic information portion selected to be modified and the genetic operation applied. The genetic information portions modified in the offspring are denoted by $\widetilde{B}^g$ (breakpoint positions), $\widetilde{\mathbf{P}}^g$ (pole-zero locations), and $\widetilde{\mathbf{C}}^g$ (pole-zero classification), respectively.

Selection between the genetic information portions corresponding to the locations of the breakpoints and locations of poles and zeros is handled randomly with $r_{pznl} \in (0, 1]$. In addition, probability for the selection is not fixed throughout the generations, and this is controlled with the parameter $\gamma(g)$. This parameter has an exponential behaviour that decreases as the generations go by. During the first generations, the probability of modifying the genetic information corresponding to the breakpoint locations is very high, and this is justified by the fact that the nonlinearity is not known, while the dynamics in a certain way are known and only require refinement. Genetic information corresponding to the locations of the breakpoints is modified through Algorithm 2, while the locations of the poles and zeros are modified with Algorithm 3.

After one of the two portions of genetic information has been modified, a random process handled by $r_c \in (0, 1]$ will determine whether the genetic information portion corresponding to the classification of poles and zeros will be modified by using Mutation M.4. The probability for this modification is controlled by the user through the parameter $\xi \in (0, 1]$.

To modify a genetic information portion (either $\mathbf{B}_{r_1}^g$ or $\mathbf{P}_{r_1}^g$), not all genetic operations are applied at the same time. In Algorithm 2, the control parameter $\delta_{nl} \in (0, 1]$ indicates the probability with which the mutation (either M.2 or M.3) or crossover C.2 will be used, while the random number $r_{nmc} \in (0, 1]$ enables the selection. In the same way, in Algorithm 3, the control parameter $\delta_{zp} \in (0, 1]$ indicates the probability with which each genetic operation will be used (either mutation M.1 or crossover C.1), while the random number $r_{lmc} \in (0, 1]$ enables the selection.

In Algorithm 2, the selection probability between mutations M.2 and M.3 is variable throughout the generations. This is justified by the fact that mutation M.2 enables an exploration in the search space to shape the static nonlinearity. This mutation is very useful in the first generations. While mutation M.3 enables an accumulation of points in the curvatures, M.3 is not useful during the first generations as nonlinearity curvatures have not yet taken shape. The variable probability of selection between the two mutations is controlled by the parameter $\eta(g)$. This parameter decreases linearly as the generations go by. Since mutation M.2 may also be useful in the final generations, the parameter $\eta_{\min} \in (0, 0.5]$ is included to control the selection probability of the two mutations. This is a user-defined parameter indicating the minimum probability with which the mutation M.2 can be selected.

3.2.3. Updation of the Population. Once an offspring has been generated, it must compete with the individuals of the

(1) Initialise the population;
(2) Evaluate fitness of all population;
(3) **for** $g = 1$ to MaxGen **do**
(4) Find $\boldsymbol{\theta}_{\text{best}}^{g}$
(5) Random selection of an individual (r_1);
(6) Compute $\gamma(g)$;
(7) **if** $r_{pznl} \leq \gamma(g)$**then**
(8) Compute $\widetilde{\mathbf{B}}^{g}$ using Algorithm 2;
(9) **else**
(10) Compute $\widetilde{\mathbf{P}}^{g}$ using Algorithm 3;
(11) **end if**
(12) **if** $r_c \leq \xi$**then**
(13) Compute $\widetilde{\mathbf{C}}^{g}$ using Mutation M.4;
(14) **end if**
(15) Update population;
(16) **end for**
(17) Print $\boldsymbol{\theta}_{\text{best}}^{\text{MaxGen}}$

Algorithm 1: Pseudocode of WH-EA.

(1) **if** $r_{nmc} \leq \delta_{nl}$ **then**
(2) Compute $\eta(g)$
(3) **if** $r_{mm} \leq \eta_{\min} + \eta(g)$**then**
(4) Mutation M.2;
(5) **else**
(6) Mutation M.3;
(7) **end if**
(8) **else**
(9) Crossover C.2;
(10) **end if**

Algorithm 2: Modifying two-dimensional points for nonlinear function.

(1) **if** $r_{lmc} \leq \delta_{zp}$ **then**
(2) Mutation M.1;
(3) **else**
(4) Crossover C.1;
(5) **end if**

Algorithm 3: Modifying pole/zero locations.

population. The fittest contestant wins the competition. The first opponent will be chosen from the population on a random basis. If the offspring wins the competition, it will occupy the position of the defeated individual in the population and the algorithm continues with the next generation. If the offspring fails to defeat the selected individual, a new competition will be held with the next individual of the population. This process will be repeated until the offspring defeats an individual. If the offspring has competed with all the individuals of the population and has not been able to defeat any, this is discarded and the algorithm continues with the next generation.

4. Application Examples

The presented approach was validated with three numerical examples and a real thermal process. In each case, the initial linear model was identified with the Matlab CONTSID Toolbox using the command *srivc*. Nonlinear identification was executed in continuous time using WH-EA. For this, simulations of the dynamic models in the objective function were performed with the *lsim* command of Matlab, while points of nonlinearity were interpolated to define a piecewise linear function. WH-EA parameters were set the same for the four identification problems: $\xi = 0.25$; $\delta_{zp} = 0.75$; $\delta_{nl} = 0.75$; and $\eta_{\min} = 0.35$. In addition, initial and final standard deviations for mutations were set to 20 and 1, respectively.

4.1. Numerical Example 1. For the first numerical example, an LTI subsystem of four poles and one zero is connected in series to a static nonlinearity to give rise to a Wiener structure (see Figure 9). Static nonlinearity consists of a sigmoid hyperbolic tangent function "tansig" (19), which symmetrically saturates large values of the independent variable.

$$S_{\text{NL}} = 50\,(1 + \text{tansig}\,(0.05\,(x - 50))). \tag{19}$$

The LTI subsystem used for this example has unitary static gain. Although the methodology proposed in this paper enables the identification of block-oriented models with a static nonlinearity and LTI subsystems with any gain, unitary gains have been assumed simply for convenience. This will allow the captured static nonlinearity to be compared with the real nonlinear function to evaluate the precision that can be achieved with WH-EA.

To estimate the initial linear model, the simulated system took half their operation range (50%). From this point, the input was modified twice consecutively to give rise to two steps. Each step had a temporary duration of 20 s. The first step had a positive amplitude of 2.5%, while the next had the same amplitude but negative, forming a rectangular pulse. To emulate a real situation, Gaussian noise with a power of −30 dB was added on the system output. Input and output data were sampled with a period of 10 ms. Figure 10 depicts the excitation signal and the response of the simulated system.

The data obtained with the first input change $t\,(15, \ldots, 35)$ were used to estimate the initial linear model, while the data belonging to the second input change $t\,(36, \ldots, 56)$ were used for validation purposes. To avoid problems with initial conditions, offset was removed from data. Fourteen linear models were estimated from second to fifth order considering only strictly proper systems (number of zeros smaller than the number of poles). For each estimated model, the quadratic mean error (MSE) was calculated on the estimation (MSE_e) and validation (MSE_v) datasets. In addition, to select the best structure, the MDL criterion was calculated using (9).

The results of the estimates are shown in Table 3. According to lowest value of MDL criterion, the best

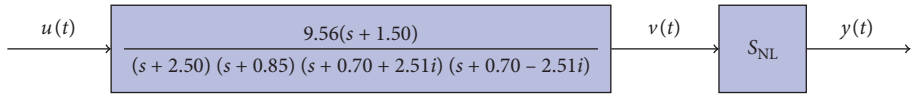

Figure 9: Numerical example 1: Wiener structure.

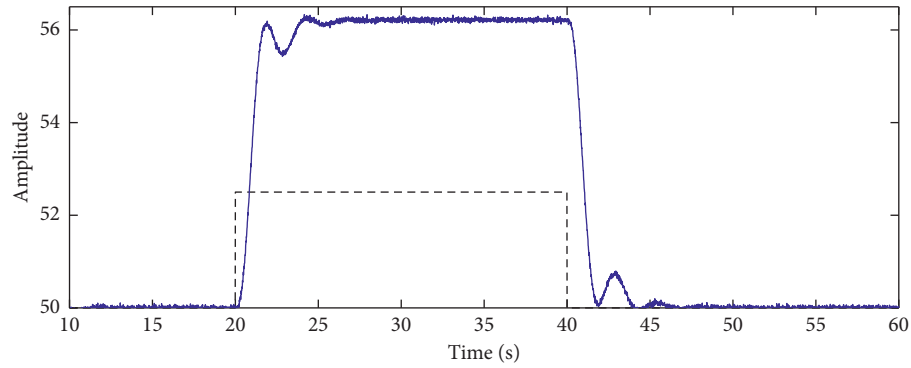

Figure 10: Input (black dashed line) and output (blue solid line) data for initial linear model estimation (numerical example 1).

estimated model was of four poles and one zero (20), which corresponds to the real structure of the linear dynamics that was used for the numerical example. This selection is corroborated by MSE_e values (from the model of four poles and a zero in cases where the MSE decreases, this decrease is practically negligible).

$$G_{w_{lne}}(s) = \frac{23.96\,(s + 1.52)}{(s + 2.51)\,(s + 0.85)\,(s + 0.70 + 2.51i)\,(s + 0.70 - 2.51i)}. \tag{20}$$

For nonlinear identification, two multistep inputs were generated, one for estimation and another for validation purposes. Both signals were designed with 50 steps of random amplitude to explore the entire operating range of the input process (0–100%). Each step had a time duration of 25 s, and the minimum difference between two consecutive steps was restricted so that it is not less than 18 units. The simulated system was excited with both signals separately. Input and output data for both cases were sampled with a period of 10 ms. From the estimation dataset, the minimum and maximum values of the input and output signals were obtained to define the search space for the static nonlinearity. These values were $u_{\min} = 0$, $u_{\max} = 100$, $y_{\min} = 0.559$, and $y_{\max} = 99.44$. Taking into account that the static gain of the estimated initial linear model is positive, the search space for static nonlinearity was defined with $(u_{\min}, y_{\min})$ and $(u_{\max}, y_{\max})$.

Once the search space for static nonlinearity was defined, WH-EA was configured according to the data of Table 4. In addition, $\mathbf{P}_1^0$ was coded with $nc = 0$, $nr = 1$, $mc = 1$, $mr = 2$, and pole/zero locations of (20). Furthermore, all bounds to search new pole-zero locations were set in ± 0.1.

At the end of the generations, a Wiener model was obtained, that is, WH-EA distributed the dynamics correctly without the need for the user to specify the type of structure to be identified. The value reached for the objective function (MAE_e) was $4.415E-2$, while the absolute error on the validation dataset (MAE_v) was 5.567×10^{-2}. Figure 11 depicts a comparison on the validation dataset between the Wiener system output and the estimated model one. A magnification on a portion of data is also shown to demonstrate the great precision of the estimated model. Figure 12 shows how the 18 points representing the static nonlinearity were located within the search space. To verify that it has been captured with great precision, the nonlinear function tansig was included in the graph.

Table 3: Ranking of estimated linear models for numerical example 1 (Wiener system). Models $4p$, $2z/5p$, $3z/5p$, and $4z/5p$ have been excluded due to their high MCL values.

Structure	MSE_e	MSE_v	MDL
$2p$	$4.61E-2$	$4.66E-2$	$2.34E-2$
$1z/2p$	$3.13E-2$	$3.19E-2$	$1.59E-2$
$3p$	$2.38E-3$	$2.49E-3$	$1.21E-3$
$1z/3p$	$1.50E-3$	$1.51E-3$	$7.71E-4$
$2z/3p$	$1.17E-3$	$1.18E-3$	$6.05E-4$
1z/4p	**1.01E − 3**	**9.81E − 4**	**5.20E − 4**
$2z/4p$	$1.01E-3$	$9.82E-4$	$5.22E-4$
$3z/4p$	$1.01E-3$	$9.92E-4$	$5.24E-4$
$5p$	$4.46E-2$	$4.42E-2$	$2.29E-2$
$1z/5p$	$1.01E-3$	$9.83E-4$	$5.22E-4$

Table 4: Summary of WH-EA parameter settings for numerical examples.

Parameter	Description	Value
MaxGen	Generations number	$5e6$
NP	Population size	$5e3$
n	Number of points to represent nonlinearity	18
α	Minimum distance between two points	0.9

4.2. Numerical Example 2. For this numerical example, the same linear subsystem and the same static nonlinearity of the

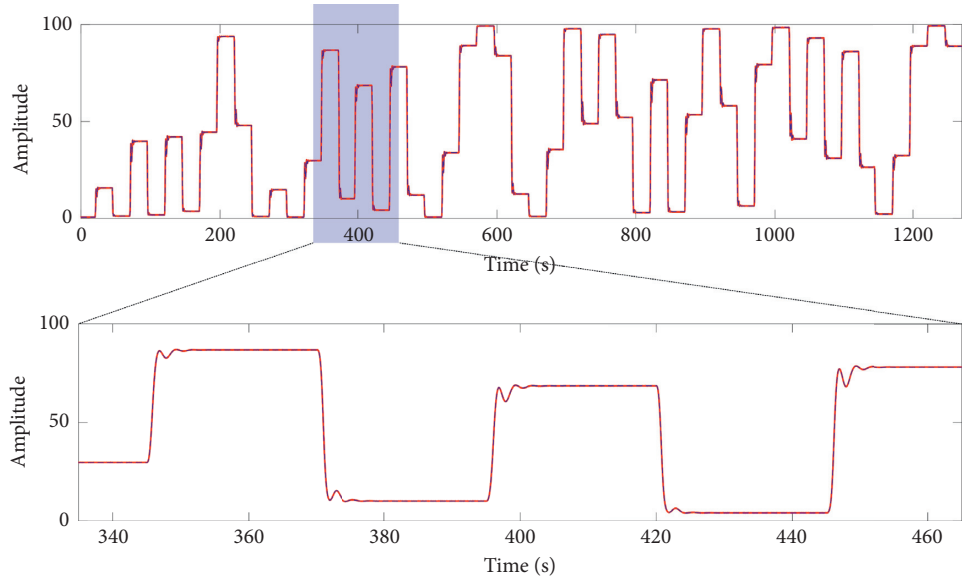

Figure 11: Validation results for numerical example 1: real output (red solid line) and model output (blue dashed line).

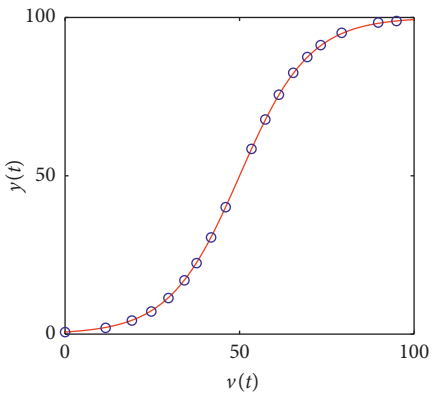

Figure 12: Numerical example 1: comparison between real nonlinear function tansig (red) and captured nonlinearity (blue circles).

previous numerical example were used; however, the blocks were permuted to give rise to a Hammerstein model (see Figure 13). Similarly, the same input signals that were used in the previous example were used to excite this simulated model. With the corresponding dataset for linear estimation, fourteen different linear models were tried. As in the previous case, only strictly proper models from second to fifth order were considered. The results of the estimates are shown in Table 5. The best linear model (21) according to the MDL criterion was four poles and one zero corresponding to the order of the real system.

$$G_{h_{lne}}(s) = \frac{23.87\,(s+1.53)}{(s+2.51)\,(s+0.85)\,(s+0.70+2.51i)\,(s+0.70-2.51i)}. \tag{21}$$

From the nonlinear estimation dataset, the search space for static nonlinearity was defined in the same way as it was for the previous numerical example. For this case, the minimum and maximum values of the input and output signals were $u_{\min} = 0$, $u_{\max} = 100$, $y_{\min} = 0.236$, and $y_{\max} = 99.45$.

For nonlinear estimation, WH-EA was executed considering the configuration parameters of Table 4. In addition, $\mathbf{P}_1^0$ was coded with $nc = 0$, $nr = 1$, $mc = 1$, and $mr = 2$, and pole/zero locations of (21) were used. Furthermore, all bounds to search new pole-zero locations were set in ± 0.1. At the end of the generations, WH-EA distributed the dynamics correctly, that is, a Hammerstein model was obtained. The value reached for the objective function (MAE_e) was 4.328×10^{-2}, while the absolute error on the validation dataset (MAE_v) was 6.526×10^{-2}. Figure 14 depicts a comparison on the validation dataset between the simulated output generated by the numerical example and the output of the estimated model. On the other hand, Figure 15 shows how the 18 points were distributed within the search space to capture the static nonlinearity. As in the previous case, the real nonlinear function was introduced in this graph to visualise the precision achieved with WH-EA.

4.3. Numerical Example 3. For this numerical example, a Wiener–Hammerstein model was constructed using the same dynamics and the same static nonlinearity of the previous examples. In this case, the front LTI subsystem was formed with the two complex poles and a gain of 6.80, while the back LTI subsystem was formed with the two real poles, the zero, and a gain of 1.41 (see Figure 16). The excitation signals and the procedures for linear and nonlinear estimation were the same as those used in the previous examples. Ranking of linear estimates is shown in Table 6. As in the previous cases, the best linear model according to the MDL criterion was of four poles and one zero (22), which is consistent with the dynamics of the real system even though for this case the dynamics was distributed around the static nonlinearity. This demonstrates the great effectiveness of the linear estimation method used in this approach.

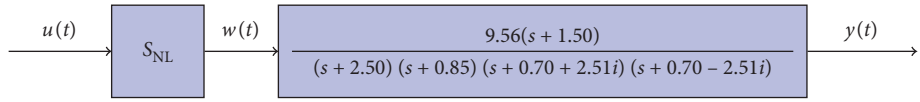

Figure 13: Numerical example 2: Hammerstein structure.

Table 5: Ranking of estimated linear models for numerical example 2 (Hammerstein system). Models $4p$, $3z/5p$, and $4z/5p$ have been excluded since their MDL values were very high.

Structure	MSE_e	MSE_v	MDL
$2p$	$4.57E-2$	$4.565E-2$	$2.32E-2$
$1z/2p$	$3.29E-2$	$3.29E-2$	$1.68E-2$
$3p$	$2.29E-3$	$2.48E-3$	$1.17E-3$
$1z/3p$	$1.38E-3$	$1.45E-3$	$7.08E-4$
$2z/3p$	$1.13E-3$	$1.14E-3$	$5.82E-4$
1z/4p	**9.45E – 4**	**9.59E – 4**	**4.85E – 4**
$2z/4p$	$9.43E-4$	$9.59E-4$	$4.86E-4$
$3z/4p$	$9.42E-4$	$9.60E-4$	$4.87E-4$
$5p$	$4.26E-2$	$4.28E-2$	$2.19E-2$
$2z/5p$	$9.46E-4$	$9.59E-4$	$4.89E-4$

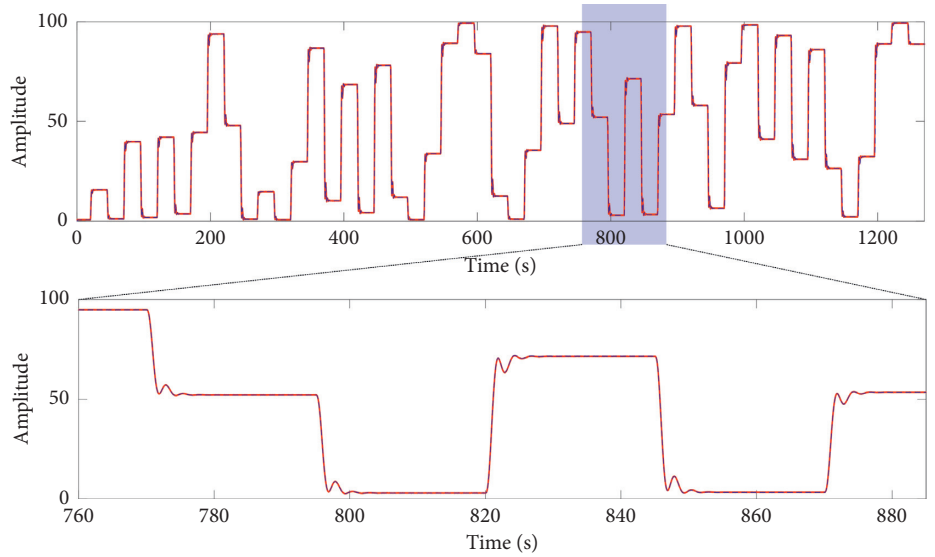

Figure 14: Validation results for numerical example 2: real output (red solid line) and model output (blue dashed line).

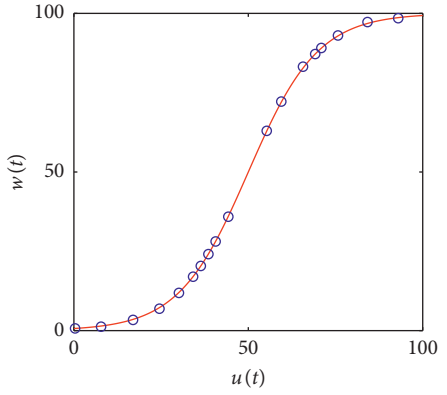

Figure 15: Comparison between real nonlinear function tansig (red) and captured nonlinearity (blue circles). Results obtained on numerical example 2.

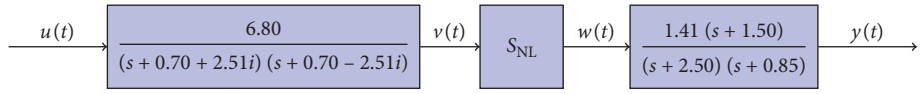

Figure 16: Numerical example 3: Wiener–Hammerstein structure.

Table 6: Ranking of estimated linear models for numerical example 3 (Wiener–Hammerstein system). Models $4p$, $1z/5p$, and $2z/5p$ have been excluded due to high MDL values.

Structure	MSE_e	MSE_v	MDL
$2p$	$4.53E-2$	$4.61E-2$	$2.30E-2$
$1z/2p$	$3.09E-2$	$3.11E-2$	$1.57E-2$
$3p$	$2.50E-3$	$2.32E-3$	$1.27E-3$
$1z/3p$	$1.50E-3$	$1.46E-3$	$7.68E-4$
$2z/3p$	$1.18E-3$	$1.11E-3$	$6.07E-4$
1z/4p	**1.02E − 3**	**9.67E − 4**	**5.23E − 4**
$2z/4p$	$1.02E-3$	$9.69E-4$	$5.25E-4$
$3z/4p$	$1.02E-3$	$9.70E-4$	$5.26E-4$
$5p$	$4.96E-2$	$4.96E-2$	$2.55E-2$
$3z/5p$	$1.01E-3$	$9.72E-4$	$5.28E-4$
$4z/5p$	$1.01E-3$	$9.73E-4$	$5.30E-4$

$$G_{wh_{lne}}(s) = \frac{24.195\,(s + 1.549)}{(s + 2.598)\,(s + 0.854)\,(s + 0.709 + 2.507i)\,(s + 0.709 - 2.507i)}. \tag{22}$$

As can be seen, the linear models obtained in (20)–(22) differ very little from each other and are almost equal to the real dynamic model. This is because the step signal used for the three identification experiments has a small amplitude which hides the effect of nonlinearity. This corroborates what was indicated in Section 2.5. A step signal with a small amplitude change is useful for linear estimation; however, for nonlinear estimation, it is necessary that the nonlinearity is notorious, for this the amplitude changes of the step signal must be large.

As in the previous cases, WH-EA was configured with the parameters of Table 4. In addition, the first individual of the population ($\mathbf{P}_1^0$) was coded with $nc = 0$, $nr = 1$, $mc = 1$, $mr = 2$, and pole/zero locations of (22). According to the minimum and maximum values of the input and output signals, the search space of the static nonlinearity was defined with the coordinates: $(0, 0.5546)$ and $(100, 99.443)$.

At the end of the generations, a Wiener–Hammerstein model was obtained and the dynamics of both LTI subsystems were consistent with the real system. The value reached for the objective function (MAE_e) was 3.768×10^{-2}, while the absolute error on the validation dataset (MAE_v) was 5.117×10^{-2}. Figure 17 depicts a comparison on the validation dataset between the simulated output generated by the numerical example and the output of the estimated model. On the other hand, Figure 18 shows a comparison between the real and estimated nonlinearity.

4.4. Thermal Process Identification. The real process used to validate the paper proposal consists of a lab scale thermal process based on a Peltier cell. Principle of operation of this device is based on nonlinear Peltier and Seebeck effects. Figure 19 shows the architecture of the system that was assembled to operate the process and acquire its output variables. As can be seen, a fan radiator has been coupled to the hot face of the Peltier cell. To measure the temperature of the cold face (T_{cold}), a type k thermocouple was used, while the temperature of the hot face (T_{hot}) was measured with an LM35 sensor. A power supply regulated with an external voltage signal u_a $(0, \ldots, 4.5V_{\text{dc}})$ was used as an actuator to apply voltage to the Peltier cell. For all the experiments involved, the input/output process signals were sampled at 100 ms using a general purpose acquisition card with 12 bits A/D and D/A converters. The process was identified based on the input signal u_a and the temperature gradient between the cold and hot faces ($\Delta_T = T_{\text{cold}} - T_{\text{hot}}$).

A two-step signal was designed to identify and validate the initial linear model. This signal was injected after the process was taken to the middle of its operating range (2.25 V). The first step had a positive amplitude of 0.225 V (5% of the maximum voltage), while the next step had the same amplitude but negative. To ensure that the process reaches steady state, each step had a temporary duration of 700 s. The applied input signal and the response of the system are shown in Figure 20.

The data obtained with the first step change $t\,(0, \ldots, 750)$ were used to estimate the initial linear model, while the data belonging to the second input change $t\,(751, \ldots, 1451)$ were used for validation. To avoid problems with initial conditions, offset was removed from datasets. Different linear models were estimated from second to fifth order. Results of the estimates are shown in Table 7. For each estimated model, the MDL criterion, error on estimation, and error on validation datasets were computed. Models $2z/3p$, $3z/4p$, and $4z/5p$ were not considered, since they were of nonminimum phase, which is not consistent with the reality of the process. The rest of the discarded models had pole/zero cancellations or there were zeros far removed from the imaginary axis.

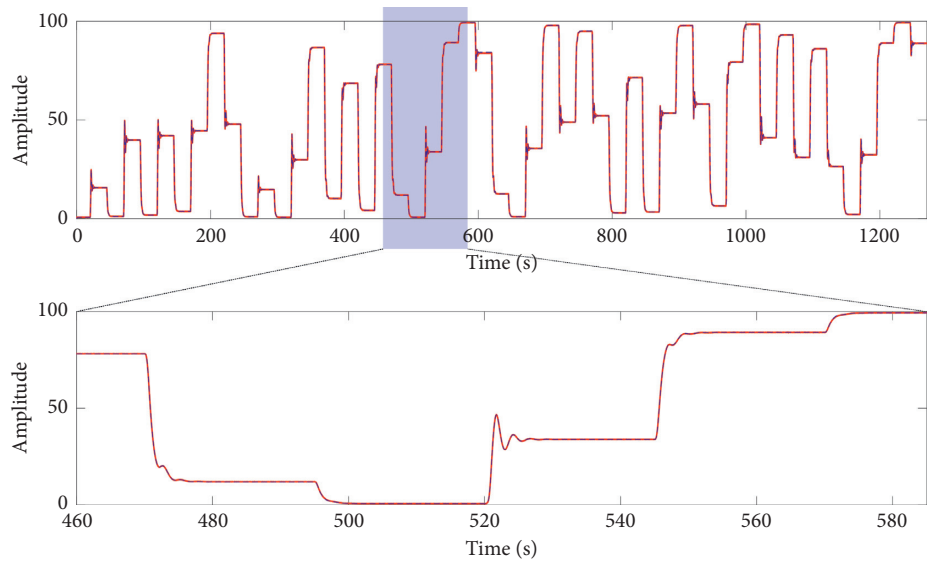

Figure 17: Validation results for numerical example 3: real output (red) and model output (blue dashed line).

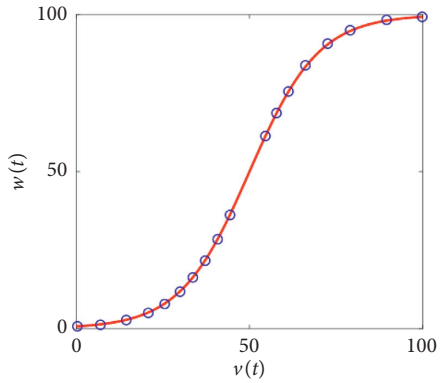

Figure 18: Example 3: comparison between real nonlinear function tansig (red) and captured nonlinearity (blue circles).

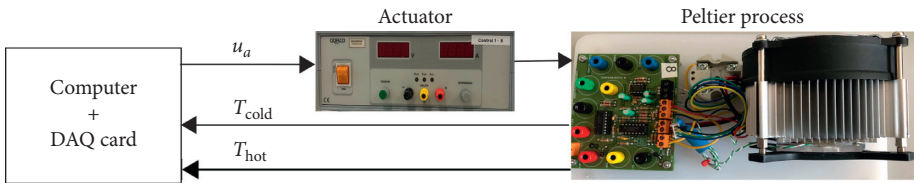

Figure 19: The real process based on a Peltier cell.

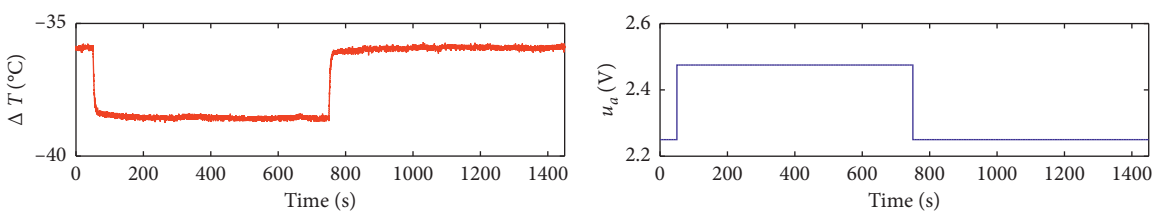

Figure 20: Input and output data for estimation of initial linear model (thermal process). (a) Excitation signal (blue). (b) Output signal of the thermal process (red).

Table 7: Ranking of estimated linear models for the thermal process. Models 4p and 5p have been excluded due to their MDL high values.

Structure	$MSE_e(C)$	$MSE_v(C)$	MDL
2p	3.994$E-3$	4.475$E-3$	13.981
1z/2p	3.991$E-3$	4.473$E-3$	13.972
3p	3.982$E-3$	4.470$E-3$	13.940
1z/3p	2.577$E-3$	2.853$E-3$	9.020
1z/4p	**2.575E−3**	**2.852E−4**	**9.014**
1z/5p	2.576$E-3$	2.854$E-4$	9.018

The best structure according to the MDL criterion was four poles and one zero (23). Figure 21 shows a comparison between the estimated model output and the real process output. This comparison has been made considering the validation dataset.

$$G_{lm}(s) = \frac{-41.186(s+0.015)}{(s+4.473)(s+2.519)(s+0.3406)(s+0.014)}. \quad (23)$$

For the nonlinear identification, two multistep signals were generated, one for identification and another for validation purposes (see Figure 22). The estimation signal was designed with 38 steps, while the validation one was designed with 24 steps. The temporary duration of the steps in both signals was 700 s, and the amplitude changes were handled randomly within the entire range of the actuator $u_a(0,\ldots,4.5v)$, whereas the minimum difference between two consecutive steps was constrained to be greater than 1.5 V. Both signals were injected separately to the process, and the input and output data were recorded after the transient corresponding to the first step was extinguished.

WH-EA was configured with the parameters of Table 8, and according to the linear model structure, vector $\mathbf{P}_1^0$ was coded with $nc = 0$, $nr = 1$, $mc = 0$, and $mr = 4$, as follows:

$$\mathbf{P}_1^0 = [-0.015, -4.473, -2.519, -0.3406, -0.014]. \quad (24)$$

The bounds to explore new locations of poles and zeros were set to ± 0.03 for poles/zeros close to the imaginary axis, while all other bounds were set to ± 0.1. As in the numerical examples, the minimum and maximum values of the input and output signal were extracted from the estimation dataset: $u_{\min} = 0$, $u_{\max} = 4.5000$, $y_{\min} = -53.957$, and $y_{\max} = -0.1810$. Since the static gain of the estimated initial linear model is negative, the search space for static nonlinearity was defined with $(0, -0.1810)$ and $(4.5000, -53.957)$.

With this information, WH-EA was parameterized and executed. At the end of generations, the algorithm divided the dynamics into two linear subsystems, therefore the best structure to represent the thermal process was a Wiener-Hammrestein model.. Table 9 presents the coordinates of the nine points that were assigned to the static nonlinearity, while a plot of this nonlinearity is presented in Figure 23. Equations (25) and (26) show the two resulting subsystems, while performance of the WH identified model on estimation and validation datasets is shown in Figure 24. To quantify the accuracy of the estimated model, the MAE was calculated on the estimation and validation datasets with values of 0.1435 and 0.2184, respectively. To calculate both errors, the first 3000 samples of the datasets were not considered to avoid the transient effects.

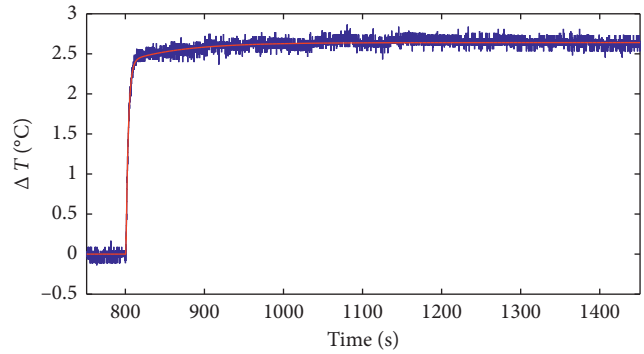

Figure 21: Comparison between the estimated model output (red) and the real process output (blue).

$$\widehat{G}_w(s) = \frac{11.393}{(s+4.394)(s+2.593)}, \quad (25)$$

$$\widehat{G}_h(s) = \frac{0.293(s+0.024)}{(s+0.3263)(s+0.022)}. \quad (26)$$

4.5. Discussion. The results obtained from the numerical examples show the effectiveness of the method to distribute the poles and zeros of the initial linear model around the static nonlinearity. For all three cases, a nonlinear model of 41 parameters has been estimated: 5 parameters for the linear dynamic model and 36 parameters for static nonlinearity. This number of parameters is due to the complexity of nonlinear function tansig, which was introduced intentionally to demonstrate the potential of the WH-EA genetic operators when capturing the nonlinearity. A comparison of the errors obtained from the estimation and validation datasets shows that these are very similar for each case. This shows that estimated models have a good predictive capacity, which can also be verified in Figures 11, 14, and 17, where the output of the estimated model has been compared with data not used in the identification procedure. However, it must be taken into account that the accuracy of the estimated model, as in all identification methods, depends on the amount of input and output data that feeds the procedure. In the specific case of the models addressed in this paper, it also depends on the number of points assigned to capture the static nonlinearity and the quality of the initial linear model.

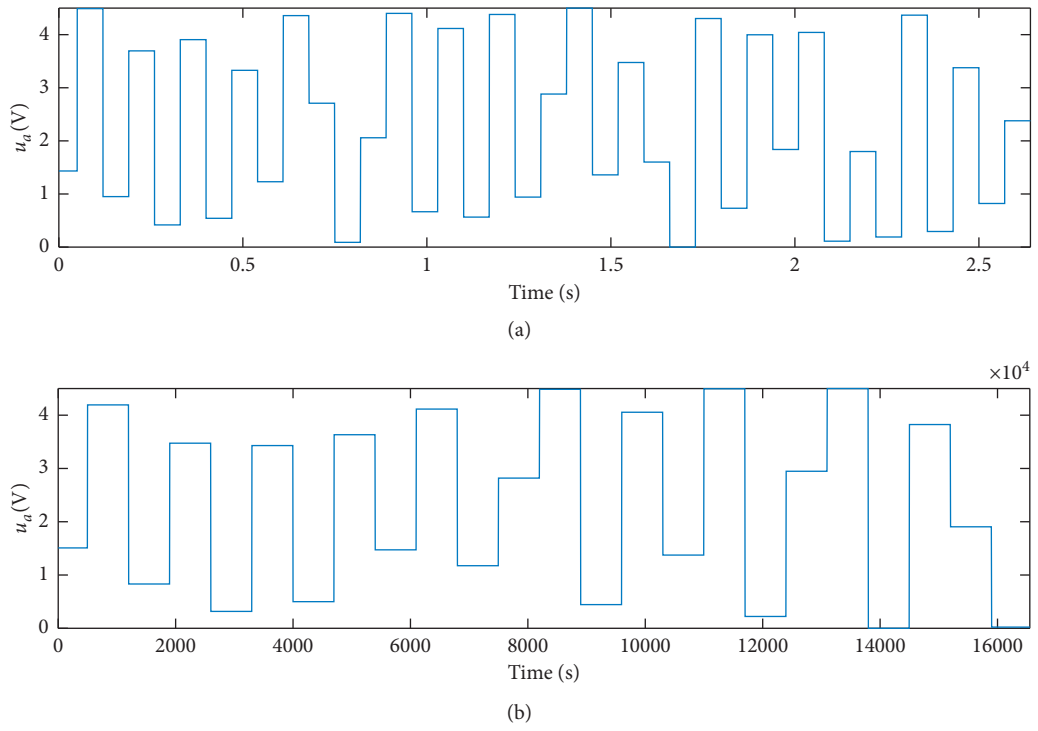

Figure 22: Input signals for nonlinear identification of the Peltier process. (a) Signal for estimation. (b) Signal for validation.

Table 8: Summary of WH-EA parameter settings for nonlinear identification of the thermal process.

Parameter	Description	Value
MaxGen	Generations number	2*e*6
NP	Population size	5*e*3
n	Number of points to represent nonlinearity	9
α	Minimum distance between two points	0.075

Table 9: Nonlinearity coordinates ($n = 9$) estimated by WH-EA from thermal process.

i	1	2	3	4	5	6	7	8	9
v_i	0.0027	0.0887	0.7726	1.5100	2.2692	3.2030	3.8501	4.2461	4.3485
w_i	−0.5143	−1.0959	−14.5081	−26.8456	−36.9569	−46.0773	−50.3862	−52.5096	−52.8295

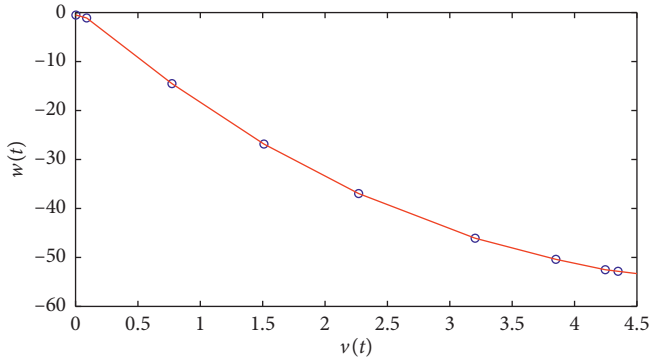

Figure 23: Captured nonlinearity as a piecewise linear function (red) from the estimated breaking points (blue circles).

The real process was estimated with 23 parameters: 5 for the linear dynamic part and 18 for static nonlinearity. The results obtained are very coherent given the structure of the thermal process. A Wiener–Hammerstein model has been estimated, where the fast dynamic of the actuator $\widehat{G}_w(s)$ has been separated from the slow dynamics of the Peltier cell $\widehat{G}_h(s)$.

A great advantage of using multistep signals for estimation of this type of models is that one can have a better panorama to analyse the graphical results. For example, an extended visual exploration of the results shown in Figure 24 showed that the process presents small changes in the dynamics, probably due to thermal drifts and other phenomena that may occur in real processes (see Figure 25) (variation of the dynamics shown in Figure 25 are not the only ones; other similar variations were detected over other portions of estimation and validation data). With a Gaussian excitation signal, in the event of a discrepancy between real output and model output, it would not be so easy to determine if this lack of precision is due to unmodeled dynamics, variation of the dynamics, or static nonlinearity that was not well captured.

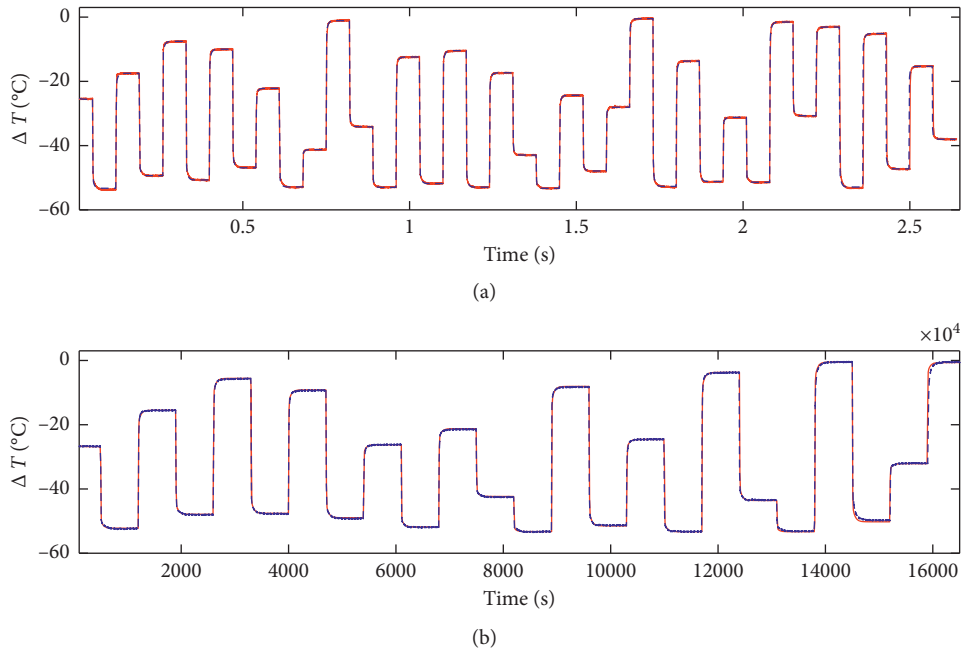

Figure 24: Comparison between thermal process output (red) and estimated model output (blue dashed line). (a) Comparison on estimation dataset. (b) Comparison on validation dataset.

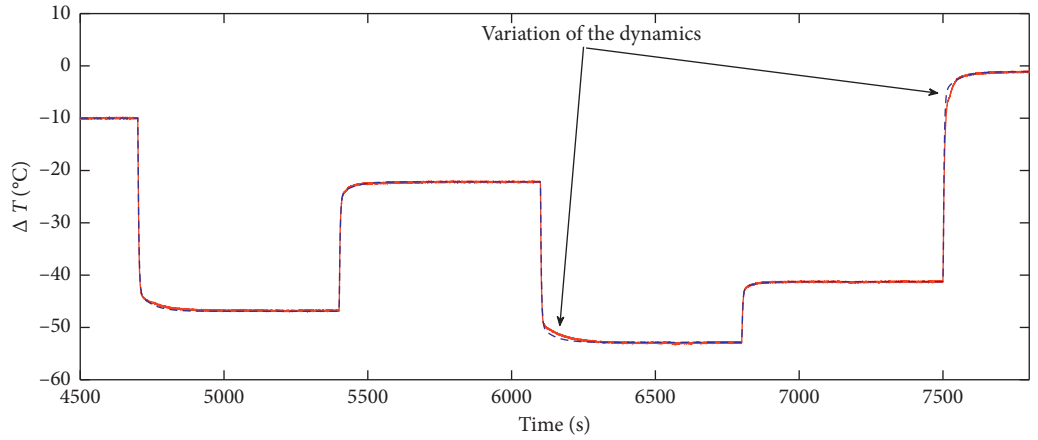

Figure 25: Variation of the dynamics detected on estimation dataset for the thermal process. Red: output of the thermal process. Blue dashed line: output of the estimated model.

The precision achieved in both the numerical examples and the real application depend to a large extent on the number of breakpoints used to capture the static nonlinearity. It is evident that a hard nonlinearity will require many points; however, this is not possible to determine until an initial estimate is made. After an initial estimation, the value reached by the objective function (index J) can give an idea of whether it is necessary to add more points to the piecewise function to reach a greater precision. This index can be compared with the process noise level or with the precision of the measuring instrument. If this information is not available, the precision of the nonlinear estimation can be evaluated with the index J and the range of the process output. Another way to establish if more points are required is through a visual comparison between the real and the modeled output. Since nonlinearity is static, the number of chosen points directly affects the steady-state error that may exist between the two outputs. This comparison is not possible when using Gaussian-type signals since these signals do not lead the system output to steady state.

In the case of the real application, the process output was bounded between −53.957°C and −0.181°C; therefore, the operating range was 53.776°C. For this operating range, the MAE between the real output and estimated output was 0.1435°C. As can be noted, the precision achieved with $n = 9$ was quite acceptable. Other estimates with a greater number of points were executed; however, the decrease in the error was negligible. In the case of the numerical examples, a noise

signal of −30 dB was added to the output of each simulated model. The mean absolute value of this noise signal was 2.52×10^{-2}, and the MAE achieved by the three models is very close to the noise levels. It should be noted that in order to conclude that a good precision has been reached, the signal-to-noise ratio (SNR) must be considered. The three examples were excited with the same signal, and the SNR was approximately 60 dB. Although the results of the three numerical examples were quite acceptable, other estimates were made with the same algorithm configuration but with $n = 24$. The results obtained were slightly above those obtained with $n = 18$; however, it is very likely that the algorithm requires an increase in population size and generations to deal with more complex models. In this sense, it is not ruled out that in the numerical examples, it is possible to improve the accuracy of the models but surely a higher computational cost will be required for the algorithm execution and obviously the models will be more complex.

To date there is no recipe for assigning an optimal number of points for static nonlinearity. Since in the context of systems identification, precision and complexity are two conflicting objectives, a very interesting way to address this problem would be through a multiobjective optimisation approach.

Regarding computational cost of WH-EA (WH-EA was run on a computer with Intel Core I7 processor of 2.8 GHz and 8.0 Gb of RAM), a reference can be obtained. For example, in Section 4.3 (Wiener–Hammerstein example), the average time to run a generation was 0.07 s; however, it should be taken into consideration that the time required by the algorithm to execute all the tasks performed in a generation (mutations, crossovers, and selection) is only 1.42% (0, 99 ms) of the total time spent in a generation. The remaining 98.58% corresponds to the time it takes to evaluate the objective function. This evaluation involves an interpolation process and the simulation of one or two continuous LTI systems with a large amount of input data. It should be taken into account that the execution time of a generation is highly sensitive to the amount of data used for the nonlinear estimation. In both the numerical examples and the practical application, large amounts of data were used to demonstrate the great accuracy that can be achieved with WH-EA.

5. Conclusions

A unified approach to identify Wiener, Hammerstein, and Wiener–Hammerstein models has been presented. This paper shows that a smart parameter selection enables WH-EA to be used to independently identify Wiener, Hammerstein, and Wiener–Hammerstein models without a priori specification of the type of model to be estimated. This is highly attractive especially when a process must be identified and there is uncertainty about the distribution of the dynamics around nonlinearity. The performance of this approach has been evaluated with three numerical examples containing complex static nonlinearity and through a real process consisting of a lab scale thermal process based on a Peltier cell. The results show that WH-EA is enabled to estimate nonlinear models with good accuracy from an initial linear model that is not necessarily the BLA.

Data Availability

The data used to support the findings of this study are available from the corresponding author upon request.

Conflicts of Interest

The authors declare no conflicts of interest.

Acknowledgments

This work was partially supported by projects DPI2015-71443-R and RTI2018-096904-B-I00 from the Spanish Ministry of Economy and Competitiveness and was also supported by Salesian Polytechnic University in Ecuador through a PhD scholarship granted to J. Z.

References

[1] A. Janczak, *Identification of Nonlinear Systems Using Neural Networks and Polynomial Models: A Block-Oriented Approach*, Vol. 310, Springer Science & Business Media, Berlin, Germany, 2004.

[2] F. Giri and E.-W. Bai, *Block-Oriented Nonlinear System Identification*, Vol. 1, Springer, Berlin, Germany, 2010.

[3] M. Schoukens and K. Tiels, "Identification of nonlinear block-oriented systems starting from linear approximations: a survey," 2016, https://arxiv.org/abs/1607.01217.

[4] I. W. Hunter and M. J. Korenberg, "The identification of nonlinear biological systems: wiener and hammerstein cascade models," *Biological Cybernetics*, vol. 55, no. 2-3, pp. 135–144, 1986.

[5] K. J. Hunt, M. Munih, N. d. N. Donaldson, and F. M. D. Barr, "Investigation of the hammerstein hypothesis in the modeling of electrically stimulated muscle," *IEEE Transactions on Biomedical Engineering*, vol. 45, no. 8, pp. 998–1009, 1998.

[6] F. Le, I. Markovsky, C. T. Freeman, and E. Rogers, "Recursive identification of Hammerstein systems with application to electrically stimulated muscle," *Control Engineering Practice*, vol. 20, no. 4, pp. 386–396, 2012.

[7] A. Kalafatis, N. Arifin, L. Wang, and W. R. Cluett, "A new approach to the identification of pH processes based on the wiener model," *Chemical Engineering Science*, vol. 50, no. 23, pp. 3693–3701, 1995.

[8] J. C. Gómez and E. Baeyens, "Subspace-based identification algorithms for Hammerstein and Wiener models," *European Journal of Control*, vol. 11, no. 2, pp. 127–136, 2005.

[9] Y. Zhu, "Distillation column identification for control using wiener model," in *Proceedings of the 1999 American Control Conference (Cat. No. 99CH36251)*, vol. 5, pp. 3462–3466, IEEE, San Diego, CA, USA, June 1999.

[10] J. Oliver, R. Prieto, J. Cobos, O. Garcia, and P. Alou, "Hybrid Wiener-Hammerstein structure for grey-box modeling of DC-DC converters," in *Proceedings of the 2009 Twenty-Fourth Annual IEEE Applied Power Electronics Conference and Exposition*, pp. 280–285, IEEE, Washington, DC, USA, February 2009.

[11] N. Patcharaprakiti, K. Kirtikara, V. Monyakul et al., "Modeling of single phase inverter of photovoltaic system using

Hammerstein-Wiener nonlinear system identification," *Current Applied Physics*, vol. 10, no. 3, pp. S532–S536, 2010.

[12] A. Haryanto and K.-S. Hong, "Maximum likelihood identification of Wiener–Hammerstein models," *Mechanical Systems and Signal Processing*, vol. 41, no. 1-2, pp. 54–70, 2013.

[13] O. P. Dewhirst, D. M. Simpson, N. Angarita, R. Allen, and P. L. Newland, "Wiener-Hammerstein parameter estimation using differential evolution," in *Proceedings of the International Conference on Bio-inspired Systems and Signal Processing*, pp. 271–276, Valencia, Spain, January 2010.

[14] K. P. Fruzzetti, A. Palazoğlu, and K. A. McDonald, "Nolinear model predictive control using Hammerstein models," *Journal of Process Control*, vol. 7, no. 1, pp. 31–41, 1997.

[15] J. C. Gómez, A. Jutan, and E. Baeyens, "Wiener model identification and predictive control of a pH neutralisation process," *IEE Proceedings—Control Theory and Applications*, vol. 151, no. 3, pp. 329–338, 2004.

[16] T. Patikirikorala, L. Wang, A. Colman, and J. Han, "Hammerstein-Wiener nonlinear model based predictive control for relative QoS performance and resource management of software systems," *Control Engineering Practice*, vol. 20, no. 1, pp. 49–61, 2012.

[17] S. Li and Y. Li, "Model predictive control of an intensified continuous reactor using a neural network wiener model," *Neurocomputing*, vol. 185, pp. 93–104, 2016.

[18] G. Shafiee, M. Arefi, M. Jahed-Motlagh, and A. Jalali, "Nonlinear predictive control of a polymerization reactor based on piecewise linear wiener model," *Chemical Engineering Journal*, vol. 143, no. 1-3, pp. 282–292, 2008.

[19] W. Greblicki and M. Pawlak, *Nonparametric System Identification*, Vol. 1, Cambridge University Press, Cambridge, UK, 2008.

[20] G. Mzyk, *Combined Parametric-Nonparametric Identification of Block-Oriented Systems*, Vol. 238, Springer, Berlin, Germany, 2014.

[21] J. Schoukens, J. Lataire, R. Pintelon, G. Vandersteen, and T. Dobrowiecki, "Robustness issues of the best linear approximation of a nonlinear system," *IEEE Transactions on Instrumentation and Measurement*, vol. 58, no. 5, pp. 1737–1745, 2009.

[22] J. Schoukens, R. Pintelon, and Y. Rolain, *Mastering System Identification in 100 Exercises*, John Wiley & Sons, Hoboken, NJ, USA, 2012.

[23] J. Schoukens and R. Pintelon, "Study of the variance of parametric estimates of the best linear approximation of nonlinear systems," *IEEE Transactions on Instrumentation and Measurement*, vol. 59, no. 12, pp. 3159–3167, 2010.

[24] H. K. R. Wong, *Study of the Best Linear Approximation of Nonlinear Systems with Arbitrary Inputs*, Ph.D. thesis, University of Warwick, Coventry, UK, 2013.

[25] P. L. dos Santos, J. A. Ramos, and J. M. de Carvalho, "Identification of a benchmark Wiener–Hammerstein: a bilinear and Hammerstein–bilinear model approach," *Control Engineering Practice*, vol. 20, no. 11, pp. 1156–1164, 2012.

[26] J. Sjöberg, L. Lauwers, and J. Schoukens, "Identification of Wiener-Hammerstein models: two algorithms based on the best split of a linear model applied to the SYSID'09 benchmark problem," *Control Engineering Practice*, vol. 20, no. 11, pp. 1119–1125, 2012.

[27] D. T. Westwick and J. Schoukens, "Classification of the poles and zeros of the best linear approximations of Wiener-Hammerstein systems," *IFAC Proceedings Volumes*, vol. 45, no. 16, pp. 470–475, 2012a.

[28] A. H. Tan, H. K. Wong, and K. Godfrey, "Identification of a Wiener-Hammerstein system using an incremental nonlinear optimisation technique," *Control Engineering Practice*, vol. 20, no. 11, pp. 1140–1148, 2012.

[29] M. Schoukens, R. Pintelon, and Y. Rolain, "Identification of Wiener-Hammerstein systems by a nonparametric separation of the best linear approximation," *Automatica*, vol. 50, no. 2, pp. 628–634, 2014.

[30] D. T. Westwick and J. Schoukens, "Initial estimates of the linear subsystems of Wiener-Hammerstein models," *Automatica*, vol. 48, no. 11, pp. 2931–2936, 2012b.

[31] J. Sjöberg and J. Schoukens, "Initializing Wiener-Hammerstein models based on partitioning of the best linear approximation," *Automatica*, vol. 48, no. 2, pp. 353–359, 2012.

[32] L. Vanbeylen, "A fractional approach to identify Wiener-Hammerstein systems," *Automatica*, vol. 50, no. 3, pp. 903–909, 2014.

[33] G. Giordano, S. Gros, and J. Sjöberg, "An improved method for Wiener-Hammerstein system identification based on the fractional approach," *Automatica*, vol. 94, pp. 349–360, 2018.

[34] J. Zambrano, J. Sanchis, J. Herrero, and M. Martínez, "WH-EA: an evolutionary algorithm for Wiener-Hammerstein system identification," *Complexity*, vol. 2018, Article ID 1753262, 17 pages, 2018.

[35] R. Pintelon and J. Schoukens, *System Identification: A Frequency Domain Approach*, John Wiley & Sons, Hoboken, NJ, USA, 2012.

[36] K. Tiels, M. Schoukens, and J. Schoukens, "Initial estimates for Wiener-Hammerstein models using phase-coupled multisines," *Automatica*, vol. 60, pp. 201–209, 2015.

[37] P. Young and A. Jakeman, "Refined instrumental variable methods of recursive time-series analysis part I: single input, single output systems," *International Journal of Control*, vol. 29, no. 1, pp. 1–30, 1979.

[38] H. Garnier and P. C. Young, "The advantages of directly identifying continuous-time transfer function models in practical applications," *International Journal of Control*, vol. 87, no. 7, pp. 1319–1338, 2014.

[39] H. Gamier and M. Mensler, "Contsida continuous-time system identification toolbox for matlab®," in *Proceedings of the 1999 European Control Conference (ECC)*, pp. 3322–3327, IEEE, Karlsruhe, Germany, September 1999.

[40] A. Padilla, H. Garnier, and M. Gilson, "Version 7.0 of the CONTSID toolbox," *IFAC-PapersOnLine*, vol. 48, no. 28, pp. 757–762, 2015.

[41] H. Garnier, M. Mensler, and A. Richard, "Continuous-time model identification from sampled data: implementation issues and performance evaluation," *International Journal of Control*, vol. 76, no. 13, pp. 1337–1357, 2003.

[42] F. DeRidder, R. Pintelon, J. Schoukens, and D. P. Gillikin, "Modified AIC and MDL model selection criteria for short data records," *IEEE Transactions on Instrumentation and Measurement*, vol. 54, no. 1, pp. 144–150, 2005.

Hindawi
Complexity
Volume 2020, Article ID 3497689, 7 pages
https://doi.org/10.1155/2020/3497689

Research Article

Trading Strategies of a Leveraged ETF in a Continuous Double Auction Market Using an Agent-Based Simulation

Isao Yagi,[1] **Shunya Maruyama**,[2] **and Takanobu Mizuta**[3]

[1]*Faculty of Information Technology, Kanagawa Institute of Technology, Atsugi 243-0292, Japan*
[2]*Course of Information and Computer Sciences, Graduate School of Kanagawa Institute of Technology, Atsugi 243-0292, Japan*
[3]*SPARX Asset Management Co., Ltd., Minato-ku 108-0075, Japan*

Correspondence should be addressed to Isao Yagi; iyagi2005@gmail.com

Received 29 August 2019; Revised 7 January 2020; Accepted 16 January 2020; Published 11 February 2020

Guest Editor: Murari Andrea

A leveraged ETF is a fund aimed at achieving a rate of return several times greater than that of the underlying asset such as Nikkei 225 futures. Recently, it has been suggested that rebalancing trades of a leveraged ETF may destabilize the financial markets. An empirical study using an agent-based simulation indicated that a rebalancing trade strategy could affect the price formation of an underlying asset market. However, no leveraged ETF trading method for suppressing the increase in volatility as much as possible has yet been proposed. In this paper, we compare different strategies of trading for a proposed trading model and report the results of our investigation regarding how best to suppress an increase in market volatility. As a result, it was found that as the minimum number of orders in a rebalancing trade increases, the impact on the market price formation decreases.

1. Introduction

A leveraged exchange-traded fund (ETF) is a fund aimed at achieving a rate of return several times greater than that of the underlying asset, such as Nikkei 225 and S&P futures. These kinds of leveraged ETFs invest in financial market indexes, so they are generally less risky than individual stocks. However, through their use of leveraging, they are able to provide high returns, so the volume of assets under their management has dramatically expanded. Therefore, the risk of a leveraged ETF is also high. Note that we cannot necessarily say that the risk of a leveraged ETF is higher than that of individual stocks. Leveraged ETFs have to execute rebalancing trades on a daily basis—that is, buy the underlying asset when its price goes up and sell it when it goes down—in order to maintain their level of leverage. Therefore, it has been suggested that rebalancing trades of a leveraged ETF may cause destabilization of the prices of the underlying assets [1].

There have been some empirical studies reporting that a leveraged ETF affects the underlying asset markets [2–6]. Chen and Madhavan [2] suggested that by purchasing assets following positive returns and selling assets following negative returns, leveraged ETFs exert additional upward price pressure on the underlying assets following positive returns and additional downward pressure following negative returns, both of which amplify market movements. Rompotis [5] examined how UK leveraged ETFs affected their underlying indexes and found that they could perform their daily rebalancing trades correctly but tracking errors—which refers to the divergence between the daily return of the leveraged ETF and the leverage ratio of the ETF times the corresponding return of underlying asset—became larger as market volatility increased. However, it is difficult for us to determine whether these findings are the pure contribution of the rebalancing trades of the leveraged ETFs to the underlying asset markets, since many factors can affect price formation in actual markets.

One way of analysing how particular transactions influence the financial market is to use an artificial market [7–9]. An artificial market is a multiagent-based model of financial markets. Each of the agents is assigned a specific trading (i.e., buying and selling) rule and then set to trade financial assets as an investor. The market can then be

observed to see how the agents behave. At the same time, it is possible to examine what kinds of effects their behaviours induce in the market.

As described in our previous paper [10], artificial markets have been proposed and refined by many researchers. For example, Chiarella et al. [7] succeeded in structuring a simple agent model which reproduced the statistical characteristics of the kinds of long-term price fluctuations observed in empirical analyses. Chen et al. [8] suggested that a simple a model which can reproduce the desired stylized facts should be made as possible.

Studies on artificial markets have had some success in market analysis, such as investigation of the impact of market regulations on the market [11–13]. In particular, Yagi and Mizuta [11] observed the correlation between the amount of leveraged ETF trading and the volatility of the underlying market and found that the rebalancing trades can destroy the underlying asset's market if the rebalancing trade impact on the market is greater than that of ordinary volatility of the underlying assets.

However, there have been no proposals of a leveraged ETF trading method that suppresses the increase in volatility as much as possible. In actual markets, it is up to the fund managers to decide whether to carry out the rebalancing trades at once or disperse them throughout the day. According to Yagi and Mizuta [11], since a larger amount of the managed assets of leveraged ETFs corresponds to a higher volatility of the underlying asset markets, it seems preferable to perform the rebalancing trades dispersed through the day.

In this paper, we consider a rebalancing trade method that has as little influence on the underlying market volatility as possible while maintaining small tracking errors by implementing a leveraged ETF trading model in the artificial market developed by Yagi et al. [14]. The amount of the rebalancing trading orders depends on the size of the tracking error. In our study, the rebalancing trade orders are placed when the amount of the rebalancing orders is larger than a preset threshold, which means the minimum amount of orders that are actually placed as the rebalancing orders. Hereinafter, we call the preset threshold the "order quantity threshold."

We investigated the appropriate rebalancing trade method by changing the order quantity threshold. As a result, we observed that the number of rebalancing trades and the total amount of rebalancing orders can be reduced by increasing the order quantity threshold. Moreover, we can also confirm that the underlying market volatility increases as the amount of the managed underlying asset increases when the order quantity threshold is small.

2. Artificial Market Model

In view of the discussion of artificial market models in Introduction, for this study, we built a new artificial market model with an investor agent who manages leveraged assets on the basis of the artificial market models of Yagi et al. [14]. This choice was made because Yagi et al. [14] built a simple agent and pricing mechanism which could reproduce the statistical characteristics of the kinds of long-term price fluctuations observed in empirical analyses, to investigate the relationship among four market liquidity indicators by changing the parameters. Hereafter, we call the investor agent, who manages leveraged assets with the aim of achieving a rate of return several times greater than that of the underlying asset, a leveraged ETF agent. Therefore, there are two types of agents in our model, namely, a normal agent as a general investor and a leveraged ETF agent, as described in the following subsections. Specifically, there are n normal agents, agents $j = 1, \ldots, n$, and one leveraged ETF in our market.

In the proposed model, only one risk asset (i.e., the underlying asset of a leveraged ETF) is available for trading. The mechanism for determining the price in this model is a continuous double auction (continuous trading session) [14]. It means that if there are some sell (buy) order prices in the order book that are lower (higher) than the agent's buy (sell) order price, then the agent's order is immediately matched to the lowest sell order (highest buy order) in the order book. Hereafter, we call this a "market order." If there are no such orders in the order book, then the order does not match any other order and remains in the order book. The remaining orders in the order book are cancelled time t_c (order effective period) after the order was placed. The tick size, which is the minimum unit for the price, is δP. An agent can possess assets indefinitely because the quantity of cash of the agent is set indefinitely. Agents can also short sell.

2.1. Order Process. As described above, there are two types of investor agents: a normal agent [14] and a leveraged ETF agent.

A normal agent selected at random sends an order whose quantity is one. However, the same agent will not order more than once until all normal agents have ordered. A leveraged ETF agent places a rebalancing order as needed as each normal agent places an order. The time t is incremented by 1 whenever a normal agent places an order except when a rebalancing trade is not successful. Thus, the process moves one step forward even when a trade of a normal agent does not occur and this new order is placed on the order book.

The order prices of normal agent j by transaction are determined as shown below. The rate of change of the price expected by agent j at time t (the expected return) r_{ej}^t is given by

$$r_{ej}^t = \frac{1}{w_{1j}^t + w_{2j}^t + u_j} \left(w_{1j}^t r_{e1,j}^t + w_{2j}^t r_{e2,j}^t + u_j \epsilon_j^t \right), \quad (1)$$

where w_{ij}^t is the weight of the i-th term for agent j and is set according to the uniform distribution between 0 and $w_{i,\max}$ at the start of the simulation and then varied by using the learning process described later. Furthermore, u_j is the weight of the third term and is set according to the uniform distribution between 0 and $u_{\max}$ at the start of the simulation and kept constant thereafter. We assume that the degree of the three trading strategies, which are fundamental strategy, technical strategy, and noise trading, will be spread across

agents, as we will explain in detail later. Thus, we model the trading weights as random variables independently chosen.

Equation (1) is composed of the three trading strategies: fundamental strategy, technical strategy, and noise trading. The reason why these strategies are implemented in our model is that many empirical studies found that the fundamental strategy, technical strategy, or both were used generally for any market and any time (e.g., Menkhoff and Taylor [15]). We also implement noise trading to model objectively investors' desire for a better strategy through trial and error. The meaning of the term fundamental strategy is as follows. The risk assets have their own fundamental prices measured based on related economic and financial factors. In theory, the market price is equal to the fundamental price. However, in the actual market, the market price is not always equal to the fundamental price. Fundamentalists who are fundamental strategy investors predict that the market price is going to converge to the fundamental price in the future and buy (sell) the stocks when the market price is lower (higher) than the fundamental price. The meaning of the term technical strategy is as follows. A technical strategy focuses on patterns of price movements, trading signals, and various other analytical charting tools to evaluate a stock's strength or weakness. There are many technical strategies in actual markets. We implement the trend following strategy, which buys the asset when its price trend goes up and sells when its trend goes down, expecting price movements to continue, because Iihara et al. [16] showed that many investors including institutional investors use the trend following strategy in their empirical analysis.

The initial term in equation (1) normalizes the impact of the three trading strategies. The first term in parentheses on the right-hand side of equation (1) represents the fundamental strategy, which indicates that an agent expects a positive (negative) return when the market price is lower (higher) than the fundamental price. The term $r^t_{e1,j}$ is the expected return of the fundamental strategy for agent j at time t, given by $r^t_{e1,j} = \ln(P_f/P^{t-1})$, where P_f is the fundamental price, which is constant over time, and P^t is the market price at time t. The market price is set to the most recent price at the time if no trading is occurring. The initial market price is set to the fundamental price, i.e., $P^0 = P_f$.

The second term represents the technical strategy, which indicates that an agent expects a positive (negative) return when the historical return is positive (negative). Here, $r^t_{e2,j}$ is the expected return of the technical strategy for agent j at time t, given by $r^t_{e2,j} = \ln(P^{t-1}/P^{t-1-\tau_j})$, where τ_j is set according to the uniform distribution between 1 and $\tau_{\max}$ at the start of the simulation.

The third term represents the noise strategy. Here, ϵ^t_j is a normally distributed random error with mean zero and standard deviation σ_ϵ.

Based on the expected return r^t_{ej}, the expected price P^t_{ej} is found using the following equation:

$$P^t_{ej} = P^{t-1}\exp\left(r^t_{ej}\right). \tag{2}$$

The order price P^t_{oj} is set according to the uniform distribution between $P^t_{ej} - P_d$ and $P^t_{ej} + P_d$, where P_d is constant. The choice between buying and selling is determined by the relative sizes of the expected price P^t_{ej} and the order price P^t_{oj}.

(i) An agent places a buy order for one share if $P^t_{ej} > P^t_{oj}$

(ii) An agent places a sell order for one share if $P^t_{ej} < P^t_{oj}$

On the other hand, the leveraged ETF agent places an order when the amount of the rebalancing trade required by the calculation method as described below exceeds the order quantity threshold V_{thr}.

Assume that NAV^t and L^t are the net asset value and the actual leverage ratio of the leveraged ETF agent at time t, respectively. Then NAV^t and L^t are defined as follows:

$$\begin{aligned} \text{NAV}^t &= P^{t-1}S^t + C^t, \\ L^t &= \frac{P^{t-1}S^t}{\text{NAV}^t}, \end{aligned} \tag{3}$$

where S^t and C^t are the number of the underlying assets and the amount of cash that the leveraged ETF agent possesses at time t, respectively. The leveraged ETF has to achieve a rate of return the target leverage ratio of the ETF L times greater than that of the underlying asset. Therefore, the leveraged ETF agent's trading starts under conditions that satisfy L. In other words, the initial number of the underlying assets is set as $S^0 = LC^{\text{init}}/P^0$, where C^{init} is the initial cash, and the initial cash after the leveraged ETF is set as $C^0 = C^{\text{init}} - P^0S^0 = C^{\text{init}} - P^0LC^{\text{init}}/P^0 = (1-L)C^{\text{init}}$. Note that the leveraged ETF agent borrows cash and buys the underlying asset when it cannot satisfy the target leveraged ratio of the ETF. The initial NAV of the leveraged ETF agent NAV^0 is defined as $\text{NAV}^0 = P^0S^0 + C^0$.

The amount of the rebalancing trade V^t is calculated as follows [11]:

$$V^t = \frac{\lfloor\{(L-1)P^{t-1}S^t + L^tC^t\}\rfloor}{P^{t-1}}. \tag{4}$$

The rebalancing trade of the leveraged ETF agent is performed when the absolute value of V^t exceeds the order quantity threshold V_{thr}. When the sign of V^t is positive, the leveraged ETF agent sends a sell order. When the sign of V^t is negative, the leveraged ETF agent sends a buy order. These orders are market orders because the leveraged ETF agent has to trade so that L^t becomes equal to L.

2.2. Learning Process. We modelled the learning process as follows based on Mizuta et al. [12]. The reason why the learning process is necessary and why the process should be modelled as described below is given in Mizuta et al. [12].

For $r^t_{ei,j}$, learning is performed by each agent immediately before the agent places an order. That is, when $r^t_{ei,j}$ and $r^t_l = \ln(P^{t-1}/P^{t-1-t_l})$, where r^t_l is the return for the agents' learning process, are the same sign, the value of $w^t_{i,j}$ is updated to $w^t_{i,j} + k_l|r^t_l|q^t_j(w_{i,\max} - w^t_{i,j})$, where k_l is a constant and q^t_j is set according to the uniform distribution between 0 and 1. When $r^t_{ei,j}$ and r^t_l have opposite signs, the value of $w^t_{i,j}$ is updated to $w^t_{i,j} - k_l|r^t_l|q^t_j w^t_{i,j}$.

Separately from the process for learning based on past performance, $w^t_{i,j}$ is reset with a small probability m,

according to the uniform distribution between 0 and $w_{i,\max}$, to model objectively investors' desire for a better weight through trial and error. On the other hand, the learning process of the leveraged ETF agent is not modelled, because the strategy of the leveraged ETF agent depends on the size of the tracking error.

3. Simulation

3.1. Overview. In this paper, we consider the rebalancing trade method that has as little influence on the underlying asset market volatility as possible while maintaining small tracking errors. In this section, we conduct experiments to find a reasonable rebalancing trade method by changing the order quantity threshold. We also analyse the impact of the leveraged ETF agent's net asset value (NAV) on the underlying asset market by changing the initial cash of the leveraged ETF agent.

The initial cash of the leveraged ETF agent C^{init} is defined as $C^{\text{init}} = 1{,}000{,}000 \times C_{\text{mag}}$. We express the NAV of the leveraged ETF agent by changing the initial cash coefficient C_{mag}. We set C_{mag} at each of 10, 20, 30, 40, 50, 60, 70, 80, 90, and 100. The reason why we implemented C_{mag} in our model is to control the relative amount of the initial cash C^{init}. By changing C_{mag}, we examine the effect of the rebalancing trades of the leveraged ETFs with different initial cash amounts on the underlying asset market. The initial cash of the leveraged ETFs in actual markets corresponds to C^{init}, not C_{mag}.

The order quantity threshold V_{thr} is set according one of five patterns: 1, 2, 3, 4, and 5 when the initial cash coefficient C_{mag} is 10 and proportionally larger for larger values of C_{mag}, as shown in Table 1.

Here, we introduce V_{nor}, which is calculated as the order quantity threshold divided by the initial cash coefficient (i.e., $V_{\text{thr}}/C_{\text{mag}}$), for our discussion of the patterns of the order quantity threshold. In the experimental environment, for a given value of V_{nor}, the results indicate that the order quantity threshold increases as the initial cash coefficient increases, so there is no need to consider the effect of the initial cash amount on the rebalancing trade.

The order quantity threshold V_{thr} decides the minimum order quantity per rebalancing trade. The rebalancing trade is performed when the order quantity per rebalancing trade is larger than V_{thr}. By changing V_{thr}, we attempt to confirm the effect of the order quantity per rebalancing trade and the number of rebalancing trades on the underlying asset market. However, as C^{init} increases, the order quantity per rebalancing trade also increases. If V_{thr} is used as the order quantity threshold in the experiments, the number of rebalancing trades inevitably increases when C^{init} is large. Therefore, we introduced V_{nor} as V_{thr} divided by C_{mag}, so that the number of rebalancing trades does not depend on the size of C^{init}. Finally, by changing V_{nor}, we examine the effect of the order quantity per rebalancing trade and the number of rebalancing trades on the underlying asset market. Note that V_{thr} corresponds to the minimum order quantity in the actual market, if the leveraged ETF manager sets a minimum order quantity per rebalancing trade and performs the rebalancing trade.

Table 1: Order quantity threshold (V_{thr}) for each set of conditions.

		V_{nor}				
		0.1	0.2	0.3	0.4	0.5
C_{mag}	10	1	2	3	4	5
	20	2	4	6	8	10
	30	3	6	9	12	15
	40	4	8	12	16	20
	50	5	10	15	20	25
	60	6	12	18	24	30
	70	7	14	21	28	35
	80	8	16	24	32	40
	90	9	18	27	36	45
	100	10	20	30	40	50

From the above, V_{nor} is set to one of five values, 0.1, 0.2, 0.3, 0.4, or 0.5, and C_{mag} is set to 10, 20, 30, 40, 50, 60, 70, 80, 90, or 100. Simulations were performed for all combinations, and simulation results each represent the averages of 100 simulation runs.

We set the initial values of the model parameters as follows. $n = 1{,}000$, $w_{1,\max} = 1$, $w_{2,\max} = 5$, $u_{\max} = 1$, $\tau_{\max} = 15{,}000$, $\sigma_\epsilon = 0.03$, $P_d = 1{,}000$, $t_c = 10{,}000$, $t_l = 10{,}000$, $k_l = 4$, $m = 0.01$, $\delta P = 1$, $P_f = 10{,}000$, $t_{\max} = 1{,}000{,}000$, and $L = 2.0$.

3.2. Validation of Proposed Artificial Market. As many empirical studies have mentioned [17, 18], a fat tail and volatility clustering appear in actual markets, which are two stylized facts of financial markets. Therefore, we set the artificial market parameters so as to replicate these features.

Table 2 shows the statistics for stylized facts in the case that the initial cash coefficient is 10 for which we calculated the price returns, i.e., $\ln(P^t/P^{t-1})$, at intervals of 100 time units. As shown, both kurtosis and autocorrelation coefficients for squared returns with several lags are positive, which means that the runs for all five patterns replicate a fat tail and volatility clustering. This indicates that the model replicates long-term statistical characteristics observed in real financial markets. Since similar results were obtained for the other values of the initial cash coefficient, those results are omitted here due to space limitations.

A previous empirical study showed that kurtosis of returns and autocorrelation coefficients for squared returns with several lags are positive when a fat tail and volatility clustering appear in actual markets [19]. For example, the kurtoses of monthly log returns of U.S. bonds, the S&P composite index of 500 stocks, and Microsoft are 4.86, 7.77, and 1.19, respectively. Note that kurtosis of returns depend on the kinds of financial assets. Likewise, autocorrelation coefficients for squared returns with several lags of the S&P composite index of 500 stocks are 0.0536, 0.0537, 0.0537, 0.0538, and 0.0538 when lags are from 1 to 5, respectively. It seems that the results of our model do not differ significantly

from these results. Therefore, it can be confirmed that the proposed model is valid.

3.3. Simulation Results. We observed the number of rebalancing trades, the total rebalancing order quantity, and the rebalancing order quantity per trade, for which results are shown in Tables 3–5, respectively. For these tables and Table 6 discussed below, entries with dashes indicate that the market collapsed, so that the stylized facts of the market were not obtained and the corresponding value could not be measured.

Table 3 shows that the number of rebalancing trades decreases as V_{nor} increases and C_{mag} increases. Table 4 indicates that the total rebalancing order quantity decreases as V_{nor} increases, but increases as C_{mag} increases. The rebalancing order quantity per trade increases as V_{nor} increases and C_{mag} increases, as shown in Table 5.

Table 6 shows that the market volatility, specifically the standard deviation of market price volatility, decreases as V_{nor} increases. On the other hand, the market volatility increases as C_{mag} increases when V_{nor} is small, whereas when V_{nor} is large, it does not change significantly. Note that market collapses occur when C_{mag} is large and V_{nor} is small.

4. Discussion

In this section, first, we discuss what constitutes an appropriate rebalancing trading method for leveraged ETF managers, meaning a trading method that maintains the actual leverage ratio at the target leverage ratio of the ETF with a small rebalancing order quantity. Next, we discuss the impact of the leveraged ETF agent's NAV on the underlying market. Finally, we attempt to suggest what rebalancing trade method would be most appropriate based on those market impacts.

4.1. Impact of the Order Quantity Threshold on the Market. For the leveraged ETF managers, it is preferable to keep the actual leverage ratio at the target leverage ratio of the ETF with a small rebalancing order quantity. Therefore, we will discuss how changes in the order quantity threshold affect the rebalance trading. Here, we will fix C_{mag} and discuss the impact of changes in V_{nor}.

The results in Table 4 indicate that the total rebalancing order quantity decreases as V_{nor} increases. In other words, Table 4 shows that the rebalancing order quantity can be reduced by increasing the order quantity threshold. The reason for this can be intuitively understood because the results in Table 4 are a combination of the results in Tables 3 and 5, but are discussed in more detail below.

The number of rebalancing trades decreases as V_{nor} increases is shown in Table 3. This phenomenon is thought to depend on the magnitude of the change in market price from the previous period when the rebalancing order quantity is equal to the order quantity threshold. The magnitudes of change in market price are shown in Table 7. For example, the V_{nor} 0.1 column of Table 7 indicates that a rebalancing trade is performed when the market price

Table 2: Stylized facts. $C_{\text{mag}} = 10$.

		V_{nor}				
		0.1	0.2	0.3	0.4	0.5
Kurtosis		8.93	7.26	4.18	2.54	2.13
Autocorrelation coefficients for squared returns	Lag					
	1	0.23	0.22	0.17	0.16	0.13
	2	0.19	0.17	0.12	0.11	0.10
	3	0.17	0.15	0.11	0.08	0.07
	4	0.15	0.11	0.09	0.07	0.05
	5	0.12	0.10	0.06	0.05	0.04

Table 3: Number of rebalancing trades.

		V_{nor}				
		0.1	0.2	0.3	0.4	0.5
C_{mag}	10	6,785	2,152	705	248	100
	20	5,286	1,788	616	218	91
	30	4,855	1,531	564	201	86
	40	—	1,400	504	187	83
	50	—	1,290	463	179	81
	60	—	—	440	178	79
	70	—	—	424	173	79
	80	—	—	425	169	80
	90	—	—	421	176	81
	100	—	—	433	182	87

Table 4: Total rebalancing order quantity.

		V_{nor}				
		0.1	0.2	0.3	0.4	0.5
C_{mag}	10	12,851	5,595	2,337	1,028	508
	20	26,515	10,727	4,366	1,849	926
	30	41,780	14,557	6,176	2,569	1,318
	40	—	18,395	7,400	3,187	1,692
	50	—	21,401	8,517	3,806	2,058
	60	—	—	9,717	4,583	2,420
	70	—	—	10,859	5,151	2,844
	80	—	—	12,430	5,744	3,292
	90	—	—	13,782	6,721	3,731
	100	—	—	15,524	7,705	4,471

Table 5: Rebalancing order quantity per trade.

		V_{nor}				
		0.1	0.2	0.3	0.4	0.5
C_{mag}	10	1	2	3	4	5
	20	4	5	6	8	10
	30	8	8	10	12	15
	40	—	12	14	16	20
	50	—	16	17	20	25
	60	—	—	21	25	30
	70	—	—	25	29	35
	80	—	—	28	33	40
	90	—	—	32	37	45
	100	—	—	35	41	50

Table 6: Underlying market volatility ($\times 10^{-3}$).

		V_{nor}				
		0.1	0.2	0.3	0.4	0.5
C_{mag}	10	1.35	0.95	0.81	0.79	0.78
	20	1.78	1.03	0.82	0.78	0.78
	30	2.27	1.07	0.81	0.79	0.78
	40	—	1.12	0.81	0.77	0.77
	50	—	1.16	0.80	0.76	0.77
	60	—	—	0.79	0.76	0.76
	70	—	—	0.78	0.74	0.75
	80	—	—	0.78	0.73	0.74
	90	—	—	0.78	0.73	0.74
	100	—	—	0.78	0.72	0.73

Table 7: Magnitude of change from previous market price when rebalancing order quantity is equal to order quantity threshold.

	V_{nor}				
	0.1	0.2	0.3	0.4	0.5
Price change	5	10	15	20	25

changes ± 5 from the previous rebalancing trade price. As a result, when the market price increases from 10,000 to 10,005, a rebalancing trade is performed for V_{nor} equal to 0.1, though it is not performed if V_{nor} is equal to 0.2. If the price goes on to increase further to 10,010, then a rebalancing trade is performed both when V_{nor} is 0.1 and when V_{nor} is 0.2. As a result, the number of rebalancing trades is 2 when V_{nor} is 0.1 and 1 when V_{nor} is 0.2. Thus, the number of rebalancing trades decreases as V_{nor} increases.

The results in Table 5 show that the rebalancing order quantity per trade increases as V_{nor} increases. However, the number of rebalancing trades decreases rapidly as V_{nor} increases, as shown in Table 3. Thus, the total rebalancing order quantity decreases when V_{nor} increases.

4.2. Impact of the Leveraged ETF Agent's NAV on the Market. The rebalancing order quantity is also affected by the leveraged ETF agent's NAV. In this section, we will discuss the impact on the underlying market by changing the leveraged ETF agent's NAV. Here, we discuss the impact of changes in C_{mag} with V_{nor} fixed.

Table 6 confirms that market volatility increases as C_{mag} increases when V_{nor} is small. However, if C_{mag} increases too much, the market will collapse. Therefore, the following findings were obtained: rebalancing trades of leveraged ETFs having large NAVs have a significant impact on the market in the sense of increased market volatility. In particular, the increase in market volatility becomes significant when rebalancing transactions with a small order volume are frequently performed.

The reason for the above can be explained by the following two points. One is that the rebalancing order quantity per trade greatly exceeds the order quantity threshold for large C_{mag}, especially when V_{nor} is small, as can be seen by comparing Tables 1 and 5. The other is that the market volatility increases as the rebalancing order quantity per trade increases.

The former reason can be explained using the following example. When V_{nor} is 0.1, regardless of the size of C_{mag}, if the magnitude of change in market price exceeds 5, then a rebalancing trade occurs. The order quantities at this time calculated based on equation (3) are 1 and 3 when C_{mag} is 10 and 30, respectively. These values are consistent with the order quantity threshold for both of these C_{mag} values. However, if the change in market price is ± 9, the quantities of orders for rebalancing trade are 1 and 5 from equation (6) when C_{mag} is 10 and 30, respectively. In the case of $C_{mag} = 30$, the order quantity is larger than the order quantity threshold. Thus, as C_{mag} increases, the actual order quantity per rebalancing trade eventually becomes greater than the order quantity threshold. This is more likely to occur as V_{nor} is smaller. This is because as V_{nor} becomes small, the magnitude of change in market price from the previous period when the rebalancing order quantity equal to the order quantity threshold also becomes small, so the actual order quantity more easily exceeds the order quantity threshold. On the other hand, as V_{nor} becomes large, the magnitude of change in market price from the previous period when the rebalancing order quantity equal to the order quantity threshold also becomes large, so the actual order quantity is less likely to exceed the order quantity threshold.

Next, the reason why market volatility increases as the rebalancing order quantity per trade greatly exceeds the order number threshold is described. As the leveraged ETF agent's orders are market orders, once the rebalancing trade orders are placed, the trade always takes place, and the best quote in the order book for the market is always removed. As C_{mag} increases, the quantity of each order becomes larger, and the market price after the rebalancing trade is higher from the previous price. As a result, market volatility can be considered to have increased.

4.3. Suggestion for the Appropriate Rebalancing Trade Method. As can be seen from the above discussion, increasing V_{nor} reduces the total rebalancing order quantity and also reduces market volatility. This finding also holds when C_{mag} is large, as long as the market does not collapses. In other words, when the mechanism for determining the price is the continuous double auction, it is possible to reduce the total rebalancing order quantity and the impact on the price formation by making several trades with a large rebalancing order quantity rather than making many more trades with small rebalancing order quantities. This result suggests that increasing the minimum number of orders in a rebalance trade can reduce the impact of such a rebalancing trade on the market and leads to keeping the actual leverage ratio at the target leverage ratio of the ETF.

5. Conclusions and Future Work

In this study, we investigated what rebalancing trading method has the least influence on the underlying market

volatility while maintaining small tracking errors by using an artificial market. The following findings were obtained. First, increasing the order quantity threshold reduces the total rebalancing order quantity and decreases market volatility. Next, increasing the NAV of the leveraged ETF agent causes increased market volatility, and in particular, the market volatility significantly increases as the order quantity threshold becomes smaller, although it does not change significantly when the order quantity threshold is large. From these findings, we conclude that increasing the minimum number of orders in a rebalancing trade defines an appropriate trading method from the perspective of the leveraged ETF manager, as well as that of the underlying market.

Our future work can be summarized as follows. In this study, by investigating the trading method focusing on the effect of rebalancing trade on the underlying market, it was found that it is effective to increase the order quantity threshold for the rebalancing trades. However, a larger-order quantity threshold results in a longer period during which a tracking error occurs. Therefore, we should discuss how to avoid such a situation. Furthermore, when the order quantity threshold is large, the market volatility does not change significantly even if the NAV of the leveraged ETF increases. Therefore, we intend to investigate the reason for this.

Data Availability

All data used to support the findings of this study are included within the article.

Disclosure

Note that the opinions expressed herein are solely those of the authors and do not necessarily reflect those of SPARX Asset Management Co., Ltd.

Conflicts of Interest

The authors declare that they have no conflicts of interest.

References

[1] M. Childs, *Fink Says Leveraged ETFs May "Blow up" Industry*, Bloomberg, New York, NY, USA, 2014.

[2] M. Cheng and A. Madhavan, "Dynamics of leveraged and inverse exchange-traded funds," *Journal of Investment Management*, vol. 7, no. 4, pp. 43–62, 2009.

[3] M. Deshpande, D. Mallick, and R. Bhatia, "Understanding ultrashort ETFs," Barclays Capital Special Report, 2009.

[4] W. J. Trainor Jr., "Do leveraged ETFs increase volatility," *Technology and Investment*, vol. 1, no. 3, pp. 215–220, 2010.

[5] G. G. Rompotis, "Empirical insights on the trading behavior of the UK leveraged ETFs," *Journal of Financial Innovation*, vol. 1, no. 3, pp. 159–197, 2017.

[6] I. T. Ivanov and S. L. Lenkey, "Do leveraged ETFs really amplify late-day returns and volatility?" *Journal of Financial Markets*, vol. 41, pp. 36–56, 2018.

[7] C. Chiarella, G. Iori, and J. Perelló, "The impact of heterogeneous trading rules on the limit order book and order flows," *Journal of Economic Dynamics and Control*, vol. 33, no. 3, pp. 525–537, 2009.

[8] S.-H. Chen, C.-L. Chang, and Y.-R. Du, "Agent-based economic models and econometrics," *The Knowledge Engineering Review*, vol. 27, no. 2, pp. 187–219, 2012.

[9] B. LeBaron, "Agent-based financial markets: matching stylized facts with style," in *Post Walrasian Macroeconomics beyond the Dynamic Stochastic General Equilibrium Model (Chapter 3)*, pp. 221–238, Cambridge University Press, Cambridge, UK, 2006.

[10] A. Nozaki, T. Mizuta, and I. Yagi, "A study on the market impact of the rule for investment diversification at the time of a market crash using a multi-agent simulation," *IEICE Transactions on Information and Systems*, vol. E100.D, no. 12, pp. 2878–2887, 2017.

[11] I. Yagi and T. Mizuta, "Analysis of the impact of leveraged ETF rebalancing trades on the underlying asset market using artificial market simulation," in *Proceedings of the 12th Artificial Economics Conference*, pp. 1–11, Rome, Italy, September 2016.

[12] T. Mizuta, K. Izumi, I. Yagi, and S. Yoshimura, "Regulations' effectiveness for market turbulence by large erroneous orders using multi-agent simulation," in *Proceedings of the IEEE Conference on Computational Intelligence for Financial Engineering Economics (CIFEr)*, pp. 138–143, London, UK, March 2014.

[13] S. Kobayashi and T. Hashimoto, "Analysis of institutional evolution in circuit breakers using the concepts of replicator and interactor," in *Proceedings of the 9th Asia-Pacific Complex Systems Conference*, pp. 80–86, Tokyo, Japan, November 2009.

[14] I. Yagi, Y. Masuda, and T. Mizuta, "Detection of factors influencing market liquidity using an agent-based simulation," in *Proceedings of the 2018 5th International Conference on Behavioral, Economic, and Socio-Cultural Computing (BESC)*, pp. 173–178, IEEE, Kaohsiung, Taiwan, November 2018.

[15] L. Menkhoff and M. P. Taylor, "The obstinate passion of foreign exchange professionals: technical analysis," *Journal of Economic Literature*, vol. 45, no. 4, pp. 936–972, 2007.

[16] Y. Iihara, H. Kato, and T. Tokunaga, "Investors' herding on the Tokyo stock exchange," *International Review of Finance*, vol. 2, no. 1-2, pp. 71–98, 2001.

[17] M. Sewell, "Characterization of financial time series," *UCL Department of Computer Science*, vol. 11, no. 1, pp. 1–35, 2011.

[18] R. Cont, "Empirical properties of asset returns: stylized facts and statistical issues," *Quantitative Finance*, vol. 1, no. 2, pp. 223–236, 2001.

[19] R. S. Tsay, *Analysis of Financial Time Series*, Wiley-Interscience, Hoboken, NJ, USA, 2nd edition, 2005.

Hindawi
Complexity
Volume 2020, Article ID 1743973, 12 pages
https://doi.org/10.1155/2020/1743973

Research Article

Intelligent Prediction of Refrigerant Amounts Based on Internet of Things

Jincai Chang, Qiuling Pan, Zhihao Shen, and Hao Qin

College of Sciences, North China University of Science and Technology, Tangshan, China

Correspondence should be addressed to Jincai Chang; jincai@ncst.edu.cn

Received 24 August 2019; Revised 3 January 2020; Accepted 8 January 2020; Published 3 February 2020

Guest Editor: Michela Gelfusa

In a refrigeration unit, the amount of refrigerant has a substantial influence on the entire refrigeration system. To predict the amount of refrigerant in refrigerators with the best performance, this study used refrigerator data collected in real time via the Internet of Things, which were screened to include only the effective parameters related to the compressor and refrigeration properties (based on their practical significance and the research background) and cleaned by applying longitudinal dimensionality reduction and transverse dimensionality reduction. Then, on the basis of an idealized model for refrigerator data, a model of the relationships between refrigerant amount (the dependent variable) and temperature variation, refrigerator compartment temperature, freezer temperature, and other relevant parameters (independent variables) was established. A refrigeration model based on a neural network was then established for predicting the amount of refrigerant and was used to predict five unknown amounts of refrigerant from data sets. BP neural network and RBF neural network models were used to compare the prediction results and analyze the loss functions. From the results, it was concluded that the unknown amount of refrigerant was most likely to be 32.5 g. It is of great practical significance for refrigerator production and maintenance to study the prediction of the amount of refrigerant remaining in a refrigerator.

1. Introduction

Against the backdrop of the highly developed state of network technology and the ongoing development of sensor acquisition technology and communication technology, a new type of relationship between objects emerges. In this environment, all objects related to the Internet are connected through radio frequency identification devices (RFIDs) [1], image recognition technology [2], wireless data communication, and other information-sensing technologies, thereby forming a network with certain intelligent identification and intelligent management functions [3], called the Internet of things (IoT). With the rapid development of smart home appliances [4], digital computer technology, information network technology, and sensing technology can be applied to household appliances [5, 6], enabling smart home appliances to generate "thought," acquire perceptual abilities, and perform information network functions [7]. As smart home appliances in the family continuously exchange information with the outside world, they can help people optimize their lifestyles and use household appliances more conveniently.

The combination of IoT with refrigerators to produce the smart refrigerator is an inevitable result of the development of IoT technology and a direct reflection of people's pursuit of higher quality and a more convenient life [8]. In contrast with the traditional ordinary refrigerator, the smart refrigerator can remind users of foods stored in the refrigerator in a timely way, collect data relevant to the refrigerator's operation to issue early warnings and to prompt maintenance, and help people use it more easily [9, 10], changing people's living habits to a certain extent and increasing convenience in people's lives [11]. Figure 1 shows a diagram of the structure of a smart home appliance system.

In refrigeration appliances, the cooling effect is affected by many factors. As a fully closed refrigeration system, it is limited by many factors, and compactness of the physical structure is a strict design requirement [12]. Under the

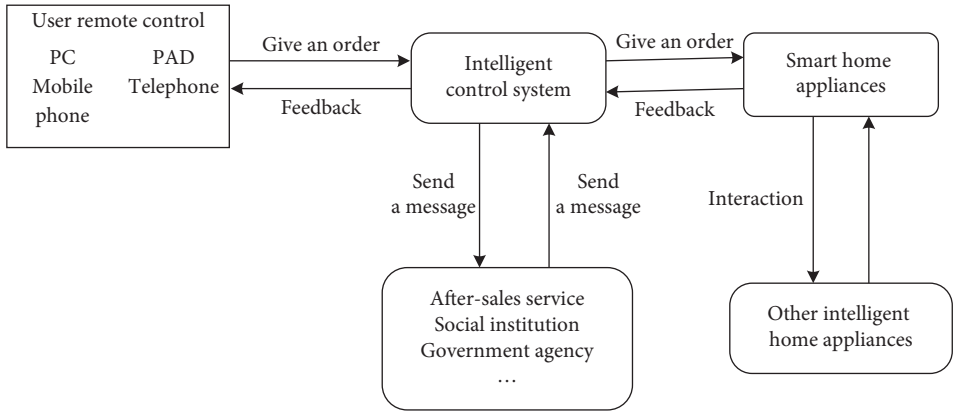

Figure 1: Diagram of smart home appliance and its relationships.

condition of close coordination of key components such as the evaporator, capillary [13], condenser, and compressor, the amount of refrigerant has a substantial influence on the entire refrigeration system [14]. With too much or too little refrigerant, the refrigerant cannot be freely converted [15], the internal pressure will be unbalanced, efficiency of the system will be reduced, and energy consumption will increase, resulting in poor refrigeration [16, 17]. Therefore, it is highly important to precisely control the amount of refrigerant, and this necessitates accurate analysis of the system data [18, 19].

It is the responsibility of refrigerator manufacturers to maintain the quality of refrigerators, addressing issues such as the normal loss of refrigerant, leakage problems, insufficient or excessive filling in later stages, and the question of how much refrigerant should be added when it is clear that the amount is insufficient. If the problem would affect actual use, prompt maintenance can significantly improve the user experience. However, as frequent on-site inspection is not very feasible, it is important to collect and analyze refrigerator data in real time through the Internet of Things, calculate the amount of refrigerant remaining, and prompt users or manufacturers when it falls to a preset threshold so that they can perform advance maintenance.

This study investigated the effect of changes in refrigerant amount on selected parameters such as the refrigerator compartment temperature, variations in temperature, freezing temperatures, and refrigerator frost temperature and established a model of the relationships between refrigerant amount and these parameters, in which the refrigerant amount is the dependent variable and the relevant acquisition parameter is an independent variable. Then, the refrigerant amount was predicted in an experiment by studying the effect of changes in relevant parameters.

2. Refrigerator Characteristics

Through the real-time collection of existing refrigerator data through the Internet of Things, it is feasible to estimate the amount of refrigerant remaining in the refrigerator and to add a proper amount of refrigerant, which is important for the production and maintenance of the refrigerator. As the refrigerator structure, operating mechanism, and data acquisition environment have an impact on the collected data, it is necessary to provide a basic description of the type of refrigerator investigated in this study.

2.1. Physical Structure and Function. Different physical structures of refrigerators produce different types of data and affect the temperature changes within each chamber. Table 1 shows the main physical structure of the refrigerator.

2.2. Control Panel

2.2.1. Principle. By adjusting the digital resistance of the analog sensor, various working states of the refrigerator's computer board can be activated, thereby simulating the process of using the refrigerator.

Throughout the experiment, the R-on of the refrigerator compartment was 7 degrees, the R-off was 3 degrees, the change in the temperature of the variable-temperature compartment was 0 degrees (the "keeping fresh" mode), the startup point was 1 degree, the shutdown point was −1 degree; the temperature of the freezing compartment was the same as that of the refrigerator compartment, F-on was −16 degrees, and F-off was −19 degrees. In order to ensure triggering, the corresponding temperature point was 1 degree lower than the OFF point and 1 degree higher than the ON point.

By default, the refrigerator runs with a load when a profile is formulated.

2.2.2. Typical Working Activities

(i) Pull-down mode (boot): when the computer board is charged, the freezer sensor detects whether the temperature is below −5 degrees, and the computer board enters the pull-down mode. Refrigeration, freezing, and temperature variations occur until the shutdown point is reached, at which time the pull-down mode is exited.

(ii) Thermal insulation refrigeration: if the heat preservation stage compressor is not operating, the

Table 1: Physical structure and function of the refrigerator.

Sequence number	Unit	Component	Function
1	Refrigerator compartment	Refrigerator sensor	Senses the temperature and sends the data to the control panel to control the cooling of the refrigeration section
2		Refrigerator defrosting heating element	Defrosts the refrigeration evaporator
3		Refrigerator door	Senses the switch status and sends the data to the control panel to control lights, air doors, fans, and compressor switches
4		Refrigerator defrost sensor	Senses the defrosting temperature and sends the data to the control panel to control the end of the defrosting
5		Refrigerator damper	Controls refrigerator cooling through the damper switch
6	Chilling chamber	Chilling chamber sensor	Senses the temperature and sends the data to the control panel to control the cooling of the chilling chamber
7		Chilling chamber heating element	Heats the chamber, turning on when the storage function of the chamber is set
8		Chilling chamber damper	Controls the cooling of the chamber through the damper switch
9	Variable-temperature compartment	Variable-temperature sensor	Senses the variations in temperature and sends the data to the control panel to control the cooling of the compartment
10		Variable-temperature damper	Controls the cooling of the compartment through the damper switch
11	Freezer compartment	Freezer sensor	Senses the temperature and sends the data to the control panel to control the cooling of the freezer
12		Freezer defrost sensor	Senses the temperature during defrosting and sends the data to the control panel to control whether defrosting is over
13		Freezer door switch	Detects status of door and sends the data to the main control board, thereby controlling lights, dampers, fans, and compressor switches
14		Freezer fan	Supplies air to the compartments
15		Freezer defrosting heating element	Defrosts the freezer evaporator
16	Ballast machine	Compressor	Circulates refrigerant in the system, thereby accomplishing refrigeration

temperature will rise. After a period of time, if the refrigerator sensor reaches the start point, the refrigerator fan starts working, and the air door opens. If the freezer sensor reaches the start point, the compressor starts working, the refrigerator fan starts working, and the air door opens. If the refrigerator sensor reaches the freezer shutdown point and the refrigerator sensor does not reach the start point, the compressor stops working.

(iii) Moisturizing: when the refrigeration compartment is uncooled and the refrigerator defrost sensor detects that the temperature is less than −3 degrees, the moisturizing function is triggered. When the refrigerator defrost sensor detects that the temperature is greater than 3 degrees, moisturizing ends.

(iv) Opening and closing the door: opening and closing the door simulates the temperature change caused by cold storage and the opening and closing of the freezer. The trigger mechanism is the same as that in the moisturizing mode.

(v) Defrosting: after booting, the compressor works for 8 h, triggering defrosting, and the defrosting heating element starts to work. During this time, the compressor does not operate, and the temperatures rise. When the defrost sensor reaches a specified temperature, defrosting stops. Defrost recovery mode is entered and cooling starts.

(vi) Stopped mode: after working for a period of time, the power supply of the computer board is switched off, simulating a loss of power to the user.

3. Data Acquisition, Screening, and Processing

3.1. Data Acquisition. There were seven refrigerators: BX001, BX002, BX004, BX005, BX006, BX007, and BX009. Each refrigerator was statically injected with a certain amount of refrigerant at a certain time, for example, the BX001 refrigerator was injected with 35 g of refrigerant on January 24, 2018; 35 g on January 25, 2018; and 42.5 g on March 6, 2018. Each file name included the refrigerator ID, the number of grams of refrigerant, and the data collection document number.

By setting up each sensor and collecting data from each one and from the refrigerator computer board, we obtained discrete data for the following parameters at various time points: refrigerator compartment temperature, temperature variation, freezer compartment temperature, freezing temperature, refrigerator defrosting temperature, freezer defrosting temperature, ambient temperature, humidity,

refrigerator evaporator outlet temperature, freezer evaporator outlet temperature, compressor outlet temperature, machine input voltage, machine input current, inverter input current, network speed, packet loss rate, working mode, refrigerator fan status, refrigerator damper A status, refrigerator damper B status, refrigerator defrosting status, freezer status, freezer defrosting status, refrigerator solenoid valve status, refrigerator solenoid valve, vertical beam heating element status, storage heating element status, refrigerator lamp status, UV module working status, ozone module working status, refrigerator compartment left-door status, refrigerator compartment right-door status, freezer door status, freezer door lower-door status, refrigerator compartment left-door duration open, refrigerator compartment right-door duration open, freezer door opening time, compressor operation frequency, refrigerator temperature setting, variable-temperature compartment function setting value, storage function setting value, freezer temperature set point, unlock button time stamp, and unlock button duration.

A total of 124 TXT files were created, 624 MB each, corresponding to the temperature change data under 10 different refrigerant amounts, as well as five files for prediction.

3.2. Data Screening. We established an idealized model of refrigerator data. We assumed that the refrigerator was in a normal state during operation, the refrigerant amount remained stable after addition, and the external environment was stable.

We show an analysis of the data collected by each sensor, ignoring the effects of built-in lighting and UV module sterilization on temperature. Parameters such as network speed and the rate of discarding are considered to be independent of the model establishment, and the data on the status of the refrigerator solenoid valve and the working status of the ozone module have little influence on the experiment. Therefore, we selected only the first 11 data items for processing: those from the refrigerator compartment temperature to the compressor outlet temperature.

In the refrigerator cooling mode, because the refrigerator is intercooled, the refrigeration principle for each compartment is divided into two types. In the first type, a particular compartment sensor reaches the start point, triggering the compressor to start working; meanwhile, the fan starts working, the damper opens, and the fan blows cold air into the compartment for heat exchange, and refrigeration is achieved. In the second type, the sensor itself cannot trigger the compressor; only the heat exchange between the fan and other chambers can serve to achieve cooling. Since refrigerant is only added to the compressor, and our purpose is to study the changes in various parameters when the refrigerant amount changes; we only study the parameter changes under the first refrigeration principle.

During heat preservation, moisturizing, tempering of each compartment, and shutdown of the refrigerator, the compressor stops working, and the temperature of each chamber rises. At this time, any changes in the data have nothing to do with the compressor or the refrigerant. Therefore, we believe that any data changes at this time do not reflect the refrigerant. Naturally, in the door-opening phase, although the compressor continues to work, the decisive factor affecting each chamber is the ambient temperature. The data at this time are also considered irrelevant.

Thus, we only select the first refrigeration principle—that is, the data on each chamber through the fan directly exchange heat with the compressor, the nonswitching door stage, and the refrigeration phase of the refrigerator compressor—as the effective data for the next step.

3.3. Data Processing. The raw data were preprocessed as shown in Figure 2.

After data preprocessing, which reduces the data dimensionality, the data parameters finally selected are shown in Table 2.

The next step was to scan the database to process the data parameters for repeat values (see Figure 3). There are multiple lines of data every second, and the basic data remain constant. In order to reduce data redundancy, the mode value for each parameter in a given second was selected as the parameter value for that second, which reduces the data vertically.

The data as finally processed are shown in Figure 4.

To visualize the data after processing, box plots were drawn from the data (Figure 5), enabling the approximate correlation of the data and general trends to be observed. From the figure, it can be seen that the distributions of data under different amounts of refrigerant are similar. It can also be seen that there is a strong correlation between the refrigerator defrosting temperature and the refrigerator evaporator outlet temperature and between the freezer defrosting temperature and the refrigerator evaporator outlet temperature. Ambient temperature and humidity also have a strong correlation, so the data can be further reduced in dimensionality by removing the three parameters refrigerator evaporator outlet temperature, freezer evaporator outlet temperature, and humidity.

Through data visualization, it was found that the parameters of the 45 g_0806 data set were "abnormal"; the data were distributed around 25°C. By a comparison with the box plots of the previous data, these data were deemed abnormal (see Figure 6). In order to improve the accuracy of the model results, the data of this part of the abnormality were eliminated during the postoperation. The data anomaly may have been due to operational errors during data collection.

Given the data characteristics and the purpose of the modeling, analysis can be performed from three perspectives: the changes in various parameters after different amounts of refrigerant are placed, the relationship between multiple sets of data collected on the same day but at different times, and the effect of different amounts of refrigerant on different machines. Because of the influence of the quantity of data, for example, one given machine can have data for at most three different amounts of refrigerant (according to the description that the refrigerant is injected

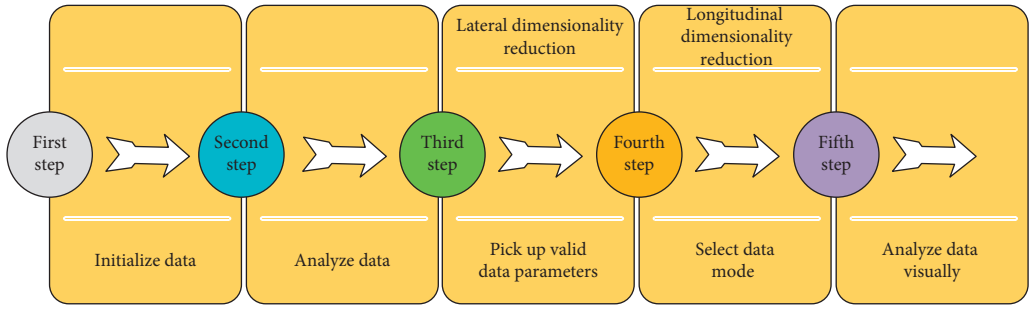

Figure 2: Data preprocessing steps.

Table 2: Valid data parameters.

Selected data parameters	
Refrigerator compartment temperature	Freezer defrosting temperature
Temperature variation	Ambient temperature
Freezer compartment temperature	Humidity
Freezing temperature	Refrigerator evaporator outlet temperature
Refrigerator defrosting temperature	Freezer evaporator outlet temperature
	Compressor outlet temperature

1		Temperature of cold storage chamber	Variable temperature	Temperature of freezing chamber	Freezing temperature	Refrigerate defrosting temperature	Freeze defrosting temperature	Environmen -tal temperature	Humidity	Refrigeration evaporator outlet temperature	Freeze evaporator outlet temperature	Compressor exit temperature
2	2018/1/25 8:06	2.5	−0.7	4.4	−14.4	−12.4	−18.8	23	20	−7.5	−19.1	47.6
3	2018/1/25 8:06	2.5	−0.7	4.4	−14.4	−12.4	−18.8	23	20	−7.5	−19.1	47.6
4	2018/1/25 8:06	2.5	−0.7	4.4	−14.4	−12.4	−18.8	23	20	−7.5	−19.1	47.6
5	2018/1/25 8:06	2.5	−0.7	4.4	−14.4	−12.4	−18.8	23	20	−7.5	−19.1	47.6
6	2018/1/25 8:06	2.5	−0.7	4.4	−14.4	−12.4	−18.8	23	20	−7.5	−19.1	47.6
7	2018/1/25 8:06	2.5	−0.7	4.4	−14.4	−12.4	−18.8	23	20	−7.5	−19.1	47.6
8	2018/1/25 8:06	2.5	−0.7	4.4	−14.4	−12.4	−18.8	23	20	−7.5	−19.1	47.6
9	2018/1/25 8:06	2.6	−0.8	4.3	−14.2	−12.2	−18.8	23	20	−7.4	−19.1	47.3
10	2018/1/25 8:06	2.6	−0.8	4.3	−14.2	−12.2	−18.8	23	20	−7.4	−19.1	47.3
11	2018/1/25 8:06	2.6	−0.8	4.3	−14.2	−12.2	−18.8	23	20	−7.4	−19.1	47.3
12	2018/1/25 8:06	2.6	−0.8	4.3	−14.2	−12.2	−18.8	23	20	−7.4	−19.1	47.3
13	2018/1/25 8:06	2.6	−0.8	4.3	−14.2	−12.2	−18.8	23	20	−7.4	−19.1	47.3
14	2018/1/25 8:06	2.6	−0.8	4.3	−14.2	−12.2	−18.8	23	20	−7.4	−19.1	47.3
15	2018/1/25 8:06	2.5	−0.8	4.4	−14.3	−11.9	−18.8	23	20	−7.1	−19.1	47.5
16	2018/1/25 8:06	2.5	−0.8	4.4	−14.3	−11.9	−18.8	23	20	−7.1	−19.1	47.5
17	2018/1/25 8:06	2.5	−0.8	4.4	−14.3	−11.9	−18.8	23	20	−7.1	−19.1	47.5
18	2018/1/25 8:06	2.5	−0.8	4.4	−14.3	−11.9	−18.8	23	20	−7.1	−19.1	47.5
19	2018/1/25 8:06	2.5	−0.8	4.4	−14.3	−11.9	−18.8	23	20	−7.1	−19.1	47.5
20	2018/1/25 8:06	2.5	−0.8	4.4	−14.3	−11.9	−18.8	23	20	−7.1	−19.1	47.5
21	2018/1/25 8:06	2.5	−0.8	4.4	−14.3	−11.9	−18.8	23	20	−7.1	−19.1	47.5
22	2018/1/25 8:06	2.7	−0.7	4.3	−14.3	−11.3	−18.8	23	20	−6.7	−19.3	47.5
23	2018/1/25 8:06	2.7	−0.7	4.3	−14.3	−11.3	−18.8	23	20	−6.7	−19.3	47.5
24	2018/1/25 8:06	2.7	−0.7	4.3	−14.3	−11.3	−18.8	23	20	−6.7	−19.3	47.5
25	2018/1/25 8:06	2.7	−0.7	4.3	−14.3	−11.3	−18.8	23	20	−6.7	−19.3	47.5

Figure 3: Raw data.

only once a day), one machine has at most four sets of data for different times of the day, and different machines do not have the same refrigeration. The amounts of the refrigerant are contrasted. Therefore, the factors influencing different machines and the changes in parameters at different times of the same day were not considered; instead, only the changes in parameters between different amounts of refrigerant were extracted for study.

4. Establishment and Solution of BP Neural Network Model

According to Kolmogorov's theorem, a three-layer BP neural network with a single hidden layer is sufficient to perform arbitrarily complex function mapping. Therefore, a three-layer BP neural network with a hidden layer was adopted.

1		Temperature of cold storage chamber	Variable temperature	Temperature of freezing chamber	Freezing temperature	Refrigerate defrosting temperature	Freeze defrosting temperature	Environmen -tal temperature	Humidity	Refrigeration evaporator outlet temperature	Freeze evaporator outlet temperature	Compressor exit temperature
2	21:32:02	8	0	2.7	−14.7	−16.6	−23.3	19	30	−17.5	−18.6	36.1
3	21:32:08	8.1	0	2.7	−14.7	−16.6	−23.3	19	30	−17.5	−18.6	36.1
4	21:32:14	8.1	0	2.6	−14.8	−16.8	−23.2	19	30	−17.6	−18.5	36.1
5	21:32:15	8	0	2.7	−14.7	−16.8	−23.2	19	30	−17.6	−18.5	36.1
6	21:52:44	3.5	−1.8	3.4	−14.3	−8	−21.2	19	30	−5.5	−21.7	39.8
7	21:52:45	3.5	−1.8	3.4	−14.3	−8	−21.2	19	30	−5.5	−21.7	39.8
8	21:52:51	3.4	−1.8	3.5	−14.2	−7.9	−21.4	19	30	−5.5	−21.8	39.8
9	21:53:04	3.5	−1.9	3.5	−14.3	−7.5	−21.5	19	30	−5.3	−21.7	40
10	21:53:04	3.5	−1.9	3.5	−14.3	−7.4	−21.4	19	30	−5.3	−21.7	40
11	21:53:10	3.5	−2	3.5	−14.3	−7.4	−21.4	19	30	−5.3	−21.8	39.9
12	21:53:17	3.4	−1.9	3.5	−14.3	−7.2	−21.5	19	30	−5.2	−22	39.7
13	21:53:24	3.5	−1.9	3.4	−14.4	−7.2	−21.6	19	30	−5.1	−21.9	39.7
14	21:53:30	3.5	−2	3.6	−14.4	−7	−21.6	19	30	−5.1	−21.9	39.7
15	21:53:37	3.5	−1.9	3.6	−14.4	−7	−21.7	19	30	−5.1	−22	39.8
16	21:54:03	3.4	−1.9	3.5	−14.6	−6.3	−21.9	18	30	−5.1	−22.2	39.8
17	21:54:10	3.6	−1.9	3.4	−14.5	−6.2	−21.9	19	30	−4.8	−22.1	39.8
18	21:54:16	3.5	−1.7	3.4	−14.6	−6.2	−21.9	18	30	−4.9	−22.1	39.8
19	21:54:23	3.5	−1.9	3.4	−14.6	−6	−22	19	30	−4.9	−22.3	39.8
20	21:54:29	3.6	−1.9	3.6	−14.6	−5.9	−22.1	19	30	−4.8	−22.2	39.8
21	21:54:36	3.6	−1.9	3.5	−14.6	−5.8	−22	19	30	−4.7	−22.3	39.6
22	21:54:43	3.6	−1.9	3.5	−14.7	−5.7	−22.1	19	30	−4.6	−22.2	39.7
23	21:54:49	3.6	−1.9	3.6	−14.7	−5.6	−22.1	19	30	−4.6	−22.4	39.7
24	21:54:55	3.6	−1.9	3.6	−14.7	−5.5	−22.1	19	30	−4.5	−22.2	39.6
25	21:54:56	3.6	−1.8	3.6	−14.7	−5.5	−22.1	19	30	−4.6	−22.4	39.7

Figure 4: Preprocessed data.

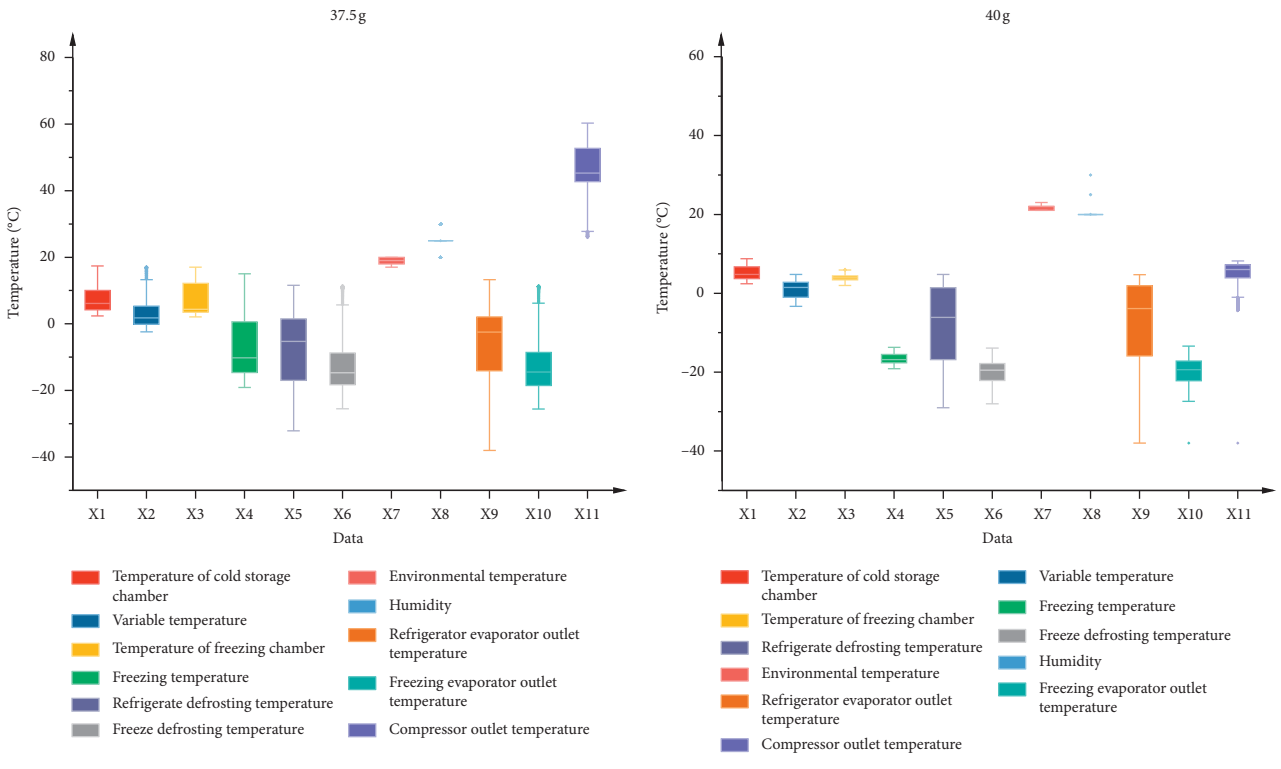

Figure 5: Continued.

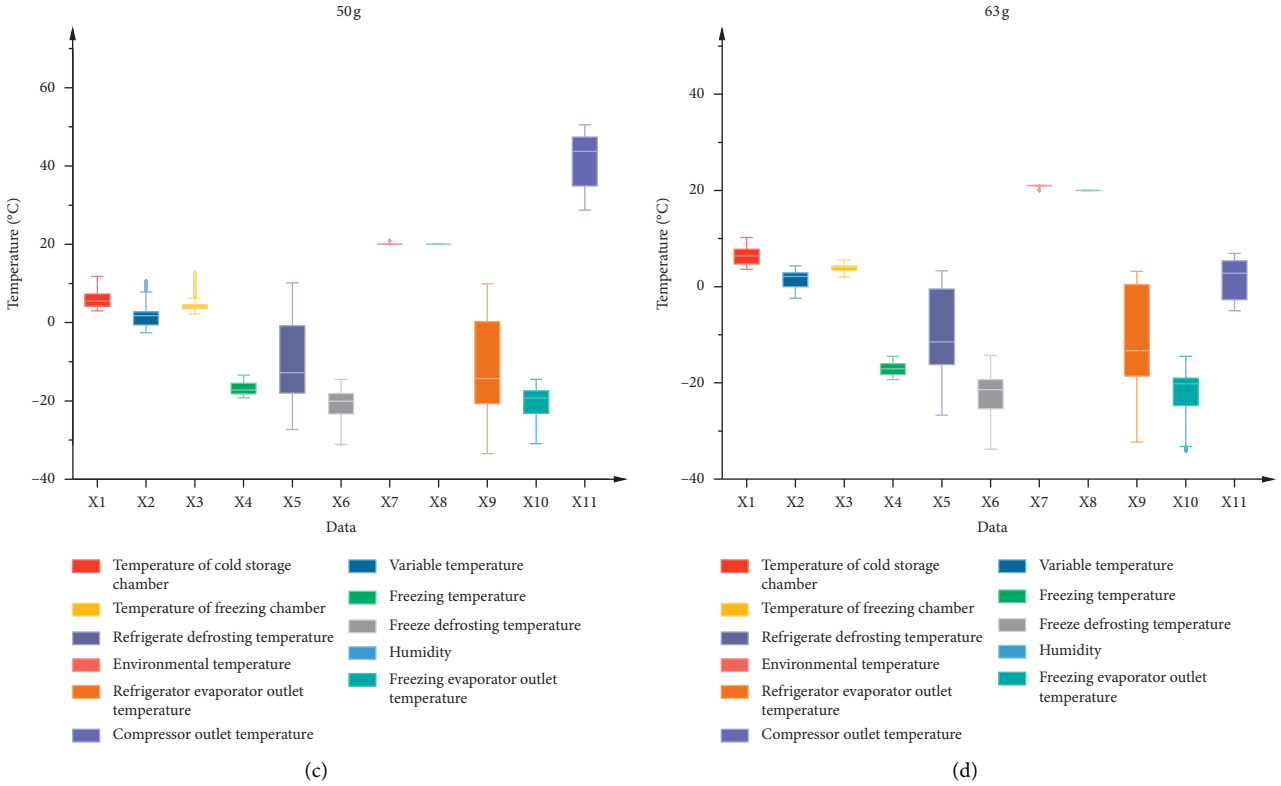

Figure 5: Box plots by refrigerant amount: (a) 37.5 g, (b) 40 g, (c) 50 g, and (d) 63 g.

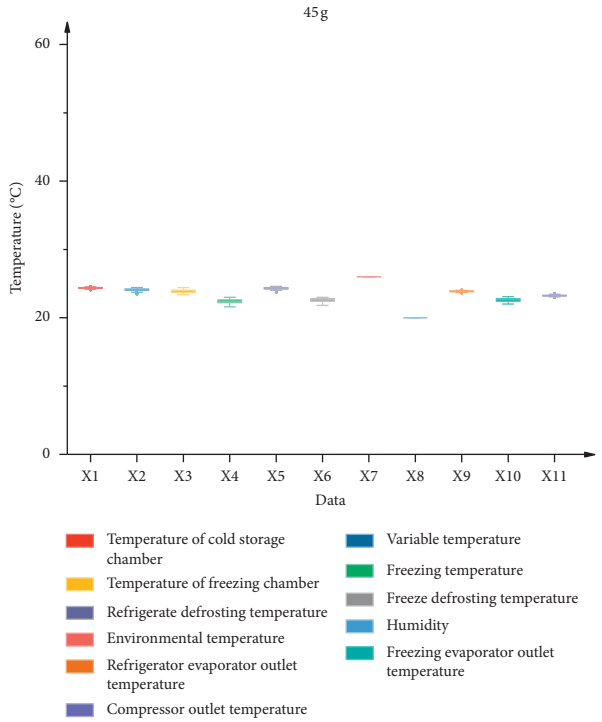

Figure 6: Exception data (refrigerant amount, 45 g).

4.1. Overview of BP Neural Network Model. A list of symbols and their descriptions is shown in Table 3.

4.2. Neural Network Model for Predicting Refrigerant Amount. Figure 7 shows the structure of the BP neural network model.

Table 3: Symbol descriptions.

Symbol	Meaning
I_n	Input layer neurons
O_n	Output layer neurons
X_i	Amount of refrigerant corresponding to the ith prediction category ($i = 1, 3, 5, 7$)
$P(X_i)$	Percentage of refrigerant amount records corresponding to the ith prediction category ($i = 1, 3, 5, 7$)

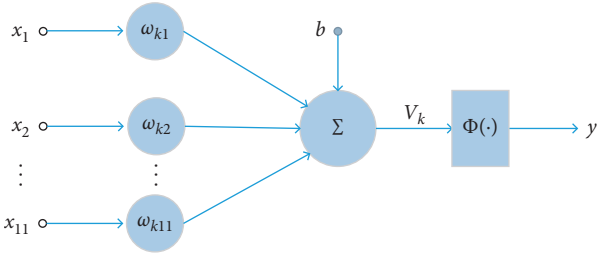

Figure 7: Diagram of model structure.

The number of input layer neurons is 11, corresponding to the 11 data parameters. The number of output neurons is 1, corresponding to the unknown amount of refrigerant. For quantitative analysis, the category values for the different refrigerant amounts are sequentially assigned: 0, 1, 2, 3, 4, 5, 6, 7, 8, and 9. The categories corresponding to the specific refrigerant amounts are shown in Table 4.

The number of neurons in the hidden layer is set as variable n and is calculated according to the following empirical formula:

$$n = \sqrt{I_n \times (O_n + 4)} + a, \tag{1}$$

where $a \in [1, 10]$. The number of hidden layer neurons was selected as $n \in [6, 15]$, and after repeated verification, we let $n = 12$.

The tansig transfer function was used from the input layer to hidden layer, and the purelin transfer function was used from the hidden layer to output layer. The training algorithm adopts a nonlinear damped least-squares optimization algorithm with the trainlm function. Regarding training error, the maximum number of cycles was 100, and the error between network training results and training samples could be controlled within 1×10^{-6}, so the accuracy requirement was considered to be reached. The learning coefficient was 0.05.

4.3. Loss Function. Using 80% of the labeled data as the training set and 20% as the test set, a simple neural network model was selected for training to obtain the loss curve of the model (Figure 8). According to the figure, the minimum loss function value of the model training can reach below 0.045.

4.4. Model Result Distribution Table. Table 5 shows the prediction result details for five XXg data sets.

Table 4: Categories corresponding to refrigerant amounts.

Amount of refrigerant (g)	Corresponding category
30	0
32.5	1
35	2
37.5	3
40	4
42.5	5
45	6
50	7
55	8
63	9

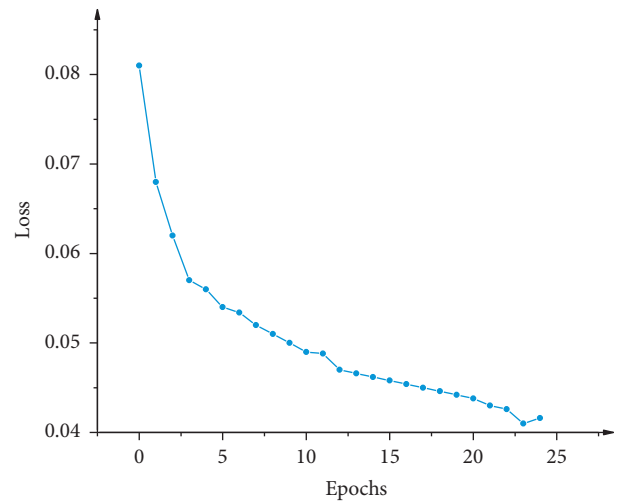

Figure 8: Loss function of model.

Table 5: Distributions of category predictions.

Data set	Predicted category	Number of corresponding records	Proportion of records (%)
BX006_XXg_0115_2051	1	1281	73.24
	3	140	8.00
	5	9	0.51
	7	318	18.18
BX006_XXg_0116_1129	1	832	96.63
	3	13	1.51
	5	15	1.74
BX006_XXg_0116_2316	1	2704	56.20
	3	1339	27.83
	5	18	0.37
	7	749	15.57
BX006_XXg_0117_0716	1	2713	55.67
	3	1505	30.88
	7	654	13.42
BX006_XXg_0117_1044	1	1325	61.40
	3	832	38.55

4.5. Visualization of Prediction Results. Five files with unknown refrigerant amounts were preprocessed, the XX data set for an unknown refrigerant amount was predicted by the model generated by training, and the prediction results were processed visually. Then, pie charts were drawn to intuitively display the distributions of different categories (Figure 9). As

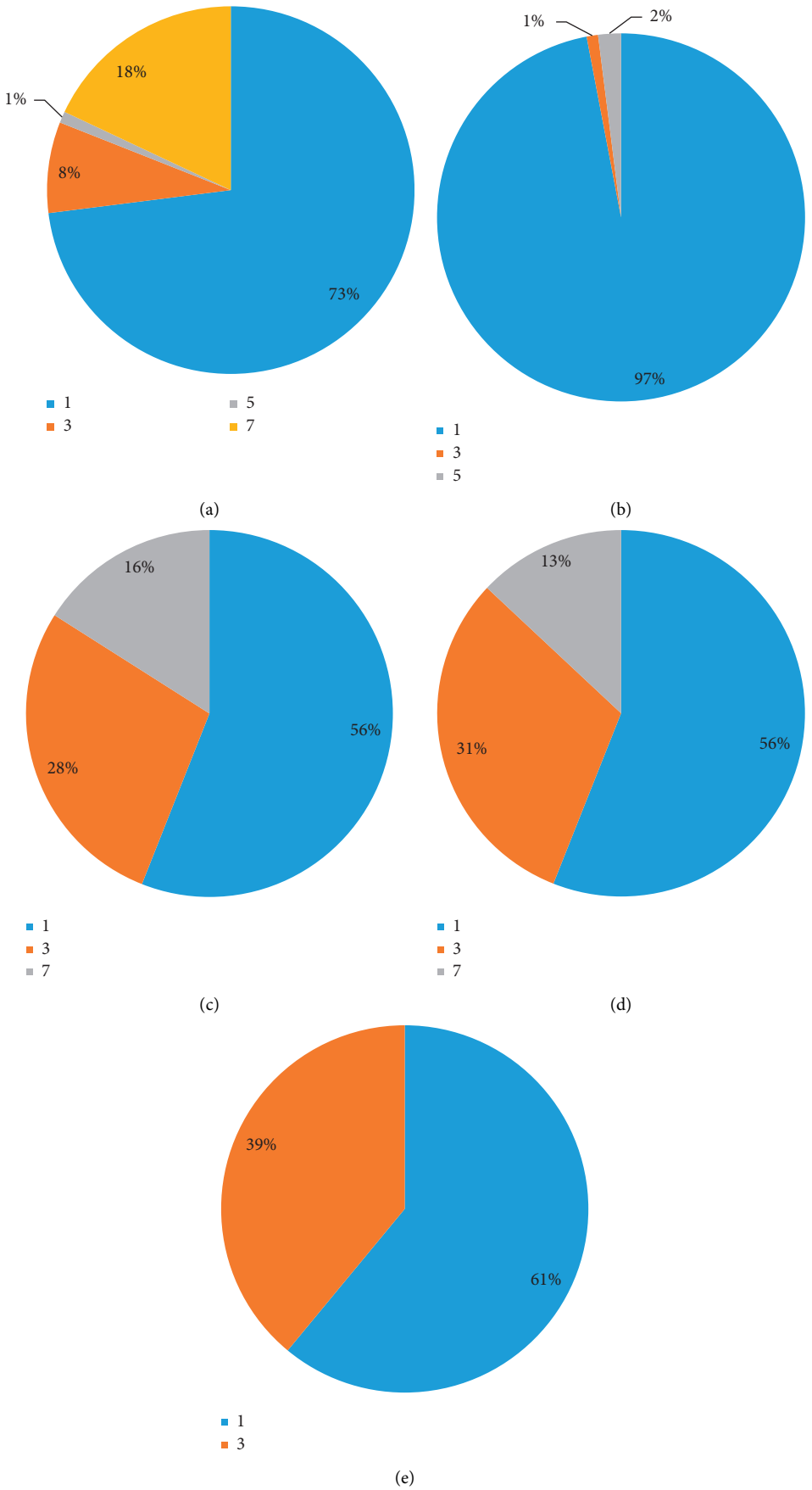

Figure 9: Visualization of prediction results.

can be seen from the figure, based on the qualitative data for five unknown refrigerant amounts, categories 1 and 3 account for the largest proportion; that is, the corresponding refrigerant may range from 30 g to 37.5 g.

4.6. Analysis of Results. There are two explanations for the above results.

4.6.1. Refrigerant Amount Varies Discretely according to the Label Given. For each data set, according to the prediction results, the predicted refrigerant amount having the highest percentage was selected as the optimal refrigerant amount for that data set. Table 6 shows the optimal amounts for the above five groups of refrigerants.

4.7. Future Model Modifications. The temperature variation rule for the original data is segmented cooling. After data cleaning, a breakpoint occurs in the second cooling after each temperature rise. Therefore, the most appropriate data processing method should be applied to the section cooling data as a whole. There has been no internal correlation analysis of data parameters and no specific analysis of the internal correlations of parameters, and the model could also be modified in this regard.

4.8. Summary. This section has introduced the BP neural network, defined the symbols, categorized the refrigerant amounts, and then applied the BP neural network to training data, training the generated model to predict the unknown refrigerant amount of XXg data, set refrigerant amount data set, and drawn the following conclusion: The value for the unknown amounts of refrigerants was most likely to be 32.5 g.

Next, in order to verify the BP results, an RBF radial basis neural network will be used to make predictions, and the results will be compared.

5. Establishment of RBF Model and Analysis of Loss Function

According to RBF theory, before implementing the algorithm, the center of the basis function should first be determined, as it can directly affect the time and space used for network training. Second, from the hidden layer to the output layer, the weight w and the bias value b are involved, and these cannot be determined in advance. To address the above problems, the following solutions are proposed for implementation at the beginning of the algorithm:

(1) Determination of the location of the center of the basis function: for a data set with a small quantity of data, when the spatiotemporal complexity (time complexity and space complexity) is not limited, take random points to determine the center of the basis function. For a data set with a large quantity of data, having higher precision requirements and certain requirements on space-time complexity, apply the clustering algorithm to obtain the center of the initial basis function for testing, such as the K-means RBF neural network [20].

(2) Determination of weight and bias values from the hidden layer to output layer of neural network: refer to the BP neural network for reverse error propagation, and update ω and b iteratively.

Table 6: Optimal refrigerant amounts.

Data set	Amount of refrigerant (g)
BX006_XXg_0115_2051	32.5
BX006_XXg_0116_1129	32.5
BX006_XXg_0116_2316	32.5
BX006_XXg_0117_0716	32.5
BX006_XXg_0117_1044	32.5

The flow chart and implementation design of this algorithm when used for nonlinear function fitting are shown in Figure 10. It can be seen from the figure that when the algorithm is applied to nonlinear neural network fitting, it can be divided into three steps: parameter initialization, network training, and network testing.

5.1. Implementation of Algorithm. The RBF neural network for nonlinear fitting is defined as an RBF class. First, the neurons and the numbers of input layers, hidden layers, and output layers are initialized according to the sample data, and the weights and basis function centers are randomly assigned. Then, the forward propagation process is constructed, the Gaussian function is selected in the hidden layer, and weight w is trained by back propagation according to the data. Finally, the test data are brought into the network to obtain the predicted value. Some parameters of the established RBF network are shown in Table 7.

5.2. Loss Function Analysis. The loss function adopts the mean square error and runs the RBF neural network. When the number of iterations was set to 500, it was found that the loss function rapidly converges to 8.72 (Figure 11). This indicates that the training of the RBF radial basis neural network is not as good as that of the BP neural network for this problem and the parameter values used.

The parameters were adjusted several times, but the results were similar. Therefore, we believe that the RBF model does not successfully extract ΔT (temperature variation), the change in temperature over time.

5.3. Summary. In order to formulate a basis for comparison with the prediction results obtained by the BP neural network, this section used the RBF radial basis neural network to conduct code design and loss function analysis on the nonlinear fitting problem. The RBF neural network characteristically has the best unique approximation, a quickly converging learning process, good classification capability, multidimensional nonlinear mapping capability, good

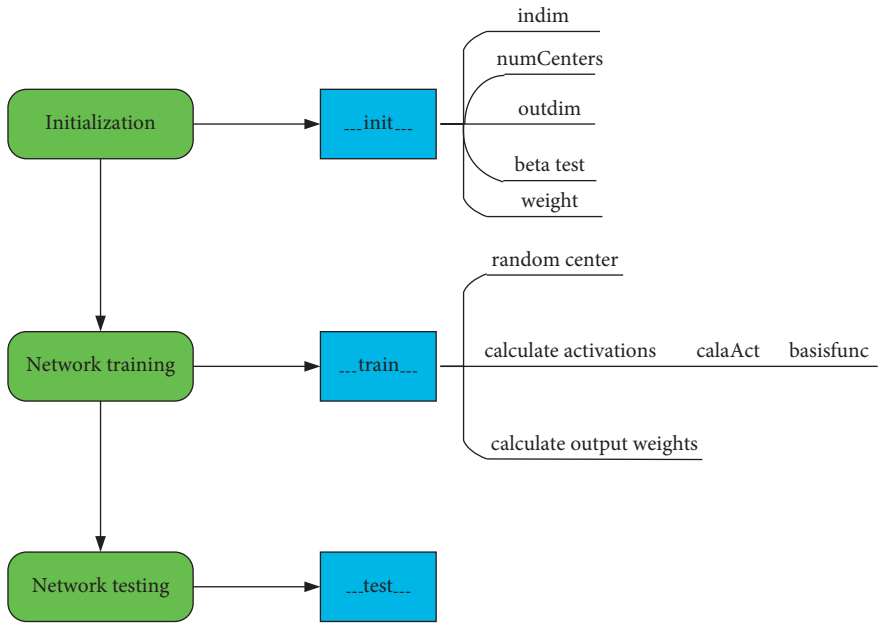

Figure 10: Algorithm flow chart and implementation design.

Table 7: Some of the RBF parameters.

Parameter	Value(s)
maxCycle	5000
Alpha	0.1
batch_size	50
Label	0, 1, 2, 3, 4, 5, 6, 7, 8, 9
n_hidden	25
n_output	1
Cost function threshold setting	Cost < 0.03

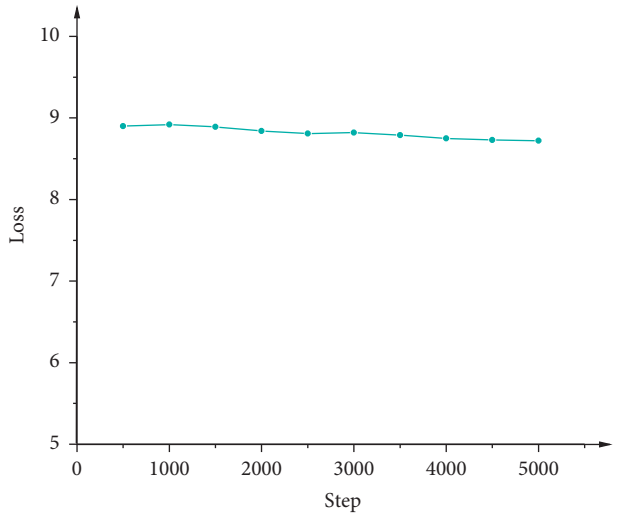

Figure 11: Loss function of RBF model.

generalizability, parallel information processing capability, and a simple and convenient learning algorithm.

However, the network still has the disadvantage of uncertain parameters, and a training process for adjusting parameters is required for different data sets. In this practical application, the RBF neural network was not as effective as the BP neural network for feature extraction of numerical changes. Therefore, the BP neural network is to be preferred when encountering a similar problem.

6. Conclusions

Different amounts of refrigerant will produce different temperature change data. After data cleaning and pretreatment, a model was established and trained to obtain a model that can predict refrigerant amount according to changes in temperature. Using this model, the relation between refrigerant amount and relevant parameters (temperature variation, cold storage temperature, etc.) can be established, in which the amount of refrigerant is the dependent variable, and the relevant collection parameters are independent variables. The amount of refrigerant can be predicted by studying the changes in relevant parameters through experiments. In this experiment, it was found that the unknown amount of refrigerant was most likely 32.5 g.

In practical production and in life, this model can be used to predict the amount of refrigerant in refrigerators with the best performance and to test and properly maintain refrigerators that have been sold or whose refrigerant needs replenishing.

Data Availability

The raw data were preprocessed as shown in Figure 2.

Conflicts of Interest

The authors declare that there are no conflicts of interest regarding the publication of this paper.

Acknowledgments

This research was funded by the National Science Foundation of China (nos. 51674121 and 61702184), the Returned Overseas Scholar Funding of Hebei Province (no. C2015005014), the Hebei Key Laboratory of Science and Application, and Tangshan Innovation Team Project (no. 18130209B).

References

[1] M. Asadpour and M. T. Dashti, "Scalable, privacy preserving radio-frequency identification protocol for the internet of things," *Concurrency and Computation: Practice and Experience*, vol. 27, no. 8, pp. 1932–1950, 2015.

[2] T. Nagato, H. Shibuya, H. Okamoto, and T. Koezuka, "Machine learning technology applied to production lines: image recognition system," *Fujitsu Scientific & Technical Journal*, vol. 53, no. 4, pp. 52–58, 2017.

[3] A. Al-Fuqaha, M. Guizani, M. Mohammadi, M. Aledhari, and M. Ayyash, "Internet of things: a survey on enabling technologies, protocols, and applications," *IEEE Communications Surveys & Tutorials*, vol. 17, no. 4, pp. 2347–2376, 2015.

[4] S. Sicari, A. Rizzardi, L. A. Grieco, and A. Coen-Porisini, "Security, privacy and trust in internet of things: the road ahead," *Computer Networks*, vol. 76, pp. 146–164, 2015.

[5] A. Botta, W. de Donato, V. Persico, and A. Pescapé, "Integration of cloud computing and internet of things: a survey," *Future Generation Computer Systems*, vol. 56, pp. 684–700, 2016.

[6] J. Lin, W. Yu, N. Zhang, X. Yang, H. Zhang, and W. Zhao, "A survey on Internet of things: architecture, enabling technologies, security and privacy, and applications," *IEEE Internet of Things Journal*, vol. 4, no. 5, pp. 1125–1142, 2017.

[7] T. Zhang, Q. Li, and F. Ma, "Remote control system of smart appliances based on wireless sensor network," in *Proceedings of the 2013 25th Chinese Control and Decision Conference (CCDC)*, pp. 3704–3709, Guiyang, China, May 2013.

[8] T. Takenaka, Y. Yamamoto, K. Fukuda, A. Kimura, and K. Ueda, "Enhancing products and services using smart appliance networks," *CIRP Annals*, vol. 65, no. 1, pp. 397–400, 2016.

[9] S. Nistor, J. Wu, M. Sooriyabandara, and J. Ekanayake, "Capability of smart appliances to provide reserve services," *Applied Energy*, vol. 138, pp. 590–597, 2015.

[10] A. Coskun, G. Kaner, and İ. Bostan, "Is smart home a necessity or a fantasy for the mainstream user? A study on users' expectations of smart household appliances," *International Journal of Design*, vol. 12, no. 1, pp. 7–20, 2018.

[11] J. Wan, S. Tang, Z. Shu et al., "Software-defined industrial Internet of things in the context of industry 4.0," *IEEE Sensors Journal*, vol. 16, no. 20, pp. 7373–7380, 2016.

[12] M. Tosun, B. Doğan, M. M. Öztürk, and L. B. Erbay, "Integration of a mini-channel condenser into a household refrigerator with regard to accurate capillary tube length and refrigerant amount," *International Journal of Refrigeration*, vol. 98, pp. 428–435, 2019.

[13] A. Pisano, S. Martínez-Ballester, J. M. Corberán, and A. W. Mauro, "Optimal design of a light commercial freezer through the analysis of the combined effects of capillary tube diameter and refrigerant charge on the performance," *International Journal of Refrigeration*, vol. 52, pp. 1–10, 2015.

[14] A. Maiorino, C. Aprea, M. G. Del Duca, R. Llopis, D. Sánchez, and R. Cabello, "R-152a as an alternative refrigerant to R-134a in domestic refrigerators: an experimental analysis," *International Journal of Refrigeration*, vol. 96, pp. 106–116, 2018.

[15] M. Deymi-Dashtebayaz, M. Farahnak, M. Moraffa, A. Ghalami, and N. Mohammadi, "Experimental evaluation of refrigerant mass charge and ambient air temperature effects on performance of air-conditioning systems," *Heat and Mass Transfer*, vol. 54, no. 3, pp. 803–812, 2018.

[16] T. Wang, B. Gu, B. Wu, H. Ma, and C. Qian, "Modeling for multi-pass parallel flow condenser with the effect of refrigerant mal-distribution," *International Journal of Refrigeration*, vol. 60, pp. 234–246, 2015.

[17] Y. Li, K. Wang, W. Wu, X. Xia, B. Niu, and Z. Zhang, "Study on the effect of refrigerant distributing nonuniformity on the performance of falling-film evaporator with liquid recirculation system," *International Journal of Refrigeration*, vol. 82, pp. 199–211, 2017.

[18] E. Björk and B. Palm, "Performance of a domestic refrigerator under influence of varied expansion device capacity, refrigerant charge and ambient temperature," *International Journal of Refrigeration*, vol. 29, no. 5, pp. 789–798, 2006.

[19] B. O. Bolaji, A. E. Adeleke, M. R. Adu, M. U. Olanipekun, and E. Akinnibosun, "Theoretical investigation of energy-saving potential of eco-friendly R430A, R440A and R450A refrigerants in a domestic refrigerator," *Iranian Journal of Science and Technology, Transactions of Mechanical Engineering*, vol. 43, no. 1, pp. 103–112, 2019.

[20] J. Platt, *A Resource-Allocating Network for Function Interpolation*, MIT Press, Cambridge, MA, USA, 1991.

Hindawi
Complexity
Volume 2020, Article ID 8543131, 9 pages
https://doi.org/10.1155/2020/8543131

Research Article

Multifractional Brownian Motion and Quantum-Behaved Partial Swarm Optimization for Bearing Degradation Forecasting

Song Wanqing,[1] **Xiaoxian Chen**,[1] **Carlo Cattani**,[2] **and Enrico Zio**[3]

[1]*School of Electronic and Electrical Engineering, Shanghai University of Engineering Science, No. 333 Longteng Road, Songjiang District, Shanghai 201620, China*
[2]*Engineering School (DEIM), University of Tuscia, Viterbo, Italy*
[3]*Energy Department, Politecnico di Milano, Campus Bovisa, Via La Masa 34/3, Milano, MI 20156, Italy*

Correspondence should be addressed to Song Wanqing; swqls@126.com

Received 15 September 2019; Accepted 20 December 2019; Published 31 January 2020

Academic Editor: Michele Scarpiniti

Gradual degradation of the bearing vibration signal is usually studied as a nonstationary stochastic time series. Roller bearings are working at high speed in a heavy load environment so that the combination of bearing faults gradually degraded during the rotation might lead to unpredicted catastrophic accidents. The degradation process has the property of long-range dependence (LRD), so that the fractional Brownian motion (fBm) is taken into account for a prediction model. Because of the dramatic changes in the bearing degradation process, the Hurst exponent that describes the fBm will change during the degradation process. A priori Hurst value of the conventional fBm in the prediction is fixed, thus inducing a minor accuracy of the prediction. To avoid this problem, we propose an improved prediction method. Based on the following steps, at the initial data processing, a skip-over factor is selected as the characteristics parameter of the bearing degradation process. A multifractional Brownian motion (mfBm) replaces the fBm for the degradation modeling. We will show that also our mfBm has the same property of long-range dependence as the fBm. Moreover, a time-varying Hurst exponent $H(t)$ is taken to replace the constant H in fBm. Finally, we apply the quantum-behaved partial swarm optimization (QPSO) to optimize $H(t)$ for a finite interval. Some tests and corresponding experimental results will show that our model QPSO + mfBm have a much better performance on the prediction effect than fBm.

1. Introduction

ROLLER bearings represent the largest application of rotating mechanisms. Since they are usually working in high speed and heavy load environment, then bearing faults might gradually lead to some catastrophic accidents [1]. Therefore, it is important to study the long-range time forecasting of the bearing life to optimize the service assistance [2].

There already exist some models for the analysis of bearing faults. The grey model (GM) was applied to forecast bearing vibration signal [3]. However, under heavy load conditions, the accuracy of forecasting for the bearing vibration signal is usually influenced by many factors, such as deterioration [4], pitting, cracking, etc. Moreover, the GM model lacks a reflection on the randomness of the data; it implies that the GM model should be enhanced. Because of the lacking information, the GM approach only considers the size of the instant forecasting value. Also the hidden Markov model (HMM) has been applied to forecast the bearing fault [5, 6]. But the disadvantage of the HMM is that a state of the HMM depends only on the state itself, and this dependence is time-independent. Besides, the HMM can only predict discrete (step) catastrophe failures and cannot forecast the trend of continuous fault changes. The error back-propagation (BP) algorithm is also widely used in forecasting bearing vibration, but the selection structure of the BP algorithm is not single, its training efficiency is not high, so that overcomplicated structure may cause the overfitting phenomenon. As a result, it is impossible to achieve accurate forecasting results [7]. Compared to the artificial neural network algorithm [8], support vector

machine (SVM) is based on the structural risk minimization principle, which has a better performance [9]. However, the SVM needs to set the penalty parameter that makes the prediction model more complex. Moreover, the calculation of the remaining useful life for the bearing is crucial. For this reason, some methods were developed, such as the Gaussian process (GP) model [10] and the recursive maximum likelihood estimation (RMLE) [11]. When using the RMLE to solve the unknown noise in the system caused by nonstationary operating conditions, the noise value is relatively large. The shortcoming of the GP is that the prediction results are performed on a relatively limited data set. Such studies employed the regression-based adaptive predictive models [12], the exponential model [13], and the Extended Kalman Filtering [14].

Since the bearing failure is a slowly varying process, the degradation process has a long-range time memory. The past states can affect the future degradation states. This property is called long-range dependent (LRD). There are two kinds of methods to identify whether the process is of LRD. The autocorrelation function (ACF) is nonintegrable [15], or the power spectrum density (PSD) of the process is divergent at the origin [16].

Fractional Brownian motion (fBm) is a nonstationary stochastic process with fractal properties of self-similarity and LRD [17] and is widely applied in many forecasting problems, like, e.g., image processing [18] and network traffic analysis [19]. FBm has also some applications in degradation modeling and remaining useful life prediction [20]. Zhang et al. [21] use fBm to describe the degradation of the blast furnace wall. Qin and Lin [22] combine fBm with Delft3D, WRF model, and GIS to predict the trajectory of harmful algal blooms. Xi et al. [23] apply fBm to predict the remaining useful life of lithium batteries. Song et al. [24] use fBm for short-term power load forecasting. Gupta et al. [25] establish the relationship between DCT and discrete fBm to provide a theoretical basis for applying DCT to fBm signal reconstruction. FBm can be considered as a generalized form of the Brownian Motion (BM). Consequently, the forecasting results of the fBm model are more flexible than those obtained from the BM model. FBm is characterized by one parameter called Hurst exponent. The expression range of Hurst exponent is $0 < H < 1$. Except for $H = 0.5$, fBm is an LRD model. Under the condition of $H = 0.5$, fBm degenerates to the BM, which is a model with independent increment process.

However, the conventional fBm degradation model has some restrictions. In fact, in the process of bearing degradation, the degradation process at the early stage of the fault is relatively stable, so that there will be a huge oscillation in the later stage. The dramatic change for the bearing degradation process indicates that the Hurst exponent will change at different stages of degradation, thus implying that H usually has multiple values. The Hurst value of fBm is a constant and will not change again during the current prediction phase.

In order to solve this problem, we propose an improved model called multifractional Brownian motion (mfBm). Compared with fBm, the fixed exponent H will be replaced by a time-varying exponent $H(t)$. Moreover the quantum-behaved particle swarm optimization (QPSO) will be proposed to optimize the fundamental parameters [26]. The main idea of QPSO is to optimize the search strategy of the particle swarm optimization (PSO) to get the global optimum solution.

In order to extract the data from bearing degradation, the skip-over factor is proposed to measure the tendency of the gradual collapse [27]. In our model, we propose an integrated approach for the mfBm and QPSO for forecasting a bearing skip-over series. The computed H for the skip-over series will be used to deduce parameters in the mfBm model. The QPSO will be used to get the global optimal $H(t)$ value in the mfBm model; the optimal can be used to make the accurate forecasting. Finally, we adopt mfBm and mfBm-QPSO models for the forecasting experiment. Monte Carlo method is used to show that the combination of mfBm and QPSO is superior to the fBm model of bearing degradation forecasting.

This paper is organized as follows. Section 2 describes the fBm model to forecast the bearing skip-over series. The optimization of $H(t)$ by QPSO for mfBm model is given in Section 3. Section 4 introduces the computation of the skip-over factor. Some examples and experimental tests are given in Section 5, together with a discussion on our model compared with previous ones. Conclusion is given in Section 6.

2. The Forecasting Model of fBm

Let the fBm model be denoted by $B_H(t)$. Thus, $B_H(t)$ is defined as follows [28]:

$$\begin{aligned} B_H(0) &= b_0, \\ B_H(t) - B_H(0) &= \frac{1}{\Gamma(H + (1/2))} \\ &\quad \times \left\{ \int_{-\infty}^{0} \left[(t-s)^{H-(1/2)} - (-s)^{H-(1/2)} \right] dB(s) \right. \\ &\quad \left. + \int_{0}^{t} (t-s)^{H-(1/2)} dB(s) \right\}, \end{aligned} \tag{1}$$

where $\Gamma(.)$ is the gamma function, τ is the time lag. H is the Hurst exponent. Reported methods for estimating H are variance method, absolute value method, curve fitting method, rescaled range analysis (R/S), periodic graph method, and wavelet method [28–31]. Here R/S is used to estimate the Hurst exponent. The time series of length T is divided into k subinterval of length n, where $T = kn$. The average value of each subinterval composes a new series $Y(i)$. The difference between the maximum and minimum values of the new series and the standard of deviation $S^2(n)$ are calculated. Then the ratio between the two values is as follows:

$$\left(\frac{R}{S}\right)_n = \frac{\left(\max\left(Y_i\right) - \min\left(Y_i\right)\right)}{\sqrt{S^2(n)}},$$
$$Y(i) = \sum_{j=1}^{n} X_j - \overline{X_n}, \tag{2}$$

where $\overline{X_n}$ and $S^2(n)$ are the mean and variance of the subinterval, respectively. The value of R/S looks like cn^H as $n \longrightarrow \infty$, where c is a constant independent of n.

The increment process of the fBm called fractional Gaussian noise (fGn) is stationary. The ACF of the fGn is expressed as

$$R_H(\tau) = \frac{\sigma^2 \varepsilon^{2H-2}}{2} \times \left[\left(\left(\frac{|\tau|}{\varepsilon} + 1\right)^{2H} - 2\left(\frac{|\tau|}{\varepsilon}\right)^{2H} + \left(\frac{|\tau|}{\varepsilon} - 1\right)^{2H}\right], \tag{3}$$

where $\varepsilon > 0$ is used by smoothing fBm so that the smoothed fBm is differentiable. σ^2 is the intensity of the fGn, and it is written by

$$\sigma^2 = \Gamma(1 - 2H)\frac{\cos(\pi H)}{\pi H}. \tag{4}$$

Then the fBm can generate a specific stochastic time series as the prediction for next power load series. The stochastic differential equations (SDEs) [32, 33] of the prediction model is written by

$$\mathrm{d}X_t = \mu X_t \mathrm{d}t + \sigma X_t \mathrm{d}B_H(t), \tag{5}$$

where μ is the drift parameter, σ is the diffusion coefficient. The Hurst exponent is the most significant parameter in fBm; once it is obtained, the two parameters μ and σ of the fBm model can be calculated by maximum likelihood estimation (MLE) [34, 35].

Discretize (5), the increments of the series are in the form

$$\Delta X_t = \mu X_t \Delta t + \sigma X_t w(t)(\Delta t)^H, \tag{6}$$

where $w(t)$ is unit white noise. The prediction model of the fBm is rewritten as

$$X_{t+1} = \mathrm{X}_t + \mu X_t \Delta t + \sigma X_t w(t)(\Delta t)^H. \tag{7}$$

In fBm, the Hurst exponent H is a constant, and it will not change again during the current prediction phase. However, as the degradation progresses, the Hurst exponent is time-varying; thus, the series generated by (6) cannot characterize the nonlinear trend. Therefore, fBm is replaced by the mfBm. For mfBm, $H(t)$ will change at different stages of degradation, and it is a time-varying parameter. To further improve the prediction accuracy, the QPSO is used to optimize the $H(t)$ of the mfBm.

3. Quantum-Behaved Particle Swarm for the Hurst Exponent Optimization

The QPSO introduces quantum computing into the PSO, so that each particle in the space has the quantum behavior. Since each particle of the PSO moves in the search space with a velocity vector to find its local optimum and the global optimum, the disadvantage of the PSO is that it will be trapped in its optimal local solution and cannot reach the optimal global one. To avoid this problem, the particles in QPSO have a probability to appear anywhere in space; thus, QPSO has the ability to avoid falling into a locally optimal solution by searching a globally optimal solution. It has also fewer parameters to be adjusted. The optimization computation of $H(t)$ by QPSO will be exhibited as follows.

Clerc and Kennedy [36] have proved that each particle must converge to the local attractor $p_{i,j}$ to provide the convergence for the PSO algorithm. They defined it as

$$p_{i,j}(t) = \varphi P_{i,j}(t) + (1 - \varphi)P_{g,j}(t), \quad \varphi \sim U(0,1). \tag{8}$$

Comparing with the convergence of the PSO, the QPSO defines one-dimensional delta potential well for each dimension at the point $p_i(t)$, and each particle has a quantum behavior, which can be described by the Schrödinger [37]. The distribution function of the particle position is given as

$$F\left(H_{ij}(t+1)\right) = e^{-2\left|p_{i,j}(t) - H_{i,j}(t+1)\right|/L_{i,j}(t)}. \tag{9}$$

where $L_{i,j}(t)$ is the standard deviation of the distribution. The position of each particle can be obtained by [38]

$$H_{i,j}(t+1) = p_{i,j}(t) \pm \frac{L_{i,j}(t)}{2}\ln\left(\frac{1}{u}\right), \tag{10}$$

where $u \sim U(0,1)$, $m(t)$ is defined as the average of a global mean best position:

$$m(t) = \left(m_1(t), m_2(t), \ldots, m_2(t)\right) = \left(\frac{1}{N}\sum_{i=1}^{N} P_{i,1}(t), \frac{1}{N}\sum_{i=1}^{N} P_{i,2}(t), \ldots, \frac{1}{N}\sum_{i=1}^{N} P_{i,D}(t), \right), \tag{11}$$

where N is the population size, and p_i is the local best position of ith particle. The values of $L_{i,j}(t)$ and the position $H_{i,j}(t+1)$ are evaluated as follows:

$$L_{i,j}(t) = 2\beta \cdot \left|m_j(t) - H_{i,j}(t)\right|,$$
$$H_{i,j}(t+1) = p_{i,j}(t) \pm \beta \cdot \left|m_j(t) - H_{i,j}(t)\right| \cdot \ln\left(\frac{1}{u}\right), \tag{12}$$

where $\beta < 1.781$, which is the only parameter that can guarantee the convergence of the particle. Continuing with the previous example, we use the previous 30 point to forecast next 30 point.

(1) Initialize H, let the number of particles $N = 20$, and each $H_{i,j}(t) = 2 * \mathrm{randint}(1, 1, [0, 2])$ with dimension equal to 3, and the number of iterations $t = 20$. The 20 particles of H is shown in Table 1. Initialize the current position, individual optical positions, and the population's global optimal position. Then each particle is used to find the global optimal solution.

(2) Initialize the local optimal position $P_{i,j}(0)$ for the current position $H_{i,j}(0)$. The mean optimal position

Table 1: The 20 particles of H.

0.7513	0.8909	0.1493	0.8143	0.1966
0.2551	0.9593	0.2575	0.2435	0.2511
0.5060	0.5472	0.8407	0.9293	0.6160
0.6991	0.1386	0.2543	0.3500	0.4733

$m_j(t)$ is computed by (11). Select a suitable value $\hat{I}^2$ and evaluate the objective function value $f(H_{i,j}(t))$.

(3) The local attractor $p_{i,j}(t)$ is computed by (8). If $\text{rand}(0,1) > 0.5$, then

$$H_{i,j}(t+1) = p_{i,j}(t) + \beta \cdot \left| m_j(t) - H_{i,j}(t) \right| \cdot \ln\left(\frac{1}{u}\right), \quad (13)$$

else

$$H_{i,j}(t+1) = p_{i,j}(t) - \beta \cdot \left| m_j(t) - H_{i,j}(t) \right| \cdot \ln\left(\frac{1}{u}\right). \quad (14)$$

(4) The optimal position $p_{i,j}(t)$ of each particle $H_{i,j}(t)$ is updated by $P_{g,j} = \arg\min_{P_i}(P_i)$.

(5) The global optimal position is given by $H_{gbest} = \arg\min_{P_g}(P_g)$.

(6) End of iteration.

During the process of updating the particle's position, it is necessary to have a comparison between the fitness value of the current individual position of each particle and the fitness value of the global optimal position. The loop iteration is used to find the global optimal solution. Once the iteration number or minimum error is reached in QPSO, the optimal approximation power curve for the H can be found. This effective value of H parameter will be used by the mfBm model for the next data series forecasting.

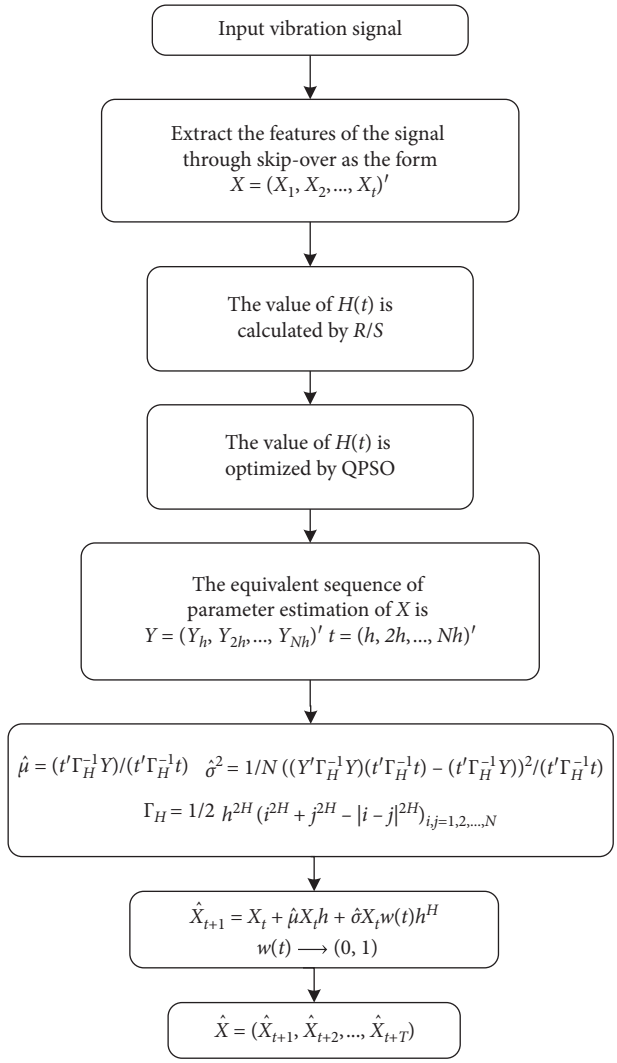

Figure 1: The prediction flowchart of the QPSO + mfBm.

4. Computing the Skip-Over Series

The dimensionless parameter skip-over factor is essentially an improvement of variance. Variance is an indicator related to energy. Energy-related indices will be disturbed by drastic operating load changes. The skip-over factor reduces the sensitivity to energy; thus, the gradual degradation trend can be reflected better. The skip-over factor is the average of the sum of squares of the difference between the data and the mean of the minimum and the measure of the difference between the source data and the expected value of the minimum value. Based on the whole-period sampling, the vibration waveforms of bearings often show skip-over characteristic, such as the failure of foundation loosening. With the faults deteriorating, the skip-over factor also changes. The essence of the skip-over factor is amplitude modulation of a waveform. The computation of skip-over factor is as follows:

(1) Firstly, the bearing vibration signals are sampled and normalized:

$$x_i = \frac{kx_i}{|x_{\max}|}, \quad k > 1,\ i = 1, 2, \ldots, n, \quad (15)$$

where k is a scale factor.

(2) The vibration signals of the bearing after normalization are divided into $x_{11}, x_{12}, \ldots, x_{1m}; \ldots; x_{n1}, x_{n2}, \ldots, x_{nm}$.

(3) Let $m = 1024$ [27], among set $x_{11}, x_{12}, \ldots, x_{1m}$, extract minimum value $x_{\min} = x_{1,p}$, $1 < p < m$; then get the average value for all m sets:

$$\overline{x} = \frac{1}{n}\sum_{i=1}^{n} x_{ip}. \quad (16)$$

(4) Calculated variance

$$D_x = \frac{1}{n}\sum_{i=1}^{n}\left(x_{ip} - \overline{x}\right)^2. \quad (17)$$

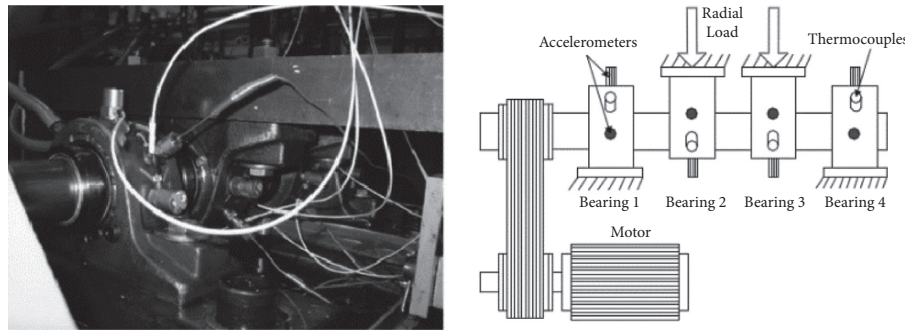

Figure 2: Bearing test rig.

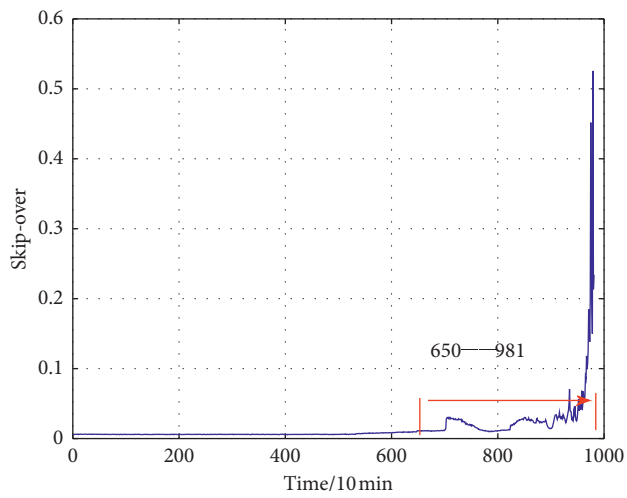

Figure 3: Skip-over series for full-life tendency of bearing 7 days.

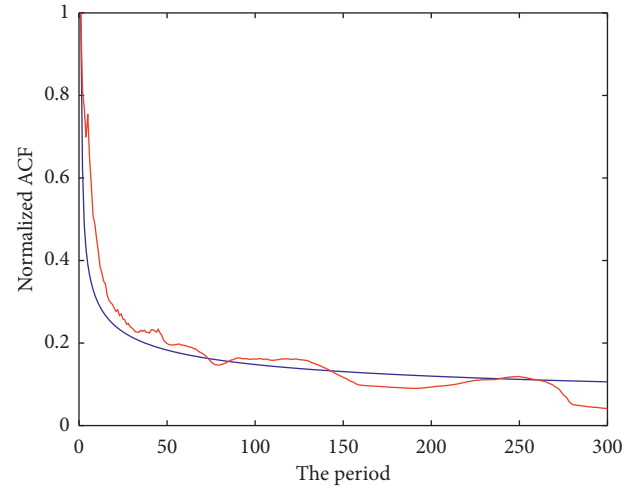

Figure 4: The fitting ACF curve. Red line is the ACF of real data; blue line is the ACF of the theoretical curve.

Define D_x as the skip-over factor.

Figure 1 shows the prediction flowchart of the QPSO + mfBm.

5. Experiment

The actual data was generated from accelerated life test of roller bearing Center for Intelligent Maintenance Systems (IMS), University of Cincinnati. Four Rexnord ZA-2115 double-row bearings were installed on the shaft as shown in Figure 2. The shaft is driven by an AC motor and coupled by rub belts. Accelerometers were installed on the bearing housing. The rotation speed of the shaft was 2000 rpm, the sampling rate was set at 20 kHz, and the data length was 20,480 points. Bearing 1 of vibration signals with an outer race failure is selected.

Figure 3 shows the full-lifecycle tendency of bearing within 7 days of the skip-over series. The skip-over series has relative stability and sensitivity to initial fault. The initial fault appears about 7000 min. Here the ACF method is used to calculate the Hurst exponent of the series. Denote the measured ACF of the skip-over series by $r(k)$, $R(k)$ be the modeled ACF. For simplicity, we use the normalized ACF. Equation (7) is rewritten as

$$R(k) = \frac{1}{2}\left[(k+1)^{2H} - 2k^{2H} + |k-1|^{2H}\right]. \quad (18)$$

Table 2: The parameters value of model.

Model	μ	σ
FBm	0.1345	321.9634
PSO + mfBm	78.3264	$4.2128e+04$
QPSO + mfBm	97.6945	$2.7573e+05$

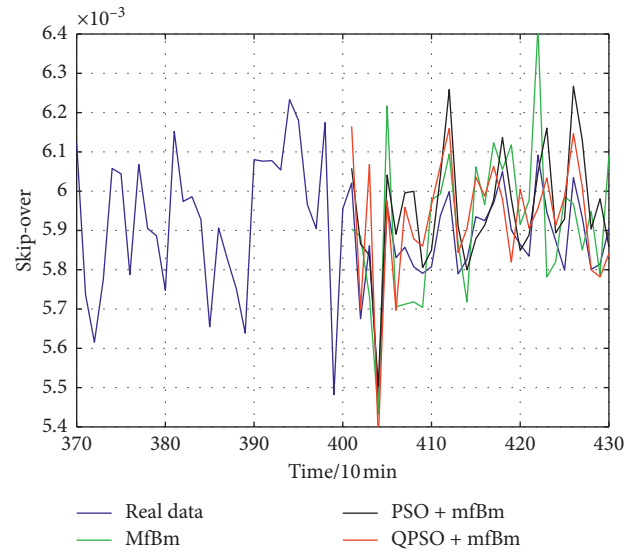

Figure 5: Forecasting with different models.

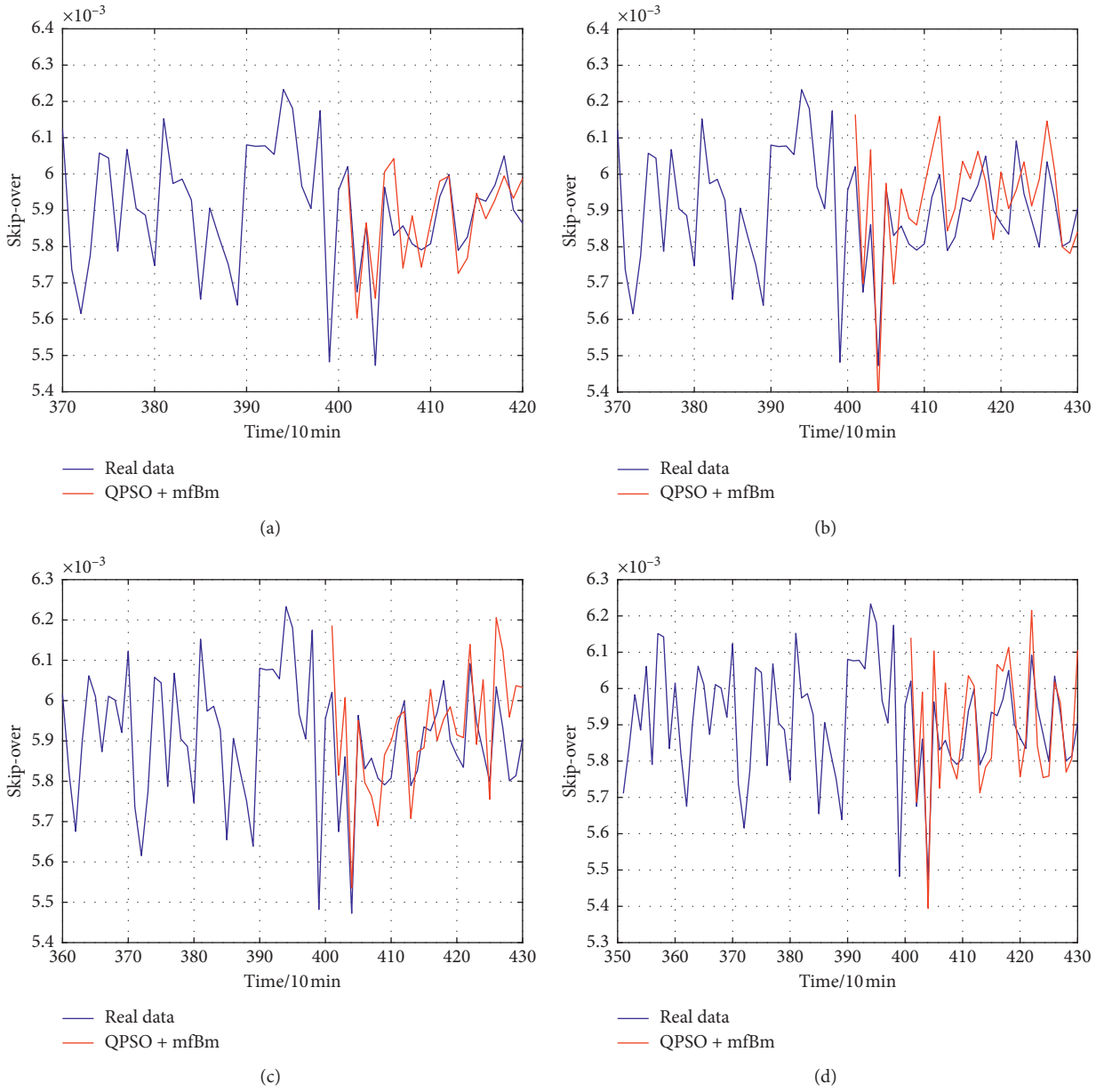

Figure 6: Forecasting skip-over series difference step long.

Let $M = E[(R - r)^2]$ be the mean square errors. As the M is minimized, the corresponding H value is the Hurst exponent. Figure 4 shows the fitting ACF curve, the calculated Hurst exponent is $H = 0.849$. The high fit of the measured curve to the model curve also indicates that the skip-over series is in accordance with the fBm.

The H of this skip-over series is $0.5 < H < 1$. We focus on fBm, PSO + mfBm, and QPSO + mfBm models. The value of each 30 points is selected to calculate one H, the model parameters μ, and σ of the fBm change with H. Then, we can deduce $\widehat{X}_{t+1} \longleftarrow \widehat{X}_t$ by (6), the fBm can generate the approximation series. The parameter estimation results are shown in Table 2. In this prediction model, the estimation of parameters is affected by two aspects: the observed value and the time interval. The feature extraction process is to integrate multiple points of the original vibration signal into one point, that is, skip-over factor. After feature extraction, the values of skip-over factor are determined, and the time interval is changed. When the time interval is small, the calculated parameter values will increase. The larger the time interval, the smaller the corresponding parameter values. Here, the time interval is set as $\Delta t = 0.1$, resulting in a large calculated value. Figure 5 shows the prediction by three models. In the fBm prediction, the average relative error of fBm is 4.0%. In PSO + mfBm prediction, the average relative error of mfBm is 3.2%. In QPSO + mfBm prediction, the average relative error of the QPSO + mfBm can be reduced to 2.5%. Obviously, QPSO + mfBm has performed better on prediction accuracy.

In order to obtain the best prediction accuracy, different combinations of observation data length and prediction step

Table 3: The parameter value of QPSO + MfBm

Figure 1	μ	σ
6(a)	97.6945	$2.7573e+05$
6(b)	97.6945	$2.7573e+05$
6(c)	106.8199	$4.6921e+05$
6(d)	80.4281	$8.8612e+07$

Table 4: Average relative error of different steps.

a (%)	b (%)	c (%)	d (%)
2.68	2.49	2.59	2.54

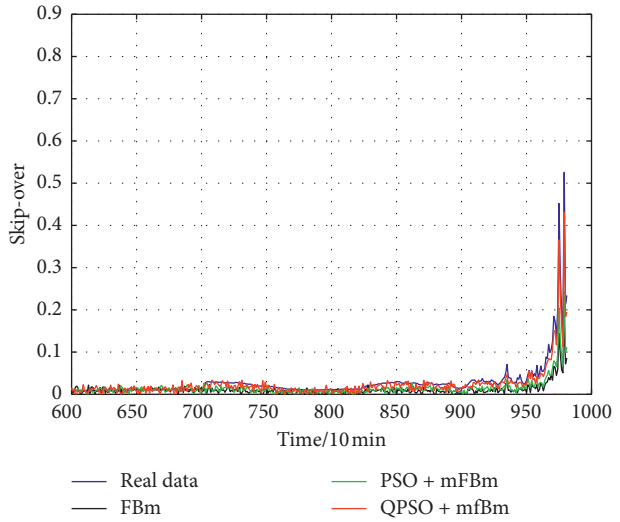

Figure 7: Forecasting bearing skip-over series by two models.

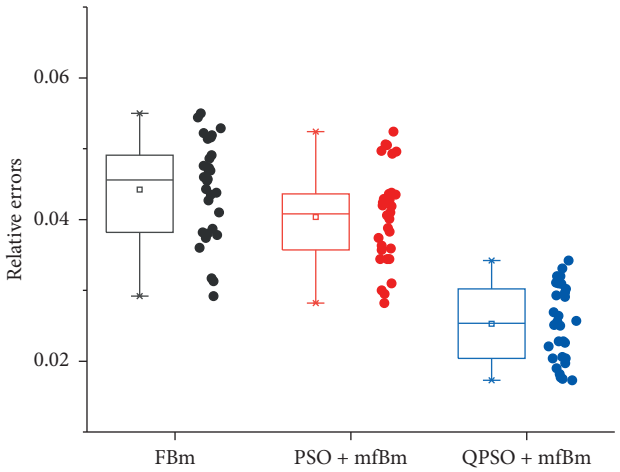

Figure 8: Box-scatter plot of relative error distribution in three models.

length are tested. Figures 6(a)–6(d) show that 30 points to forecast next 20 points, 30 points to forecast next 30 points, 40 points to forecast next 30 points, 50 points to forecast the next 30 points, respectively. The parameter estimation results are shown in Table 3 and the average relative error is shown in Table 4.

Obviously, 30 points predict next 30 points has minimum average error in statistic meaning. Figure 7 shows prediction results by three models from 600th to 981th points.

Figure 8 shows a box-scatter plot describing the relative error distribution of the forecasting skip-over series. The mean relative error of the QPSO + mfBm is lower than the other two models. Meanwhile, the relative error distribution of the QPSO + mfBm is more concentrated than the other two models; it means the QPSO + mfBm has lower relative error and stable prediction performance.

6. Conclusion

In this paper, a hybrid framework (mfBm and QPSO) for predicting a bearing skip-over series is proposed. We have used the ACF method to estimate the Hurst value of the entire degradation process. The fitting results show that the degradation process of the bearing has the LRD property; moreover, the fBm-based model gives the more reasonable description of the process. However, we have shown that the fBM-based model can be significantly improved by adopting the QPSO + mfBm. By using this improved method, we have shown that the predicted value is more consistent with the actual value, and the average relative error is significantly lower. In terms of relative error distribution, the QPSO + mfBm is more efficient. The experimental results have also shown that the improvement to the LRD prediction method for fBm is effective.

Data Availability

The data used to support the findings of this study are available at (https://ti.arc.nasa.gov/tech/dash/groups/pcoe/prognostic-data-repository/#bearing).

Conflicts of Interest

The authors declare that they have no conflicts of interest.

Acknowledgments

This project is supported in part by Shanghai Natural Science Foundation of China under the Project Grant nos. 14ZR141850 and 17ZR1411900, and Shanghai University of Engineering Science under the Project Grant no. 18XJC002.

References

[1] Z. Wang, L. Zheng, J. Wang, and W. Du, "Research on novel bearing fault diagnosis method based on improved krill herd algorithm and kernel extreme learning machine," *Complexity*, vol. 2019, Article ID 4031795, 19 pages, 2019.

[2] L. Guo, N. Li, F. Jia, Y. Lei, and J. Lin, "A recurrent neural network based health indicator for remaining useful life prediction of bearings," *Neurocomputing*, vol. 240, no. 5, pp. 98–109, 2017.

[3] X. Ma and Z. B. Liu, "Research on the novel recursive discrete multivariate grey prediction model and its applications," *Applied Mathematical Modelling*, vol. 40, no. 7-8, pp. 4876–4890, 2016.

[4] Z. Wang, L. Zheng, W. Du et al., "Application of an improved ensemble local mean decomposition method for gearbox composite fault diagnosis," *Complexity*, vol. 2019, Article ID 1564243, 17 pages, 2019.

[5] Z. Liu, Q. Li, X. Liu, and C. Mu, "A hybrid LSSVR/HMM-based prognostic approach," *Sensors*, vol. 13, no. 5, pp. 5542–5560, 2013.

[6] Y. Gao, F. Villecco, M. Li, and W. Song, "Multi-scale permutation entropy based on improved LMD and HMM for rolling bearing diagnosis," *Entropy*, vol. 19, no. 4, p. 176, 2017.

[7] R. Razavi-Far, M. Farajzadeh-Zanjani, and M. Saif, "An integrated class-imbalanced learning scheme for diagnosing bearing defects in induction motors," *IEEE Transactions on Industrial Informatics*, vol. 13, no. 6, pp. 2758–2769, 2017.

[8] Z. Wang, L. Zheng, W. Du et al., "A novel method for intelligent fault diagnosis of bearing based on capsule neural network," *Complexity*, vol. 2019, Article ID 6943234, 17 pages, 2019.

[9] S. J. Dong, J. L. Sheng, Z. Liu, L. Zhong, and H. B. Wei, "Bearing remain life prediction based on weighted complex SVM models," *Journal of Vibroengineering*, vol. 18, no. 6, pp. 3636–3653, 2016.

[10] P. Boskoski, M. Gasperin, D. Petelin, and D. Juricic, "Bearing fault prognostics using rényi entropy based features and Gaussian process models," *Mechanical Systems and Signal Processing*, vol. 52-53, no. 2, pp. 327–337, 2015.

[11] X. Liu, P. Song, C. Yang, C. Hao, and W. Peng, "Prognostics and health management of bearings based on logarithmic linear recursive least-squares and recursive maximum likelihood estimation," *IEEE Transactions on Industrial Electronics*, vol. 65, no. 2, pp. 1549–1558, 2018.

[12] W. Ahmad, S. A. Khan, and J.-M. Kim, "A hybrid prognostics technique for rolling element bearings using adaptive predictive models," *IEEE Transactions on Industrial Electronics*, vol. 65, no. 2, pp. 1577–1584, 2018.

[13] N. Li, Y. Lei, J. Lin, and S. X. Ding, "An improved exponential model for predicting remaining useful life of rolling element bearings," *IEEE Transactions on Industrial Electronics*, vol. 62, no. 12, pp. 7762–7773, 2015.

[14] R. K. Singleton, E. G. Strangas, and S. Aviyente, "Extended kalman filtering for remaining-useful-life estimation of bearings," *IEEE Transactions on Industrial Electronics*, vol. 62, no. 3, pp. 1781–1790, 2015.

[15] J. Beran, *Statistics for Long Memory Processes: Monographs on Statistics and Applied Probability*, Chapman & Hall, New York, NY, USA, 1994.

[16] B. B. Mandelbrot, *Multifractals and 1/f Noise*, Springer, Berlin, Germany, 1999.

[17] H.-T. Yau, S.-Y. Wu, C.-L. Chen, and Y.-C. Li, "Fractional-order chaotic self-synchronization-based tracking faults diagnosis of ball bearing systems," *IEEE Transactions on Industrial Electronics*, vol. 63, no. 6, pp. 3824–3833, 2016.

[18] I. Zachevsky and Y. Y. Zeevi, "Single-image superresolution of natural stochastic textures based on fractional brownian motion," *IEEE Transactions on Image Processing*, vol. 23, no. 5, pp. 2096–2108, 2014.

[19] C. Vamos, M. Craciun, and N. Suciu, "Automatic algorithm to decompose discrete paths of fractional brownian motion into self-similar intrinsic components," *The European Physical Journal B*, vol. 88, no. 10, pp. 1–10, 2015.

[20] X. Xi, M. Chen, and D. Zhou, "Remaining useful life prediction for degradation processes with memory effects," *IEEE Transactions on Reliability*, vol. 66, no. 3, pp. 751–760, 2017.

[21] H. Zhang, M. Chen, X. Xi, and D. Zhou, "Remaining useful life prediction for degradation processes with long-range dependence," *IEEE Transactions on Reliability*, vol. 66, no. 4, pp. 1368–1379, 2017.

[22] R. Qin and L. Lin, "Integration of gis and a Lagrangian particle-tracking model for harmful algal bloom trajectories prediction," *Water*, vol. 11, no. 1, pp. 1–14, 2019.

[23] X. Xi, M. Chen, H. Zhang, and D. Zhou, "An improved non-markovian degradation model with long-term dependency and item-to-item uncertainty," *Mechanical Systems and Signal Processing*, vol. 105, no. 5, pp. 467–480, 2018.

[24] W. Song, C. Cattani, and C.-H. Chi, "Fractional brownian motion and quantum-behaved particle swarm optimization for short term power load forecasting: an integrated approach," *Energy*, vol. 194, Article ID 116847, 2019.

[25] A. Gupta, S. D. Joshi, and P. Singh, "On the approximate discrete klt of fractional brownian motion and applications," *Journal of the Franklin Institute*, vol. 355, no. 17, pp. 8989–9016, 2018.

[26] S. Djemame, M. Batouche, H. Oulhadj, and P. Siarry, "Solving reverse emergence with quantum pso application to image processing," *Soft Computing*, vol. 23, no. 16, pp. 6921–6935, 2019.

[27] G. Koren and D. Shasha, "Skip-over: algorithms and complexity for overloaded systems that allow skips," in *Proceedings of the 16th IEEE Real-Time Systems Symposium*, pp. 110–117, Pisa, Italy, December 1995.

[28] L. Yan, "The fractional derivative for fractional brownian local time with hurst index large than 1/2," *Mathematische Zeitschrift*, vol. 283, no. 1-2, pp. 437–468, 2016.

[29] J. Barunik and L. Kristoufek, "On hurst exponent estimation under heavy-tailed distributions," *Physica A: Statistical Mechanics and Its Applications*, vol. 389, no. 18, pp. 3844–3855, 2010.

[30] J. Kent and A. Wood, "Estimating the fractal dimension of a locally self-similar Gaussian process using increments," *Journal of the Royal Statistical Society. Series B (Methodological)*, vol. 59, no. 3, pp. 679–699, 1997.

[31] L. Lacasa, B. Luque, J. Luque, and J. C. Nuno, "The visibility graph: a new method for estimating the hurst exponent of fractional brownian motion," *EPL (Europhysics Letters)*, vol. 86, no. 3, pp. 1–5, 2009.

[32] M. Xu, L. Zhang, B. Du, L. Zhang, Y. Fan, and D. Song, "A mutation operator accelerated quantum-behaved particle swarm optimization algorithm for hyperspectral endmember extraction," *Remote Sensing*, vol. 9, no. 3, pp. 1–18, 2017.

[33] T. Xue, R. Li, M. Tokgo, J. Ri, and G. Han, "Trajectory planning for autonomous mobile robot using a hybrid improved qpso algorithm," *Soft Computing*, vol. 21, no. 9, pp. 2421–2437, 2017.

[34] J.-H. Jeon and R. Metzler, "Fractional brownian motion and motion governed by the fractional Langevin equation in confined geometries," *Physical Review E*, vol. 81, no. 2, pp. 1–13, 2010.

[35] L. Longjin, F.-Y. Ren, and W.-Y. Qiu, "The application of fractional derivatives in stochastic models driven by fractional brownian motion," *Physica A: Statistical Mechanics and Its Applications*, vol. 389, no. 21, pp. 4809–4818, 2010.

[36] M. Clerc and J. Kennedy, "The particle swarm—explosion, stability, and convergence in a multidimensional complex space," *IEEE Transactions on Evolutionary Computation*, vol. 6, no. 1, pp. 58–73, 2002.

[37] W. Li, D. H. Zhang, and Z. Sun, "Efficient fourth-order split operator for solving the triatomic reactive schrodinger

equation in the time-dependent wavepacket approach," *The Journal of Physical Chemistry A*, vol. 118, no. 42, pp. 9801–9810, 2014.

[38] M. Xi, Z. Qi, Y. Zou, G. S. V. Raghavan, and J. Sun, "Calibrating RZWQM2 model using quantum-behaved particle swarm optimization algorithm," *Computers and Electronics in Agriculture*, vol. 113, no. 4, pp. 72–80, 2015.

Hindawi
Complexity
Volume 2020, Article ID 1357853, 9 pages
https://doi.org/10.1155/2020/1357853

Research Article

Multichannel Deep Attention Neural Networks for the Classification of Autism Spectrum Disorder Using Neuroimaging and Personal Characteristic Data

Ke Niu,[1,2] **Jiayang Guo**,[3] **Yijie Pan**,[4] **Xin Gao**,[5] **Xueping Peng**,[2] **Ning Li**,[1] **and Hailong Li**[6]

[1]*Computer School, Beijing Information Science and Technology University, Beijing 100101, China*
[2]*CAI, School of Computer Science, Faculty of Engineering and Information Technology, University of Technology Sydney, Ultimo, Australia*
[3]*Department of Electrical Engineering and Computer Science, University of Cincinnati, Cincinnati, OH 45221, USA*
[4]*Ningbo Institute of Information Technology Application, CAS, Beijing, China*
[5]*Computational Bioscience Research Center (CBRC), Computer Electrical and Mathematical Sciences and Engineering (CEMSE) Division, King Abdullah University of Science and Technology (KAUST), Thuwal 23955, Saudi Arabia*
[6]*Department of Pediatrics, Cincinnati Children's Hospital Medical Center, Cincinnati, OH, USA*

Correspondence should be addressed to Jiayang Guo; guojy@mail.uc.edu, Xueping Peng; xueping.peng@uts.edu.au, and Hailong Li; hailong.li@cchmc.org

Received 12 June 2019; Revised 1 January 2020; Accepted 4 January 2020; Published 31 January 2020

Guest Editor: Gonzalo Farias

Autism spectrum disorder (ASD) is a developmental disorder that impacts more than 1.6% of children aged 8 across the United States. It is characterized by impairments in social interaction and communication, as well as by a restricted repertoire of activity and interests. The current standardized clinical diagnosis of ASD remains to be a subjective diagnosis, mainly relying on behavior-based tests. However, the diagnostic process for ASD is not only time consuming, but also costly, causing a tremendous financial burden for patients' families. Therefore, automated diagnosis approaches have been an attractive solution for earlier identification of ASD. In this work, we set to develop a deep learning model for automated diagnosis of ASD. Specifically, a multichannel deep attention neural network (DANN) was proposed by integrating multiple layers of neural networks, attention mechanism, and feature fusion to capture the interrelationships in multimodality data. We evaluated the proposed multichannel DANN model on the Autism Brain Imaging Data Exchange (ABIDE) repository with 809 subjects (408 ASD patients and 401 typical development controls). Our model achieved a state-of-the-art accuracy of 0.732 on ASD classification by integrating three scales of brain functional connectomes and personal characteristic data, outperforming multiple peer machine learning models in a k-fold cross validation experiment. Additional k-fold and leave-one-site-out cross validation were conducted to test the generalizability and robustness of the proposed multichannel DANN model. The results show promise for deep learning models to aid the future automated clinical diagnosis of ASD.

1. Introduction

Autism spectrum disorder (ASD) has been estimated to occur in more than 1.6% of children aged 8 across the United States [1]. As a chronic neurological condition, ASD is characterized by impairments in social interaction and communication, as well as by a restricted repertoire of activity and interests [2–5]. Patients with ASD exhibit different levels of impairments, ranging from above average to intellectual disability. In neuroscience, ASD remains a formidable challenge, due to their high prevalence, complexity, and substantial heterogeneity, which require multidisciplinary efforts [6–8]. Although clinical therapies have been developed to treat the symptoms, the diagnosis of ASD

remains to be a challenging task. Currently, behavior-based test is the standard clinical method for diagnosing ASD [9]. However, the diagnostic process for ASD is not only time consuming but also costly [10]. This results in a tremendous financial burden for patients' families. Meanwhile, with this lifetime ASD, the patients may have difficulties in normal socialization and working environments, increasing the overall social costs. Therefore, an automated diagnosis approach is desirable for earlier identification of ASD.

Machine learning is a promising tool for investigating the replicability of patterns across larger, more heterogeneous datasets [11–13]. For automated diagnosis of ASD, personal characteristic (PC) data, such as intelligence quotient (IQ) and Social Responsiveness Scale (SRS) score have been adopted in several studies [14–16]. In the study of ASD, IQ is a type of standard score that is derived from several standardized tests designed to assess human intelligence, and the SRS score includes a 65-item standardized questionnaire regarding behaviors that are associated with ASD [17]. ASD is highly associated with intellectual disability which is mainly measured by IQ. Meanwhile, some studies [18, 19] indicate that IQ discrepancy marks a meaningful phenotype in ASDs. In this way, IQ becomes an important biomarker to classify the ASD.

Neuroimaging data have also been investigated to explore ASD biomarkers in recent decades. To facilitate the ASD research community, Autism Brain Imaging Data Exchange (ABIDE), an international collaborative project, has collected data from over 1,000 subjects (e.g., structure MRI (sMRI), resting-state functional MRI (rs-fMRI), and PC data) and made the whole database publicly available. This provided a common platform to test hypotheses, search key biomarkers, and develop advanced statistical and machine learning algorithms. For example, Ghiassian et al. [20] proposed an automated classifier by combining the histogram of orientated gradients approach for feature extraction from sMRI and rs-fMRI data and support vector machines (SVMs) for decision making. Their method was tested on the ABIDE dataset and achieved 65.0% accuracy on hold-out set. Of late, Sen et al. [21] developed a LEFMS learner, which applies sparse autoencoder to extract features from sMRI and spatial nonstationary independent components on rs-fMRI data. SVM was the utilized to classify ASD and improved accuracy by 0.042. Katuwal et al. [22] applied a random forest classifier to classify ASD and achieved an AUC of 0.61. Adding verbal IQ and age to morphometric features, AUC was improved to 0.68. By introducing hypergraph learning technique, Zu et al. [23] proposed a novel learning method to discover complex connectivity biomarkers that are beyond the widely used region-to-region connections in the conventional brain network analysis.

Deep learning has had a profound impact on many data analytic applications, such as speech recognition, image classification, computer vision, and natural language processing [24]. Based on data-driven feature construction, deep learning provides a new direction for data analytic modelling. Over the past few years, an increasing body of the literature confirmed the success of feature construction using deep learning methods. Deep learning has been demonstrated to outperform traditional machine learning algorithms on numerous recognition and classification tasks [24–29], which inspires the researchers in the ASD community to apply deep learning approaches on ASD classification. Earlier, deep neural networks (DNNs) have been applied to identify ASD patients using rs-fMRI [26]. Their model achieved 70% on accuracy by using the functional connectivity (FC) matrix as features for model training.

Kong et al. [27] constructed individual functional brain networks using the rs-fMRI data from 182 subjects of NYU Langone Medical Center, a data site within ABIDE repository. FC features were used to represent the networks of all subjects and further ranked using F-score. Then, a stacked sparse autoencoder-based DNN model was developed. Significant performance improvement was achieved by comparing the proposed method with two existing algorithms.

More recently, an ASD-DiagNet, a joint learning procedure using an autoencoder and a single layer perceptron, was presented [28]. A data augmentation strategy was also designed for the FC features of functional brain networks based on linear interpolation of available feature vectors to ensure the robust training of the ASD-DiagNet. By evaluating the model on 1035 subjects from 17 different sites of ABIDE repository, ASD-DiagNet achieves 70.1% on the accuracy, 67.8% on sensitivity, and 72.8% on specificity in 10-fold cross validation. In the mode evaluation of individual data centers, ASD-DiagNet outperformed other state-of-the-art methods and increased the accuracy performance up to 20% with a maximum accuracy of 80%.

In this work, we aim to develop a novel deep learning model for automated diagnosis of ASD. Specifically, we proposed a multichannel deep attention neural network, called DANN, by integrating multiple layers of neural networks, attention mechanism, and feature fusion to capture the interrelationships in multimodality data (functional neuroimaging data and PC data) to distinguish ASD patients from typical development controls (TDCs). The attention mechanism-based learning is a type of deep learning which is a recent trend for understanding what part of historical information weighs more in predicting diseases [30, 31]. Taking advantage of large heterogeneous dataset from ABIDE, multiscale brain functional connectomes and PC data were obtained as the features. We systematically evaluated the diagnosis power of our multichannel DANN on ASD classification and compared the performance of the proposed model with peer machine learning models.

The rest of paper is organized as follows. Section 2 describes ASD data and multichannel deep attention neural network. The experimental setup is shown in Section 3, followed by the experimental results and discussion in Section 4. Finally, the conclusion of this work is described in Section 5.

2. Materials and Methods

2.1. Subjects. We collected preprocessed rs-fMRI and PC data from 809 subjects from publicly accessible ABIDE repository, including 408 ASD subjects and 401 TDC subjects. Detailed demographic information of subjects is listed in Table 1. The incidence of ASD between male and female

Table 1: Demographic information of 809 subjects from ABIDE.

Type	Number	Gender (M/F)	Age	FIQ	PIQ	VIQ
ASD	408	330/78	16.47 ± 6.70	110.63 ± 12.67	107.85 ± 13.41	111.17 ± 13.31
TDC	401	352/49	16.80 ± 7.80	105.28 ± 16.64	105.10 ± 17.10	104.60 ± 17.81
p value	—	0.017	0.785	<0.001	0.003	<0.001

ASD: autism spectrum disorder; TDC: typical development control; M: male; F: female; VIQ: the verbal IQ; PIQ: the performance IQ; FIQ: the full-scale IQ. The values are denoted as mean and standard deviation.

subjects is significantly different, and thus the majority of the subjects in ABIDE dataset are male. There is no significant difference between the age of ASD and TDC groups. All three IQ scores had significant difference between two groups. Later, the variables' gender, age, and three IQs were used as PC data in our ASD classification experiments.

2.2. Data Preprocessing. Each of rs-fMRI data has been preprocessed using Configurable Pipeline for the Analysis of Connectomes (CPAC) preprocessing pipeline, which includes slice timing correction, motion realignment, and intensity normalization. Nuisance variable regression was implemented through bandpass filtering and global signal regression strategies to clean confounding variations introduced by heartbeats and respiration, head motion, and low-frequency scanner drifts. Furthermore, boundary-based rigid body and FMRIB's linear and nonlinear image registration tools were used to register functional to anatomical images. Then, both functional and anatomical images were normalized to template space (MNI 152). Three scales of brain functional connectomes were extracted in this work. Mean blood oxygen-level dependent (BOLD) time-series signals for three sets of regions of interests (ROIs), i.e., atlases, including the Automated Anatomical Labeling (AAL) atlas, Harvard-Oxford (HO) atlas, and Craddock 200 (CC200), were calculated. The weights of functional brain connectivity were defined using Pearson's correlation coefficient between any pair of two ROIs. For AAL atlas, each subject was represented by a 90×90 FC adjacency matrix, symmetric along diagonal, in which each entry represents the brain connectivity between each pair of ROIs. Similarly, each rs-fMRI data was also represented by 110×110 and 200×200 symmetric FC adjacency matrices using HO and CC200 atlases, respectively. In addition, from 809 subjects, we obtained five PC data, including sex, handedness, full-scale IQ (FIQ), verbal IQ (VIQ), and performance IQ (PIQ).

2.3. Multichannel Deep Attention Neural Network

2.3.1. Overview Structure. An overview of multichannel DANN is given in Figure 1. It consists of blocks of multichannel inputs, multilayer perceptron (MLP), self-attention, fusion, and aggregation. The various components are described in the following sections.

2.3.2. MLP. The MLP block is composed of 5 layers, which are one dropout layer and four dense layers. The details of the block are shown in Figure 2.

A dropout layer, which prevents overfitting during training the model, is applied on input data, e.g. AAL FC (input size is 4005). The white circle in Figure 2 denotes dropped units according to dropout probability. The dropout layer is followed by four dense layers, whose hidden units are 1024, 512, 128, and 32, respectively, and corresponding activation functions are "elu," "tanh," "tanh," and "relu," respectively.

2.3.3. Self-Attention. The attention is proposed to compute an alignment score between elements from two sources [32]. In particular, given an input FC adjacency matrix, which can be transformed into a FC adjacency sequence, $\mathbf{x} = [x_1, x_2, \ldots, x_d]$ and a representation of a query $q \in \mathbb{R}^d$, attention [33] computes the alignment score between q and each element x_i using a compatibility function $f(x_i, q)$. A softmax function then transforms the alignment scores $[f(x_i, q)]_{i=1}^d$ to a probability distribution $p(z \mid \mathbf{x}, q)$, where z is an indicator of which element is important to q. That is, a large $p(z = i \mid \mathbf{x}, q)$ means that x_i contributes important information to q. This attention process can be formalized as

$$\begin{aligned} \alpha &= \left[f\left(x_i, q\right)\right]_{i=1}^d, \\ p\left(z = i \mid \mathbf{x}, q\right) &= \operatorname{softmax}\left(\alpha\right). \end{aligned} \tag{1}$$

The output s_i is the weighted element according to its importance, i.e.,

$$s_i = p\left(z = i \mid \mathbf{x}, q\right) x_i. \tag{2}$$

Additive attention mechanisms [33, 34] are commonly used attention mechanisms where the compatibility function $f(\cdot)$ is parameterized by a MLP, i.e.,

$$f\left(x_i, q\right) = w^T \sigma\left(W^{(1)} x_i + W^{(2)} q\right), \tag{3}$$

where $W^{(1)} \in \mathbb{R}^{d \times d}$, $W^{(2)} \in \mathbb{R}^{d \times d}$, $w \in \mathbb{R}^d$ are learnable parameters, d is the dimension of x_i, and $\sigma(\cdot)$ is an activation function. In contrast to additive attention, multiplicative attention [35, 36] uses cosine similarity or inner product as the compatibility function for $f(x_i, q)$, i.e.,

$$f\left(x_i, q\right) = \langle W^{(1)} x_i, W^{(2)} q \rangle. \tag{4}$$

In practice, although additive attention is expensive in time cost and memory consumption, it usually achieves better empirical performance for downstream tasks.

Self-attention [37, 38] explores the importance of each feature to the entire FC given a specific task. In particular, q is removed from the common compatibility function which is formally written as the following equation:

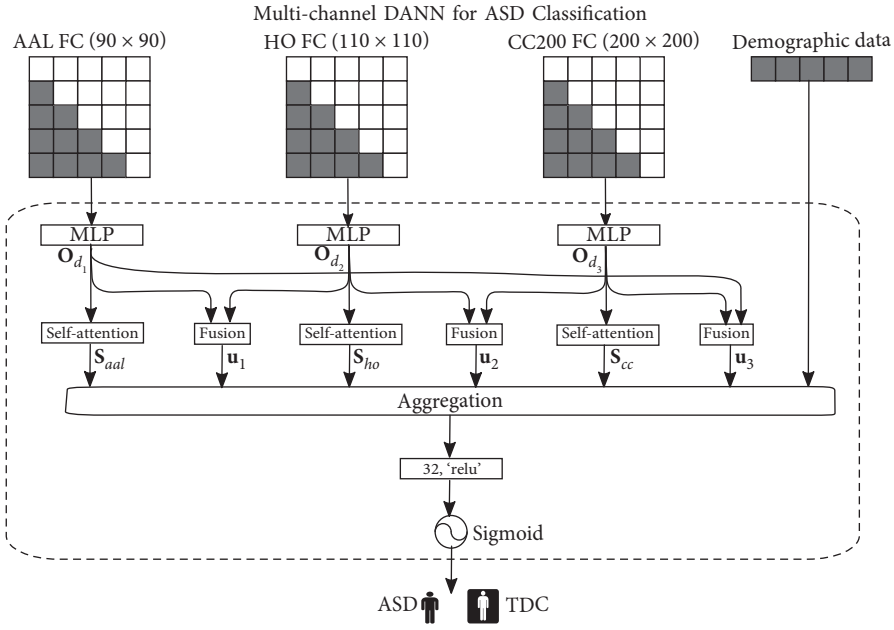

Figure 1: A DANN structure for ASD classification in this study.

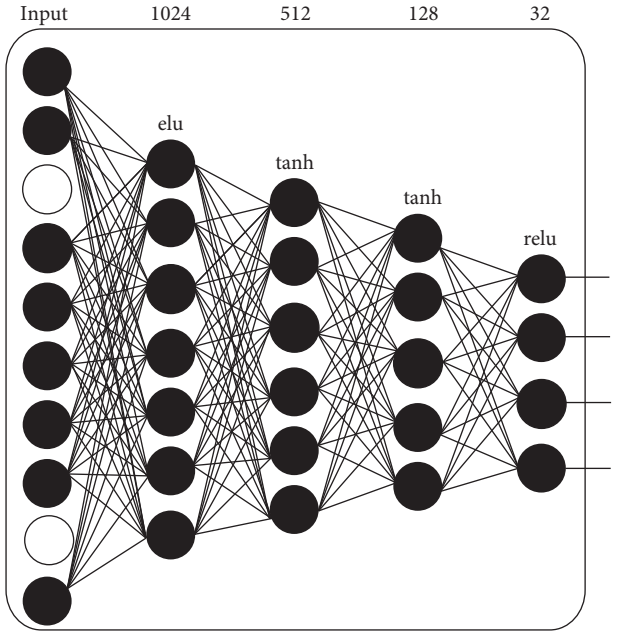

Figure 2: Detailed MLP block in DANN structure.

$$f(x_i) = w^T \sigma\left(W^{(1)} x_i\right),$$
$$\alpha = \left[f(x_i)\right]_{i=1}^{d}, \tag{5}$$
$$p(z = i \mid \mathbf{x}) = \text{softmax}(\alpha).$$

The output s_i is the weighted element according to its importance, i.e.,

$$s_i = p(z = i \mid \mathbf{x}) x_i. \tag{6}$$

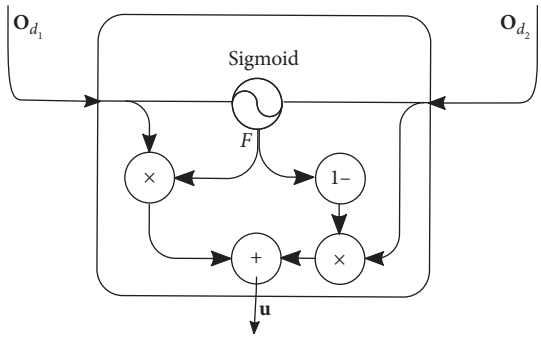

Figure 3: Detailed fusion gate in DANN structure.

2.3.4. Fusion. The fusion output u is obtained by combining the outputs of the two dense layer blocks, which can capture the correlation between the types of spaces. The combination is accomplished by a fusion gate, as shown in Figure 3, i.e.,

$$F = \text{sigmoid}\left(W^{(f_1)} o_{d_1} + W^{(f_2)} o_{d_2} + b^{(f)}\right).$$
$$u = F \odot o_{d_1} + (1 - F) \odot o_{d_2}, \tag{7}$$

where $W^{(f1)}, W^{(f2)} \in \mathbb{R}^{d_o}$, d_o is the dimension of output o_d, and $b^{(f)} \in \mathbb{R}$ are the learnable parameters of the fusion gate.

2.3.5. Aggregation. To aggregate dense layer, self-attention, and fusion into a DANN, the outputs of self-attention and fusion blocks can be concatenated, multiplied, or averaged. In our implementation, the outputs of both the self-attention blocks and the fusion blocks are concatenated, followed by a dense layer and sigmoid layer for classification:

$$l_d = \text{relu}(W_d \mathbf{v} + b_d),$$
$$\text{Comb} = \text{sigmoid}(W_c l_d + b_c), \tag{8}$$

where $\mathbf{v}$ is a vector of the combined outputs of both the self-attention blocks and the fusion blocks. $\mathbf{v} = [\mathbf{s}_{\text{aal}}, \mathbf{s}_{\text{ho}}, \mathbf{s}_{\text{cc}}, \mathbf{u}_1, \mathbf{u}_2, \mathbf{u}_3, \mathbf{Demo}]$ represents the concatenation of outputs $\mathbf{s}_{\text{aal}}$, $\mathbf{s}_{\text{ho}}$, $\mathbf{s}_{\text{cc}}$ from the self-attention blocks, $\mathbf{u}_1$, $\mathbf{u}_2$, $\mathbf{u}_3$ from the fusion blocks, and **Demo** from demographic data. A sigmoid function on dense lay is then used for data classification.

3. Experiment Setup

3.1. Model Evaluation. We conducted a comprehensive evaluation in this study by employing the proposed multichannel DANN on ABIDE dataset to classify the ASD subjects from TDC subjects. Two evaluation strategies, k-fold cross validation and leave-one-site-out cross validation, were designed in our experiments. For k-fold cross validation, whole ABIDE dataset would be divided into k portions. In each repeated iteration, we randomly used one portion of the data as testing data and applied the remaining $(k-1)$ portions of the data as training data. This process would be repeated k times until all data have been tested once. For the leave-one-site-out cross validation, we separated the whole ABIDE dataset according to their data sites. We removed the SBL site from this experiment due to its small subject size ($N = 4$). This resulted in a total of 12 data sites. We randomly used data from one site as testing data and treated the remaining data from 11 data sites as training data. This is repeated 12 times until data from all sites have been evaluated as testing data. Both the k-fold cross validation and leave-one-site-out experiments were repeated 50 times to understand the variability of the results. Mean and standard deviation (SD) were calculated. Student's T-test was applied to test the difference between continuous values, and chi-square test was used for discrete values. One-way analysis of variance (ANOVA) was utilized to compare multiple conditions (i.e., multiple k-fold cross validation experiments). A p value < 0.05 was used for inferring statistical significance.

We calculated true positive (TP), false positive (FP), true negative (TN), and false negative (FN) for the classification by comparing the classified labels and gold-standard labels. Then, we calculated accuracy, sensitivity, precision, and F-score by

$$\text{accuracy} = \frac{\text{TP} + \text{TN}}{\text{TP} + \text{TN} + \text{FP} + \text{FN}},$$
$$\text{sensitivity} = \frac{\text{TP}}{\text{TP} + \text{FN}},$$
$$\text{precision} = \frac{\text{TP}}{\text{TP} + \text{FP}}, \tag{9}$$
$$F - \text{score} = 2 \times \frac{\text{precision} \times \text{sensitivity}}{\text{precision} + \text{sensitivity}},$$
$$\text{specificity} = \frac{\text{TN}}{\text{TN} + \text{FP}}.$$

3.2. Peer Machine Learning Models. To compare our multichannel DANN with existing machine learning models, we also implemented random forest (RF), support vector machine (SVM) models, and multichannel DNN. Each model was designed to take multimodality data as inputs.

3.2.1. Random Forest (RF). RF is one of the classic ensemble learning methods by learning multiple decision trees to improve classification performance and control overfitting. The number of trees in the forest was optimized from empirical values [20, 40, 60, 80, 100]. We set the maximal depth of the tree as 10.

3.2.2. Support Vector Machine (SVM). A SVM model was developed to perform ASD classification by using vectorized FC features. We applied a linear kernel and searched the margin penalty with empirical values [0.2, 0.4, 0.6, 0.8, 1.0].

3.2.3. Deep Neural Networks (DNNs). In terms of existing deep learning model, we compared our model with a DNN model developed previously for ASD classification [26]. In brief, the compared existing DNN model is a 5-layer DNN, with input number of nodes in input layer, followed by 1024, 512, 128, and 32 nodes in hidden layers, and the output layer contains two output units. A cross entropy loss function was adopted. Learning rate was set as 0.0001. 10 epochs were applied to ensure the convergence of the model.

3.3. Developmental Environment. The proposed DANN and peer machine learning models were implemented in the Python 3.7 environment. To build the deep learning related models, we applied Keras (2.2.4) package with TensorFlow (1.13.1) backend. For the traditional models, we adopted the models from Sklearn 0.20 [39]. Statistical analyses were performed using Matlab 2019b.

All the experiments were conducted on a workstation with 10 cores of Intel Core i9 CPU and 64 GB RAM. Due to the high computation cost of deep learning algorithm, we configured one GPU (Nvidia TITAN Xp, 12 GB RAM) to accelerate the training speed of the models.

4. Results and Discussion

4.1. Performance Comparison on the Whole ABIDE Dataset. We first compared the ASD classification performance of the proposed multichannel DANN model and multiple peer machine learning models, including RF, SVM, and multichannel DNN. The results were calculated based on 50 repeats of 10-fold cross validation experiments by using the entire ABIDE dataset. The mean and SD of the performance metrics are listed in Table 2. The proposed multichannel DANN exhibited a significantly higher accuracy than multichannel DNN ($p = 0.01$), SVM ($p = 0.014$), and RF ($p = 0.008$) models. Similarly, the multichannel DANN also had better F-score than multichannel DNN ($p = 0.004$), SVM ($p < 0.001$), and RF ($p < 0.001$) models. The sensitivity of the multichannel

Table 2: Comparison of random forest (RF), support vector machine (SVM), multichannel deep neural network (DNN), and multichannel deep attention neural network (DANN) classifiers trained using 10-fold cross validation on the entire dataset.

Method	Accuracy	Sensitivity	Precision	F-Score	Specificity
RF	0.659 ± 0.018	0.689 ± 0.106	0.656 ± 0.012	0.671 ± 0.023	0.628 ± 0.081
SVM	0.693 ± 0.059	0.713 ± 0.059	0.696 ± 0.072	0.702 ± 0.048	0.673 ± 0.113
Multichannel DNN	0.707 ± 0.027	0.673 ± 0.088	$\mathbf{0.740 \pm 0.106}$	0.718 ± 0.060	0.700 ± 0.067
Multichannel DANN	$\mathbf{0.732 \pm 0.024}$	$\mathbf{0.745 \pm 0.115}$	0.730 ± 0.053	$\mathbf{0.736 \pm 0.042}$	$\mathbf{0.717 \pm 0.101}$

All data are mean and standard deviation. The highest metrics were marked as bold.

DANN was significantly higher than that of multichannel DNN ($p = 0.009$), SVM ($p = 0.015$), and RF ($p = 0.005$) models. The specificity of the multichannel DANN was significantly higher than that of SVM ($p = 0.004$) and RF ($p < 0.001$) models but was not significantly better than multichannel DNN ($p = 0.082$). Since the multichannel DNN had a relatively lower sensitivity (0.673), it achieved the best mean precision in our experiments. No significant difference ($p = 0.219$) was found between multichannel DNN and DANN on precision. The multichannel DANN model still exhibited higher precision than SVM ($p = 0.003$) and RF ($p < 0.001$). Overall, the proposed multichannel DANN achieved improved ASD classification accuracy, sensitivity, *F*-score, and specificity among compared machine learning models, while the multichannel DNN had the highest precision.

Inspiringly, the proposed multichannel DANN significantly outperformed multichannel DNN on four of five performance metrics, increasing mean accuracy by 0.025, sensitivity by 0.072, *F*-score by 0.018, and specificity by 0.017. Although no significance was found, the precision of the proposed approach is slightly lower than multichannel DNN by 0.01. The attention mechanism in our model, as the name implies, aids the deep learning model to make choices about which features it should pay attention. Our model can allocate attention by adjusting the weights they assign to individual FC features. This process can decide which FC features are more important than others in terms of the ASD classification task. In another word, it optimizes the feature selection during the learning of a deep learning model. The improved performance of DANN over DNN demonstrated the validity of the attention mechanism. The results in Table 2 also showed that multichannel DANN achieved significantly improved performance, compared to traditional models SVM and RF. This is consistent with multiple previous ASD classification studies [26, 27]. The improvement was likely due to a combination of attention mechanism and the superior capability of deep learning model on complex data patterns, such as FC features.

4.2. Leave-One-Site-Out Cross Validation of Multichannel DANN. To test the generalizability of the proposed model on unseen data from different data sites, we performed a leave-one-site-out cross validation. Similar to *k*-fold cross validation, we reserved data from one data site as testing data and trained our model by using all data from the rest of the 11 data sites. But, since the training data were the same across all repeats, the performances have much smaller variations than *k*-fold cross validation. Table 3 shows the classification performance of our model and the size of subjects for each data site.

In the NYU data site that contains the largest sample size, our model achieved an accuracy of 0.709 ± 0.019, sensitivity of 0.720 ± 0.086, the precision of 0.758 ± 0.127, *F*-score of 0.738 ± 0.069, and specificity of 0.689 ± 0.072. When examining data sites with more than 40 subjects, we found that our model achieved the highest accuracy (0.803 ± 0.045) on the USM site and the best *F*-score (0.745 ± 0.052) on the UCLA site. These two sites contain nearly 100 subjects, so the results are very informative. We also noted that the lowest accuracy our model returned was 0.684 ± 0.026 from UM site, suggesting that the data here may have variability that is different from other sites. Overall, our model reached a mean accuracy of 0.713 ± 0.022 and mean *F*-score 0.707 ± 0.043. This was significantly lower than accuracy ($p = 0.002$) and *F*-score ($p < 0.001$) from the cross validation results in Table 2, indicating a large data variability among different data sites.

4.3. Robustness of Multichannel DANN on Varying Data Split Schemes. Next, the robustness of our DANN was further tested using varying *k*-fold cross validation. A classification model that is not robust may appear to perform very differently with different *k*. Figure 4 shows plots of the accuracy, sensitivity, precision, *F*-score, and specificity of the proposed DANN over *k*-fold cross validation strategies ($k = [6, 7, 8, 9, 10]$). Using one-way ANOVA, the proposed DANN exhibited no significantly different performance across varying *k*-fold experiments ($p = 0.082$), indicating the robustness of the proposed multichannel DANN model.

4.4. Impact of Data Modality on the Classification Performance. At the end, we set to test the performance of the multichannel DANN when different data modalities are used for ASD classification. All results were based on 50 repeats of 10-fold cross validation experiment. Table 4 lists the performance of multichannel DANN on varying combinations of FC data (marked as AAL, HO, and CC200) and PC data (marked as Demo). The upper part of Table 4 contains results based on both FC and PC data, while the lower part of the table focuses on FC data only. The combined FC and PC data (AAL + HO + CC + Demo) had a better accuracy ($p = 0.011$), sensitivity ($p = 0.039$), and specificity ($p = 0.025$) than FC data alone (AAL + HO + CC), while no significant differences were

Table 3: Leave-one-site-out cross validation results using multichannel DANN.

Site-out	Size	Accuracy	Sensitivity	Precision	*F*-score	Specificity
TRINITY	46	0.696 ± 0.012	0.640 ± 0.012	0.762 ± 0.036	0.696 ± 0.004	0.679 ± 0.070
YALE	56	0.696 ± 0.025	0.679 ± 0.029	0.714 ± 0.032	0.691 ± 0.034	0.682 ± 0.065
STANFORD	39	0.615 ± 0.018	0.350 ± 0.025	0.778 ± 0.039	0.483 ± 0.015	0.685 ± 0.032
SDSU	36	0.694 ± 0.024	0.727 ± 0.095	0.762 ± 0.072	0.744 ± 0.059	0.705 ± 0.067
CALTECH	36	0.667 ± 0.029	0.556 ± 0.016	0.714 ± 0.029	0.625 ± 0.015	0.693 ± 0.038
UCLA	98	0.755 ± 0.015	0.795 ± 0.017	0.700 ± 0.009	0.745 ± 0.012	0.701 ± 0.019
CMU	27	0.630 ± 0.019	0.692 ± 0.044	0.600 ± 0.037	0.643 ± 0.044	0.684 ± 0.035
USM	71	0.803 ± 0.015	0.560 ± 0.028	0.824 ± 0.034	0.667 ± 0.029	0.685 ± 0.038
NYU	175	0.709 ± 0.019	0.720 ± 0.026	0.758 ± 0.027	0.738 ± 0.039	0.689 ± 0.022
PITT	56	0.696 ± 0.022	0.778 ± 0.023	0.656 ± 0.002	0.712 ± 0.027	0.717 ± 0.013
LEUVEN	29	0.621 ± 0.017	1.000 ± 0.017	0.577 ± 0.027	0.732 ± 0.028	0.674 ± 0.022
UM	126	0.684 ± 0.026	0.761 ± 0.008	0.675 ± 0.009	0.715 ± 0.008	0.671 ± 0.012
Mean	62	0.713 ± 0.022	0.712 ± 0.081	0.731 ± 0.087	0.707 ± 0.043	0.713 ± 0.057

All data are mean and standard deviation.

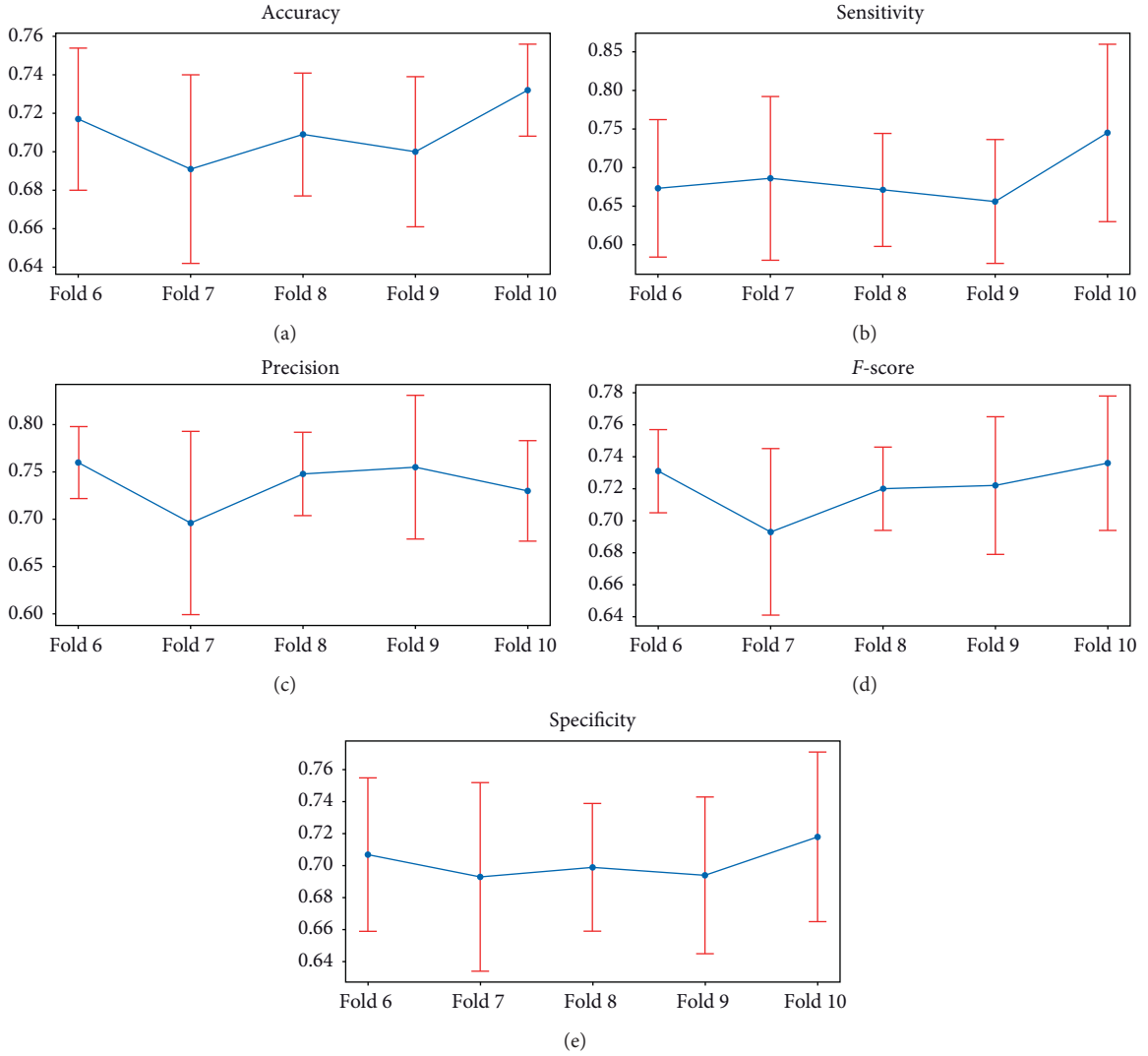

Figure 4: Performance of multichannel DANN over varying data split schemes with k-fold cross validation strategies ($k = [6, 7, 8, 9, 10]$). Mean and standard deviation are displayed.

Table 4: Comparison of multichannel DANN on different data combinations using 10-fold cross validation on the entire dataset.

Data	Accuracy	Sensitivity	Precision	*F*-score	Specificity
AAL + HO + CC + Demo	0.732 ± 0.024	0.745 ± 0.115	0.730 ± 0.053	0.736 ± 0.042	0.717 ± 0.101
AAL + HO + Demo	0.700 ± 0.035	0.698 ± 0.068	0.701 ± 0.035	0.702 ± 0.004	0.673 ± 0.401
AAL + CC + Demo	0.703 ± 0.009	0.721 ± 0.084	0.686 ± 0.071	0.699 ± 0.067	0.697 ± 0.060
HO + CC + Demo	0.691 ± 0.018	0.696 ± 0.098	0.686 ± 0.106	0.690 ± 0.054	0.687 ± 0.065
AAL + Demo	0.666 ± 0.002	0.683 ± 0.080	0.650 ± 0.071	0.659 ± 0.006	0.679 ± 0.031
HO + Demo	0.689 ± 0.027	0.681 ± 0.078	0.696 ± 0.106	0.691 ± 0.011	0.685 ± 0.057
CC + Demo	0.692 ± 0.053	0.703 ± 0.092	0.681 ± 0.141	0.689 ± 0.043	0.704 ± 0.055
AAL + HO + CC	0.720 ± 0.062	0.696 ± 0.097	0.738 ± 0.212	0.724 ± 0.078	0.695 ± 0.056
AAL + HO	0.684 ± 0.027	0.636 ± 0.084	0.730 ± 0.018	0.699 ± 0.035	0.673 ± 0.050
AAL + CC	0.695 ± 0.018	0.683 ± 0.083	0.706 ± 0.124	0.700 ± 0.030	0.683 ± 0.052
HO + CC	0.688 ± 0.027	0.666 ± 0.086	0.711 ± 0.053	0.697 ± 0.020	0.683 ± 0.055
AAL	0.658 ± 0.009	0.641 ± 0.078	0.674 ± 0.141	0.663 ± 0.035	0.658 ± 0.032
HO	0.679 ± 0.009	0.683 ± 0.065	0.674 ± 0.071	0.677 ± 0.007	0.691 ± 0.029
CC	0.682 ± 0.005	0.651 ± 0.071	0.713 ± 0.106	0.693 ± 0.034	0.677 ± 0.046

AAL: AAL atlas-based FC; HO: HO atlas-based FC; CC: CC200 atlas-based FC; Demo: PC data. All data are mean and standard deviation.

observed on precision ($p = 0.231$) and *F*-score ($p = 0.347$). This demonstrated the predictive power of PC data.

Without PC data, our model achieved the highest performance by combining FC from all three brain atlases. This suggests that brain connected data from different atlases may have complementary information so as to assist the ASD classification. Interestingly, the model using CC200 FC data (marked as CC in the table) performed better than FC data derived from AAL ($p = 0.012$) and HO ($p = 0.023$). It is likely because that CC200 atlas is constructed from rs-fMRI data, representing a brain functional parcellation.

5. Conclusion

In summary, we developed a multichannel DANN model by applying the state-of-the-art attention mechanism-based deep learning techniques for automated diagnosis of ASD. The *k*-fold cross validation experiments have shown that our multichannel DANN achieved an accuracy of 0.732, outperforming multiple peer machine learning models. The results of the leave-one-site-out cross validation experiments showed promise for our model to be applied to clinical data with unseen variations. The experiments using varying combinations of data modalities demonstrated discriminative power of individual data modalities such as brain functional connectome and PC data. This suggests a future direction of combining additional data modalities to move the machine learning applications towards clinical usage of ASD computer-aided diagnosis tools. One limitation of the current work is that the selected cohort is in the adolescent and young adult population, which limits the generalizability of the model, since the ASD diagnosis was performed much earlier. In the future study, we would retrain the model with additional data from a wider age range of population.

Data Availability

The dataset used to support the findings of this study is available in http://fcon_1000.projects.nitrc.org/indi/abide/.

Conflicts of Interest

The authors declare that there are no conflicts of interest regarding the publication of this paper.

Acknowledgments

This work was supported in part by the Beijing Education Commission Research Project of China under grant no. KM201911232004, National Natural Science Foundation of China under grant no. 61672105, and National Key Research and Development Program of China under grant no. 2018YFB1004100.

References

[1] J. Baio, *Prevalence of Autism Spectrum Disorder Among Children Aged 8 Years-Autism and Developmental Disabilities Monitoring Network, 11 Sites*, Centers for Disease Control and Prevention, Atlanta, GA, USA, 2010.

[2] L. Tonello, L. Giacobbi, A. Pettenon et al., "Crisis behavior in autism spectrum disorders: a self-organized criticality approach," *Complexity*, vol. 2018, pp. 1–7, 2018.

[3] E. Simonoff, A. Pickles, T. Charman, S. Chandler, T. Loucas, and G. Baird, "Psychiatric disorders in children with autism spectrum disorders: prevalence, comorbidity, and associated factors in a population-derived sample," *Journal of the American Academy of Child & Adolescent Psychiatry*, vol. 47, no. 8, pp. 921–929, 2008.

[4] S. Goldstein and S. Ozonoff, *Assessment of Autism Spectrum Disorder*, Guilford Publications, New York, NY, USA, 2018.

[5] I. Riquelme, S. M. Hatem, and P. Montoya, "Abnormal pressure pain, touch sensitivity, proprioception, and manual dexterity in children with autism spectrum disorders," *Neural Plasticity*, vol. 2016, Article ID 1723401, 9 pages, 2016.

[6] R. Djemal, K. AlSharabi, S. Ibrahim, and A. Alsuwailem, "EEG-based computer aided diagnosis of autism spectrum disorder using wavelet, entropy, and ann," *BioMed Research International*, vol. 2017, Article ID 9816591, 9 pages, 2017.

[7] K. B. Schauder and L. Bennetto, "Toward an interdisciplinary understanding of sensory dysfunction in autism spectrum disorder: an integration of the neural and symptom literatures," *Frontiers in Neuroscience*, vol. 10, p. 268, 2016.

[8] N. Newbutt, C. Sung, H. J. Kuo, and M. J. Leahy, "The acceptance, challenges, and future applications of wearable technology and virtual reality to support people with autism spectrum disorders," in *Recent Advances in Technologies for Inclusive Well-Being*, pp. 221–241, Springer, Berlin, Germany, 2017.

[9] American Psychiatric Association, *Diagnostic and Statistical Manual of Mental Disorders (DSM-5®)*, American Psychiatric Association Publishing, GA, USA, 2013.

[10] M. Galliver, E. Gowling, W. Farr, A. Gain, and I. Male, "Cost of assessing a child for possible autism spectrum disorder? an observational study of current practice in child development centres in the UK," *BMJ Paediatrics Open*, vol. 1, no. 1, Article ID e000052, 2017.

[11] K. K. Hyde, M. N. Novack, N. LaHaye et al., "Applications of supervised machine learning in autism spectrum disorder research: a review," *Review Journal of Autism and Developmental Disorders*, vol. 6, no. 2, pp. 128–146, 2019.

[12] D. Gil, M. Johnsson, H. Mora, and J. Szymanski, "Advances in architectures, big data, and machine learning techniques for complex Internet of things systems," *Complexity*, vol. 2019, Article ID 4184708, 3 pages, 2019.

[13] L. Zhou, S. Pan, J. Wang, and A. V. Vasilakos, "Machine learning on big data: opportunities and challenges," *Neurocomputing*, vol. 237, pp. 350–361, 2017.

[14] Ç. Uğur, H. Tunca, E. Sekmen et al., "A comparative study of the oxidative stress indices of children with autism and healthy children," *Anatolian Journal of Psychiatry*, vol. 19, no. 3, 2018.

[15] C. Li, H. Zhou, T. Wang et al., "Performance of the autism spectrum rating scale and social responsiveness scale in identifying autism spectrum disorder among cases of intellectual disability," *Neuroscience Bulletin*, vol. 34, no. 6, pp. 972–980, 2018.

[16] R. L. Hansen, N. J. Blum, A. Gaham et al., "Diagnosis of autism spectrum disorder by developmental-behavioral pediatricians in academic centers: a DBPNet study," *Pediatrics*, vol. 137, no. 2, pp. S79–S89, 2016.

[17] J. N. Constantino and C. P. Gruber, *Social Responsiveness Scale (SRS), Western Psychological Services*, Springer, New York, NY, USA, 2007.

[18] T. Charman, A. Pickles, E. Simonoff, S. Chandler, T. Loucas, and G. Baird, "IQ in children with autism spectrum disorders: data from the special needs and autism project (SNAP)," *Psychological Medicine*, vol. 41, no. 3, pp. 619–627, 2011.

[19] S. L. Bishop, J. Richler, and C. Lord, "Association between restricted and repetitive behaviors and nonverbal IQ in children with autism spectrum disorders," *Child Neuropsychology*, vol. 12, no. 4-5, pp. 247–267, 2006.

[20] S. Ghiassian, R. Greiner, P. Jin, and M. R. G. Brown, "Using functional or structural magnetic resonance images and personal characteristic data to identify ADHD and autism," *PLoS One*, vol. 11, no. 12, Article ID e0166934, 2016.

[21] B. Sen, N. C. Borle, R. Greiner, and M. R. G. Brown, "A general prediction model for the detection of ADHD and autism using structural and functional MRI," *PLoS One*, vol. 13, no. 4, Article ID e0194856, 2018.

[22] G. J. Katuwal, S. A. Baum, N. D. Cahill, and M. M. Andrew, "Divide and conquer: sub-grouping of asd improves ASD detection based on brain morphometry," *PLoS One*, vol. 11, no. 4, Article ID e0153331, 2016.

[23] C. Zu, Y. Gao, B. Munsell et al., "Identifying disease-related subnetwork connectome biomarkers by sparse hypergraph learning," *Brain Imaging and Behavior*, vol. 13, no. 4, pp. 879–892, 2018.

[24] Y. LeCun, Y. Bengio, and G. Hinton, "Deep learning," *Nature*, vol. 521, no. 7553, pp. 436–444, 2015.

[25] A. Krizhevsky, I. Sutskever, and G. E. Hinton, "Imagenet classification with deep convolutional neural networks," in *Advances in Neural Information Processing Systems*, Curran Associates, Inc., Lake Tahoe, NV, USA, 2012.

[26] A. S. Heinsfeld, A. R. Franco, R. C. Craddock, A. Buchweitz, and F. Meneguzzi, "Identification of autism spectrum disorder using deep learning and the abide dataset," *NeuroImage: Clinical*, vol. 17, pp. 16–23, 2018.

[27] Y. Kong, J. Gao, Y. Xu, Y. Pan, J. Wang, and J. Liu, "Classification of autism spectrum disorder by combining brain connectivity and deep neural network classifier," *Neurocomputing*, vol. 324, pp. 63–68, 2019.

[28] T. Eslami, V. Mirjalili, A. Fong, A. Laird, and F. Saeed, "ASD-diagnet: a hybrid learning approach for detection of autism spectrum disorder using FMRI data," 2019, http://arxiv.org/abs/1904.07577.

[29] J. Guo, K. Yang, H. Liu et al., "A stacked sparse autoencoder-based detector for automatic identification of neuromagnetic high frequency oscillations in epilepsy," *IEEE Transactions on Medical Imaging*, vol. 37, no. 11, pp. 2474–2482, 2018.

[30] F. Ma, Q. You, H. Xiao, R. Chitta, J. Zhou, and J. G. Kame, "Knowledge-based attention model for diagnosis prediction in healthcare," in *Proceedings of the 27th ACM International Conference on Information and Knowledge Management*, pp. 743–752, ACM, Torino, Italy, October 2018.

[31] X. Peng, G. Long, T. Shen, S. Wang, J. Jiang, and M. Blumenstein, "Temporal self-attention network for medical concept embedding," 2019, http://arxiv.org/abs/1909.06886.

[32] T. Shen, T. Zhou, G. Long, J. Jiang, S. Pan, and C. Zhang, "Disan: directional self-attention network for RNN/CNN-free language understanding," in *Proceedings of the Thirty-Second AAAI Conference on Artificial Intelligence*, New Orleans, LA, USA, February 2018.

[33] D. Bahdanau, K. Cho, and Y. Bengio, "Neural machine translation by jointly learning to align and translate," 2014, http://arxiv.org/abs/1409.0473.

[34] L. Shang, Z. Lu, and H. Li, "Neural responding machine for short-text conversation," 2015, http://arxiv.org/abs/1503.02364.

[35] S. Sukhbaatar, J. Weston, R. Fergus et al., "End-to-end memory networks," in *Proceedings of the Conference on Neural Information Processing Systems*, Montreal, Canada, December 2015.

[36] A. M. Rush, S. Chopra, and J. Weston, "A neural attention model for abstractive sentence summarization," 2015, http://arxiv.org/abs/1509.00685.

[37] Z. Lin, M. Feng, C. Nogueira dos Santos et al., "A structured self-attentive sentence embedding," 2017, http://arxiv.org/abs/1703.03130.

[38] Y. Liu, C. Sun, L. Lin, and X. Wang, "Learning natural language inference using bidirectional LSTM model and inner-attention," 2016, http://arxiv.org/abs/1605.09090.

[39] F. Pedregosa, G. Varoquaux, A. Gramfort et al., "Scikit-learn: machine learning in Python," *Journal of Machine Learning Research*, vol. 12, pp. 2825–2830, 2011.

Hindawi
Complexity
Volume 2020, Article ID 4174857, 9 pages
https://doi.org/10.1155/2020/4174857

Research Article

Method of Depression Classification Based on Behavioral and Physiological Signals of Eye Movement

Mi Li[1,2], **Lei Cao**[1,2], **Qian Zhai**[3,4], **Peng Li**[1,2], **Sa Liu**[1,2], **Richeng Li**[1,2], **Lei Feng**[3,4], **Gang Wang**[3,4], **Bin Hu**[1,5] and **Shengfu Lu**[1,2]

[1]*Department of Automation, Faculty of Information Technology, Beijing University of Technology, Beijing 100124, China*
[2]*The Beijing International Collaboration Base on Brain Informatics and Wisdom Services, Beijing 100124, China*
[3]*The National Clinical Research Center for Mental Disorders & Beijing Key Laboratory of Mental Disorders, Beijing Anding Hospital, Capital Medical University, Beijing, China*
[4]*The Advanced Innovation Center for Human Brain Protection, Capital Medical University, Beijing, China*
[5]*Gansu Provincial Key Laboratory of Wearable Computing, School of Information Science and Engineering, Lanzhou University, Lanzhou, China*

Correspondence should be addressed to Shengfu Lu; lusf@bjut.edu.cn

Received 16 August 2019; Accepted 20 December 2019; Published 14 January 2020

Guest Editor: Michela Gelfusa

This paper presents a method of depression recognition based on direct measurement of affective disorder. Firstly, visual emotional stimuli are used to obtain eye movement behavior signals and physiological signals directly related to mood. Then, in order to eliminate noise and redundant information and obtain better classification features, statistical methods (FDR corrected *t*-test) and principal component analysis (PCA) are used to select features of eye movement behavior and physiological signals. Finally, based on feature extraction, we use kernel extreme learning machine (KELM) to recognize depression based on PCA features. The results show that, on the one hand, the classification performance based on the fusion features of eye movement behavior and physiological signals is better than using a single behavior feature and a single physiological feature; on the other hand, compared with previous methods, the proposed method for depression recognition achieves better classification results. This study is of great value for the establishment of an automatic depression diagnosis system for clinical use.

1. Introduction

Depression is a psychiatric disorder characterized by significant and persistent loss of pleasure, anhedonia, and decreased interest. To date, no specific biological markers have been found for the diagnosis of depression. Therefore, in clinic, the diagnosis of depression is mainly carried out by psychiatrists through structured interviews based on diagnostic manuals (e.g., DSM-IV). With the development of artificial intelligence technology, pattern recognition technology based on machine learning has been widely studied in the recognition or diagnosis of depression.

Recently, a lot of research has been done on the depression classification based on resting-state fMRI brain image signals. For example, Cao et al. classified the severe depression patients based on functional connections of resting-state fMRI by feature selection and SVM and obtained 84.21% classification accuracy [1]. Qin et al. used SVM to identify patients with severe depression based on the diffusion tensor imaging (DTI) of resting-state fMRI, and the highest classification accuracy was 83.05% [2]. Sato et al. classified the patients with severe depression based on fMRI signals and achieved an accuracy of 78.26%, sensitivity of 72.00%, and specificity of 85.71% [3]. Bhaumik et al. used SVM to classify remitted major depressive patients based on the functional connectivity of resting-state fMRI and achieved an accuracy of 76.1%, sensitivity of 81.5%, and specificity of 68.9% [4]. Schnyer et al. used DTI and SVM to identify patients with severe depression, and the highest classification accuracy, specificity, and sensitivity were

74.0%, 80.0%, and 68.0% [5]. Ramasubbu et al. used SVM based on the voxel space of resting-state fMRI to classify mild-moderate, severe, and very severe patients, and the classification accuracy was 58%, 52%, and 66%, respectively [6].

In addition to using fMRI signals to identify depression, in recent years, EEG-based depression recognition has also been widely studied. For example, Liao et al. used SVM to classify severe depression patients based on resting-state EEG signals, and 80% of the classification accuracy is obtained [7]. Bairy et al. used the decision tree algorithm to classify based on EEG signal, and the classification accuracy, sensitivity, and specificity were 94.30%, 91.46%, and 97.45% [8]. Mumtaz et al., based on resting-state EEG using SVM for classification, achieved an accuracy of 98.4%, sensitivity of 96.66%, and specificity of 100% [9]. Acharya et al. used deep convolution neural network to recognize depression based on EEG signals and achieved the highest accuracy of 96% [10].

Compared with EEG and fMRI signals, the behavior data such as expression and voice are easier to obtain. Therefore, a lot of research has been done on the method of depression classification based on behavior data. For example, Valstar et al. used linear SVM with random gradient descent to classify depression based on video expression, audio, and multimodality, and the F1 scores were 0.583, 0.889, and 0.467, respectively [11]. Ma et al. proposed a depth classification model (DepAudioNet) combining convolutional neural network (CNN) with long-term and short-term memory (LSTM) based on audio signals, and the optimal F1 score is 0.52 (0.70), classification accuracy is 0.35 (1.00), and recall is 1.00 (0.54) (nondepressive results in parentheses) [12].

In addition to using a single physiological or behavioral signal for depression classification, many studies have recognized depression based on multimodal data. For example, Zhao et al. used the multimodal data of resting-state fMRI and DTI for classification with an accuracy of 80.95% [13]. Le et al. fused audio, video, language, and sleep multimodal data at feature level and obtained F1 scores of 57.1% and 87.7% in depression patients and normal control group, respectively, by using decision tree algorithm [14]. Al Hanai et al. used LSTM to classify depression based on multimodal data of audio/text, and the optimal F1 score and recall rate were 0.77 and 0.83, respectively [15]. Haque et al. used causal convolution neural network (C-CNN) to identify depression in patients with severe depression based on multimodality of expression, voice, and linguistic (text), and 83.3% sensitivity and 82.6% specificity were obtained [16].

Compared with EEG/fMRI, behavioral signals are easier to collect and low in cost from the source of classified signals. Therefore, the method of depression recognition based on behavioral signals and deep learning methods has attracted the attention of researchers. However, whether it is physiological signal (fMRI, EEG) or behavioral signal (expression, voice, etc.), the common characteristics of these signals are acquired in the natural state of the individual; for example, resting-state EEG and fMRI signals are all acquired when the individual is in the state of closing eyes, relaxing, and not thinking about anything. Behavioral signals such as expressions and voices are natural state signals obtained during interviews (usually using virtual agents). That is to say, at present, the classification signals collected in the natural state are not directly related to affective disorders but indirect measurement of affective disorders. However, the core symptoms of depression patients are low and bad mood is caused by emotional injury, so the signals obtained by direct measurement of emotions are of great value for the study of depression recognition.

Eye movement technology opens up a new way for the study of automatic detection of depression. The eye is the window of the mind and the important organ for humans to observe the world directly. Eye movement signals, such as gaze objects, gaze time, gaze shift, and pupil size, acquired by eye tracking technology, are all direct reflections of the brain's information processing demand and can quantitatively characterize emotional perception. Therefore, eye movement signals are a direct measurement of emotional state. Alghowinem et al., firstly based on the eye movement features (horizontal, vertical, and eyelid movement) obtained by emotional language stimulation to classify 30 depressive patients and 30 normal people, achieved 75% of the classification accuracy by using the Gauss mixture model and SVM [17]. Li et al. used random forest algorithm to classify 9 depressive patients and 25 normal people based on the eye movement features (pupil size, gaze position, gaze time, etc.) obtained by emotional expression picture stimulation, and the classification accuracy was 80.1% [18]. It can be seen that the above studies using eye movement behavior signals and physiological signals (pupil diameter) as classification features still do not get a high classification accuracy. Although the pupil diameter signal can reflect the change of emotion, the physical size of the pupil diameter varies greatly and cannot be directly used for emotional measurement. Therefore, this study further processed behavior and pupil diameter signals of eye movement in order to extract classification features that can better reflect the differences between depressed patients and normal people.

Many previous eye movement studies have shown that, on the one hand, depressed patients tend to have emotional attention bias [19], i.e., reduced attention to happy emotions and excessive attention to sad emotions, which represented that positive attention bias scores (the difference between the total fixation time at happy expressions and the total fixation time at calm expressions) of depressed patients were significantly greater than those of the normal people, while the negative attention bias scores (the difference between the total fixation time at sad expressions and the total fixation time at calm expressions) of depressed patients were significantly smaller than those of the normal people [20]. On the other hand, the processing of emotional information in the brain can cause changes in pupil diameter. The change in pupil diameter directly reflects the change of people's emotion. Positive emotional visual stimulation can cause people to have happy emotional experience, accompanied by the enlargement of pupil diameter, whereas negative emotional visual stimulation can cause people to have sad emotional experience, accompanied by the smaller pupil

diameter [21–23]. Studies have shown that there are significant differences in pupil diameter between depressive patients and normal people under different emotional stimuli [24, 25].

In this study, two kinds of classification features are extracted from eye movement signals directly related to emotion when evoked by different emotional pictures: one is the attention bias score [20] which reflects eye movement behavior signals, and the other is the emotional bandwidth [26] which reflects physiological signals based on pupil diameter. Noise and redundant information often exist in the acquired physiological and behavioral signal features, so feature selection and feature extraction are needed.

In addition, the performance of classification model directly affects the classification results. The data collected in this study are tabular data, and the data scale is small, which is not suitable for deep learning methods. For relatively small-scale data, SVM implements the suboptimal solution learning method, while the extreme learning machine (ELM) [27, 28] shows better classification performance. ELM is a feedforward neural network model based on a single hidden layer, which has been widely used for its advantages of simple calculation process, fast speed, and good generalization performance. At present, basic ELM and kernel ELM have developed. Compared with basic ELM, kernel ELM has the advantages of fewer adjustable parameters and no need to set hidden layer nodes manually. Therefore, to improve the recognition accuracy of depression, this study used kernel ELM as a classifier. At the same time, to compare the impact of different classification models on the classification results, we also used SVM, KNN, and random forest to classify depression.

2. Materials and Methods

2.1. Signal Acquisition. There were 96 participants in the data collection, including 48 depressed patients and 48 normal people. From the international standard expression library, the NimStim set [29], three facial expressions (neutral, happy, and sad) images of 36 people (18 males and 18 females), was selected. On the one hand, to reduce the eye movement caused by nonexpressive factors, the ears and hair should be masked as much as possible. On the other hand, the size, resolution, and gray level of all facial expression pictures were consistent through picture manager software.

Data acquisition tasks were divided into two categories: One was eye movement behavioral signals, that is, acquisition of the position and time of each gaze point when a participant views positive or negative bias tasks. Positive bias task is composed of 36 pictures of happy and neutral expressions, while negative bias task is composed of 36 pictures of sad and neutral expressions. Figure 1 shows an example of eye movements when a depressed patient views positive bias task and negative bias task. Each circle represents a gaze point, and its size indicates the length of fixation time.

The other is eye movement physiological signal (pupil diameter) acquisition, that is, the size of pupil diameter produced by each fixation point during a participant viewing positive, negative, or neutral tasks. Positive tasks consist of two pictures of happy expressions (36 in total), negative tasks consist of two pictures of sad expressions (36 in total), and neutral tasks consist of two pictures of neutral expressions (36 in total), as shown in Figure 2.

The eye-tracking device Tobii T120 was used to collect and record the position, time, and pupil size of each fixation point at a frequency of 120 Hz. As shown in Figure 3, the data acquisition process was as follows: Firstly, a 1000 ms white "+" appeared in the center of the black screen to focus on it [10]. Then, the screen presented a pair of pictures with a time of 3500 ms, followed by a "∗" of 2000 ms, prompting them to rest for the next trial.

2.2. Classification Feature Calculation. Firstly, the eye movement behavioral and physiological features are calculated according to the collected behavioral data and physiological data of eye movement.

2.2.1. Behavioral Features—Emotional Attentional Bias. Emotional attention bias includes positive bias and negative bias [20]. Among them, positive attention bias refers to the total fixation time of happy expression subtracted from the total fixation time of neutral expression in the "positive bias" task of Figure 1; negative attention bias refers to the total fixation time of sad expression subtracted from the total gaze time of neutral expression in the "negative bias" task of Figure 1.

2.2.2. Physiological Features—Affective Bandwidth and Change Rate of Pupil Diameter. Affective bandwidth includes positive affective bandwidth and negative affective bandwidth. Although pupil size is affected by external emotional stimuli, the pupil size of each person is different and is also affected by light, mental load, and so on. Therefore, the use of individual pupil size cannot simply express the effect of emotion. Here, affective bandwidth [26] is used to characterize the effect of emotion on pupil size, including positive and negative affective bandwidth. Positive affective bandwidth indicates the ability of individuals to process and experience happy emotions. The larger the positive affective bandwidth, the stronger the ability of individuals to process and experience happy information. Negative affective bandwidth indicates the ability of individuals to process and experience negative emotions. The larger the negative affective bandwidth, the stronger the ability of individuals to process and experience negative information.

Positive affective bandwidth is calculated that the mean pupil diameter of all fixation points in the "neutral" task (Figure 2(a)) is subtracted from that of all fixation points in the "positive" task (Figure 2(c)). Negative affective bandwidth is calculated that the mean pupil diameter of all fixation points in the "neutral" task (Figure 2(b)) is subtracted from that of all fixation points in the "negative" task (Figure 2(c)).

At the same time, the change rate of positive pupil diameter and negative pupil diameter is calculated with the mean pupil diameter in the "neutral" task as the baseline.

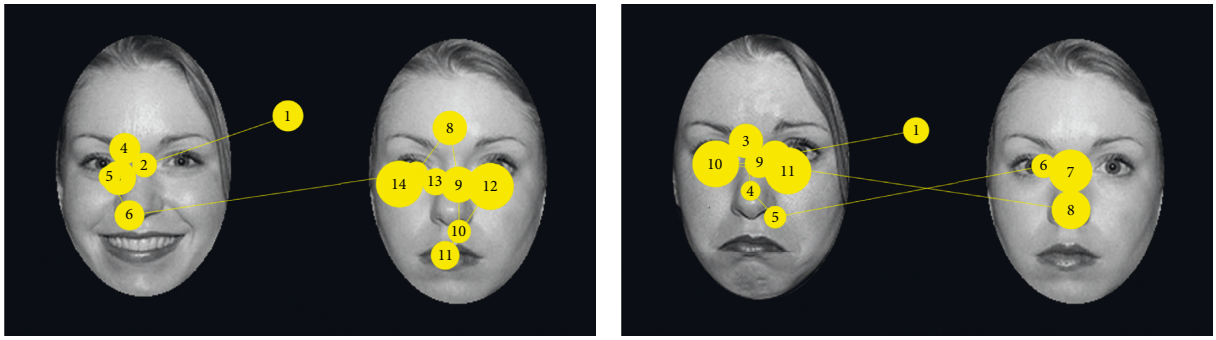

(a) (b)

Figure 1: An example of eye movements when a depressed patient views (a) positive bias tasks and (b) negative bias tasks. Each circle represents a gaze point, and its size represents the length of fixation time.

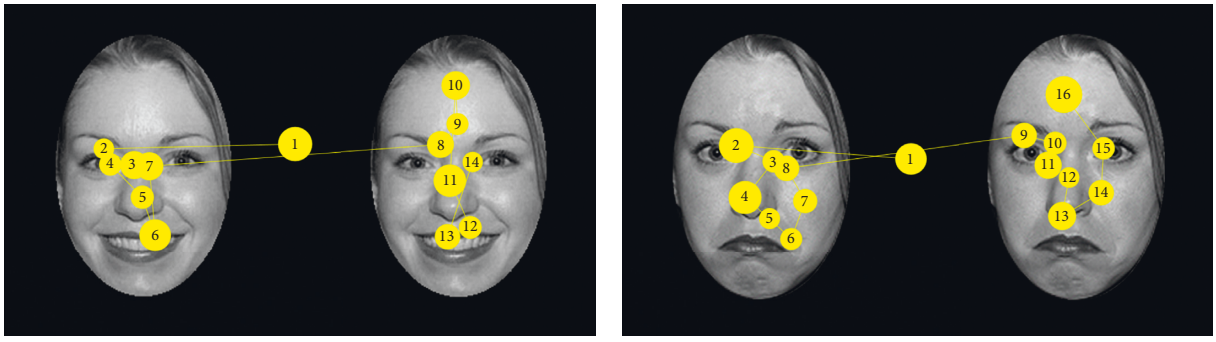

(a) (b)

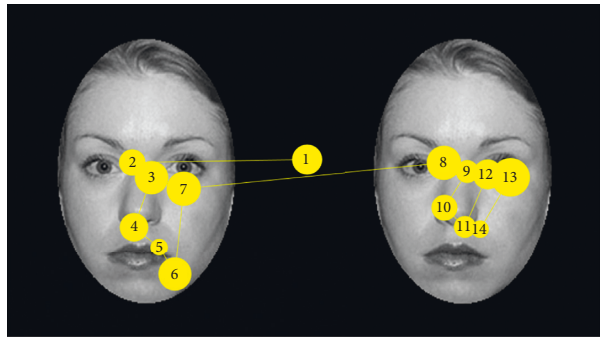

(c)

Figure 2: An example of eye movements when a depressed patient views (a) positive task, (b) negative task, and (c) neutral task. Each circle represents a gaze point, and its size represents the length of fixation time.

On this basis, the statistical indicators of each eye movement behavioral feature (positive attention bias and negative attention bias) and each eye movement physiological feature (positive/negative affective bandwidth, positive/negative pupil diameter change rate) are calculated, including minimum, lower quartile, median, upper quartile, maximum, mean, and standard deviation. This constitutes 42 classification features, including 14 behavioral features and 28 physiological features of eye movement, as shown in Table 1.

2.3. Classification Feature Reduction. Since there may be irrelevant and redundant information in eye movement features, dimensionality reduction is carried out after normalization. Here, feature selection and feature extraction are used to complete dimensionality reduction.

2.3.1. Feature Selection. Feature selection is to select a subset of features that are effective for classification from all features. Here, the FDR corrected t-test was used to analyze whether there was a significant difference between the depression group and healthy control group ($P < 0.05$). As shown in Table 1, only 24 of the 42 features showed significant differences among groups (including 11 behavioral and 13 physiological features).

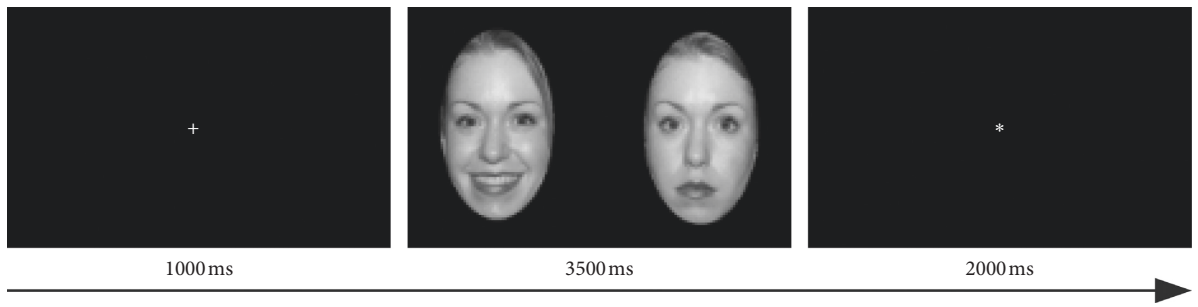

Figure 3: Data acquisition process.

Table 1: Analysis of differences between groups in 42 classification features (FDR corrected t-test).

	Minimum	Lower quartile	Median	Upper quartile	Maximum	Mean	Standard deviation
Positive bias	−1.47	1.73	5.71***	7.59***	6.58***	6.00***	6.30***
Negative bias	−5.45***	−6.99***	−8.25***	−8.3***	−8.25***	−8.15***	−0.10
Positive affective bandwidth	6.50***	6.49***	5.74***	4.68***	3.32**	5.97***	−2.06
Negative affective bandwidth	1.63	1.03	0.62	0.14	−1.02	0.50	−2.60*
Positive pupil diameter change rate	6.49***	6.95***	6.21***	5.44***	4.17***	6.70***	−1.14
Negative pupil diameter change rate	1.64	1.25	1.02	0.63	−0.24	0.92	−1.47

*$P < 0.05$; **$P < 0.01$; ***$P < 0.001$.

The positions of the 24 selected features in Table 1 are expressed as F1~F24 in the order of left to right and top to bottom. Among them, F1~F11 are the behavioral signal features and F12~F24 are the physiological signal feature.

2.3.2. Feature Extraction. There may be redundancy in the 24 features obtained by feature selection; that is, there may be correlation between features. Therefore, feature extraction is needed.

In order to determine whether there is redundant information between features, we use the Pearson correlation coefficient to calculate the correlation between these features. The calculation formula is as follows:

$$\rho_{X,Y} = \frac{E(XY) - E(X)E(Y)}{\sqrt{E(X)^2 - E^2(X)}\sqrt{E(Y)^2 - E^2(Y)}}, \quad (1)$$

where $E(X)$ represents the mathematical expectation of variable X. When $|\rho_{X,Y}| \geq 0.6$, there is a strong correlation between variables X and Y. On the contrary, there is a weak correlation or no correlation between them.

The correlations between behavioral features and physiological features are shown in Figure 4. It can be seen that there is a strong correlation between some behavioral features (Figure 4(a)) and some physiological features (Figure 4(b)).

To eliminate redundant information and further reduce the dimension of features, principal component analysis (PCA) is used to extract features. The behavioral and physiological features are processed with PCA, respectively. Figure 5 shows the single variance contribution rate and accumulated variance contribution rate of behavioral features PCA (PCA1, PCA2, ..., PCA11) and physiological features PCA (PCA1, PCA2, ..., PCA13).

2.4. Classification Model

2.4.1. KELM Classification Model. The output function for extreme learning machine (ELM) is

$$f(x) = h(x)\mathbf{H}^{\mathrm{T}}\left(\frac{I}{C} + \mathbf{H}\mathbf{H}^{\mathrm{T}}\right)^{-1} O, \quad (2)$$

where $f(x)$ is the actual output, O is the expected output of neural networks, C is the regularization factor, $h(x)$ is the function of hidden layer, and $\mathbf{H}$ is the output matrix of hidden layer.

Kernel extreme learning machine (KELM) introduces the kernel function based on ELM and solves the problem that the low-dimensional space is inseparable. The kernel function is defined as

$$\Omega_{\mathbf{i},\mathbf{j}} = h(x_i)h(x_j) = K(x_i, x_j), \quad (3)$$

$$\Omega = \mathbf{H}\mathbf{H}^{\mathrm{T}} = \begin{bmatrix} K(x_1, x_1) & \cdots & K(x_1, x_N) \\ \vdots & \ddots & \vdots \\ K(x_N, x_1) & \cdots & K(x_N, x_N) \end{bmatrix}. \quad (4)$$

The final output function of KELM is

$$f(x) = h(x)\mathbf{H}^{\mathrm{T}}\left(\frac{1}{C} + \mathbf{H}\mathbf{H}^{\mathrm{T}}\right)^{-1} O = \begin{bmatrix} K(x, x_1) \\ \cdots \\ K(x, x_N) \end{bmatrix}^T \left(\frac{1}{C} + \Omega\right)^{-1} O, \quad (5)$$

where N is the number of input samples.

Since the RBF kernel function has the advantage of strong learning ability and fewer parameters to be optimized,

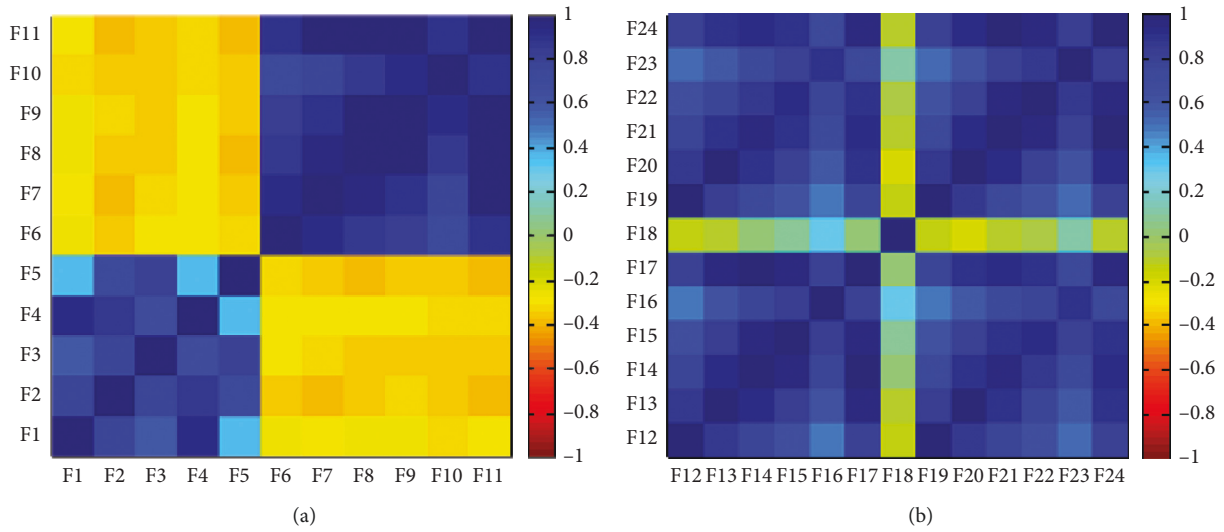

Figure 4: Analysis of correlations between selected features: (a) behavioral features; (b) physiological features.

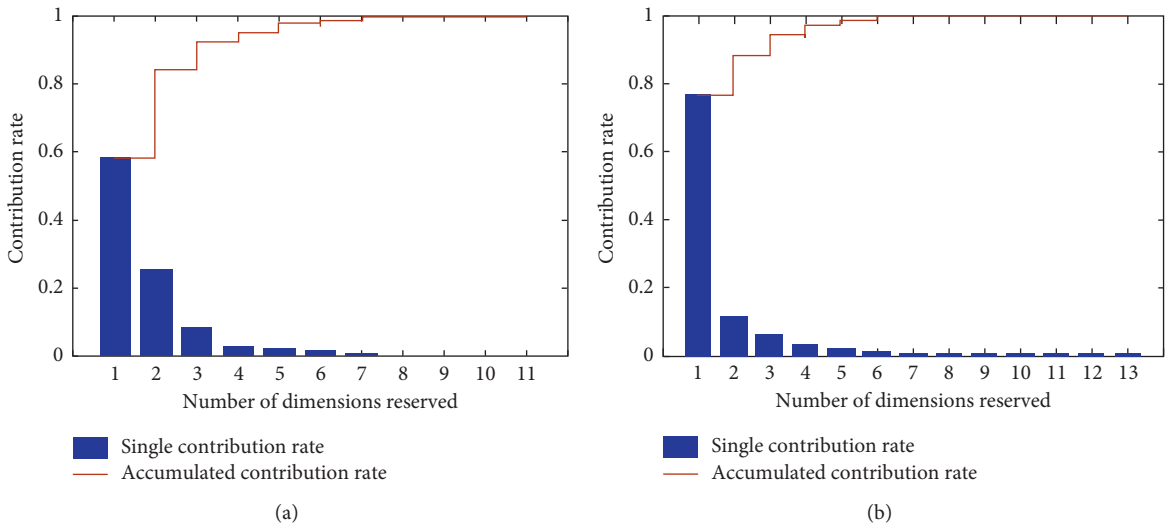

Figure 5: Single and accumulated variance contribution rate after PCA processing: (a) behavioral features; (b) physiological features.

RBF kernel function is adopted in this study, as shown in the following formula:

$$K(x_i, x_j) = \exp\left(-\frac{\|x_i - x_j\|^2}{\sigma^2}\right). \quad (6)$$

2.4.2. Model Training Strategy. The number of participants was 96 (48 for normal subjects and 48 for depressed patients). The training process of the model uses 10-fold cross-validation. The training set is randomly divided into 10 disjoint subsets of the same size, in which 9 subsets are used as the training set and the remaining one is used as the validation set. Ten models are trained in turn, and the mean values of the classification results of the test set on 10 models are calculated.

3. Results and Discussion

In this section, the depressed patients group is regarded as positive class, while the normal control group is regarded as negative class. The results are analyzed from four aspects: accuracy, specificity, sensitivity, and F1 score. Among them, the accuracy reflects the ability of the model to distinguish depressed patients from normal people, the sensitivity reflects the proportion of depressed patients correctly classified, the specificity reflects the proportion of normal people correctly classified, and F1 score takes into account the precision and recall of the classification model.

3.1. Selection of Optimal Feature Subset. Feature selection is carried out inside the cross-validation folds to make the classification algorithm more robust. To do this, the top k

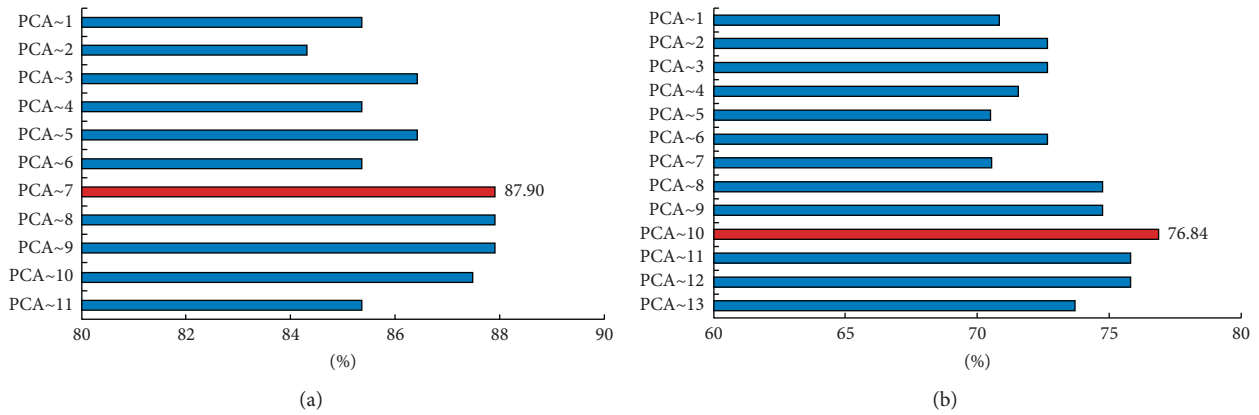

Figure 6: Classification accuracy of different PCA feature subsets: (a) behavioral features; (b) physiological features. PCA~m represents PCA1 + PCA2 +. . .+ PCAm.

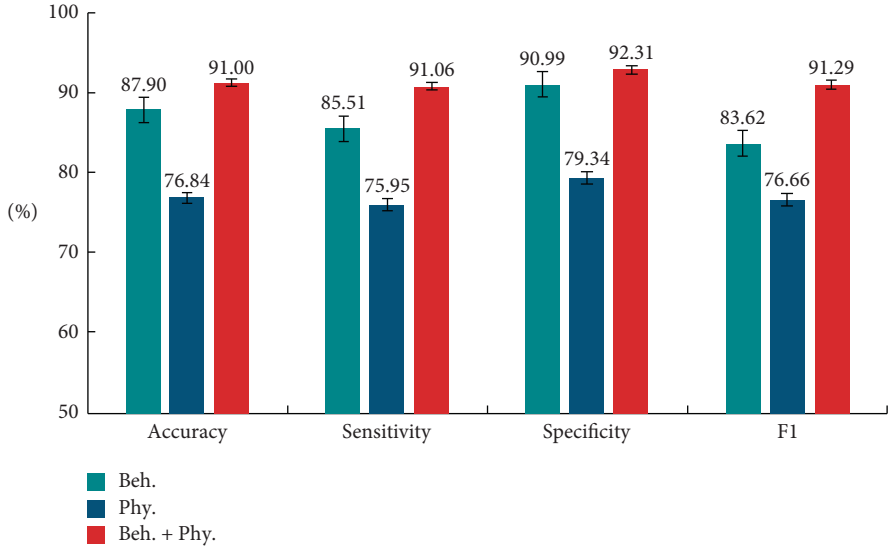

Figure 7: Classification results for different signal features. Beh. represents the eye movement behavioral signals; Phy. represents the eye movement physiological signals; Beh.+ Phy. represents the fusion features of eye movement behavioral and physiological signals.

PCA features (k is less than or equal to the number of PCA features) are selected iteratively as the classification features, and the 10-fold cross-validation method is used to train the model. Finally, the optimal feature subset is selected from multiple PCA feature subsets based on the classification accuracy.

Figure 6 shows the classification accuracy based on different PCA feature subsets. It can be seen that as the number of PCA features increases, the classification accuracy generally increases first and then decreases. According to the classification results, the optimal feature subset of behavioral signal PCA features is PCA1~PCA7, and the optimal feature subset of physiological signal PCA features is PCA1~PCA10.

3.2. Comparison of Classification Results of Different Signal Features. The classification results based on the features of eye movement behavioral signals, physiological signals, and their fusion signals are shown in Figure 7. It can be seen that the classification accuracy, sensitivity, specificity, and F1 score of behavioral signals are much higher than those of physiological signals, which indicate that the difference of attentional function in the emotional information between depressed patients and normal people is much greater than that of pupil size changes. When behavioral and physiological signals are used together in modeling, the classification results are better than those using single eye movement behavioral signals and single physiological signals.

3.3. Comparison with Other Methods. Table 2 shows the comparison with other methods for depression classification based on eye movement signals. It can be seen that our proposed classification method is much better than other methods.

Table 3 shows the comparison with other methods of depression classification based on fusion signals, and our proposed classification method is also much better than other methods.

Table 2: Comparison with other methods of depression classification based on eye movement signals.

	Accuracy (%)	Sensitivity (%)	Specificity (%)	F1 (%)
Reference [17]	—	75	—	—
Reference [18]	80.1	81.1	—	—
Proposed	**91.00**	**91.06**	**92.31**	**91.29**

Table 3: Comparison with other methods of depression classification based on fusion signals.

	Accuracy (%)	Sensitivity (%)	Specificity (%)	F1 (%)
Reference [13]	80.95	72.73	90	—
Reference [14]	—	66.7	—	57.1
Reference [15]	—	83	—	77
Reference [16]	—	83.3	82.6	—
Proposed	**91.00**	**91.06**	**92.31**	**91.29**

Table 4: Comparison of depression classification methods based on fusion signals (behavior and physiology) and different classification models.

	Accuracy (%)	Sensitivity (%)	Specificity (%)	F1 (%)
SVM	88.95	90.48	88.23	87.86
KNN	90.21	90.74	90.60	89.56
Random forests	**91.37**	**91.32**	90.96	90.78
KELM	91.00	91.06	**92.31**	**91.29**

We also compare the effects of different classification models on the classification results, as shown in Table 4. It can be seen that the KELM model and random forest model have better classification results.

From the comparison of the classification results in Tables 2 and 3, we can see that the proposed classification results based on the fusion of eye movement behavioral and physiological signals are better. There are three main aspects: first, compared with the previous resting-state EEG/fMRI signals and expression/voice, we obtain emotional information of eye movement under external emotional stimulation, which reflects the current mood of depressed patients; second, we use the relative change indicators such as attention bias and affective bandwidth features as classification features and, based on this, extract statistical indicators (minimum, lower quartile, median, upper quartile, maximum, mean, and standard deviation) directly related to the data distribution, which effectively improves the difference between depressed patients and normal people; third, through statistical feature selection and PCA-based feature extraction, the irrelevant features and redundant information are effectively removed, and the classification performance of depression is improved. In addition, compared with other methods, our proposed method also has the advantages of simple data acquisition and fewer features for classification.

4. Conclusion

In view of the lack of physiological and behavioral signals directly related to affective disorders in current research on depression recognition, this paper designs and extracts physiological signals based on the changes of affective bandwidth and pupil diameter and attentional bias signals based on gaze behavior. Statistical FDR corrected t-test and PCA are used for feature selection and feature extraction to eliminate noise and redundant information in behavioral and physiological signals of eye movement. The KELM classifier is used to classify depression based on behavioral features, physiological features, and fusion of behavior and physiological features. The results show that behavioral and physiological features are the main features of depression, and the fusion features improve the classification performance of depression.

In addition, we also use other classifiers (SVM, KNN, and random forest) to classify depression based on the fusion features of eye movement behavioral and physiological signals. The results show that the random forest model also achieved satisfactory classification results.

Data Availability

Since these data relate to personal, private information of patients and health subjects, there are ethical restrictions. All original data referred to in the paper will be made available upon request to the corresponding author.

Conflicts of Interest

The authors declare that they have no conflicts of interest.

Authors' Contributions

Mi Li, Lei Cao, and Qian Zhai contributed equally to this work.

Acknowledgments

This work was supported by the National Natural Science Foundation of China (61602017), the National Basic Research Programme of China (2014CB744600), "Rixin Scientist" Foundation of Beijing University of Technology (2017-RX(1)-03), the Beijing Natural Science Foundation (4164080), the Beijing Outstanding Talent Training Foundation (2014000020124G039), the National Natural Science Foundation of China (61420106005), the International Science & Technology Cooperation Program of China (2013DFA32180), the Special Fund of Beijing Municipal Science and Technology Commission (Z171100000117004), the Beijing Hospitals Authority Youth Programme (QML20181904), the Beijing Municipal Administration of Hospitals Clinical Medicine Development of Special

Funding Support (ZYLX201607), and the Beijing Municipal Administration of Hospitals' Ascent Plan (DFL20151801).

References

[1] L. Cao, S. Guo, Z. Xue et al., "Aberrant functional connectivity for diagnosis of major depressive disorder: a discriminant analysis," *Psychiatry and Clinical Neurosciences*, vol. 68, no. 2, pp. 110–119, 2014.

[2] J. Qin, M. Wei, H. Liu et al., "Abnormal hubs of white matter networks in the frontal-parieto circuit contribute to depression discrimination via pattern classification," *Magnetic Resonance Imaging*, vol. 32, no. 10, pp. 1314–1320, 2014.

[3] J. R. Sato, J. Moll, S. Green, J. F. W. Deakin, C. E. Thomaz, and R. Zahn, "Machine learning algorithm accurately detects fMRI signature of vulnerability to major depression," *Psychiatry Research: Neuroimaging*, vol. 233, no. 2, pp. 289–291, 2015.

[4] R. Bhaumik, L. M. Jenkins, J. R. Gowins et al., "Multivariate pattern analysis strategies in detection of remitted major depressive disorder using resting state functional connectivity," *NeuroImage: Clinical*, vol. 16, pp. 390–398, 2017.

[5] D. M. Schnyer, P. C. Clasen, C. Gonzalez, and C. G. Beevers, "Evaluating the diagnostic utility of applying a machine learning algorithm to diffusion tensor MRI measures in individuals with major depressive disorder," *Psychiatry Research: Neuroimaging*, vol. 264, pp. 1–9, 2017.

[6] R. Ramasubbu, M. R. G. Brown, F. Cortese et al., "Accuracy of automated classification of major depressive disorder as a function of symptom severity," *NeuroImage: Clinical*, vol. 12, pp. 320–331, 2016.

[7] S.-C. Liao, C.-T. Wu, H.-C. Huang, W.-T. Cheng, and Y.-H. Liu, "Major depression detection from EEG signals using kernel eigen-filter-bank common spatial patterns," *Sensors*, vol. 17, no. 6, p. 1385, 2017.

[8] G. M. Bairy, O. S. Lih, Y. Hagiwara et al., "Automated diagnosis of depression electroencephalograph signals using linear prediction coding and higher order spectra features," *Journal of Medical Imaging and Health Informatics*, vol. 7, no. 8, pp. 1857–1862, 2017.

[9] W. Mumtaz, L. Xia, S. S. A. Ali, M. A. M. Yasin, M. Hussain, and A. S. Malik, "Electroencephalogram (EEG)-based computer-aided technique to diagnose major depressive disorder (MDD)," *Biomedical Signal Processing and Control*, vol. 31, pp. 108–115, 2017.

[10] U. R. Acharya, S. L. Oh, Y. Hagiwara, J. H. Tan, H. Adeli, and D. P. Subha, "Automated EEG-based screening of depression using deep convolutional neural network," *Computer Methods and Programs in Biomedicine*, vol. 161, pp. 103–113, 2018.

[11] M. Valstar, J. Gratch, B. Schuller et al., "Avec 2016: depression, mood, and emotion recognition workshop and challenge," in *Proceedings of the 6th International Workshop on Audio/visual Emotion Challenge*, pp. 3–10, ACM, Amsterdam, Netherlands, October 2016.

[12] X. Ma, H. Yang, Q. Chen, D. Huang, and Y. Wang, "Depaudionet: an efficient deep model for audio based depression classification," in *Proceedings of the 6th International Workshop on Audio/visual Emotion Challenge*, pp. 35–42, ACM, Amsterdam, Netherlands, October 2016.

[13] J. Zhao, G. Luo, Z. Yao, and Q. Lu, "Depression discrimination using fMRI and DTI data by wavelet based fusion scheme," *Journal of Southeast University*, vol. 28, no. 1, pp. 25–28, 2012.

[14] Y. Le, D. Jiang, H. Lang, E. Pei, and H. Sahli, "Decision tree based depression classification from audio video and language information," in *Proceedings of the 6th International Workshop on Audio/visual Emotion Challenge*, pp. 89–96, ACM, Amsterdam, Netherlands, October 2016.

[15] T. Al Hanai, M. M. Ghassemi, and J. R. Glass, "Detecting depression with audio/text sequence modeling of interviews," in *Proceedings of the Interspeech*, pp. 1716–1720, Hyderabad, India, September 2018.

[16] A. Haque, M. Guo, A. S. Miner, and L. Fei-Fei, "Measuring depression symptom severity from spoken language and 3d facial expressions," 2018, http://arxiv.org/abs/1811.08592.

[17] S. Alghowinem, R. Goecke, M. Wagner, G. Parker, and M. Breakspear, "Eye movement analysis for depression detection," in *Proceedings of the 2013 IEEE International Conference on Image Processing*, pp. 4220–4224, IEEE, Melbourne, Australia, September 2013.

[18] X. Li, T. Cao, S. Sun, B. Hu, and M. Ratcliffe, "Classification study on eye movement data: towards a new approach in depression detection," in *Proceedings of the 2016 IEEE Congress on Evolutionary Computation*, pp. 1227–1232, Vancouver, BC, Canada, July 2016.

[19] T. Armstrong and B. O. Olatunji, "Eye tracking of attention in the affective disorders: a meta-analytic review and synthesis," *Clinical Psychology Review*, vol. 32, no. 8, pp. 704–723, 2012.

[20] A. Duque and C. Vázquez, "Double attention bias for positive and negative emotional faces in clinical depression: evidence from an eye-tracking study," *Journal of Behavior Therapy and Experimental Psychiatry*, vol. 46, pp. 107–114, 2015.

[21] E. H. Hess and J. M. Polt, "Pupil size as related to interest value of visual stimuli," *Science*, vol. 132, no. 3423, pp. 349-350, 1960.

[22] E. H. Hess, "Attitude and pupil size," *Scientific American*, vol. 212, no. 4, pp. 46–54, 1965.

[23] R. A. Hicks, S. L. Williams, and F. Ferrante, "Pupillary attributions of college students to happy and angry faces," *Perceptual and Motor Skills*, vol. 48, no. 2, pp. 401-402, 1979.

[24] M. Li, S. Lu, G. Wang, L. Feng, B. Fu, and N. Zhong, "Emotion, working memory, and cognitive control in patients with first-onset and previously untreated minor depressive disorders," *Journal of International Medical Research*, vol. 44, no. 3, pp. 529–541, 2016.

[25] M. Li, S. Lu, L. Feng, F. Bingbing, and G. Wang, "Emotional experience and the mood-congruent working memory effect in first-onset and untreated depressive disorder patients," *Journal of Psychiatry*, vol. 19, no. 4, p. 2, 2016.

[26] M. Li, S. Lu, G. Wang, and N. Zhong, "Affective bandwidth measurement and affective disorder determination," US Patent No. US9532711B2, 2017.

[27] G.-B. Huang, Q.-Y. Zhu, and C.-K. Siew, "Extreme learning machine: theory and applications," *Neurocomputing*, vol. 70, no. 1-3, pp. 489–501, 2006.

[28] G. B. Huang, H. Zhou, X. Ding, and R. Zhang, "Extreme learning machine for regression and multiclass classification," *IEEE Transactions on Systems, Man and Cybernetics, Part B (Cybernetics)*, vol. 42, no. 2, pp. 513–529, 2011.

[29] N. Tottenham, J. W. Tanaka, A. C. Leon et al., "The NimStim set of facial expressions: judgments from untrained research participants," *Psychiatry Research*, vol. 168, no. 3, pp. 242–249, 2009.

Hindawi
Complexity
Volume 2020, Article ID 7607545, 11 pages
https://doi.org/10.1155/2020/7607545

Research Article

Application of Soft Computing Techniques for the Analysis of Tractive Properties of a Low-Power Agricultural Tractor under Various Soil Conditions

Katarzyna Pentoś, Krzysztof Pieczarka, and Krzysztof Lejman

Wroclaw University of Environmental and Life Sciences, ul. J. Chełmońskiego 37, 51-630 Wrocław, Poland

Correspondence should be addressed to Katarzyna Pentoś; katarzyna.pentos@upwr.edu.pl

Received 27 May 2019; Accepted 17 December 2019; Published 10 January 2020

Guest Editor: Murari Andrea

Considering the fuel consumption and soil compaction, optimization of the performance of tractors is crucial for modern agricultural practices. The tractive performance is influenced by many factors, making it difficult to be modeled. In this work, the traction force and tractive efficiency of a low-power tractor, as affected by soil coefficient, vertical load, horizontal deformation, soil compaction, and soil moisture, were studied. The optimal work of a tractor is a compromise between the maximum traction force and the maximum tractive efficiency. Optimizing these factors is complex and requires accurate models. To this end, the performances of soft computing approaches, including neural networks, genetic algorithms, and adaptive network fuzzy inference system, were evaluated. The optimal performance was realized by neural networks trained by backpropagation as well as backpropagation combined with a genetic algorithm, with a coefficient of determination of 0.955 for the traction force and 0.954 for the tractive efficiency. Based on models with the best accuracy, a sensitivity analysis was performed. The results showed that the traction performance is mainly influenced by the soil type; nevertheless, the vertical load and soil moisture also exhibited a relatively strong influence.

1. Introduction

The mechanization of agricultural operations is essential for modern agricultural practices. Most agricultural operations are conducted using tractors that exert a high traction force (e.g., during tilling, cultivation, and seeding) or a light traction force (e.g., during harvesting and haymaking). Studies have found that 20–55% of the available tractor power is lost because of the interaction between the tires and topsoil [1]. The traction performance of a tractor significantly affects the fuel consumption and field performance resulting from soil compaction. Therefore, optimizing the performance is crucial for tillage management. The parameters significantly influencing the performance of drive wheels include the tire inflation pressures, wheel slip, and vertical wheel loads [2–5].

A mathematical modeling of the soil-tire interaction process can help improve the tractor design and minimize fuel consumption. Such models can be based on empirical, semiempirical, or analytical methods [6]. Analytical models have been developed for predicting traction parameters [7, 8]. However, Tiwari et al. emphasized some of the difficulties limiting the widespread use of analytical models, including the complex tire-soil interaction [6]. Semiempirical models are based on the vertical deformation of the soil and the shear deformation of the soil under a traction device. Rosca et al. proposed using experimentally derived parameters in semianalytical models to predict the traction performance of a driving tractor tire [9]. Empirical models are simpler than analytical and semiempirical models; however, their applicability is limited to cases in which the service and experimental conditions used to develop the model are similar.

The complex soil-tire interaction and the limitations in implementing the mathematical models described above have encouraged researchers to develop models based on

soft computing techniques. Artificial neural networks (ANNs) have been employed for predicting draught requirement of tillage implements under sandy clay loam soil conditions [10], prognosticating the energy efficiency indices of driven wheels [11], and modeling the relationship between travel reduction-to-net traction ratio and tractive efficiency [12]. Although an ANN is a powerful tool for solving stochastic and complex problems and can produce highly accurate prediction models, more sophisticated (hybrid) soft computing techniques have also been employed [13]. An ANN-genetic algorithm (GA) has been used to model the power of agricultural tractors as a function of the wheel load, slip, and speed [14] and to model the dynamic characteristics of a tractor on sloping terrain [15]. Another hybrid method used for modeling complex relationships in the agricultural field is the adaptive network fuzzy inference system (ANFIS), which combines the advantages of neural networks and fuzzy logic [16, 17].

Most studies on topsoil-tire interactions were conducted for high-power tractors (engine power > 73 kW). Studies concerning low-power tractors (engine power < 15 kW) are lacking. A high-power tractor is not always necessary. For example, in horticulture, vineyards, maintenance of green spaces, or in foothill areas on sloping terrain, the use of big, high-power tractors may be difficult. Furthermore, using low-power tractors is likely to reduce machinery costs and decrease soil compaction as a result of low tractor weight [18]. When high traction force is not required, the use of low-power tractors will result in lower fuel consumption, exhaust emissions reduction, and reduction of environmental pollution.

The tractive properties of agricultural tractors need to be optimized to minimize fuel consumption. However, the optimization process requires an accurate objective function. Nevertheless, based on measurement data, it is relatively easy to develop an empirical model of soil-tire interaction to be used as the objective function for an optimization algorithm. Considering the nonlinearity and complexity of a soil-tire interaction, soft computing techniques can be used to develop highly accurate models.

The objective of this study was to develop ANN, ANN trained by GA, ANN trained by backpropagation (BP) and GA, and ANFIS models to estimate the traction force or tractive efficiency of a low-power tractor as a function of the soil coefficient (which is indicative of soil texture as defined in equation (1)), vertical load, horizontal deformation, soil compaction, and soil moisture. Additionally, various modeling methodologies were compared to determine their accuracy in predicting the experimentally measured traction force or tractive efficiency. An analysis on the importance of predictor variables was conducted with highly accurate models. The parameters that significantly affect the tractive properties and can be varied by the tractor operator to optimize the traction force and tractive efficiency were found.

2. Materials and Methods

2.1. Experimental Data Acquisition. The tests were conducted on the following types of soil: sand, fine sandy loam, sandy loam, and silty clay loam. To obtain a universal model that can be used for different soil types, the soil texture was determined according to the USDA Comprehensive Soil Survey System [19]. The soil coefficient was calculated as follows:

$$S_c = \frac{c_1 + c_2 + c_3}{100}, \quad (1)$$

where S_c is the soil coefficient [−], c_1 is the proportion of medium silt in the test sample [%], c_2 is the proportion of fine silt in the test sample [%], and c_3 is the proportion of clay in the test sample [%].

Based on equation (1), the values of S_c for sand, fine sandy loam, sandy loam, and silty clay loam were calculated to be 0.08, 0.21, 0.33, and 0.68, respectively. Table 1 lists the values of soil moisture corresponding to various soil types, field capacity, beginning of plant growth inhibition, and strong inhibition of plant growth.

A soil bin testing facility (see Figure 1) was used in the laboratory to provide a controlled environment for evaluating the interaction between the soil and the tire. The tractive force was measured using a load cell with a measurement range of up to 1 kN and a precision of 1 N.

Low-power tractors are usually equipped with wheels having a rim diameter of 10 inches. On this type of rim, tires with different overall widths can be mounted, e.g., 4.00–10, 4.50–10, and 5.00–10. In the case of 5.00–10 tires, the contact area is the largest, resulting in a low-unit pressure and less soil compaction. Therefore, this tire is particularly advantageous for soils of low compaction because the larger tread blocks are unlikely to penetrate a highly compact soil. Conversely, in the case of highly compact soils, a 4.00–10 tire would be most beneficial, as the narrow tread blocks will be able to extend deeper into the soil ensuring an optimum traction force. In this work, experiments were conducted on soils of both low and high compactions. Therefore, the drive tire Kenda 4.50–10, type K365 for small agricultural tractors was used for the measurements. Considering that tractor tires must to some extent be universal, the results obtained for Kenda 4.50–10 can be extended to other tires manufactured for low-power tractors.

During the measurement, the peripheral speed of the wheel was constant and low (0.3 rad/s). The decision to use a low speed value was caused by the need to eliminate the impact of dynamic phenomena that could affect the results when the tests were performed on soils with different textures. The following five vertical load values were used in this work: 375, 490, 638, 785, and 932 N. The values of the vertical load were chosen on the basis of technical documentation provided by the manufacturers of the low-power tractors. The average vertical load recommended for low-power tractors is in the range of 800–900 N. The aim of this research was to develop mathematical models of the relationships under study, which can subsequently be used for optimizing the selected operating parameters in order to minimize soil compaction. Therefore, the authors selected three values of the vertical load, all of which were lower than that recommended for low-power tractors. The influence of tire inflation pressure on the tractive properties was not a subject

Table 1: Values of soil moisture (%).

	1.25 field water capacity	Field water capacity	Beginning of plant growth inhibition	Strong inhibition of plant growth
Sand	15.31	12.25	10.00	7.00
Fine sandy loam	24.38	19.50	16.00	11.20
Sandy loam	25.63	20.50	18.00	12.60
Silty clay loam	37.81	30.25	27.00	18.90

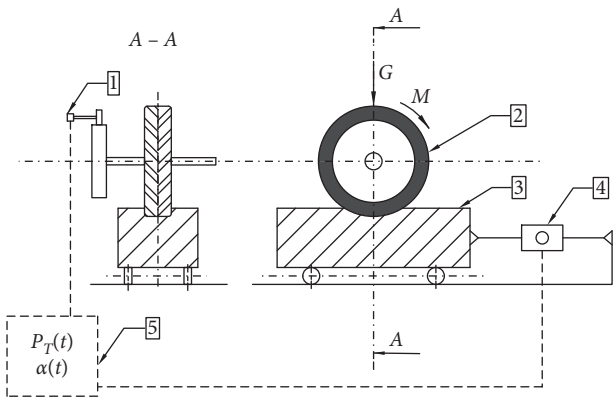

Figure 1: Schematic of a soil bin testing facility: 1, linear potentiometer; 2, wheel, 3, box with soil; 4, load cell; 5, data agent.

of this research. Thus, all the measurements were conducted using a constant pressure of 0.16 MPa (as recommended by the tire manufacturer).

For measuring the static-loaded radius, the tire deflection under certain vertical load and tire inflation pressures was determined. The measurement method is detailed in Figure 2(a).

The static loaded radius was calculated as follows:

$$r_s = r - e, \tag{2}$$

where r_s is the static loaded radius, r is the tire radius when the vertical load is equal to 0, and e is the tire deflection.

Based on the static loaded radius values and wheel rotation angle, the horizontal deformation can be calculated as follows:

$$j = \frac{\alpha \cdot r_s \cdot \pi}{180}, \tag{3}$$

where j is the horizontal deformation, α is the wheel rotation angle, and r_s is the static loaded radius (see Figure 2(b)).

The result of the measurements conducted using the soil bin testing facility (see Figure 1) was the traction force as a function of the rotation angle of the wheel. For each combination of the independent variables, the traction force increases with an increase in the horizontal deformation. Consequently, the maximum traction force could not be determined. Therefore, the horizontal deformation that produced a wheel slip of 20% (the slip limit accepted in the case of agricultural tractors) was determined analytically, and the traction force corresponding to this horizontal deformation was considered the maximum. The wheel slip depends on both the horizontal and vertical deformations. Hence, the horizontal deformation that produces a wheel slip of 20% can be determined only for a certain value of the vertical deformation (affected by vertical load, soil type, soil moisture, and soil compaction). In this research, the vertical deformation was calculated as an arithmetic mean of the maximum values measured for each soil type. The horizontal deformation corresponding to this vertical deformation and under a slip of 20% is found to be 0.05 m. Therefore, the traction force measured for a horizontal deformation of 0.05 m was considered the maximum. To determine the relationship between the traction force and the horizontal deformation, measurements were also taken for horizontal deformations of 0.02, 0.03, and 0.04 m (corresponding to slips of 5, 10, and 15%, respectively).

The tractive efficiency was calculated as follows:

$$\eta = \frac{\int_0^j P_T(j)\mathrm{d}j}{\int_0^j P_T(j)\mathrm{d}j + G \cdot h}, \tag{4}$$

where η is the tractive efficiency, P_T is the traction force (N), j is the horizontal deformation (m), G is the vertical load of the wheel (N), and h is the rut depth (m).

Table 2 lists the statistics of the experimental data.

The 1600 datasets (the vectors of measured parameters) obtained during the measurement process were randomly separated into training (80%) and validation (20%) sets. Table 2 lists the minimum and maximum input and output parameter values. Prior to utilizing the dataset for model development, the data were normalized to a range of 0-1 using the following equation:

$$NV = \frac{V - V_{\min}}{V_{\max} - V_{\min}}, \tag{5}$$

where NV is the input or output normalized vector, V is the input or output data, $V_{\max}$ is the maximum of the input or output data, and $V_{\min}$ is the minimum of the input or output data. We followed the methods of Pentoś and Pieczarka [20].

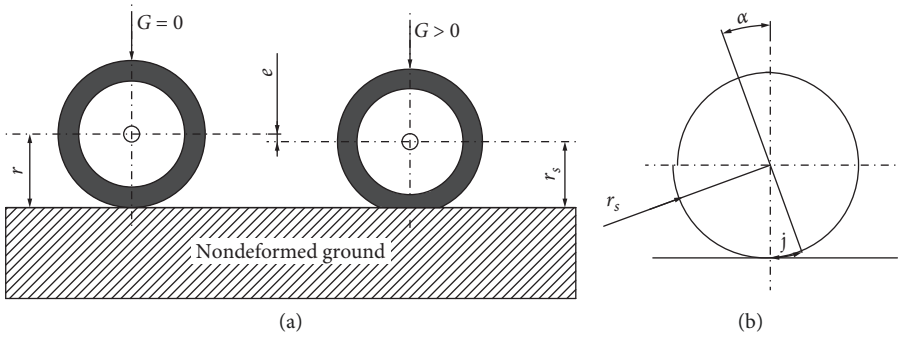

Figure 2: Method of static loaded radius measurement (a) and graphical representation of the parameters used for horizontal deformation calculation (b).

Table 2: Statistics of experimental data by the soil type.

The parameter	Minimum	Maximum	Mean	Standard deviation
Horizontal deformation (m)	0.01	0.05	0.03	0.01
Vertical load (N)	375.00	932.00	644.00	199.53
Sand				
Soil compaction (kPa)	201.04	571.85	386.45	124.51
Soil moisture (%)	7.00	15.00	11.00	2.91
Traction force (N)	65.81	596.56	284.91	114.27
Tractive efficiency (%)	5.04	85.55	33.61	17.43
Fine sandy loam				
Soil compaction (kPa)	102.69	498.11	300.85	125.92
Soil moisture (%)	11.00	24.00	17.76	4.82
Traction force (N)	99.78	787.63	339.94	140.15
Tractive efficiency (%)	4.45	85.71	33.44	17.39
Sandy loam				
Soil compaction (kPa)	90.88	486.30	288.59	125.84
Soil moisture (%)	13.00	26.00	19.50	4.72
Traction force (N)	36.09	683.61	326.27	133.30
Tractive efficiency (%)	0.99	64.98	27.97	14.38
Silty clay loam				
Soil compaction (kPa)	95.89	520.83	308.36	128.13
Soil moisture (%)	19.00	38.00	28.50	6.81
Traction force (N)	48.83	770.65	362.24	150.15
Tractive efficiency (%)	2.05	73.77	31.80	14.91

2.2. Artificial Neural Networks. An ANN is a highly simplified model of the biological structure of neurons in the human nervous system. An ANN is considered an effective substitute for the empirical and statistical process modeling techniques and is widely used in agricultural applications. In this work, a feed-forward neural network, namely, multilayer perceptron (MLP), was used. The ability of an ANN strongly depends on its topology, i.e., the number of hidden layers and the number of neurons in these layers. The optimal topology and learning parameters are usually determined by a trial and error method, requiring many simulations. For this study, an MLP with a single hidden layer was chosen as the ANN architecture. The input layer was composed of five nodes (soil coefficient, vertical load, horizontal deformation, soil compaction, and soil moisture). The number of neurons in the hidden layer was set to a range of 10–40, and nonlinear sigmoid neurons were implemented in this layer. There was one neuron in the output layer, producing the predicted value of the traction force or tractive efficiency. For each ANN architecture, 10 simulations were performed, and as a result, 310 ANNs were trained for each output parameter. The following were the three training methods used for the simulations: resilient backpropagation with and without weight backtracking and a modified globally convergent algorithm. The resilient backpropagation algorithm is based on the traditional backpropagation; however, in this algorithm, a separate learning rate η_k is used for each weight in the network and can be changed during the training process. Contrary to the traditional backpropagation, in resilient backpropagation, only the sign of the partial derivatives is used to indicate the direction of weight updation. The weights were modified using the following equation [21]:

$$w_k^{(t+1)} = w_k^{(t)} - \eta_k^{(t)} \cdot \operatorname{sign}\left(\frac{\partial E^{(t)}}{\partial w_k^{(t)}}\right), \tag{6}$$

where w_k is the k^{th} connection weight and E is the error function. Weight backtracking implies weight update reversal when the sign of the partial derivative changes [22]:

$$\Delta w_k^{(t)} = -\Delta w_k^{(t-1)}, \quad \text{if } \frac{\partial E^{(t-1)}}{\partial w_k^{(t)}} \cdot \frac{\partial E^{(t)}}{\partial w_k^{(t)}} < 0. \tag{7}$$

The modified globally convergent algorithm presented by Anastasiadis et al. is based on resilient backpropagation. A new modification to the learning rate is proposed [23]:

$$\eta_i^{(t)} = -\frac{\sum_{k;k\neq i}^{n} \eta_k^{(t)} \cdot \left(\partial E^{(t)}/\partial w_k^{(t)}\right) + \delta}{\partial E^{(t)}/\partial w_i^{(t)}}, \tag{8}$$

where $(\partial E^{(t)}/\partial w_i^{(t)}) \neq 0$ and $0 < \delta << \infty$. This modification improves the convergence speed and stability of the learning algorithm.

The "neuralnet" package, version 1.44.2, for the R environment (R Foundation for Statistical Computing (https://www.r-project.org/)), was used for the simulations [24].

2.3. Artificial Neural Network Combined with Genetic Algorithm. A typical problem with the ANN trained by an algorithm based on backpropagation is the possibility of falling into a local minimum of the error function, resulting in a slow convergence. Therefore, this technique needs to be improved by hybridizing the ANN with an optimization tool such as the GA. The GA, suggested by Holland, can be a pragmatic alternative to conventional local search methods [25]. In this study, two hybridizations of the ANN combined with GA were used. The first one (ANN + GA) utilizes a GA to realize the optimal allocation for the given network weights and biases starting from the random values. The second one (ANN_BP + GA) uses one of the algorithms based on backpropagation (resilient backpropagation with and without weight backtracking and modified globally convergent algorithm) for initial ANN training. The GA is then employed for the final optimization starting from the initial chromosome population produced by the ANN training. The chromosome in this work is the vector of genes, real numbers representing the ANN weights and biases. The following operations are performed on chromosome population during GA: selection and genetic operations (crossover and mutation). During the selection, the population of the chromosomes is chosen based on the fitness function for genetic operations. In the selection procedure, the probability that an individual can become a parent should be higher for higher fitness functions. A crossover operation is when two individuals (parents) exchange genes with each other. A crossover is performed with probability P_c, which is usually high. Mutation is a small random tweak in the chromosome that leads to a new individual. It is performed with probability P_m, which is usually low. The function of a mutation operation is to ensure a higher population diversity, consequently preventing the GA from falling into local extremes. After reaching the maximum generation, the GA converges to produce the best chromosome, which represents an optimal or near-optimal solution. In this work, the population size was set to 100 chromosomes, the crossover probability was set to 0.8, and the mutation probability was set to 0.01. As a fitness function, the root mean square error (RMSE) of the ANN was used for the validation dataset. The following were the three selection methods used: roulette wheel, tournament selection, and fitness proportional selection with fitness linear scaling. The genetic operations were performed with local arithmetic crossover and uniform random mutation. An R package, "GA" version 3.0.2, for optimization with the GA was used for the simulations [26].

2.4. Adaptive Network Fuzzy Inference System. The ANFIS is a global search soft computing technique, which combines the advantages of fuzzy logic and ANN. It is based on the first-order Takagi–Sugeno fuzzy inference system introduced by Jang [27]. This machine-learning technique generates fuzzy rules from a given input/output dataset and can adjust the membership function parameters directly from the data during the training process. The membership function parameters are adjusted using a combination of gradient descent and the least squares method. The typical fuzzy IF-THEN rules for the first-order Takagi–Sugeno fuzzy model are as follows:

$$\begin{aligned} &\text{IF } x_1 = A_1 \text{ and } x_2 = A_3 \text{ THEN } f = p_1^1 x_1 + p_2^1 x_2 + r^1, \\ &\text{IF } x_1 = A_2 \text{ and } x_2 = A_4 \text{ THEN } f = p_1^2 x_1 + p_2^2 x_2 + r^2. \end{aligned} \tag{9}$$

The ANFIS architecture contains a five-layer feed-forward neural network. Figure 3 shows the architecture used in the present work.

Layer 1 is the fuzzification layer. Each node in this layer represents a membership function (MF) and defines the membership grades for each set of input. There are various types of MFs. Because a normalized Gaussian function is used in this study, the output of this layer is given by

$$O_{1,n} = \mu_{An}(x) = \exp\left(\frac{-(x - c_n)^2}{2\sigma_n^2}\right), \tag{10}$$

where c_n and σ_n are the parameters that make up a premise set.

Layer 2 is a multiplicative layer. Each node uses a multiplication operator and calculates the firing strength of the rule as a product of the previous membership grades. For instance, for the first node, this is given by

$$O_{2,1} = w_1 = \mu_{A1}(x_1)\mu_{A4}(x_2)\mu_{A7}(x_3)\mu_{A10}(x_4)\mu_{A13}(x_5). \tag{11}$$

Layer 3 normalizes the firing strength of the rules:

$$O_{3,n} = \overline{w}_n = \frac{w_n}{\sum_j w_j}. \tag{12}$$

Layer 4 consists adaptive nodes that compute a linear function in which the parameters p^n and r^n are adapted using the error function of the feed-forward neural network:

$$O_{4,n} = \overline{w}_n \cdot f_n = \overline{w}_n \cdot \left(\sum_k p_k^n x_k + r^n\right). \tag{13}$$

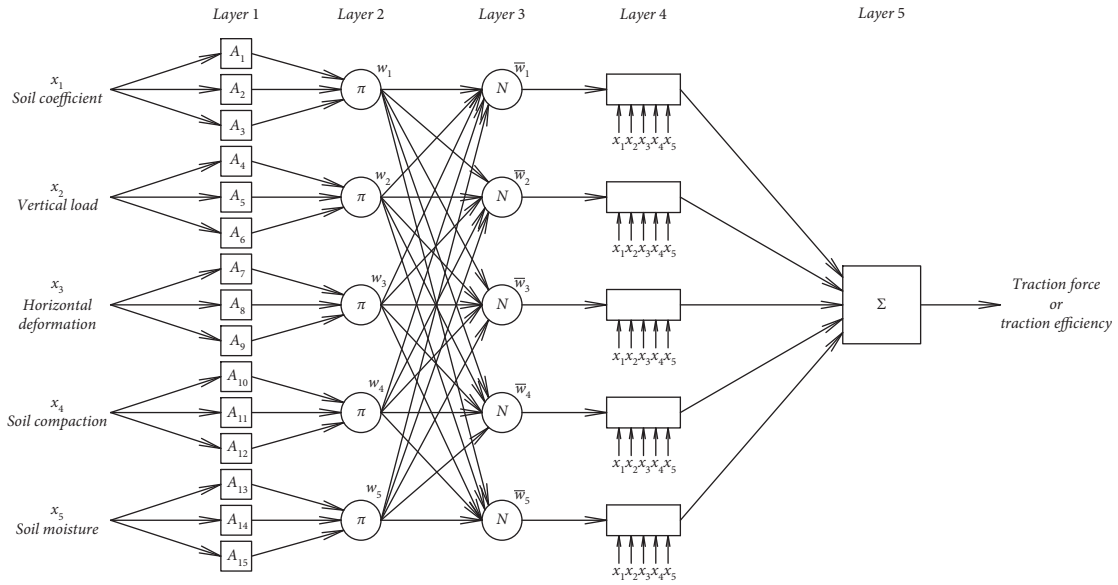

Figure 3: Adaptive neurofuzzy inference system structure.

Layer 5 has a single node and produces the output signal of the ANFIS, which is the sum of the outputs of the nodes from layer 4:

$$O_{5,1} = \sum_{n} O_{4,n}. \tag{14}$$

The package "anfis"—Adaptive Neurofuzzy Inference System in R, version 0.99.1, was used for the simulations. Excessive membership functions in the ANFIS model is not appropriate because many parameters need to be predicted. Therefore, the number of membership functions was set to 3, and the number of iterations was set to 20.

2.5. Comparison Criteria. The accuracy of the models were compared in terms of the mean absolute error (MAE), RMSE, and coefficient of determination (R^2), which are expressed as follows:

$$\mathrm{MAE} = \frac{1}{n}\sum_{i=1}^{n}\left|Y_{\mathrm{predicted}} - Y_{\mathrm{measured}}\right|,$$

$$\mathrm{RMSE} = \sqrt{\frac{1}{n}\sum_{i=1}^{n}\left(Y_{\mathrm{predicted}} - Y_{\mathrm{measured}}\right)^2},$$

$$R^2 = \left[\frac{\sum\left(Y_{\mathrm{measured}} - Y_{\mathrm{mean\_meas}}\right)\left(Y_{\mathrm{predicted}} - Y_{\mathrm{mean\_predict}}\right)}{\sqrt{\sum\left(Y_{\mathrm{measured}} - Y_{\mathrm{mean\_meas}}\right)^2 \sum\left(Y_{\mathrm{predicted}} - Y_{\mathrm{mean\_predict}}\right)^2}}\right]^2, \tag{15}$$

where $Y_{\mathrm{predicted}}$ and $Y_{\mathrm{mean\_predict}}$ are the absolute and average predicted values and Y_{measured} and $Y_{\mathrm{mean\_meas}}$ are the absolute and average measured values, respectively.

The MAE, using the absolute values of the differences between the measured and predicted values, rates over- and underestimations equally. The RMSE is an indicator of the distribution of positive and negative errors of the estimated values. R^2 estimates the strength of the relationship between the output value calculated using a model and the expected value. Therefore, the closer MAE and RMSE are to 0 and the closer R^2 is to 1, the better is the accuracy of the model in estimating the dependent variable.

2.6. Sensitivity Analysis. Based on the mathematical model, the importance of the independent variables can be estimated. Many methods have been proposed for model sensitivity analysis. The relevance of the method depends on the characteristics of the particular model. In this research, the partial derivatives method, dedicated for a neural network model, was used, whereby the contribution of the input variables is determined based on the connection weights and a bias matrix [28]. It is difficult to select an optimal ANN model architecture; thus, the contribution of the predictor variables should be determined based on a group of ANN models [29]. In the present research, a group of twenty ANN models with the highest R^2 values and the lowest MAE and RMSE values was selected. As the final result for each dependent variable (traction force and tractive efficiency), the arithmetical mean of the results produced by the twenty ANNs was calculated.

3. Results and Discussion

3.1. Soft Computing Models. The optimal solution, according to energy savings, is to have high values of both traction force and tractive efficiency. Figure 4 shows the dependence of the traction force and tractive efficiency on the vertical load and soil moisture measured on sand, for a horizontal deformation of 0.05 m.

As shown in Figure 4, the optimal traction force is produced under a high vertical load, whereas an optimal tractive efficiency can be achieved under a rather low vertical load. Therefore, achieving an optimal balance between the

traction force and the tractive efficiency is very difficult and requires accurate mathematical models of the tractive properties.

Before the development of the models based on the ANN, linearly dependent predictor variables must be removed from the dataset. Therefore, Pearson's correlation coefficients between the explanatory variables were calculated. A high positive correlation was observed only between the soil coefficient and the soil moisture ($r = 0.767$). However, after analyzing the experimental procedures, it was evident that both soil coefficient and soil moisture must be considered as input variables and used for model development. The correlation coefficient is high because the soil moisture range (Table 1) was determined depending on the soil texture.

Table 3 lists the statistical parameters, namely, R^2, RMSE, and MAE, for the best configurations of the mentioned models. The calculations were performed using normalized data (equation (5)).

In the case of the traction force model, the best architecture of the ANN was a network with 28 neurons in the hidden layer, and this network was chosen for weights optimization by the GA. The best ANN architecture trained by the GA starting from random values (ANN + GA) was a network with 14 neurons in the hidden layer. The best neural network for the tractive efficiency model had 26 neurons in the hidden layer, and the best ANN + GA model contained 17 neurons in the hidden layer.

Figures 5 and 6 show the measured and predicted traction force and tractive efficiency values for all the predictive models on the validation dataset. These graphs show the number of data points located very close to the diagonal line, thus facilitating the assessment of the model accuracy.

As listed in Table 3 and shown in Figures 5 and 6, for both output model parameters, among all the computational models, the ANN and ANN_BP + GA models exhibit the best performance, as indicated by high values of R^2 (0.954 and 0.955 for traction force and 0.954 for tractive efficiency) and low values of MAE and RMSE for the validation dataset. The use of the GA for optimizing the weights and biases adjusted by the BP algorithm produced slightly better accuracy in the case of the traction force model. The accuracy of the ANFIS model was lower than those of the ANN and ANN_BP + GA models, with R^2 values below 0.9. Additionally, the computational time required for the calculations during the ANFIS model development was significantly higher than that required in the case of models based on MLP. The ANN + GA technique seems to be unsuitable, exhibiting a low accuracy in estimating the traction force and tractive efficiency ($R^2 = 0.820$ and 0.752 for the validation dataset, respectively). Generally, it can be stated that, in agriculture, mathematical models (also based on machine learning) with coefficient of determination (R^2) exceeding 0.9 are useful for real life applications [30].

Neural networks and hybrid methods were also used by other researchers to model the behavior of agricultural tractors. The ANFIS-based modeling was found to be a promising technique for prognosticating the traction coefficient and tractive power efficiency, with R^2 values of 0.98 and 0.97, respectively [17] and for prognosticating the drawbar pull energy of tractor driving wheels, with MSE and R^2 values of 0.00236 and 0.995, respectively [16]. In the case of ANN combined with a GA, Taghavifar et al. demonstrated that this method drastically decreased the error and increased the performance of the model of power provided by agricultural tractors as affected by wheel load, slip, and speed [14]. They obtained high values for the coefficient of determination for the ANN + GA model: 0.9696 for the training dataset and 0.9672 for validation dataset.

Comparing the current results with those presented by other researchers, it is unclear which technique most accurately models the nonlinear and complex relationships such as the ones investigated in this study. Similar results were obtained by other researchers. Johann et al. compared computational models based on ANN and ANFIS in estimating the soil moisture from the stochastic information of the horizontal and vertical forces acting on a no-till chisel opener using autoregressive error function parameters [31]. The ANN model ($R^2 = 0.79$ and RMSE = 1.27) outperformed the ANFIS model ($R^2 = 0.69$ and RMSE = 1.62) in the test phase. Citakoglu applied ANN and ANFIS for estimating the solar radiation in Turkey using the calendar month number and pertinent meteorological data and obtained a higher accuracy when using the ANN ($R^2 = 0.930$ and RMSE = 1.650) in comparison with using the ANFIS ($R^2 = 0.926$ and RMSE = 1.691) [32]. In contrast, the ANFIS was found to be more suitable than the ANN for estimating the soil cation exchange capacity as affected by clay, silt, sand, organic carbon, and pH in arid rangeland ecosystems and for estimating the oxidation parameters of Kilka oil [33, 34]. Based on relevant error (RE) values, Ping and Fei showed that the accuracy of an ANN combined with a GA (RE = 1.48%) is better than that of a traditional ANN model (RE = 3.91%) for Guangdong port throughput forecasting [35]. Similarly, Srinivasulu and Jain found that the predictive capability of an ANN combined with GA rainfall-runoff models is better than that trained using a BP algorithm [36].

3.2. Sensitivity Analysis. A highly accurate mathematical model can give additional information about the relationships under study. A sensitivity analysis has been performed to determine the contribution of independent variables in black box data mining models. The neural network trained by backpropagation combined with a GA was found to be the best model for the relationships analyzed in the present research. This soft computing technique was used for developing the models for the sensitivity analysis. For each dependent variable (traction force and tractive efficiency), a group of twenty ANN models was developed. Table 4 lists the parameters of the models.

The results of the relative importance of the input parameters for each model were determined as the arithmetical mean of the results produced by the group of twenty ANN models. The results revealed that the traction force and tractive efficiency are most affected by the soil type (58.3 and 74.5%, respectively). This is in agreement with the results reported by other authors [37, 38]. The two additional

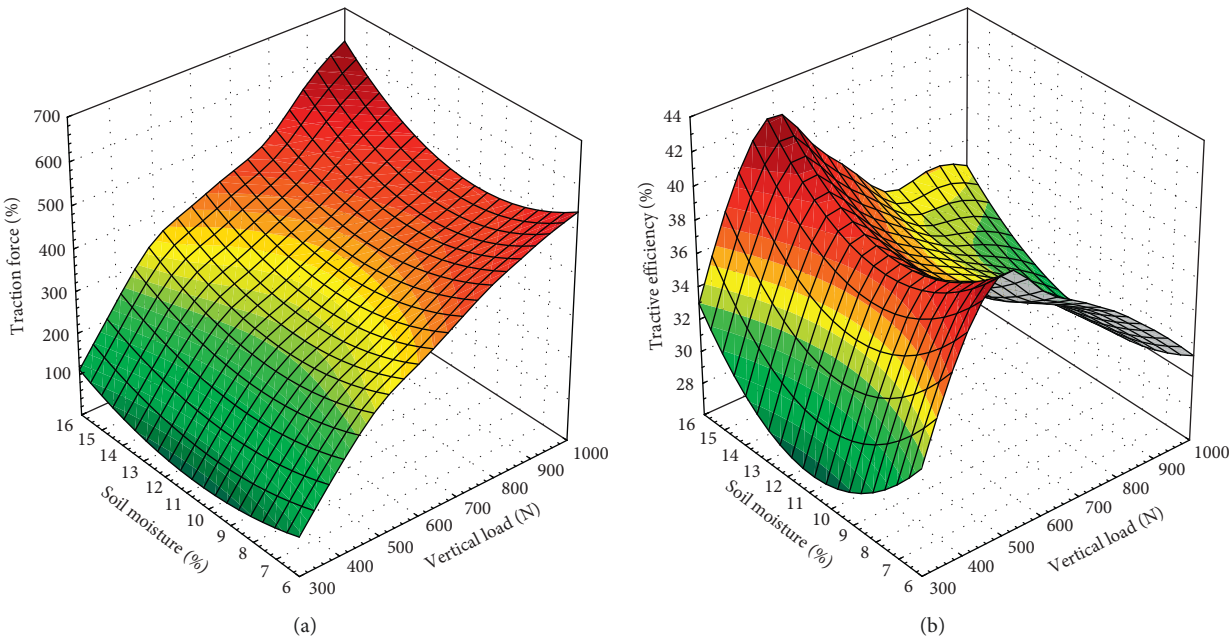

Figure 4: 3D surface curves of traction force (a) and tractive efficiency (b) as affected by the interactions of vertical load and soil moisture.

Table 3: Error metrics of best model performances.

Model	Train			Validation		
	MAE	RMSE	R^2	MAE	RMSE	R^2
Traction force						
ANN	0.026	0.037	0.957	0.029	0.040	0.954
ANN + GA	0.064	0.084	0.808	0.063	0.087	0.820
ANN_BP + GA	0.026	0.037	0.958	0.028	0.040	0.955
ANFIS	0.042	0.061	0.892	0.045	0.064	0.888
Tractive efficiency						
ANN	0.022	0.030	0.975	0.024	0.037	0.954
ANN + GA	0.076	0.102	0.789	0.068	0.096	0.752
ANN_BP + GA	0.022	0.030	0.975	0.024	0.037	0.954
ANFIS	0.038	0.061	0.883	0.040	0.064	0.872

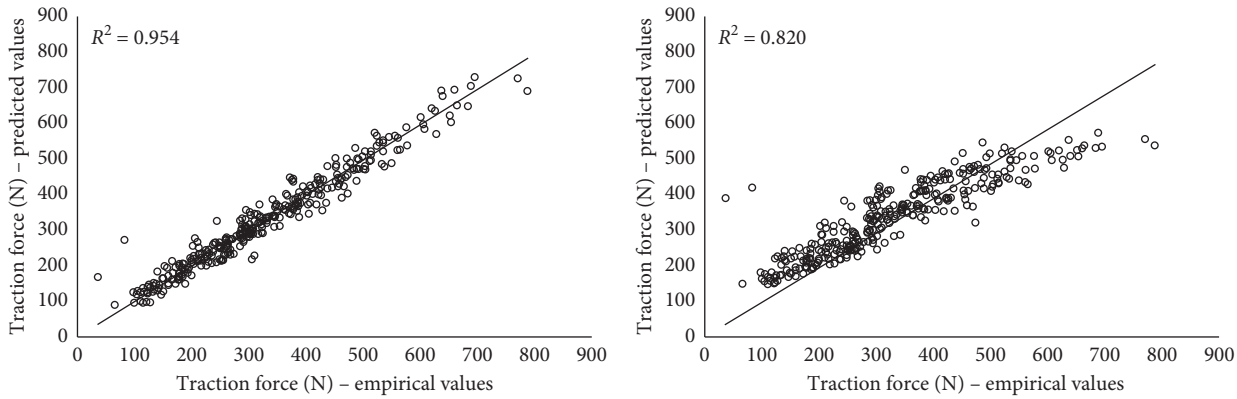

Figure 5: Continued.

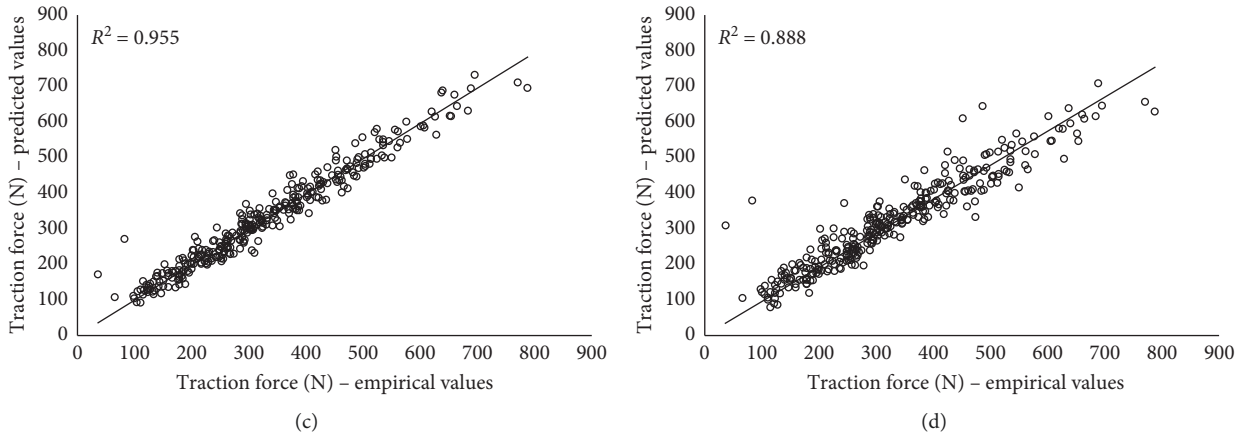

Figure 5: Scatterplot of model-predicted values versus actual values of traction force: (a) ANN, (b) ANN + GA, (c) ANN_BP + GA, and (d) ANFIS.

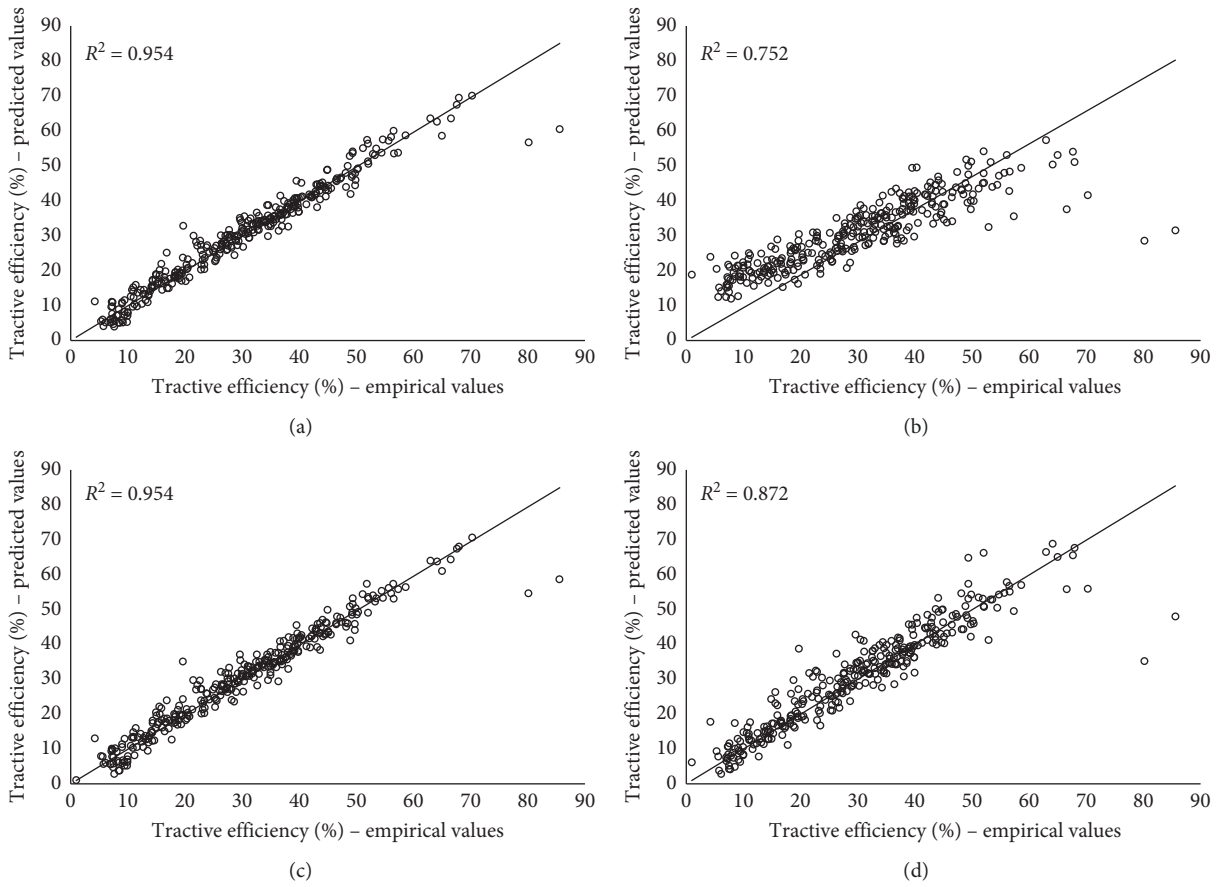

Figure 6: Scatterplot of model-predicted values versus actual values of tractive efficiency: (a) ANN, (b) ANN + GA, (c) ANN_BP + GA, and (d) ANFIS.

Table 4: Statistics of neural model architectures used for sensitivity analysis.

Dependent variable	The range of number of neurons in hidden layer	The range of R^2 for validation dataset	The range of MAE for validation dataset	The range of RMSE for validation dataset
Traction force	16–40	0.944–0.955	0.028–0.032	0.040–0.045
Tractive efficiency	16–38	0.928–0.954	0.024–0.032	0.037–0.047

parameters that significantly influenced the traction force and tractive efficiency are the vertical load (18.3 and 10.1%, respectively) and soil moisture (19.8 and 10.3%, respectively). The significant effects of these parameters on the tractive performance have been highlighted in other studies as well [11, 39]. It is worth emphasizing that the vertical load is one of the more easily manageable parameters during traction performance optimization. Soil moisture can also be varied in a certain range, as the operator can advance or delay agricultural operation depending on the weather condition. The influence of both horizontal deformation and soil compaction on the traction performance is very low (does not exceed 4%).

4. Conclusions

The optimization of the traction performance of an agricultural tractor is essential considering fuel economy. The development of highly accurate mathematical models that describe the tractive properties is an integral part of the optimization process. In this work, four soft computing techniques were used for predicting the traction force and tractive efficiency of a low-power tractor as affected by the soil type (expressed as soil coefficient), vertical load, horizontal deformation, soil compaction, and soil moisture. Comparisons of the error statistics revealed that the neural network model trained by a traditional BP algorithm or by a combination of BP and GA performs better in estimating both the traction force and tractive efficiency than an ANFIS model or an ANN trained by only a GA. An ANN structure with 28 neurons in the hidden layer produced the best model of the traction force, with an R^2 value of 0.954, a mean absolute error of 0.029, and an RMSE of 0.040. Similarly, an ANN with 26 neurons in the hidden layer was found to be the best structure for the tractive efficiency model, with $R^2 = 0.954$, MAE = 0.024, and RMSE = 0.037. Using GA for optimizing the weights and biases in the ANN model trained by BP led to a slight improvement in model accuracy. Considering the results presented by other authors, it can be stated that the potential usability of a certain technique depends strongly on the data characteristics. Moreover, the behavior of each machine-learning algorithm is affected by its parameters. Thus, for improving the optimization process, different techniques should be employed, and the model with the highest accuracy should be chosen. Considering the computational time required for ANFIS model development, the neural network trained by the backpropagation algorithm seems to be the best soft computing technique. The results of a sensitivity analysis conducted on a group of models with the highest accuracy showed that the soil type is the parameter most affecting the traction performance of a low-power tractor. A relatively strong influence was also found for the vertical load and soil moisture, which can be varied by the tractor operator to optimize the traction performance.

The results of this research are expected to be useful in saving energy in agricultural production systems. However, it should be noted that the application of the empirical models obtained by the authors is limited to conditions similar to those present during the measurements.

Data Availability

The data samples used to support the findings of this study are available from the corresponding author upon request.

Conflicts of Interest

The authors have no conflicts of interest to declare.

References

[1] T. Smerda and J. Cupera, "Tire inflation and its influence on drawbar characteristics and performance—energetic indicators of a tractor set," *Journal of Terramechanics*, vol. 47, no. 6, pp. 395–400, 2010.

[2] A. Janulevicius and V. Damanauskas, "How to select air pressures in the tires of MFWD (mechanical front-wheel drive) tractor to minimize fuel consumption for the case of reasonable wheel slip," *Energy*, vol. 90, pp. 691–700, 2015.

[3] H. Taghavifar, A. Mardani, and H. Karim-Maslak, "Multi-criteria optimization model to investigate the energy waste of off-road vehicles utilizing soil bin facility," *Energy*, vol. 73, pp. 762–770, 2014.

[4] J. H. Lee and K. Gard, "Vehicle-soil interaction: testing, modeling, calibration and validation," *Journal of Terramechanics*, vol. 52, pp. 9–21, 2014.

[5] F. M. Zoz and R. D. Grisso, "Traction and tractor performance," in *ASAE Distinguished Lecture Series*, Vol. 27, American Society of Agricultural Engineers, Tractor Design No. 27, St. Joseph, MI, USA, 2003.

[6] V. K. Tiwari, K. P. Pandey, and P. K. Pranav, "A review on traction prediction equations," *Journal of Terramechanics*, vol. 47, no. 3, pp. 191–199, 2010.

[7] C. W. Fervers, "Improved FEM simulation model for tire-soil interaction," *Journal of Terramechanics*, vol. 41, no. 2-3, pp. 87–100, 2004.

[8] H. Nakashima and A. Oida, "Algorithm and implementation of soil-tire contact analysis code based on dynamic FE-DE method," *Journal of Terramechanics*, vol. 41, no. 2-3, pp. 127–137, 2004.

[9] R. Rosca, P. Carlescu, and I. Tenu, "A semi-empirical traction prediction model for an agricultural tyre, based on the super ellipse shape of the contact surface," *Soil and Tillage Research*, vol. 141, pp. 10–18, 2014.

[10] A. K. Roul, H. Raheman, M. S. Pansare, and R. Machavaram, "Predicting the draught requirement of tillage implements in sandy clay loam soil using an artificial neural network," *Biosystems Engineering*, vol. 104, no. 4, pp. 476–485, 2009.

[11] H. Taghavifar and A. Mardani, "Applying a supervised ANN (artificial neural network) approach to the prognostication of driven wheel energy efficiency indices," *Energy*, vol. 68, pp. 651–657, 2014.

[12] K. Çarman and A. Taner, "Prediction of tire tractive performance by using artificial neural networks," *Mathematical and Computational Applications*, vol. 17, no. 3, pp. 182–192, 2012.

[13] S. A. Hoseinpour, A. Barati-Harooni, P. Nadali et al., "Accurate model based on artificial intelligence for prediction of carbon dioxide solubility in aqueoustetra-n-butylammonium bromide solutions," *Journal of Chemometrics*, vol. 32, no. 2, Article ID e2956, 2018.

[14] H. Taghavifar, A. Mardani, and A. H. Hosseinloo, "Appraisal of artificial neural network-genetic algorithm based model for

prediction of the power provided by the agricultural tractors," *Energy*, vol. 93, pp. 1704–1710, 2015.

[15] Z. X. Zhu, R. Torisu, J. I. Takeda, E. R. Mao, and Q. Zhang, "Neural network for estimating vehicle behaviour on sloping terrain," *Biosystems Engineering*, vol. 91, no. 4, pp. 403–411, 2005.

[16] H. Taghavifar and A. Mardani, "Evaluating the effect of tire parameters on required drawbar pull energy model using adaptive neuro-fuzzy inference system," *Energy*, vol. 85, pp. 586–593, 2015.

[17] H. Taghavifar and A. Mardani, "On the modeling of energy efficiency indices of agricultural tractor driving wheels applying adaptive neuro-fuzzy inference system," *Journal of Terramechanics*, vol. 56, pp. 37–47, 2014.

[18] N. H. Abu-Hamdeh, "The disturbance of topsoil using ultrasonic waves," *Soil and Tillage Research*, vol. 75, no. 1, pp. 87–92, 2004.

[19] N. C. Brady and R. R. Weil, *The Nature and Properties of Soils*, Pearson Education International, London, UK, 15th edition, 2008.

[20] K. Pentoś and K. Pieczarka, "Applying an artificial neural network approach to the analysis of tractive properties in changing soil conditions," *Soil and Tillage Research*, vol. 165, pp. 113–120, 2017.

[21] G. Frauke and S. Fritsch, "Neuralnet: training of neural networks," 2010, https://journal.r-project.org/archive/2010/RJ-2010-006/RJ-2010-006.pdf.

[22] M. Riedmiller, "Advanced supervised learning in multi-layer perceptrons-from backpropagation to adaptive learning algorithms," *Computer Standards & Interfaces*, vol. 16, no. 3, pp. 265–278, 1994.

[23] A. D. Anastasiadis, G. D. Magoulas, and M. N. Vrahatis, "New globally convergent training scheme based on the resilient propagation algorithm," *Neurocomputing*, vol. 64, pp. 253–270, 2005.

[24] S. Fritsch, F. Guenther, M. N. Wright, M. Suling, S. M. Mueller, 2019 https://cran.r-project.org/web/packages/neuralnet/index.html.

[25] J. H. Holland, *Adaptation in Natural and Artificial Systems*, University of Michigan Press, Ann Arbor, MI, USA, 1975.

[26] L. G. A. Scrucca, "A package for genetic algorithms in R," *Journal of Statistical Software*, vol. 53, no. 4, pp. 1–37, 2013.

[27] J.-S. R. Jang, "ANFIS—adaptive-network-based fuzzy inference system," *IEEE Transactions on Systems, Man, and Cybernetics*, vol. 23, no. 3, pp. 665–685, 1993.

[28] Y. Dimopoulos, P. Bourret, and S. Lek, "Use of some sensitivity criteria for choosing networks with good generalization ability," *Neural Processing Letters*, vol. 2, no. 6, pp. 1–4, 1995.

[29] K. Pentoś, "The methods of extracting the contribution of variables in artificial neural network models—comparison of inherent instability," *Computers and Electronics in Agriculture*, vol. 127, pp. 141–146, 2016.

[30] K. Liakos, P. Busato, D. Moshou, S. Pearson, and D. Bochtis, "Machine learning in agriculture: a review," *Sensors*, vol. 18, no. 8, p. 2674, 2018.

[31] A. L. Johann, A. G. de Araújo, H. C. Delalibera, and A. R. Hirakawa, "Soil moisture modeling based on stochastic behavior of forces on a no-till chisel opener," *Computers and Electronics in Agriculture*, vol. 121, pp. 420–428, 2016.

[32] H. Citakoglu, "Comparison of artificial intelligence techniques via empirical equations for prediction of solar radiation," *Computers and Electronics in Agriculture*, vol. 118, pp. 28–37, 2015.

[33] H. Ghorbani, H. Kashi, N. Hafezi Moghadas, and S. Emamgholizadeh, "Estimation of soil cation exchange capacity using multiple regression, artificial neural networks, and adaptive neuro-fuzzy inference system models in Golestan province, Iran," *Communications in Soil Science and Plant Analysis*, vol. 46, no. 6, pp. 763–780, 2015.

[34] M. Asnaashari, R. Farhoosh, and R. Farahmandfar, "Prediction of oxidation parameters of purified Kilka fish oil including gallic acid and methyl gallate by adaptive neuro-fuzzy inference system (ANFIS) and artificial neural network," *Journal of the Science of Food and Agriculture*, vol. 96, no. 13, pp. 4594–4602, 2016.

[35] F. F. Ping and F. X. Fei, "Multivariant forecasting mode of Guangdong Province port throughput with genetic algorithms and Back Propagation neural network," in *Proceedings from the 13th Cota International Conference of Transportation Professionals*, vol. 96, pp. 1165–1174, Shenzhen, China, August 2013.

[36] S. Srinivasulu and A. Jain, "A comparative analysis of training methods for artificial neural network rainfall-runoff models," *Applied Soft Computing*, vol. 6, no. 3, pp. 295–306, 2006.

[37] E. V. McKyes, *Soil Cutting and Tillage*, Elsevier Science Publishers BV, Amsterdam, Netherlands, 1985.

[38] F. M. Zoz, *Predicting Tractor Field Performance*, Vol. 49085, ASAE, St. Joseph, MI, USA, 1970.

[39] M. I. Lyasko, "How to calculate the effect of soil conditions on tractive performance," *Journal of Terramechanics*, vol. 47, no. 6, pp. 423–445, 2010.

Hindawi
Complexity
Volume 2020, Article ID 7190169, 20 pages
https://doi.org/10.1155/2020/7190169

WILEY | Hindawi

Research Article

A "User-Knowledge-Product" Co-Creation Cyberspace Model for Product Innovation

Yu Wang[1], **Jiacong Wu**[2], **Ru Zhang**[1], **Sara Shafiee**[3] **and Cheng Li**[1]

[1]*School of International Business, Jinan University (Zhuhai Campus), Zhuhai 519070, China*
[2]*School of Management, Jinan University, Guangzhou 510632, China*
[3]*Department of Mechanical Engineering, Technical University of Denmark, Kgs. Lyngby 2800, Denmark*

Correspondence should be addressed to Jiacong Wu; skywu@stu2017.jnu.edu.cn and Ru Zhang; zhangru@stu2016.jnu.edu.cn

Received 9 April 2019; Accepted 8 October 2019; Published 10 January 2020

Guest Editor: Murari Andrea

To benefit from users' co-creation knowledge in online communities, enterprises need effective methods to discover and manage co-creation users and knowledge as suggested in existing research. However, the existing methods still have their own limitations when analysing different relationships and networks. Therefore, first, this paper proposes a co-creation cyberspace super-network model for product innovation from a "user-knowledge-product" perspective to integrate the co-creation information of users, knowledge, and products. Second, to increase the accuracy of discovering, managing, and using the co-creation knowledge, three subnetworks including co-creation user network, co-creation knowledge network, and co-creation product network as well as the relationships among them are constructed and improved. Third, a well-known co-creation community in China is selected as a case to verify the feasibility and validity of the proposed model for enterprise's product innovation. Three subnetworks and the mapping relationships among them are constructed and visualized based on the introduced User-Knowledge-Product Cyberspace model. The results from the case study validate the co-creation cyberspace constructed in this paper and provide enterprises with a comprehensive and detailed integration framework analysis model. Hence, the enterprises can use this model for user discovery, product innovation knowledge mining, and dynamic innovation knowledge basement and forecast hotspot trend in co-creation communities.

1. Introduction

As product innovation has become more complex and its costs have increased in recent years, enterprises can no longer realize continuous innovation through their internal innovation capabilities; rather they increasingly co-create with external stakeholders [1]. With the advances in information technology, online co-creation communities with a large volume of user-generated content provide enterprises a new way to communicate with customers [2, 3]. In online co-creation communities, customers can interact actively with each other and are absorbed in product development process. They provide inputs in the form of ideas, suggestions, and solutions, serving as product conceptualizers, product designers, product testers, product observers, and product marketers [4]. Therefore, enterprises can select the pertinent ideas for their innovation development to improve their products and service, expand markets, and even accelerate innovation processes [3, 5]. Furthermore, enterprises can also improve customer relationship management, such as brand loyalty, brand trust, and brand commitment in online co-creation communities [6–8].

As argued by Irani et al. [9], users' co-creation knowledge is a unique and nonduplicated resource and serves as a driven force in promoting product innovation. In a complex social network system, the co-creation knowledge generated between enterprises and users is critical for enterprises' product innovation and their continued competitiveness in markets [10]. However, enterprises can hardly utilize co-creation knowledge in online communities for efficient product innovation [11] and the probable reasons are as follows. (1) There is overload of information and overflow of

spam messages that present significant challenges in co-creation knowledge discovery, management, and application [11]. (2) It is difficult to manage online co-creation communities as they are easy to access with no time and geographical constraint [12]. (3) The knowledge from co-creation communities is unstructured, diverse, and heterogeneous [13], which is one of the reasons in hindering knowledge discovery and classification, and product innovation [14].

The issue of constructing a co-creation knowledge network to discover, manage, and apply co-creation knowledge for product innovation has been recognized by a few research [14–17]. However, most of the existing research has its own limitations when analysing different relationships of users and knowledge and constructing different subnetworks. First, most of the existing research ignored the collaborative relationship between co-creation users when constructing co-creation user network [14], which influences the accuracy of identifying leading users. Second, when constructing co-creation knowledge network, the co-occurrence relationship of knowledge points was considered, but the similarity relationship among knowledge points was not taken into account, resulting in information overload. In addition, lack of comprehensive consideration of knowledge point weights lead to inaccurate identification of hot knowledge points. Third, most of the existing research only considered two-tier networks, the co-creation users and knowledge network [14], which influences the accuracy and efficiency when mapping co-creation knowledge with product innovation. Therefore, to address these limitations, this paper aims to answer the following research questions: (1) How to fully consider the relationships between co-creation users to better manage users and identify leading users? (2) How to integrate highly similar co-creation knowledge points to avoid information overload and comprehensively consider knowledge point weights to better identify hot co-creation knowledge points? (3) How to construct a product network (includes the nodes of product names and product feature network) to map with co-creation knowledge points for more accurate product innovation?

To address those research questions and considering the limitations of the existing research, we develop a co-creation cyberspace super-network model for product innovation to help enterprises to discover, manage and apply co-creation knowledge in an effective way. This paper contributes from three different perspectives. The first is to understand the relationships among co-creation users more comprehensively and discover the leading co-creation users more accurately. So, both the interaction and collaboration relationships among co-creation users are considered when constructing co-creation user network. Second, to avoid information overload, this paper uses the words similarity algorithm to avoid the repeated calculation of co-creation knowledge when constructing co-creation knowledge network. In addition, knowledge frequency, attention, and character are considered adequately when constructing knowledge weight set. Third, a co-creation product network is further constructed to map with co-creation user network and co-creation knowledge network for better product innovation.

This paper is organized as follows: The next section reviews relevant studies already conducted in this research area. Section 3 describes the construction of the "user-knowledge-product" co-creation cyberspace model. Three subnetworks are constructed and the mapping relationships among them are analysed in details. Section 4 uses a case study of a well-known co-creation community in China to visualise and validate the proposed co-creation cyberspace model. Finally, contribution to theory and industry and limitations and future directions of this paper are discussed.

2. Literature Review

In recent years, in order to mine the value of co-creation knowledge and take advantage of the useful co-creation knowledge for business purpose, various research areas have been explored. However, there are three streams of literature relevant to this paper. First, several studies researched in online community knowledge creation process and mechanism to understand how users participate in online communities and generate co-creation knowledge. Second, some studies further researched in online community knowledge discovery and management and proposed multiple methods and tools for it. Third, few studies further investigated in knowledge application to explore how the discovered and managed co-creation knowledge can be used for business purpose. The three streams of relevant literature are reviewed in subsections below in details.

2.1. Studies on Online Community Knowledge Creation Processes and Mechanisms. Knowledge is created through two generic processes: combination and exchange [18], and thus online community knowledge creation processes and mechanisms should be studied from not only an individual perspective but also a community perspective [19]. Two streams of studies have examined knowledge creation. First, from an individual perspective, leading users are often important initiators and contributors of innovative knowledge such as product concepts. For example, Von Hippel [20] proposed that leading users can present the main requirements which will become general in a marketplace in few months or years, and they can provide new product concept and design data as well. In addition, as a strong cornerstone for product innovation, leading users often maintain more frequent interactions with other members in the community and inspire other users to participate in co-creation process [21]. Second, from a community perspective, interactions in one community are the key driver in knowledge creation [1]. For example, Hau and Kim [22] proposed that social capital is the major concern that prompts users to share their innovative knowledge voluntarily. The greater social capital and relationship facilitate the access of individuals to other sources of knowledge within and outside the organisation and increase their willingness and efficiency of knowledge co-creation [18]. Hafkesbrink and Schroll [23] found that,

basically, co-creation community is a learning community involving users and managers and they collaboratively conduct a learning and innovation process.

However, such studies can only keep practitioners informed of the gained benefits from co-creation knowledge for enterprises' product innovation. There is limited practicability to provide guidance on how to better coordinate online users" innovative knowledge creation and the internal new product development in an enterprise. Therefore, there is a great practical significance and theoretical value in analysing their connection.

2.2. Studies on Online Community Knowledge Discovery and Management. As for online knowledge discovery and management, existing research has explored multiple methods and tools for analysing the co-creation knowledge network structures and knowledge development process such as concept map, domain knowledge map, and knowledge super-network. Divakaran [24] proposed a "community-aided brand concept map" to collect user-generated data and analyse the evolution and the dynamic pattern of brand associations. According to the domain feature set defined by domain experts, Hao et al. [25] proposed a domain knowledge map construction method using latent semantic analysis, so that various types of knowledge can be classified into different domains based on their semantics for better knowledge management. Due to the lack of research in the construction of semantic knowledge base and the semantic expression model in the context of big data, Liu et al. [26] proposed a model and construction method on dynamic knowledge network. Liao et al. [27] proposed modelling and analysing methods of user-innovation knowledge in enterprise communities based on a weighted knowledge network, so that the importance of each knowledge and the closeness among each knowledge can be clearly indicated in the network. Furthermore, based on a super-network model for public innovation, Tang et al. [14] proposed an analytical framework for enterprises to manage all elements of knowledge in online communities conveniently. Comprehensively considering the users, attention, and frequency of knowledge, the authors constructed user network, text network, and semantics network of knowledge and the relationship among them.

Such research provided great methods and technical support for the discovery and management of co-creation knowledge and they could be the base of this study. However, these knowledge network construction methods also have their own limitations which need to be improved in this study. For example, when analysing the relationships among co-creation users, only the collaboration relationship was considered and the interaction relationship was ignored [14], which create biases for the accurate discovery and management of co-creation users. The concern, reply, forwarding, and comment among co-creation users are more and more frequent, and this interaction information among users is valuable and necessary to be taken into account for accurate co-creation user identification. Furthermore, when analysing the relationships between knowledge points, only the co-occurrence of knowledge points was considered, but the similarity relationship among knowledge points was not taken into account [14, 26, 27], resulting in information overload and inaccurate hot co-creation knowledge discovery. As different users may use similar but different words to express same meaning, Wang and Shao [28] have indicated the importance of considering the similarity among words and merging similar words for more accurate word frequency statistics. It is obvious that the management and discovery of co-creation knowledge will be disturbed without considering the similarity among knowledge. Moreover, the factors considered when setting the knowledge point weights were not comprehensive enough [14, 25–27], interfering the discovery of hot knowledge. Based on a Co-word model [28], keywords with different position, part-of-speech, or span have different importance significantly. Therefore, these characters of knowledge points are necessary to be considered for more comprehensive co-creation knowledge management and discovery.

2.3. Studies on Knowledge Application. Chen et al. [15] proposed a knowledge super-network model to provide support for knowledge acquisition and integration in the process of innovation, and the exploration and evaluation of innovation issues. Yang et al. [16] proposed a knowledge-driven product innovation design model based on complex networks according to the application characteristics of design knowledge in innovation and many-to-many relationship of functions, behaviours, and structures. Yassine and Bradley [17] built a knowledge network model based on data acquisition, transformation, and utilization to support product development and design.

Such research sheds light on co-creation knowledge application and gives support to enterprises during their product innovation process. However, most of the existing research only considered two-tier networks, the co-creation user network, and the co-creation knowledge network, which influence the accuracy and efficiency when mapping co-creation knowledge with product innovation.

2.4. Literature Summary. This section presented and overview on different research available on online community knowledge co-creation, online community knowledge discovery and management (e.g. concept map, various knowledge network, etc.), and also business cases and applications for the industries. Table 1 summarizes few discussed research in the previous subsections and categorizes them based the area of application and lists the positive contribution and remaining gaps in the field "Detailed contribution (+)/Gap in the research (−)." The table has been divided into four columns to determine the research contribution in three co-creation network construction. As it is illustrated, most of the previous research focused on co-creation knowledge network construction, and we rarely found studies on co-creation user network and product network construction, which are also valuable and important for product innovation. Therefore, it is the motivation and contribution of this paper to extend the previous co-creation network to a more comprehensive and systematic "user-knowledge-product" co-creation cyberspace model for better product innovation.

Table 1: Previous research summary.

Related research	Co-creation user network	Co-creation knowledge network	Co-creation product network	Detailed contribution (+)/gap in the research (-)
Divakaran [24]		✓		+ Analysed the evolution and the dynamic pattern of brand associations. − The considered weights and relationship of knowledge are simple.
Hao et al. [25]		✓		+ Various types of knowledge can be classified into different domains based on their semantics for better knowledge management. − Only the co-occurrence relationship among knowledge was considered. The weights of knowledge were neglected.
Liu et al. [26]		✓		+ Constructed a semantic expression model of dynamic knowledge network in the context of big data. − Only considered the semantic relationship among knowledge. No attention to the relation between user and knowledge and product for product innovation.
Liao et al. [27]		✓		+ The importance of each knowledge and the closeness among each knowledge can be clearly indicated in the network. − Some character weights of knowledge and the similarity relationship among knowledge were neglected.
Tang et al. [14]	✓	✓		+ Comprehensively considering the users, attention, and frequency of knowledge, the authors constructed user network, text network, and semantics network of knowledge and the relationship among them. − Some character weights of knowledge and the similarity relationship among knowledge were neglected.
Chen et al. [15]		✓		+ Support for knowledge acquisition and integration in the process of innovation and the exploration and evaluation of innovation issues. − No attention to the relation between user and knowledge.
Yang et al. [16]		✓		+ Proposed a knowledge-driven product innovation design model. − No attention to the relation between user and knowledge.
Yassine and Bradley [17]		✓		+ Constructed a knowledge network model based on data acquisition, transformation, and utilization to support product development and design. − No attention to the relation between user and knowledge.
This paper	✓	✓	✓	+ (1) Combined some of the advantages of the construction of co-creation user and knowledge network in the related literature. (2) Further considered some important but neglected weights and relationships of users and knowledge to make the network more comprehensive. (3) Extend the previous network to a more systematic "user-knowledge-product" co-creation cyberspace model for better product innovation. − The comparative analysis with the related research is required in the future to prove the priority of the model.

3. Construction of the "User-Knowledge-Product" Co-Creation Cyberspace Model

To address the limitations ascertained from the literature, as summarized in Section 2, we propose a "user-knowledge-product" co-creation cyberspace super-network model to provide a more comprehensive, detailed, and integrated analysis model for user discovery and management and product innovative knowledge mining and management, which is shown in Figure 1.

This model is novel due to the following design considerations:

(1) When constructing the co-creation user network, not only collaboration relationship but also interaction relationship among co-creation users are considered for better user management and leading user identification. Based on the attention relationship, reply relationship, forwarding relationship, and review relationship among co-creation users, the direct interaction relationship among co-creation users is built.

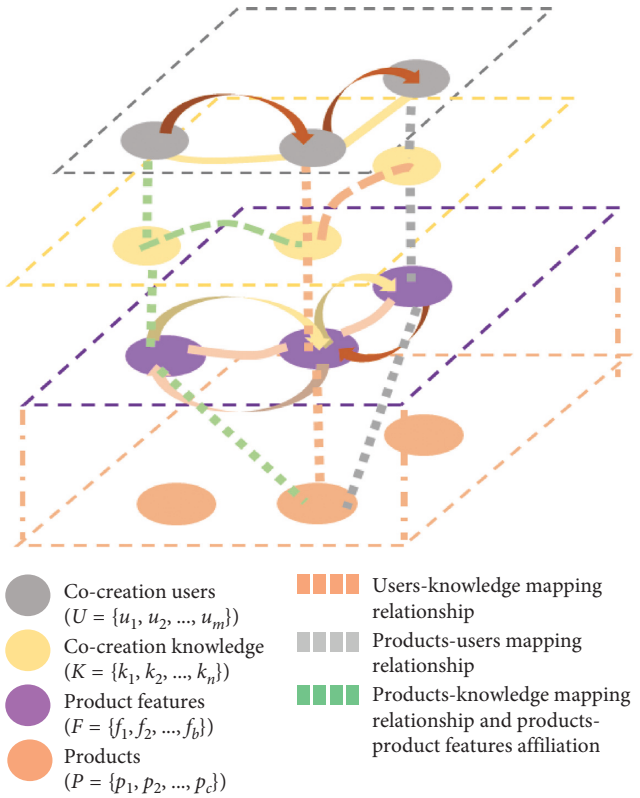

Figure 1: Co-creation knowledge network cyberspace for product innovation.

(2) When constructing the co-creation knowledge network, repetitiveness and similarities among knowledge points are further considered by calculating the semantic similarities among them to avoid information overload. Besides, in addition to the frequency and attention weights of knowledge points, character weights including the position, part-of-speech, and span of the knowledge points are considered for more accurate hot knowledge point identification.

(3) A co-creation product network is constructed to map with the previous two-tier co-creation network for applying co-creation knowledge into product innovation. Thus, a comprehensive co-creation cyberspace for product innovation is integrated for enterprises to better manage the co-creation users and knowledge systematically and identify the useful information for product innovation.

Based on the earlier version of this paper presented in 11th CIRP Conference on Industrial Product-Service Systems [29], three subnetworks are constructed and the mapping relationships among them are analysed in detail in the following subsections.

3.1. Co-Creation User Network Construction. With regard to co-creation users, an online social network model [30] reveals two major factors of social network formation: social choice and social influence [31]. Hence, a multidimensional online interest network model [32] classifies co-creation user relationship into interaction relationship caused by social influence and collaboration relationship caused by social choice, which are shown in Table 2.

Most of the existing research only considered the collaboration relationship and neglected the interaction relationship among co-creation users when constructing the co-creation user network [14], which resulted in inaccurate discovery of co-creation users and poor management in online co-creation communities. To address this limitation, this paper uses co-creation users as nodes and uses their interaction and collaboration relationships as two-dimensional edges to construct co-creation user network, shown in Figure 2.

The co-creation user network "G_U" is expressed as

$$G_U = \{U, E_{UD}, E_{UA}, W(E_{UD}), W(E_{UA})\}, \quad (1)$$

where "U" is the set of co-creation users with amount "m" as follows:

$$U = \{u_1, u_2, \ldots, u_m\}. \quad (2)$$

The co-creation user relationship set "E_U" includes interaction relationship set "E_{UD}" with weight set "$W(E_{UD})$" and collaboration relationship set "E_{UA}" with weight set "$W(E_{UA})$." As mentioned in Table 2, the co-creation user network includes two parts:

(1) The interaction relationship set of co-creation users "E_{UD}" is established based on attention relationship, reply relationship, forwarding relationship, and review relationship. If user "u_j" pays attention, responds, forwards, or comments on user "u_i" for more than "w_{ud}" times, an interaction relationship "$e_{ud}(u_i, u_j)$" is constructed from user "u_j" to user "u_i," as shown in Figure 3.

The interaction relationship set of co-creation users and its weight set are expressed as follows:

$$E_{UD} = \left\{ \left(e_{ud}(u_i, u_j) \right) \middle| w(u_i, u_j), \geq w_{ud} \right\}, \quad (3)$$

$$W(E_{UD}) = \left\{ \left(w(u_i, u_j) \right) \middle| w(u_i, u_j) \geq w_{ud} \right\}. \quad (4)$$

(2) The collaboration relationship set of co-creation users "E_{UA}" is established based on common friends and common topic participation. If the amount of collaboration activities "$w(u_i, u_j)$" between user "u_i" and user "u_j" is not less than "w_{ua}" times, a collaboration relationship "$e_{ua}(u_i, u_j)$" is constructed between them. The conceptual diagram is shown in Figure 4.

The collaboration relationship set of co-creation users and its weight set are expressed as follows:

$$E_{UA} = \left\{ \left(e_{ua}(u_i, u_j) \right) \middle| w(u_i, u_j) \geq w_{ua} \right\}, \quad (5)$$

$$W(E_{UA}) = \left\{ \left(w(u_i, u_j) \right) \middle| w(u_i, u_j) \geq w_{ua} \right\}. \quad (6)$$

Table 2: Types of co-creation user relationships.

User relationship	Formation mechanism	User behaviour	Network type
Interaction	Social influence	Concern, reply, forwarding, comment	Direct weighted interaction network
Collaboration	Social choice	Common friend's attention, common topic participation and common post comments	Indirect weighted collaboration network

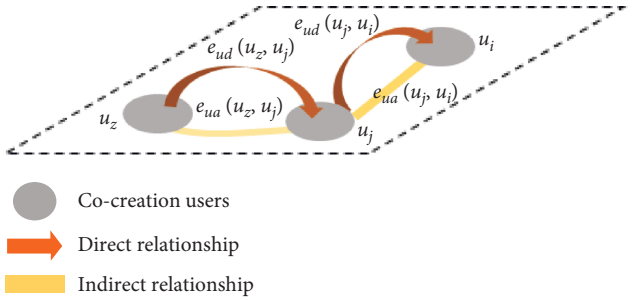

Figure 2: Co-creation user network.

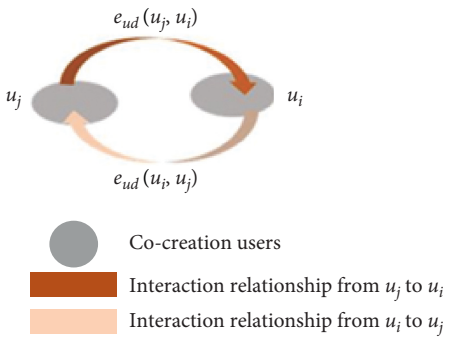

Figure 3: Co-creation user interaction network.

3.2. Co-Creation Knowledge Network Construction. Most of the existing research only considered the co-occurrence relationship and neglected the similarity relationship among co-creation knowledge points when constructing the co-creation knowledge network [14], which resulted in information overload, repeated calculation of co-creation knowledge points, and interference of hot knowledge discovery. In addition, there is still enough room for further improvements regarding the construction of knowledge point weight sets, which will interfere with the accuracy of hot knowledge point discovery. To address these limitations, this paper uses knowledge point keywords as nodes; uses attention, frequency, and character of them as their weights; and uses co-occurrence and similarity relationships as two-dimensional edges to construct co-creation user network, as shown in Figure 5.

The co-creation knowledge network "G_K" is expressed as

$$G_K = \{K, Q(K), H(K), O(K), E_{KC}, E_{KS}, W(E_{KC}), W(E_{KS})\}, \tag{7}$$

where "K" is knowledge point set with frequency weight set "$Q(K)$," attention weight set "$H(K)$," and character weight set "$O(K)$.""E_K" is knowledge relationship set including

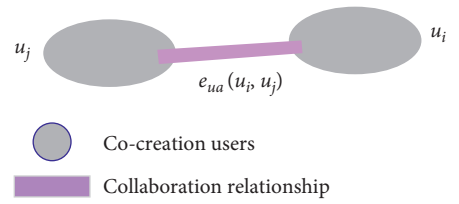

Figure 4: Co-creation user collaboration network.

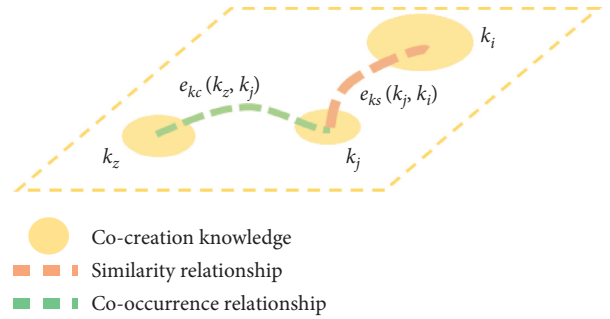

Figure 5: Co-creation knowledge network.

co-occurrence relationship set "E_{KC}" with weight set "$W(E_{KC})$" and similarity relationship "E_{KS}" with weight set "$W(E_{KS})$." The knowledge point set with various weight sets and the knowledge relationship sets are constructed, respectively, in details as follows.

3.2.1. The Weight Sets of Knowledge Points. This paper comprehensively considers the frequency, attention, and characters of co-creation knowledge points to establish knowledge point weight sets, as described below:

(1) The frequency weight set of knowledge points "$Q(K)$" is established based on their mentioned frequency, which is calculated as follows:

$$q(k_i) = \sum_{j=1}^{a} \eta(k_i, b_j), \tag{8}$$

where "$\eta(k_i, b_j) = 1$" indicates that the knowledge point "k_i" is the keyword of the post "b_j"; otherwise, "$\eta(k_i, b_j) = 0$." Hence, the knowledge point frequency weight set is expressed as

$$Q(K) = \{q(k_i) \mid k_i \in \{k_1, k_2, \ldots, k_n\}\}. \tag{9}$$

(2) The attention weight set of knowledge points "$H(K)$" is established based on the browsing popularity and response heat of their carrier post, which is calculated as follows:

$$h(k_i) = \sum_{j=1}^{a} \left[h(b_j) * \eta(k_i, b_j) \right], \tag{10}$$

where "$h(b_j)$" is the attention of the knowledge point, "k_i" 's carrier post "b_j" including browse popularity "$\mathrm{HB}(b_j)$" and response heat "$\mathrm{HR}(b_j)$," which is calculated as follows [27]:

$$\begin{aligned} h(b_j) &= \alpha * \mathrm{HB}(b_j) + \beta * \mathrm{HR}(b_j) \\ &= \alpha * \frac{v(b_j)}{\sqrt{\sum_{j=1}^{a} v^2(b_j)}} * e^{v(b_j)/\sqrt{\sum_{j=1}^{a} v(b_j)}} \\ &\quad + \beta * \frac{r(b_j)}{\sqrt{\sum_{j=1}^{a} r^2(b_j)}} * e^{r(b_j)/\sqrt{\sum_{j=1}^{a} r(b_j)}}, \end{aligned} \tag{11}$$

where "α"and "β" represent the importance of the reply and browsing behaviour, respectively, "$v(b_j)$" is the browse amount of the post "b_j" and "$r(b_j)$" is the reply amount of the post "b_j."

(3) The character weight set of knowledge points "$O(K)$" is established based on their position, part-of-speech, and span [28] including position weight set "$O_L(K)$," part-of-speech weight set "$O_R(K)$," and span weight set "$O_T(K)$."

For the position weight set of knowledge points "$O_L(K)$," the importance of knowledge points in different position of a post varies significantly. For example, knowledge points in the title of a post can summarize the main idea of the post, which should be paid more attention to. Thus, knowledge points in different position should be weighted differently, which is expressed as

$$\begin{aligned} O_L(K) &= \left\{ (o_l(k_i)) \mid i = 1, 2, \ldots, n \right\} \\ \text{s.t. } o_l(k_i) &= \begin{cases} o_{l_1}(\text{title}) \\ o_{l_2}(\text{text}) \\ o_{l_3}(\text{comment}) \end{cases} \quad 1 \geq o_{l_1} \geq o_{l_2} \geq o_{l_3} > 0. \end{aligned} \tag{12}$$

For the part-of-speech weight set of knowledge points "$O_R(K)$," similarly, the importance of knowledge points with different part-of-speech varies significantly. A noun knowledge points can better represent innovative topics and their connotations [28]. Therefore, knowledge points of different part-of-speech should be weighted differently, which is expressed as

$$\begin{aligned} O_R(K) &= \left\{ (o_r(k_i)) \mid i = 1, 2, \ldots, n \right\} \\ \text{s.t. } o_r(k_i) &= \begin{cases} o_{r_1}(\text{nouns}) \\ o_{r_2}(\text{other}) \end{cases} \quad 1 \geq o_{r_1} > o_{r_2} > 0. \end{aligned} \tag{13}$$

For the span weight set of knowledge points "$O_T(K)$," a knowledge point with larger span indicates that it can represent the main idea of a post more, so that it should be weighed greater. Therefore, the span weight of knowledge points is calculated as

$$o_t(k_i) = \frac{pn}{3}, \tag{14}$$

where "pn" indicates how many parts of a post the knowledge points are mentioned in, including title, text, and comments part.

3.2.2. The Co-Creation Knowledge Relationship Set. The co-creation user relationship set "E_K" includes co-occurrence relationship set "E_{KC}" with weight set "$W(E_{KC})$" and similarity relationship set "E_{KS}" with weight set "$W(E_{KS})$" and is described in details as follows:

(1) The co-occurrence relationship set of knowledge points "E_{KC}" is established based on the co-occurrence of knowledge points. If the co-occurrence frequency "$w(k_i, k_j)$" between two knowledge points is not less than "w_{kc}," a co-occurrence relationship is constructed between them. And the co-occurrence relationship set of knowledge points "E_{KC}" and its weight set are expressed as

$$E_{KC} = \left\{ e_{kc}(k_i, k_j) \mid w(k_i, k_j) \geq w_{kc} \right\}, \tag{15}$$

$$W(E_{KC}) = \left\{ w(k_i, k_j) \mid w(k_i, k_j) \geq w_{kc} \right\}. \tag{16}$$

(2) The similarity relationship set of knowledge points "E_{KS}" is established based on the similarity "$s(k_i, k_j)$" between knowledge points calculated by the words similarity algorithm based on Tongyici Cilin [28]. According to Tongyici Cilin, similarity "$s(k_i, k_j)$" between knowledge points "k_i" and "k_j" is calculated by using the amount of knowledge points in the word forest to get semantic distance and similarity. The specific calculation method is shown in Table 3.

In Table 3, "n" is the amount of nodes in one branch layer where the knowledge point word is located and "m" is the distance between two branches and the coefficients are generally customized and optimized according to experimental conditions. If the similarity "$s(k_i, k_j)$" is between the upper and lower similarity thresholds "s_{ku}" and "s_{kl}," it indicates that the knowledge points "k_i" and "k_j" are highly similar but are not exactly the same. If the similarity

Table 3: Similarity calculation method [28].

Tree level position	Sense level position	Coefficient	Semantic similarity
Not in the same word forest tree	None	f	$s(k_i, k_j) = f$
In the same word forest tree	Layer 2 branch	a	$s(k_i, k_j) = a \times \cos(n\pi/180) \times ((n-m+1)/n)$
In the same word forest tree	Layer 3 branch	b	$s(k_i, k_j) = b \times \cos(n\pi/180) \times ((n-m+1)/n)$
In the same word forest tree	Layer 4 branch	c	$s(k_i, k_j) = c \times \cos(n\pi/180) \times ((n-m+1)/n)$
In the same word forest tree	Layer 5 branch	d	$s(k_i, k_j) = d \times \cos(n\pi/180) \times ((n-m+1)/n)$

"$s(k_i, k_j)$" is less than the lower similarity threshold "s_{kl}," it means that there is no semantic similarity and semantic relevance between the knowledge points "k_i" and "k_j." If the similarity "$s(k_i, k_j)$" is higher than the upper similarity threshold "s_{ku}," it shows that knowledge points "k_i" and "k_j" are the same. Furthermore, these two knowledge points will be combined as one knowledge point "k" with the highest frequency weight, because the knowledge point with higher frequency weights means more likely to be hot knowledge points. The frequency, attention, and character weights of the merged knowledge point "k" are equal to the sum of the frequency, attention, and character weights of these two knowledge points, respectively (Figure 6).

The similarity relationship set of knowledge points "E_{KS}" and its weight set are expressed as

$$E_{KS} = \left\{ e_{ks}(k_i, k_j) \,\middle|\, s_{ku} \geq s(k_i, k_j) \geq s_{kl} \right\}, \tag{17}$$

$$W(E_{KS}) = \left\{ e_{ks}(k_i, k_j) \,\middle|\, s_{ku} \geq s(k_i, k_j) \geq s_{kl} \right\}. \tag{18}$$

3.3. Co-Creation Product Network Construction. To apply co-creation knowledge into product innovation effectively, this paper further constructs a co-creation product network to map with co-creation user and knowledge networks. Co-creation product network includes the nodes of product names and product feature network, shown in Figure 7. Based on the improved feature extraction and clustering [33] and a feature comparison network for competitiveness [34], this paper uses product features as nodes; uses attention and frequency of them as their weights; and uses co-occurrence, similarity, frequency comparison, and attention comparison relationships as four-dimensional edges to construct co-creation product feature network, shown in Figure 8. Besides, the nodes of product names are extracted and constructed with their weights of frequency and attention. And the mapping relationship between the nodes of product names and product feature network is constructed. The nodes of product names are used as the indexes to manage and analyse the information of every product's product features, so that the product feature networks belonged to every product can be constructed into a systematic product network.

Hence, the co-creation product network is expressed as

$$G_P = (P, F, E_F, E_{P-F}, Q(P), H(P), Q(F), H(F), W(E_F)), \tag{19}$$

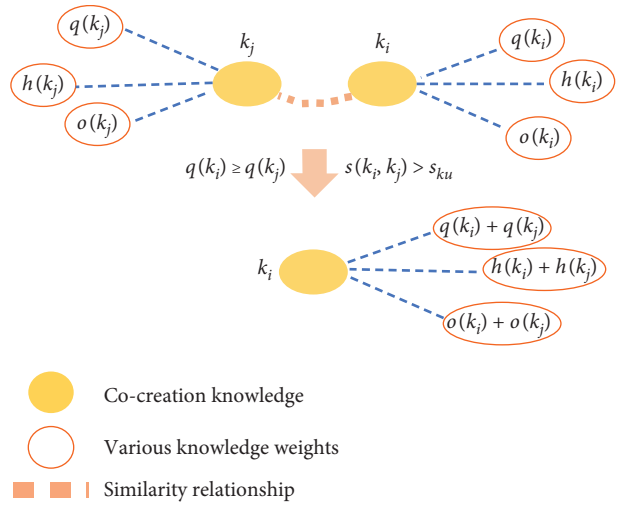

Figure 6: Knowledge points merging process.

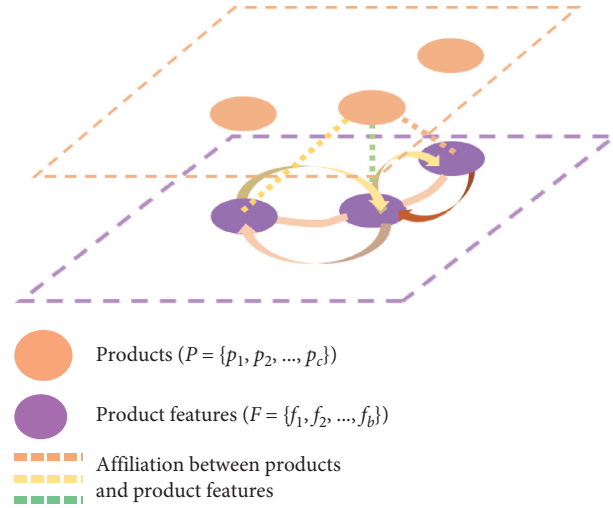

Figure 7: Co-creation product network.

where "P" is the product set with frequency weight set "$Q(P)$" and attention weight set "$H(P)$.""F" is the product feature set with frequency weight set "$Q(F)$" and attention weight set "$H(F)$.""E_F" is product feature relationship set with weight set "$W(E_F)$." And "E_{P-F}" is the product-to-product feature mapping relationship set.

The product set and product feature set with various weight sets and the product feature relationship sets are constructed, respectively, in detail as follows:

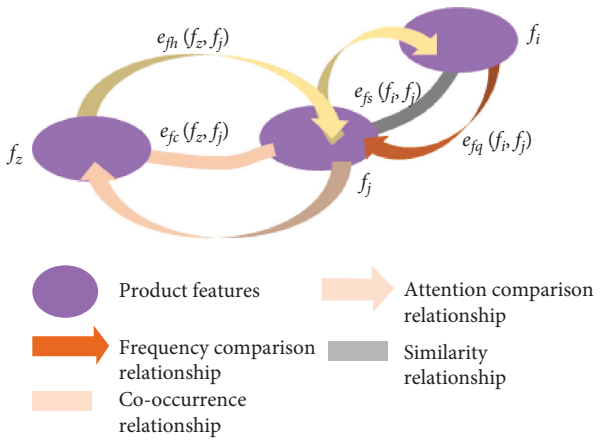

Figure 8: Co-creation product feature network.

3.3.1. The Weight Sets of Products and Product Features

(1) The frequency weight set of product features "$Q(F)$" is established based on their mentioned frequency, which is calculated similarly as formula (13).

(2) The attention weight set of product features "$H(F)$" is established based on the browsing popularity and response heat of their carrier post, which is calculated similarly as formulas (10) and (11).

(3) The frequency weight set "$Q(P)$" and attention weight set "$H(P)$" of products are established based on frequency weight set "$Q(F)$" and attention weight set "$H(F)$" of product features, respectively. They are calculated as

$$q(p_i) = \sum_{j=1}^{b} q(f_j)\mu(p_i, f_j), \tag{20}$$

$$h(p_i) = \sum_{j=1}^{b} h(f_j)\mu(p_i, f_j). \tag{21}$$

If the product feature "f_j" belongs to the product "p_i," "$\mu(p_i, f_j) = 1$"; otherwise, "$\mu(p_i, f_j) = 0$."

3.3.2. The Product Feature Relationship Set. The product feature relationship set "E_F" includes co-occurrence relationship set "E_{FC}" with weight set "$W(E_{FC})$," similarity relationship set "E_{FS}" with weight set "$W(E_{FS})$," frequency comparison relationship set "E_{FQ}" with weight set "$W(E_{FQ})$" and attention comparison relationship set "E_{FH}" with weight set "$W(E_{FH})$" and elaborated as follows.

(1) The co-occurrence relationship set of product feature "E_{FC}" is established based on the co-occurrence of product feature. If the co-occurrence frequency "$w(f_i, f_j)$" between two product features is not less than "w_{fc}," a co-occurrence relationship is constructed between them. And the co-occurrence relationship set of product features "E_{FC}" and its weight set are expressed as

$$E_{FC} = \left\{ e_{fc}(f_i, f_j) \,\middle|\, w(f_i, f_j) \geq w_{fc} \right\}, \tag{22}$$

$$W(E_{FC}) = \left\{ w(f_i, f_j) \,\middle|\, w(f_i, f_j) \geq w_{fc} \right\}. \tag{23}$$

(2) The similarity relationship set of product features "E_{FS}" is established based on the similarity "$s(f_i, f_j)$" between product features calculated by the words similarity algorithm based on Tongyici Cilin [33] similarly as the similarity relationship set of knowledge points. The similarity relationship set of product features "E_{FS}" and its weight set are expressed as

$$E_{FS} = \left\{ e_{fs}(f_i, f_j) \,\middle|\, s_{fu} \geq s(f_i, f_j) \geq s_{fl} \right\}, \tag{24}$$

$$W(E_{FS}) = \left\{ s(f_i, f_j) \,\middle|\, s_{fu} \geq s(f_i, f_j) \geq s_{fl} \right\}. \tag{25}$$

(3) The frequency comparison relationship set "E_{FQ}" and the attention comparison relationship set "E_{FH}" of product features are established based on the comparison of the product feature's mentioned frequency and attention. If the mentioned frequency of the product feature "f_i" is higher than that of "f_j", a frequency comparison relationship "$e_{fq}(f_i, f_j)$" is constructed from "f_i" to "f_j." Similarly, if the attention of the product feature "f_i" is higher than that of "f_j", an attention comparison relationship "$e_{fh}(f_i, f_j)$" is constructed from "f_i" to "f_j."

Finally, product features are mapped with products based on which product section the product features are extracted from. And the co-creation product network is constructed.

3.4. Analysis of the Mapping Relationships among Subnetworks. After the construction of the three subnetworks, the mapping relationships among them need to be established to complete the whole cyberspace.

3.4.1. Co-Creation User Network and Co-Creation Knowledge Network. The mapping relationship between co-creation user network and knowledge network, shown in Figure 9, is established based on if (1) users' focused post contains knowledge point keywords, or (2) knowledge point keywords are mentioned when users post or comment. If yes, a mapping relationship is constructed between the co-creation user "u_i" and the co-creation knowledge point "k_j," "$\chi(u_i, k_j) = 1$." And the weight of this mapping relationship is established based on its frequency. Therefore, the mapping

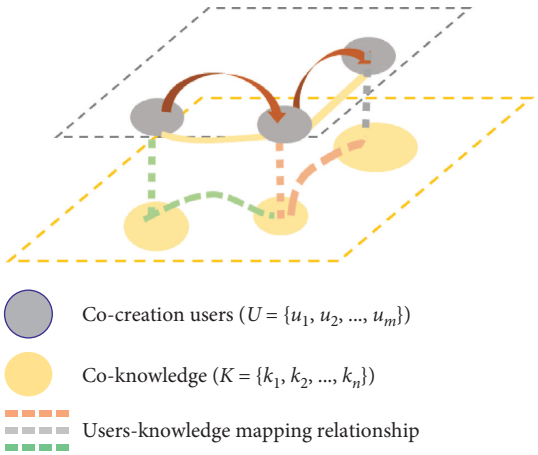

Figure 9: Co-creation user network-knowledge network mapping relationship.

relationship set "E_{U-K}" between co-creation users and knowledge and its weight set "$W(E_{U-K})$"are expressed as

$$E_{U-K} = \left\{ e_{u-k}(u_i, k_j) \,\middle|\, \chi(u_i, k_j) = 1 \right\}, \tag{26}$$

$$W(E_{U-K}) = \left(w(u_i, k_j) \,\middle|\, \chi(u_i, k_j) = 1 \right). \tag{27}$$

3.4.2. Co-Creation Users Network and Co-Creation Product Network. The mapping relationship between co-creation user network and product network, shown in Figure 10, is established based on if (1) product names or product features are mentioned in the text data generated by co-creation users, or (2) co-creation users' generated behaviour data such as attention, forwarding, reply, and comment mention product names or product features. If yes, a mapping relationship is constructed between the co-creation user "u_i" and the co-creation product feature "f_j," "$\alpha(u_i, f_j) = 1$." And the weight of this mapping relationship is established based on its frequency. Therefore, the mapping relationship set "E_{U-F}" between co-creation users and product feature and its weight set "$W(E_{U-F})$"are expressed as

$$E_{U-F} = \left\{ e_{u-f}(u_i, f_j) \,\middle|\, \alpha(u_i, f_j) = 1 \right\}, \tag{28}$$

$$W(E_{U-F}) = \left(w(u_i, f_j) \,\middle|\, \alpha(u_i, f_j) = 1 \right). \tag{29}$$

3.4.3. Co-Creation Product Network and Co-Creation Knowledge Network. The mapping relationship between co-creation product network and knowledge network, shown in Figure 11, is established based on the affiliation relationship between co-creation knowledge and product features. If yes, a mapping relationship is constructed between the co-creation product feature "f_i" and the co-creation knowledge point "k_j," "$\beta(f_i, k_j) = 1$." Therefore, the mapping relationship set "E_{F-K}" between co-creation product feature and knowledge and its weight set "$W(E_{F-K})$"are expressed as

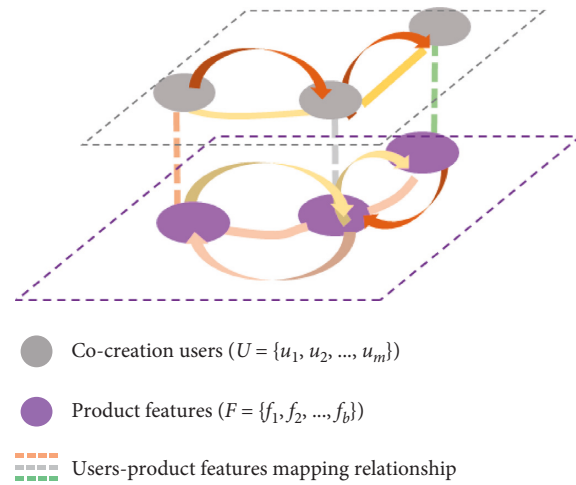

Figure 10: User network-product network mapping relationship.

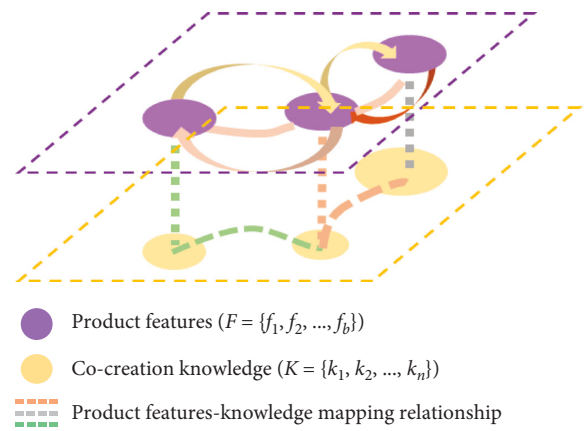

Figure 11: Product network-knowledge network mapping relationship.

$$E_{F-K} = \left\{ e_{f-k}(f_i, k_j) \,\middle|\, \beta(f_i, k_j) = 1 \right\}, \tag{30}$$

$$W(E_{F-K}) = \left\{ w(f_i, k_j) \,\middle|\, \beta(f_i, k_j) = 1 \right\}. \tag{31}$$

4. Case Study

The focus of this study is to add some important but neglected relationships, weights, and dimension to make the previous co-creation network more comprehensive. Accordingly, the reasons why mentioned elements are necessary to be considered in the construction of co-creation knowledge cyberspace have been clearly explained in the literature review. Thus, in this section, we do not want to prove the priority of our model but only to prove the usability and application of the model in one case study. Therefore, this paper selects the MIUI community of Xiaomi enterprise as an application example. It is a well-known co-creation community with more than 1900 million registered users in China. MIUI community focuses on the customer-generated content on their products and allows its registered

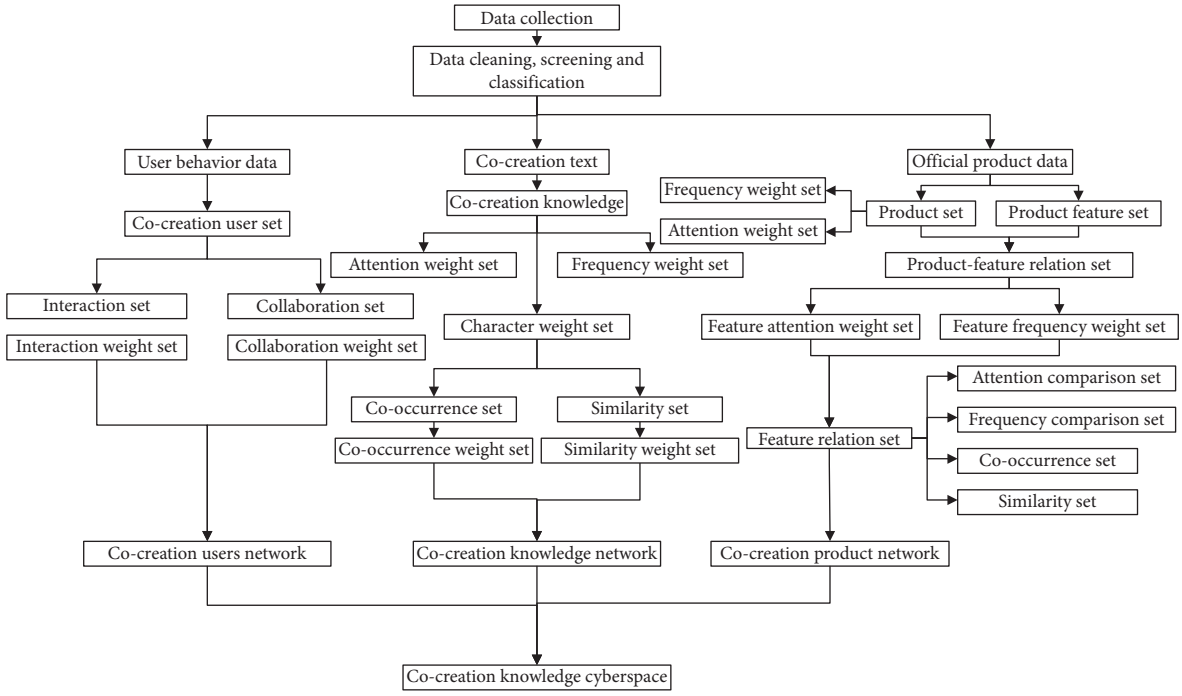

Figure 12: Case study application analysis flow chart.

users to establish their own personal homepages. All registered users may contact each other through favouring, sharing, and commenting on valuable content. As it generates a large amount of interactive data and text data every day, MIUI community is a suitable analytical case for this model. The application analysis process is shown in Figure 12.

First, this paper uses "Octopus" collector to collect post data in Red Rice Note 5/5A/4X panel on March 17th, 2018, excluding the useless and repetitive posts, and the posts with the browsing number less than 300. Three types of data per post are collected as follows:

(1) Co-creation user behaviour data, including post author ID, reviewer ID, post browsing number, and comment number

(2) Co-creation text data, including post titles, text, and comments

(3) Official product data, including product list and text data posted by the official operation team

Then, python's jieba segmentation toolkit and nltk natural language processing toolkit are used to process the text data. And the three subnetworks are constructed respectively according to the collected and processed data. Finally, the co-creation cyberspace is integrated for Xiaomi enterprise to support its user management, knowledge management, and product innovation.

4.1. Co-Creation User Network Construction. For co-creation user network construction, this study first encodes the user IDs in MIUI community by establishing a co-creation user set "$U = \{u_1, u_2, \ldots, u_{184}\}$" and then uses the excel software to screen the collaboration and interaction relationships among users that occur no less than two times. According to Section 3.1, a collaboration relationship set of co-creation users "$E_{UD} = \{e_{ud1}, e_{ud2}, \ldots, e_{ud396}\}$" with its weight set "$W(E_{UD})$" and an interaction relationship set of co-creation users "$E_{UA} = \{e_{ua1}, e_{ua2}, \ldots, e_{ua3590}\}$" with its weight set "$W(E_{UA})$" can be obtained. Besides, co-creation users are ranked by the node degree in descending order and the co-creation users with top 60 node degree as shown in Table 4.

The co-creation user network is visualized by Gephi 0.9.2 software in Figure 13. The Fruchterman Reingold algorithm in the Gephi layout function was used to rearrange the network, and Gephi's own community detection algorithm was used to group the main nodes where the size of the node is proportional to the size of the node degree. This means that the larger the user node is, the larger the degree is. Meanwhile, if the node is closer to the centre, the behaviour of the user has more social influence and importance. In this visualized co-creation user network, "U108" is the largest user node, indicating that he interacts with other users the most. Besides, "U108" is in the centre of the co-creation user network, meaning that he has a lot of influence over other users. Therefore, "U108" obviously is the opinion leaders. Xiaomi enterprise needs to pay more attention to him, taking incentives to encourage him to improve his innovation rate and taking advantage of his big influence to motivate other users to co-create as well. Similarly, "U109" and "U61" are the users that Xiaomi enterprise needs to pay more attention to. Moreover, in the visualized co-creation network, user nodes with the same colour mean that these users have closer social relationships. The users are divided into small groups so that Xiaomi enterprise can manage them more effectively based on the character of each group.

Table 4: The users with top 60 node degree in co-creation user network.

Rank	User ID	Node degree
1	U108	390
2	U109	42
3	U61	38
4	U2	33
5	U3	32
6	U28	29
7	U154	24
8	U158	23
9	U145	21
10	U26	20
11	U69	18
12	U82	18
13	U115	18
14	U130	18
15	U144	18
16	U94	17
17	U101	17
18	U75	16
19	U168	16
20	U72	15
21	U105	15
22	U122	15
23	U137	15
24	U151	15
25	U138	14
26	U22	13
27	U51	13
28	U139	12
29	U6	11
30	U8	11
31	U9	11
32	U32	11
33	U157	11
34	U19	10
35	U41	10
36	U83	10
37	U146	10
38	U165	10
39	U177	10
40	U53	9
41	U73	9
42	U76	9
43	U135	9
44	U143	9
45	U14	8
46	U42	8
47	U92	8
48	U97	8
49	U103	8
50	U111	8
51	U113	8
52	U123	8
53	U181	8
54	U25	7
55	U30	7
56	U58	7
57	U74	7
58	U129	7
59	U147	7
60	U38	6

4.2. Co-Creation Knowledge Network Construction. For co-creation knowledge network construction, this study first uses HIT pyltp, jieba segmentation, and natural language tools in python to perform sentence segmentation, word segmentation, part-of-speech tagging, and word frequency statistics on the text content of posts. Then, with the calculation of frequency weight, attention weight, and character weight for knowledge point keywords, a preliminary knowledge points set and its weight set can be obtained. The extracted knowledge point keywords with top 15 frequency weights are shown in Table 5 with their attention weight and character weight.

In Table 5, "Note 5A" is the keyword with the largest frequency weight, which means that it is the knowledge point keyword mentioned most by the community users. It also has a large attention weight, which means that it is the knowledge point keyword that many community users browsed and responded. Besides, it has large position weight, part-of-speech weight, and span weight as well, which means that it is an important keyword of the posts. Similarly, "Fans," "System," Battery," and "Screen" are the knowledge point keywords with large weights.

In addition, this study uses the HIT University pyltp Tongyici Cilin expansion to calculate the similarity of keywords and merges highly similar knowledge points to obtain a revised set of co-creation knowledge points. Meanwhile, knowledge point weight set and knowledge co-occurrence relationship are reorganized, and a similar relationship set of knowledge points is constructed. Some synonymous knowledge point keywords are shown in Table 6, and the merged knowledge point keywords and their weights are shown in Table 7. The reason for use of Chinese in Table 6 is that some of the translation of knowledge point 1 and knowledge point 2 is the same words in English, while these two words and their intended meaning is different in China.

After synonymous knowledge point keyword merging, Table 7 shows that "Photography" is the merged knowledge point keyword with the largest frequency weight and character weight, which shows different results compared with Table 5. Therefore, it proves that repetitiveness and similarity among knowledge points would disturb hot knowledge discovery.

The co-creation knowledge network is visualized by Gephi 0.9.2 software in Figure 14 and the Fruchterman Reingold algorithm in the Gephi layout function is used to rearrange the network. Hence, the knowledge nodes are clustered and divided using Gephi's own community detection algorithm, where the size of the knowledge node is proportional to its weights. The names of nodes are automatically generated by Gephi software based on the Chinese posts data collected in MIUI community, and they are translated into English for better understanding. The larger the knowledge node is, the larger the weight it has and the more the concern it receives from the users in the co-creation community. And the closer the knowledge node is to the centre of the network, the more important is this knowledge point for the users. In the visualized co-creation knowledge network, "photography" is the largest knowledge

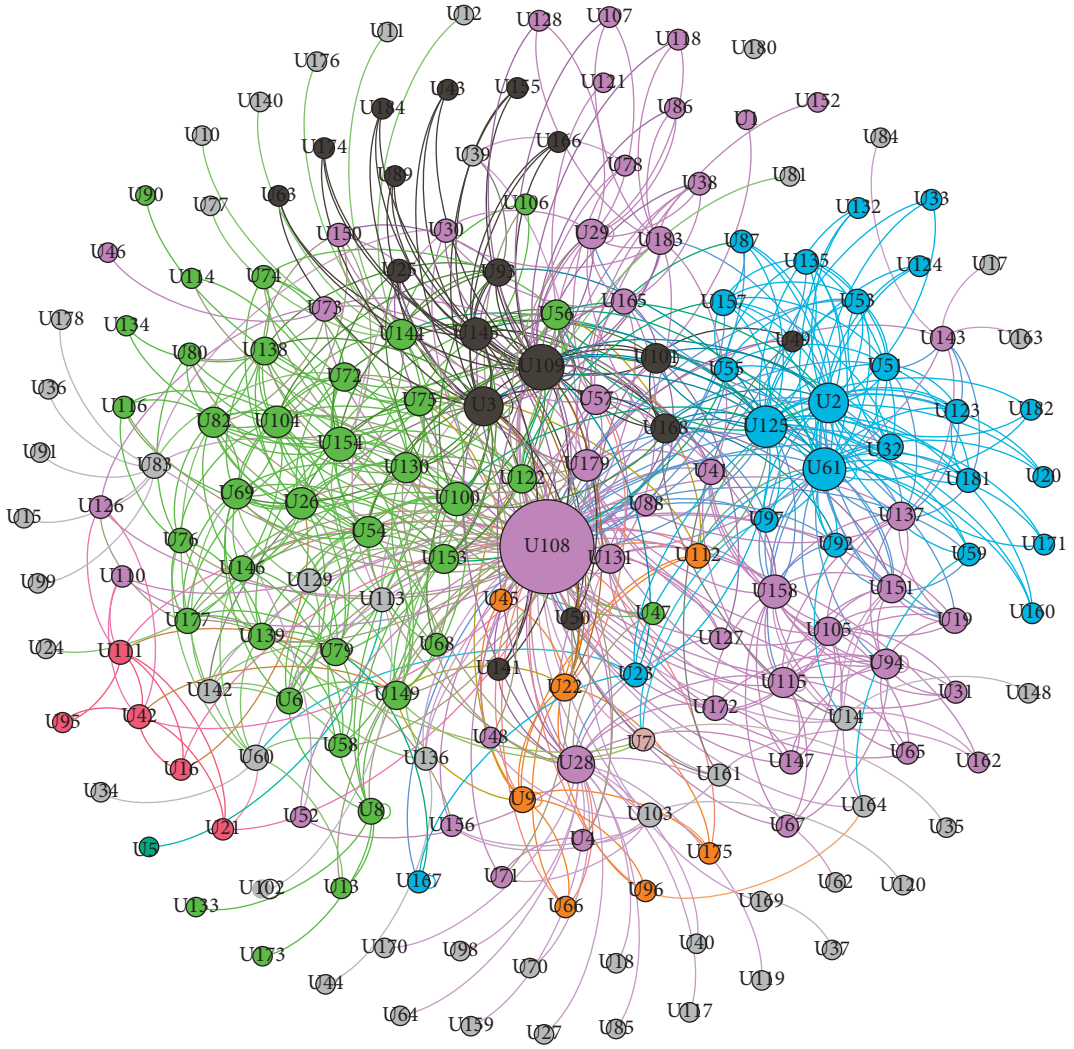

Figure 13: Visualized co-creation user network.

Table 5: The extracted knowledge point keywords with top 15 frequency weight and their various weights.

Keywords	Frequency weight	Attention weight	Character weight		
			Position weight	Part-of-speech weight	Span weight
Note 5A	80	$3.51817E+11$	78.6	1	75.33333
Fans	37	$3.51817E+11$	5.4	1	3
Purchase	32	1581825.91	2.6	0.6	1.333333
Discount	30	1581787.063	0	0.6	0
System	19	1581326.577	6.4	1	3.333333
Battery	16	$3.51817E+11$	7	1	3.333333
Use	15	1081.948809	7.6	0.6	4.333333
Edition	15	1160.523897	5.2	1	2.666667
Screen	15	$3.51817E+11$	6	1	3.333333
Software	13	1581226.719	4.2	1	2.333333
Express	13	705.2475923	5.2	0.6	2.333333
Wakeup	12	655.3813314	6.8	0.6	3.666667
Settings	12	679.439974	2.4	0.6	1.333333
Mode	11	1580806.593	4.4	1	2.333333
WeChat	10	1581228.874	1.8	1	1

node, indicating that it is the knowledge point the users mostly concern about. Besides, "photography" knowledge point is in the centre of the green co-creation knowledge network, meaning that it is the core knowledge point connecting many other knowledge points, so that it is a very important knowledge point for product innovation.

Table 6: Example of some synonymous knowledge point keywords.

Similarity	Knowledge point 1	Knowledge point 2
1	Photography	Photograph
1	Price	Value
1	Earphone	Earpiece
1	Phone	Machine
1	Cheap	Inexpensive
1	Beautiful	Perfect
1	Beautiful	Wonderful
1	Message	Information

Table 7: Example of the merged knowledge point keywords and their weights.

Knowledge points	Knowledge points				
	Frequency weight	Attention weight	Position weight	Part-of-speech weight	Span weight
Photography	28.00	86.49	26.00	23.60	24.00
Price	9.00	351814930895.95	1.20	2.00	0.67
Earphone	9.00	790.28	3.20	2.00	1.33
Phone	10.00	836.29	3.00	2.00	1.67
Cheap	6.00	351816511887.58	0.60	1.20	0.33
Beautiful	18.00	351814930835.20	14.20	14.60	13.67
Message	5.00	65.89	2.40	2.00	1.33

Similarly, the knowledge point nodes such as "cost-performance," "screen", "battery" and "storage" are larger, and therefore, Xiaomi enterprise should focus more on these knowledge points to do product innovation. Furthermore, in the visualized co-creation knowledge network, knowledge point nodes with the same colour mean that these knowledge points have closer co-occurrence and similar relationships. The knowledge points are divided into small groups so that Xiaomi enterprise can manage the co-creation knowledge more effectively.

4.3. Co-Creation Product Network Construction. For co-creation product network construction, this study extracts and filters product names from the product list and then obtains the product name set. The frequently mentioned product features are extracted from the post text based on the improved Apriori algorithm and the preliminary product feature set is obtained with PMI thresholds. Then, similar to the relevant calculation indexes of the co-creation knowledge network, this study (1) calculates the frequency weight and attention weight of each product feature keyword as shown in Table 8, (2) calculates the similarity among product feature keywords based on Tongyici Cilin, and (3) finally merges synonymous product feature keywords and reconstructs the product feature set.

In Table 8, "Price," "Edition," "Function," "CNC," and "CPU" are the product features with large frequency and attention weights, which means that these are the product features the community users most mentioned, browsed, and responded. Therefore, Xiaomi enterprise should pay more attention to these product features for product innovation.

The co-creation product network is visualized by Gephi 0.9.2 software in Figure 15. As illustrated, like the co-creation knowledge network, the product feature node size is proportional to the various weights of the nodes. However, the names of nodes are automatically generated by Gephi software based on the Chinese posts data collected in MIUI community, and they are translated into English for better understanding. The larger the product feature node is, the larger the weight it has and the more the concern it receives from the users in the co-creation community. And the closer the product feature node is to the centre of the network, the more important is this product feature for the users. In the visualized co-creation product network, "DPI," "two-core," "module," and "light" are the nodes near the centre of the network, indicating that they are the important product features the users most concern. Therefore, Xiaomi enterprise should pay more attention to these product features and mine the relevant knowledge for product innovation. Furthermore, in the visualized co-creation product network, product feature nodes with the same colour mean that these product features have closer co-occurrence and similar relationships. The product features are divided into small groups so that Xiaomi enterprise can manage these product features more effectively.

4.4. Construction of Co-Creation Cyberspace Model for Product Innovation. Finally, by counting the mentioned frequency of keywords that each user of the co-creation user set posted, focused, forwarded, replied, and commented, this study constructs the mapping relationship set between the co-creation user network and co-creation knowledge network, and the mapping relationship set between the co-creation user network and co-creation product network, respectively. Besides, considering the affiliation relationship between co-creation knowledge and product features, a mapping relationship set between co-creation knowledge

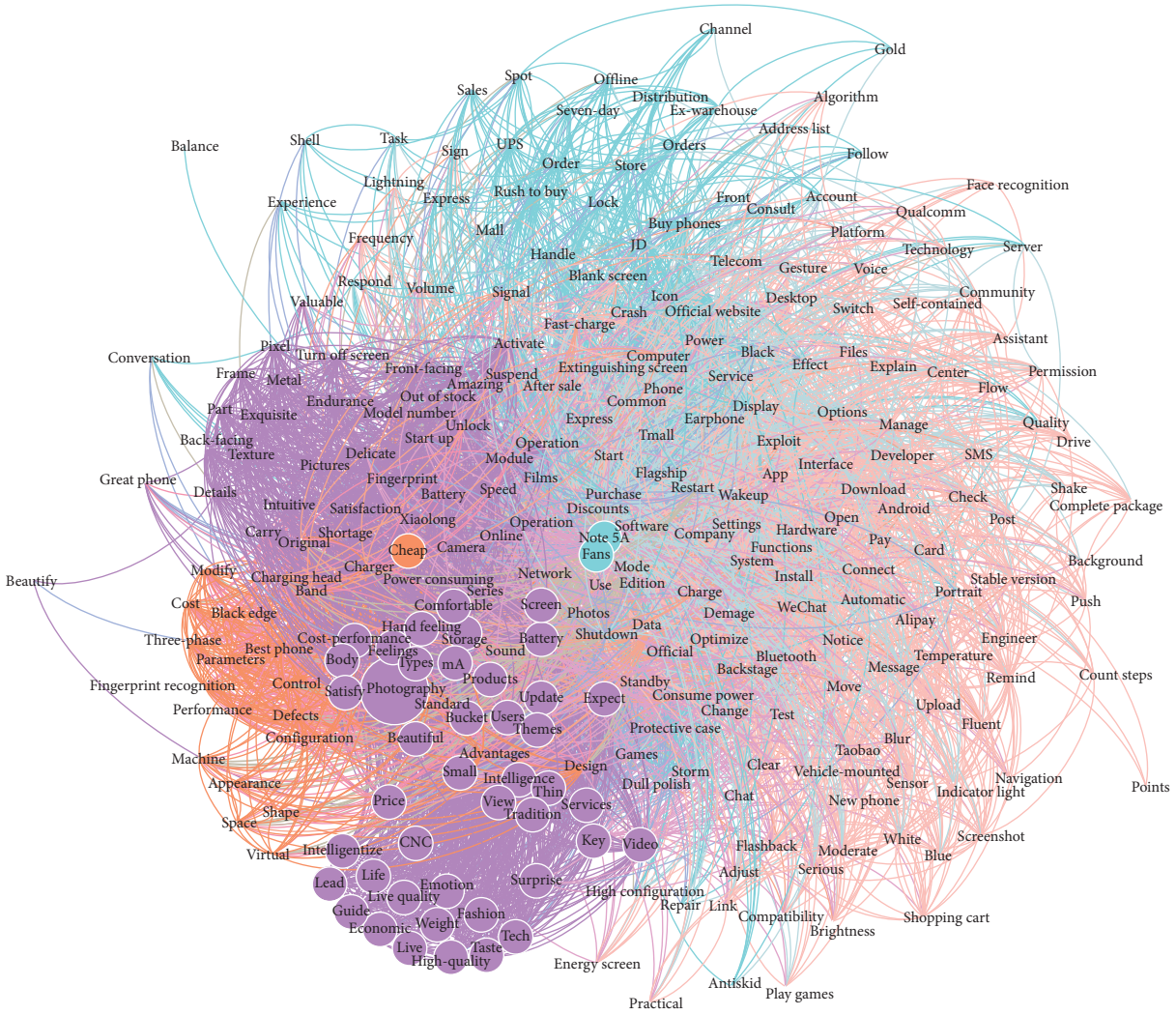

Figure 14: Visualized co-creation knowledge network.

Table 8: Example of some extracted product features and their weights.

Product features	Frequency weight	Attention weight	Product features	Frequency weight	Attention weight
Price	59	756462.7	Data	4	31118.08
Edition	18	378954.4	Games	3	31109.38
Function	21	349008.8	Positioning	3	31109.38
CNC	10	348859.6	Great phone	3	31094.95
CPU	8	348768.9	Reduce price	5	30995.03
Brand	4	347274.6	Capacity	5	30995.03
Playing games	3	347097.1	Platform	5	30995.03
Phone	2	347097.1	Dual channel	5	30995.03
Low version	1	347097.1	Price difference	5	30995.03
Test data	1	347097.1	Button	5	30995.03
Option	2	144088	Screen	5	30995.03
Fingerprint	6	144082.7	Gesture	5	30995.03
Camera	15	32873.97	System	5	30995.03
Storage	16	32603.31	Cost	5	30995.03
Performance	14	31401.37	Front-facing	5	30995.03

network and co-creation product network is constructed. The integrated construction of co-creation knowledge network cyberspace model for product innovation is visualized in Figure 16.

In Figure 16, the co-creation users, knowledge, products, and product features are connected together in the integrated cyberspace model. Again, as we used Chinese posts data collected in MIUI community, the names are

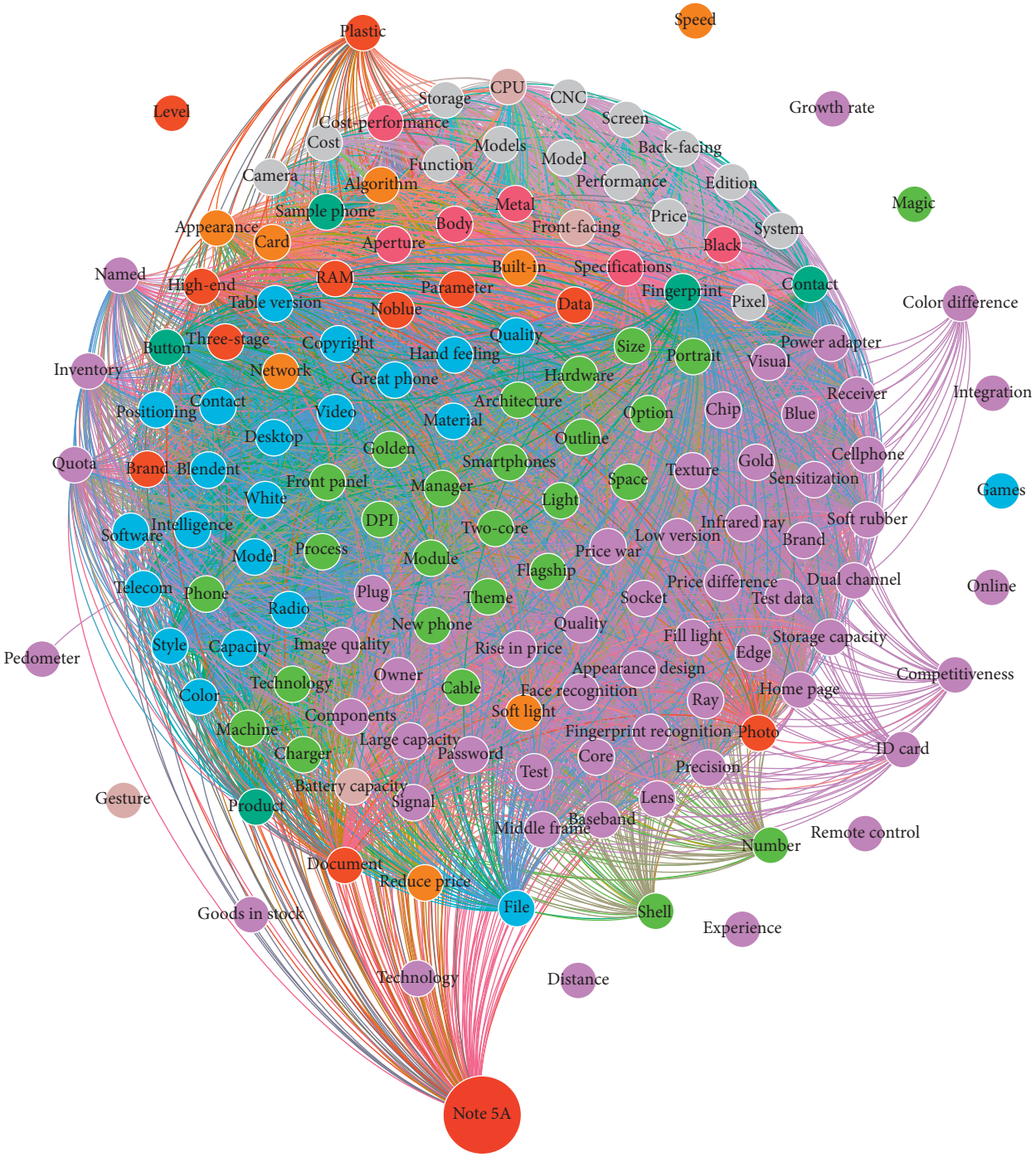

Figure 15: Visualized co-creation product network.

automatically generated by Gephi software in Chinese and they are translated into English for better understanding. The grey nodes represent co-creation users, the apricot nodes represent co-creation knowledge, the purple nodes represent co-creation product features and the orange node represents the co-creation product. In this integrated model, co-creation knowledge and its related users, products, and product features can be managed systematically and the co-creation knowledge of each user and each product can be traced, respectively. Therefore, Xiaomi enterprise can do product innovation according to the relevant co-creation knowledge of the focused product and motivate the corresponding users to co-create actively in the MIUI community. For example, if Xiaomi enterprise wants to do some product innovation in Red Rice Note 5A mobile phone's "performance," it should focus on the product feature "performance" connected co-creation knowledge "Xiaolong" and try to motivate the co-creation users who connect to "Xiaolong," such as the users "U151" and "U94," to co-create more actively.

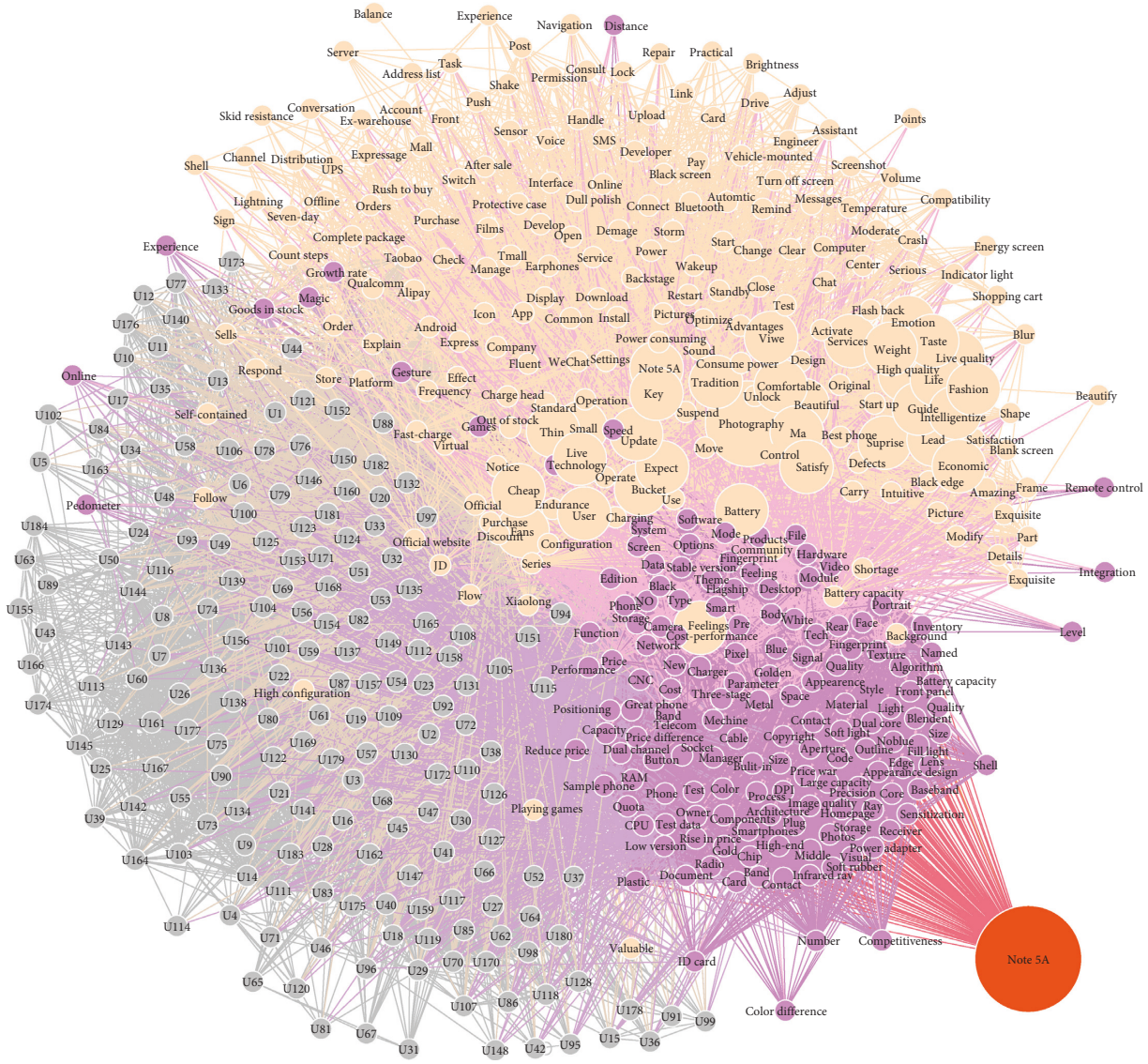

Figure 16: Visualized co-creation cyberspace model for product innovation.

5. Discussion and Conclusion

Several existing research studies have shown great importance of knowledge management and application during product innovation in co-creation community. However, most of the existing research studies only considered co-creation user and knowledge network, failing to map co-creation knowledge with product innovation accurately. Besides, when constructing each co-creation network, the weights and relationships of users and knowledge were not considered comprehensively. Therefore, this paper constructs a "user-knowledge-product" co-creation cyberspace super-network model to address these limitations. The contribution to theory and industry and the limitations of this paper are discussed in detail as follows.

5.1. Contribution to Theory. Aiming at the limitations of the existing research, this paper contributes to the theory from three different perspectives comparing with relevant literature, shown in Table 9. First, for better co-creation user management, the co-creation user network is improved by further considering the interaction relationship among co-creation users. Both the collaboration network caused by social choice and the interaction network caused by social influence are constructed. Second, a comprehensive co-creation knowledge network further considering the similarity relationship and the character weights is constructed to avoid information overload and make hot co-creation knowledge identification more accurate. Third, the two-tier co-creation networks are expanded by constructing a co-creation product network to map with each of them for more effective product innovation. Moreover, the co-creation users, knowledge, and products are integrated into a co-creation cyberspace super-network model for systematic management.

5.2. Contribution to Industry. A well-known co-creation community in China is selected as a case to verify the

Table 9: Comparison with relevant literature.

		Tang et al. [14]	Hao et al. [25]	Liu et al. [26]	Liao et al. [27]	This paper
User network	Interaction relationship					✓
	Collaboration relationship	✓				✓
Knowledge network	Frequency weight	✓			✓	✓
	Attention weight				✓	✓
	Character weight	✓				✓
	TF-IDF weight		✓			
	Co-occurrence relationship	✓		✓	✓	✓
	Similarity relationship		✓			✓
	Synonymy relationship			✓		✓
Product network	Frequency weight					✓
	Attention weight					✓
	Co-occurrence relationship					✓
	Similarity relationship					✓
	Frequency comparison relationship					✓
	Attention comparison relationship					✓

feasibility and validity of the proposed co-creation cyberspace super-network model. The proposed model can provide enterprises with a more comprehensive and detailed integration framework for user discovery, knowledge mining, and application for product innovation in co-creation communities. Through identifying leading users and hot knowledge together with product features, enterprises can:

(1) Grasp the prevailing customer needs and expectations of the consuming products and respond to these needs in time with proper quality for higher customer satisfaction.

(2) Involve customers in product development and improvement process and benefit from their innovation knowledge in the form of ideas, suggestions, and solutions about their consuming products. However, customer involvement can reduce the time and resources as the product innovation and ideation is outsourced to the leading users who may be the best resource to perform this task.

(3) Eliminate the unnecessary and unpopular products from the market based on the received real data from the customers; which will lead to a significant reduction in product/process complexity and cost saving.

(4) Build a dynamic innovation knowledge basement and forecast hotspot trend to gain the initiative in products or service design.

5.3. Limitations of the Study and Threats to Validity. The scope of this study only explained why those important but neglected relationships, weights, and dimension were necessary based on the related literature and used a case study to prove the usability of our proposed model. However, a comparative analysis in order to prove the priority of our model worth investing further in future projects of this nature. Moreover, a separate study to compare and report other available methods of co-creation network construction should be considered in the future. Besides, due to the limitation of time and resources when constructing the co-creation cyberspace, this paper does not consider its dynamic evolution with time. In the future, the dynamic research of network and the use of dynamic network indicators will be applied to this model after further research. Furthermore, in the co-creation community, user-generated context is not only in the form of text, but also in the form of pictures, links, and videos. Future study could take various types of user-generated content into account to mine co-creation knowledge comprehensively. Finally, this paper collected data only from MIUI community and only considered the text in the form of Chinese. It would be interesting to consider replicating this study with other co-creation communities under different language backgrounds.

Data Availability

The data used to support the findings of this study are available from the corresponding author upon request.

Disclosure

Any opinions, findings, conclusions, or recommendations expressed in this paper are those of the authors and do not necessarily reflect the views of the above funding agencies.

Conflicts of Interest

The authors declare that there are no conflicts of interest regarding the publication of this paper.

Authors' Contributions

Yu Wang was responsible for conceptualization, project administration, and supervision. Jiacong Wu performed formal analysis and reviewed, revised, and edited the article. Ru Zhang was responsible for methodology, data curation, and original draft of the manuscript. Sara Shafiee reviewed the manuscript. Cheng Li performed discussion and format editing.

Acknowledgments

This research was partially supported by Jinan University, the National Natural Science Foundation of China under Grant nos. 71772075, 71302153, and 71672074, the Technology R&D Foundation of Guangzhou, China, under Grant no. 201607010012, the Social Science Foundation of Guangzhou, China, under Grant no. 2018GZYB31, and the Foundation of Chinese Government Scholarship No. 201806785010.

References

[1] K. Kazadi, A. Lievens, and D. Mahr, "Stakeholder co-creation during the innovation process: identifying capabilities for knowledge creation among multiple stakeholders," *Journal of Business Research*, vol. 69, no. 2, pp. 525–540, 2016.

[2] E. Constantinides, L. A. Brünink, and C. L. Romero, "Customer motives and benefits for participating in online co-creation activities," *International Journal of Internet Marketing and Advertising*, vol. 9, no. 1, pp. 21–48, 2015.

[3] J. Q. Dong and W. Wu, "Business value of social media technologies: evidence from online user innovation communities," *The Journal of Strategic Information Systems*, vol. 24, no. 2, pp. 113–127, 2015.

[4] W. Guo, Q. Zheng, W. An, and W. Peng, "User roles and contributions during the new product development process in collaborative innovation communities," *Applied Ergonomics*, vol. 63, pp. 106–114, 2017.

[5] L. Bengtsson and N. Ryzhkova, "Managing a strategic source of innovation: online users," *International Journal of Information Management*, vol. 33, no. 4, pp. 655–662, 2013.

[6] S. Kamboj, B. Sarmah, S. Gupta, and Y. Dwivedi, "Examining branding co-creation in brand communities on social media: applying the paradigm of stimulus-organism-response," *International Journal of Information Management*, vol. 39, pp. 169–185, 2018.

[7] N. Zhang, Z.-M. Zhou, C.-T. Su, and N. Zhou, "How do different types of community commitment influence brand commitment? The mediation of brand attachment," *Cyberpsychology, Behavior, and Social Networking*, vol. 16, no. 11, pp. 836–842, 2013.

[8] N. Hajli, M. Shanmugam, S. Papagiannidis, D. Zahay, and M.-O. Richard, "Branding co-creation with members of online brand communities," *Journal of Business Research*, vol. 70, pp. 136–144, 2017.

[9] M. A. Irani, T. S. M. Z. bin Tan, and S. M. Ghazali, "Role of customer knowledge in developing new products and services," in *Proceedings of the 2014 4th International Conference on Engineering Technology and Technopreneuship (ICE2T)*, pp. 6–9, IEEE, Kuala Lumpur, Malaysia, August 2014.

[10] Y. Ding, C. W. Phang, X. Lu, C. H. Tan, and J. Sutanto, "The role of marketer-and user-generated content in sustaining the growth of a social media brand community," in *Proceedings of the 2014 47th Hawaii International Conference on System Sciences*, pp. 1785–1792, IEEE, Waikoloa, Hawaii, January 2014.

[11] Y.-J. Chen and Y.-M. Chen, "Knowledge evolution course discovery in a professional virtual community," *Knowledge-Based Systems*, vol. 33, pp. 1–28, 2012.

[12] Y. Zhang, "Knowledge management model of virtual community based on knowledge intensive services," *Information Science*, vol. 4, pp. 25–28, 2015.

[13] X. F. Zhang, Y. Yang, and G. D. Yu, "Collaborative customer selection based on knowledge perspective," *Computer Integrated Manufacturing System*, vol. 11, pp. 2817–2826, 2015.

[14] H. T. Tang, Z. H. Li, and R. Qin, "Research on user and knowledge model of the mass collaborative," *Chinese Journal of Management*, vol. 6, pp. 859–867, 2017.

[15] T. Chen, Y. Shao, and Y. Han, "Collaborative innovation model research based on knowledge super-network and TRIZ," in *LISS 2014*, pp. 1169–1174, Springer, Berlin, Germany, 2015.

[16] K. Yang, Y. Li, Y. Xiong et al., "Knowledge driven product innovation design based on complex network," *Computer Integrated Manufacturing System*, vol. 9, pp. 2257–2269, 2015.

[17] A. A. Yassine and J. A. Bradley, "A knowledge-driven, network-based computational framework for product development systems," *Journal of Computing and Information Science in Engineering*, vol. 13, no. 1, Article ID 011005, 2013.

[18] M. Sheng and R. Hartono, "An exploratory study of knowledge creation and sharing in online community: a social capital perspective," *Total Quality Management & Business Excellence*, vol. 26, no. 1-2, pp. 93–107, 2015.

[19] J. Swan, S. Newell, and M. Robertson, "Limits of IT-driven knowledge management initiatives for interactive innovation processes: towards a community-based approach," in *Proceedings of the 33rd Annual Hawaii International Conference on System Sciences*, p. 11, January 2000.

[20] E. Von Hippel, "Lead users: a source of novel product concepts," *Management Science*, vol. 32, no. 7, pp. 791–805, 1986.

[21] Y. S. Hau and M. Kang, "Extending lead user theory to users' innovation-related knowledge sharing in the online user community: the mediating roles of social capital and perceived behavioral control," *International Journal of Information Management*, vol. 36, no. 4, pp. 520–530, 2016.

[22] Y. S. Hau and Y.-G. Kim, "Why would online gamers share their innovation-conducive knowledge in the online game user community? Integrating individual motivations and social capital perspectives," *Computers in Human Behavior*, vol. 27, no. 2, pp. 956–970, 2011.

[23] J. Hafkesbrink and M. Schroll, "Ambidextrous organisational and individual competencies in oi: the dawn of A new research agenda," in *Open Innovation: A Multifaceted Perspective: Part II*, pp. 517–570, World Scientific, Singapore, 2016.

[24] P. K. P. Divakaran, "Community-aided brand concept maps: a new approach for eliciting brand association networks," in *Proceedings of the 2014 8th International Days of Statistics and Economics Conference*, pp. 1208–1217, Prague, Czech Republic, September 2014.

[25] J. Hao, Y. Yan, G. X. Wang et al., "LSA-based domain knowledge map construction method," *Transactions of Beijing Institute of Technology*, vol. 7, pp. 691–694, 2014.

[26] J. Liu, H. B. Xu, H. F. Tang et al., "Model and construction method on dynamic knowledge network in big data," *Journal of Computer Research and Development*, vol. 2, pp. 86–93, 2014.

[27] X. Liao, Z. H. Li, and Y. J. Xi, "Modeling and analyzing methods of user-innovation knowledge in enterprise communities based on weighted knowledge network," *Systems Engineering-Theory & Practice*, vol. 1, pp. 94–105, 2016.

[28] F. Y. Wang and Q. Shao, "Co-word analysis combining the WK and CSK co-word models," *University of Electronic Science and Technology of China*, vol. 2, pp. 110–113, 2017.

[29] Y. Wang, J. Wu, R. Zhang, and C. Li, "The construction of "user-knowledge-product" co-creation knowledge cyberspace

served for product innovation," in *Proceedings of the 2019 11th CIRP Conference on Industrial Product-Service Systems*, vol. 83, pp. 467–472, Hong Kong, China, May 2019.

[30] J. He and Y. Z. Liu, "Research on online social networks link prediction based on multidimensional social relations," *Journal of Modern Information*, vol. 7, pp. 41–46, 2017.

[31] L. Ma, R. Krishnan, and A. L. Montgomery, "Latent homophily or social influence? An empirical analysis of purchase within a social network," *Management Science*, vol. 61, no. 2, pp. 454–473, 2015.

[32] R. Barbosa and R. Santos, "Multidimensional approach to online interest networks," *DEStech Transactions on Computer Science and Engineering*, 2016.

[33] C. B. Li, C. P. Pang, Y. L. Ling et al., "Research on network review mining based on improved feature extraction and clustering," *Journal of Modern Information*, vol. 2, pp. 68–74, 2018.

[34] W. Wang and H. W. Wang, "Feature comparison network for competitiveness: emotional analysis method," *Journal of Management Science in China*, vol. 9, pp. 109–126, 2016.

Hindawi
Complexity
Volume 2020, Article ID 7157248, 24 pages
https://doi.org/10.1155/2020/7157248

Research Article

Evolution of Enterprise Competitiveness in Multiplex Networks of Standards: A Case Study of the Communication Industry in China

Fangyu Chen and Yongchang Wei

Institute of Operations Management and System Engineering, School of Business Administration, Zhongnan University of Economics and Law, Wuhan 430073, China

Correspondence should be addressed to Yongchang Wei; ivanwilts306@163.com

Received 9 June 2019; Accepted 31 July 2019; Published 9 January 2020

Academic Editor: Ludovico Minati

Competing to set industry standards is a strategic option to a variety of industries. This paper aims to investigate the role of standard drafting in the evolution of enterprises' competitiveness in multiplex networks of standards. Specifically, network-based measurements are deliberately designed to evaluate the enterprises participation, contribution, and collaboration in drafting standards. By demonstrating the development of the standard system in China's communication industry, the effectiveness of our measurement system is verified. Accompanied by empirical observation, the data analysis shows that the relevant governmental agencies dominate the whole standard system; basic-technology providers acquire greater competitiveness through participating in the standards drafting than the other kinds of enterprises. Finally, the corresponding managerial suggestions are offered.

1. Introduction

Many studies have confirmed the important roles of standards in supporting technological innovation [1–4]. In addition, it is widely accepted in China's business environments that third-tier enterprises manufacture products, their second-tier counterparts forge brands, but leading first-tier enterprises set industrial standards. Thus, we gauge enterprise can gain competitiveness through determining not only the extent to which a given company is involved in drafting standards, but also the significance of such standards. However, there is no literature in ascertaining how to evaluate the enterprises' involvement in standard setting. Fortunately, standards encompass the information such as cited standards, implementation date, and drafters. Two implications follow here. Firstly, to assess the significance of the standards, we may analyse the mutual referencing between standards in a manner analogous to analysing the networks of patents and of literatures [5–9]. Secondly, through examining the standard-drafting by drafters and the collaboration between drafters, we may underline their involvement to the entire standards system. Such analyses, coupled with experiential observation of the drafters' position in the industry, enable us to determine whether enterprises can improve their competitiveness through involvement in drafting industrial standards.

Referencing to a given set of standards reflects the recognition and inheritance of the knowledge in the literature thus referenced. Referencing to standards, citing papers, and citing patents all can demonstrate the relevance of the knowledge, but each has different characteristics. The citation of papers encompasses not only the authors' recognition and inheritance of their predecessors' knowledge, but possibly also critiques of such knowledge; there may additionally be such "referencing noise" [10, 11] as misquotation, referential bias, and intentional self-citation. The citation of patents refers to the adoption of relevant technological predecessors (known as the "prior art") by applicants of new patents, but similar "referencing noise" exists [8, 12]. This may be exemplified by Company A's filing for a new patent based on examining another patent owned by a competitor. The Company A may tend to avoid citing the examined patent and instead seek other bodies' literature, in order to minimize the risks of

copyright infringement or failure in patent filing. Such a propensity will culminate in the lack of citation between two technically most related patents. In this regard, the decision by a standardization organization in referencing a given set of standards implies its selection of the standards from its peers. In the standards-drafting process, the standards technical committee (TC) makes a coordinated, unified, and systematic demonstration of the referential relationship of the standards, thus effectively circumventing the aforesaid problem. The citation of a given set of standards by another set most directly and measurably reflects its adoption and recognition: the higher frequency of a standard being cited illustrates its wider adoption and recognition, which in turn demonstrates both its higher status in the system and the greater contribution of the drafter to establishing the standards system. Co-authorship of standards reflects the collective contributions of multiple drafters to composing them. As with papers and patents, co-authorship of standards reflects collaboration between authors; such co-authorship also implies that the drafters' interests in this area have been agreed by consensus. Greater involvement in drafting and co-authorship translates into greater potential benefits for the drafters through establishing standards, thereby improving their competitiveness. Against this backdrop, despite rich findings on networks of patents and of papers, research into citation networks of standards and the accompanying co-authorships is still lacking.

Challenges exist in identifying key standards and in measuring the drafters' impact on formulating standards. The first concerns the dynamism of the standards system. For scholarly papers, they will upon publication become permanently available in the network of citations. For patents, despite their terms of legal protection, they nonetheless will upon expiry of such terms enter into the public domain. For standards, they are assigned a defined life cycle: from their implementation to their substitution or abolition, and finally to their removal from the system altogether. In the meantime, the drafters constantly undergo organizational changes such as mergers and reorganizations. In sum, the structure and function of the whole standards system evolve continuously. The second challenge concerns the heterogeneity of elements constituting the standards system. On the one hand, the system consists of two different elements: the standards and the drafters. On the other hand, the relationship between the elements is threefold, as it includes citation between standards, drafting between standards and drafters, and the co-authorship between drafters. These challenges have hindered the modelling and analysis of citation and co-authorship networks of standards.

Rapid development in network science has yielded rich theoretical grounds and methods to the research into the aforesaid problem [13–15]. Therefore, through employing the network theory, this paper constructs a dynamic multiplex network model that considers the interactions between the standards and drafters, with focuses on the dynamism and heterogeneity of standards systems. With the communication industry in China as an example, this proposed model is used for: analysing the evolution of standards systems; determining the significance of standards and the contribution of drafters to constructing such systems; demonstrating whether enterprises can improve their competitiveness through involvement in formulating standards; elucidating the different roles of the government and enterprises in formulating standards; and providing corresponding managerial advice on establishing standards systems and on improving enterprises competitiveness.

The academic contributions of this paper follow hereafter. It proposes a general dynamic multiplex standards network model, which can be used for analysing the structural evolution of standards systems in other different industries. Secondly, based on the aforesaid model, a set of measurements is designed for evaluating enterprises' involvement in standards setting, including the extents of such aspects as participation, contribution, cooperation, co-authorship. Thirdly, the paper showcases the development of the standards system in China's communication industry in recent decades from the perspectives of time and of technology, and verifies the effectiveness of the measurement system. Lastly, critical conclusions are drawn based on the results of data analysis—such as the relevant governmental agencies predominating the whole network, and the basic-technology providers acquiring greater competitiveness through participating in the formulating standards than the terminal-equipment manufacturers; the corresponding managerial suggestions are offered.

The rest of this article is organized as follows. Section 2 provides an literature review on the citation networks, co-authorship networks, and standards and enterprises competitiveness. Section 3 not only introduces the evaluative metrics for the standard network selected in this paper and evaluative measurement designs for the drafters involvement, but also outlines the construction of dynamic multiplex standard networks. Section 4, with China's communication industry as an example, not only charts the industry's developmental course through the time and technology mode, but also attests to the rationality of the network model and of the related indicators for evaluation. Some managerial suggestions are also yielded. Finally, conclusions are provided in Section 5.

2. Literature Review

This paper elucidates the dynamic multiplex network (formed by the citation of standards and by the co-authorship between drafters) in the communication industry. Our aims are threefold: to identify the key standards; to assess the drafters' involvement, and to chart the industry's developmental course through analysing the evolution of the network. The literature relevant to this study mainly concerns analysing networks of citations and of co-authorship and the relationship between enterprises' competitiveness and standards. The following is a review of these three areas:

2.1. Analysis of Citation Networks. The citation networks embody the literature—including papers, patents, standards, etc.—and the interconnected referencing. The increasing profusion of the literature in publication not only enriches data in such networks, but also complicates their structures. Through studying the structure and evolution of citation

networks, we can effectively evaluate the importance of academic research results, predict the developmental direction of science and technology, and reveal correlations between bodies of knowledge.

Early research into the citation of papers was limited to only simple indicators. For instance, Garfield [16] first suggested evaluating papers based on the frequency of citations. In addition, in 1976, the US Institute for Scientific Information in its Journal Citation Reports proposed evaluating journals based on impact factors [17]. However, a frequently-cited paper may not necessarily be an influential one. In October 2014, Nature published two consecutive papers on the phenomenon of highly-cited papers [18, 19]: the authors found that the most highly-cited papers were not necessarily the most influential or important papers—the papers of many Nobel laureates had not entered the list of such papers. PageRank, an algorithm invented by Google to evaluate the importance of web pages, has been suggested to evaluate the significance of papers [20]. With the development of the complex network theory, some structural metrics have been used widely to evaluate the significance of papers, such as the degree centrality and betweenness centrality [6, 5, 21].

The publication of scientific articles reflect the trend of development in science, whereas the filing of patents, being an important carrier of technology, forms a requisite source of information for reference in technological innovation of enterprises. For patent citation networks, analysis of the evolution of their structure and function forms the basis underlying the evaluation, selection, and prediction for patent technologies; in addition, such analysis enables research into the transfer and diffusion of knowledge between technical organizations and fields [22–25]. Against this background, Narin [26] pioneered the application of the analysis of paper-citing to patents, thus paving the path for the new field of quantifying patent literature. In their analysis of the trend of patent citation and the mode of knowledge flow, Hu and Jaffe [27] found that the flow of technical knowledge between entities was positively correlated to technological proximity and to geographical proximity. Choe et al. [7], based on data of patent citation, studied the flow of knowledge among organizations and the structural characteristics of the network. Although patents are closely linked to corporate innovation, it is noteworthy that not all technologies can be patented, given factors such as the degree of their innovation and strategic decisions of the enterprise [8, 9, 12, 28, 29].

2.2. Analysis of the Co-Authorship Networks. In the citation networks, each literature originates from one or more authors; accordingly, the citation and drafting of the literature can be further mapped into the co-authorships and communications between authors, thereby forming co-authorship networks. Network analysis has been applied to evaluating the statuses of scholars, academic groups, and research institutions in the academic circles [15, 30]. Such application exerts a critical influence on decision-making such as recruiting talents and allocating resources. Price [31] published the first study on the co-authorship networks, thereby pioneering the research into this hitherto uncharted area. Subsequently, scholars have studied at the microscopic (individuals), mesoscopic (institutions) and macroscopic (countries) levels [30, 32, 33] into technological cooperation in areas as diverse as sociology, medicine, mathematics, intelligence and information science, materials science, etc. [6, 15, 34–37]. In establishing a network of research co-authorship covering physics, biomedicine, and computer science, Newman [13] has reported numerous findings: that the network had a "small-world" phenomenon [14]; that the network in each field contains a huge subgroup; and that the networks of different disciplines possess different characteristics. Hou et al. [35] investigated the structural characteristics of the co-authorship networks at a more microscopic level, including the network density and centrality, areas of cooperation between different sub-networks, and the centres of cooperation. White et al. [38], through examining the contact mode and social distance between co-authors, not only analysed the role of team cooperation in scientific production, but also offered insights into the formation of academic teams and schools of thought. In recent years, considerable attention has been paid to research into networks of cross-disciplinary co-authorship [39–41].

2.3. Enterprise Competitiveness and Standards. Competi tiveness is a complex and multi-facet concept that has not come to one broadly accepted, which is closely related to one enterprise's profitability, productivity and market share. The existing research has focused on the impact of different factors on w, or on the comprehensive evaluation of it through a system of indicators. Numerous factors affect enterprises competitiveness: in addition to existing technical advantages [42–46], some of the literature has focused on the mode of employment [47], prices of energy [48], free-trade agreements [49], captive finance [50], venture capital [51], and intellectual capital [52]. A contentious subject concerns whether environmental protection exerts positive or negative influences on enterprises competitiveness [53–56]. Cheng and Yiu [57] proposed four recommendations, including strengthening intellectual-property protection and implementing educational reforms, to enhance the competitiveness of Chinese enterprises. Goncalves et al. [58] proposed a model for assessing the competitiveness of small-and-medium-sized (SMEs) based on integrating cognitive mapping and the measuring attractiveness by a categorical-based evaluation technique (MACBETH). Despite their managerial suggestions on augmenting enterprises competitiveness, these studies have mostly been static and included few sample enterprises, leading to difficulty in reaching dynamic and universal conclusions.

Additionally, they have overlooked the role of standardization in promoting innovation and enhancing competitiveness [42, 59]. A common thread linking dominant design, appropriability and complementarity is the presence of standards [60]. Standards play a special role in shaping industry architecture, in part because they facilitate specialization and modularization [61]. For instance, if a company wants to get into the cell phone business, it can now buy the relevant chips sets from a company like Qualcomm. In these settings, rents

flow to the suppliers of specialized chips that create lock-in via compatibility or control over standards [62]. Competition to own the standard (or the dominant design) becomes, in some ways, competition for the market [59]. Furthermore, standards setting bodies are usually willing to forms cooperation networks to access additional technology and market knowledge, to create a minimum (critical) size for a project, and to share innovation costs and risks [63]. Therefore, this paper argues that enterprises' competitiveness is closely related to the involvement of enterprises in drafting critical standards and the co-authorship in such drafting [6].

In summary, despite rich findings on citation networks of patents and papers, research into standard citations and the accompanying co-authorships is still lacking. Additionally, in the existing research into enterprises competitiveness, little consideration has been given to how the involvement in standards-drafting may boost competitiveness. As aforesaid, industrial standards are often the fruition of complete consultation and repeated practice of the relevant TC, which are associated with an excellent systematic nature, coordination, and practicality. Standards' citations and the co-authorships reflect the inheritance and development of experience, technology and knowledge in a field. Collectively, these considerations motivate us to undertake this research.

3. Theoretical Framework

3.1. Dynamic Multiplex Network Model. Given the heterogeneity and dynamic nature of the standards system, this paper considers a dynamic multiplex network with two layers: the *standard citation layer* that reflects the citation relationship between standards, and the *drafter cooperation layer* that reflects the cooperation in drafting. The former comprises m standards, while the latter comprises n drafters, which could be governmental agencies, enterprises, etc. In this study, we only focus on enterprises' involvement because we empirically observed that enterprises dominantly affect the communications industry. Consequently, the entire standard network, which includes two kinds of node sets and three kinds of edge sets, is represented by:

$$\begin{aligned} \mathcal{G} = &\left\{\mathcal{N}_s^t, \mathcal{N}_d^t, \mathcal{E}_{citation}^t, \mathcal{E}_{drafting}^t, \mathcal{E}_{co-authorship}^t\right\}, \\ &t \in T = \{t_0, t_1, \ldots, t_k, \ldots\}, \end{aligned} \tag{1}$$

where $\mathcal{N}_s^t = \{s_1^t, s_2^t, \ldots, s_m^t\}$ denotes the node set of valid standards at time t; $\mathcal{N}_d^t = \{d_1^t, d_2^t, \ldots, d_n^t\}$ denotes the node set of drafters corresponding to those valid standards at time t; $\mathcal{E}_{citation}^t = \left\{\left\langle s_i^t, s_j^t\right\rangle \middle| s_i^t, s_j^t \in \mathcal{N}_s^t, i \neq j\right\}$ denotes the edge set of citations; $\mathcal{E}_{drafting}^t = \left\{\left\langle s_i^t, d_j^t\right\rangle \middle| s_i^t \in \mathcal{N}_s^t, d_j^t \in \mathcal{N}_d^t\right\}$ denotes the edge set of drafting relationships; $\mathcal{E}_{co-authorship}^t = \left\{\left\langle d_i^t, d_j^t\right\rangle \middle| d_i^t, d_j^t \in \mathcal{N}_d^t\right\}$ denotes the edge set of co-authorships. If the standard s_i^t is cited by the standard s_j^t, then $\left\langle s_i^t, s_j^t\right\rangle \in \mathcal{E}_{citation}^t$. Between the *standard citation layer* and *drafter cooperation layer*, if the standard s_i^t is drafted by the drafter d_j^t, then $\left\langle s_i^t, d_j^t\right\rangle \in \mathcal{E}_{drafting}^t$; if the standard s_k^t is drafted jointly by the drafters d_i^t and d_j^t, then $\left\langle d_i^t, d_j^t\right\rangle \in \mathcal{E}_{co-authorship}^t$. Apparently, the network is heterogeneous because it is composed of nodes and edges with distinct characteristics. Moreover, the network is dynamic because both node sets and edge sets only cover the standards and drafters that are valid at time t, leading to constant structural evolution.

Elements in the three kinds of edge sets can be defined by the matrix that characterizes the three kinds of relationships. Since the citation relationship is irreversible, the edges in $\mathcal{E}_{citation}^t$ are directed. Thus, the citation relationship between standards is characterized by an asymmetrical matrix $\mathbf{A}^t = \left[a_{ij}^t\right]_{m\times m}$, wherein:

$$a_{ij}^t = \begin{cases} 1, & \text{if standard } s_i^t \text{ is cited by standard } s_j^t; \\ 0, & \text{otherwise.} \end{cases} \tag{2}$$

Accordingly, the drafting relationship between m standards and n drafters is directed, which constitutes a matrix $\mathbf{B}^t = \left[b_{ij}^t\right]_{m\times n}$, wherein:

$$b_{ij}^t = \begin{cases} 1, & \text{if standard } s_i^t \text{ is drafted by drafter } d_j^t; \\ 0, & \text{otherwise.} \end{cases} \tag{3}$$

Given the possibility of their multiple occurrences, co-authorships between drafters can be expressed by a weighted matrix $\mathbf{C}^t = \left[c_{ij}^t\right]_{n\times n}$, where the weight of the co-authorship between drafters d_i^t and d_j^t, c_{ij}^t is represented by

$$c_{ij}^t = \sum_{k=1}^{m} b_{\mathrm{ki}}^t b_{kj}^t. \tag{4}$$

When $b_{ki}^t = 1$ and $b_{kj}^t = 1$, it is implied that drafters d_i^t and d_j^t have jointly drafted the standard s_k^t. Thus, the c_{ij}^t is determined by the number of standards that are jointly drafted by d_i^t and d_j^t.

Based on the above definitions, the dynamic multiplex network model can be constructed, as shown in Figure 1.

3.2. Metrics of Dynamic Multiplex Standard Network. Prior to evaluating drafters' involvement, we will firstly evaluate the significance of each standard with the out-degree of standards in the standard citation layer, which is represented by,

$$D_o(s_i^t) = \sum_{j=1}^{m} a_{ij}^t. \tag{5}$$

We select the out-degree to for two reasons. Firstly, although a lot of topological metrics, e.g., betweenness centrality and clustering coefficient, are available in measuring the significance of nodes, the most direct one is the out-degree of standards [13, 15], which is the frequency of citations. Actually, the citation count is the most frequently used metric in bibliometric analysis [16]. Secondly, this study aims at evaluating the drafters' involvement; the computational simplicity of out-degree facilitates the real application.

As aforesaid, competitiveness of an enterprise is closely related to its involvement in standards setting. Moreover, this involvement is an abstractive concept, which is intrinsically

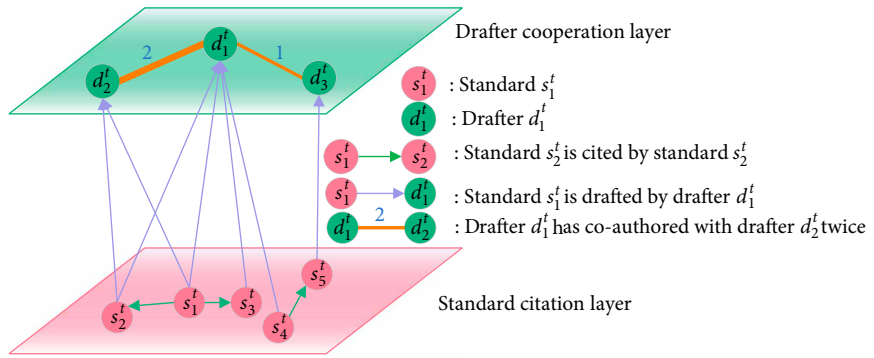

FIGURE 1: An illustration of dynamic standards network at time t.

multi-dimensional. Based on our network model, we can evaluate each enterprise's involvement with a measurement system with four dimensions: *participation degree*, *contribution degree*, *cooperation degree*, and *co-authorship degree*. Firstly, we can measure the significance of each enterprise by the number of its drafted standards, namely, *participation degree*. However, the *participation degree* disregards the quality or significance of standards, which motivates us to design the measurement of *contribution degree* by considering each standard's significance based on *participation degree*, as measured by the out-degree defined in (1). Secondly, cooperation between institutions also plays an essential role in promoting information exchange and knowledge communication. In this study, each enterprise's performance on cooperation is quantified by two aspects: cooperation width and cooperation depth, correspond to *cooperation degree*, and *co-authorship degree*, respectively. *Cooperation degree* of a drafter is determined by the number of its partners in drafting standards jointly, while *co-authorship degree* of each drafter is mainly determined by the number of cooperation times quantified by c_{ij}^t. The four measurements are subsequently defined as follows:

(1) *Participation degree*

The *participation degree* indicates the number of all standards whose drafting the drafter, d_j^t, has participated in, as defined by

$$D_p\left(d_j^t\right) = \sum_{i=1}^{m} b_{ij}^t. \tag{6}$$

A greater *participation degree* of the drafter, d_j^t, suggests a greater number of standards drafted by it.

(2) *Contribution degree*

The *contribution degree* indicates the number of citations of all drafted standards by the drafter, d_j^t, as defined by

$$D_{con}\left(d_j^t\right) = \sum_{i=1}^{m}\left(b_{ij}^t \sum_{k=1}^{m} a_{ki}^t\right). \tag{7}$$

A greater *contribution degree* of the drafter, d_j^t, suggests the greater impact of those standards drafted by it on other standards.

(3) *Cooperation degree*

The *cooperation degree* indicates the number of drafters with whom the drafter, d_j^t, has cooperated, at time t, as defined by

$$D_{coo}\left(d_j^t\right) = \left|\mathscr{C}_j^{\prime t}\right|, \tag{8}$$

where $\mathcal{C}_j^{\prime t} = \left\{c_{ji}^t \neq 0 \middle| i = 1, 2, \ldots, n\right\}$. A greater *cooperation degree* associated with the drafter, d_j^t, suggests its greater number of collaborators.

(4) *Co-authorship degree*

The *co-authorship degree* of the drafter d_j^t represents the number of all the co-authorship times with other drafters, as defined by

$$D_{coa}\left(d_j^t\right) = \sum_{i=1}^{n} c_{ji}^t. \tag{9}$$

A greater *co-authorship degree* associated with the drafter, d_j^t, suggests its greater willingness to adopt co-authorship in standards-drafting.

Finally, we select the numbers of nodes and of edges of the network as the network-level indicators to describe the dynamic evolution of the entire standards system. The number of nodes reflects the scale of the network. To distinguish between different types of nodes, we compute the numbers of standards, indicated as $m = \left|\mathcal{N}_s^t\right|$, and of drafters, indicated as $n = \left|\mathcal{N}_d^t\right|$, at time t. The number of standards nodes will rise because of the implementation of standards and decline because of their abolition, whereas the number of drafters' nodes will rise because of the participation of their new counterparts in standards-setting and decline because of institutional restructuring or mergers. On the other hand, the number of edges reflects the number of connections between nodes; for the standards network, computations are made at time t according to the edges of citation, of drafting, and of co-authorship, as determined by the formulas $\left|\mathscr{E}_{citation}^t\right|$, $\left|\mathscr{E}_{drafting}^t\right|$, and $\left|\mathscr{E}_{co-authorship}^t\right|$.

3.3. Establishing and Evaluating the Standards Network. After the architecture of the network and evaluation measurements are designed, the corresponding standard network can be generated based on our data collected from publicized web sites. The process is illustrated in Figure 2, which offers two

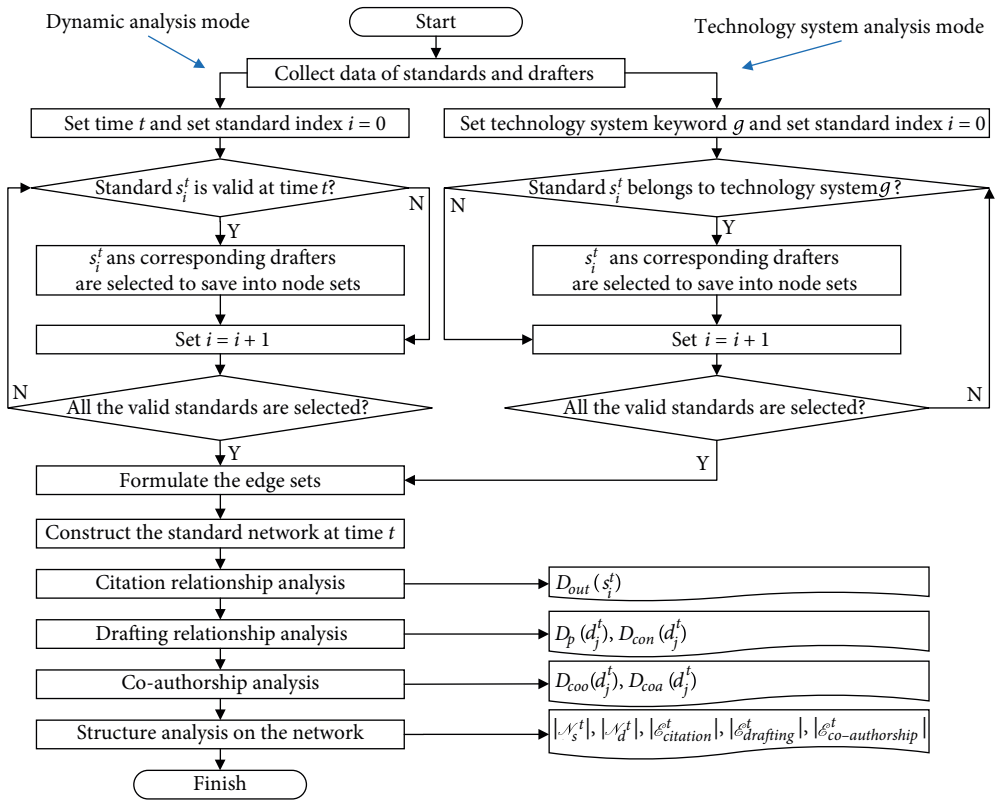

Figure 2: Flowchart depicting the construction of network and computation of indicators.

analysis modes: dynamic analysis mode and technology system analysis mode. The dynamic analysis mode begins with the screening of data of the standards and drafters at a pre-set time; only the standards in use and their corresponding drafters are retained. The technology system analysis mode screens the data by a specific keyword of technology, such as GSM, and retains the related standards and drafters. Firstly, considering the standards nodes and the citation relationship between them, we can determine the out-degree of the standards. Secondly, considering the drafting relationship between the standards and drafters, we can compute not only the drafters' *participation degree*, but also the *contribution degree*. Thirdly, considering the cooperative relationship between the drafters, we can compute the drafters' *cooperation degree* and *co-authorship degree*. Finally, the overall characteristics of the standards network at time t is analysed.

4. Case Study

4.1. Sources of Data and Processing. Taking China's communications industry as the case study, this paper considers that, in a given domain, the standards may cite their counterparts from other areas or international standards during their drafting process, and may also in turn be cited by standards in other domains; accordingly, there is a need to limit the scope of the standards thus considered. The China Communications Standards Association is the main nonprofit corporate body in communication technology that governs standardization and standards-formulation in China's communications industry, under which are 10 technical committees and 5 ad-hoc task forces. The standards under its management are largely categorized as telecommunications according to the Chinese classification, for which the prefixes are mostly "YD". Therefore, we limit the standards in our study to those under the purview of the Association. Through web crawlers, we have acquired a list of all the standards up to June 2018 from the website of the Association. Given possible missing information in registration, we then cross-compared multiple other standards' service websites based on the list. This enabled us to obtain attributes of the standards such as their name, technical field, keywords, implementation date, expiration date, reference standards, substitution standards, drafters, etc. Finally, our efforts yielded 4,642 valid standards signals (to which corresponding codes were assigned). Through collation of the drafters' signals on mergers and reorganizations, we filtered 1,036 drafters' signals (to which corresponding codes were assigned), alongside 8,266 reference signals, 10,754 co-authorship signals and 17,620 drafting signals.

To outline the dynamic evolution of the standards network, we partitioned the development of China's communications industry into five stages (before 1997, 1998–2002, 2003–2007, 2008–2012, and after 2013), thereby forming five time points: 1997, 2002, 2007, 2012, and 2017. The rationale underlying such partitioning was that China's communication standards system was not yet mature before 1997; this was followed by five-year intervals, with the more significant years being 2002, 2008, and 2013, which respectively corresponded

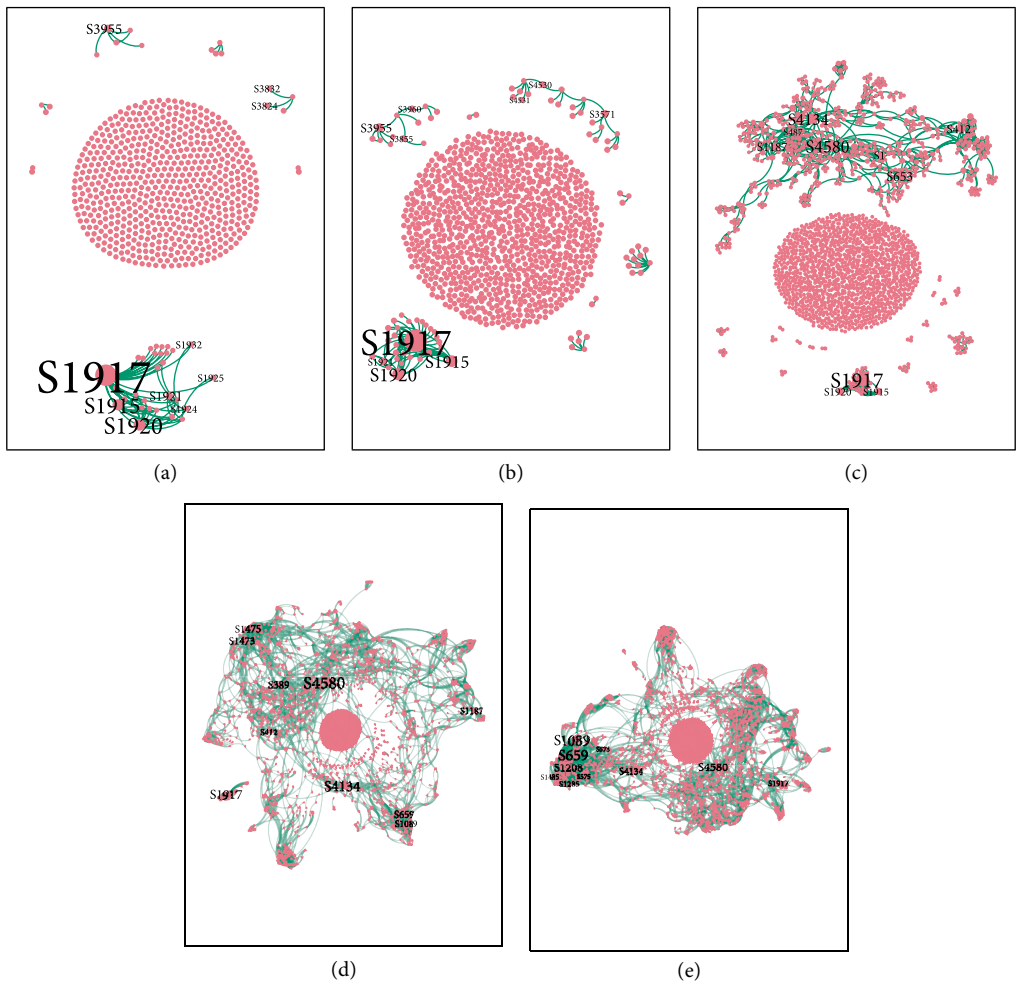

FIGURE 3: The sub-networks of citation in different stages. (a) 1997, (b) 2002, (c) 2007, (d) 2012, (e) 2017.

to the commercial application of 2G, 3G, and 4G technology in China's mobile-communications industry. The partitioning charts the evolution of the standards system in tandem with the development of the industry. In addition, apart from mobile communications, the standards system encompasses optical-fiber communications, construction of telecommunication infrastructures, and standards of other areas. To analyse the different mobile-communication technologies in China's establishment of standards system, we determine from the standards system a list of the relevant technical standards (a network of six standards sub-system)—GSM, CDMA, WCDMA, TD-SCDMA, CDMA2000, and LTE—and the accompanying indicators.

4.2. Findings

4.2.1. Dynamic Analysis of the Overall Network.

(1) 1997: In 1993, China began testing the commercial application of second-generation communication technology. Prior to this, most mobile communications in China used FDMA-based analog communication technology, and more users were using landlines.

To delineate the structural characteristics of different relationships in the standard network, three sub-networks—each of which respectively considers only the citation relationship, drafting relationship, and co-authorship—can be constructed. They can be defined by:

$$\begin{aligned} &\mathcal{G}_{citation} = \left\{\mathcal{N}_s^t, \mathcal{N}_d^t, \mathcal{E}_{citation}^t\right\}, \mathcal{G}_{citation} \subseteq \mathcal{G}, \\ &\mathcal{G}_{drafting} = \left\{\mathcal{N}_s^t, \mathcal{N}_d^t, \mathcal{E}_{drafting}^t\right\}, \mathcal{G}_{drafting} \subseteq \mathcal{G}, \\ &\text{and} \quad \mathcal{G}_{co\text{-}authorship} = \left\{\mathcal{N}_d^t, \mathcal{E}_{co\text{-}authorship}^t\right\}, \mathcal{G}_{co\text{-}authorship} \subseteq \mathcal{G}. \end{aligned} \tag{10}$$

In sub-network of citation (Figure 3(a)), the S1917 represents the most important standard, as shown in Table 1. This standard stipulates specifications for components used in the construction of overhead communication lines. This implies that China's main means of communication has not yet transitioned to the digital mobile communications as of 1997. In the end of 1997, the number of fixed-line users reaching 110 million, while mobile phone users have just exceeded 10 million. For information on the standards referred to herein, please refer to Appendix A. In the sub-networks of drafting relationship (Figure 4(a)) and of co-authorship (Figure 5(a)), we can evaluate the *participation degree*, *contribution degree*, *cooperation degree*, and *co-authorship degree* of each drafter. As the standards-citation is insufficient, only eight drafters have valid values in *contribution degree*. As shown in Table 1, the majority of the top ten are research institutes and

Table 1: The top ten standards and drafters in high indicators till 1997.

Rank	Out degree		Participation degree		Contribution degree		Cooperation degree		Co-authorship degree	
	s_i^t	$D_o(s_i^t)$	d_j^t	$D_p(d_j^t)$	d_j^t	$D_{con}(d_j^t)$	d_j^t	$D_{coo}(d_j^t)$	d_j^t	$D_{coa}(d_j^t)$
1	S1917	28	D3	179	D10	62	D3	9	D10	63
2	S1920	11	D10	83	D501	60	D10	7	D501	58
3	S1915	10	D4	52	D502	60	D334	4	D502	58
4	S3955	4	D1021	48	D1021	5	D4	4	D3	17
5	S1921	3	D135	43	D3	5	D1035	3	D135	5
6	S1925	1	D1031	35	D381	1	D501	2	D334	4
7	S1924	1	D16	32	D15	1	D502	2	D4	4
8	S1932	1	D501	29			D96	2	D96	4
9	S3832	1	D502	29			D1021	2	D1035	3
10	S3824	1	D1027	18			D115	2	D1021	3

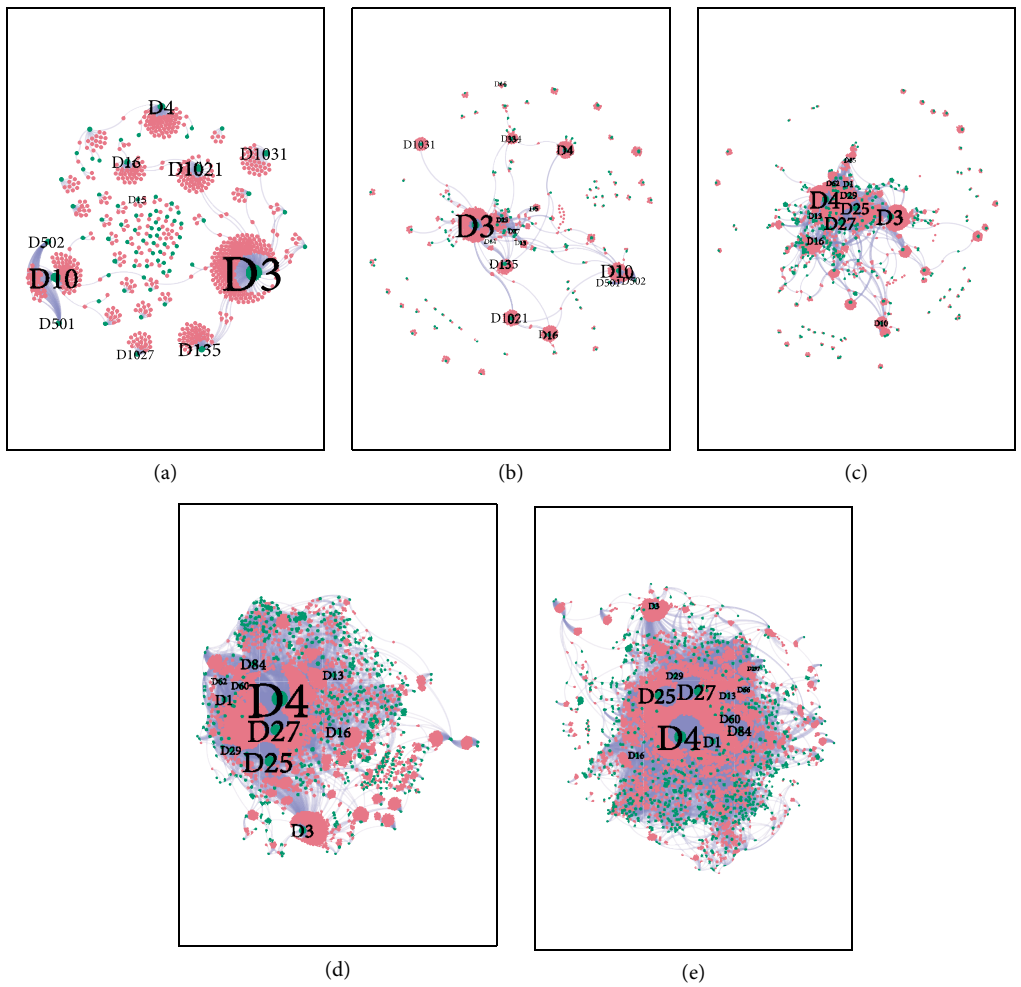

Figure 4: The sub-networks of drafting in different stages. (a) 1997, (b) 2002, (c) 2007, (d) 2012, (e) 2017.

manufacturers of communication equipment affiliated with the Ministry of Industry and Information Technology (MIIT). This suggests that, in the period leading up to 1997, standardization in China's communications industry had been dominated by governmental agencies, with relatively low participation of enterprises. For the main drafters' and their corresponding details, please refer to Appendix B. In this first stage, 658 standards were collated, alongside 74 drafters, 75 pairs of citation relationships, 33 pairs of co-authorships, and 749 pairs of drafting relationships, all of which constituted the overall network shown in Figure 6(a).

(2) 2002: The year 1998 witnessed the commercial application of 2G digital mobile-communications technology. In 2001, the use of analog mobile phones was completely phased

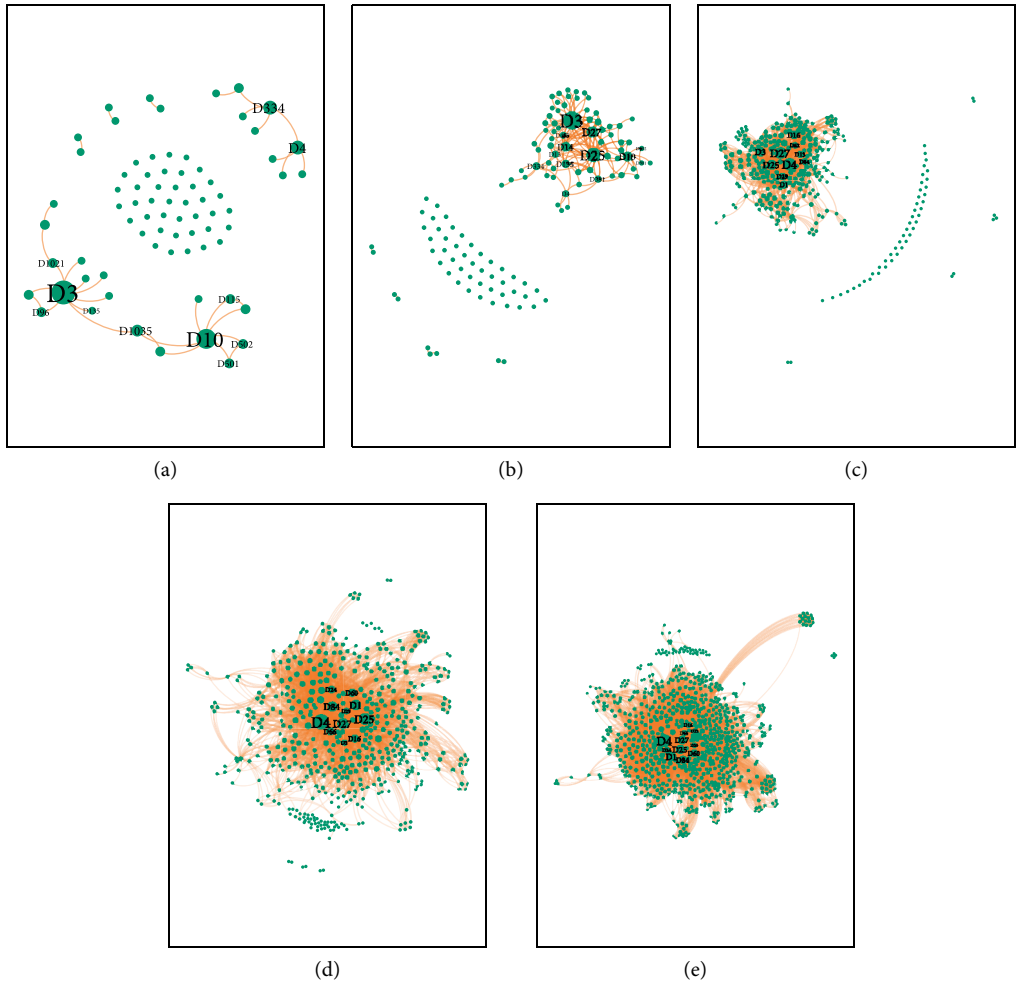

Figure 5: The sub-networks of co-authorship in different stages. (a) 1997, (b) 2002, (c) 2007, (d) 2012, (e) 2017.

out of the market. In the next year, China's mobile-phone numbers rose from 10 digits to 11, mobile-phone users reached 150 million, and fixed-line users persisted at 200 million. In the sub-network of citation (Figure 3(b)), S1917 remained as the standard with the greatest out-degree in the entire citation network, as likewise indicated in Table 2. Given the little difference between mobile-phone users and fixed-line users, despite the expanded volume in the standards system, the standards relating to fixed-line users remained as the core of the system. In the sub-networks of drafting (Figure 4(b)) and of co-authorship (Figure 5(b)), the greatest change was the beginning of a more pronounced increase in the proportion of enterprises among the drafters, especially Huawei and ZTE, as suggested in Table 2. Although the number of standards whose drafting involved them was not superior to that of the government, the two companies had performed well in cooperating with the relevant governmental agencies. In 2002, 1033 standards nodes were collected, alongside 122 drafters, 114 pairs of citation relationships, 167 pairs of co-authorships, and 1286 pairs of drafting relationships, all of which constituted the overall network shown in Figure 6(b). Within 1998–2002, the numbers of standards and drafters almost doubled, in tandem with evident development in the standards system. Of note, the standards in China's communications industry were still predominantly driven by governmental agencies. Despite rising enterprises participation, standards whose drafting involved enterprises had yet to become the core standards in the system.

(3) 2007: From 2003 to 2007, the 2G digital communication technology continued to expand the market. In October 2003, the number of mobile-phone subscribers reached 260 million, exceeding the number of fixed-line subscribers, while that of Internet users rose from 59.1 million in 2003 to 160 million in 2007. In sub network of citation (Figure 3(c)), although S1917 remained as the standard with the greatest out-degree of the entire citation network (as shown in Table 3), standards in other domains such as the Internet, telephones, optical-fiber communications, and mobile phones began to enter lists of highly-cited standards. This shows that, in the communications industry, the changes in the focus of the establishment of the standards system were consistent with the industrial structure changes. The 11th Five-Year plan outlines the need to build a next-generation communication network with independent intellectual property rights. In the sub-networks of drafting

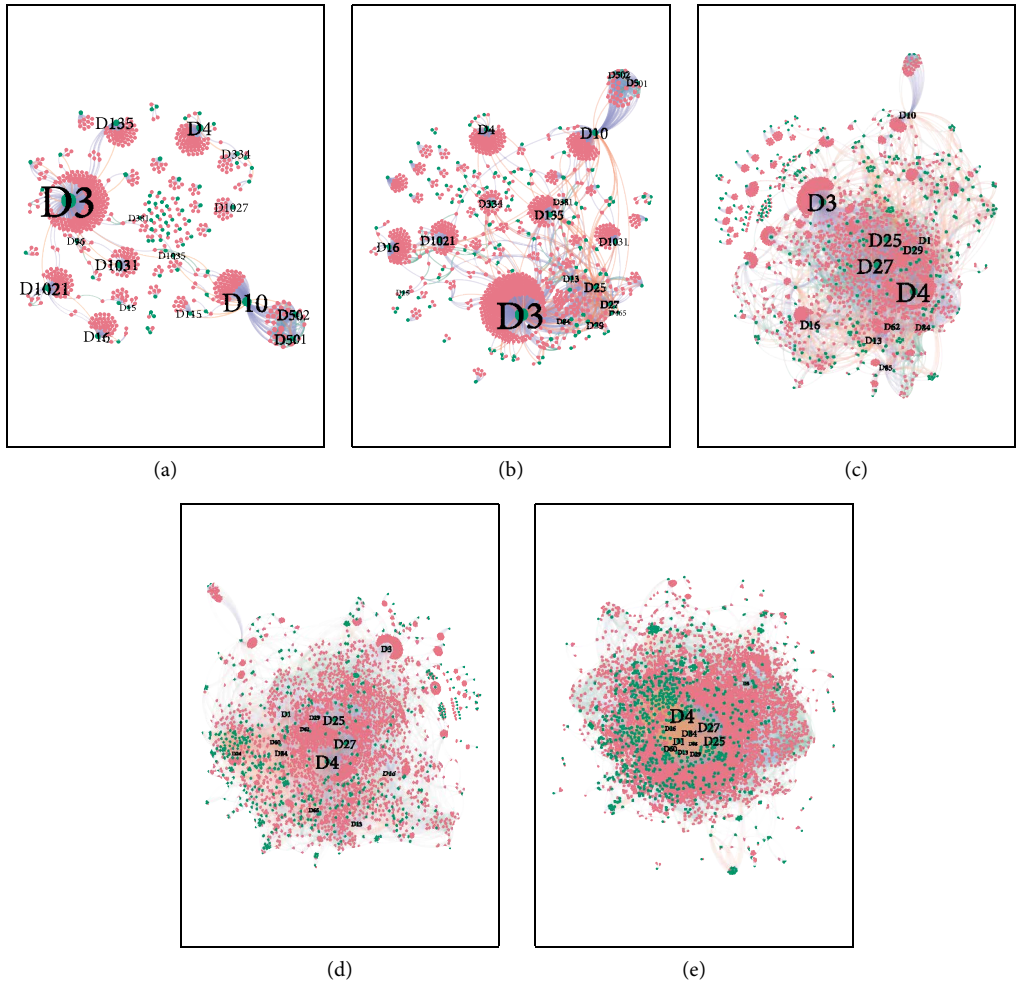

FIGURE 6: The overall networks in different stages. (a) 1997, (b) 2002, (c) 2007, (d) 2012, (e) 2017.

TABLE 2: The top ten standards and drafters in high indicators till 2002.

	Out degree		Participation degree		Contribution degree		Cooperation degree		Co-authorship degree	
Rank	s_i^t	$D_o(s_i^t)$	d_j^t	$D_p(d_j^t)$	d_j^t	$D_{con}(d_j^t)$	d_j^t	$D_{coo}(d_j^t)$	d_j^t	$D_{coa}(d_j^t)$
1	S1917	28	D3	363	D10	64	D3	40	D3	145
2	S1920	11	D10	96	D502	60	D25	28	D25	110
3	S1915	10	D4	76	D501	60	D27	18	D27	77
4	S3955	5	D16	67	D3	20	D10	15	D10	71
5	S1921	3	D1021	65	D1021	13	D29	14	D29	67
6	S3571	3	D135	64	D16	9	D135	11	D501	58
7	S3855	2	D25	47	D15	3	D334	10	D502	58
8	S3960	2	D1031	40	D13	2	D381	8	D135	23
9	S4530	2	D334	33	D5	2	D13	8	D13	16
10	S4531	1	D27	29	D84	1	D4	7	D465	15

relationship (Figure 4(c)) and of co-authorship (Figure 5(c)), the proportion of enterprises among the drafters continued to rise, as shown in Table 3. The number of standards drafted by Huawei and ZTE had become on a par with that by governmental agencies, with concomitantly significant contributions. Given the emerging segmentation in the industry, other enterprises such as Datang Telecom Technology and Fiberhome Technologies, had started to assume more important positions in the standards system. At this stage, 1,975 standards nodes were collected, alongside 303 drafters, 1,130 pairs of citation relationships, 1,185 pairs of co-authorships, and 4,070 pairs of drafting relationships, all of which constituted the overall

Table 3: The top ten standards and drafters in high indicators till 2007.

	Out degree		Participation degree		Contribution degree		Cooperation degree		Co-authorship degree	
Rank	s_i^t	$D_o(s_i^t)$	d_j^t	$D_p(d_j^t)$	d_j^t	$D_{con}(d_j^t)$	d_j^t	$D_{coo}(d_j^t)$	d_j^t	$D_{coa}(d_j^t)$
1	S1917	28	D4	577	D3	433	D4	110	D4	1174
2	S4580	22	D3	503	D25	349	D27	101	D27	1174
3	S4134	20	D27	389	D4	335	D25	80	D25	1005
4	S653	15	D25	347	D27	296	D3	74	D29	640
5	S1187	13	D29	185	D29	174	D29	64	D1	417
6	S412	13	D16	159	D62	96	D16	59	D3	385
7	S1	12	D1	97	D10	80	D1	52	D62	302
8	S1920	11	D10	97	D16	73	D13	42	D16	271
9	S1915	10	D13	93	D13	65	D84	39	D13	265
10	S487	9	D62	83	D85	63	D62	35	D84	235

Table 4: The top ten standards and drafters in high indicators till 2012.

	Out degree		Participation degree		Contribution degree		Cooperation degree		Co-authorship degree	
Rank	s_i^t	$D_o(s_i^t)$	d_j^t	$D_p(d_j^t)$	d_j^t	$D_{con}(d_j^t)$	d_j^t	$D_{coo}(d_j^t)$	d_j^t	$D_{coa}(d_j^t)$
1	S4580	36	D4	1480	D4	1511	D4	297	D4	4481
2	S4134	31	D27	869	D27	1085	D25	204	D27	3359
3	S1917	28	D25	815	D25	905	D27	186	D25	2985
4	S1473	22	D3	474	D3	653	D1	171	D29	1794
5	S1475	22	D29	452	D29	426	D84	159	D84	1705
6	S389	22	D1	333	D84	412	D29	130	D1	1695
7	S659	21	D84	329	D13	377	D16	111	D16	1044
8	S1089	19	D16	320	D1	367	D60	110	D13	941
9	S1187	19	D13	241	D16	305	D66	109	D60	875
10	S412	17	D60	178	D62	292	D24	96	D66	743

network shown in Figure 6(c). Over this five-year period, both the numbers of standards and drafters again nearly doubled, and even showed a nearly ten-fold growth in citation relationships and in co-authorships. Based on the volume, the standards system had exhibited manifest development. The citation, co-authorship, and drafting relationships between the standards and drafters had grown closer. Enterprises participation improved further still, yielding results that occupied higher core positions in the standards system.

(4) 2012: In 2008, China Telecommunications Corporation, China Mobile, and China Unicom launched 3G commercial services based on CDMA2000, TD-SCDMA, and WCDMA respectively. Over the next five years, 3G-based smartphones began to gradually replace feature phones. Internet access services had also demonstrated rapid growth: the numbers of Internet users in China surpassed their counterparts in the United States (US) in 2008 and outnumbered the total US population in 2009. In the sub-network of citation (Figure 3(d)), the majority of the highly-cited standards were related to industries that had rapidly developed over the five years such as Internet access and mobile phones, as likewise indicated in Table 4. In the sub-networks of drafting (Figure 4(d)) and of co-authorship (Figure 5(d)), as likewise indicated in Table 4, influences exerted by research-and-development enterprises such as ZTE Corporation and Huawei in the standards system had gradually stabilised, while communication service providers, such as China Mobile, had also begun to engage in drafting standards. This was mainly because commercial applications of communications technology required the corresponding service-oriented technical standards to be in place; thus, setting such standards was obligatory for service providers. Therefore, from 2008 to 2012, service providers not only became increasingly deeply involved in the standards-formulating in China's communications industry, but also began to occupy higher core positions. At this stage, 3,057 standards nodes were collected, alongside 506 drafters, 3,084 pairs of citation relationships, 3,453 pairs of co-authorships, and 9,016 pairs of drafting relationships, all of which constituted the overall network as shown in Figure 6(d).

(5) 2017: The year 2013 witnessed China's entry into the 4G commercial era. In the sub-network of citation (Figure 3(e)), as shown in Table 5, given the proliferation of smartphones, the standards of the associated functions (such as batteries) and components were highly cited in the network. In the sub-networks of drafting (Figure 4(e)) and of co-authorship (Figure 5(e)), as shown in Table 5, it is evident

Table 5: The top ten standards and drafters in high indicators till 2017.

Rank	Out degree		Participation degree		Contribution degree		Cooperation degree		Co-authorship degree	
	s_i^t	$D_o(s_i^t)$	d_j^t	$D_p(d_j^t)$	d_j^t	$D_{con}(d_j^t)$	d_j^t	$D_{coo}(d_j^t)$	d_j^t	$D_{coa}(d_j^t)$
1	S659	53	D4	2426	D4	2616	D4	553	D4	9991
2	S1089	52	D27	1428	D27	1752	D1	365	D27	7262
3	S4580	41	D25	1366	D25	1339	D25	341	D25	6747
4	S1208	39	D1	871	D84	931	D27	314	D1	4972
5	S4134	32	D84	795	D13	885	D84	301	D84	4831
6	S1917	26	D29	713	D1	759	D60	258	D29	3759
7	S1285	26	D60	653	D29	722	D29	190	D60	3746
8	S1485	24	D13	470	D3	645	D16	172	D13	2916
9	S575	21	D16	437	D66	527	D24	168	D66	2035
10	S573	21	D3	407	D297	465	D66	146	D16	1928

that the status of various types of enterprises in the entire network has stabilized. In this 3G era, given these drafters' successive considerable investments in establishing the standards system and their leading roles in the relevant domains, the 4G era has rightly come to determine those standards. It is expected that this situation will persist for long in the coming 5G era. At this stage, 4,132 standards nodes were collected, alongside 775 drafters, 4,324 pairs of citation relationships, 7,347 pairs of co-authorships, and 16,691 pairs of drafting relationships, all of which constituted the overall network shown in Figure 6(e). As 4G is still in the commercial phase, its related standards are still multiplying. No upsurge was observed in the numbers of standards and drafters relative to the 3G era; however, co-authorships notably doubled, suggesting that, in the development of 4G-related standards, co-authorship has grown to be the drafters' default option.

The time series of the highly-cited standards (Figure 7(a)) reveals two findings. The abolition of standards leads to a diminished out-degree of the standards; conversely, the upgrading of communication technology leads to an augmented out-degree of those standards associated with the new technologies. Depicted in Figures 7(b)–7(e) are the time-series characterising the *participation degree*, *contribution degree*, *cooperation degree*, and *co-authorship degree*. Herein, in establishing the standards system, the core drafters fluctuated with the development of communication technology. This cemented the superior positions of Huawei, ZTE Corporation, the three communication service providers (China Telecommunications Corporation, China Mobile, and China Unicom), and other drafters. In the meantime, although the Telecommunications Research Institute (as the governmental representative of the MIIT) has led the drafting, the role of enterprises in the development of China's communications industry has grown progressively critical. As judged from the dynamic change of the network metrics (Figure 7(f)), the scale of the network of communication standards exhibit a yearly increasing trend and is closely connected with the upgrading of communication technology. This is especially so between 2012 and 2013, when the numerous implemented new standards laid the cornerstone for the launch of 4G and its related technologies. This this same stage also saw the evident accelerated growth of the network metrics. This phenomenon was likewise noted during the promotion of 3G between 2008 and 2009.

4.2.2. Analysis of Standard Networks for Technology Systems. The dynamic analysis of the overall network of standards offers insights into the whole development of China's communications industry. However, technological systems comprising the industry's standards are too multitudinous. To investigate the relationship between the establishment of standards system for a specific technology and enterprises' involvement, we disregarded the time factor; instead, we used specific technical terminologies as keywords. We then selected from the system a series of technical standards related to the mobile-phone communication technology for analysis, as follows.

(1) Global System for Mobile Communications (GSM).

The GSM, a technological standard originating in Europe, belongs to the 2G mobile-communications technology. It was introduced and adopted in China in the 1990s. At present, China Mobile and China Unicom each earns the world's largest GSM-based mobile communications network.

The network comprises 79 standards nodes, 33 drafters, 63 pairs of citation relationship, 189 pairs of co-authorships, and 440 pairs of drafting relationships, all of which constitute the overall network shown in Figure 8(a). As shown in Table 6, the Telecommunications Research Institute (under the MIIT), Huawei, ZTE Corporation, and Datang have assumed dominant roles in establishing the standards system. In addition, enterprises holding the dominant market share in the GSM era, such as Samsung and Nokia, have likewise contributed to establishing the system. Two other types of enterprises are those responsible for GSM operations (i.e. China Mobile and China Unicom) and those manufacturing GSM terminal chips such as MediaTek and Spreadtrum Communications. As a whole, the GSM standards system is characterised by decreasing metrics such as *contribution degree*, with the MIIT as the leading contributor, followed by the basic-technology providers, service providers, and terminal-equipment manufacturers (in that order).

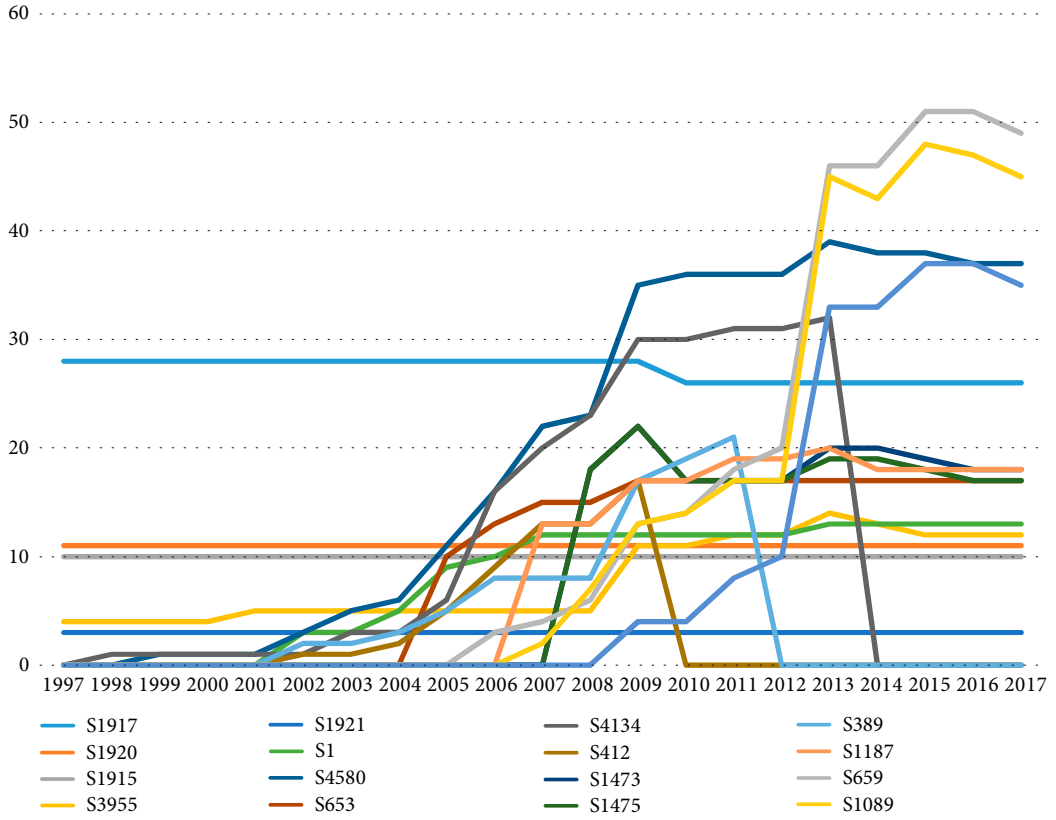

(a)

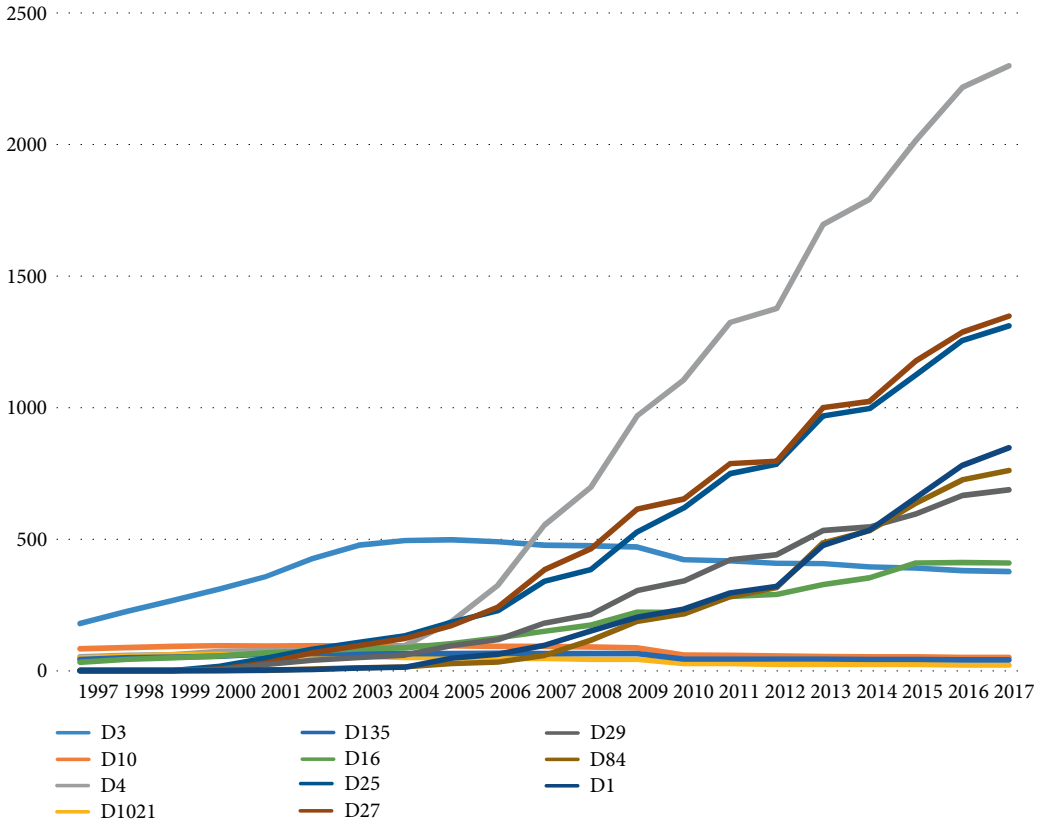

(b)

Figure 7: Continued.

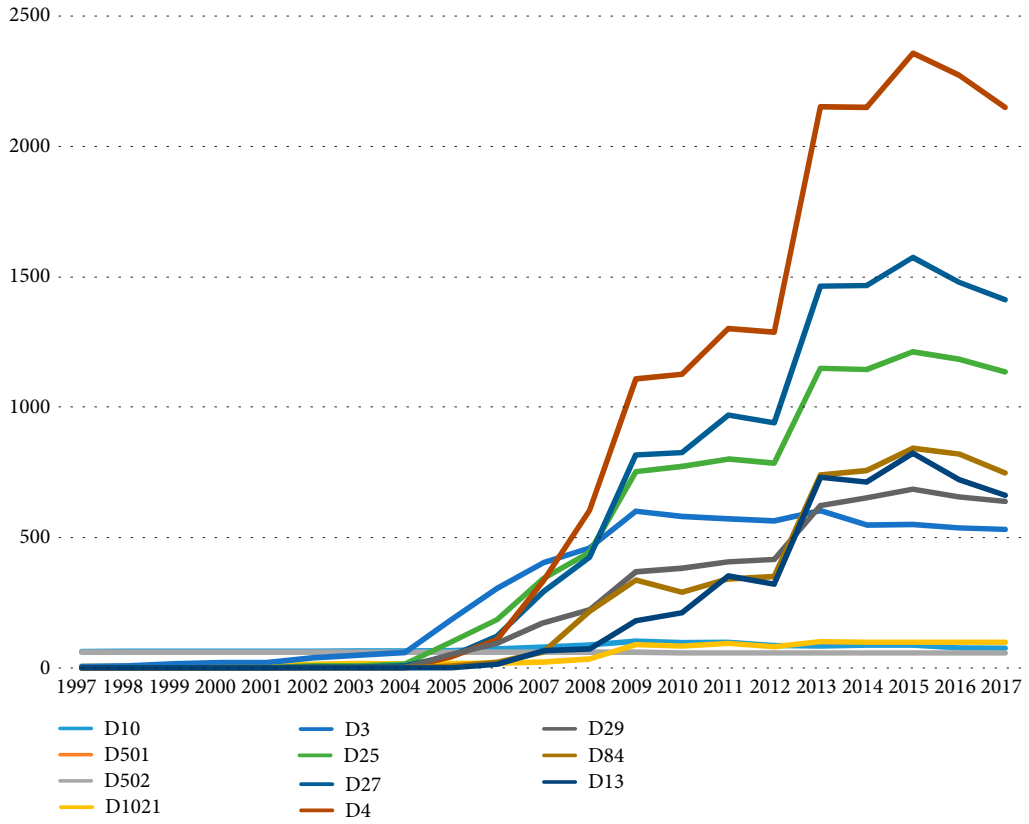

(c)

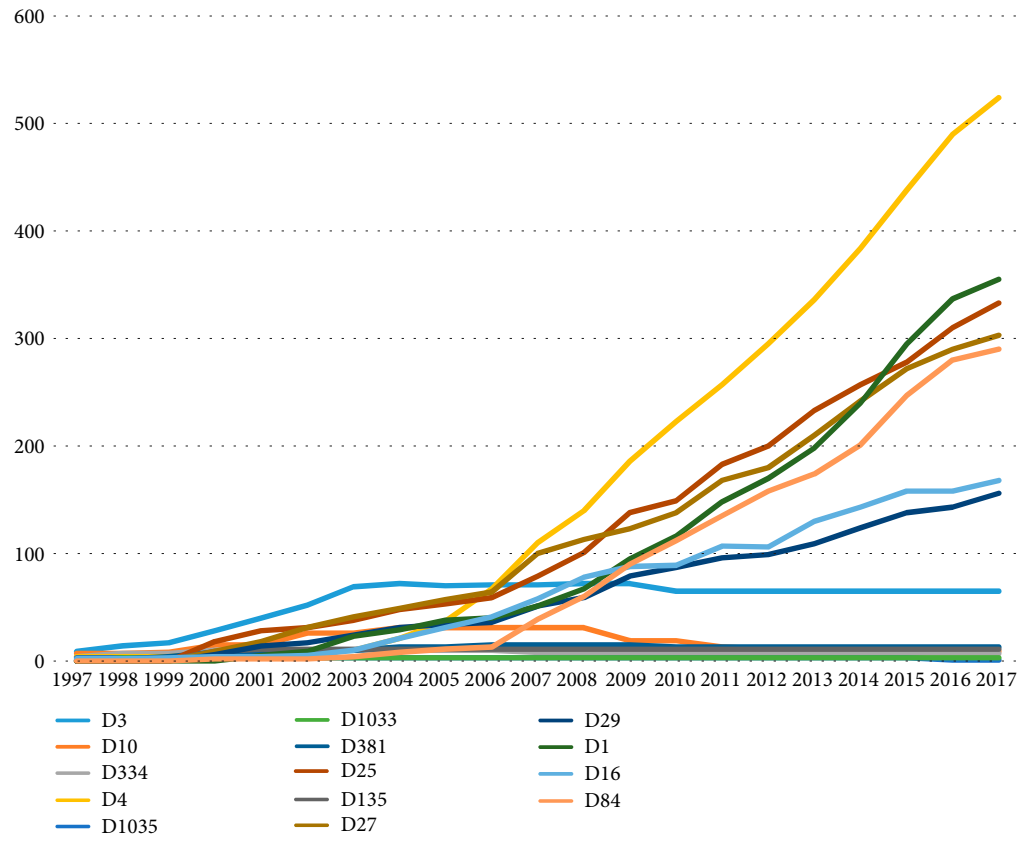

(d)

Figure 7: Continued.

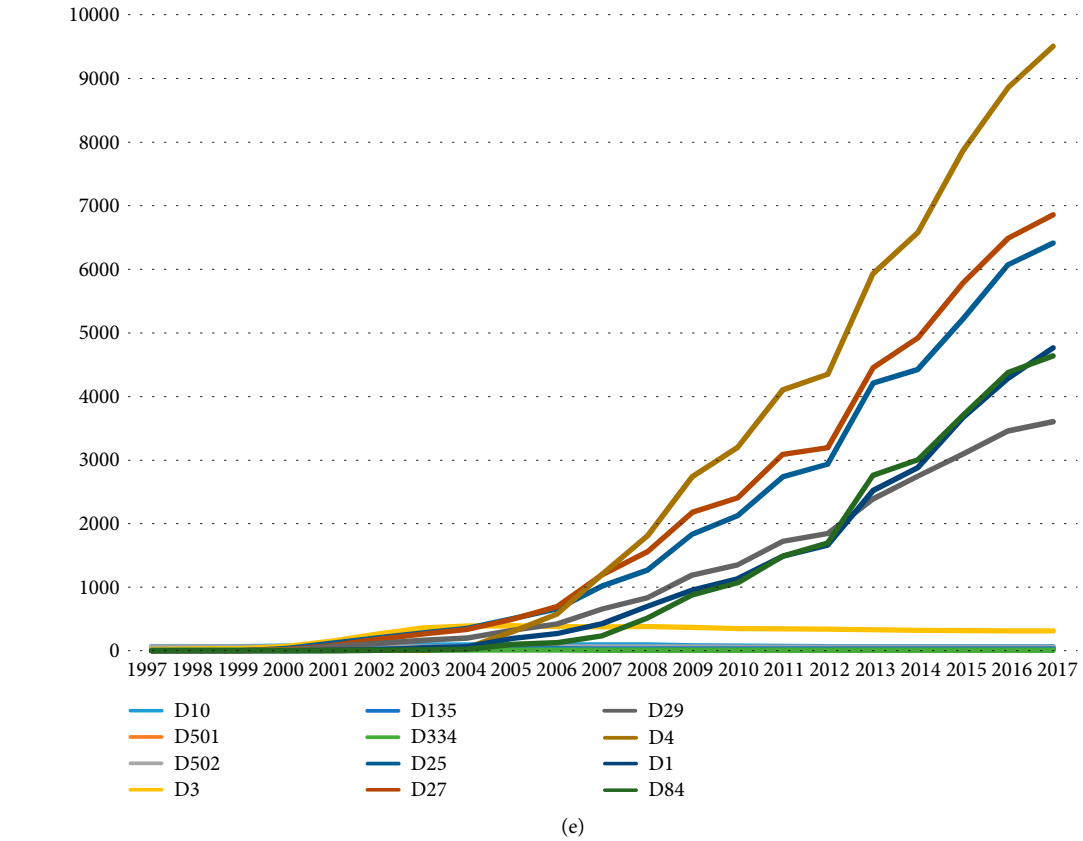

(e)

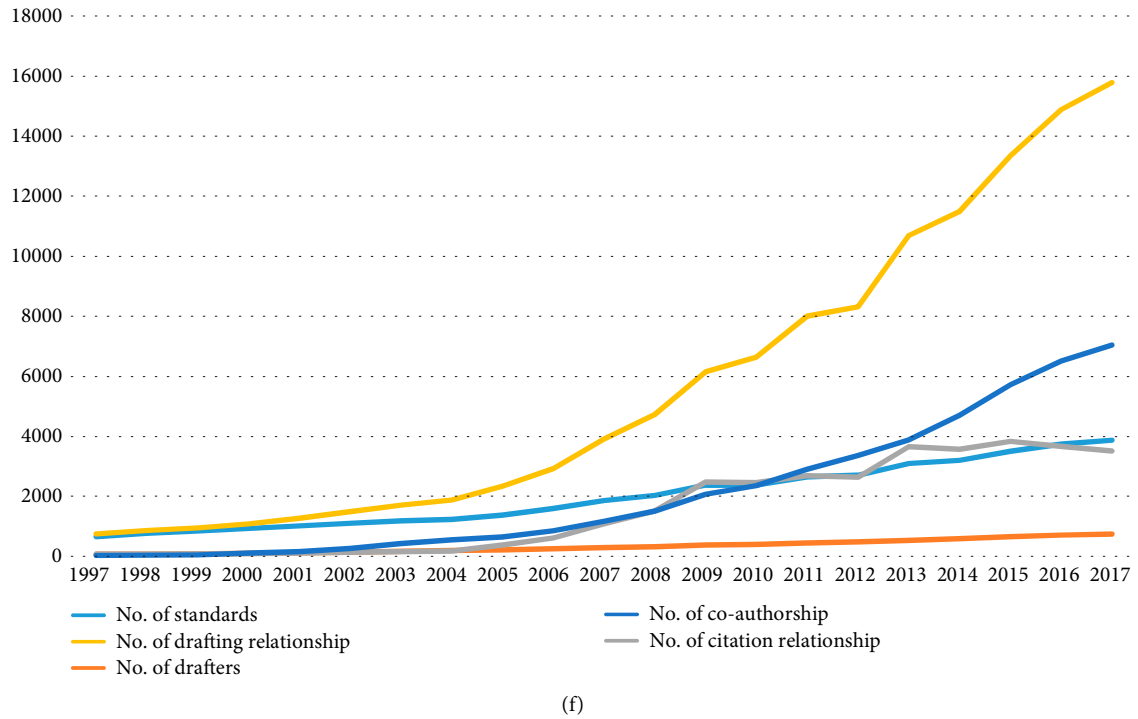

(f)

Figure 7: Dynamic changes in metrics communications standards network. Dynamic changes in (a) most highly-cited standards, (b) drafters with the greatest participation degree, (c) drafters with the greatest contribution degree, (d) drafters with the greatest cooperation degree, (e) drafters with the greatest co-authorship degree, and (f) the network metrics.

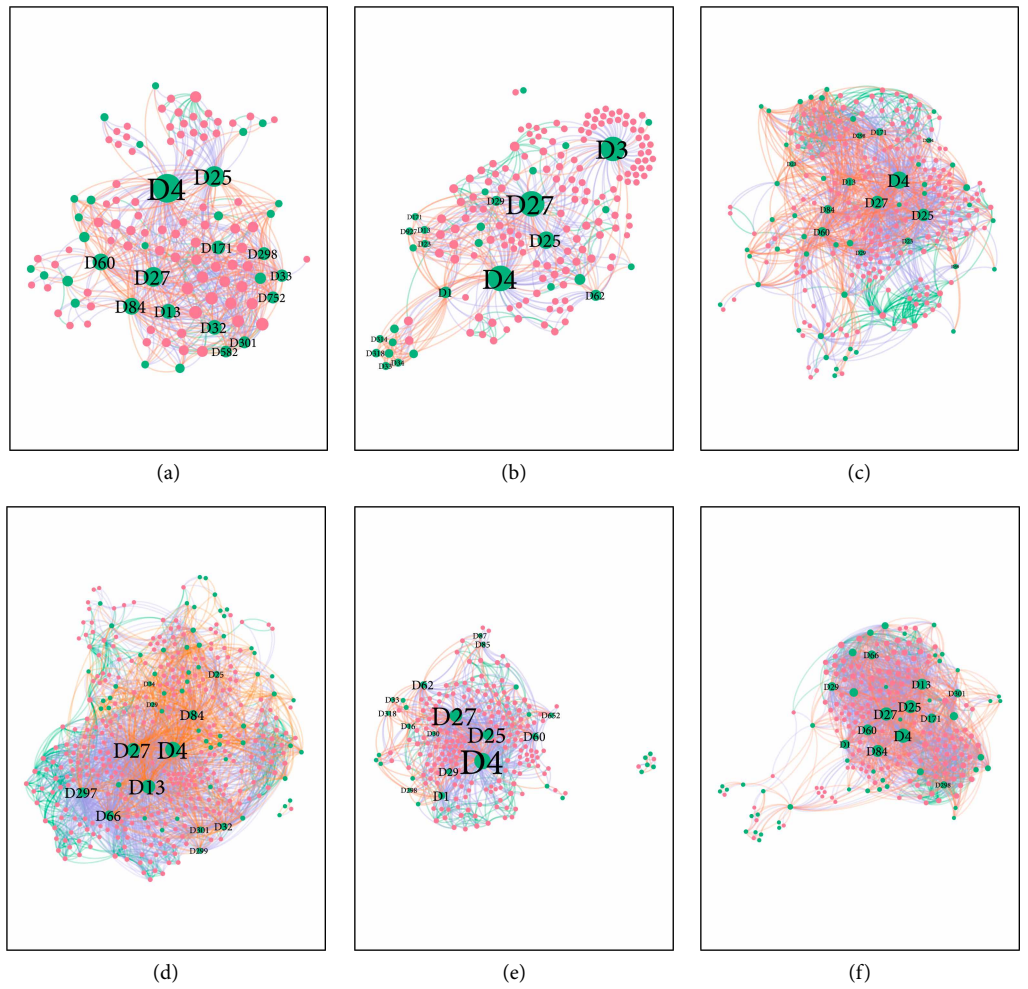

(a) (b) (c)

(d) (e) (f)

Figure 8: The standard networks of different mobile communication technology. (a) GSM, (b) CDMA, (c) WCDMA, (d) TD–SCDMA, (e) CDMA2000, (f) LTE.

Table 6: The top ten drafters with high indicators in GSM system.

	Participation degree		Contribution degree		Cooperation degree		Co-authorship degree	
Rank	d_j^t	$D_p(d_j^t)$	d_j^t	$D_{con}(d_j^t)$	d_j^t	$D_{coo}(d_j^t)$	d_j^t	$D_{coa}(d_j^t)$
1	D4	66	D4	59	D4	27	D4	274
2	D25	41	D27	37	D60	25	D27	264
3	D27	38	D25	34	D27	24	D32	228
4	D84	29	D32	26	D25	22	D13	211
5	D60	27	D13	25	D84	22	D25	198
6	D13	25	D84	22	D13	21	D84	198
7	D32	25	D582	19	D171	18	D171	185
8	D171	22	D301	19	D32	18	D752	185
9	D298	20	D33	13	D298	16	D33	179
10	D33	18	D171	13	D33	15	D298	175

(2) Code Division Multiple Access (CDMA).

The CDMA is a technological standard originating in the US and, similar to GSM, belongs to the 2G mobile-communications technology. In 2001, it was adopted by China Unicom for launching mobile-communications services; in 2008, the network in its entirety was acquired by China Telecom.

The network comprises 147 standards nodes, 31 drafters, 74 pairs of citation relationships, 129 pairs of co-authorships, and 334 pairs of drafting relationships, all of which constitute the overall network shown in Figure 8(b). As shown in Table 7, as is the case with GSM, apart from dominant institutions (such as the Telecommunications Research Institute of the

Table 7: The top ten drafters with high indicators in CDMA system.

	Participation degree		Contribution degree		Cooperation degree		Co-authorship degree	
Rank	d_j^t	$D_p(d_j^t)$	d_j^t	$D_{con}(d_j^t)$	d_j^t	$D_{coo}(d_j^t)$	d_j^t	$D_{coa}(d_j^t)$
1	D4	67	D4	54	D4	22	D27	156
2	D27	65	D27	44	D1	20	D4	140
3	D3	62	D25	22	D27	20	D25	123
4	D25	36	D29	17	D29	19	D29	99
5	D29	25	D3	16	D25	17	D1	63
6	D1	14	D1	9	D3	9	D3	39
7	D62	14	D13	4	D314	9	D13	29
8	D13	6	D23	4	D318	9	D23	26
9	D23	6	D62	4	D33	9	D171	23
10	D927	4	D5	3	D34	9	D31	23

Table 8: The top ten drafters with high indicators in WCDMA system.

	Participation degree		Contribution degree		Cooperation degree		Co-authorship degree	
Rank	d_j^t	$D_p(d_j^t)$	d_j^t	$D_{con}(d_j^t)$	d_j^t	$D_{coo}(d_j^t)$	d_j^t	$D_{coa}(d_j^t)$
1	D4	163	D4	291	D4	43	D4	611
2	D27	105	D27	146	D27	38	D27	478
3	D25	99	D25	127	D25	35	D25	475
4	D60	64	D84	86	D84	35	D60	323
5	D84	51	D13	84	D60	33	D29	255
6	D29	51	D171	60	D29	29	D84	254
7	D13	42	D29	50	D13	27	D171	229
8	D171	41	D298	41	D171	24	D13	185
9	D23	29	D294	36	D33	22	D23	173
10	D298	23	D59	34	D298	21	D298	167

Table 9: The top ten drafters with high indicators in TD-SCDMA system.

	Participation degree		Contribution degree		Cooperation degree		Co-authorship degree	
Rank	d_j^t	$D_p(d_j^t)$	d_j^t	$D_{con}(d_j^t)$	d_j^t	$D_{coo}(d_j^t)$	d_j^t	$D_{coa}(d_j^t)$
1	D4	281	D4	545	D4	59	D4	1298
2	D13	238	D13	526	D27	50	D27	1258
3	D27	236	D27	471	D84	49	D13	1191
4	D297	138	D297	324	D13	42	D84	753
5	D66	129	D66	314	D25	36	D297	744
6	D84	127	D84	173	D66	34	D66	731
7	D32	81	D32	161	D29	34	D32	560
8	D25	58	D301	116	D34	28	D301	404
9	D301	50	D299	112	D301	28	D25	361
10	D299	47	D25	60	D297	28	D299	317

MIIT, Huawei, ZTE Corporation, and Datang), China Unicom and China Telecommunications Corporation, which are in charge of CDMA operations, and CDMA-solution providers such as Bell and Ericsson, also predominate the standards system. As a whole, the CDMA standards system resemble its GSM counterpart in terms of characteristics.

(3) Wideband Code Division Multiple Access (WCDMA).

Among the 3G technologies worldwide, WCDMA—a 3G wireless communications technology based on the upgrading of GSM—not only has the greatest subscription, but also represents the most successful technical and commercial applications. After China Telecommunications Corporation acquired the CDMA network built by China Unicom in 2008, the latter, upon its restructuring in 2009, began to provide 3G mobile-communications business services based on WCDMA.

The network comprises 197 standards nodes, 54 drafters, 312 pairs of citation relationships, 343 pairs of co-authorships, and 915 pairs of drafting relationships, all of which constitute

Table 10: The top ten drafters with high indicators in CDMA2000 system.

	Participation degree		Contribution degree		Cooperation degree		Co-authorship degree	
Rank	d_j^t	$D_p(d_j^t)$	d_j^t	$D_{con}(d_j^t)$	d_j^t	$D_{coo}(d_j^t)$	d_j^t	$D_{coa}(d_j^t)$
1	D4	162	D4	180	D4	22	D4	337
2	D27	110	D27	115	D27	20	D27	302
3	D25	90	D25	82	D25	15	D25	266
4	D1	40	D62	36	D1	13	D29	114
5	D29	39	D1	34	D62	12	D1	106
6	D60	35	D29	22	D29	12	D60	77
7	D62	28	D60	21	D16	11	D62	58
8	D85	11	D85	11	D318	11	D85	21
9	D652	9	D30	9	D33	8	D16	15
10	D87	6	D652	4	D60	8	D298	15

Table 11: The top ten drafters with high indicators in LTE system.

	Participation degree		Contribution degree		Cooperation degree		Co-authorship degree	
Rank	d_j^t	$D_p(d_j^t)$	d_j^t	$D_{con}(d_j^t)$	d_j^t	$D_{coo}(d_j^t)$	d_j^t	$D_{coa}(d_j^t)$
1	D4	127	D4	336	D4	42	D4	1153
2	D27	114	D27	292	D27	38	D25	1142
3	D25	110	D25	287	D25	36	D27	1091
4	D84	101	D84	270	D84	35	D84	938
5	D13	90	D60	261	D13	34	D13	903
6	D60	86	D13	226	D60	31	D60	857
7	D171	70	D171	209	D301	29	D171	826
8	D29	64	D32	205	D66	28	D23	693
9	D1	62	D301	202	D298	27	D29	691
10	D66	61	D29	198	D1	27	D66	656

Table 12: Comparison of network indicators between different communications-technology systems.

	$\lvert\mathcal{N}_s^t\rvert$	$\lvert\mathcal{N}_d^t\rvert$	Proportion of enterprise drafters	$\lvert\mathcal{E}_{citation}^t\rvert$	$\lvert\mathcal{E}_{co-authorship}^t\rvert$	$\lvert\mathcal{E}_{drafting}^t\rvert$
GSM	79	33	84.85%	63	189	440
CDMA	147	31	80.65%	74	129	334
WCDMA	197	54	90.74%	312	343	915
TD-SCDMA	318	67	92.54%	571	493	1752
CDMA2000	181	31	87.10%	193	111	574
LTE	144	57	80.70%	336	416	1431

the overall network shown in Figure 8(c). As shown in Table 8, similarities are noted in the characteristics of WCDMA in the 2G standards system. However, interestingly, given the application of dual-mode mobile phones, China Mobile (responsible for the commercial applications of TD-SCDMA technology) has contributed to the WCDMA standards system to an extent comparable to China Unicom.

(4) Time Division-Synchronous Code Division Multiple Access (TD-SCDMA).

Relative to the other two prime 3G standards (WCDMA and CDMA2000), the TD-SCDMA started late. The historic date of June 29th, 1998 marked the proposal of this standard by China's former Ministry of Posts and Telecommunications through the Research Institute of Telecommunications Science and Technology (the predecessor of modern-day Datang Telecom Technology Co., Ltd.) to the International Telecommunication Union (the initial standards research institute was Siemens). In February 2008, China Mobile began taking charge of constructing the TD-SCDMA communications network.

The network comprises 318 standard nodes, 67 drafters, 571 pairs of citation relationships, 493 pairs of co-authorships, and 1,752 pairs of drafting relationships, all of which constitute the overall network shown in Figure 8(d). As shown in Table 9, enterprises responsible for the domestic research and

development of TD-SCDMA (among which a representative is Datang Telecom) and China Mobile, responsible for commercial applications, have contributed the most to the entire standards system, surpassing both nonlocal enterprises and joint ventures.

(5) Code Division Multiple Access 2000 (CDMA2000).

The CDMA2000, an extension of the CDMA standard among the 2G standards, is incompatible with the WCDMA, a 3G standard. In 2009, China Telecommunications Corporation launched a 3G mobile-communications service based on CDMA2000.

The system comprises 181 standards nodes, 31 drafters, 193 pairs of citation relationships, 111 pairs of co-authorships, and 574 pairs of drafting relationships, all of which constitute the overall network shown in Figure 8(e). As shown in Table 10, the drafters' distribution in the CDMA2000 standards system is approximately the same as that in other standards systems, but it is noteworthy that Beijing University of Posts and Telecommunications—the only academic institution in the top ten—is also in the system. Its presence there suggests that the standards-formulating in the CDMA2000 outperforms other standards systems in the translation of scientific research results.

(6) Long-Term Evolution (LTE)

The LTE is a global standard based on the OFDMA technology and developed by the 3rd-Generation Partnership Project (3GPP) Organizational Partners. It encompasses two modes: the Frequency Division Duplex (FDD) and the Time Division Duplex (TDD). The MIIT issued TDD-LTE business licenses to China Mobile, China Telecommunications Corporation, and China Unicom on December 4th, 2013, and then issued FDD-LTE business licenses to the latter companies on February 27, 2015. These historic dates marked the complete entry of China's communications industry into the 4G era. Given the 90% similarities between the two modes, and the stipulations common to both modes during standards-formulation, we do not distinguish between them when analysing the LTE standards system.

The system comprises 144 standard nodes, 57 drafters, 336 pairs of citation relationships, 416 pairs of co-authorships, and 1,431 pairs of drafting relationships, all of which can constitute the overall network shown in Figure 8(f). As shown in Table 11, the drafters' distribution in the LTE standards system is approximately the same as that in other standard systems; however, China Telecom, as the operator-in-charge in the system, has not invested as much as China Mobile and Chinese Unicom in establishing it.

For metrics in the standards systems of the different mobile-communications technologies, horizontal comparison can be performed, as shown in Table 12.

In different communications-technology standard systems, the TD-SCDMA is the optimal based on the metrics, mainly because the standard has been promoted chiefly by China: the standards are in greater need of China's drafters to formulating and improving the entire system. At the same time, with the expansion of China's communications market and the development of communications technology, enterprises in the industry have also begun to pay attention to the importance of standards and thereby channelled more efforts into establishing the standards system. Governmental agencies manage and guide the whole standards system only through the formulation of a minority of standards, with enterprises assuming the dominant role.

4.3. Discussions and Management Implications. The development of China's communications industry is evident from changes in the scale of the standards network; at the same time, technological changes in the industry are also reflected by changes in the core standards. Based on the indicators of the network, the drafters have performed mostly consistent in our measurements, including *participation degree*, *contribution degree*, *cooperation degree*, and *co-authorship degree*. This implies that the indicators proposed in this paper can quantify the drafters' contributions to constructing the standards system. As judged from different periods and the network characteristics of different technological systems, the standards system in China's communications industry has always been led by governmental agencies. Thereafter, for enterprise drafters, basic-technology providers play the most significant role in drafting standards, followed by service providers, while the involvement of terminal-equipment manufacturers is insufficient. This is closely related to the Chinese enterprises competitiveness in the segmentation of China's communications industry. As for basic technology, Huawei, ZTE Corporation, and other enterprises hold the dominant market shares, with correspondingly important roles in the standards system.

Conversely, as for the purveying of terminal-equipment such as mobile phones, no obvious correlation has existed between market shares owned by manufacturers and their positions in the system. This is mainly because market shares of terminal-equipment are influenced more by product designs, marketing, and pricing strategies. However, this does not mean that the terminal-equipment manufacturers need not participate in establishing the standards system. For example, Huawei, as a basic-technology provider, is also engaged in research and development of mobile phones; with its currently most sizeable sales in China's market of mobile-phone terminals, it has exhibited relatively great participation in setting the standards of such terminals. In addition, despite their lack of past contributions, enterprises with substantial shares of the mobile-phone market have been developing standards since 2017: Vivo, Xiaomi, and OPPO have, respectively, been engaged in drafting 1, 2, and 7 standards.

More interestingly, as for the provision of services, the service providers' contributions to developing technical standards related to the mode of their communications services are somewhat related to their market shares. In the 3G era, China Mobile, China Unicom, and China Telecommunications Corporation have respectively been responsible for the operations of the TD-SCDMA, WCDMA,

CDMA2000 communications networks. The three standards systems have exhibited diminution in the scale of the network (in that order), while the significance of the three enterprises in their own standards systems has also declined (in that order). Up to the commercial launch of the 4G technology, the numbers of their 3G users also dwindled in 2012 (likewise in that order). For service providers, notwithstanding their lack of direct involvement in the research and development of technologies, the development of the relevant standards will affect the quality of services offered to clients. Thus, for basic-technology providers, service providers, and terminal-equipment manufacturers, the extent of their contributions to the standards system influences their competitiveness in their domains, and this influence is correlated to the contributions of these three types of enterprises in the whole standards system. Compared with service providers and terminal-equipment manufacturers, basic-technology providers ought to be more involved in constructing standards systems.

China's communications industry has metamorphosed from a minor follower in the past to the major formulator of technical standards in the present. This change in role is attributed to not only the governmental steering of the direction of development through standards-setting, but also, more importantly, to active enterprises participation in the standards-setting. With the development of technology, enterprises in the standards system have started to assume progressively elevated positions. As world-class enterprises in the communications industry, ZTE Corporation and Huawei have exhibited performances second only to the MIIT in the entire standards system, reflecting the magnitude of their contributions to developing China's communications industry. The international standards for 5G mobile-communications technology are still in their nascent formulation, in which the participation of Huawei—the representative of Chinese enterprises—may be seen as the fruition of its aforesaid contribution.

5. Conclusions

The managerial aphorism that leading first-tier enterprises set industrial standards deserves academic explorations. To verify whether evidence suffices to support this widely-circulated view in the China's management field, this paper establishes a dynamic multiplex network that considers not only citation between standards but also co-authorship between drafting institutions. Taking the period from the introduction of the standards to their abolition as their life cycle, the model further observes the interaction between the standards, in order to ascertain whether augmenting investments in standards-formulating boosts enterprises competitiveness. To quantitatively evaluate the drafters' involvement in establishing the standards system, we selected relevant indexes in the network theory. More importantly, we also designed a series of evaluative measurements—including the *participation degree*, *contribution degree*, *cooperation degree*, and *co-authorship degree*-based on the characteristics of the system. In the case study (with China's communications industry as the case study), we combined the standard citation network and drafter co-authorship network in the industry, based on collecting data on the standards and the drafting institutions. Subsequently, we performed a dynamic analysis of the development of the standards system in China's communications industry, based on two dimensions: the era and the specific technical mode. The results show that the development of the standards system mirrors that of China's communications industry: in constructing the standards system, the situation in which governmental agencies acted as the main body is noted to have changed into another in which such agencies acted as the leader and the enterprises acted as the main body. Over time, it can be observed that early participation in standards-drafting enables enterprises to acquire advantages in the subsequent competition in the industry. Such a change has exerted a more catalytic effect on basic-technology providers than on service providers and terminal-equipment manufacturers. From the perspective of market segmentation, basic-technology providers enjoy a greater market share than terminal-equipment manufacturers in China's communication market. The aphorism "first-class enterprises set the standards" has indeed been verified to some extent.

In addition to their suitability for the communications industry, models and indicators established herein may be extended to other industrial standards or to other network systems with citation and drafting relationships, so as to provide an instructive angle for observation. Admittedly, findings on China's communications industry based on the models have their limitations. We have restricted the standards to those within the purview of the China Communications Standards Association and not considered references to other industries or international standards.

For future research, one question warrants more investigation: whether the participation, contribution, cooperation and co-authorship in establishing standards systems can improve enterprises competitiveness in other industries and international standards. If, for certain areas of segmentation, such improvement is not apparent, research should then focus on the presence of other factors. Likewise, the quantitative evaluation of such improvement in competitiveness is worth studying. In addition, our observation of the standards system in China's communications industry has revealed the leading role of governmental agencies. Against this background, two emergent questions are the most challenging for future research: (1) whether such governmental leadership likewise exists in other industries and even other countries; and (2) whether it exerts a favourable or adverse effect on the development of the industry and on the cultivation of enterprises competitiveness.

Appendix

A. Standard Information (Figure 9)

s_i^t	Standard No	Standard name
S1	GF 001-9001	Technical specification for domestic network No. 7 signalling
S389	YD/T 1082-2000	Technical requirements for the protection against overvoltages and overcurrents and the suitability in basic environment on access network equipment
S412	YD/T 1098-2001	Test Specification for Low-End Router
S487	YD/T 1156-2001	Test Specification for High-End Router
S573	YD/T 1214-2006	Technical requirement of 900/1800 MHz TDMA Digital Cellular Mobile Telecommunication Network
S575	YD/T 1215-2006	General Packet Radio Service (GPRS) Equipment: Mobile Stations Testing Methods of 900/1800 MHz TDMA Digital Cellular Mobile Telecommunication Network
S653	YD/T 1261-2003	General Packet Radio Service (GPRS) Equipment: Mobile Stations The technical specification of CAMEL3: CAMEL Application Part (CAP) for 900/1800 MHz TDMA digital cellular mobile telecommunication network
S659	YD/T 1268-2003	The safety specification and test method for lithium batteries and charger
S1089	YD/T 1539-2006	Technical Requirements and Testing Methods for Reliability of Mobile Telecommunication Handset
S1187	YD/T 1584.3-2007	Technical Specification for 2GHz Digital Cellular Mobile Communications Network Management General Part 3 Interface Analysis
S1208	YD/T 1591-2009	Technical requirements and test method for power adapter and charging/data port of mobile telecommunication terminal Equipment
S1285	YD/T 1644.1-2007	Human exposure to radio frequency fields from hand-held and body-mounted wireless communication devices-Human models, instrumentation, and procedures Part 1: Procedure to determine the specific absorption rate (SAR) for hand-held devices used in close proximity
S1473	YD/T 1754-2008	Classified Security Protection Requirements for Telecom Network and Internet for Physics Environment
S1475	YD/T 1756-2008	Classified Management Security Protection Requirements for Telecom Network and Internet
S1485	YD/T 1762.1-2011	TD-SCDMA/WCDMA digital cellular mobile telecommunication network technical requirements for UICC-ME (Cu)interface-part 1: physical, electrical and logical characteristics
S1915	YD/T 206.10-1997	Ironworks for overhead communication line: Nail
S1917	YD/T 206.1-1997	Ironworks for overhead communication line: General technology
S1920	YD/T 206.14-1997	Ironworks for overhead communication line: Nut
S1921	YD/T 206.15-1997	Ironworks for overhead communication line: Gasket
S1924	YD/T 206.18-1997	Ironworks for overhead communication line: Stay anchor
S1925	YD/T 206.19-1997	Ironworks for overhead communication line: Steel anchor
S1932	YD/T 206.25-1997	Ironworks for overhead communication line: Dog
S3571	YD/T 514-1998	Technical requirements and test methods for interface between nonvoice subscriber terminal and public telephone network
S3824	YD/T 728-1994	Telephone lightning protection technology requirements and test methods
S3832	YD/T 735-1994	Telephone electro magnetic compatibility limits and test methods
S3855	YD/T 760-1995	Polyolefine insulation materials for communication cable
S3955	YD/T 837.1-1996	Communication cable test method Part 1: General rules
S3960	YD/T 838.1-1996	Multicore and symmetrical pair/quad cables for digital communications Part 1: Generic specification
S4134	YD/T 965-1998	The safety requirement and test method for telecommunication terminal equipment
S4530	YDN 020-1996	Specification of V5.1 interface between local digital switcher and access network
S4531	YDN 021-1996	Specification of V5.2 interface between local digital switcher and access network
S4580	YDN 065-1997	Telephone switcher general technical specification

Figure 9

B. Drafter Information (Figure 10)

d_j^t	Drafter name	Type
D1	China Telecom	Enterprise
D3	Institute of Telecommunication Transmission of MIIT	Government agency
D4	Academy of Telecommunication Research of MIIT	Government agency
D5	Communication Measurement Center of MIIT	Government agency
D10	Institute of P&T Industry Standardization of MIIT	Government agency
D13	Datang	Enterprise
D15	Chengdu Datang Communication Cable Company	Enterprise
D16	FiberHome Technologies	Enterprise
D23	Nanjing Ericsson Panda Communications	Enterprise
D24	China Information Technology Designing Consulting Institute	Enterprise
D25	Huawei	Enterprise
D27	ZTE	Enterprise
D29	AlcatelLucent Shanghai Bell	Enterprise
D30	Shanghai Bell Samsung Mobile Communication	Enterprise
D31	Nokia Siemens	Enterprise
D32	Beijing Zhanxun High-Tech Communication Technology	Enterprise
D33	State Radio Monitoring Center	Government agency
D34	Comba Telecom Systems (China)	Enterprise
D59	UTStarcom	Enterprise
D60	China United Network Communications	Enterprise
D62	China United Communications	Enterprise
D66	China Potevio Company	Enterprise
D84	China Mobile	Enterprise
D85	Beijing University of Posts and Telecommunications	University
D87	Beijing Tianyuan Network	Enterprise
D96	Beijing Communications Administration	Government agency
D115	Beijing P&T Equipment Factory	Enterprise
D135	Data Communications Science Technique Research Institute	Enterprise
D171	Nokia Solutions and Networks (Shanghai)	Enterprise
D294	Motorola	Enterprise
D297	TD Tech	Enterprise
D298	Samsung Mobile R&D Center of China-Tianjin	Enterprise
D299	ST-Ericsson	Enterprise
D301	Chongqing Chongyou Information Technology	Enterprise
D314	Shenzhen Winhap Communications	Enterprise
D318	Zhongyouke Communication Technology	Enterprise
D328	Delta Greentech (China)	Enterprise
D334	China Mobile Group Design Institute	Enterprise
D381	Guangzhou Research Institute of China Telecom	Enterprise
D398	Vertiv	Enterprise
D465	Xingtang Communication Technology	Enterprise
D501	China P&T Appliances	Enterprise
D502	Maanshan Telecommunications Equipment	Enterprise
D582	Beijing Starpoint Information Technology	Enterprise
D652	Guangdong Nortel Telecommunication Equipment	Enterprise
D742	Comba Telecom Systems China (Guangzhou)	Enterprise
D752	Mediatek (Beijing)	Enterprise
D927	Ericsson	Enterprise
D1021	CEPREI	Government agency
D1027	Telecom Technology Instrument Research Institute	Government agency
D1031	Fourth Research Institute of Telecommunication Technology	Government agency
D1035	Luoyang Telephone Equipment Factory	Enterprise

Figure 10

Data Availability

The data used to support the findings of this study are available from the corresponding author upon request.

Conflicts of Interest

The authors declare that they have no conflicts of interest.

Acknowledgments

This work was supported by the National Natural Science Foundation of China [grant numbers 71701213, 71401181], the MOE (Ministry of Education in China) Project of Humanities and Social Sciences [grant numbers 15YJC630008, 14YJC630136], and the National Social Science Fund Project [grant number 16CTQ022].

References

[1] J.-Y. Ho and E. O'Sullivan, "Strategic standardisation of smart systems: a roadmapping process in support of innovation," *Technological Forecasting and Social Change*, vol. 115, pp. 301–312, 2017.

[2] H. Jiang, S. Zhao, Y. Yuan, L. Zhang, L. Duan, and W. Zhang, "The coupling relationship between standard development and technology advancement: a game theoretical perspective," *Technological Forecasting and Social Change*, vol. 135, pp. 169–177, 2018.

[3] W. S. Lee and S. Y. Sohn, "Effects of standardization on the evolution of information and communications technology," *Technological Forecasting and Social Change*, vol. 132, pp. 308–317, 2018.

[4] H. Zoo, H. J. de Vries, and H. Lee, "Interplay of innovation and standardization: exploring the relevance in developing countries," *Technological Forecasting and Social Change*, vol. 118, pp. 334–348, 2017.

[5] L. Leydesdorff, C. S. Wagner, and L. Bornmann, "Betweenness and diversity in journal citation networks as measures of interdisciplinaritya tribute to Eugene garfield," *Scientometrics*, vol. 114, no. 2, pp. 567–592, 2018.

[6] Y. Li, H. Li, N. Liu, and X. Liu, "Important institutions of interinstitutional scientific collaboration networks in materials science," *Scientometrics*, vol. 117, no. 1, pp. 85–103, 2018.

[7] H. Choe, D. H. Lee, H. D. Kim, and I. W. Seo, "Structural properties and inter-organizational knowledge flows of patent citation network: the case of organic solar cells," *Renewable & Sustainable Energy Reviews*, vol. 55, pp. 361–370, 2016.

[8] K. Blind, J. Edler, R. Frietsch, and U. Schmoch, "Motives to patent: empirical evidence from Germany," *Research Policy*, vol. 35, no. 5, pp. 655–672, 2006.

[9] K. Blind, K. Cremers, and E. Mueller, "The influence of strategic patenting on companies' patent portfolios," *Research Policy*, vol. 38, no. 2, pp. 428–436, 2009.

[10] L. Bornmann and H.-D. Daniel, "What do citation counts measure? a review of studies on citing behavior," *Journal of Documentation*, vol. 64, no. 1, pp. 45–80, 2008.

[11] D. O. Cases and G. M. Higgins, "How can we investigate citation behavior? a study of reasons for citing literature in communication," *Journal of the Association for Information Science and Technology*, vol. 51, no. 7, pp. 635–645, 2000.

[12] J. Alcácer, M. Gittelman, and B. Sampat, "Applicant and examiner citations in U.S. patents: an overview and analysis," *Research Policy*, vol. 38, no. 2, pp. 415–427, 2009.

[13] M. E. Newman, "Scientific collaboration networks. i. network construction and fundamental results," *Physical Review E*, vol. 64, no. 1, Article ID 016131, 2001.

[14] S. N. Dorogovtsev and J. F. F. Mendes, "Evolution of networks," *Advances in Physics*, vol. 51, no. 4, pp. 1079–1187, 2002.

[15] A. Barabási, H. Jeong, Z. Néda, E. Ravasz, A. Schubert, and T. Vicsek, "Evolution of the social network of scientific collaborations," *Physica A: Statistical Mechanics and its Applications*, vol. 311, no. 3–4, pp. 590–614, 2002.

[16] E. Garfield, "Citation indexes for science: a new dimension in documentation through association of ideas," *Science*, vol. 122, no. 3159, pp. 108–111, 1955.

[17] P. Doreian, "A measure of standing of journals in stratified networks," *Scientometrics*, vol. 8, no. 5–6, pp. 341–363, 1985.

[18] J. P. A. Ioannidis, K. W. Boyack, H. Small, A. Sorensen, and R. Klavans, "Bibliometrics: is your most cited work your best?," *Nature*, vol. 514, no. 7524, pp. 561–562, 2014.

[19] R. Van Noorden, B. Maher, and R. Nuzzo, "The top 100 papers," *Nature*, vol. 514, no. 7524, pp. 550–553, 2014.

[20] P. Chen, H. Xie, S. Maslov, and S. Redner, "Finding scientific gems with google's pagerank algorithm," *Journal of Informetrics*, vol. 1, no. 1, pp. 8–15, 2007.

[21] K. S. Fursov and A. R. Kadyrova, "How the analysis of transitionary references in knowledge networks and their centrality characteristics helps in understanding the genesis of growing technology areas," *Scientometrics*, vol. 111, no. 3, pp. 1947–1963, 2017.

[22] J. Kim and J. Shin, "Mapping extended technological trajectories: integration of main path, derivative paths, and technology junctures," *Scientometrics*, vol. 116, no. 3, pp. 1439–1459, 2018.

[23] X. Sun and K. Ding, "Identifying and tracking scientific and technological knowledge memes from citation networks of publications and patents," *Scientometrics*, vol. 116, no. 3, pp. 1735–1748, 2018.

[24] J. Wang and L. Zhang, "Proximal advantage in knowledge diffusion: the time dimension," *Journal of Informetrics*, vol. 12, no. 3, pp. 858–867, 2018.

[25] F. Han and C. L. Magee, "Testing the science/technology relationship by analysis of patent citations of scientific papers after decomposition of both science and technology," *Scientometrics*, vol. 116, no. 2, pp. 767–796, 2018.

[26] F. Narin, "Patent bibliometrics," *Scientometrics*, vol. 30, no. 1, pp. 147–155, 1994.

[27] A. G. Hu and A. B. Jaffe, "Patent citations and international knowledge flow: the cases of Korea and Taiwan," *International Journal of Industrial Organization*, vol. 21, no. 6, pp. 849–880, 2003.

[28] B. H. Hall, A. B. Jaffe, and M. Trajtenberg, "Market value and patent citations," *The RAND Journal of Economics*, vol. 36, no. 1, pp. 16–38, 2005.

[29] M. J. Holgersson and O. Granstrand, "Patenting motives, technology strategies, and open innovation," *Management Decision*, vol. 55, no. 6, pp. 1265–1284, 2017.

[30] J. Moody, "The structure of a social science collaboration network: disciplinary cohesion from 1963 to 1999," *American Sociological Review*, vol. 69, no. 2, pp. 213–238, 2004.

[31] D. J. D. S. Price, "Is technology historically independent of science? A study in statistical historiography," *Technology and Culture*, vol. 6, no. 4, p. 553, 1965.

[32] T. W. Pike, "Collaboration networks and scientific impact among behavioral ecologists," *Behavioral Ecology*, vol. 21, no. 2, pp. 431–435, 2010.

[33] H. Kretschmer, "Author productivity and geodesic distance in bibliographic co-authorship networks, and visibility on the web," *Scientometrics*, vol. 60, no. 3, pp. 409–420, 2004.

[34] S. Choi, J. S. Yang, and H. W. Park, "The triple helix and international collaboration in science," *Journal of the Association for Information Science and Technology*, vol. 66, no. 1, pp. 201–212, 2015.

[35] H. Hou, H. Kretschmer, and Z. Liu, "The structure of scientific collaboration networks in scientometrics," *Scientometrics*, vol. 75, no. 2, pp. 189–202, 2008.

[36] F. Landini, F. Malerba, and R. Mavilia, "The structure and dynamics of networks of scientific collaborations in northern africa," *Scientometrics*, vol. 105, no. 3, pp. 1787–1807, 2015.

[37] J. Li and Y. Li, "Patterns and evolution of coauthorship in Chinas humanities and social sciences," *Scientometrics*, vol. 102, no. 3, pp. 1997–2010, 2015.

[38] H. D. White, B. Wellman, and N. Nazer, "Does citation reflect social structure? Longitudinal evidence from the globenet interdisciplinary research group," *Journal of the Association for Information Science and Technology*, vol. 55, no. 2, pp. 111–126, 2004.

[39] P. Liu and X. Haoxiang, "Structure and evolution of co-authorship network in an interdisciplinary research field," *Scientometrics*, vol. 103, no. 1, pp. 101–134, 2015.

[40] J. Fagan, K. S. Eddens, J. Dolly, N. L. Vanderford, H. L. Weiss, and J. S. Levens, "Assessing research collaboration through co-authorship network analysis," *The Journal of Research Administration*, vol. 49, no. 1, pp. 76–99, 2018.

[41] C. S. Wagner, J. D. Roessner, K. Bobb et al., "Approaches to understanding and measuring interdisciplinary scientific research (IDR): a review of the literature," *Journal of Informetrics*, vol. 5, no. 1, pp. 14–26, 2011.

[42] D. J. Teece, "Profiting from technological innovation: implications for integration, collaboration, licensing and public policy," *Research Policy*, vol. 15, no. 6, pp. 285–305, 1986.

[43] V. Barba-Sánchez, M. José Calderón-Miláan, and C. Atienza-Sahuquillo, "A study of the value of ICT in improving corporate performance: a corporate competitiveness view," *Technological and Economic Development of Economy*, vol. 24, no. 4, pp. 1388–1407, 2018.

[44] G. Dosi, M. Grazzi, and D. Moschella, "Technology and costs in international competitiveness: from countries and sectors to firms," *Research Policy*, vol. 44, no. 10, pp. 1795–1814, 2015.

[45] P. Lii and F.-I. Kuo, "Innovation-oriented supply chain integration for combined competitiveness and firm performance," *International Journal of Production Economics*, vol. 174, pp. 142–155, 2016.

[46] V. Kveton and P. Horak, "The effect of public R&D subsidies on firms' competitiveness: regional and sectoral specifics in emerging innovation systems," *Applied Geography*, vol. 94, pp. 119–129, 2018.

[47] R. Giuliano, S. Kampelmann, B. Mahy, and F. Rycx, "Short notice, big difference? The effect of temporary employment on firm competitiveness across sectors," *British Journal of Industrial Relations*, vol. 55, no. 2, pp. 421–449, 2017.

[48] C. Rammer, S. Gottschalk, M. Peneder, M. Worter, T. Stucki, and S. Arvanitis, "Does energy policy hurt international competitiveness of firms? A comparative study for Germany, Switzerland and Austria," *Energy Policy*, vol. 109, pp. 154–180, 2017.

[49] Y. Park, P. Hong, and S. Li, "Free trade agreements and maritime supply chain costs: competitiveness of Korean firms," *Maritime Economics & Logistics*, vol. 18, no. 1, pp. 3–18, 2016.

[50] A. Bodnaruk, W. O'Brien, and A. Simonov, "Captive finance and firm's competitiveness," *Journal of Corporate Finance*, vol. 37, pp. 210–228, 2016.

[51] S. Yang, Y. Li, and X. Wang, "Cohesiveness or competitiveness: venture capital syndication networks and firms' performance in China," *Journal of Business Research*, vol. 91, pp. 295–303, 2018.

[52] J. L. Solleiro and R. Castañón, "Competitiveness and innovation systems: the challenges for Mexico's insertion in the global context," *Technovation*, vol. 25, no. 9, pp. 1059–1070, 2005.

[53] S.-P. Chuang and S.-J. Huang, "The effect of environmental corporate social responsibility on environmental performance and business competitiveness: the mediation of green information technology capital," *Journal of Business Ethics*, vol. 150, no. 4, pp. 991–1009, 2018.

[54] V. Costantini and M. Mazzanti, "On the green and innovative side of trade competitiveness? The impact of environmental policies and innovation on EU exports," *Research Policy*, vol. 41, no. 1, pp. 132–153, 2012.

[55] L. M. Ferri and M. Pedrini, "Socially and environmentally responsible purchasing: comparing the impacts on buying firm's financial performance, competitiveness and risk," *Journal of Cleaner Production*, vol. 174, pp. 880–888, 2018.

[56] M. D. Lopez-Gamero and J. F. Molina-Azorin, "Environmental management and firm competitiveness: the joint analysis of external and internal elements," *Long Range Planning*, vol. 49, no. 6, pp. 746–763, 2016.

[57] J. L. C. Cheng and D. Yiu, "China business at a crossroads: institutions, international competitiveness, and innovation," *Long Range Planning*, vol. 49, no. 5, pp. 584–588, 2016.

[58] J. M. Goncalves, F. Ferreira, J. J. Ferreira, and L. Farinha, "A multiple criteria group decision-making approach for the assessment of small and medium-sized enterprise competitiveness," *Management Decision*, vol. 57, no. 2, pp. 480–500, 2019.

[59] D. J. Teece, "Reflections on 'profiting from innovation'," *Research Policy*, vol. 35, no. 8, pp. 1131–1146, 2006.

[60] J. Dedrick, K. L. Kraemer, and G. Linden, "Who profits from innovation in global value chains?: a study of the iPod and notebook PCs," *Industrial and Corporate Change*, vol. 19, no. 1, pp. 81–116, 2010.

[61] G. P. Pisano and D. J. Teece, "How to capture value from innovation: shaping intellectual property and industry architecture," *California Management Review*, vol. 50, no. 1, pp. 278–296, 2007.

[62] G. Pisano, "Profiting from innovation and the intellectual property revolution," *Research Policy*, vol. 35, no. 8, pp. 1122–1130, 2006.

[63] E. Enkel, "Attributes required for profiting from open innovation in networks," *International Journal of Technology Management*, vol. 52, no. 3–4, pp. 344–371, 2010.

Hindawi
Complexity
Volume 2019, Article ID 6409630, 15 pages
https://doi.org/10.1155/2019/6409630

Research Article

Vehicle Attribute Recognition for Normal Targets and Small Targets Based on Multitask Cascaded Network

Fang Liu,[1] **Yong Zhang**,[2] **Hua Gong**,[1] **Ke Xu**,[1] **and Ligang Cai**[3]

[1]*College of Science, Shenyang Ligong University, Shenyang 110159, China*
[2]*Technology on Electro-Optical Information Security Control Laboratory, Tianjing 300308, China*
[3]*College of Science, Shenyang University of Technology, Shenyang 110178, China*

Correspondence should be addressed to Hua Gong; gonghua@sylu.edu.cn

Fang Liu, Yong Zhang, and Hua Gong contributed equally to this work.

Received 20 June 2019; Revised 14 October 2019; Accepted 7 November 2019; Published 6 December 2019

Guest Editor: Teddy Craciunescu

The interference of the complex background and less information of the small targets are two major problems in vehicle attribute recognition. In this paper, two cascaded networks of vehicle attribute recognition are established to solve the two problems. For vehicle targets with normal size, the multitask cascaded convolution neural network MC-CNN-NT uses the improved Faster R-CNN as the location subnetwork. The vehicle targets in the complex background are extracted by the location subnetwork to the classification subnetwork CNN for the classification. The implementation of this task decomposition strategy effectively eliminates the interference of the complex background in target detection. For vehicle targets with small size, the multitask cascaded convolution neural network MC-CNN-ST applies the network compression strategy and the multilayer feature fusion strategy to extract the feature maps. These strategies enrich the location information and semantic information of the feature maps. In order to optimize the nonlinear mapping ability and the hard-to-detect samples mining ability of the networks, the activation function and the loss function in the two cascaded networks are improved. The experimental results show that MC-CNN-NT for the normal targets and MC-CNN-ST for the small targets achieve the state-of-the-art performance compared with other attribute recognition networks.

1. Introduction

Vehicle attribute recognition can provide the support for the statistics of the road traffic flow [1], the automatic driving of the vehicles [2, 3], and the detection and the tracking of the illegal vehicles [4]. Location and recognition for the vehicles with different sizes in complex natural scenes are important issues in the intelligent transportation researches.

The traditional methods of vehicle recognition are mainly to build 3D models of the vehicles and extract the features of the vehicles manually. In the aspect of vehicle attribute recognition based on 3D models, the Bayesian algorithm is applied to generate a 3D vehicle model for matching the features and realizing the vehicle classification [5]. A 3D curve alignment method [6] is established to identify the types of the vehicles from a single image. The image gradient is used to calculate the attitude scores of the targets, and the real-time vehicle location is realized [7]. In the aspect of vehicle attribute recognition based on the feature extraction manually, the directional gradient histogram (HOG) [8] is fused with the rectangular filter. The features are extracted manually to recognize the vehicle targets. Scale-Invariant Feature Transform (SIFT) is proposed to describe the edge features and classify the vehicles [9]. The edge-oriented histogram is obtained to extract the vehicle features [10]. These features are input into the support vector machine (SVM) classifier to classify the vehicles. The traditional vehicle recognition methods essentially use the human-made features to represent the images. Since the hand-made features are sensitive to illumination, shooting angle, and target background, the generalization ability of the algorithms is weak. Moreover, the extraction speed of the manual features is slow, which does

not meet the needs for the recognition of massive data of intelligent transportation.

In recent years, since the deep convolution networks have excellent performance in dealing with the big data samples and nonlinear mapping, they are widely used in the field of target recognition. At present, there are mainly two kinds of target recognition methods based on the deep convolution networks. The first method is the region proposal method, such as R-CNN [11], Fast-CNN [12], Faster R-CNN [13], and SPP Net [14]. The other method is the region-free method, such as YOLO [15] and SSD [16]. These two deep network recognition methods are also applied in vehicle recognition. The multitask R-CNN method is established to recognize four types of vehicles (car, truck, bus, and van) [17]. The improved Faster R-CNN [18] is constructed to detect the vehicles in aerial images. The use of the hyper region proposal network (HRPN) and the multiple boosted classifiers reduces false detection. SSD with the feature fusion method [19] is proposed to recognize the six categories of vehicles (cyclist, motocycle, bus, minibus, car, and truck) and persons. In [19], an image segmentation strategy is employed to improve the recognition effect for the small targets. Vehicle attribute recognition methods based on the deep convolution networks are driven by data to extract the features; this strategy eliminates the sensibility of the hand-made features, and the methods are universal and accurate. However, the abovementioned vehicle recognition methods based on the deep convolution networks all adopt one-stage networks to complete vehicle location and recognition at the same time. The strategy of doing multiple tasks in the same network has two main shortcomings. First, it is easy to produce false acceptance and false rejection in the complex background (illumination change, local occlusion, target scale change) [20]. Second, the target images undergo several convolutions and pooling, which results in the disappearance or the transformation of the location of the feature points for the small targets. The recognition accuracy for the small targets is reduced.

In view of two shortcomings of one-stage deep convolution neural networks, the multitask cascaded neural networks and the multiscale feature fusion networks are established. In the aspect of the multitask cascaded neural networks, the two-stage multitask cascaded CNN [3] is applied to recognize the vehicles. The multitask cascaded network based on IFR-CNN and CNN [21] is obtained to recognize different types of vehicles. The two-stage cascaded YOLO [22] is established to carry out the vehicle location and license plate recognition. The multitask convolution neural networks are devised to segment the targets from the complex background firstly and then recognize the targets. These methods divide the background and the targets and eliminate the interference of the complex background for the target recognition. The accuracy of target attribute recognition is higher than that of one stage deep convolution networks. In the aspect of the multiscale feature fusion, the feature pyramid network (FPN) [23] as a feature extractor achieves the most advanced single-model recognition results on COCO datasets. The FPN network uses multiscale fusion features to describe the target information, which solves the problem of the feature disappearance for the small targets. The feature fusion networks are widely used in the fields of human body detection [24], situation assessment [25], and face recognition [26]. However, the multiscale feature fusion models for the small targets are few in the vehicle attributes recognition.

We devote this paper to the study of vehicle attribute recognition models. Our contributions are mainly as follows. (1) Two cascaded models MC-CNN-NT and MC-CNN-ST are proposed. MC-CNN-NT is applied to recognition vehicle targets with normal size. MC-CNN-ST is used to recognition vehicle targets with small size. (2) The activation function and the loss function in the two cascaded networks are improved. The performance of feature extraction and classification of two networks is enhanced. (3) The strategies of network compression and feature fusion in MC-CNN-ST are employed. The object edge information extracted by the bottom filter and semantics information extracted by the high-level filter are fused to realize the precise location of the vehicles. (4) The SYIT-Vehicle dataset and the COCO-Vehicle dataset are constructed and annotated. The target quantity and quality in the two dataset provide the guarantee for verifying network performance.

The rest of this paper is outlined as follows. Section 2 and Section 3 describe the architectures of MC-CNN-NT and MC-CNN-ST in detail, respectively. Section 4 reports the experimental results of the two multitask cascaded networks. Section 5 denotes the conclusions.

2. Architecture: The Multitask Cascaded Network MC-CNN-NT

This section demonstrates the architecture of the multitask cascaded network MC-CNN-NT for recognizing vehicle targets with normal size. Section 2.1 demonstrates the framework of MC-CNN-NT. Section 2.2 introduces the improvement of the activation function and the loss function in MC-CNN-NT. Section 2.3 shows the basic processes of attribute recognition using MC-CNN-NT in detail.

2.1. The Framework of MC-CNN-NT. Aiming at the low accuracy of the vehicle target recognition in the complex background with one stage network, a multitask cascaded network MC-CNN-NT is constructed. The problem of vehicle attribute recognition is decomposed into two subproblems: target location and target classification. The improved Faster R-CNN is employed as the location subnetwork of MC-CNN-NT. This subnetwork consists of three parts: the network of the feature extraction, the network of the region proposal (RPN), and the network of the object location. CNN is used as the classification subnetwork in the cascaded networks. The framework of MC-CNN-NT is shown in Figure 1.

The feature extraction network in the MC-CNN-NT location subnetwork applies VGG-D as the backbone network to extract the image features. 13 convolution layers and the first four subsampling layers in the VGG-D model are selected. The fifth subsampling layers and three full-connection layers

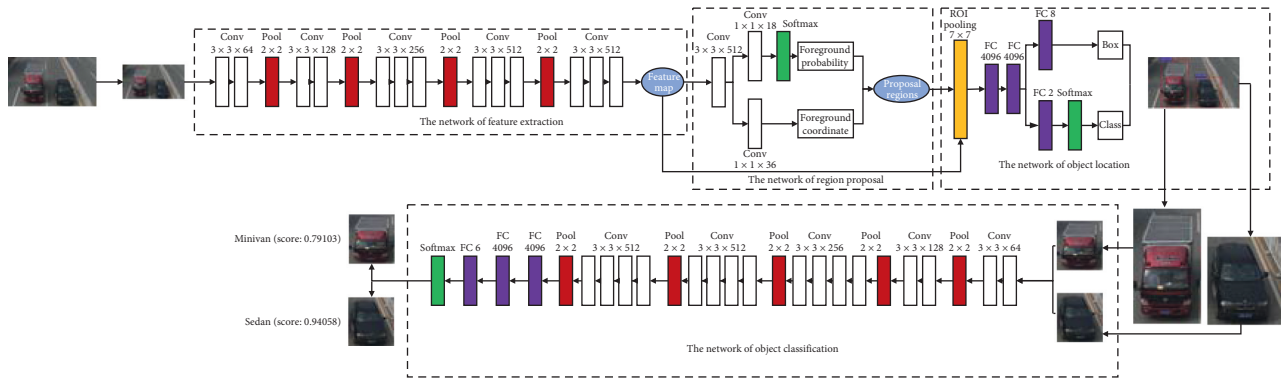

Figure 1: The framework of MC-CNN-NT.

in the VGG-D model are discarded. The parameters of the feature extraction network are detailed in Table 1. In RPN, the sizes of anchors are set to $\{128 \times 128, 256 \times 256, 512 \times 512\}$. The length-width ratios of anchors are set to $\{1:2, 1:1, 2:1\}$. The number of anchors is $3 \times 3 = 9$. A 3×3 sliding box is used to traverse the top-level feature map of the feature extraction network. Each pixel on the feature map corresponds to 9 anchors of different sizes in the original maps. In RPN, the classification layer and the regression layer output the scores of 9 anchors corresponding to each pixel and their respective location coordinates. Let the top feature map size of the shared convolution be $w \times h$. The classification layer outputs the scores of $w \times h \times 9 \times 2$ candidate regions. The regression layer outputs $w \times h \times 9 \times 4$ coordinate parameters. As Fast R-CNN, ROI pooling is carried out for the proposal regions of RPN network. The coordinate parameters of the targets are output through the multiple full-connection layers.

The classification subnetwork of MC-CNN-NT is based on CNN. VGG-E is selected as the backbone network of the classification subnetwork. According to the coordinate values output by the location subnetwork, the target regions are cut out from the original images. The extracted image size is normalized to $227 \times 227 \times 3$. The normalized single target images are input into the classification subnetwork for vehicle type recognition. The parameters of the classification subnetwork are detailed in Table 2.

2.2. Activation Function and Loss Function. In order to enhance the recognition performance of the cascaded network MC-CNN-NT, the activation function and the loss function are improved in Faster R-CNN and CNN.

2.2.1. Activation Function: PReLU. The activation function is an important part of the deep network. The form of the activation function plays a key role in the quality of the feature extraction. The activation function can be divided into two categories: the saturated activation function and the unsaturated activation function. Since the unsaturated activation function has the advantages of solving "gradient disappearance" and fast convergence speed, it attracts more attentions from researchers of deep learning [27, 28].

Table 1: Parameters of the feature extraction network of MC-CNN-NT.

Layer	Type	Number	Size	Stride	Padding
1	Conv	64	3×3	1	2
2	Conv	64	3×3	1	2
3	Pool	64	2×2	2	0
4	Conv	128	3×3	1	2
5	Conv	128	3×3	1	2
6	Pool	128	2×2	1	2
7	Conv	256	3×3	2	0
8	Conv	256	3×3	1	2
8	Conv	256	3×3	1	2
10	Pool	256	2×2	2	0
11	Conv	512	3×3	1	2
12	Conv	512	3×3	1	2
13	Conv	512	3×3	1	2
14	Pool	512	2×2	2	0
15	Conv	512	3×3	1	2
16	Conv	512	3×3	1	2
17	Conv	512	3×3	1	2

In this paper, ReLU [29] is updated to PReLU [27]. PReLU function formula is described as follows:

$$g(x_i) = \max(0, x_i) + k_i \min(0, x_i). \tag{1}$$

ReLU function formula is shown as follows:

$$g(x) = \max(0, x), \tag{2}$$

where x is the input signal of the activation function, k is a coefficient controlling the slope of the negative part in the PReLU function, and the subscript i denotes the channel i. The improved activation function PReLU adds a linear term to the negative signals. This strategy alleviates the problem of gradient disappearance when the network propagates back to the negative signals. When the activation function has better nonlinear mapping ability for different negative signals, the learning strategy is adopted for the slope k_i in model training.

In this paper, k_i is trained by using backpropagation and updated using the momentum method. According to the chain rule, the gradient derivative formula of k_i is formed as follows:

Table 2: Parameters of the classification subnetwork of MC-CNN-NT.

Layer	Type	Number	Size	Stride	Padding
1	Conv	64	3×3	1	2
2	Conv	64	3×3	1	2
3	Pool	64	2×2	2	0
4	Conv	128	3×3	1	2
5	Conv	128	3×3	1	2
6	Pool	128	2×2	2	0
7	Conv	256	3×3	1	2
8	Conv	256	3×3	1	2
8	Conv	256	3×3	1	2
10	Conv	256	3×3	1	2
11	Pool	256	2×2	2	0
12	Conv	512	3×3	1	2
13	Conv	512	3×3	1	2
14	Conv	512	3×3	1	2
15	Conv	512	3×3	1	2
16	Pool	512	2×2	2	0
17	Conv	512	3×3	1	2
18	Conv	512	3×3	1	2
19	Conv	512	3×3	1	2
20	Conv	512	3×3	1	2
21	Pool	512	2×2	2	0
22	FC	4096	1×1	—	—
23	FC	4096	1×1	—	—
24	FC	6	1×1	—	—
25	Softmax	—	—	—	—

$$\frac{\partial\sigma}{\partial k_i}=\sum_{x_i}\frac{\partial\sigma}{\partial g(x_i)}\frac{\partial g(x_i)}{\partial k_i}, \tag{3}$$

where σ is the objective function of the model and $\partial\sigma/\partial g(x_i)$ is the gradient function transferred by the deeper convolution neural network. The gradient derivative of the activation function $g(x_i)$ is demonstrated as follows:

$$\frac{\partial g(x_i)}{\partial k_i}=\begin{cases}0, & \text{if } x_i\geq 0,\\ x_i, & \text{if } x_i<0.\end{cases} \tag{4}$$

The reverse update formula of k_i is adopted as follows:

$$\Delta k_i:=\delta\Delta k_i+\eta\frac{\partial\sigma}{\partial k_i}, \tag{5}$$

where δ represents the momentum and η represents the learning rate of the network.

As shown equation (4), the gradient derivative of PReLU activation function only adds a very small number of parameters. The computational complexity of the network and the risk of overfitting can be neglected. The adaptability of rectifier parameter k_i improves the training accuracy of the cascaded network. The inherent unsaturation of PReLU function makes it perform better in controlling gradient and convergence rate.

2.2.2. Loss Function. The location subnetwork of MC-CNN-NT is the improved Faster R-CNN; it needs to train RPN and Fast R-CNN. The classification subnetwork of MC-CNN-NT needs to train CNN. For three different networks, three loss functions $L_{\mathrm{RPN}}(\{p_i\},\{t_i\})$, $L_{\mathrm{Fast}\,R\mathrm{-CNN}}(\{p_i\},\{t_i\})$, and $L_{\mathrm{CNN}}(\{p_i\})$ are described as follows:

$$L_{\mathrm{RPN}}(\{p_i\},\{t_i\})=\frac{1}{N_{\mathrm{cls}}}\sum_i \mathrm{FL}_{\mathrm{cls}}(p_i)+\omega\frac{1}{N_{\mathrm{reg}}}\sum_i \delta_i L_{\mathrm{reg}}(t_i,t_i^*), \tag{6}$$

$$L_{\mathrm{Fast}\,R\mathrm{-CNN}}(\{p_i\},\{t_i\})=\sum_i \mathrm{FL}_{\mathrm{cls}}(p_i)+\sum_i L_{\mathrm{reg}}(t_i,t_i^*), \tag{7}$$

$$L_{\mathrm{CNN}}(\{p_i\})=\sum_i \mathrm{FL}_{\mathrm{cls}}(p_i). \tag{8}$$

RPN and Fast R-CNN are two multitask networks. Their loss functions are composed of classification loss and regression loss. CNN only completes the classification task, and the loss function is only related to the classification loss. Here, $\mathrm{FL}_{\mathrm{cls}}(p_i)$ represents classification loss, and $L_{\mathrm{reg}}(t_i,t_i^*)$ represents regression loss.

In the R-CNN series network framework, the commonly used loss function of classification is the cross-entropy loss function. The cross-entropy loss function uses the logarithmic loss $\log(p_i)$ to characterize the difference between the real sample and the prediction box. Although the cross-entropy loss function has a low loss value for a single easy-to-detect sample, it still contributes a lot to the overall loss of the network due to the large number of the easy-to-detect samples. However, due to the small number of the hard-to-detect samples, the contribution of the hard-to-detect samples to the loss function is small. As a result, the training of the network is towards the easy-to-detect samples, which affects the quality of the network recognition. In this paper, we update the cross-entropy classification loss function to the Focal loss function. The strategy of assigning different weights to different samples is adopted to increase the contribution of the hard-to-detect samples in the loss function.

The Focal Loss function is defined as follows:

$$\mathrm{FL}_{\mathrm{cls}}(p_i)=-(1-p_i)^{\gamma}\log(p_i), \tag{9}$$

$$p_i=\frac{e^{z_i}}{\sum_{q=1}^{k}e^{z_q}}, \tag{10}$$

where z_i is the network output of the category i, and p_i $(0\leq p_i\leq 1)$ is the output probability of the category i. The Focal Loss function adds a modulating factor $(1-p_i)^{\gamma}$ to the standard cross-entropy loss function. As shown in Figure 2, $-\log^{p_i}$ and $(1-p_i)^{\gamma}$ are small for the easy-to-detect samples (p_i is large). They lead that $\mathrm{FL}_{\mathrm{cls}}(p_i)$ is small. The weights are slightly adjusted when the deep network backpropagation occurs. $-\log^{p_i}$ and $(1-p_i)^{\gamma}$ are large for the hard-to-detect samples (p_i is small). They lead that $\mathrm{FL}_{\mathrm{cls}}(p_i)$ is large. The weights are dramatically adjusted when the deep network backpropagation occurs. The learning of the hard-to-detect samples is strengthened. In equation (9), γ is a parameter for adjusting the weight rate, which is called focusing parameter. When $\gamma=0$, the Focal Loss function is equal to the cross-entropy loss function. The influence of the modulation factor is increased with the increase of the value γ.

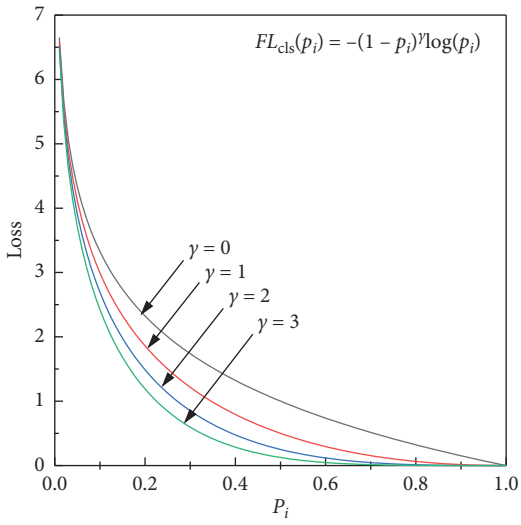

Figure 2: The curve of Focal Loss function.

The Smooth L_1 function is used as the regression loss in $L_{\mathrm{RPN}}(\{p_i\},\{t_i\})$ and $L_{\mathrm{Fast}\,R-\mathrm{CNN}}(\{p_i\},\{t_i\})$ functions [30]. The definition of the $L_{\mathrm{reg}}(t_i,t_i^*)$ function is denoted in the following equation:

$$L_{\mathrm{reg}}(t_i,t_i^*) = \mathrm{Smooth}_{L_1}(t_i,t_i^*) = \begin{cases} 0.5(t_i-t_i^*)^2, & |t_i-t_i^*| \prec 1, \\ |t_i-t_i^*| - 0.5, & \text{otherwise}, \end{cases} \tag{11}$$

where $t_i = (t_{ix}, t_{iy}, t_{iw}, t_{ih})$ represents the translation scaling values of the four prediction boxes. $t_i^* = (t_{ix}^*, t_{iy}^*, t_{iw}^*, t_{ih}^*)$ is the four coordinates of the ground-true box. δ_i is a label function in equations (6) and (7). If the label of the prediction box is a positive sample, $\delta_i = 1$. Otherwise, $\delta_i = 0$. According to the definitions of the regression loss of RPN and Fast R-CNN, it can be seen that the regression losses of two networks are calculated only for the positive samples. Here, the definitions of the positive samples and the negative samples in PRN and Fast R-CNN adopt the definitions of reference [13] and reference [12], respectively.

In equation (6), the classification loss is normalized by the mini-batch size N_{cls}. The regression loss is normalized by the number of anchors N_{reg}. Set $N_{\mathrm{cls}} = 256$, $\omega = 10$, $N_{\mathrm{reg}} = 2400$. By using the normalization strategy, the weight of the classification loss is approximately equal to the weight of the regression loss in RPN. In equation (7), the weight of the classification loss and the regression loss in Fast R-CNN is set to 1, and the contribution of two kinds of losses to the total loss is equal.

2.3. The Basic Procedures of the Multitask Cascaded Network MC-CNN-NT. The specific steps using MC-CNN-NT to recognize the vehicles are as follows:

Step 1 (partitioning the dataset): firstly, according to the ratio of 9 : 1, the dataset is divided into two parts: the training verification set and the testing set. Then, according to the ratio of 9 : 1, the training verification set is divided into two parts: the training set and the verification set. According to such partitioning rules, the original dataset is divided into three parts: the training set, the verification set, and the testing set.

Step 2 (annotating the dataset): the positions of the vehicle targets in the images are labeled. The coordinates of the upper left corner and the lower right corner of the vehicle targets in the images are recorded. The generated annotation information is saved in the corresponding XML file.

Step 3 (preprocessing the image data): the images are scaled. The color formats of the images are converted. Let the zoom ratio be S, the input image size be $W \times H$, and the zoomed image size be $W' \times H'$. Here, $S = W/W' = H/H'$. When the images are scaled, the long side is less than 1000, and the short side is less than 600 (at least one is equal). The target regions in the images are also scaled at the same scale. Since the Caffe frame recognizes the BGR color format, the RGB (Red-Green-Blue) color format of the images is converted to the BGR (Blue-Green-Red) color format.

Step 4 (setting the hyperparameters of the cascaded network): let the maximum number of the iterations in the location subnetwork and the classification subnetwork of MC-CNN-NT be $N_{\mathrm{max}}^{\mathrm{loc}}$ and $N_{\mathrm{max}}^{\mathrm{clc}}$, respectively. Let the initial learning rate in the location subnetwork and the classification subnetwork of MC-CNN-NT be η_{loc} and η_{clc}, respectively.

Step 5 (initializing the weights and the thresholds of the cascaded network): for the location subnetwork of MC-CNN-NT, the VGG-D model parameters are applied to initialize the parameters of the convolution layer shared by RPN and Fast R-CNN. The parameters of the unique layers of RPN and Fast R-CNN are initialized by Gaussian distribution with the mean of 0 and the standard deviation of 0.01. The thresholds of each layer are initialized by the constant 0.

For the classification subnetwork of MC-CNN-NT, the VGG-A model parameters are used to initialize the parameters of the first four convolution layers and the last three full connection layers of VGG-E. The parameters of the other layers are initialized by Gaussian distribution with the mean of 0 and the standard deviation of 0.01. The thresholds of each layer are initialized by the constant 0.

Step 6 (training the location subnetwork): train the location subnetwork using the images coming from the training set. The weights and the thresholds of the location subnetwork are adjusted by cyclic iterations. When the number of the iterations of the location subnetwork is greater than $N_{\mathrm{max}}^{\mathrm{loc}}$, execute step 7.

Step 7 (testing the location subnetwork): test the location subnetwork using the images coming from the testing set. The target prediction boxes on the testing images are output. The position coordinates of the prediction boxes are obtained.

Step 8 (extracting the targets from the location subnetwork): according to the coordinates of the target prediction boxes in the location subnetwork, the target regions are extracted from the original images as the input images of the classification subnetwork.

Step 9 (preprocessing the classification subnetwork images): the size of the images that are input into the classification subnetwork is adjusted to $227 \times 227 \times 3$.

Step 10 (training the classification subnetwork): the weights and the thresholds of the classification network are adjusted by cyclic iterations. When the number of the iterations is greater than the number of the iterations $N_{\max}^{\text{clc}}$, execute step 11.

Step 11 (testing the classification subnetwork): the classification subnetwork is tested with the images coming from the testing set. The confidence scores of each testing image belonging to different categories are obtained. The category with the highest confidence score is the recognized category of the target.

3. Architecture: The Multitask Cascaded Network MC-CNN-ST

The regions of the small target images contain few pixels. If the deep convolution neural network is used to extract information from the deep feature maps, the edge and the detailed information of the images is lost. The recognition accuracy of the small targets is reduced. In this section, in order to solve this problem, the cascaded strategy of the multitask network is employed and a cascaded network MC-CNN-ST is established. This new network is more practical for the attribute recognition of the small targets. Section 3.1 introduces the structure of the location subnetwork in MC-CNN-ST. Section 3.2 demonstrates the structure of the classification subnetwork in MC-CNN-ST. The data augmentation section is described in Section 3.3.

3.1. The Location Subnetwork of MC-CNN-ST. In Figure 3, the convolution layer i is represented as Conv i, the subsampling layer i is represented as Dpool i, and the upsampling layer is represented as Upool i. FC represents the full connection layer. RS is the abbreviation of reshape, and it is a data reorganization layer. Softmax is a classifier.

In the location subnetwork of MC-CNN-ST, the network compression strategy and the feature fusion strategy are proposed to improve the feature extraction quality. The location sub network of MC-CNN-ST inherits RPN and the object location network in the location sub network of MC-CNN-NT. The improved activation function and the loss function in MC-CNN-NT are also applied to MC-CNN-ST. Figure 3 shows the framework of MC-CNN-ST.

In the network of the feature extraction of MC-CNN-ST, the last seven convolution layers of VGG-D in the location sub network of MC-CNN-NT are abandoned. The number of the network layers is compressed to 6. The first six convolution layers of VGG-D use 3×3 size convolution cores. The second convolution layer and the fourth convolution layer connect a 2×2 size subsampling layer, respectively. This forward propagation network structure with six convolution layers and two subsampling layers is called as the backbone network of the feature extraction. In order to extract richer feature information, the lateral connection structure in the feature extraction network is constructed. The first convolution layer, the third convolution layer, and the sixth convolution layer of the backbone network connect two convolution cores of 3×3 size in the lateral connection paths, respectively. The three branches of the network are called Branch 1, Branch 2, and Branch 3, respectively. Branch 1 consists of Conv1, Dpool3, Conv7, and Conv8. Branch 2 consists of Conv2, Dpool1, Conv3, Conv9, and Conv10. Branch 3 consists of Conv4, Dpool2, Conv5, Conv6, Upool1, Conv11, and Conv12. The composition of the three branches is shown in Figure 3.

Branch 1 integrates the information of the first convolution layer into the feature maps, and the footprints of the target locations are well preserved. Branch 2 integrates the information of the third convolution layer into the feature maps, which includes the edge information of the targets and the semantic information of the images. Branch 3 integrates the information of the sixth convolution layer into the feature maps, and the strong semantic information of the targets is incorporated into the feature maps. The extracted features of the three branches include the details of the vehicle edges in the shallow feature maps and the strong semantic information in the high-level feature maps. The implementation of the network fusion strategy enriches the diversity of the extracted features. A 2×2 subsampling layer and a 2×2 upsampling layer are added to Branch 1 and Branch 3, respectively. Using this scheme, the scale of the feature maps output by each branch is consistent. After one subsampling and multiple convolutions, the size of the feature maps becomes a quarter of the original ones. The processes of the size change of the feature maps in three branches are demonstrated in Figure 4. As shown in Figure 4, Branch 1 generates 32 feature maps, Branch 2 generates 64 feature maps, and Branch 3 generates 128 feature maps. The feature extraction network stacks and fuses the output feature maps of three branches and generates 224 feature maps for RPN.

3.2. The Classification Subnetwork of MC-CNN-ST. A new shallow convolution network is constructed as a classification sub network of MC-CNN-ST. The shallow network applies the activation function PReLU and the loss function Focal Loss in MC-CNN-NT. The network structure is shown in Figure 3. The network consists of three convolution layers Conv16, Conv17, Conv18, two maximum pooling layers Dpool4, Dpool5, a data reorganization layer reshape, and a softmax classifier. The images to be classified are the single target images extracted by the location sub network of MC-CNN-ST. The image size is normalized to 28×28. The number of the input images for each batch is set to 50. Since each image has three channel charts of blue, green, and red, the number of Conv16 images that input into the classification network is $3 \times 50 = 150$. The size transition processes

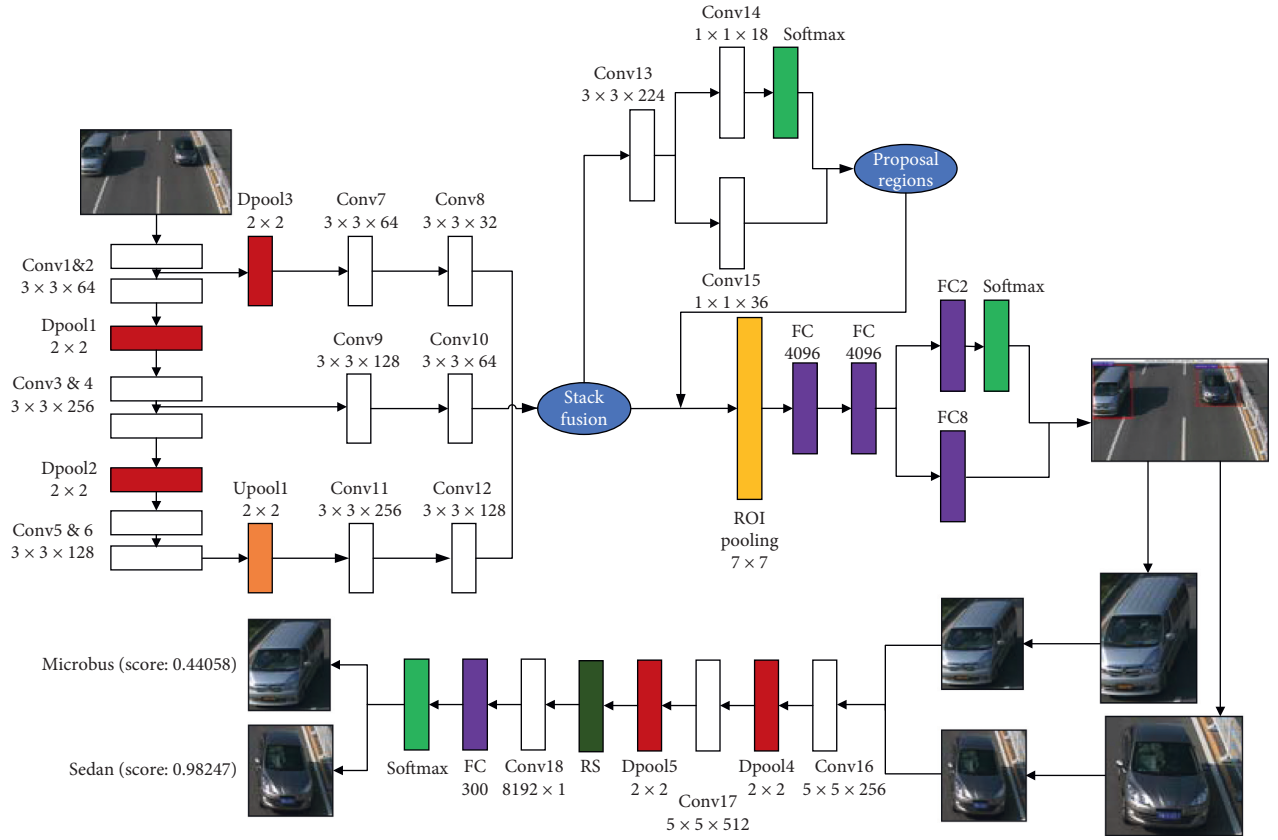

Figure 3: The framework of MC-CNN-ST.

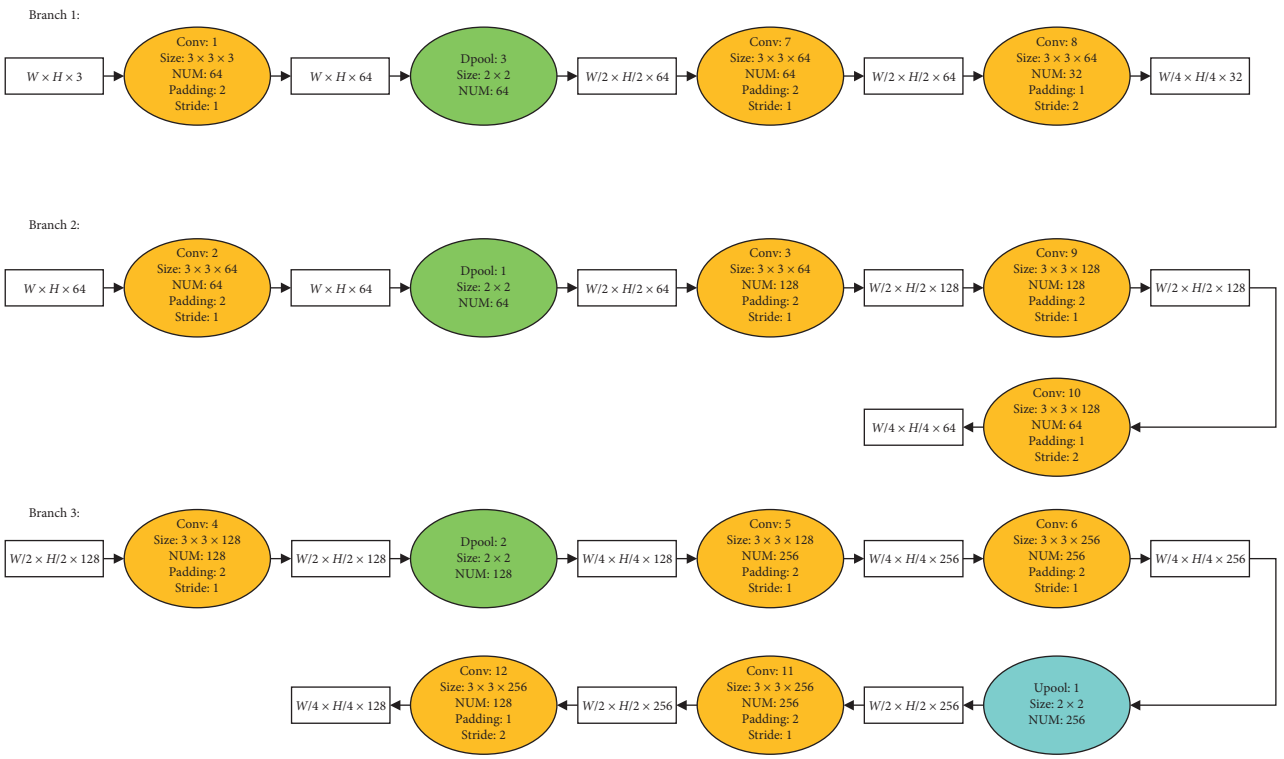

Figure 4: The processes of the size change of the feature maps in three branches.

from Conv16 to Conv18 are shown in Table 3. Here, the reshape layer reorganizes the features coming from Dpool5, the size of the feature map vectors becomes 8192×150. Conv18 uses six convolution cores of 8192×1 size to extract the features. The width of the feature maps output by Conv18 is $(8192 - 8192 + 0)/1 + 1 = 1$. The height of the feature maps output by Conv18 is $(150 - 1 + 0)/1 + 1 = 150$. The full connection layer maps the distributed feature extracted from Conv18 to the sample label space. The number of neural nodes in the full connection layer is set to $50 \times 6 = 300$. Here, 50 is the number of the images input in each batch and 6 is the number of the vehicle categories. Softmax classifier outputs the probability values of each target belonging to six type vehicles. The category that obtains the maximum probability value is the vehicle recognition category. The network adopts the strategies of inputting multiple images in the same batch and the shallow network, the recognition speed of the network is enhanced.

3.3. Data Augmentation. When MC-CNN-ST has robust localization performance for small targets with different sizes, positions, and perspectives, we use random sampling to translate, rotate, flip, and cut the images. The specific operations are presented as follows. (1) Targets are randomly translated $10k$ ($k = \pm 5, \pm 10, \pm 15, \pm 20$) pixels along X or Y axis. (2) The images are rotated 180 degrees. (3) The images are flipped along the axis of the image center. (4) The length of the original images is randomly clipped as the input images. These samples contain at least one central point of the targets. Four data augmentation schemes can effectively avoid overfitting of the model.

4. Experiments

In this section, two groups of experiments are designed to verify the effectiveness of the cascaded network MC-CNN-NT and MC-CNN-ST. Section 4.1 introduces the hardware and software environment of the experiments and the initial setting of the network parameters. Section 4.2 shows the experimental results for the normal targets using MC-CNN-NT. Section 4.3 demonstrates the experimental results for the small targets using MC-CNN-ST.

4.1. Environment and the Initial Value Settings. The experiments use Caffe framework to implement the target detection algorithms. The hardware in the experiments is used as follows: 32 GB RAM, Intel i7 CPU and NVIDIA Geforce GTX1080Ti 11 GB GPU. The software in the experiments is applied as follows: Ubutu 16.04, Python 2.7.14, CUDA8.0 and CUDNN 6.0.

In MC-CNN-NT, some network initial weights are pretrained on the ImageNet dataset. These weights partly locates in the convolution layers shared by PRN and Fast R-CNN in the location sub network, and partly locates in the first four convolution layers and the last three full connection layers of VGG-E in the classification sub network. The other convolution layer initial weights are initialized by Gaussian distribution with the mean value of 0 and the standard deviation of 0.01. The maximum number of the iterations is set to 70,000. The learning rate of the first 50,000 iterations is set to 0.001. The learning rate of the last 20,000 iterations is reduced to 0.0001.

In MC-CNN-ST, the Gaussian distribution with the mean value of 0 and the standard deviation of 0.01 is used to initialize the weights of the whole network randomly. The maximum number of the iterations is set to 100,000. The learning rate of the first 50,000 iterations is set to 0.001. The learning rate of the last 50,000 iterations is reduced to 0.0001.

The other initial parameters of two groups of experiments use the same setting strategy. The thresholds of two cascaded networks are initially set to 0. The focusing parameter of the Focal Loss function γ is set to 2. The momentum term is set to 0.9. The weight-decay coefficient is set to 0.0005. Dropout method is applied to prevent overfitting, and the probability of discarding network neurons is 0.5.

4.2. Experiments of Vehicle Attributes Recognition for the Normal Targets. In the experiments of vehicle attribute recognition for the normal targets, two datasets are selected: the SYIT-Vehicle dataset and BIT-Vehicle dataset [31]. The common feature of the two datasets is that they contain six categories of vehicles: bus, microbus, minivan, sedan, SUV, and truck. The differences of the two datasets are that the location, size, environment, and quantity of the images.

4.2.1. Datasets. The vehicle images in the BIT-Vehicle dataset are derived from the road monitoring. The images are obtained directly above the road surveillance camera. The sizes of images are 1600×1200 and 1600×1080, respectively. The dataset contains 9850 images with 10053 vehicle targets. Among them, the number of bus, microbus, minivan, sedan, SUV, and truck is 558, 883, 476, 5922, 1392, and 822, respectively. The sample images of the dataset are shown in Figure 5.

The vehicle images in SYIT-Vehicle dataset are derived from the image capturing equipment of the Institute of Optimization Theory and Process Control in Shenyang Ligong University. The dataset contains the vehicle images with multi-region, multi-angle, and multi-illumination. The dataset contains 12000 images with 12161 vehicle targets. Among them, the number of bus, microbus, minivan, sedan, SUV, and truck is 1770, 2174, 1817, 2626, 1891, and 1883, respectively. The sizes of images are not fixed. The background of the vehicle targets of the SYIT-Vehicle dataset is more complex than that of the BIT-Vehicle dataset. The sizes of vehicle targets of the SYIT-Vehicle dataset are more diverse than those of the BIT-Vehicle dataset. The sample images of the SYIT-Vehicle dataset are shown in Figure 6.

In this paper, the SYIT-Vehicle dataset is employed as the training validation set and the testing set. The sample ratio of the training validation set and the testing set is 9 : 1. The sample ratio of the training set and the verification set is set to 9 : 1. The BIT-Vehicle dataset is used as the migration dataset. The robustness of the algorithm is verified by randomly selecting 3600 images from the BIT-Vehicle dataset.

Table 3: Parameters of the classification sub network in MC-CNN-ST.

Position	Feature map input size	Kernel size	Kernel number	Stride	Padding	Feature map output size
Conv16	28×28	5×5	256×150	1	0	24×24
Dpool4	24×24	2×2	256×150	2	0	12×12
Conv17	12×12	5×5	512×150	1	0	8×8
Dpool5	8×8	2×2	512×150	2	0	4×4
Reshape	4×4	—	—	—	—	8192×150
Conv18	8192×150	8192×1	6	1	0	1×150

Figure 5: The samples of the BIT-Vehicle dataset.

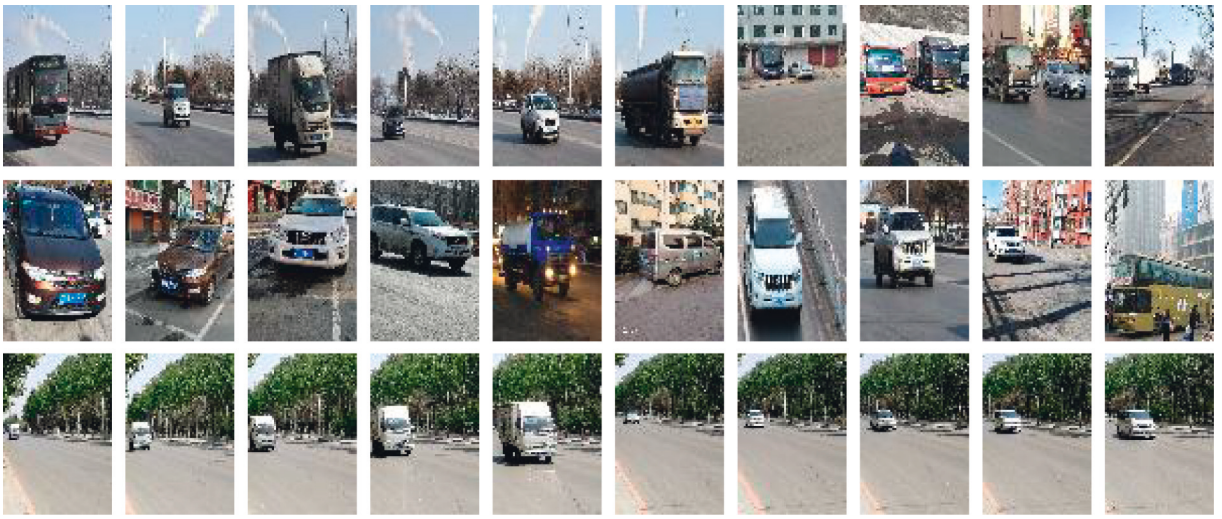

Figure 6: The samples of the SYIT-Vehicle dataset.

4.2.2. Results and Analysis. In this section, the target attribute recognition experiments using MC-CNN-NT are described. Nine networks are selected as the comparison networks. Three noncascaded networks (CNN, Fast R-CNN, and Faster R-CNN) and six cascaded networks (CNN + CNN [3], IFR-CNN + CNN [21], MC-CNN, MC-CNN-P, MC-CNN-F, and MC-CNN-NT) are included in nine networks. Table 4 describes the principal structures of nine networks participating in the comparison.

The results of vehicle attribute recognition using MC-CNN-NT are shown in Tables 5 and 6. The attribute recognition accuracy of the cascaded network MC-CNN is significantly higher than that of the noncascaded network. The recognition accuracy of MC-CNN is 84.24% on the

Table 4: The main structures of nine networks.

Method	Structure
CNN	One stage + exhaustive sliding window + CNN + SVM + single loss
Fast R-CNN	One stage + selective search + CNN + softmax + multi loss
Faster R-CNN	One stage + RPN + CNN + softmax + multi loss
CNN + CNN	Two stages + CNN + CNN
IFR-CNN + CNN	Two stages + IFR-CNN + CNN
MC-CNN	Two stages + faster R-CNN + CNN
MC-CNN-P	MC-CNN + PReLU
MC-CNN-F	MC-CNN + Focal Loss
MC-CNN-NT	MC-CNN + PReLU + Focal Loss

Table 5: The attribute recognition results for the normal targets on the SYIT-Vehicle dataset.

Method	Bus (%)	Microbus (%)	Minivan (%)	Sedan (%)	SUV (%)	Truck (%)	Total (%)
CNN	80.00	68.65	75.14	63.25	64.33	68.65	70.00
Fast R-CNN	78.92	70.81	73.51	68.33	70.27	76.22	72.97
Faster R-CNN	87.03	76.76	78.92	69.73	81.62	77.30	79.82
CNN + CNN	88.94	79.31	80.14	75.23	83.20	79.41	81.89
IFR-CNN + CNN	92.49	84.23	83.74	82.23	84.02	81.41	84.96
MC-CNN	91.35	83.70	83.70	80.92	84.78	81.00	84.24
MC-CNN-P	94.05	84.67	83.62	83.16	84.78	80.46	85.12
MC-CNN-F	94.60	84.62	84.24	84.08	87.57	83.62	86.46
MC-CNN-NT	97.30	91.11	90.57	88.41	90.73	89.49	91.27

Table 6: The attribute recognition results for the normal targets on the BIT-Vehicle dataset.

Method	Bus (%)	Microbus (%)	Minivan (%)	Sedan (%)	SUV (%)	Truck (%)	Total (%)
CNN	60.00	41.08	48.11	44.87	52.44	50.27	52.88
Fast R-CNN	78.92	42.17	48.11	45.95	54.60	58.92	57.30
Faster R-CNN	81.24	64.33	64.33	62.17	66.49	65.95	69.46
CNN + CNN	82.24	66.03	67.00	65.57	67.3	68.03	71.44
IFR-CNN + CNN	85.24	70.43	78.01	70.21	73.68	76.24	75.64
MC-CNN	83.70	70.19	76.68	69.11	70.19	76.14	74.33
MC-CNN-P	88.03	71.77	82.08	70.73	73.98	75.60	77.03
MC-CNN-F	89.11	73.52	83.70	72.35	75.22	77.00	78.48
MC-CNN-NT	90.19	77.76	86.41	75.60	79.38	86.41	82.63

SYIT-Vehicle dataset, which is 4.42% higher than that of Faster R-CNN. The recognition accuracy of MC-CNN is 74.33% on the BIT-Vehicle dataset, which is 4.87% higher than that of Faster R-CNN. The multitask decomposition strategy of the cascaded network MC-CNN improves the recognition accuracy of the network. The cascaded network MC-CNN-P enhances the recognition accuracy by 0.88% and 2.7% compared with MC-CNN in two datasets, respectively. The cascaded network MC-CNN-F enhances the recognition accuracy by 2.22% and 4.15% compared with MC-CNN in two datasets, respectively. The adaptive learning strategy for the negative values of the activation function PReLU and the hard-to-detect sample reinforcement learning strategy of the Focal loss function both improve the quality of the cascaded network target recognition. MC-CNN-NT gets 91.27% recognition accuracy on the SYIT-Vehicle dataset. The increases of MC-CNN-NT accuracy are 11.45%, 9.38%, 6.31%, 7.03%, 6.15%, and 4.81% than Faster R-CNN, CNN + CNN, IFR-CNN + CNN, MC-CNN, MC-CNN-P, and MC-CNN-F, respectively. MC-CNN-NT gets 82.63% recognition accuracy on the BIT-Vehicle dataset. The increases of MC-CNN-NT accuracy are 13.17%, 11.19%, 6.99%, 8.3%, 5.6%, and 4.15% than Faster R-CNN, CNN + CNN, IFR-CNN + CNN, MC-CNN, MC-CNN-P, and MC-CNN-F, respectively. MC-CNN-NT that combines the PReLU function with the Focal loss function achieves the best performance of target attribute recognition. Simultaneously, MC-CNN-NT achieves high accuracy in the migration datasets, which verifies that the model has good robustness.

4.3. Experiments of Vehicle Attributes Recognition for the Small Targets

4.3.1. Datasets. The COCO-Vehicle dataset is used to carry out the experiments of vehicle attribute recognition for the small targets. The COCO-Vehicle dataset contains seven category targets: person, bus, microbus, minivan, sedan, SUV, and truck. The dataset is manually annotated according to the file of the COCO dataset [32]. The person, car, and bus in the COCO dataset are extracted, and the car in COCO dataset is subdivided into sedan, minivan, microbus, SUV, and truck. Since the number of trucks in the COCO dataset is few, 300 trucks from the VOC2007 dataset are selected to supplement them. The sample images of the COCO-Vehicle dataset are shown in Figure 7.

In this paper, the definition of small target, medium target, and large target is based on the standard of reference [33]: P_{pix} represents the percentage of ROIS pixels in the whole image. The targets with $P_{pix} \le 2.4\%$ are defined as the small targets. The targets with $2.4\% \le P_{pix} \le 47.2\%$ are defined as the medium targets. The targets with $P_{pix} \ge 47.2\%$ are defined as the large targets. In the COCO-Vehicle dataset, the number of small targets accounts for 63.10%, the number of medium targets accounts for 32.86%, and the number of large targets accounts for 4.04%. The statistical results of the COCO-Vehicle dataset are shown in Table 7.

4.3.2. Experiments of the Location for the Small Targets. In order to verify the small target location performance of MC-CNN-ST, the contrast experiments of six networks are designed in this paper. The main structures of the six networks are shown in Table 8. Net-A network is an original Faster R-CNN Network. Net-B network is based on the original Faster R-CNN, which compresses the number of convolution layers in the feature extraction network to 6. Net-C network and Net-D network fuse the second, fourth, and sixth convolution layers of VGG-E. Net-C network adds a 5×5 convolution layer to the three branches of the fusion network. Net-D network adds two 3×3 convolution layers

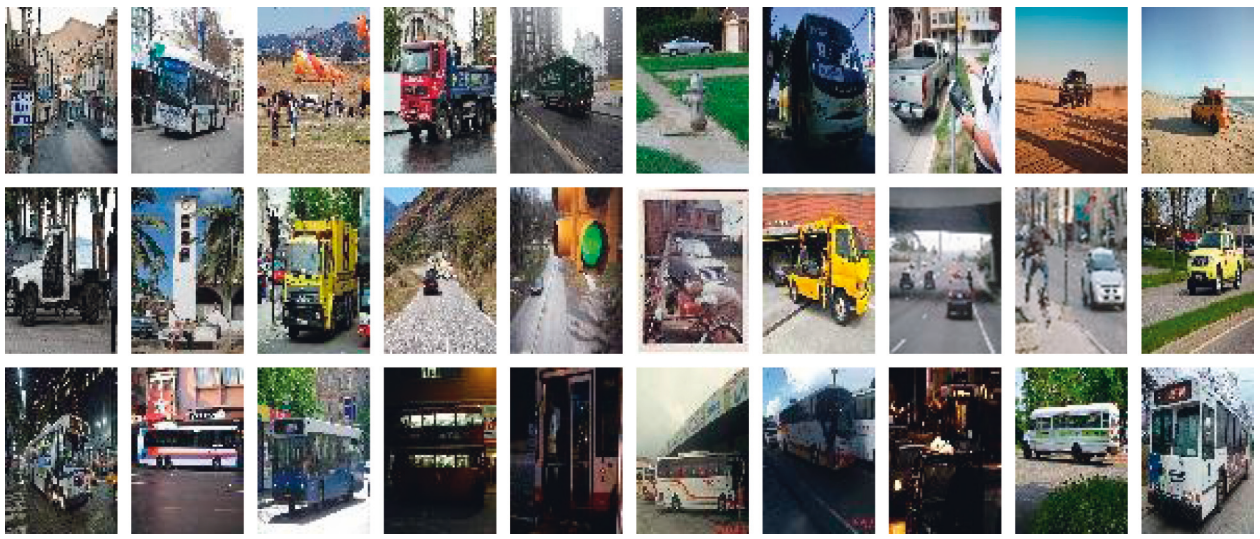

Figure 7: The samples of the COCO-Vehicle dataset.

Table 7: The sample statistics of the COCO-Vehicle datasets.

Target type	Person	Bus	Microbus	Minivan	Sedan	SUV	Truck	Total
Small	5083	240	356	261	3249	900	40	10129
Middle	1783	796	176	235	1430	483	372	5275
Big	16	240	9	38	273	40	32	648
Total	6882	1276	541	534	4952	1423	444	16052

Table 8: The structures of six location networks.

Method	Description of comparative experiments
Net-A	The original faster R-CNN
Net-B	Faster R-CNN + structure compression
Net-C	Structure compression + the fusion of 2, 4, 6 feature map + using one 5×5
Net-D	Structure compression + the fusion of 2, 4, 6 feature map + using two 3×3
Net-E	Structure compression + the fusion of 1, 3, 6 feature map + using one 5×5
Net-F	Structure compression + the fusion of 1, 3, 6 feature map + using two 3×3

to the three branches of the fusion network. Net-E network and Net-F network fuse the first, third, and sixth convolution layers of VGG-E. Net-F network is the location subnetwork of the cascaded network MC-CNN-ST. Different from Net-F network, Net-E network adds a 5×5 convolution layer to the three branches of the network.

The location results of six networks are shown in Table 9 and Figure 8. As shown in Table 9, the MC-CNN-ST location network (Net-F) using the network compression strategy has better recognition ability for the background region of the suspected targets. The number of false acceptances is reduced. The increase of Net-F network recognition precision is 21.23%, 8.55%, 5.03%, 2.42%, and 2.7% more than Net-A, Net-B, Net-C, Net-D, and Net-E, respectively. Net-F network using the network fusion strategy enhances the expressive ability for the target features and reduces the

Table 9: The location results for the small targets on the COCO-Vehicle dataset.

Method	Vehicle	TP	FP	FN	Precision (%)	Recall (%)
Net-A	1913	1237	546	676	69.38	64.66
Net-B	1913	1459	319	454	82.06	76.27
Net-C	1913	1555	262	358	85.58	81.29
Net-D	1913	1576	211	337	88.19	82.38
Net-E	1913	1614	222	299	87.91	84.37
Net-F	1913	1651	171	262	90.61	86.30

number of false rejection. The increase of the recall rate of Net-F network is 21.64%, 10.03%, 5.01%, 3.92%, and 1.93% than Net-A, Net-B, Net-C, Net-D, and Net-E, respectively.

The location results of Net-A, Net-B, and Net-F correspond to the images of the first, second, and third columns of Figures 8(a) and 8(b), respectively. As shown in Figure 8(a), Net-A network recognizes 8 and 10 targets in two different images, respectively. Net-B network recognizes 11 and 13 targets in two images, respectively. Net-F network recognizes 12 and 14 targets in two images, respectively. Net-F network recognizes the largest number of the targets. Longitudinal network compression strategy and horizontal network fuse strategy of Net-F network reduce the number of false rejection in the model and improve the recall rate of the network. In Figure 8(b), the vehicles marked with the red borders are correctly identified as the foreground. Buildings, billboards, and other backgrounds are misidentified as vehicles marked with the green borders. As shown in Figure 8(b), the number of false detections in Net-F network

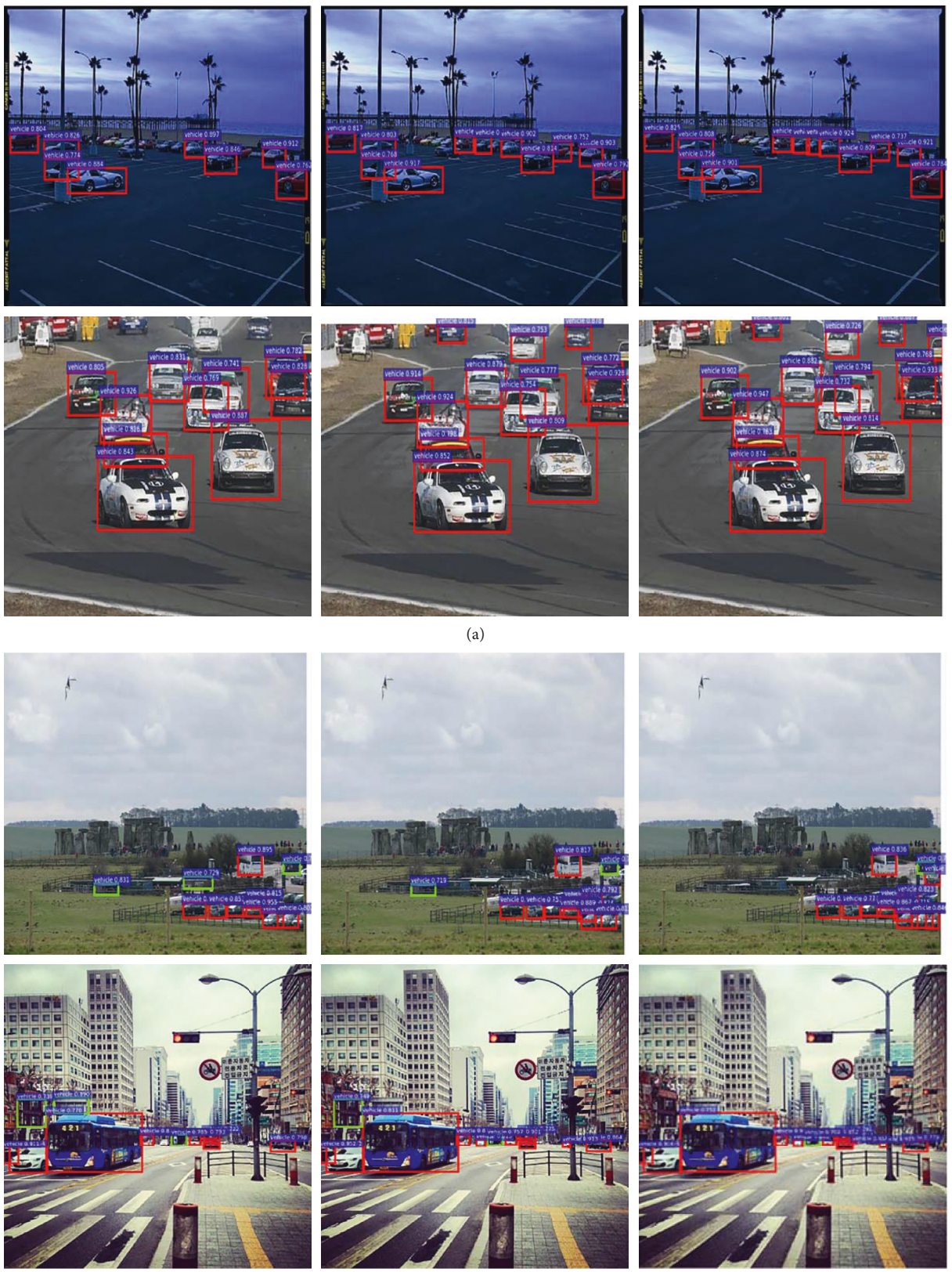

(a)

(b)

Figure 8: The results of the comparative experiments. (a) The reduction of false negative. (b) The reduction of false positive.

Table 10: The attribute recognition results for the small targets on the COCO-Vehicle dataset.

Method	Bus (%)	Microbus (%)	Minivan (%)	Sedan (%)	SUV (%)	Truck (%)	Total (%)
CNN	65.25	37.70	38.36	43.93	38.36	51.14	45.79
Fast R-CNN	70.50	49.18	53.77	44.59	54.09	57.70	54.97
Faster R-CNN	74.10	53.12	59.67	51.15	55.41	60.62	59.34
CNN + CNN	74.99	54.89	59.80	52.53	56.99	61.39	60.10
IFR-CNN + CNN	75.70	55.12	59.97	53.45	57.41	62.51	60.71
MC-CNN-NT	77.70	57.04	60.00	54.75	58.36	62.62	61.75
MC-CNN-ST	88.27	79.46	75.67	75.10	77.52	79.95	79.33

Figure 9: The classification results for the small targets using MC-CNN-ST.

is 1, which is less than the number of false detections in Net-A and Net-B.

4.3.3. Experiments of Attribute Recognition for the Small Targets. In order to verify the small target recognition performance of MC-CNN-ST, the contrast experiments of seven networks are designed in this paper. These seven networks include three noncascaded networks (CNN, Fast R-CNN, and Faster R-CNN) and four cascaded networks (CNN + CNN, IFR-CNN + CNN, MC-CNN-NT, and MC-CNN-ST). The results of attribute recognition are demonstrated in Table 10 and Figure 9.

As shown in Table 10, MC-CNN-ST achieves the superior recognition results in seven networks. The increases of the accuracy of MC-CNN-ST are 33.54%, 24.36%, 19.99%, 19.23%, 18.62%, and 17.58 than CNN, Fast R-CNN, Faster R-CNN, CNN + CNN, IFR-CNN + CNN, and MC-CNN-NT, respectively. As shown in Figure 9, MC-CNN-ST has good attribute recognition ability for six category vehicles.

5. Conclusions

This paper is devoted to solving the problem of vehicle attribute recognition. The multitask cascaded networks MC-CNN-NT and MC-CNN-ST are established to recognize vehicle attributes with normal size and small size, respectively. The cascaded multitask networks improve the recognition effect of one-stage networks in the complex background. The implementation of the network compression strategy and the feature fusion strategy reduces the false acceptance rate and improves the recall rate for the small targets. The use of the activation function PReLU and the loss function Focal Loss improves the nonlinear mapping ability of the networks and the mining ability for the hard-to-detect samples. The experimental results show that the

increase of the recognition accuracy of MC-CNN-NT for the normal targets is 18.3%, 11.45%, 9.38%, 6.31%, and 7.03% more than Fast R-CNN, Faster R-CNN, CNN + CNN, IFR-CNN + CNN, and MC-CNN, respectively. The increase of the recognition accuracy of MC-CNN-ST for the small targets is 24.36%, 19.99%, 19.23%, 18.62%, and 17.58% than Fast R-CNN, Faster R-CNN, CNN + CNN, IFR-CNN + CNN, and MC-CNN-NT, respectively. In the future research, we consider fusing the infrared image features with the visible image features to enhance the recognition accuracy for the small target vehicles.

Data Availability

The three datasets (SYIT-Vehicle dataset, BIT-Vehicle dataset, and COCO-Vehicle dataset) used in the paper can be obtained through e-mail (liufang5208@sylu.edu.cn and xuke@sylu.edu.cn).

Conflicts of Interest

The authors declare that they have no conflicts of interest.

Acknowledgments

This work was supported by Open Foundation of Science and Technology on Electro-Optical Information Security Control Laboratory (Grant no. 61421070104), Science and Technology Project of Educational Department of Liaoning Province (Grant no. LG201715), Natural Science Foundation of Liaoning Province (Grant no. 20170540790), and (Grant no. 2019-ZD-0256).

References

[1] Q. W. Li, H. S. Cheng, Y. Zhou, and G. Y. Huo, "Road vehicle monitoring system based on intelligent visual internet of things," *Journal of Sensors*, vol. 2015, Article ID 720308, 16 pages, 2015.

[2] Q. W. Xue, K. Wang, J. J. Lu, and Y. J. Liu, "Rapid driving style recognition in car-following using machine learning and vehicle trajectory data," *Journal of Advanced Transportation*, vol. 2019, Article ID 9085238, 11 pages, 2019.

[3] B. Hu, J.-H. Lai, and C.-C. Guo, "Location-aware fine-grained vehicle type recognition using multi-task deep networks," *Neurocomputing*, vol. 243, pp. 60–68, 2017.

[4] R. Feris, B. Siddiquie, Y. Zhai, J. Petterson, L. Brown, and S. Pankanti, "Attribute-based Vehicle Search in Crowded Surveillance videos," in *Proceedings of the 1st International Conference on Multimedia Retrieval*, Trento, Italy, April 2011.

[5] J. Prokaj and G. Medioni, "3-D model based vehicle recognition," in *Proceedings of the 2009 IEEE Workshop on Applications of Computer Vision (WACV)*, pp. 1–7, Salt Lake County, UT, USA, January 2009.

[6] K. Ramnath, S. N. Sinha, R. Szeliski, and E. Hsiao, "Car make and model recognition using 3D curve alignment," in *in Proceedings of the 2014 IEEE Winter Conference on Applications of Computer Vision (WACV)*, pp. 285–292, Steamboat Springs, CO, USA, March 2014.

[7] T. N. Tan and K. D. Baker, "Efficient image gradient based vehicle localization," *IEEE Transactions on Image Processing*, vol. 9, no. 8, pp. 1343–1356, 2000.

[8] P. Negri, X. Clady, S. M. Hanif, and L. Prevost, "A cascade of boosted generative and discriminative classifiers for vehicle detection," *EURASIP Journal on Advances in Signal Processing*, vol. 2008, no. 1, Article ID 782432, 2008.

[9] X. X. Ma and W. E. L. Grimson, "Edge-based rich representation for vehicle classification," in *Proceedings of the Tenth IEEE International Conference on Computer Vision*, pp. 1185–1192, Beijing, China, October 2005.

[10] S. S. Teoh and T. Bräunl, "Symmetry-based monocular vehicle detection system," *Machine Vision and Applications*, vol. 23, no. 5, pp. 831–842, 2012.

[11] R. Bräunl, J. Donahue, T. Darrelland, and J. Malik, "Rich feature hierarchies for object detection and semantic segmentation," in *Proceedings of the 2014 IEEE Conference on Computer Vision and Pattern Recognition*, pp. 580–587, Columbus, OH, USA, June 2014.

[12] R. Girshick, "Fast R-CNN," in *Proceedings of the 2015 IEEE International Conference on Computer Vision (ICCV)*, pp. 1440–1448, Santiago, Chile, December 2015.

[13] S. Ren, K. He, R. Girshick, and J. Sun, "Faster R-CNN: towards real-time object detection with region proposal networks," in *Proceedings of the International Conference on Neural Information Processing Systems*, pp. 1137–1149, Istanbul, Turkey, 2015.

[14] K. He, X. Zhang, S. Ren, and J. Sun, "Spatial pyramid pooling in deep convolutional networks for visual recognition," *IEEE Transactions on Pattern Analysis & Machine Intelligence*, vol. 37, no. 9, pp. 1904–1916, 2014.

[15] J. Redmon, S. Divvala, R. Girshick, and A. Farhadi, "You only look once: unified, real-time object detection," in *Proceedings of the 2016 IEEE Conference on Computer Vision and Pattern Recognition*, pp. 779–788, CVPR, Las Vegas, NV, USA, June 2016.

[16] W. Liu, D. Anguelov, D. Erhan et al., "SSD: single shot multiBox detector," in *Proceedings of the 14th European Conference on Computer Vision*, pp. 21–37, Amsterdam, Netherlands, October 2016.

[17] Z. Q. Huo, Y. Z. Xia, and B. L. Zhang, "Vehicle type classification and attribute prediction using multi-task rcnn," in *Proceedings of the International Congress on Image & Signal Processing*, pp. 564–569, IEEE, Shanghai, China, October 2017.

[18] T. Y. Tang, S. L. Zhou, Z. P. Deng, H. X. Zou, and L. Lei, "Vehicle detection in aerial images based on region convolutional neural networks and hard negative example mining," *Sensors*, vol. 17, no. 2, p. 336, 2017.

[19] Q. Meng, H. S. Song, G. Li, Y. A. Zhang, and X. Q. Zhang, "A block object detection method based on feature fusion networks for autonomous vehicles," *Complexity*, vol. 2019, Article ID 4042624, 14 pages, 2019.

[20] Z. Wang, P. Chen, and J. X. Pan, "Target detection in complex background based on depth learning," *Journal of Chongqing University of Technology: Natural Science*, vol. 32, no. 4, pp. 171–176, 2018.

[21] H. Gong, Y. Zhang, F. Liu, and K. Xu, "Vehicle recognition using multi-task cascaded network," in *Proceedings of Fifth Symposium on Novel Optoelectronic Detection Technology and Application*, pp. 1–8, Xian, China, October 2018.

[22] P. Fu and S. P. Xie, "License plate location based on cascaded convolution neural network," *Computer Technology and Development*, vol. 28, no. 1, pp. 1362–1451, 2018.

[23] T. Y. Lin, P. Dollár, R. Girshick, K. He, B. Hariharan, and S. Belongie, "Feature pyramid networks for object detection," in *Proceedings of the 2017 IEEE Conference Computer Vision*

and Pattern Recognition (CVPR), pp. 936–944, Honolulu, HI, USA, July 2017.

[24] N. Dalal and B. Triggs, "Histograms of oriented gradients for human detection," in *Proceedings of the 2005 IEEE Conference Computer Vision and Pattern Recognition (CVPR)*, no. 8, pp. 886–893, Diego, CA, USA, 2005.

[25] D. G. Lowe, "Distinctive image features from scale-invariant keypoints," *International Journal of Computer Vision*, vol. 60, no. 2, pp. 91–110, 2004.

[26] S. Karungaru, M. Fukumi, and N. Akamatsu, "Human face detection in visual scenes using neural networks," *IEEJ Transactions on Electronics Information and Systems*, vol. 122, no. 6, pp. 995–1000, 2008.

[27] K. He, X. Zhang, S. Ren, and J. Sun, "Delving deep into rectifiers: surpassing human-level performance on ImageNet classification," in *Proceedings of the 2015 IEEE International Conference on Computer Vision*, pp. 1026–1034, Santiago, Chile, December 2015.

[28] F. Agostinelli, M. Hoffman, P. Sadowski, and P. Baldi, "Learning activation functions to improve deep neural networks," in *Proceedings of the International Conference on Learning Representations (ICLR)*, Banff, Canada, April 2014.

[29] V. Nair and G. E. Hintion, "Rectified linear units improve restricted Boltzmann machines," in *Proceedings of the 27th International Conference on International Conference on Machine Learning (ICML)*, pp. 807–814, Haifa, Israel, June 2010.

[30] R. Girshick, J. Donahue, T. Darrell, and J. Malik, "Rich feature hierarchies for accurate object detection and semantic segmentation," in *Proceedings of the 2014 IEEE Conference on Computer Vision and Pattern Recognition (CVPR)*, pp. 580–587, Colorado Springs, CO, USA, June 2014.

[31] Z. Dong, Y. Wu, M. Pei, and Y. Jia, "Vehicle type classification using a semisupervised convolutional neural network," *IEEE Transactions on Intelligent Transportation Systems*, vol. 16, no. 4, pp. 2247–2256, 2015.

[32] T. Y. Lin, M. Maire, S. Belongie et al., "Microsoft coco: common objects in context," in *Proceedings of the 13th European Conference On Computer Vision*, pp. 740–755, Zurich, Switzerland, September 2014.

[33] B. Singh and L. S. Davis, "An analysis of scale invariance in object detection – SNIP," in *Proceedings of the IEEE Conference on Computer Vision and Pattern Recognition*, pp. 3578–3587, Salt Lake City, USA, June 2018.

Hindawi
Complexity
Volume 2019, Article ID 1712569, 10 pages
https://doi.org/10.1155/2019/1712569

Research Article

Analysis of College Students' Public Opinion Based on Machine Learning and Evolutionary Algorithm

Jinqing Zhang[1], **Pengchao Zhang**[2] **and Bin Xu**[3,4]

[1]*School of Automation Science and Electrical Engineering, Beihang University, Beijing, China*
[2]*Shaanxi Provincial Key Laboratory of Industrial Automation, Shaanxi University of Technology, Hanzhong, Shaanxi 723000, China*
[3]*Major Public Information Research Center of Shaanxi Province, Northwestern Polytechnical University, Xi'an, China*
[4]*School of Marxism, Northwestern Polytechnical University, Xi'an, China*

Correspondence should be addressed to Bin Xu; smileface.binxu@gmail.com

Received 21 April 2019; Accepted 9 September 2019; Published 11 November 2019

Guest Editor: Gonzalo Farias

The recent information explosion may have many negative impacts on college students, such as distraction from learning and addiction to meaningless and fake news. To avoid these phenomena, it is necessary to verify the students' state of mind and give them appropriate guidance. However, many peculiarities, including subject focused, multiaspect, and low consistency on different samples' interests, bring great challenges while leveraging the mainstream opinion mining method. To solve this problem, this paper proposes a new way by using a questionnaire which covers most aspects of a student's life to collect comprehensive information and feed the information into a neural network. With reliable prediction on students' state of mind and awareness of feature importance, colleges can give students guidance associated with their own experience and make macroscopic policies more effective. A pipeline is proposed to relieve overfitting during the collected information training. First, the singular value decomposition is used in pretreatment of data set which includes outlier detection and dimension reduction. Then, the genetic algorithm is introduced in the training process to find the proper initial parameters of network, and in this way, it can prevent the network from falling into the local minimum. A method of calculating the importance of students' features is also proposed. The experiment result shows that the new pipeline works well, and the predictor has high accuracy on predicting fresh samples. The design procedure and the prediction design will provide suggestions to deal with students' state of mind and the college's public opinion.

1. Introduction

Youth is the most important period for college students to establish a mature outlook on life and values. In college, students' perception on life and various things includes public opinion, which can also influence the ideology of students in turn. The advent of Internet has increased the diversification of mass media, which makes it possible for people to obtain information that they are interested in at anytime and anywhere. However, the quality and reliability of information show increasing difference. Some untrue and negative information might pollute public opinion in college and cause harmful influence on students' state of mind. For personality, research studies have shown that students who are addicted to Internet and wireless mobile devices such as smartphones relate to increase in stress and anxiety while decrease in academic performance and satisfaction with life [1, 2]. These impacts could make students take a pessimistic view and feel their lives meaningless which show strong relationship with depressive disorder and even suicide. For society, the spread of rumors could make students more suspicious and treat social media and government as liars instead [3]. When students enter society after graduation, their distrust on government will leave room to disharmony. A student's state of mind is the cell of public opinion in college, and there have been strong evidences showing that students in positive environments are more likely to make great achievements [4]. To protect students from the

negative impact of information explosion, colleges should focus on giving guidance to students with problems in mind, take responsibility for helping them correct their outlook on life and values, and make them be willing to fight for the development of the whole human race.

However, students are usually not willing to seek guidance on state of mind because many of them do not want to be regarded as "sick." This requires the colleges to actively implement guidance on students. But if students tend to hide their problem, there will be problems for colleges to know who needs to be guided when facing thousands of students. One of the methods is using machine learning (ML) tools such as the neural network (NN) to predict students' state of mind. ML tools can automatically learn the function from students' features to their state of mind and make prediction quickly and accurately as long as there are enough training data. With precise prediction on students' state of mind, colleges can adjust the guidance according to the students' own features to enhance its effectiveness [5].

ML has been widely used to predict people's opinion on things by doing text analysis on data collected from Internet, but it might not be so much useful when predicting students' state of mind. That is because prediction of student's state of mind has several peculiarities: (1) focus on subject: this work is focused on the people who make judgements, but not the judgements they have made; (2) multiaspect: to enhance the correctness of the analysis, the predictor should learn plenty of information from different aspects, but students might not publish some of this information forwardly on the Internet; (3) low consistency on aspects: different students would like to pay attention to different matters, thus it is opinionated to make an answer on a certain question as a public criterion. To meet these peculiarities, more abundant data should be collected for a single sample which covers most aspects of opinions related to a student's daily life, and the data of different samples should have good consistency on their content. If only text-based data from the internet are collected, the data set will be not effective enough. On the contrary, the traditional method of using the questionnaire to get the data can better meet the requirements. The questionnaire used is well designed to cover most of the aspects about college students, and the questions with scale can help quantify students' sentiment on different issues. The way of using a questionnaire can also force students to answer the same question so that the data between different samples can have high consistency on aspects of content.

The ML tool used as predictor is the NN. For a predictor, one of the most important criteria is generalization performance, which means the prediction accuracy on fresh samples. However, the high dimension of samples will make itself too sparse to fill the sample space. In the training process of NN, the lack of samples can cause overfitting [6]. An overfitting NN fits the training set well but has poor prediction accuracy on fresh samples. As a result, a new way is needed to solve this problem. This paper will introduce a way that uses singular value decomposition (SVD) to reduce the dimension directly and add a closed loop based on genetic algorithm (GA) on the training process to relieve overfitting. After obtaining a NN with good generalization performance, a method of calculating importance of each features is also proposed, which can help colleges combine macroscopic policies and microscopic guidance and strengthen the overall effectiveness.

Section 2 reviews the related work. Section 3 introduces the process of using SVD to pretreat the data set. Section 4 introduces the method of getting a predictor with good generalization performance, also the way of calculating features importance. Section 5 describes the details of the experiment and shows the results. Section 6 concludes our study and introduces future work.

2. Related Works

Early research studies on mining humans' opinions have been done. Pang et al. [7] collected the review data from IMDb and used different tools of machine learning such as naive Bayes classification, maximum entropy classification, and support vector machines to classify audiences' sentiment towards movies. Khan et al. [8] analyzed abundant text on Twitter that related to specific products and services and summarized the user's overall views of those objects to help the producers and servers improve their works. Zhan et al. [9] designed an algorithm that not only mined opinion from customs reviews but also automatically pointed out the salient topics from these opinions, which can make the analysis more targeted. Zhou et al. [10] did the research to transfer customs' reviews into answers of a questionnaire generated by the algorithm automatically and analyzed the collected data to point out what were the main points to improve user's experience. Not only there are research studies focusing on objects, but also several others that try to focus on people. For example, Kosinski et al. [11] used "Facebook Likes" to predict a range of highly sensitive personal attributes and get high accuracy on some classification problems. Baik et al. [12] used buying behaviors to predict people's score on four different personality traits and showed better precision when compared with previous studies. Besides the abovementioned research studies in different applications, some researchers also summarize the work in the whole field of public opinion mining. Pang and Lee [13] focused on improving the methods to address the new challenges raised by opinion mining. Tsytsarau and Palpanas [14] tried to give a definition on opinion mining to clarify what is the basic work that should be done to mine public opinion. Ravi and Ravi [15] divided research studies into different levels and summarized the characteristics of each levels. These summaries provide researchers powerful tools to do opinion mining and give criteria to assess their work.

The method of using a questionnaire to collect data has been widely used in many situations when it is necessary to establish a person's comprehensive personality profile. Topp et al. [16] reviewed 213 relevant articles to check the utility of a questionnaire named the WHO-5 Well-Being Index and confirmed its validity both in depression screening and outcome measuring in clinical trials. Garfinkel et al. [17] used a questionnaire to measure interoceptive sensibility,

which is an important dimension of one's interception. It could help explain cognitive, emotional, and clinical associations of interoceptive ability. Duckworth and Yeager [18] considered a self-report questionnaire is more efficient in studies of assessing internal psychological states like feelings of belonging when compared with other measures.

From previous research studies, it is clear that the method of using a questionnaire is good at collecting comprehensive data from a single person, and the data between different persons have high consistency on aspects. The collected data can be a good training material for human-focused opinion mining to learn the inner connection between students' behaviors and their state of mind. In this paper, the combination of the two methods overcomes the peculiarities and can make precise prediction on students' state of mind.

3. Data Collection and Pretreatment

This section will introduce what is the source of the data about college students' state of mind and describe the pretreatment method on data, including outlier detection and dimension reduction. Both of them are based on SVD.

3.1. Data Source. The data used in experiment come from a survey on students' state of mind that was conducted by Northwestern Polytechnical University in September, 2017. The students who had been surveyed were from different grades (including some masters and doctoral students). Under screening and checking, the total number of efficient sample data is 953.

The questionnaire consists of 30 questions, which are well designed to cover most aspects of students' daily life and their opinions. In terms of content, these questions can be divided as follows: (1) basic information: gender, grade, subject, and so on; (2) individual development: information of personal development since university entrance and future plan after graduation; (3) focus of attention: the focus of event happened recently; (4) mind identity: agreement on some policies and opinions; (5) school work evaluation: satisfaction with school work and direction of improvement. In terms of form, these questions can be divided into a single-choice question, multiple-choice question, scale question, and essay question.

Questions in different types need different primary pretreatments to get the original data set. Options in single-choice questions and multiple-choice questions are extended to independent variables, and the variable values were decided according to whether the options are selected or not; the answers of scale questions can be directly added into the data set; most of the questionnaires were left blank on essay questions so that they are ignored. After primary pretreatment, the sample vector dimension is extended to 160 dimensions. One of the variables is selected as sample label, and the rest are features of students. The sample label is given according to the students' evaluation on their own state of mind: the label 1 is positive, which means they do not need to be guided; the label 0 means the students are not mature and need to be guided.

3.2. Meaning of SVD. SVD can be considered as the generalization of eigen decomposition from square matrix to matrix in any size [19]. In this case, the original data set is $S \in \mathbb{R}^{m \times n}$, which means there is m samples in the data set and each sample has n features. After the SVD process, there will be orthogonal matrixes $U \in \mathbb{R}^{m \times m}$ and $V \in \mathbb{R}^{n \times n}$ that present S as follows:

$$S = U \Sigma V^T. \tag{1}$$

In (1), Σ has the structure of $\Sigma = [\mathrm{diag}(\sigma_1, \sigma_2, \ldots, \sigma_n), 0]^T$ as $m > n$, where $\mathrm{diag}(\sigma_1, \sigma_2, \ldots, \sigma_n)$ is a diagonal matrix and 0 is the zero matrix. σ_i is the singular values of S sorted in the descending order. If 0 is removed, the related vectors in U can be deleted so that $\Sigma = \mathrm{diag}(\sigma_1, \sigma_2, \ldots, \sigma_n)$ and $U \in \mathbb{R}^{m \times n}$.

An n dimension coordinate system can be established in the space of student samples whose axes relate to sample features, and every student samples can be represented by a point. The coordinate of sample is s_i, which is the row vectors of S. Then, the process of SVD can be considered as a coordinate transformation within the sample space, and each column vector v_i of V represents a base vector of the new coordinate system. The new base vectors can be given abstract meanings according to their relationship with original features. All the new base vectors are perpendicular to each other because V is an orthogonal matrix. Let $\widehat{S} = U\Sigma$, so that

$$\widehat{S} = SV. \tag{2}$$

From (2), it can be found that each row vector $\widehat{s}_i$ in $\widehat{S}$ represents the coordinate of a sample in the new coordinate system. Meanwhile, the singular values that relate to different base vectors represent the dispersion of samples on these directions. If the singular value is large, the samples' projections on its related base vector are widely distributed, which means there is abundant information stored.

3.3. Application of SVD in Outlier Detection. As larger singular value related to base vector which has a scattered distribution, it can be known that the bias on the base vector with small singular value will contribute more to a sample's deviation. As a result, the bias on base vector with small singular value should be given a high weight when calculating the total deviation of a sample. Before calculating sample's deviation, the singulars need to be sorted in the descending order as $\sigma_1 \geq \sigma_2 \geq \cdots \geq \sigma_n$. The calculation formula of weight is as follows:

$$w_j = \frac{\sum_{k=1}^{j} \sigma_k^2}{\sum_{k=1}^{n} \sigma_k^2}. \tag{3}$$

The bias of student sample i on new base vector v_j can be represented by Z-score. The calculation formula of Z-score is as follows:

$$z_{ij} = \frac{\widehat{s}_{ij} - \mu_j}{\sqrt{\sum_{k=1}^{m}\left(\widehat{s}_{ij} - \mu_j\right)^2}}, \tag{4}$$

where $\widehat{s}_{ij}$ is the element of $\widehat{S}$ and μ_j represents the mean of all elements in column vector $\widehat{s}_j = (\widehat{s}_{1j}, \widehat{s}_{2j}, \ldots, \widehat{s}_{nj})$. The total deviation of the sample is calculated by the following equation:

$$d_i = \sum_{j=1}^{n} z_{ij} w_j. \tag{5}$$

After calculating deviations of all samples, a self-adapting threshold will be set. If a sample's deviation goes beyond the threshold, it will be deleted as outliers to make the data set more credible. A training set with high reliability will improve the generalization performance of the predictor.

3.4. Application of SVD in Dimension Reduction. It is found that larger singular value relates to more information, which means singular value can be used to help reduce the dimension of data set. The specific way to reduce dimension is to delete singulars with small values and its related vectors in U and V. Then, matrixes can be reconstructed as $\Sigma' = \mathrm{diag}(\sigma_1, \sigma_2, \ldots, \sigma_k)$, $U' \in \mathbb{R}^{m\times k}$, and $V' \in \mathbb{R}^{n\times k}$. k is the number of reserved singulars, and formula (1) will be written as $= U'\Sigma' V'^T$.

However, even some new base vectors with small singulars might have high correlation with label, which means they can help increase the classification accuracy of the predictor. To protect them, the correlation between a base vector and sample label should be added in criterion. The importance score of a base vector is calculated by the following equation:

$$\mathrm{score}_j = \sqrt{\sigma_j} \sum_{i=1}^{n} |c_i| v_{ij}^2, \tag{6}$$

where c_i is the correction between original features and label and v_{ij} is the element of V, which represent the relationship of original features and new base vectors.

The amount of information carried by a matrix can be measure by its Frobenius norm (F-norm). The F-norm of is calculated by the following equation:

$$||S||_F = \sqrt{\sum_{i=1}^{m}\sum_{j=1}^{n} s_{ij}^2} = \sqrt{\mathrm{tr}\left(S^T S\right)} = \sqrt{\sum_{i=1}^{n} \sigma_i^2}, \tag{7}$$

where singular value σ_i is sorted by its score_i in the descending order. After base vectors with smaller scores have been deleted, the amount of remaining information can be represented by the F-norm of S'. And the percentage of the information reserved can be calculated by the following equation:

$$\mathrm{percentage} = \frac{||S'||_F}{||S||_F} = \frac{\sqrt{\sum_{i=1}^{k} \sigma_i^2}}{\sqrt{\sum_{i=1}^{n} \sigma_i^2}}, \tag{8}$$

where k is the number of reserved base vectors.

The reduction on dimension of the sample space can prevent overfitting caused by sparsity of samples and strengthen the generalization performance of the predictor. Furthermore, because the noise carried by the data set is more likely to have smaller variance than the useful information, the dimension reduction can also weaken the impact of random noise on the data set.

4. Prediction on Students' State of Mind

This section will describe how the BP algorithm can be used in training NN for predicting students' state of mind. However, it is found using only BP algorithm will lead to overfitting, so a new algorithm which combines GA is proposed to relieve overfitting. After getting a NN with good generalization performance, a method of calculating importance of different features are also proposed.

4.1. BP-NN. BP algorithm is a common algorithm in ML. So, a NN trained by BP algorithm is established to predict the student's state of mind at first. After dimension reduction, the data of student samples can be represented by $\widehat{S}' \in \mathbb{R}^{m\times k}$. Here, m is not the total number of student samples, but the sample number after deleting outliers from the data set, and k is the number of remained new features of each sample student. Also, it should be $\widehat{S}' = U'\Sigma'$, but in fact, $\widehat{S}'$ is Z-scored by (4) to fit the standard normal distribution on each features. This pretreatment will balance the learning rate of parameters in different nodes. Then, a data set $D = \{(\mathbf{x}_1, y_1), (\mathbf{x}_2, y_2), \ldots, (\mathbf{x}_m, y_m)\}$ is obtained, where $\mathbf{x}_i = \widehat{s}_i'$ is a row vector of $\widehat{S}'$ and y_i is the label of the ith student sample.

The NN that is used to predict includes three layers. The input layer consists of k nodes for inputting the data vector $\mathbf{x}_i$. The output layer has only one node for outputting the prediction $\widehat{y}_i$ of samples. The hidden layer's node number l is adjustable to fit the actual demand. I_i, H_h, and O, respectively, represent the ith input node, hth hidden node, and output node. The parameters of NN include connection weights ω_{ih} between I_i and H_h, connection weights ν_{ih} between H_h and O, thresholds γ_h of H_h, and threshold θ of O. The thresholds of nodes make NN become a nonlinear function, so that $f(\mathbf{x})$ is used as its equivalent function, and the output of NN is

$$\widehat{y}_i = f(\mathbf{x}_i). \tag{9}$$

The optimization goal of BP algorithm is usually the mean square error (MSE) between the output and label. The MSE can be calculated by the following equation:

$$E = \frac{1}{m}\sum_{i=1}^{m}\left(\widehat{y}_i - y_i\right)^2. \tag{10}$$

BP algorithm uses the strategy of adjusting parameters along the adverse direction of the gradient of E to decrease the error between prediction and real label. For example, the variation of ω_{ih} for each training round can be calculated by the following equation:

$$\Delta\omega_{ih} = -\mu \frac{\partial E}{\partial \omega_{ih}}, \tag{11}$$

where μ is the learning rate, which decides the speed of training.

Set the function between a student's features $\mathbf{x}_i$ and his state of mind y_i as $F(\mathbf{x})$. The use of BP algorithm can help decrease the difference between $f(\mathbf{x})$ and $F(\mathbf{x})$ rapidly, so that the trained NN can be used as a predictor to make good prediction on student's state of mind.

4.2. Description and Analysis on Overfitting. However, BP algorithm did not work well in the primary experiment. To test the usefulness of the predictor, the data set D was divided into training set D_{train} and test set D_{test} randomly. It can be found from Figure 1 that the variation of the MSE of the NN's prediction on D_{train} and D_{test} shows difference.

As the number of training round increases, the MSE of NN on the training set approaches 0, which means the predictor fits the training set well. However, the MSE on the test set is still at a large value. This indicates that a well-trained NN may not have high prediction accuracy on fresh samples. $F1$-measure (the harmonic mean of the recall and precision ratio) can represent the prediction accuracy of the predictor, and the mean $F1$-measure on the training set is 0.97, while the mean $F1$-measure on the test set is only 0.76. It means overfitting occurs.

Generally, the noise and unrelated features carried by the training set is considered as the reason of overfitting [20]. As the function between students' features and state of mind is set as $F(\mathbf{x})$, the influence on state of mind caused by noise and unrelated features can be defined as characteristic function $N(\mathbf{x})$, then the function of student samples in the training set is $F_{\text{train}}(\mathbf{x}) = F(\mathbf{x}) + N_{\text{train}}(\mathbf{x})$ and the function of student samples in the test set is $F_{\text{test}}(\mathbf{x}) = F(\mathbf{x}) + N_{\text{test}}(\mathbf{x})$.

All of the parameters in NN can be represented as $\mathbf{p} = (\omega_{11}, \ldots, \omega_{kj}, \nu_1, \ldots, \nu_l, \gamma_1, \ldots, \gamma_l, \theta)$. Let MSE function $M(\mathbf{p})$ be the function from $\mathbf{p}$ to the MSE between prediction and labels, and it can be known that the parameters of optimal NN is the global minimum point $\mathbf{p}^g$ of $M(\mathbf{p})$. Due to the difference between $F_{\text{train}}(\mathbf{x})$ and $F_{\text{test}}(\mathbf{x})$, there will be difference between $M_{\text{train}}(\mathbf{p})$ and $M_{\text{test}}(\mathbf{p})$, thus difference between p^g_{train} and p^g_{test}. If a NN selects p^g_{train} as its optimal parameter, it will fit $F_{\text{train}}(\mathbf{x})$ well, but the accuracy of its prediction on the test set may be not good. That is why overfitting occurs in BP-NN.

4.3. A Method of Relieving Overfitting. Although the experiment shows there is big difference between p^g_{train} and p^g_{test}, $M_{\text{train}}(\mathbf{p})$ and $M_{\text{test}}(\mathbf{p})$ should be approximate. This can be verified by putting "prospect holes" on them. Putting "prospect holes" means to use same input $\mathbf{p}_0$ to predict different sample sets and compare the difference between $M_{\text{train}}(\mathbf{p}_0)$ and $M_{\text{test}}(\mathbf{p})$. After putting "prospect holes" randomly for 1000 times, the calculated mean percentage of MSE difference is 1.14%, which verifies the approximation. As a result, there can be several similar local minimum points $\mathbf{p}^l$ in different $M(\mathbf{p})$ values. If the NN with parameters

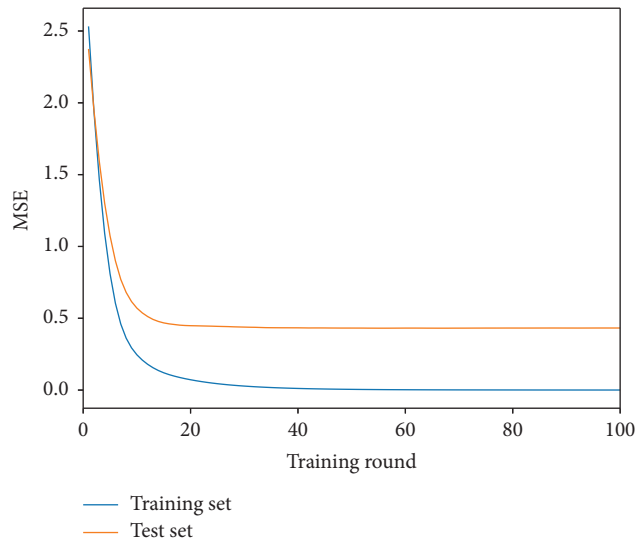

Figure 1: MSE on different data set.

of p^g_{train} does not fit the test set, then one of the $\mathbf{p}^l_{\text{train}}$ values which has high similarity with one of the $\mathbf{p}^l_{\text{test}}$ values can be used as the approximate optimal solution. Although the $M_{\text{train}}(\mathbf{p}^l_{\text{train}})$ is slightly larger than $M_{\text{train}}(\mathbf{p}^g_{\text{train}})$, it can fit both the training set and the test set well, which means to have good generalization performance.

In fact, the above method changes the criterion from only considering the MSE value to considering both the MSE values and the similarity with the test set. The optimization task of the MSE value can be handled by BP algorithm as usual. However, the similarity with the test set is difficult to quantify, but it can be indicated by $F1$-measure of prediction on the test set.

To improve the similarity, an evolutionary algorithm is needed, so GA is introduced. It is known that different initial parameters of NN $\mathbf{p}^i$ can make the network converge to different $\mathbf{p}^l$ values when the training set is constant [21], and the training process can be represented as $\mathbf{p}^l = T(\mathbf{p}^i)$. So that $\mathbf{p}^i$ can be regarded as an individual of population in GA, and population can be represented by $P = (\mathbf{p}^i_1, \mathbf{p}^i_2, \ldots, \mathbf{p}^i_N)$ where N is the population size. After the NN with p^i has been trained, the fitness of the individual will be calculated as the $F1$-measure on the test set. After the operations of mate, mutate, and selection to generate, p^i tends to fit both the training set and test set well.

However, using D_{test} to calculate individuals' fitness means D_{test} is also involved in the closed loop of algorithm, thus it loses the representation on fresh samples. To test whether the generalization performance of NN is improved, it is necessary to separate a set of samples before the algorithm to show the change of prediction accuracy on fresh samples. This sample set is called verification set D_{ver}.

After the primary experiment, if D_{test} which is used to calculate fitness is constant, the prediction accuracy of the test set will be improved greatly, but the prediction accuracy on verification set does not have a distinct change. This may be caused by the difference between $F_{\text{test}}(\mathbf{x})$ and $F(\mathbf{x})$. In order to make the algorithm effective, D_{test} is divided into

three parts as temporary test sets D_{temp} randomly, and a punishment is added if the network only performs well in one of the temporary test sets. Then, the fitness of individuals will be calculated as follows:

$$\text{fitness} = F1_{\text{mean}} - \sqrt{\frac{1}{3}\sum_{i=1}^{3}\left(F1_i - F1_{\text{mean}}\right)^2}. \tag{12}$$

The $F1_i$ in (12) is the $F1$-measure on the ith D_{temp}, and $F1_{\text{mean}}$ is the mean of $F1_i$. After modification of the algorithm, each individual faces different D_{temp} values when calculating fitness. This method will dilute $N_{\text{test}}(\mathbf{x})$, so that the evolutionary direction is to fit $F(\mathbf{x})$ rather than to fit $F_{\text{test}}(\mathbf{x})$. It can make sure that the NN is going to have better generalization performance.

It has been found that overfitting when predicting students' state of mind is caused by difference between $F_{\text{train}}(\mathbf{x})$ and $F(\mathbf{x})$, so it will be of benefit to use the above algorithm. Just as the process represented in Figure 2, the whole data set is divided into D_{train}, D_{test}, and D_{ver} at first. Then, the initial P is generated randomly, and all of the NNs with $\mathbf{p}^i$ will be trained by the same training set. To keep genetic advantage of the individual with high fitness, elite strategy is used when generating the next population. This strategy produces offsprings by mating and mutating before selecting individuals in the next population, and the offspring has the same size of current population which is N. All of the individuals in the current population and offsprings are sorted by their fitness in the descending order, and the first N individuals are selected as the next population. When the population reaches the largest generation, the individual that relates to the NN who has the largest prediction accuracy on D_{ver} will be chosen as optimal solution $\mathbf{p}^o$. Finally, a new network whose initial parameter is $\mathbf{p}^o$ will be trained by the whole data set to get the predictor that can predict students' state of mind with high accuracy.

4.4. Feature Importance Calculation. BP algorithm combined with GA helps obtain a predictor on students' state of mind with high accuracy, but the predictor is a "black box" which means the mechanism of making prediction is still unknown. Though NN is known as an unilluminated method, there are still some ways to evaluate the importance of different features [22]. After a NN is trained by D, it has nearly perfect prediction accuracy on D. But if one feature is sheltered (replace the mean of this feature. which is 0 after z-scored) in each student sample, there would likely be a recession on accuracy [23]. Then, the importance of features in D can be calculated by the following equation:

$$im_i = F1_i' - F1_0, \tag{13}$$

where $F1_0$ is the accuracy before sheltering and $F1_i'$ is the accuracy after ith has been sheltered. The features in D are abstraction of original features, which means the importance of original features can also be calculated according to V' which represents the relationship between new features and original features by the following equation:

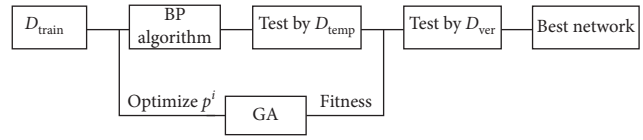

Figure 2: Structure of the algorithm.

$$im_i' = \sum_j = 1^k im_j v_{ij}. \tag{14}$$

The importance analysis on single NN lacks credibility, so the total importance of original features is accumulated after analyzing 500 NNs. The importance can help colleges know what is important in guiding students' state of mind.

5. Experiment Results and Discussion

This section will show the experiment results which can support the hypotheses that have been proposed above. They can also show the actual effectiveness of this new method on predicting students' state of mind.

5.1. Implementation Details. The first step of experiment is the pretreatment of data. The raw data collected are already numbered according to the order of answers or whether an answer has been ticked, and the data set expansion strategy described in Section 3.1 is used to make it regular. Then, the whole data set is regard as a matrix, and SVD is performed. The attained matrixes after SVD are used in the process of outlier detection and dimension reduction which are described in Sections 3.3 and 3.4. After pretreatment, each sample is represented by a vector in the new coordinate system and a label of state of mind. Then, the samples are used to start the operation of the algorithm described in Section 4.3. The algorithm will train many NNs, and the NN with best generalization performance will be selected to make precise prediction on students' state of mind. The rest of the trained NNs also show part of inner connection between students' behaviors and their state of mind, so all of the trained NNs are used to calculate importance of different features by the method described in Section 4.4.

5.2. Experiment on Data Pretreatment. The pretreatment of data set includes outlier detection and dimension reduction. Both of them have been detailed in Section 3. After calculating deviations of all samples, the distribution of deviations is represented in Figure 3. It can be found that the distribution of sample's deviation roughly conforms to the normal distribution. The normal distribution which is shown in Figure 3 is obtained by fitting the original distribution approximately. The mean of normal distribution is $\mu = 105.18$, and the standard deviation is $\sigma = 13.97$. Then the self-adaption threshold is calculated by threshold $= \mu + 2\sigma = 133.12$, and the number of outliers is 27.

After checking the content of deleted outliers, many of them are found with contradictions in context. For example, a student said his counselor is the one who gives the best help in development of his state of mind, but he also said he was

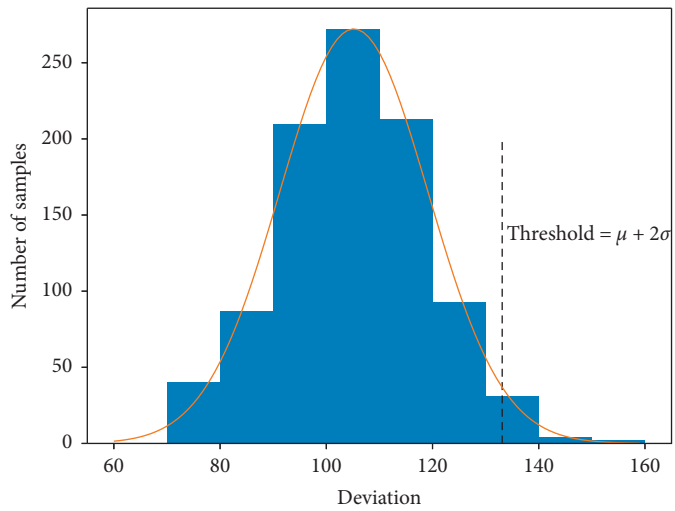

Figure 3: The distribution of samples' deviation.

dissatisfied with counselors' work. This might be his real thought, but will confuse the predictor, so he is removed from the sample set. Other outliers can make mistakes while answering questions, such as making multiple choices on single-choice question. It will also change the potential importance of a variable so that they should be removed. The experiment result on outlier detection shows that the algorithm is effective and reasonable. The application of outlier detection will purify the data set and help improve the generalization performance of the predictor.

Figure 4 shows the change in the number of reserved inputs with the increase in percentage, which represents the percentage of reserved information calculated by F-norm. It can be found that the number of inputs have a sharp increase when the percentage is large. It confirms that there are many inputs related to small singular values and have a low correlation with label that should be deleted to reduce the dimension of sample space. In experiment, 90% information is reserved, and the number of inputs changes from 159 to 71.

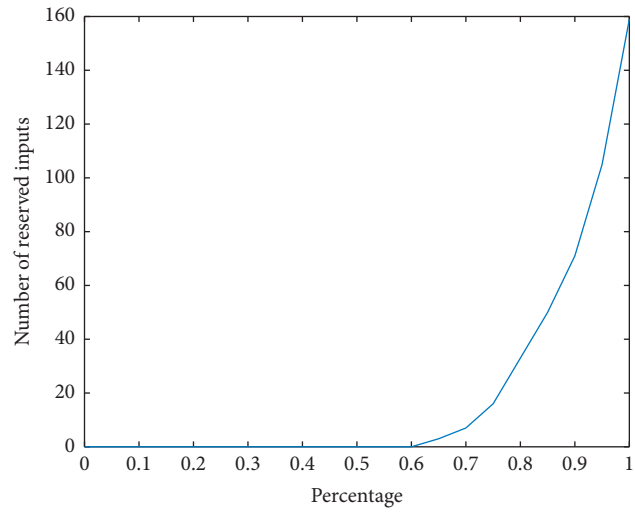

Figure 4: Number of reserved inputs in different percentages.

5.3. Experiment Results on Overfitting Relief. The overfitting relief experiment is designed according to the algorithm mentioned in Section 4. Abnormal samples have been previously excluded by the outlier detection based on SVD, and 926 samples are used. Under the principle of randomness, 70% samples are selected as D_{train}, 20% samples are selected as D_{test}, and the rest 10% are used as D_{ver}. The number of individuals in a population is set to 10, and the maximum number of generations is set to 50. The population crossover rate is 0.7, and the mutation rate is 0.3. Figures 5(a) and 5(b) show the change on population's mean $F1$-measure on different data sets when using constant D_{test} to calculate individuals' fitness, and Figures 6(a) and 6(b) show the changes when using D_{temp} to calculate fitness.

Figures 5(a) and 5(b) show the different tendency of population's mean $F1$-measure on D_{test} and D_{ver}. It can be found the prediction accuracy on D_{test} has an obvious increase, but the prediction accuracy on D_{ver} decreases slightly, which means population tends to fit $F_{\text{test}}(\mathbf{x})$ when using D_{test} to calculate fitness. If $D_{\text{temp}}s$ are used, it can be found in Figure 6(a) that the prediction accuracy on D_{test} does not reach the same increase shown in Figure 5(a). But on D_{ver}, the prediction accuracy increases obviously. This tells the hypothesis in Section 4 is reliable.

In Figure 6(b), it can be observed that the mean $F1$-measure of the initial population on the verification set is 0.7662. After the evolution, the mean $F1$-measure of the last generation reaches 0.8080. When applying the network as a predictor in real engineering, the one with best accuracy from the current population will be chosen. The data show that the biggest $F1$-measure is 0.8315, which represents high prediction accuracy. With reliable prediction of students' state of mind, colleges can make effective guidance to help students get rid of bad influences of information explosion.

5.4. Experiment on Feature Importance. To evaluate the importance of different students' features, 500 NNs are trained by the whole data set D. The calculated importance of

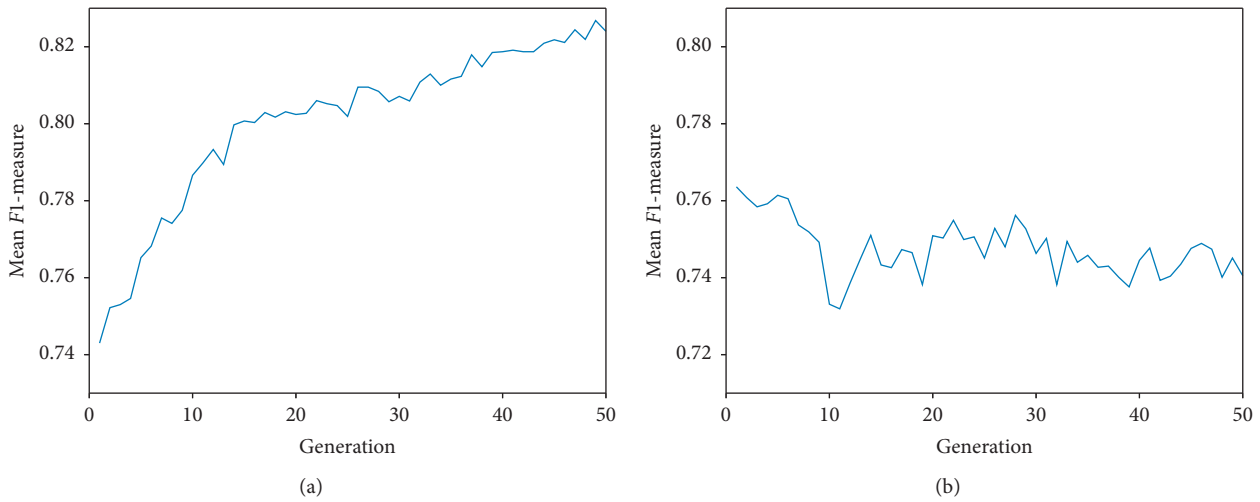

Figure 5: Using constant test set to calculate fitness. (a) Test set. (b) Verification set.

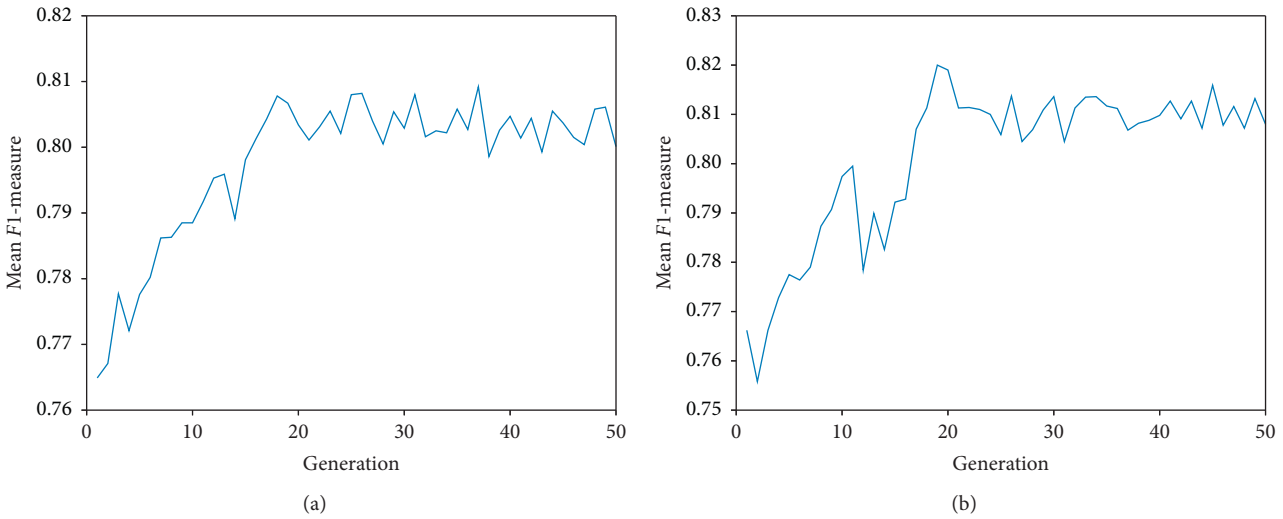

Figure 6: Using temporary test set to calculate fitness. (a) Temporary test set. (b) Verification set.

original features are partly shown in Table 1. The features are sorted by their absolute importance and only top 10 are listed in Table 1. It can be found some features positively relate to students' state of mind while others negatively. Also, some features show a potential causal relationship with state of mind such as "focus on politics news" and "benefit more from ideology education," while others may not such as "use QQ often" and "benefit more from club activities" though they do have correlation. It can also be noticed that the features classified as "individual development" have the best power in indicating students' state of mind.

With analysis on feature importance, colleges will be aware of what are the key points of guidance on students' state of mind. For example, they can help students interest in politics news, strengthen the relationship between students and their tutors, and enrich social practice. These macroscopic policies can combine with the microscopic guidance on students' state of mind and enhance overall effectiveness.

6. Conclusion

The main purpose of this paper is to change the traditional method on mining humans' opinion to make it effective when predicting students' state of mind. This changed method requires more data aspects of samples, and using a questionnaire is a good choice to get comprehensive data about students. However, the expansion of sample space's dimension makes samples sparser and causes overfitting while training NN. To solve this problem, SVD is used to reduce the dimension of sample space directly, and a closed loop based on GA is added to help NN have better prediction accuracy on fresh samples. The result of the experiment shows that the new algorithm works well and the predictor obtained has good generalization performance. Also a simple method of calculating features' importance is proposed, which can help colleges make policies.

The new method lets the predictor make reliable predictions on students' state of mind. With these predictions,

Table 1: Feature importance.

Rank	Importance	Description	Classification
1	1.5069	Focus on politics news	Individual development
2	0.7620	Benefit more from tutor	Individual development
3	0.7487	Focus on the broadcasting of *The truth of 731 troop* in NHK	Focus of attention
4	0.7358	Think addiction to smartphone is common	Individual development
5	−0.7055	Focus on relaxation news	Individual development
6	−0.6830	Benefit more from club activities	Individual development
7	−0.6364	Use QQ often	Individual development
8	0.6281	Satisfy on school's politics education	School work evaluation
9	0.5388	Benefit more from ideology education	Individual development
10	0.5348	Benefit more from social practice	Individual development

colleges can apply guidance associated with students' personal experience which will make it more genial and effective. Furthermore, the macroscopic policies made according to feature importance can supplement microscopic guidance to have better effectiveness.

For further research, a questionnaire used to collect data will be redesigned. The aim of questions in the questionnaire should be more covert to make sure to collect real information, and the content of questions should be more various especially in "individual development" to collect more data that might be necessary. Also, the classification problem on students' state of mind will be changed into quantization problem to get a student's certain score on different aspects of state of mind. The method of calculating feature importance will be improved too. These future studies will be able to further strengthen the effect of guidance on students' state of mind.

Data Availability

The students' state of mind data used to support the findings of this study are included within the article.

Conflicts of Interest

The authors declare that they have no conflicts of interest.

Acknowledgments

This work was supported by the Fundamental Research Funds for the Central Universities (3102018jcc041 and 3102018jcc028) and the 2011 Collaborative Center Innovation Project under Grant QBXT-17-7.

References

[1] N. A. Cheever, L. D. Rosen, L. M. Carrier, and A. Chavez, "Out of sight is not out of mind: the impact of restricting wireless mobile device use on anxiety levels among low, moderate and high users," *Computers in Human Behavior*, vol. 37, pp. 290–297, 2014.

[2] M. Samaha and N. S. Hawi, "Relationships among smartphone addiction, stress, academic performance, and satisfaction with life," *Computers in Human Behavior*, vol. 57, pp. 321–325, 2016.

[3] L. Zhao, J. Yin, and Y. Song, "An exploration of rumor combating behavior on social media in the context of social crises," *Computers in Human Behavior*, vol. 58, pp. 25–36, 2016.

[4] Z. Demirtas, "The relationship between school culture and student achievement," *Egitim Ve Bilim-Education and Science*, vol. 35, no. 158, pp. 3–13, 2010.

[5] L. Yu and S. Ding, "Broad learning based optimization and prediction of questionnaire survey: application to mind status of college students," *Complexity*, vol. 2018, Article ID 5736030, 9 pages, 2018.

[6] N. Srivastava, G. Hinton, A. Krizhevsky, I. Sutskever, and R. Salakhutdinov, "Dropout: a simple way to prevent NNs from overfitting," *Journal of Machine Learning Research*, vol. 15, pp. 1929–1958, 2014.

[7] B. Pang, L. Lee, and S. Vaithyanathan, "Thumbs up?: sentiment classification using machine learning techniques," *in Proceedings of the ACL-02 conference on Empirical methods in natural language processing—EMNLP '02*, J. Hajic and Y. Matsumoto, Eds., vol. 10, pp. 79–86, Association for Computational Linguistics, Stroudsburg, PA, USA, July 2002.

[8] F. H. Khan, S. Bashir, and U. Qamar, "TOM: Twitter opinion mining framework using hybrid classification scheme," *Decision Support Systems*, vol. 57, pp. 245–257, 2014.

[9] J. Zhan, H. T. Loh, and Y. Liu, "Gather customer concerns from online product reviews—a text summarization approach," *Expert Systems with Applications*, vol. 36, no. 2, pp. 2107–2115, 2009.

[10] Y. Zhou, J. Chen, and Y. Kuo, "Fairness resource allocation for parallel multi-radio access in cognitive multi-cell," *Wireless Personal Communications*, vol. 88, no. 3, pp. 587–602, 2016.

[11] M. Kosinski, D. Stillwell, and T. Graepel, "Private traits and attributes are predictable from digital records of human behavior," *Proceedings of the National Academy of Sciences of the United States of America*, vol. 110, no. 15, pp. 5802–5805, 2013.

[12] J. Baik, K. Lee, S. Lee, Y. Kim, and J. Choi, "Predicting personality traits related to consumer behavior using SNS analysis," *New Review of Hypermedia and Multimedia*, vol. 22, no. 3, pp. 189–206, 2016.

[13] B. Pang and L. Lee, "Opinion mining and sentiment analysis," *Foundations and Trends in Information Retrieval*, vol. 1, no. 2, pp. 1–135, 2008.

[14] M. Tsytsarau and T. Palpanas, "Survey on mining subjective data on the web," *Data Mining and Knowledge Discovery*, vol. 24, no. 3, pp. 478–514, 2012.

[15] K. Ravi and V. Ravi, "A survey on opinion mining and sentiment analysis: tasks, approaches and applications," *Knowledge-Based Systems*, vol. 89, pp. 14–46, 2015.

[16] C. W. Topp, S. D. Østergaard, S. Sondergaard, and P. Bech, "The WHO-5 well-being Index: a systematic review of the literature," *Psychotherapy and Psychosomatics*, vol. 84, no. 3, pp. 167–176, 2015.

[17] S. N. Garfinkel, A. K. Seth, A. B. Barrett, K. Suzuki, and H. D. Critchley, "Knowing your own heart: distinguishing interoceptive accuracy from interoceptive awareness," *Biological Psychology*, vol. 104, pp. 65–74, 2015.

[18] A. L. Duckworth and D. S. Yeager, "Measurement matters: assessing personal qualities other than cognitive ability for educational purposes," *Educational Researcher*, vol. 44, no. 4, pp. 237–251, 2015.

[19] G. H. Golub and W. Kahan, "Calculating the singular values and pseudo-inverse of a matrix," *Journal of the Society for Industrial and Applied Mathematics*, vol. 2, no. 2, pp. 205–224, 1965.

[20] D. M. Hawkins, "The problem of overfitting," *Journal of Chemical Information and Computer Sciences*, vol. 44, no. 1, pp. 1–12, 2004.

[21] C. Ren, N. An, J. Z. Wang, L. Li, B. Hu, and D. Shang, "Optimal parameters selection for BP NN based on particle swarm optimization: a case study of wind speed forecasting," *Knowledge-Based Systems*, vol. 56, pp. 226–239, 2013.

[22] R. Guidotti, A. Monreale, S. Ruggieri, F. Turini, F. Giannotti, and D. Pedreschi, "A survey of methods for explaining black box models," *ACM Computing Surveys*, vol. 51, no. 5, pp. 1–42, 2018.

[23] W. Samek, A. Binder, G. Montavon, S. Lapuschkin, and K.-R. Müller, "Evaluating the visualization of what a deep neural network has learned," *IEEE Transactions on Neural Networks and Learning Systems*, vol. 28, no. 11, pp. 2660–2673, 2017.

Hindawi
Complexity
Volume 2019, Article ID 5034025, 15 pages
https://doi.org/10.1155/2019/5034025

Research Article

Some Novel Complex Dynamic Behaviors of a Class of Four-Dimensional Chaotic or Hyperchaotic Systems Based on a Meshless Collocation Method

Du Mingjing[1] **and Yulan Wang**[2]

[1]*Institute of Computer Information Management, Inner Mongolia University of Finance and Economics, Hohhot 010070, China*
[2]*Department of Mathematics, Inner Mongolia University of Technology, Hohhot 010051, China*

Correspondence should be addressed to Yulan Wang; wylnei@163.com

Received 29 May 2019; Revised 15 August 2019; Accepted 10 September 2019; Published 20 October 2019

Guest Editor: Murari Andrea

In the field of complex systems, there is a need for better methods of knowledge discovery due to their nonlinear dynamics. The numerical simulation of chaotic or hyperchaotic system is mainly performed by the fourth-order Runge–Kutta method, and other methods are rarely reported in previous work. A new method, which divides the entire intervals into N equal subintervals based on a meshless collocation method, has been constructed in this paper. Some new complex dynamical behaviors are shown by using this new approach, and the results are in good agreement with those obtained by the fourth-order Runge–Kutta method.

1. Introduction

This paper shows some novel complex dynamical behaviors of a class of four-dimensional chaotic or hyperchaotic systems, and a four-dimensional system (1) is adopted as an example to elucidate the solution process.

We consider the following four-dimensional system:

$$\begin{bmatrix} \frac{dx}{dt} \\ \frac{dy}{dt} \\ \frac{dz}{dt} \\ \frac{dw}{dt} \end{bmatrix} = \begin{bmatrix} a_{11} & a_{12} & a_{13} & a_{14} \\ a_{21} & a_{22} & a_{23} & a_{24} \\ a_{31} & a_{32} & a_{33} & a_{34} \\ a_{41} & a_{42} & a_{43} & a_{44} \end{bmatrix} \begin{bmatrix} x \\ y \\ z \\ w \end{bmatrix} - \begin{bmatrix} 0 \\ a_1 xz \\ a_2 x^2 + a_3 y^2 + a_4 xy \\ 0 \end{bmatrix}, \quad 0 \le t \le T, \tag{1}$$

with the following initial conditions:

$$\begin{aligned} x(0) &= c_1, \\ y(0) &= c_2, \\ z(0) &= c_3, \\ w(0) &= c_4, \end{aligned} \tag{2}$$

where $x, y, z,$ and w are the state variables and $a_{ij}, a_i,$ and c_i are the positive parameters of the system. We assume that the solution of systems (1) and (2) exists and it is unique.

In recent years, some new four-dimensional chaotic or hyperchaotic systems [1–7] are presented. In [1], the authors presented a four-dimensional hyperchaotic system and investigated and analyzed some complex dynamical behaviors such as ultimate boundedness, chaos, and hyperchaos. In [2], the authors reported a four-dimensional dissipative chaotic system, and the coexistence of rich chaotic dynamics in the system was investigated through the Lyapunov spectrum, bifurcation diagram, Poincarė map, frequency spectrum, and attractor plot. In [3], the authors discussed the synchronization between two chaotic dynamical systems of different order using an adaptive control scheme. In [4],

a four-dimensional autonomous system with complex hyperchaotic dynamics was presented, and the complex dynamical behaviors were investigated by dynamical analysis approaches, such as time series, Lyapunov exponent spectra, bifurcation diagram, and phase portraits. In [1–8], the authors used the fourth-order Runge–Kutta method to simulate chaotic or hyperchaotic systems. In this paper, we mainly introduce an improved meshless collocation method to simulate hyperchaotic systems with long-time dynamic behavior.

2. The Meshless Collocation Method

A hyperchaotic system has two or more positive Lyapunov exponents. At least four dimensions for the integer order continuous autonomous system are needed in order to generate a hyperchaotic system. Chaotic sequences of such system are more dependent on the parameters and initial conditions, and their dynamic behaviors are more difficult to predict. Its attractors are more complex than general attractor. Diffusion and confusion can be carried out simultaneously in several dimensional spaces. Therefore, the hyperchaotic system has a distinct advantage over low dimensional chaos, and its high-precision numerical solution is very important.

In this section, we introduce an improved meshless collocation method to solve the four-dimensional chaotic or hyperchaotic system, and the main points are as follows.

We transform system (1) into equation (5) using the meshless collocation method [9]. We construct the following linear iterative format of system (1):

$$\begin{bmatrix} \frac{dx_n}{dt} \\ \frac{dy_n}{dt} \\ \frac{dz_n}{dt} \\ \frac{dw_n}{dt} \end{bmatrix} = \begin{bmatrix} a_{11} & a_{12} & a_{13} & a_{14} \\ a_{21} & a_{22} & a_{23} & a_{24} \\ a_{31} & a_{32} & a_{33} & a_{34} \\ a_{41} & a_{42} & a_{43} & a_{44} \end{bmatrix} \begin{bmatrix} x_n \\ y_n \\ z_n \\ w_n \end{bmatrix} - \begin{bmatrix} 0 \\ a_1 x_{n-1} z_n \\ a_2 x_{n-1} x_n + a_3 y_{n-1} y_n + a_4 x_{n-1} z_n \\ 0 \end{bmatrix}. \tag{3}$$

Using the meshless collocation method, $x_n(t), y_n(t), z_n(t), w_n(t)\,(n = 1, 2, 3, \ldots)$ can be written as [9, 10]

$$x_n(t) = \sum_{j=1}^{M} r_j(t) x_n\left(t_j\right),$$

$$y_n(t) = \sum_{j=1}^{M} r_j(t) y_n\left(t_j\right),$$

$$z_n(t) = \sum_{j=1}^{M} r_j(t) z_n\left(t_j\right),$$

$$w_n(t) = \sum_{j=1}^{M} r_j(t) w_n\left(t_j\right), \tag{4}$$

where the barycentric interpolation primary function $r_j(t) = (\omega_j/t - t_j)/\sum_{k=1}^{M}(\omega_k/t - t_k)$ and $\omega_j = 1/\prod_{i=1, j\neq k}^{M}(t_i - t_j)$ is the center of gravity interpolation weight.

Inserting (4) into (3) and then letting $t = t_i$, the format (3) can be transformed into the following linear algebraic equations [9, 10]:

$$\begin{bmatrix} D - a_{11}I & -a_{12}I & -a_{13}I & -a_{14}I \\ -a_{21}I & D - a_{22}I & -a_{23}I + a_1\mathrm{diag}\left(x_{n-1}\right) & -a_{24}I \\ -a_{31}I + a_2\mathrm{diag}\left(x_{n-1}\right) & -a_{32}I + a_3\mathrm{diag}\left(y_{n-1}\right) & D - a_{33}I + a_4\mathrm{diag}\left(x_{n-1}\right) & -a_{34}I \\ -a_{41}I & -a_{42}I & -a_{43}I & D - a_{44}I \end{bmatrix} \begin{bmatrix} x_n \\ y_n \\ z_n \\ w_n \end{bmatrix} = \begin{bmatrix} 0 \\ 0 \\ 0 \\ 0 \end{bmatrix}, \tag{5}$$

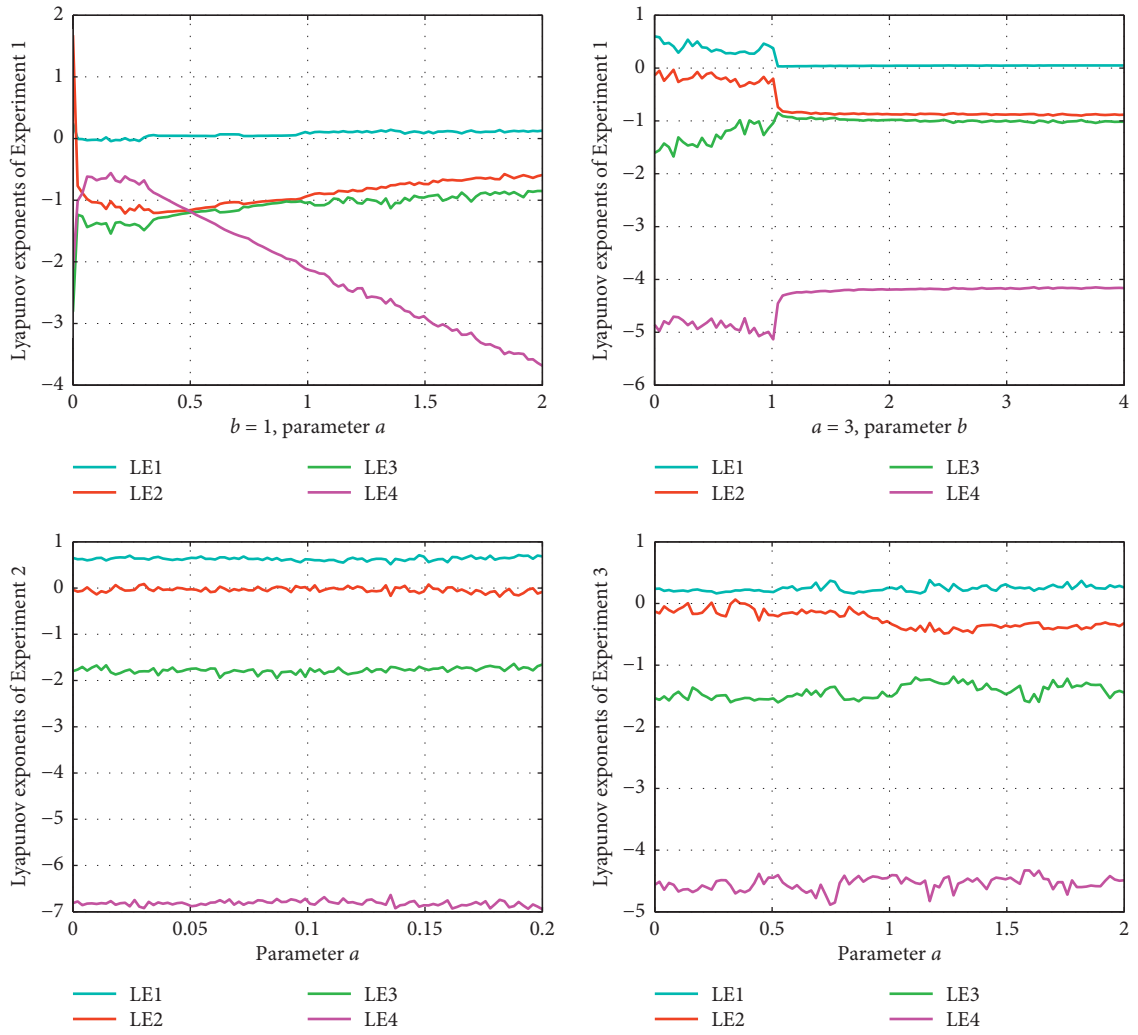

Figure 1: Lyapunov exponents of Experiment 1–3.

where $D = (r_j'(t_i))_{i,j=1,2,\ldots,M}$ is the M-order matrix, I is the M-order unit matrix, and the vector $[x_n, y_n, z_n, w_n] = [x_n(t_1), x_n(t_2), \ldots, x_n(t_M), y_n(t_1), y_n(t_2), \ldots, y_n(t_M), z_n(t_1), \ldots, z_n(t_M), w_n(t_1), \ldots, w_n(t_M)]$.

Schneiaer and Werner [11] introduced the meshless collocation method by using higher-order rational interpolation functions. The barycentric representation of the rational interpolation function possesses various advantages in comparison with other representations such as continued fractions. Baltensperger and Berrut [12] introduced the meshless collocation method for solving general hyperbolic problems and proved its stability and its convergence in weighted norms. Li and Wang [13, 14] presented the algorithm and program of the meshless collocation method and had indicated the meshless collocation method has a high accuracy, good stability, and convergence [15–19]. However, the method cannot apply directly the solving of hyperchaotic system due to great errors. Therefore, an improved mesheless collocation method, which divides the entire intervals $[0, T]$ into N equal subintervals, is constructed in the following section.

We obtain the solution of equation (5) on every intervals $[T_j, T_{j+1}]$.

Dividing the interval $[0, T]$ into N equal subintervals $[T_j, T_{j+1}]$, $j = 0, 1, \ldots, N-1$, letting $\Delta T = T_{j+1} - T_j$ with $T_0 = 0$ and $T_N = T$. On $[T_0, T_1]$, selecting the second kind Chebyshev nodes $t_i = T_1/2\,(1 - \cos(\pi i/M))$, $i = 0, 1, 2, \ldots, M$, and using (4) and the initial conditions (2), we can get

$$\begin{aligned}
\sum_{i=1}^{M} r_i(0) x_n(t_i) &= c_1,\\
\sum_{i=1}^{M} r_i(0) y_n(t_i) &= c_2,\\
\sum_{i=1}^{M} r_i(0) z_n(t_i) &= c_3,\\
\sum_{i=1}^{M} r_i(0) w_n(t_i) &= c_4.
\end{aligned} \tag{6}$$

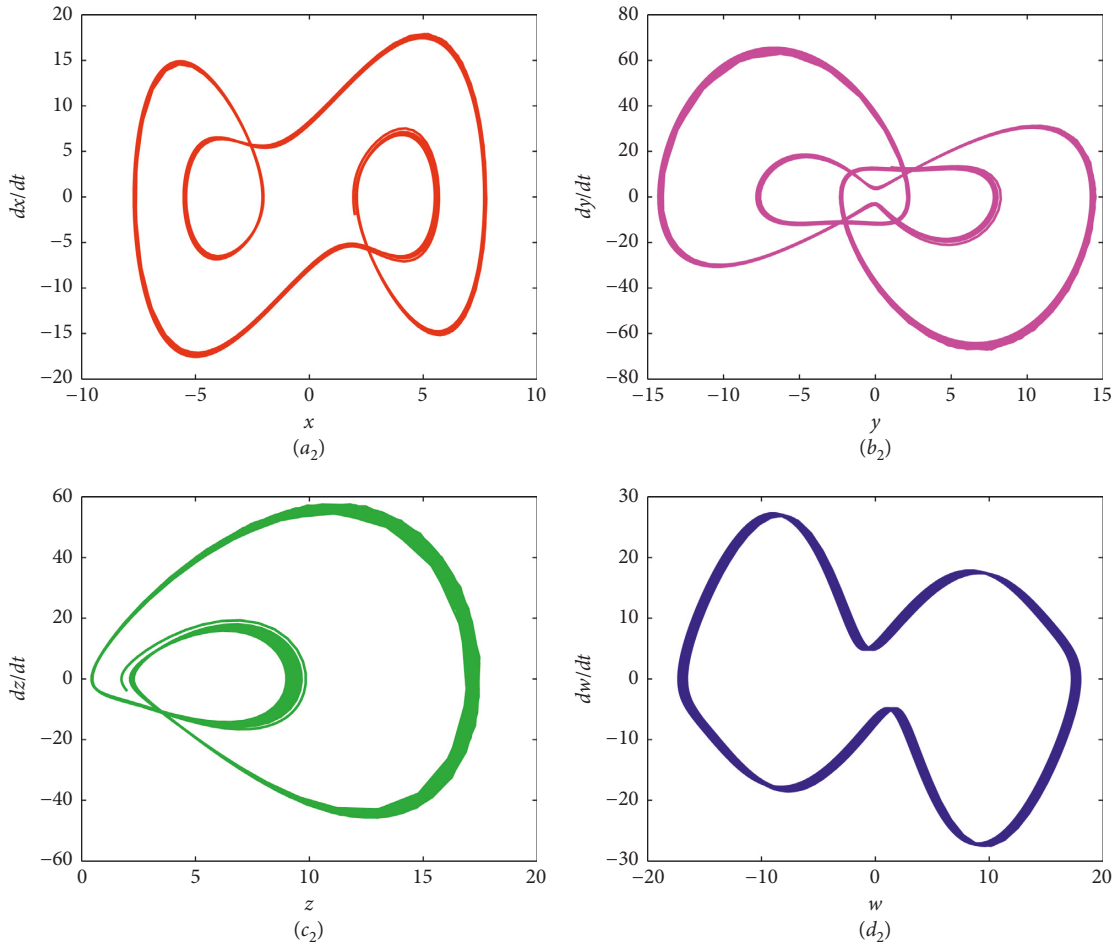

FIGURE 2: Phase diagrams of Experiment 1 with $a = 2, b = 1$, $t = 1000$: (a_2) phase diagram of x; (b_2) phase diagram of y; (c_2) phase diagram of z; (d_2) phase diagram of w.

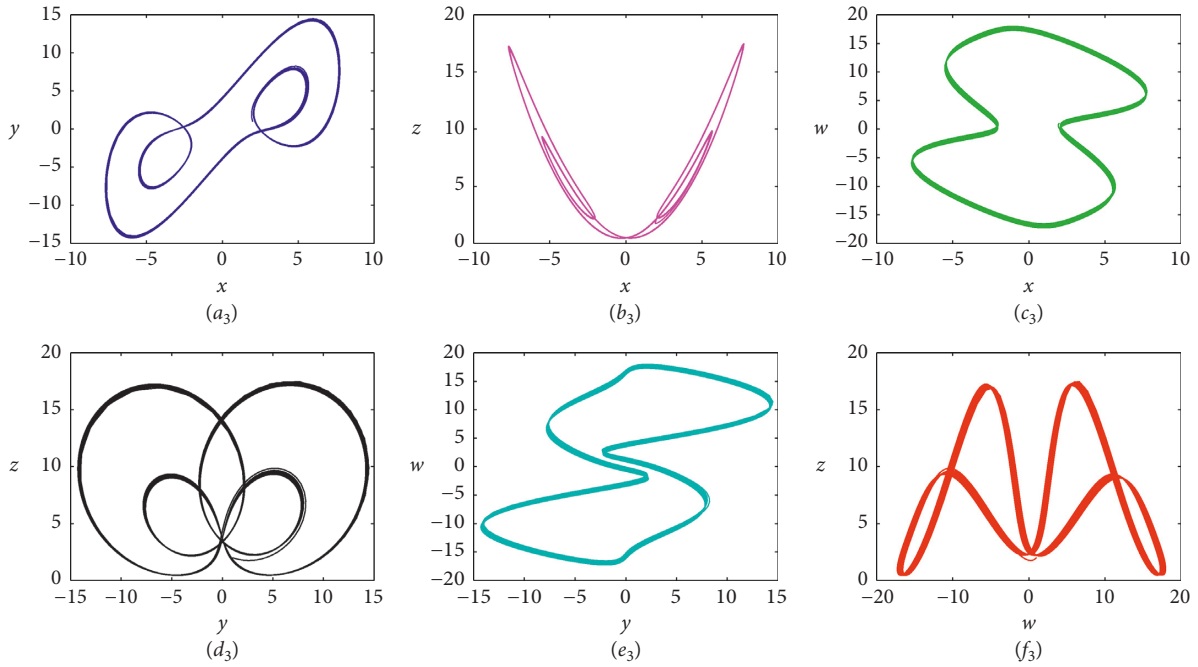

FIGURE 3: Phase portraits of Experiment 1 with $a = 2, b = 1$, $t = 1000$: (a_3) on $x - y$ plane; (b_3) on $x - z$ plane; (c_3) on $x - w$ plane; (d_3) on $y - z$ plane; (e_3) on $y - w$ plane; (f_3) in $z - w$ space.

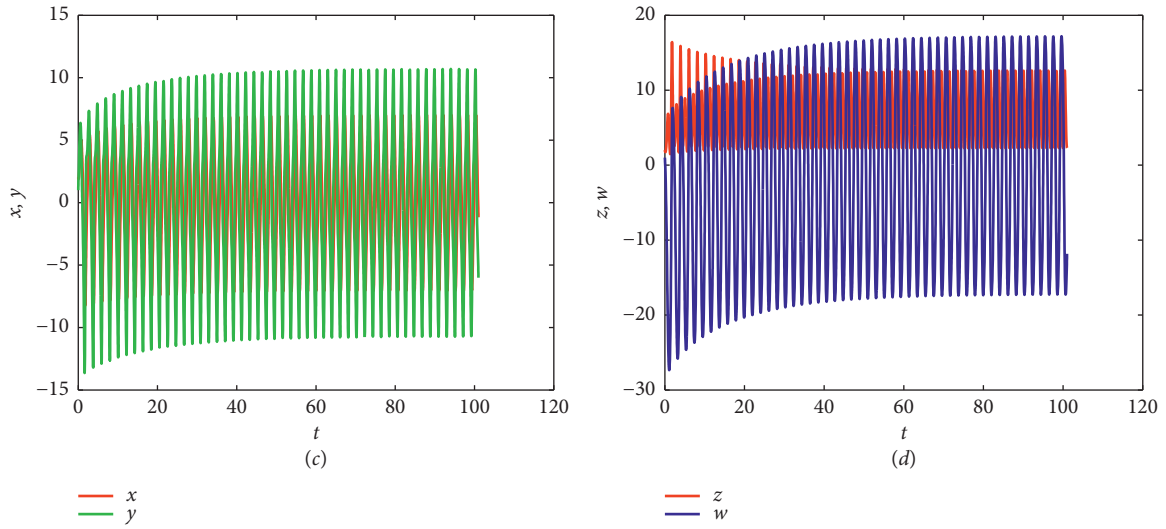

Figure 4: Time evolutions of Experiment 1 with $a = 3$, $b = 5$: (c) x, y states; (d), z, w states.

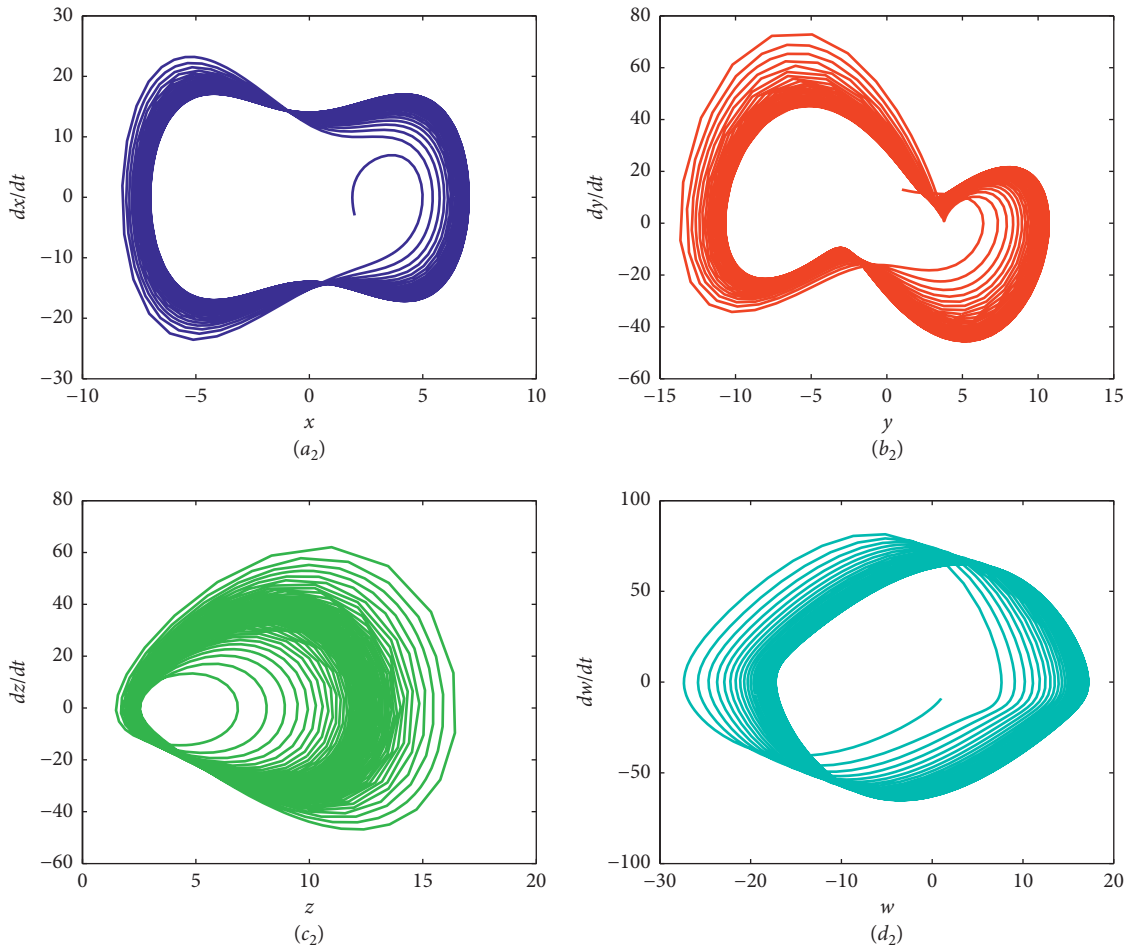

Figure 5: Phase diagrams of Experiment 1 with $a = 3, b = 5$, $t = 100$: (a_2) phase diagram of x; (b_2) phase diagram of y; (c_2) phase diagram of z; (d_2) phase diagram of w.

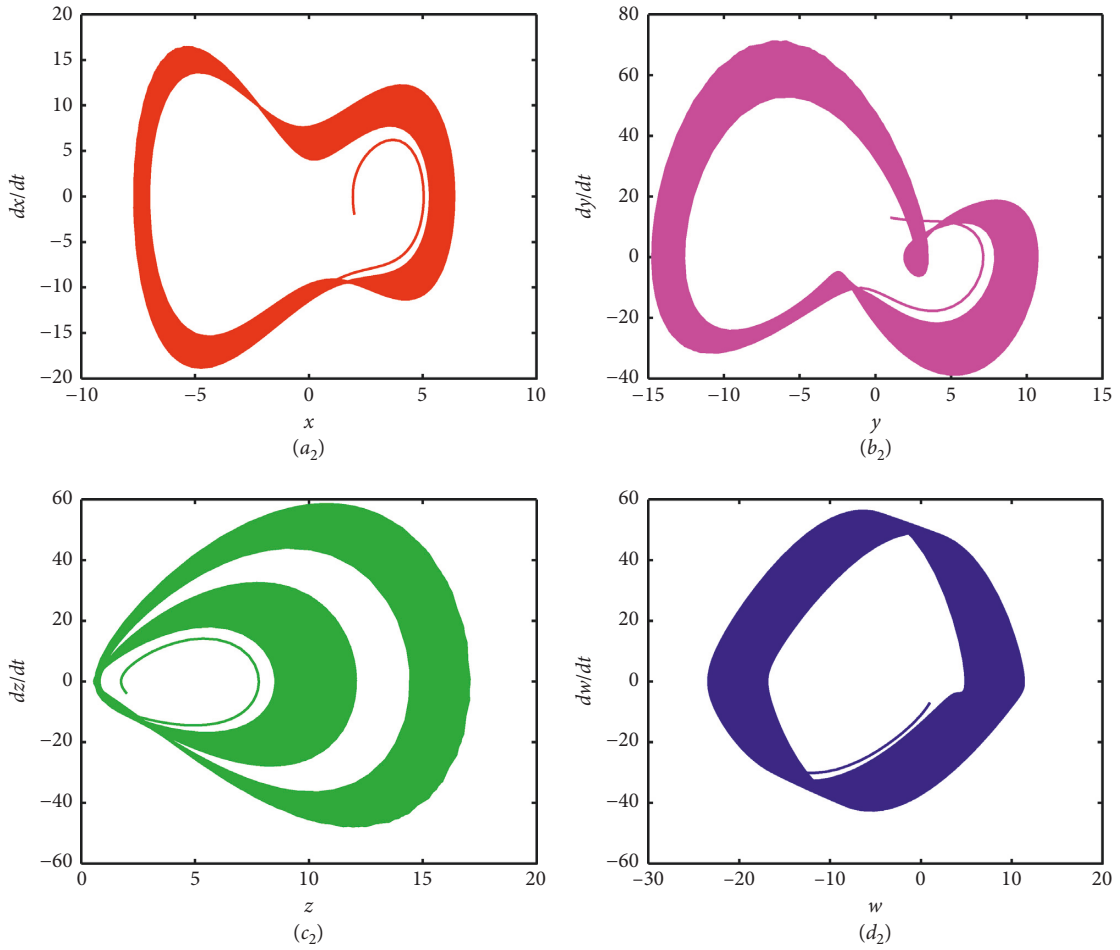

FIGURE 6: Phase diagrams of Experiment 1 with $a = 2, b = 3, t = 1000$: (a_2) phase diagram of x; (b_2) phase diagram of y; (c_2) phase diagram of z; (d_2) phase diagram of w.

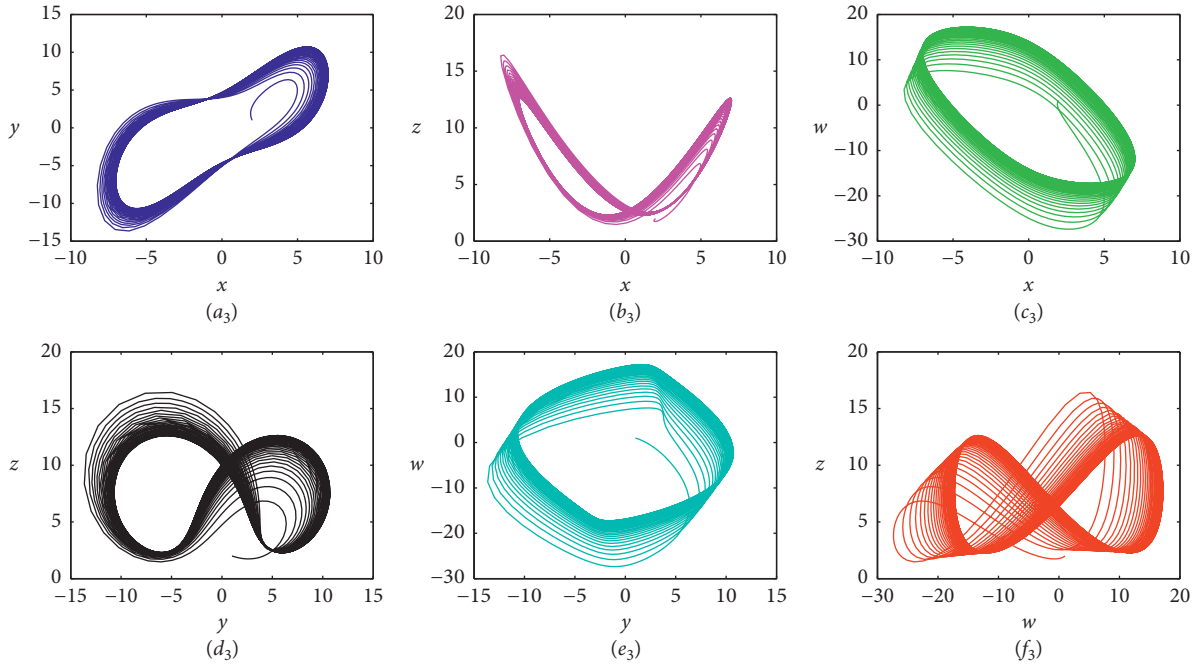

FIGURE 7: Phase portraits of Experiment 1 with $a = 3, b = 5, t = 100$: (a_3) on $x - y$ plane; (b_3) on $x - z$ plane; (c_3) on $x - w$ plane; (d_3) on $y - z$ plane; (e_3) on $y - w$ plane; (f_3) in $z - w$ space.

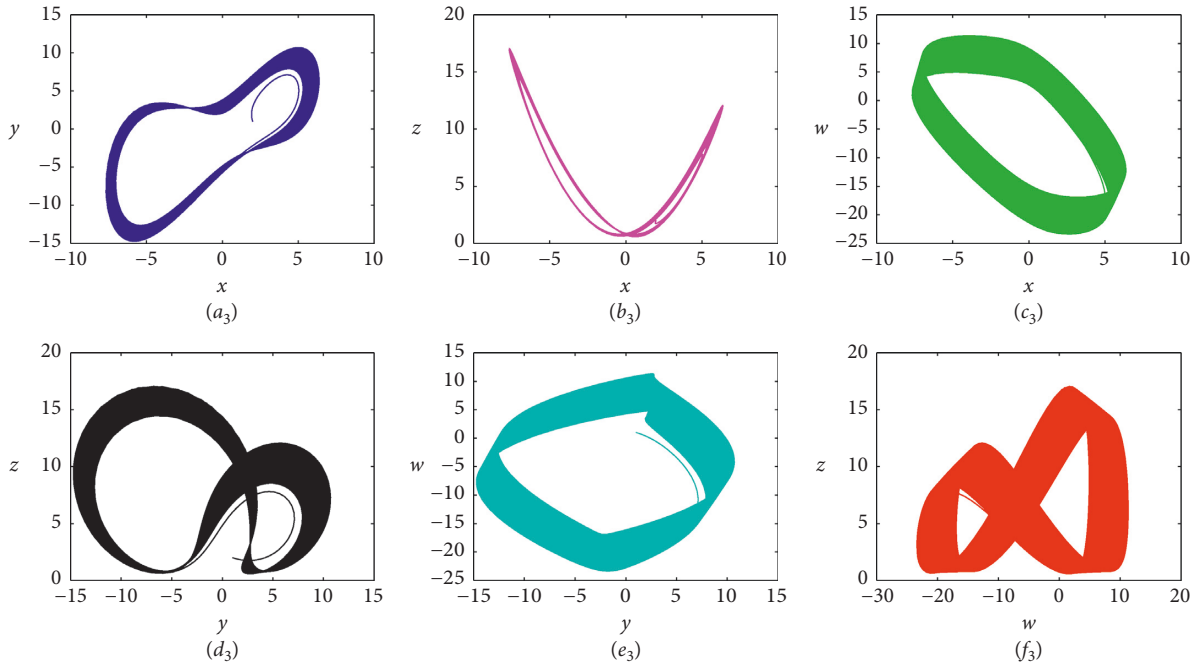

FIGURE 8: Phase portraits of Experiment 1 with $a = 2, b = 3, t = 1000$: (a_3) on $x - y$ plane; (b_3) on $x - z$ plane; (c_3) on $x - w$ plane; (d_3) on $y - z$ plane; (e_3) on $y - w$ plane; (f_3) in $z - w$ space.

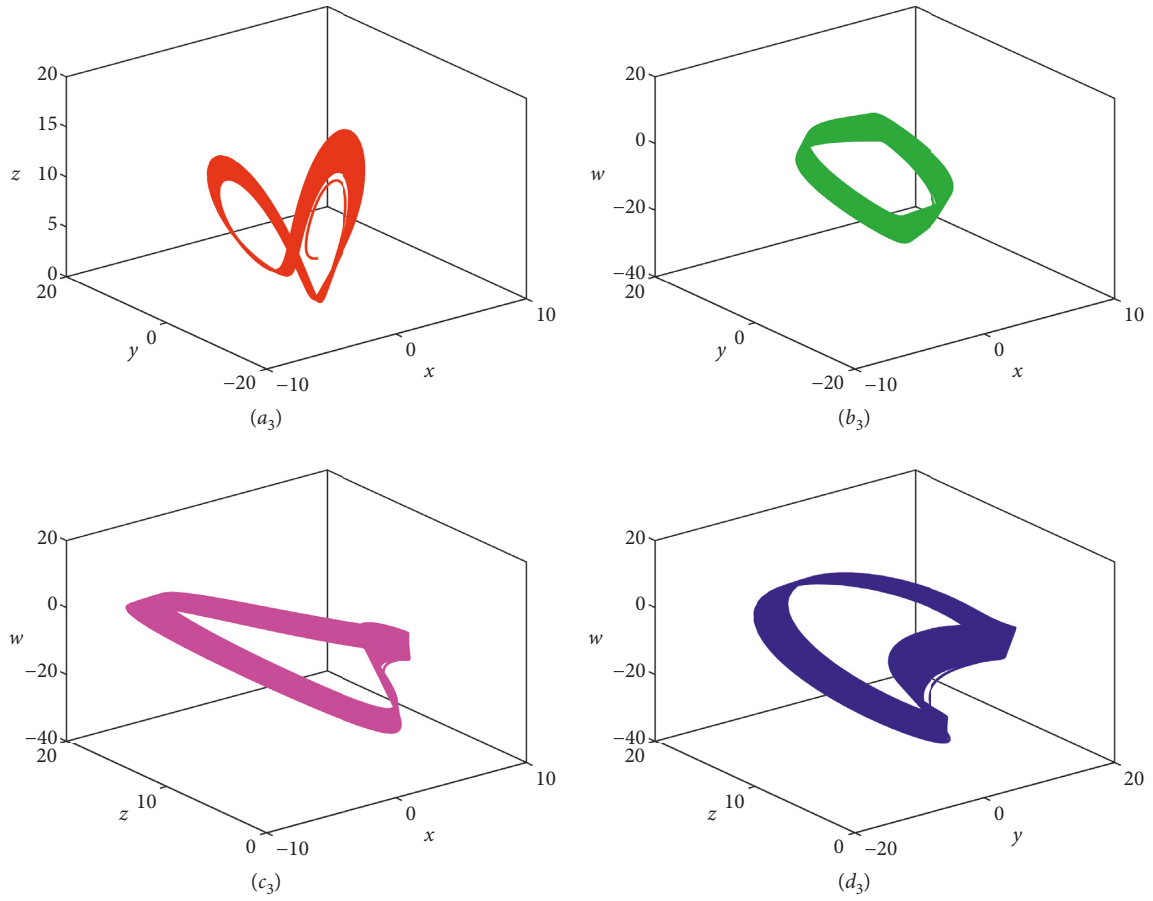

FIGURE 9: Phase portraits of Experiment 1 with $a = 2, b = 3, t = 1000$: (a_3) on $x - y - z$ plane; (b_3) on $x - y - w$ plane; (c_3) on $x - z - w$ plane; (d_3) on $y - z - w$ plane.

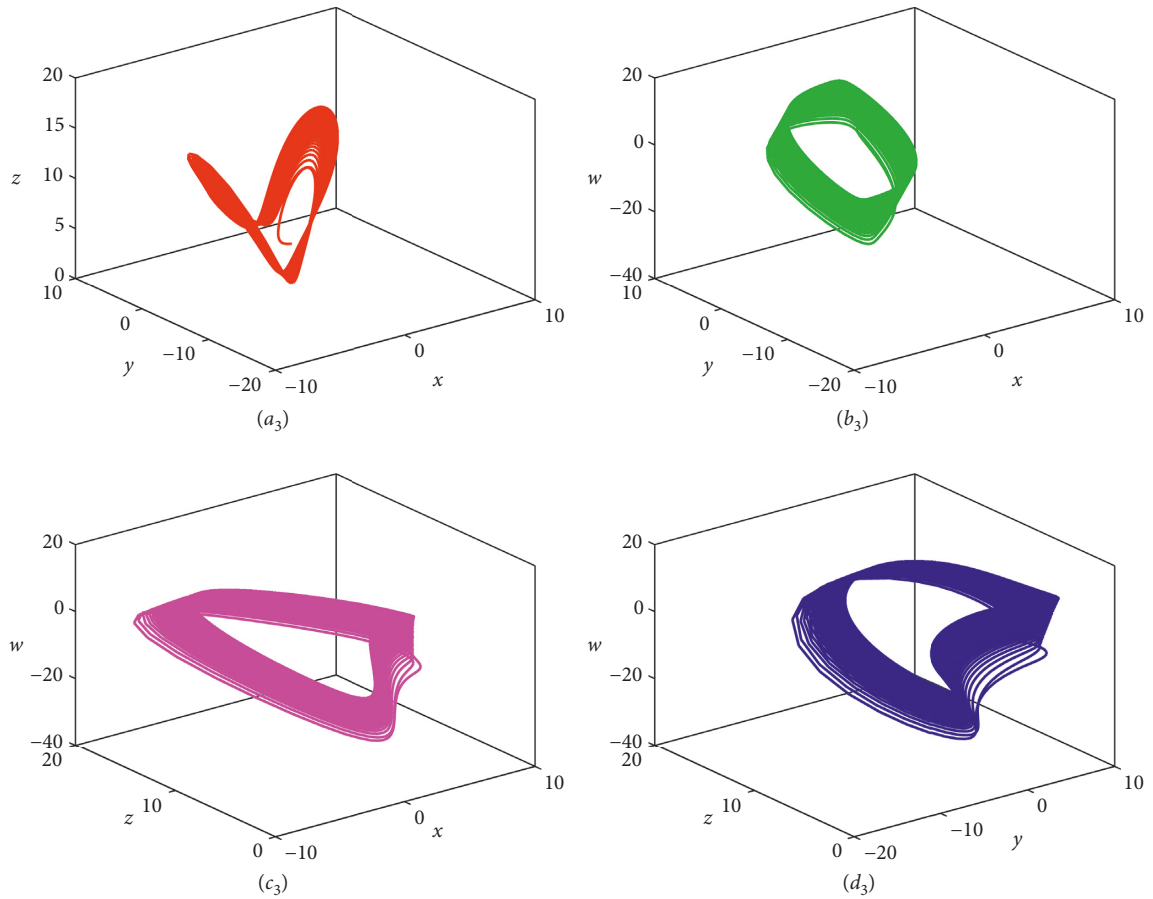

FIGURE 10: Phase portraits of Experiment 1 with $a = 4, b = 5, t = 1000$: (a_3) on $x - y - z$ plane; (b_3) on $x - y - w$ plane; (c_3) on $x - z - w$ plane; (d_3) on $y - z - w$ plane.

Replacing the first line of equation (5) with the initial conditions (6) and solving equation (5) that has been replaced by the initial conditions (6), we can get a numerical solution $x_n(t_j), y_n(t_j), z_n(t_j), w_n(t_j)$ of systems (1) and (2) on $[T_0, T_1]$.

On $[T_1, T_2]$, select the second kind Chebyshev nodes $t_i = (T_2 + T_1/2) - (T_2 - T_1/2)\cos(\pi i/M), i = 0, 1, 2, \ldots, M$ because $x_n(T_1), y_n(T_1), z_n(T_1), w_n(T_1)$ have been obtained on $[T_0, T_1]$. Using (4), we can get

$$\begin{aligned}
\sum_{i=1}^{M} r_i(T_1)x_n(t_i) &= x_n(T_1),\\
\sum_{i=1}^{M} r_i(T_1)y_n(t_i) &= y_n(T_1),\\
\sum_{i=1}^{M} r_i(T_1)z_n(t_i) &= z_n(T_1),\\
\sum_{i=1}^{M} r_i(T_1)w_n(t_i) &= w_n(T_1).
\end{aligned} \tag{7}$$

Replacing the first line of equation (5) with the initial conditions (7) and solving equation (5) that has been replaced by the initial conditions (7), we can get a numerical solution $x_n(t_j), y_n(t_j), z_n(t_j), w_n(t_j)$ of systems (1) and (2) on $[T_1, T_2]$.

Similarly, on $[T_{i-1}, T_i]$, $i = 3, 4, \ldots, N$, we can get the numerical solution of systems (1) and (2) on $[T_{i-1}, T_i]$. After obtaining the numerical solution for all subintervals, these solutions are combined to obtain a numerical solution to equation (1) over the entire interval $[0, T]$.

It is easy to see that the present method provides a globally smooth numerical solution due to the continuity of the numerical solution obtained and its first-order derivative at the common end point of two adjacent intervals.

Based on above formulas, a computer code has been programmed. The existence, uniqueness, and convergence of the approximate solution are ensured by using the computer code.

From above the meshless collocation method, we can get the following theorem.

Theorem 1. *If $\{t_j\}_{j=1}^{\infty}$ is the countable dense point in $[0, T]$, the linear iterative format (3) is the convergence, $x(t), y(t), z(t), w(t)$ is the solution of equation (1), $x_n(t), y_n(t), z_n(t), w_n(t)$ is the solution of equation (3), and $x_n(t_j), y_n(t_j), z_n(t_j), w_n(t_j)$ is the solution of equation (5). Then,*

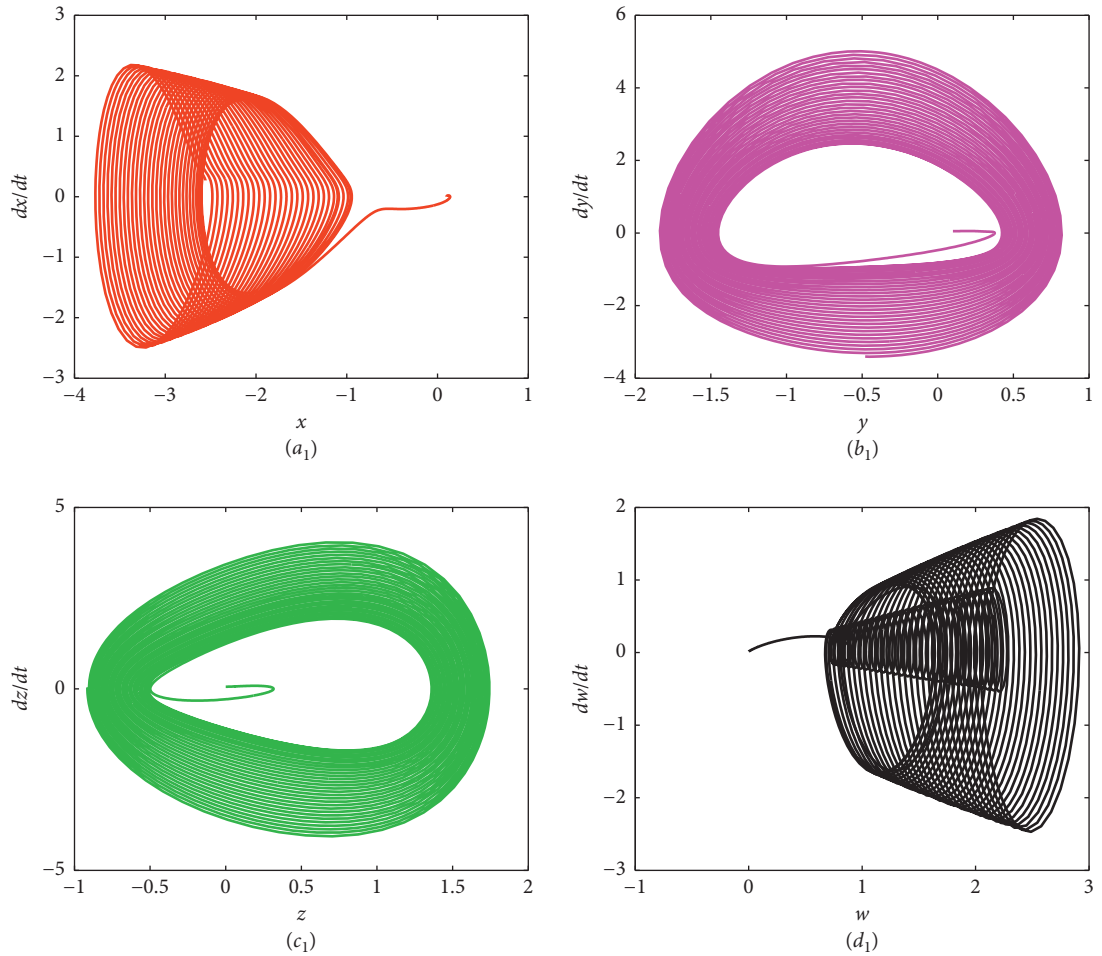

Figure 11: Phase portraits of Experiment 2 with $a = 0.1, t = 100$: (a_1) phase diagram of x; (b_1) phase diagram of y; (c_1) phase diagram of z; (d_1) phase diagram of w.

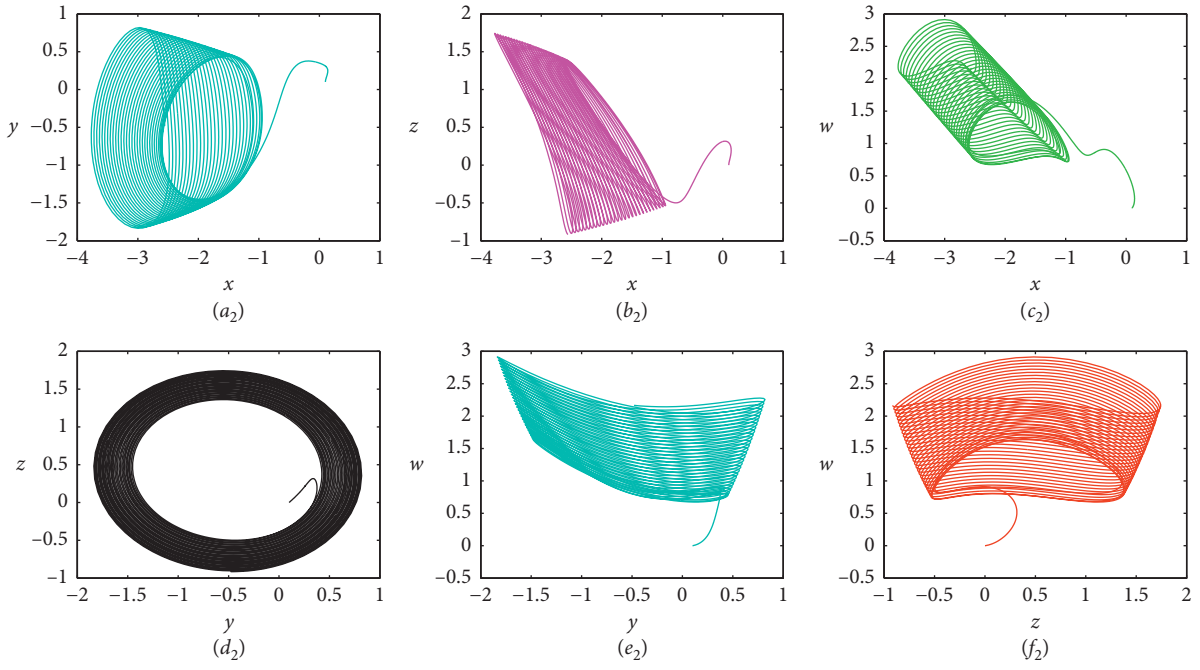

Figure 12: Phase portraits of Experiment 2 with $a = 0.1, t = 100$: (a_2) on $x - y$ plane; (b_2) on $x - z$ plane; (c_2) on $x - w$ plane; (d_2) on $y - z$ plane; (e_2) on $y - w$ plane; (f_2) on $z - w$ plane.

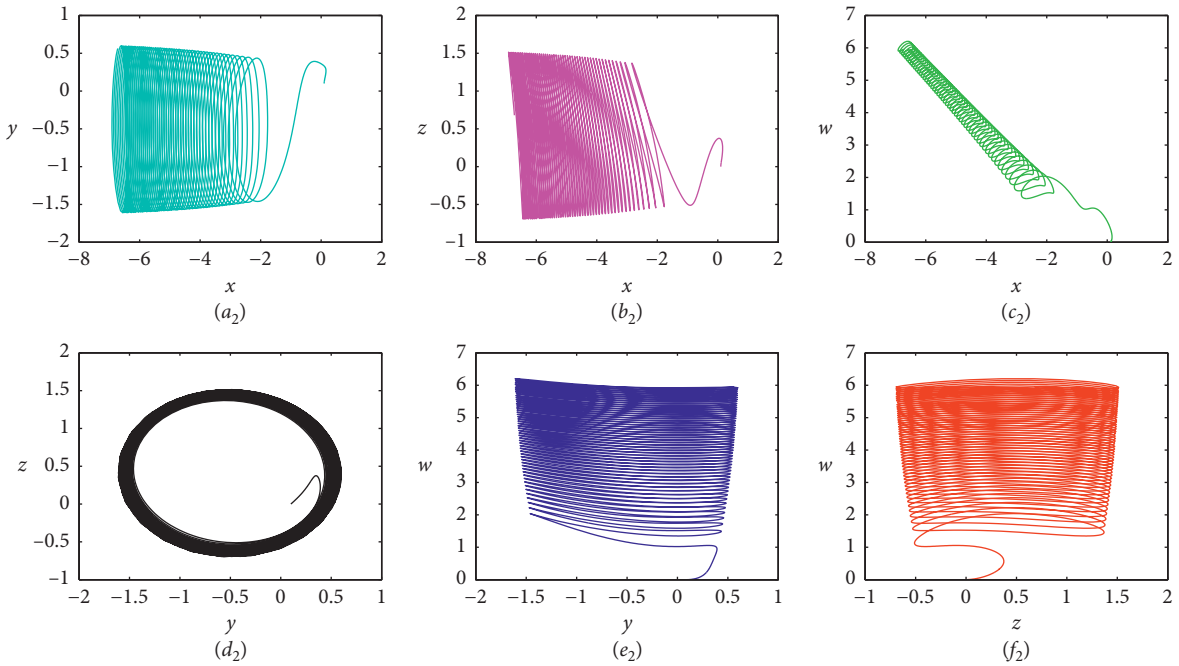

FIGURE 13: Phase portraits of Experiment 2 with $a = 0.01, t = 80$: (a_2) on $x - y$ plane; (b_2) on $x - z$ plane; (c_2) on $x - w$ plane; (d_2) on $y - z$ plane; (e_2) on $y - w$ plane; (f_2) on $z - w$ plane.

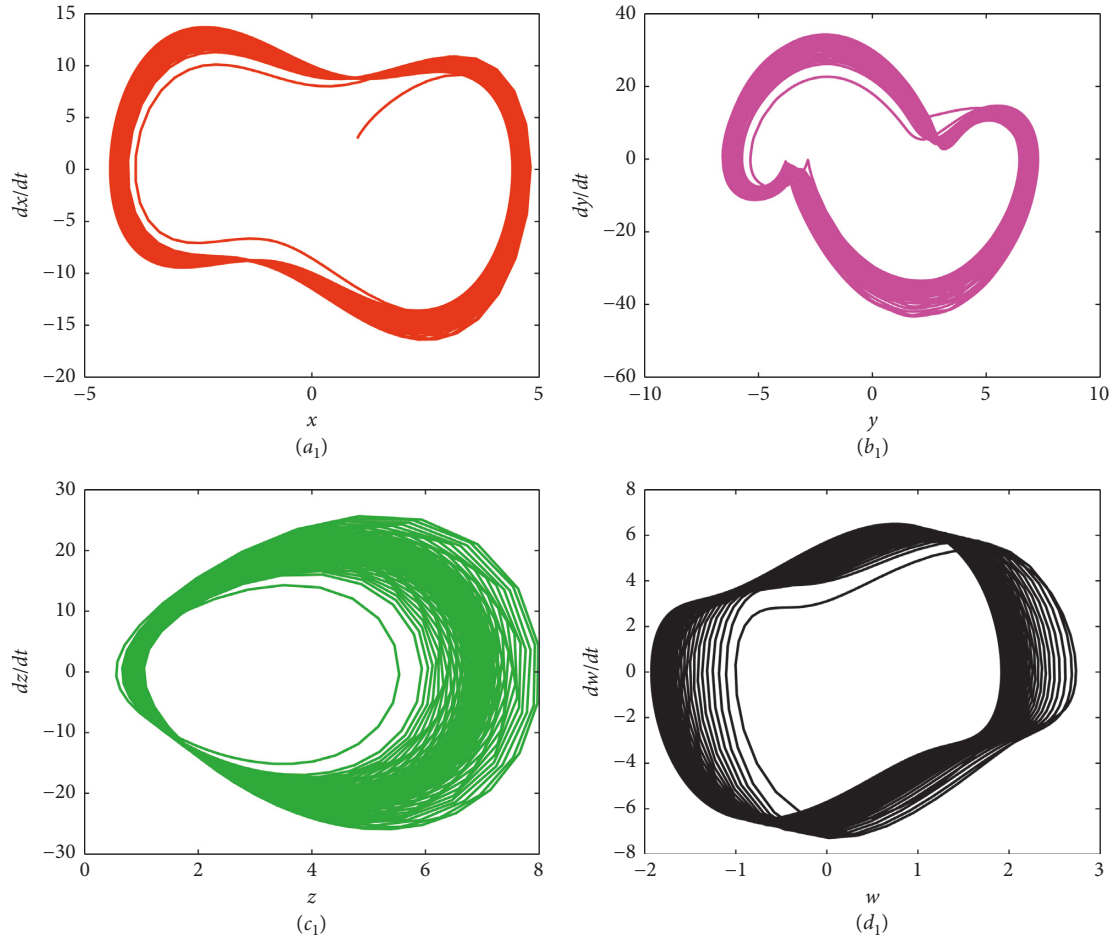

FIGURE 14: Phase portraits of Experiment 3 with $a = 3, t = 3000$: (a_1) phase diagram of x; (b_1) phase diagram of y; (c_1) phase diagram of z; (d_1) phase diagram of w.

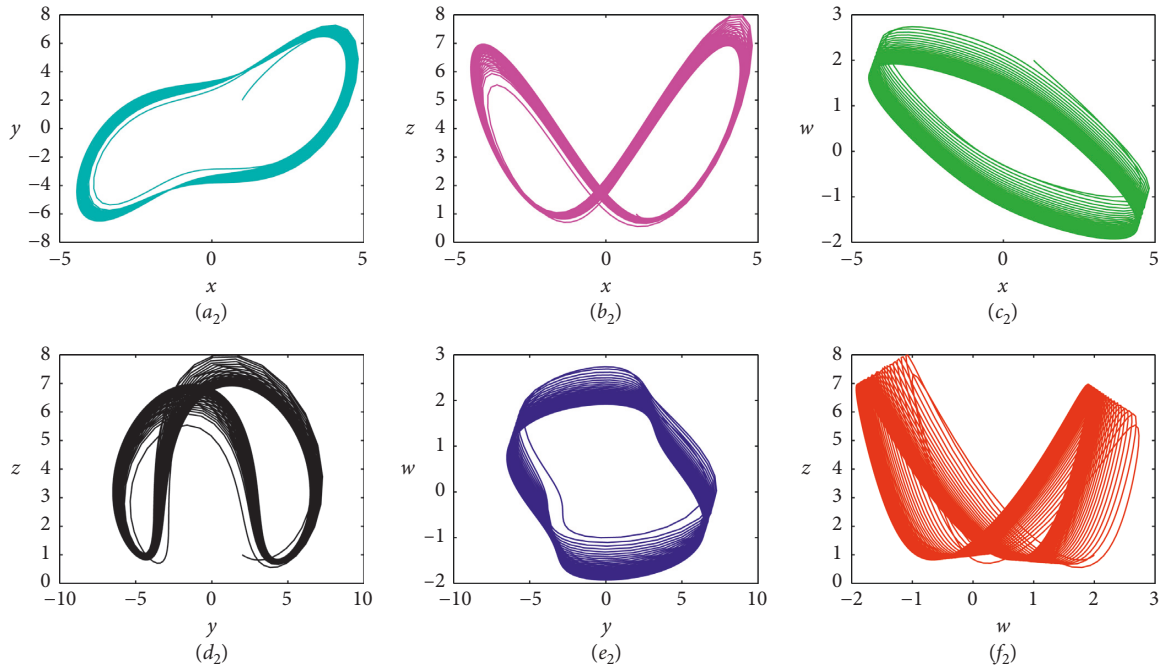

FIGURE 15: Phase portraits of Experiment 3 with $a = 3, t = 3000$: (a_2) on $x - y$ plane; (b_2) on $x - z$ plane; (c_2) on $x - w$ plane; (d_2) on $y - z$ plane; (e_2) on $y - w$ plane; (f_2) on $z - w$ plane.

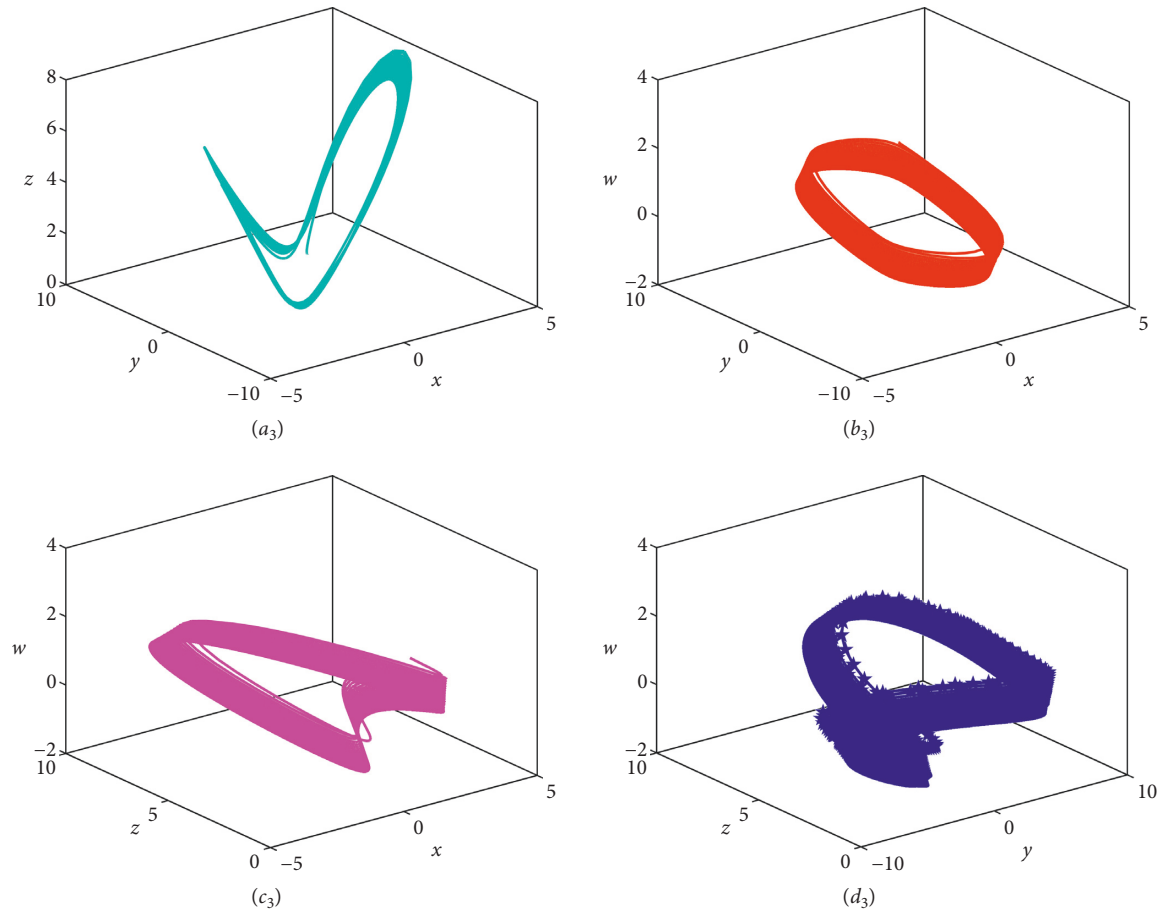

FIGURE 16: Phase portraits of Experiment 3 with $a = 3, t = 3000$: (a_3) in $x - y - z$ space; (b_3) in $x - y - w$ space; (c_3) in $x - z - w$ space; (d_3) in $y - z - w$ space.

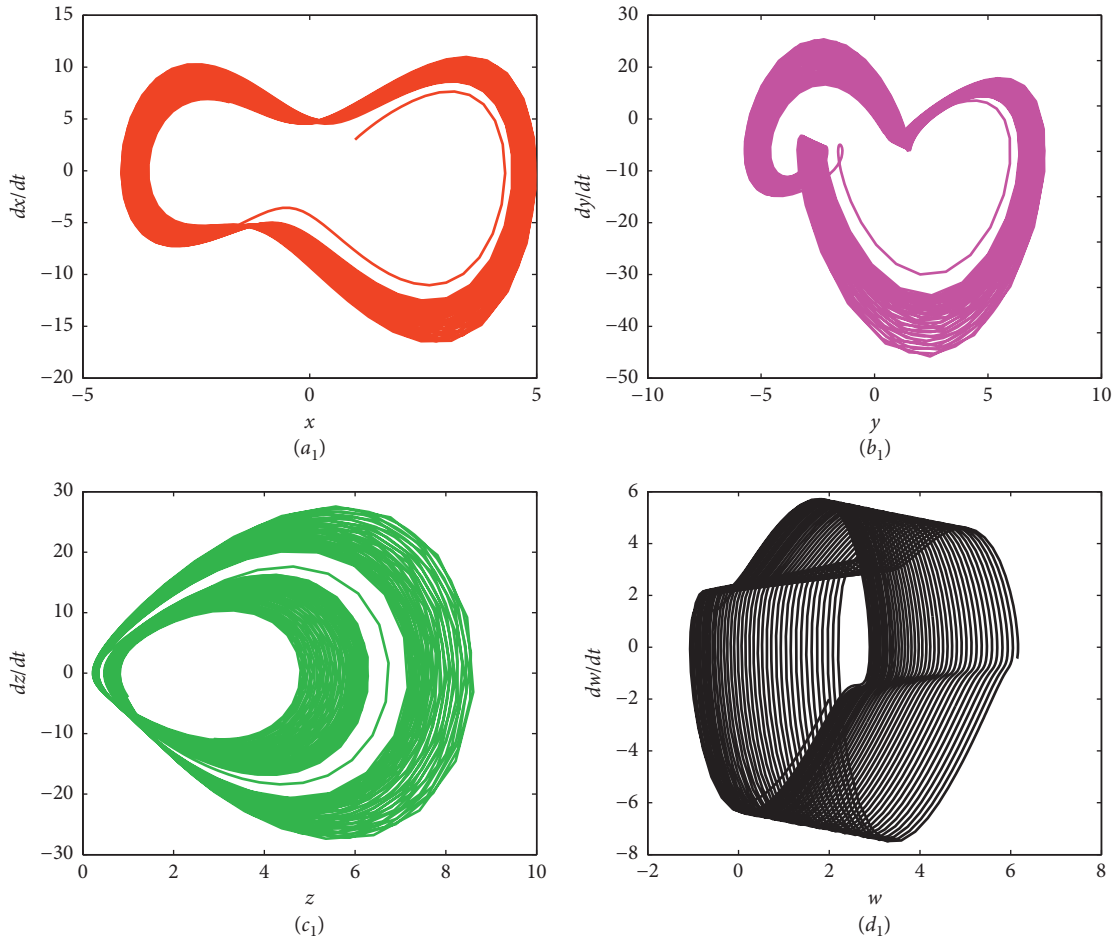

Figure 17: Phase portraits of Experiment 3 with $a = 0.1, t = 100$: (a_1) phase diagram of x; (b_1) phase diagram of y; (c_1) phase diagram of z; (d_1) phase diagram of w.

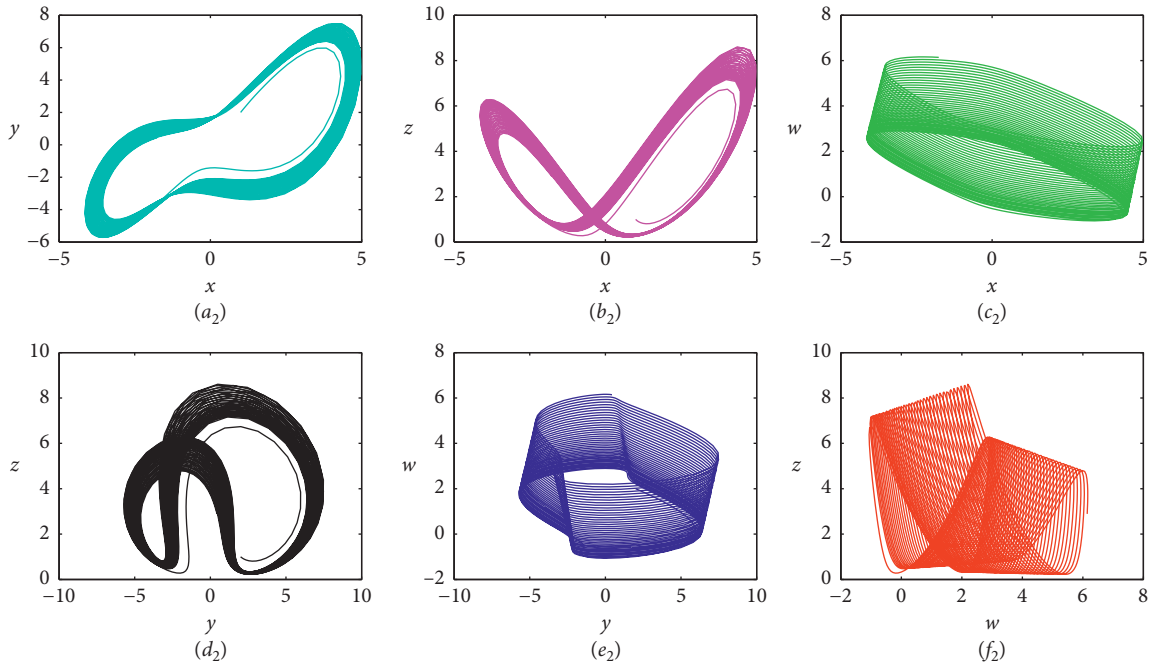

Figure 18: Phase portraits of Experiment 3 with $a = 0.1, t = 100$: (a_2) on $x - y$ plane; (b_2) on $x - z$ plane; (c_2) on $x - w$ plane; (d_2) on $y - z$ plane; (e_2) on $y - w$ plane; (f_2) on $w - z$ plane.

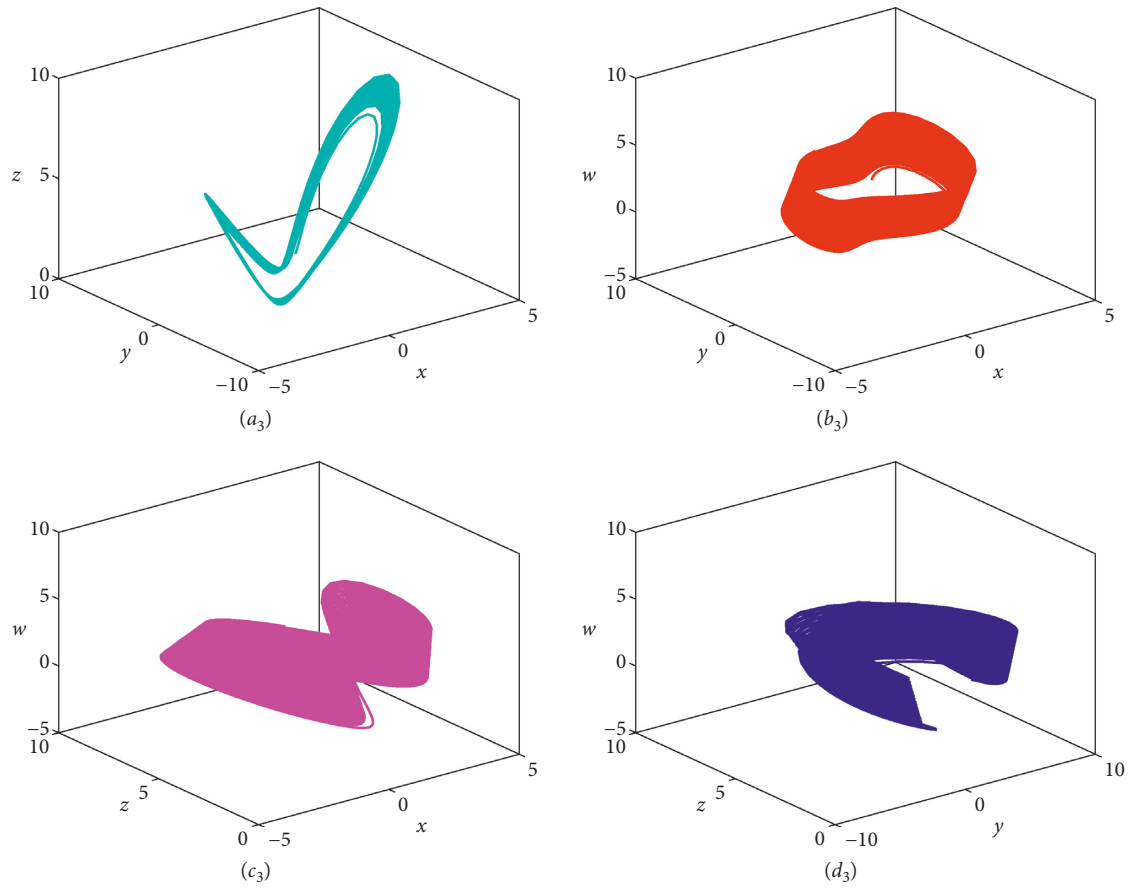

FIGURE 19: Phase portraits of Experiment 3 with $a = 0.1, t = 100$: (a_3) in $x - y - z$ space; (b_3) in $x - y - w$ space; (c_3) in $x - z - w$ space; (d_3) in $y - z - w$ space.

$$\begin{aligned}
\lim_{n\longrightarrow\infty}\left[\lim_{N\longrightarrow\infty} x_n(t_j)\right] &= \lim_{n\longrightarrow\infty} x_n(t) = x(t),\\
\lim_{n\longrightarrow\infty}\left[\lim_{N\longrightarrow\infty} y_n(t_j)\right] &= \lim_{n\longrightarrow\infty} y_n(t) = y(t),\\
\lim_{n\longrightarrow\infty}\left[\lim_{N\longrightarrow\infty} z_n(t_j)\right] &= \lim_{n\longrightarrow\infty} z_n(t) = z(t),\\
\lim_{n\longrightarrow\infty}\left[\lim_{N\longrightarrow\infty} w_n(t_j)\right] &= \lim_{n\longrightarrow\infty} w_n(t) = w(t).
\end{aligned} \tag{8}$$

In numerical experiments, we select the initial iteration value $x_0 = y_0 = z_0 = w_0 = 0; x_1(t_i) = y_1(t_i) = z_1(t_i) = w_1(t_i) = t_i$. *The accuracy of iteration control is* $\varepsilon = 10^{-10}$, *and let* $M = 35, N = T$.

3. Numerical Experiment

In this section, some numerical experiments are studied to demonstrate the accuracy of the present method. The experiments are computed using Matlab R2017a.

Experiment 1. We consider the following four-dimensional system [1]:

$$\begin{bmatrix} \frac{dx}{dt} \\ \frac{dy}{dt} \\ \frac{dz}{dt} \\ \frac{dw}{dt} \end{bmatrix} = \begin{bmatrix} -a & a & 0 & 0 \\ 8 & 0 & 0 & 1 \\ 0 & 0 & -3 & 0 \\ -2 & -b & 0 & 0 \end{bmatrix} \begin{bmatrix} x \\ y \\ z \\ w \end{bmatrix} - \begin{bmatrix} 0 \\ xz \\ -xy \\ 0 \end{bmatrix}, \tag{9}$$

where a and b are the positive parameters of the system, which satisfy the following initial conditions:

$$\begin{aligned}
x(0) &= 2,\\
y(0) &= 1,\\
z(0) &= 2,\\
w(0) &= 1.
\end{aligned} \tag{10}$$

Lyapunov exponents of Experiment 1 are shown in Figure 1. The complex dynamic behaviors of Experiment 1 are shown in Figures 2–9.

Experiment 2. We consider the following four-dimensional system:

$$\begin{bmatrix} \frac{dx}{dt} \\ \frac{dy}{dt} \\ \frac{dz}{dt} \\ \frac{dw}{dt} \end{bmatrix} = \begin{bmatrix} -0.9 & 0.9 & 0 & -0.9 \\ 0.4 & 0.1 & 0 & 0 \\ 0.5 & 0 & -0.1 & 0 \\ a & 0 & 0 & 0 \end{bmatrix} \begin{bmatrix} x \\ y \\ z \\ w \end{bmatrix} + \begin{bmatrix} 0.8yz \\ -xz \\ xy \\ 0.15yz + 0.5y^2 \end{bmatrix}, \tag{11}$$

where a is the real parameter, which satisfies the following initial conditions (Figure 10):

$$\begin{aligned} x(0) &= 0.1, \\ y(0) &= 0.1, \\ z(0) &= 0, \\ w(0) &= 0. \end{aligned} \tag{12}$$

Lyapunov exponents of Experiment 2 are shown in Figure 1. The complex dynamic behaviors of Experiment 2 are shown in Figures 11–13.

Experiment 3. We consider the following four-dimensional system [7]:

$$\begin{bmatrix} \frac{dx}{dt} \\ \frac{dy}{dt} \\ \frac{dz}{dt} \\ \frac{dw}{dt} \end{bmatrix} = \begin{bmatrix} -3 & 3 & 0 & 0 \\ 7 & 0 & 0 & a \\ 0 & 0 & -3 & 0 \\ 0 & -1 & 0 & 0 \end{bmatrix} \begin{bmatrix} x \\ y \\ z \\ w \end{bmatrix} - \begin{bmatrix} 0 \\ 2xz \\ -3x^2 \\ 0 \end{bmatrix}, \tag{13}$$

where a is the parameter of the system, which satisfies the following initial conditions:

$$\begin{aligned} x(0) &= 1, \\ y(0) &= 2, \\ z(0) &= 1, \\ w(0) &= 2. \end{aligned} \tag{14}$$

Lyapunov exponents of Experiment 3 are shown in Figure 1. The complex dynamic behaviors of Experiment 3 are shown in Figures 14–19.

4. Conclusions and Remarks

In this paper, an improved meshless collocation method, which divides the entire intervals $[0, T]$ into N equal subintervals, has been constructed for a class of four-dimensional chaotic or hyperchaotic systems. The numerical results demonstrate that this approach is more effective and accurate than other mesheless collocation methods. Some new complex dynamical behaviors are shown by using the improved method. It is worth noting that the improved method can also be used to solve other similar problems [19, 20]. In the further work, we will be devoted to studying some fractional-order chaotic systems.

Data Availability

The data used to support the findings of this study are available from the corresponding author upon request.

Conflicts of Interest

The authors declare that there are no conflicts of interest regarding the publication of this article.

Acknowledgments

This study was supported by the Natural Science Foundation of Inner Mongolia (2017MS0103), Inner Mongolia Maker Collaborative Innovation Center of Jining Normal University, and National Natural Science Foundation of China (11361037).

References

[1] Q. Yang and Y. Liu, "A hyperchaotic system from a chaotic system with one saddle and two stable node-foci," *Journal of Mathematical Analysis and Applications*, vol. 360, no. 1, pp. 293–306, 2009.

[2] J. P. Singh and B. K. Roy, "Coexistence of asymmetric hidden chaotic attractors in a new simple 4-D chaotic system with curve of equilibria," *Optik*, vol. 145, pp. 209–217, 2017.

[3] S. Bowong and P. V. E. McClintock, "Adaptive synchronization between chaotic dynamical systems of different order," *Physics Letters A*, vol. 358, no. 2, pp. 134–141, 2006.

[4] W. Wu and Z. Chen, "Hopf bifurcation and intermittent transition to hyperchaos in a novel strong four-dimensional hyperchaotic system," *Nonlinear Dynamics*, vol. 60, no. 4, pp. 615–630, 2010.

[5] X.-J. Tong, M. Zhang, Z. Wang, Y. Liu, and J. Ma, "An image encryption scheme based on a new hyperchaotic finance system," *Optik*, vol. 126, no. 20, pp. 2445–2452, 2015.

[6] W. Wu, Z. Chen, and Z. Yuan, "The evolution of a novel four-dimensional autonomous system: among 3-torus, limit cycle, 2-torus, chaos and hyperchaos," *Chaos, Solitons & Fractals*, vol. 39, no. 5, pp. 2340–2356, 2009.

[7] J. P. Singh and B. K. Roy, "The nature of Lyapunov exponents is (+, +, −, −). Is it a hyperchaotic system?," *Chaos, Solitons & Fractals*, vol. 92, pp. 73–85, 2016.

[8] S. Dadras and H. R. Momeni, "Four-scroll hyperchaos and four-scroll chaos evolved from a novel 4D nonlinear smooth autonomous system," *Physics Letters A*, vol. 374, no. 11-12, pp. 1368–1373, 2010.

[9] J.-P. Berrut, "Rational functions for guaranteed and experimentally well-conditioned global interpolation," *Computers & Mathematics with Applications*, vol. 15, no. 1, pp. 1–16, 1988.
[10] J.-P. Berrut and L. N. Trefethen, "Barycentric Lagrange interpolation," *SIAM Review*, vol. 46, no. 3, pp. 501–517, 2004.
[11] C. Schneiaer and W. Werner, "Some new aspects of rational interpolation," *Mathematics of Computation*, vol. 175, pp. 285–299, 1986.
[12] R. Baltensperger and J.-P. Berrut, "The linear rational collocation method," *Journal of Computational and Applied Mathematics*, vol. 134, no. 1-2, pp. 243–258, 2001.
[13] S. P. Li and Z. Q. Wang, *Barycentric Interpolation Collocation Method for Nonlinear Problems*, National Defense Industry Press, Beijing China, 2015.
[14] S. P. Li and Z. Q. Wang, *High-Precision Non-grid Center of Gravity Interpolation Collocation Method: Algorithm, Program and Engineering Application*, Science Press, Beijing China, 2012.
[15] Y. Wang, D. Tian, and Z. Li, "Numerical method for singularly perturbed delay parabolic partial differential equations," *Thermal Science*, vol. 21, no. 4, pp. 1595–1599, 2017.
[16] F. Liu, Y. Wang, and S. Li, "Barycentric interpolation collocation method for solving the coupled viscous Burgers' equations," *International Journal of Computer Mathematics*, vol. 95, no. 11, pp. 2162–2173, 2018.
[17] X. Zhou, J. Li, Y. Wang, and W. Zhang, "Numerical simulation of a class of hyperchaotic system using barycentric Lagrange interpolation collocation method," *Complexity*, vol. 2019, Article ID 1739785, 13 pages, 2019.
[18] M. J. Du, J. M. Li, Y. L. Wang, and W. Zhang, "Numerical simulation of a class of three-dimensional Kolmogorov model with chaotic dynamic behavior by using barycentric interpolation collocation method," *Complexity*, vol. 2019, Article ID 3426974, 14 pages, 2019.
[19] J. Vega, A. Murari, S. González, A. Pereira, and I. Pastor, "Spatial location of local perturbations in plasma emissivity derived from projections using conformal predictors," *Nuclear Instruments and Methods in Physics Research Section A: Accelerators, Spectrometers, Detectors and Associated Equipment*, vol. 720, pp. 14–19, 2013.
[20] A. Murari, N. Bekris, J. Figueiredo et al., "Implementation and exploitation of JET enhancements at different fuel mixtures in preparation for DT operation and next step devices," *Fusion Engineering and Design*, vol. 146, pp. 741–744, 2019.

Hindawi
Complexity
Volume 2019, Article ID 9107167, 11 pages
https://doi.org/10.1155/2019/9107167

Research Article

Compound Autoregressive Network for Prediction of Multivariate Time Series

Yuting Bai[1,2], **Xuebo Jin**[1,2], **Xiaoyi Wang**[1,2], **Tingli Su**[1,2], **Jianlei Kong**[1,2] and **Yutian Lu**[3]

[1]*School of Computer and Information Engineering, Beijing Technology and Business University, Beijing 100048, China*
[2]*Beijing Key Laboratory of Big Data Technology for Food Safety, Beijing Technology and Business University, Beijing 100048, China*
[3]*State Grid Beijing Electric Power Company, Beijing 100031, China*

Correspondence should be addressed to Xuebo Jin; jinxuebo@btbu.edu.cn

Received 16 July 2019; Revised 31 August 2019; Accepted 4 September 2019; Published 22 September 2019

Guest Editor: Teddy Craciunescu

The prediction information has effects on the emergency prevention and advanced control in various complex systems. There are obvious nonlinear, nonstationary, and complicated characteristics in the time series. Moreover, multiple variables in the time-series impact on each other to make the prediction more difficult. Then, a solution of time-series prediction for the multivariate was explored in this paper. Firstly, a compound neural network framework was designed with the primary and auxiliary networks. The framework attempted to extract the change features of the time series as well as the interactive relation of multiple related variables. Secondly, the structures of the primary and auxiliary networks were studied based on the nonlinear autoregressive model. The learning method was also introduced to obtain the available models. Thirdly, the prediction algorithm was concluded for the time series with multiple variables. Finally, the experiments on environment-monitoring data were conducted to verify the methods. The results prove that the proposed method can obtain the accurate prediction value in the short term.

1. Introduction

In the information era, data play a significant role in various artificial and natural systems. Data provide the basis for machine control, industrial system running, economical market, environment management, etc. For the complex systems above, the accurate real-time data are essential for the control and operation. Moreover, the future information is also very important, which is predicted with the historical data and can guide the beforehand operation for the system adjustment, environmental adaptation, and accident avoidance. Therefore, the reliable prediction of the data in the time domain becomes an urgent issue for the complex systems. For the complicated composition and internal mechanism, the time-series data in the systems are usually nonstationary, nonlinear, and noisy. The complicated features make the prediction difficult. Besides, the variables in the time-series impact on each other to perplex the nonlinear relation. Then, the prediction issue becomes the challenge in front of the complicated time-series characteristics and multivariate correlativity.

In the prediction issue, various explorations have been conducted to excavate the potential rules and features in the time-series data. For the practice application in some fields, the prediction methods are proposed based on mechanism models. In the methods, the inner mechanism of a system is studied deeply, in which the relations between system components are built with the approach of physics, chemistry, and biology, such as models of water environment (WASP [1] and EFDC [2]) and models of atmospheric diffusion (Gaussian puff and plume model [3]). The system change can be predicted based on the mechanism model in the view of model simulation. However, the models are difficult to build because of the complex and unknown inner structure. Moreover, the professional and interdisciplinary knowledge is also required for the mechanism analysis.

The data-driven solution has been an effective complement for the mechanism methods. Different from the mechanism methods, the data-driven methods focus on the external data characteristic instead of the inner structure relation. It develops from the statistical method to the machine learning method which can excavate more features from the mass data. Machine learning solves mainly the problem of the parametric model setting and adaption in the statistical methods such as autoregression (AR), moving average (MA), autoregressive moving average (ARMA), and autoregressive integrated moving average (ARIMA) models [4]. Machine learning including the traditional neural network and deep learning also face some problems in the time-series analysis. First, multiple variables usually need to be considered for the target predicted variable. In the multivariable analysis, the traditional networks mainly model the multivariable mapping relations, while neglecting the sequential features. And the deep learning methods are specialized in the sequential feature extraction of the univariate. Second, the computational efficiency should be considered in the prediction models, especially for the terminal application which cannot provide the high configuration. Third, the training methods affect the network performance largely. A suitable and extensible learning framework should be designed for the neural network. Based on the analysis of the existing research, we explore an access to the time-series prediction, in the view of multivariable modelling performance, computational efficiency, and training methods.

The rest of this paper is organized as follows: Section 2 introduces the related prediction methods, including the statistical model and machine learning method. In Section 3, the main prediction model is proposed and the compound autoregressive network is presented with the prediction algorithm. Experiments are conducted in Section 4 to test the network. The methods and results are discussed in Section 5. Finally, the paper is concluded in Section 5.

2. Related Works

The direct solution of the prediction is to figure out the change rule of the system, which is the basic thought of the mechanism-based prediction methods. Obviously, it is difficult to build the completed mechanism model to describe the system composition and change rule. Then, the data-driven method becomes a feasible solution with the external characteristic irrespective of the system inner construction and relation. The data-driven methods can be divided into two categories: statistical model and machine learning model.

2.1. Prediction Models Based on Statistics. The statistical model is based on the mathematical description and calculation of the data. The classical statistical models are built on the autocorrelation function and exponential decays of the time series. The typical models include AR, MA, and hybrid models. The AR model describes the change process of the regressor variable itself. In the model, the random variables in the next time steps are expressed with the linear combination of the variables in the previous moments. The MA model uses the sliding window to extract the time-series features in the view of the adjacent data segment. Because the length of the sliding window impacts the feature extraction ability mainly, some exponential smoothing methods are proposed to optimize the MA model, in which the cubic exponential smoothing method is applied widely. Based on AR and MA models, the hybrid model is proposed for accurate modelling, including the ARMA and ARIMA. The ARIMA has been the typical hybrid model for the nonstationary regressive issue. It was applied in the prediction problems of environment monitoring [5], financial economy [6, 7], food safety [8], traffic system [9], etc.

The statistical model can be expressed as follows. x_t is the value of the time series at t, p is the number of autoregressive terms, q is the number of moving average terms, d is the differential order, ε_t is the white noise at t, L is the lag operator, and $\alpha_1, \cdots, \alpha_p$ and $\beta_1, \cdots, \beta_q$ are the weights. Then, the AR model can be expressed as

$$x_t = \sum_{i=1}^{p} \alpha_i x_{t-i} + \varepsilon_t. \tag{1}$$

The MA model is

$$x_t = \sum_{i=1}^{q} \beta_i \varepsilon_{t-i} + \varepsilon_t. \tag{2}$$

The ARMA model is

$$x_t = \sum_{i=1}^{p} \alpha_i x_{t-i} + \sum_{i=1}^{q} \beta_i \varepsilon_{t-i} + \varepsilon_t. \tag{3}$$

The ARIMA model is

$$\left(1 - \sum_{i=1}^{p} \alpha_i L^i\right)(1-L)^d x_t = \left(1 + \sum_{i=1}^{q} \beta_i L^i\right)\varepsilon_t. \tag{4}$$

The statistical models rely on the assumption of stationarity in the time series. Although the models are improved and evolved, they are still limited by the transformation and process of the stationary data. Besides, it is a problem on how to select a proper model and estimate the model parameters. The practice indicates that the models perform well in the linear short-term prediction. The prediction accuracy declines markedly in the complex and long-term time series. It becomes a demand to seek new prediction solutions to the nonstationary time series.

2.2. Prediction Model Based on Machine Learning. Machine learning develops fast in the classification and regression research. The black-box thought of machine learning seems to provide the extensive possibility for the complex modelling problems. The backpropagation neural network (BP), radial basis function neural network (RBF), nonlinear autoregressive neural network (NAR), support vector machine (SVM), and Bayes network have been studied and applied in the prediction problems [10].

Some studies have been conducted to improve the network and prediction performance. Pradeepkumar [11] proposed a novel particle swarm optimization algorithm to train the quantile regression neural network, which was applied in the financial data prediction. Daly [12] designed the structure of the NAR to predict the video traffic in the Ethernet passive optical network. Wang [13] proposed an adaptive method based on the multiple-rate network to predict the parameters in industrial control. Liu [14] studied an improved grayscale neural network which was tested to predict the traffic stop. Some combinations of different methods are also a hotspot in the machine learning studies. Doucoure [15] predicted the wind speed with wavelet analysis and neural network. Wang [16] improved the BP with the self-adaptive differential evolution algorithm.

The machine learning methods above are mainly the shallow networks. They are suitable for multivariate modelling because of the network structure of multiple input nodes. The data in different time steps are imported independently into the network circularly, which place emphasis on the nonlinear mapping relation instead of the sequence connection in the time domain. Generally, they are limited in mass data processing and complex time-series relation modelling. Especially for the prediction issue, the sequence feature should be extracted which is difficult to realize in the traditional fully connected network. The recurrent neural network (RNN) [17] draws much attention in the sequence features. In the RNN, the nodes between the hidden layers are connected, and the input of the hidden layer includes not only the output of the input layer but also the output of the previous hidden layer. The RNN develops to the multidimensional recurrent neural network (MDRNN) [18] and to the bidirectional recurrent neural network (BiRNN) [19] for the higher performance. The long short-term memory network (LSTM) [20] is proposed for the long-term dependency problem in the traditional RNN. Some variants of the LSTM appear with the improvement and redesign of the structure or gate in the LSTM, including the bidirectional LSTM network (BiLSTM) [21] and gated recurrent unit (GRU) [22]. Although the deep networks usually perform better than the traditional networks, they are studied and applied more with the univariate instead of the multivariate. Besides, their structures are more complex, and they need more training time and computing resources.

In the prediction problem of the time series, on the one hand, we should consider the sequence feature of the time series as well as the mutual effect of the related variables. On the other hand, we should balance the network prediction accuracy with the calculating speed and resources occupied. Considering the related works mentioned above, the advantages of different networks should be utilized, including the simple structure and multivariate analysis ability in the shallow networks, as well as the sequence feature extraction in the recurrent networks. Then, the shallow recurrent neural network NAR [23] is selected as the basic network which can extract the nonlinear and sequence features in the time series. And a compound network structure and algorithm are designed to analyse multiple variables. The novel framework of the compound network can be applied in the prediction problem of complex systems, providing an alternative solution to analyse the data change in the data-driven view.

3. Compound Autoregressive Prediction Network

For the time series in the systems, the main feature is the trend in their changing process, as well as the incidence relation among different variables. The trend means that there are potential rules in the changing data, which can be linear, periodic, or stochastic. The incidence relation means the effect on multiple variables. For example, the temperature value fluctuates in its change rule, and it is impacted by other meteorological variables such as the precipitation and humidity. Based on the two important factors in the time series, a compound neural network is built to predict the object variable. The overall network structure is introduced firstly. Then, the components and training methods are analysed. The prediction algorithm for the multivariate time series is proposed finally.

3.1. Compound Autoregressive Network. In the traditional neural networks, the NAR can realize the regression analysis of the time series itself. The network has been applied in practice and performs well in the short-term prediction. Besides, the data needed in the network training are obviously less than those of deep networks such as the LSTM and GRU. Then, the NAR can be an effective tool in the univariate prediction. Moreover, the nonlinear autoregressive network with external input (NARX) develops based on the NAR, in view of the incidence relation in the multiple variables. With the advantages of the NAR and NARX, the compound network is designed for the multivariate prediction issue, as shown in Figure 1. The compound autoregressive network proposed in this paper is abbreviated as CARN.

The CARN consists of two parts, namely, the primary network and auxiliary network. In the prediction issue, a variable is the main target to be predicted, and some variables are selected as the correlated variables according to their correlation degrees. The components in the compound network are corresponding to different types of variables. The primary network is built based on the structure of the NARX to predict the object variable. And the auxiliary network is built based on the NAR to provide the reference of the correlated variables.

For the primary network, the inputs include the object variable (Y in Figure 1) and the correlated variables (U in Figure 1). The nonlinear and complex relation in the variables is usually difficult to be analysed with mechanism modelling. But the network performs well in the black-box mapping relation mining. Then, the design of the two types of inputs can excavate the associate relation in multiple variables. Besides the two types of inputs, the other characteristic of the network is the feedback of the object variable from the output to the input. The changing trend in the object variable itself is usually more important than the multivariable relation. And the self-trend is constructed based on the feedback in the time dimension.

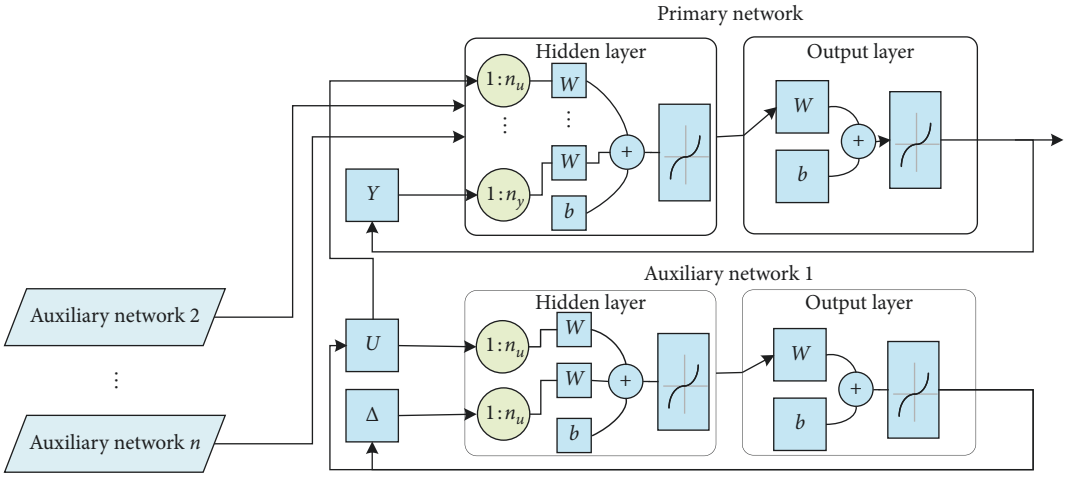

Figure 1: Compound autoregressive network for the multivariable time-series prediction.

For the auxiliary network, the main inputs are the variables associated with the object variable. The network mainly sets up the time-series trend with the structure of the feedback. In the feedback, the data change gradient is also set as the input to compensate the prediction. The NAR-based auxiliary network realizes the regression of the univariate. Moreover, there is not only one effect variable of the object variable. Therefore, there are some auxiliary networks in practice, and the number of auxiliary networks equals the variable number.

3.2. Design and Train of Discrete Networks. In the framework of the compound network, the primary and auxiliary networks are set up to predict the variables. There are two issues to be solved including the concrete network structure and the network training method. The structures of the networks are shown in Figure 2.

There are three layers in the primary network, namely, the input, hidden, and output layers. The inputs include the effect variables which are from the auxiliary networks and the object variable. In the view of the time dimension, the data of the object variable in the past are used to predict the data in the next time steps. The data at present are provided by the auxiliary networks. The nonlinear regressive function of the network can be expressed as

$$y(t) = f\Big(u(t), u(t-1), \ldots, u\big(t-n_u\big), y(t-1), y(t-2), \ldots, y\big(t-n_y\big)\Big), \tag{5}$$

where $y(t)$ is the prediction output, $u(t)$ is the effect variable input, $(t-i)$ means the time step, n_u is the input delay, and n_y is the output delay.

The relation between the input and hidden layers is

$$H_j = f\left(\sum_{i^1=1}^{n_u} W_{i_1 j} u_{i_1} + \sum_{i^2=1}^{n_y} W_{i_2 j} y_{i_2} + A_j\right), \tag{6}$$

where $j = 1, 2, \ldots, l$, i_1 is the number of historical input data, u_{i_1} is the i_1-th input, i_2 is the number of historical output data, y_{i_2} is the i_2-th output, l is the number of hidden-layer neurons, f is the activation function in the hidden layer, $W_{i_1 j}$ is the connection weight between the i_1-th input and the j-th neuron in the hidden layer, $W_{i_2 j}$ is the connection

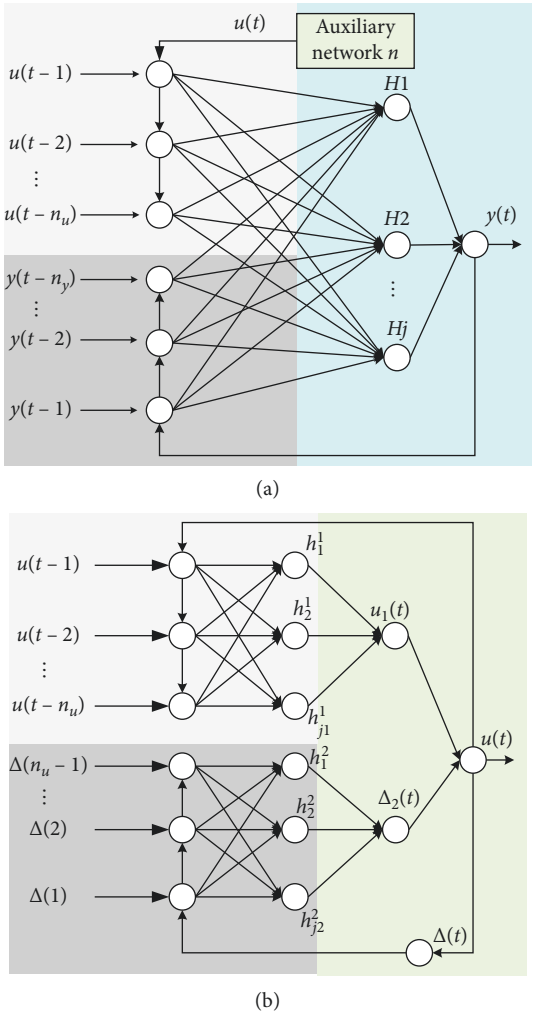

Figure 2: Structure design of the networks: (a) primary network; (b) auxiliary network.

weight between the i_1-th linear relation weight and the j-th neuron in the hidden layer, and A_j is the threshold value of the j-th hidden neuron.

The network output O can be obtained with the hidden-layer output H_j:

$$O = f\left(\sum_{j=1}^{i} H_j W_j + B\right), \tag{7}$$

where W_j is the connection weight between the output neuron and the j-th neuron in the hidden layer and B is the threshold value of the output neuron.

Similar to the primary network, there are also input, hidden, and output layers in the auxiliary network. But the hidden layers are extended to two layers. The inputs include the effect variable itself and the data change gradient which can be the reference to promote the prediction accuracy. The network can be expressed as

$$u(t) = f\Big(u(t-1), u(t-2), \ldots, u(t-n_u), \Delta(t-1), \Delta(t-2), \ldots, \Delta(t-n_u)\Big), \tag{8}$$

where $u(t)$ is the effect variable input and $\Delta(t)$ is the data change gradient given by

$$\Delta(t) = \frac{\left(u(t-n_u) - u\left(t-(n_u-1)\right)\right)}{t_0}, \tag{9}$$

where n_u is the input delay and t_0 is the time step interval.

The concrete model of the auxiliary network is

$$\begin{aligned} h_{j_1} &= f\left(\sum_{i_1=1}^{n_u} \omega_{i_1 j_1} u_{i_1} + a_{j_1}\right), \\ h_{j_2} &= f\left(\sum_{i_2=1}^{n_u-1} \omega_{i_2 j_2} \Delta_{i_2} + a_{j_2}\right), \end{aligned} \tag{10}$$

where $j_1 = 1, 2, ..., l_1$, $j_2 = 1, 2, ..., l_2$, i_1 is the number of historical input data, i_2 is the number of linear relation weights between $u(t)$ and $u(t-1)$, l_1 and l_2 are the number of hidden-layer neurons, n_u is the input delay, f is the activation function of the hidden layer, u_{i_1} is the i_1-th input number, ω is the connection weight between input and hidden neurons, and a is the threshold value of the hidden neuron. The output is derived from the hidden layer:

$$o = f\left(f\left(\sum_{j_1=1}^{l_1} h_{j_1}\omega_{j_1} + b_1\right) + f\left(\sum_{j_2=1}^{l_2} h_{j_2}\omega_{j_2} + b_2\right) + c\right), \tag{11}$$

where b is the threshold of the second hidden layer and c is the threshold of the output layer.

Based on the design of the networks above, the training method should be studied. The basic learning method is from the algorithm of backpropagation through time, in which the variable from the feedback can be regarded as a new variable.

The errors of the primary and auxiliary networks between the prediction output and the designed output are

$$\begin{cases} e_1 = \dfrac{1}{2}(y-o)^2, \\ e_2 = \dfrac{1}{2}(Y-O)^2, \end{cases} \tag{12}$$

where e_1 and e_2 are the errors, o and O are the prediction outputs, and y and Y are the designed outputs.

The connection weights $\omega_{i_1 j_1}, \omega_{i_2 j_2}, \omega_{j_1}, \omega_{j_2}, W_{i_1 j}, W_{i_2 j}, W_j, a_{j_1}, a_{j_2}, b_1, b_2, A_j$, and B are adjusted with the errors until the global error or the training iterations reach the preset value. Based on the backpropagation algorithm, the weights are obtained as

$$\begin{cases} \omega_{i_1 j_1} = \omega_{i_1 j_1} + \eta_1 h_{j_1}\left(1-h_{j_1}\right) x_{i_1} \omega_{j_1} e_1, \\ \omega_{i_2 j_2} = \omega_{i_2 j_2} + \eta_1 h_{j_2}\left(1-h_{j_2}\right) x_{i_2} \omega_{j_2} e_1, \\ \omega_{j_1} = \omega_{j_1} + \eta_1 h_{j_1} e_1, \\ \omega_{j_2} = \omega_{j_2} + \eta_1 h_{j_2} e_1, \\ a_{j_1} = a_{j_1} + \eta_1 h_{j_1}\left(1-h_{j_1}\right)\omega_{j_1} e_1, \\ a_{j_2} = a_{j_2} + \eta_1 h_{j_2}\left(1-h_{j_2}\right)\omega_{j_2} e_1, \\ b_1 = b_1 + e_1, \\ b_2 = b_2 + e_1, \\ c = c + e_1, \\ E_1 = \dfrac{1}{2m_1}\displaystyle\sum_{k_1=1}^{m_1} (y-o)^2, \end{cases} \tag{13}$$

$$\begin{cases} W_{i_1 j} = W_{i_1 j} + \eta_2 H_j\left(1-H_j\right) x_{i_1} W_j e_2, \\ W_{i_2 j} = W_{i_2 j} + \eta_2 H_j\left(1-H_j\right) x_{i_2} W_j e_2, \\ W_j = W_j + \eta_2 H_j e_2, \\ A_j = A_j + \eta_2 H_j\left(1-H_j\right) W_j e_2, \\ B = B + e_2, \\ E_2 = \dfrac{1}{2m_2}\displaystyle\sum_{k_2=1}^{m_2} (Y-O)^2, \end{cases}$$

where η_1 and η_2 are the learning rate and E_1 and E_2 are the global errors of the two networks.

3.3. Prediction Algorithm for Multivariate Time Series. Based on the CARN proposed above, the data in practice can be used to train and obtain the networks which can predict the object variable with the effect variables. The prediction algorithm for the multivariate time series is designed based on the network model. In the algorithm, the data processing and calculation process is ascertained to obtain the final prediction results. The algorithm flow is shown in Figure 3.

The inputs of the prediction algorithm include the historical data of the object variable and effect variables and the data change gradient. The output is the series of the object variable in the next time steps. The steps of the algorithm are as follows:

(1) The effect variables are selected with the correlation degrees between the object and effect variables. The historical data of the object variable and selected effect variables are preprocessed with the normalization method. In the preprocessing, the data change gradients of the effect variables should be calculated for the auxiliary networks.

(2) The historical data which have been processed are imported into the auxiliary networks. The networks are trained with the method in Section 3.2.

(3) The outputs of the auxiliary networks and the historical data of the object variable are imported into the primary network to obtain the main prediction model.

(4) The time step is set forward, and the updated data in the next time step can be obtained by repeating the steps above.

The compound network and the prediction algorithm for the multivariate time series have been proposed so far. In practice, the prediction length should be set, and the effect variables should be selected reasonably. Then, the designed prediction results of the object variable can be obtained with the historical data.

4. Experiment and Results

4.1. Experiment Data and Setting. In the experiment, we focus on the data prediction issue in the complex environment system. Two sets of the environment data are chosen to be tested. One is the atmospheric quality data from the monitoring system of an industrial park. And the other one is the meteorological forecast data.

For the atmospheric quality data, 3240 sets of data are truncated from the monitoring system in an industrial park of Hebei Province, China. The data are from different time periods which can represent different trends. The time periods include June to August in 2016 (set A), September to November in 2016 (set B), and December in 2016 to February in 2017 (set C). The monitored variables are SO_2, NO_2, CO, O_3, VOC, humidity, temperature, wind speed, atmospheric pressure, etc. And they were recorded every hour in the monitoring system. SO_2 is the main factor in the atmospheric environment management in the industrial park. Then, SO_2 is set as the object variable to be predicted, and the correlation degrees between other variables and SO_2 were calculated, as shown in Figure 4. Then, the main effect variables were selected including NO_2, CO, O_3, humidity, and wind speed.

For the meteorological forecast data, there are 24 sets of data in a day. And every set is about the meteorological factors, including the temperature, humidity, wind speed, precipitation, and atmospheric pressure. Similar to the atmospheric quality data, the most relevant variables are selected for the object variable temperature. The effect variables are the humidity, wind speed, and precipitation.

In the setting of the prediction models, the data were preprocessed firstly with the method of maximum and minimum. The prediction network output should be denormalized. The data were divided into the training, validation, and test sets. Their proportions are 70%, 15%, and 15%. The numbers of various sets are listed in Table 1.

In the experiments, the parameters of the network structure and training were obtained and are listed in Table 2. Then, the networks are trained to run the prediction algorithm in Section 3.3. The prediction results are presented in Section 4.2.

Some typical prediction methods are set as the contrast methods, including the ARIMA model, BP, RNN, and LSTM. The contrast methods cover the main types of the classic statistical model and machine learning methods. In the concrete experiments, the ARIMA and RNN are used to predict the object variable. The BP and LSTM are designed with multiple inputs including the object variable and effect variables.

4.2. Results of Atmospheric Quality Data. In the experiments, 162 sets of atmospheric quality data are tested for the prediction performance. The prediction results are shown in Figure 5. According to the experiment setting, the input delay means the historical data used, and the output delay means the prediction steps. For the atmospheric quality data, the historical data of the latest 6 hours are used to output the prediction, and the prediction results are the SO_2 concentration in the next 6 hours. The data are used forward circularly. In Figure 5, the reference true value and the prediction results of various methods are presented with lines in different colours, and some parts are enlarged for the obvious comparison.

For the prediction results in Figure 5, all methods can trace the general trend of the SO_2 concentration data. The results of the ARIMA and RNN fluctuate more acutely than the others. The results of the CARN are closer to the true value so that the black line seems to be hidden in the figure.

For the obvious comparison of different methods, the errors are calculated and shown in Figure 6. The mean absolute error (MAE) and root-mean-squared error (RMSE) are selected as the evaluation indicators. The indicators are listed in Table 3.

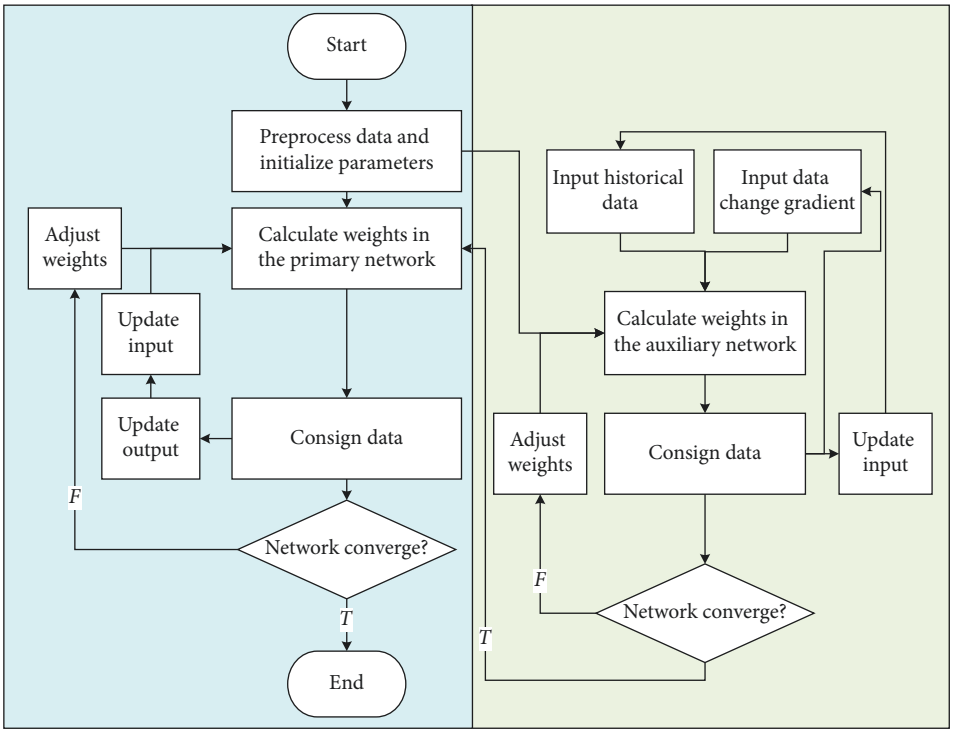

Figure 3: Prediction algorithm flow for the multivariate time series.

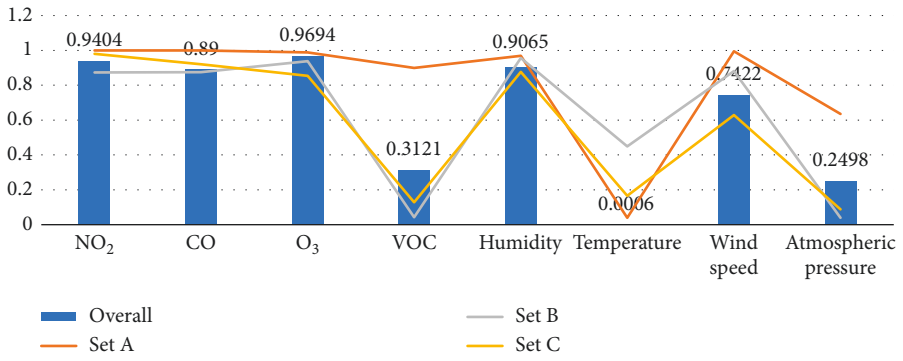

Figure 4: Correlation degrees between SO_2 and effect variables.

Table 1: Number of data in the experiments.

Datasets	Training data	Validation data	Test data
Atmospheric quality data (for each subset)	756	162	162
Meteorological forecast data	1008	216	216

The absolute errors show the similar trend of the prediction results in Figure 5. In the general view, the CARN performs more stably than other methods, in which the errors of the ARIMA and RNN change more sharply. The prediction performance can be evaluated objectively with the indicators in Table 3. The MAE is the average of all errors in their absolute value. In the indicator MAE, the CARN and LSTM perform better than the others. The MAE of results in the ARIMA is largest, while the RNN and BP show a similar MAE. The RMSE reflects the overall closeness of the results to the average value. It can indicate the stability of the prediction methods. The sort of the RMSE in different methods is similar to the trend of the MAE, and the CARN is more stable than the others in prediction.

4.3. Results of Meteorological Forecast Data. For the prediction of meteorological forecast data, 1224 sets of data are used to train and verify the network. Then, 216 sets of data are set as the testing data. The 216 sets of the prediction results are shown in Figure 7 which also includes the reference true value and results of different methods. Different

Table 2: Parameters of the network structure and training.

Datasets	Atmospheric quality data		Meteorological forecast data	
Networks	Primary network	Auxiliary network	Primary network	Auxiliary network
Number of networks	1	5	1	3
Number of training times	1000	1000	1000	1000
Learning rate	0.01	0.01	0.02	0.02
Convergence error	0.002	0.002	0.001	0.001
Input delay	1 : 6	1 : 6	1 : 12	1 : 12
Output delay	1 : 6	1 : 6	1 : 12	1 : 12
Number of inputs	6	10	4	6
Number of outputs	1	10	1	6
Number of hidden-layer neurons	10	14	7	10

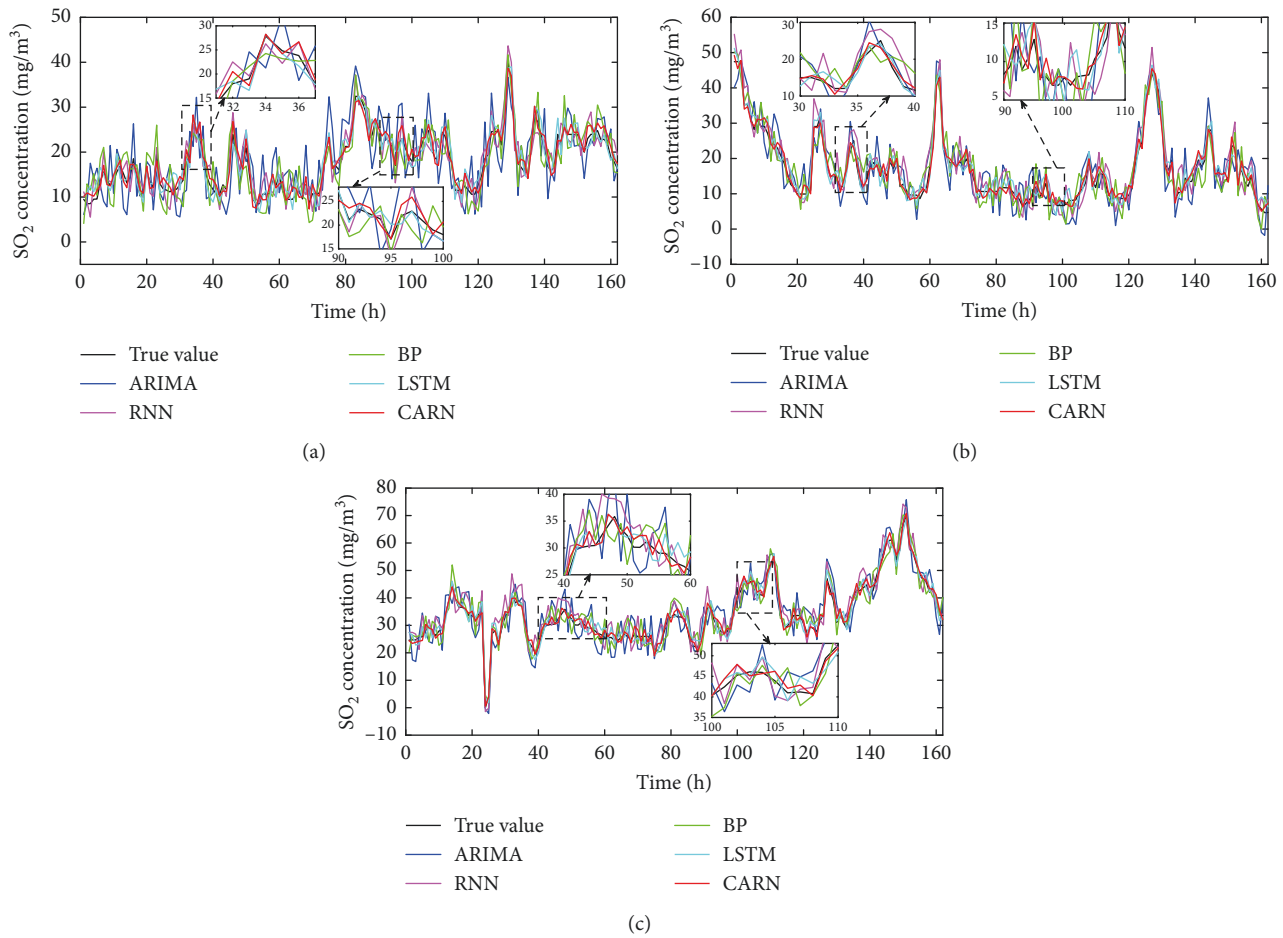

Figure 5: Prediction results of atmospheric quality data in three time periods: subset data (a) from June to August in 2016, (b) from September to November in 2016, and (c) from December in 2016 to February in 2017.

from the experiment of atmospheric quality data, the input and output delays are set to 12. The latest 12 sets of data are used to predict the temperature in the next 12 hours.

The data shown in Figure 7 present an obvious periodic trend. In fact, 216 sets of data are the meteorological data in 9 days. The temperature changes circularly in the period of one day. Then, the data change rule is more distinct. The prediction results of the CARN are closer to the true value than the others, in which the ARIMA and RNN fluctuate because they are predicted only with the object variable and other methods use the object variable with effect variables.

The errors are calculated and presented in Figure 8 and Table 4. Figure 8 shows the errors of different prediction results. Table 4 lists the error evaluation indicators MAE and RMSE.

From the prediction results in Figure 7 and errors in Figure 8, it can be seen that all methods can trace the data change rule closely because of the periodicity in the meteorological data. The errors mainly occur in the fluctuation. The maximal MAE reaches 4.43°C in the ARIMA which is near to

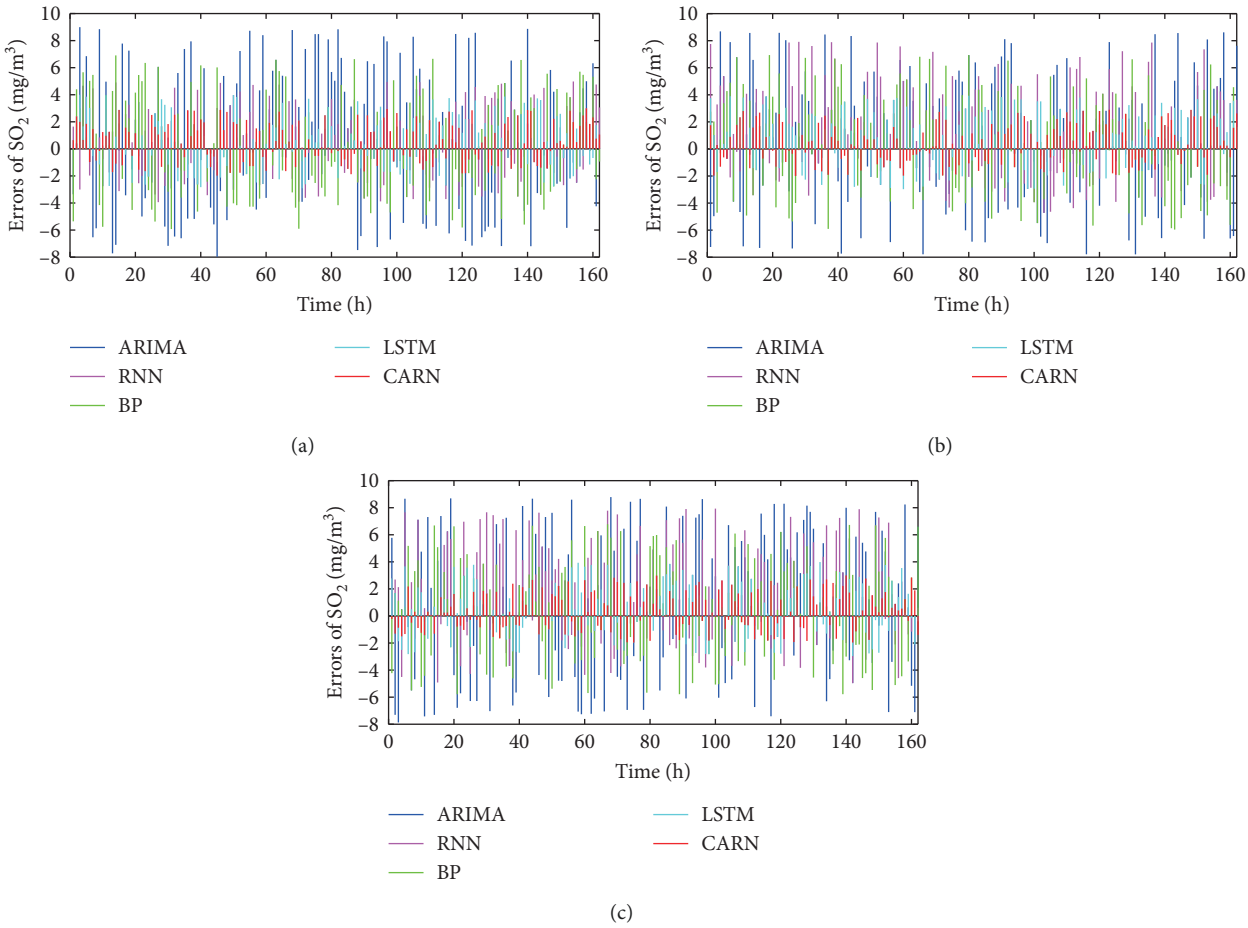

Figure 6: Errors of the prediction results of atmospheric quality data in different methods: subset data (a) from June to August in 2016, (b) from September to November in 2016, and (c) from December in 2016 to February in 2017.

Table 3: Error evaluation indicators of the prediction results of atmospheric quality data.

Data subsets		ARIMA	RNN	BP	LSTM	CARN
A	MAE	4.3617	2.3389	3.0917	1.6595	1.3275
	RMSE	5.0748	2.7257	3.6026	1.9791	1.5546
B	MAE	4.1136	2.9919	3.1235	1.8687	1.2421
	RMSE	4.7969	3.6575	3.6624	2.1634	1.4779
C	MAE	4.6690	3.3906	3.1084	1.7715	1.2660
	RMSE	5.3136	4.0724	3.6529	2.0841	1.4966

20% of the original measurement. The errors of the ARIMA, RNN, and BP exceed the usual expectation, while the errors of the CARN and LSTM (lower than 2°C) are acceptable.

5. Discussion

For the prediction issue of the multivariate time series, a compound network framework is introduced in which the structure of the nonlinear autoregressive network and the prediction algorithm are designed. The experiments are conducted within the environment data, including the atmospheric quality data and meteorological forecast data. The prediction methods and results will be discussed in this section.

Firstly, the method shows the favourable short-term tracking performance in the data change rule. Generally, the prediction methods cannot avoid the divergency in the long term. It seems that there is not divergency in our prediction results. It is not that our approach is perfect, while the good regressive results derive from the setting of prediction time. The prediction time steps of the experiment are 6 and 12, which belong to the short-term prediction. The practical true values are imported into the model circularly to output the data in the future. Therefore, the prediction results show the good regressive effects. The results indicate that the proposed method can meet the short-term prediction need.

Secondly, the proposed method focuses on the prediction problem with multiple variables. For the accurate prediction, the related variables should be considered based on the target variable to be predicted. In the experiments, SO_2 and temperature are set as the object variable, and the related variables are selected as the effect variables. In the comparison methods, the ARIMA and RNN only use the object variable to predict the data themselves. The BP, LSTM, and CARN use multiple variables to obtain more accurate results. It is indicted that the effect variables help

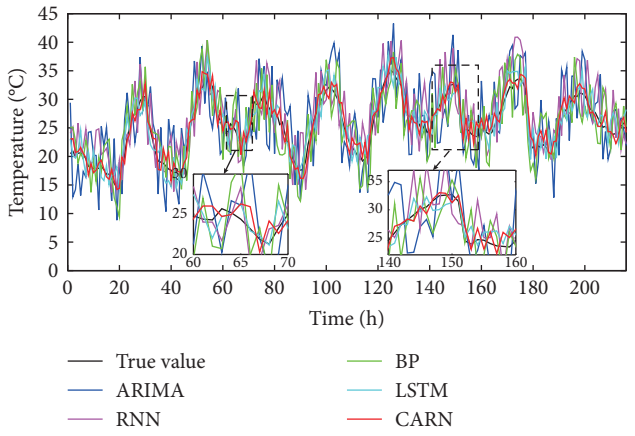

Figure 7: Prediction results of meteorological forecast data.

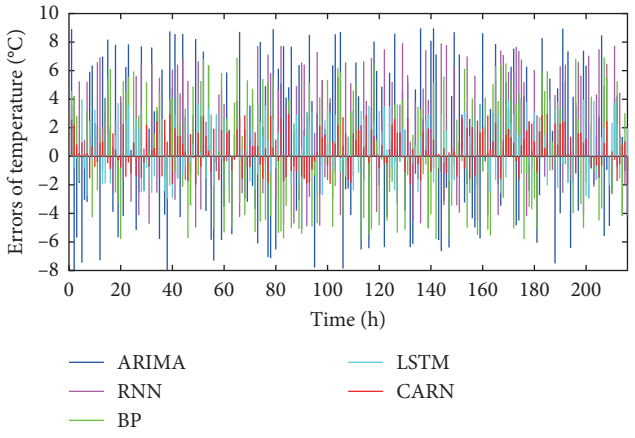

Figure 8: Errors of the prediction results of meteorological forecast data in different methods.

Table 4: Error evaluation indicators of the prediction results of meteorological forecast data.

	ARIMA	RNN	BP	LSTM	CARN
MAE	4.4331	3.3896	3.4048	1.7582	1.2564
RMSE	5.0999	4.0747	3.8864	2.0608	1.4829

improve the prediction performance. In the proposed method, the design of the auxiliary network meets the need of multivariate analysis.

Thirdly, the proposed method seeks the balance of precision performance and calculation resource occupancy. As mentioned in the introduction of related works, deep learning shows the excellent performance in prediction. It can be proved in the experiment where the result of the LSTM is similar to that of the CARN. However, the structure of the deep network is more complex than that of the network NAR, which may lead to the large consumption of the calculation resources. In the proposed method, networks based on the NAR are combined to obtain the expected prediction accuracy. Meanwhile, the simple structure of the NAR can reduce the calculation resource demand. The balance of accuracy and calculation resource in our method is beneficial to the application in practice.

The proposed CARN reaches the expectant effect in the time-series prediction. The effect is guaranteed with the compound structure of the primary and auxiliary networks to model the multivariable relation. Meanwhile, the training method in the CARN is also tested with experimental results based on the adjustment of the network parameters.

For the objective appraisal, the performance and application of the proposed network can be extended in the future. For the network performance, the training method is derived from the framework of backpropagation through time, which is an effective and simple solution in network learning. The related works on the backpropagation learning method are abundant. The improvement methods can be imitated based on the compound network structure. For the application, the proposed network can solve the direct prediction problems, such as the forecast of the weather, environment, economic market, and health management. It can also solve the data prediction in other complex systems indirectly. For example, the network may help the prediction of the control parameter in the nonlinear time-delay system [24]. The prediction result will be the important information for the control and management issues.

6. Conclusion

For the intelligent and advance management in the information era, the data-driven prediction method is studied in this paper. Considering the characteristic of the nonstationary and multivariate effect in the nonlinear time series, a compound prediction framework is designed based on the autoregressive neural network. The experiments on the environment data are conducted to verify the performance of the method. The method shows the favourable accuracy and appropriate calculation scale. The proposed network realizes the prediction of the multivariate. Besides, it takes the computational efficiency into account as well as the prediction performance. Furthermore, the principle of the network training in this paper is practical. It provides a feasible solution to the nonlinear multivariate time series with the shallow neural network. In the future work, the training method can be improved based on the advanced research, and the long-term prediction performance should be promoted. Moreover, the compound autoregressive network can be applied in other fields, including the direct forecasting of the time series and indirect prediction of the parameters and components in the complex systems.

Data Availability

The CSV data used to support the findings of this study are currently under embargo, while the research findings are commercialized. Requests for data, 6 months after publication of this article, will be considered by the corresponding author.

Conflicts of Interest

The authors declare that there are no conflicts of interest regarding the publication of this paper.

Acknowledgments

This work was supported in part by the National Key Research and Development Program of China under No. 2017YFC1600605, National Natural Science Foundation of China under Nos. 61673002 and 61903009, and Beijing Municipal Education Commission under Nos. KM201910011010 and KM201810011005.

References

[1] H. Yao, W. Zhuang, Y. Qian et al., "Estimating and predicting metal concentration using online turbidity values and water quality models in two rivers of the Taihu Basin, Eastern China," *PLoS One*, vol. 11, no. 3, Article ID e0152491, 2016.

[2] X. Liu, H. Liu, L. Wang et al., "The EFDC model integration and application in the Three Gorges reservoir," *Research of Environmental Sciences*, vol. 31, no. 2, pp. 283–294, 2018.

[3] K. M. Mok, A. I. Miranda, K. U. Leong, and C. Borrego, "A Gaussian puff model with optimal interpolation for air pollution modelling assessment," *International Journal of Environment and Pollution*, vol. 35, no. 1, pp. 111–137, 2008.

[4] G. E. P. Borrego and G. M. Jenkins, *Time Series Analysis: Forecasting and Control*, Holden Day, San Francisco, CA, USA, 1976.

[5] Y. Wang, C. Wang, C. Shi, and B. Borrego, "Short-term cloud coverage prediction using the ARIMA time series model," *Remote Sensing Letters*, vol. 9, no. 3, pp. 274–283, 2018.

[6] Z. H. Xiao and M. Khashei, "A least squares-based parallel hybridization of statistical and intelligent models for time series forecasting," *Computers & Industrial Engineering*, vol. 118, pp. 44–53, 2018.

[7] M. Khashei and Z. Hajirahimi, "A comparative study of series ARIMA/MLP hybrid models for stock price forecasting," *Communication in Statistics-Simulation and Computation*, vol. 48, no. 9, pp. 2625–2640, 2018.

[8] L. Chen and H. Xu, "Autoregressive integrated moving average model in food poisoning prediction in Hunan province," *Journal of Central South University*, vol. 37, no. 2, pp. 142–146, 2012.

[9] D.-w. Xu, Y.-d. Wang, L.-m. Jia, Y. Qin, and H.-h. Dong, "Real-time road traffic state prediction based on ARIMA and Kalman filter," *Frontiers of Information Technology & Electronic Engineering*, vol. 18, no. 2, pp. 287–302, 2017.

[10] H. Yang, Z. Pan, and W. Bai, "Review of time series prediction methods," *Computer Science*, vol. 46, no. 1, pp. 21–28, 2019.

[11] D. Pradeepkumar and V. Ravi, "Forecasting financial time series volatility using particle swarm optimization trained quantile regression neural network," *Applied Soft Computing*, vol. 58, pp. 35–52, 2017.

[12] C. Daly, D. L. Moore, and R. J. Haddad, "Nonlinear autoregressive neural network model for forecasting Hi-Def H.265 video traffic over Ethernet passive optical networks," in *Proceedings of the IEEE SoutheastCon 2017*, pp. 1–7, IEEE, Charlotte, NC, USA, March 2017.

[13] T. Wang, H. Gao, and J. Qiu, "A combined adaptive neural network and nonlinear model predictive control for multirate networked industrial process control," *IEEE Transactions on Neural Networks and Learning Systems*, vol. 27, no. 2, pp. 416–425, 2015.

[14] C. Liu, T. Shu, S. Chen, S. Wang, K. K. Lai, and L. Gan, "An improved grey neural network model for predicting transportation disruptions," *Expert Systems with Applications*, vol. 45, pp. 331–340, 2016.

[15] B. Doucoure, K. Agbossou, and A. Cardenas, "Time series prediction using artificial wavelet neural network and multi-resolution analysis: application to wind speed data," *Renewable Energy*, vol. 92, pp. 202–211, 2016.

[16] L. Wang, Y. Zeng, and T. Chen, "Back propagation neural network with adaptive differential evolution algorithm for time series forecasting," *Expert Systems with Applications*, vol. 42, no. 2, pp. 855–863, 2015.

[17] P. Rodriguez, J. Wiles, and J. L. Elman, "A recurrent neural network that learns to count," *Connection Science*, vol. 11, no. 1, pp. 5–40, 1999.

[18] A. Graves, S. Fernández, and J. Schmidhuber, "Multi-dimensional recurrent neural networks," *Lecture Notes in Computer Science* in *Proceedings of the International Conference on Artificial Neural Networks*, vol. 4668, pp. 549–558, 2007.

[19] M. Schuster and K. K. Paliwal, "Bidirectional recurrent neural networks," *IEEE Transactions on Signal Processing*, vol. 45, no. 11, pp. 2673–2681, 1997.

[20] S. Hochreiter and J. Schmidhuber, "Long short-term memory," *Neural Computation*, vol. 9, no. 8, pp. 1735–1780, 1997.

[21] A. Graves, S. Fernández, and J. Schmidhuber, "Bidirectional LSTM networks for improved phoneme classification and recognition," in *Proceedings of the International Conference on Artificial Neural Networks*, pp. 799–804, Munich, Germany, September 2005.

[22] K. Cho, B. V. Merrienboer, C. Gulcehre et al., "Learning phrase representations using RNN encoder-decoder for statistical machine translation," in *Proceedings of the Conference on Empirical Methods in Natural Language Processing*, pp. 1–14, Lisbon, Portugal, September 2014.

[23] R. Matkovskyy and T. Bouraoui, "Application of neural networks to short time series composite indexes: evidence from the nonlinear autoregressive with exogenous inputs (NARX) model," *Journal of Quantitative Economics*, vol. 17, no. 2, pp. 433–446, 2019.

[24] T. Wang, J. Qiu, and H. Gao, "Adaptive neural control of stochastic nonlinear time-delay systems with multiple constraints," *IEEE Transactions on Systems, Man, and Cybernetics: Systems*, vol. 47, no. 8, pp. 1875–1883, 2017.

Hindawi
Complexity
Volume 2019, Article ID 5986562, 24 pages
https://doi.org/10.1155/2019/5986562

Research Article

Geodesic Distance on Gaussian Manifolds to Reduce the Statistical Errors in the Investigation of Complex Systems

Michele Lungaroni,[1] **Andrea Murari**,[2] **Emmanuele Peluso**,[1] **Pasqualino Gaudio**,[1] **and Michela Gelfusa**[1]

[1]*Department of Industrial Engineering, University of Rome Tor Vergata, Via del Politecnico 1, 00133 Rome, Italy*
[2]*Consorzio RFX (CNR, ENEA, INFN, Universita' di Padova, Acciaierie Venete SpA), Corso Stati Uniti 4, 35127 Padova, Italy*

Correspondence should be addressed to Michele Lungaroni; michele.lungaroni@uniroma2.it

Received 18 March 2019; Revised 17 July 2019; Accepted 21 July 2019; Published 18 August 2019

Academic Editor: Dan Selişteanu

In the last years the reputation of medical, economic, and scientific expertise has been strongly damaged by a series of false predictions and contradictory studies. The lax application of statistical principles has certainly contributed to the uncertainty and loss of confidence in the sciences. Various assumptions, generally held as valid in statistical treatments, have proved their limits. In particular, since some time it has emerged quite clearly that even slightly departures from normality and homoscedasticity can affect significantly classic significance tests. Robust statistical methods have been developed, which can provide much more reliable estimates. On the other hand, they do not address an additional problem typical of the natural sciences, whose data are often the output of delicate measurements. The data can therefore not only be sampled from a nonnormal pdf but also be affected by significant levels of Gaussian additive noise of various amplitude. To tackle this additional source of uncertainty, in this paper it is shown how already developed robust statistical tools can be usefully complemented with the Geodesic Distance on Gaussian Manifolds. This metric is conceptually more appropriate and practically more effective, in handling noise of Gaussian distribution, than the traditional Euclidean distance. The results of a series of systematic numerical tests show the advantages of the proposed approach in all the main aspects of statistical inference, from measures of location and scale to size effects and hypothesis testing. Particularly relevant is the reduction even of 35% in Type II errors, proving the important improvement in power obtained by applying the methods proposed in the paper. It is worth emphasizing that the proposed approach provides a general framework, in which also noise of different statistical distributions can be dealt with.

1. Robust Statistics and Measurement Errors in the Science of Complex Systems

In the last decades the number of contradictory, inaccurate, and/or misleading scientific pronouncements reported in the media about complex systems has increased exponentially. From medicine to finance, very often opposing studies and findings have generated a quite high level of confusion. Moreover various expectations, predictions, and evaluations have been very often completely contradicted by reality; a very evident example is the financial crisis of 2008. This situation has considerably corroded the public confidence in expert knowledge [1] and even more generally in the sciences. The status of peer reviewed journals in various fields is not more reassuring. In a famous paper and subsequent works, it has been shown how many studies, published in the most highly respected medical journals, are refuted by other investigations in a matter of months or at the most a few years [2].

There are many causes to the worrying situation previously described, from the reduction in public funding to the corporate takeover of public functions and institutions. However, also the misguided application of inadequate statistical tools has certainly played a role and contributed to exacerbate the problem. Indeed classic significance tests are the main statistical tools in many disciplines, ranging from medicine and education to economics and psychology. In the last decades, hypothesis tests have been increasingly used also

in the so called exact sciences, such as physics, chemistry and engineering, particularly when complex systems have to be studied. These classic methods are based on certain specific assumptions, which have to be reasonably satisfied; otherwise the accuracy of the results can be seriously compromised. One fundamental assumption is that the data are randomly sampled from a Gaussian distribution. In case of hypothesis testing and comparison between independent groups, it is also typically assumed that the distributions have a common variance (even if they present different means); this is the so called homogeneity of variance or homoscedasticity hypothesis. Conversely, in practical applications the data available do not necessarily conform to these assumptions. The probability density functions sampled in experiments are not necessarily Gaussians and can present heavy tails or be skewed. Homoscedasticity is even more frequently violated.

Some of the classic parametric tests are quite robust against violation of the normality assumption, in the sense that they can preserve both the expected rates of Type I and Type II errors, even if they have quite low power compared to their nonparametric counterparts. This has been reported extensively in Sawilowsky [3] and Sawilowsky and Blair [4]. On the contrary, in the last decades, a lot of evidences have emerged showing how a blind reliance on the assumption of homoscedasticity can produce rather inaccurate results as reported in Wilcox [5, 6] and in this respect rank-based nonparametric statistics can fare even worse. In Wilcox [6] it is shown that the violation of homoscedasticity significantly affects type I errors, up to 0.5 at a significant level of 0.05. The power of the tests can be even more severely compromised by violation of the previous assumptions; indeed for distributions characterized by small departures from normality, as reported in Wilcox [5], the power of the t test can be reduced from 0.96 to 0.28. Therefore a lot of efforts have been recently devoted to developing robust tools, which seek to provide methods that compare well with popular statistical techniques, when the classic hypotheses are satisfied, but which are not unduly affected by departures from model assumptions. Developed in the framework of robust statistics, as reported in Huber and Ricchetti [7], these techniques provide quite accurate, even if slightly suboptimal results, in the case the assumptions of normality and homoscedasticity are correct, but are not compromised, if the data have been sampled from a different distribution. However, even if they are quite successful in terms of descriptive statistics, robust techniques can be affected by significant increase in Type I errors when converted into inference statistics. The developments proposed in this paper are indeed meant to improve robust statistics explicitly in this direction.

The tools developed in the framework of robust statistics in the last decades have achieved very impressive results but they do not address at all a problem typical of the experimental sciences. In the vast majority of natural science applications, the data are measurements affected by error bars. Therefore, the available data can be not only sampled from a distribution, which is quite far from a Gaussian, but they can also be affected by significant additive noise. Robust statistical methods address only the first of these two problems, the fact that the assumptions about the probability density function (pdf) generating the data are not satisfied. However, the additional uncertainty introduced by the additive noise in the measurements is not considered.

In all the formulas developed in the framework of robust statistics, the Euclidean distance is implicitly assumed to be the proper metric to adopt. The Euclidean distance, however, implicitly requires considering all data as single infinitely precise values. This assumption can be appropriate in other applications but it is obviously not so in the natural sciences, since all the measurements are typically affected by noise. As will be shown later, an inappropriate evaluation of the uncertainties in the measurements can have a major impact even on the determination of the basic statistical measures such as the mean. An alternative approach is to use a new distance between data, which would take into account the measurement uncertainties. The idea, behind the method proposed in this paper, consists of considering the measurements not as points, but as Gaussian distributions. This is a valid assumption in many scientific applications, because the measurements are affected by a wide range of noise sources, which, from a statistical point of view, can be considered random variables.

Modelling measurements not as punctual values, but as Gaussian distributions, requires defining a distance between Gaussians. This distance is the Geodesic on the Gaussian Manifold (GDGM) and can be expressed as a closed formula (see Section 3). As shown in the rest of the paper, adopting this geodesic distance increases significantly the accuracy of robust statistical tools, even when the data are affected by a limited level of noise, particularly for hypotheses testing.

With regard to the structure of the paper, next section is devoted to an introductory discussion about the importance of a proper evaluation of the errors associated with the experimental measurements in the framework of a modern theory of uncertainty. Section 3 provides the background on the main mathematical tool introduced in the paper: the Geodesic Distance on Gaussian Manifolds. The probability density functions used in the paper to test the proposed new approach are reviewed in Section 4. The main ideas behind robust statistics are introduced in Section 5. The proposed new method is applied first to the measurements of location and scale, as described in Sections 6 and 7. The impact of using the GDGM in hypothesis testing is described in Section 8. The performance of GDGM in the case the sampled pdf is asymmetric and the additive noise is heteroscedastic is exemplified in Section 9. Conclusions and lines of future work are provided in the last Section 10 of the paper.

2. The Theory of Uncertainty and the Experimental Measurements

In the science of complex systems, measurements are the basic inputs required to provide quantitative knowledge about phenomena. However, all the measurements provide limited information about the measure and since they are affected by uncertainties. At the end of last century, the theory of uncertainty was consolidated and became the dominant paradigm with the publication of the IEC-ISO “Guide to

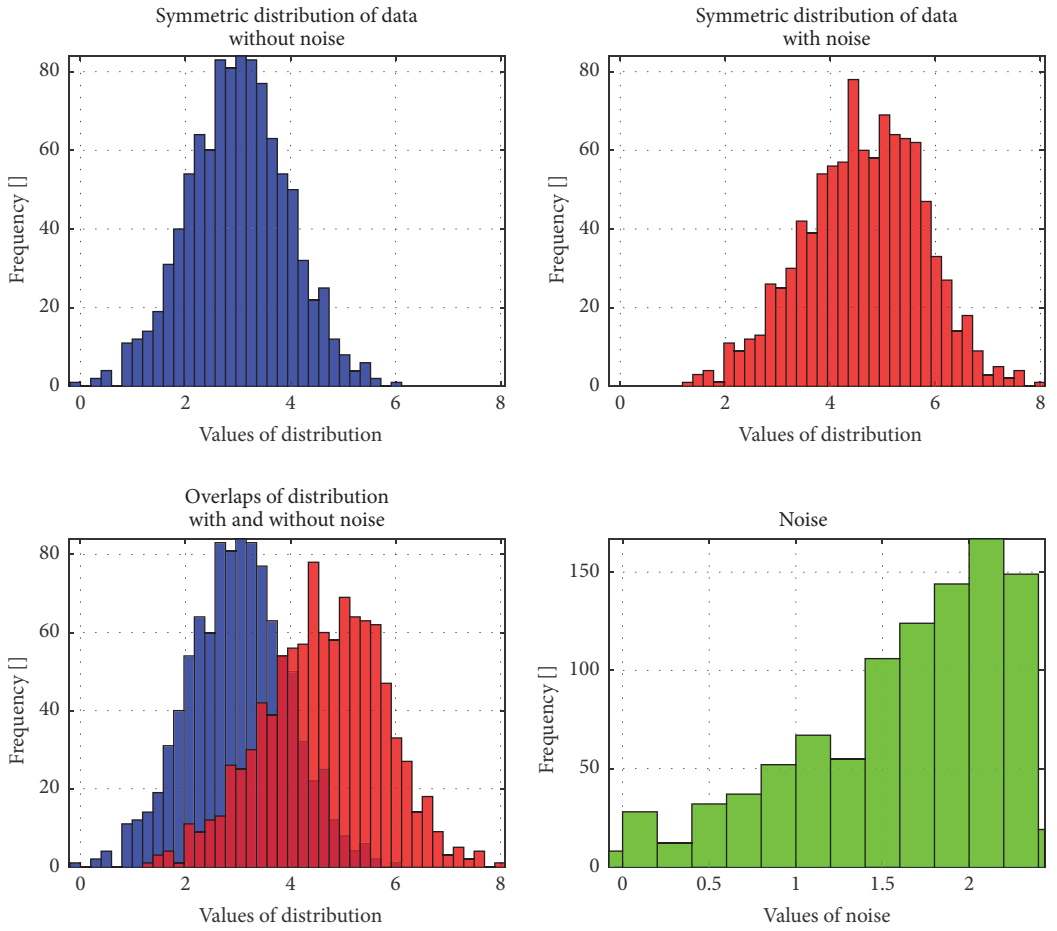

Figure 1: Distribution of data sampled from a Gaussian distribution (of $\overline{x}$=3 and s=1) affected by Gaussian noise of zero mean and standard deviation basically proportional to the absolute value of the data (see bottom right plot).

the Expression of Uncertainty in Measurement" (GUM) in 1992 [8]. Assuming that all the systematic errors have been eliminated, the uncertainty to be associated with the results of a series of measurements x_i is their standard deviation, defined as

$$s = \sqrt{\frac{\sum_{i=1}^{n} \left[(x_i) - \overline{x}\right]^2}{n-1}} \quad (1)$$

In the previous equation, the standard deviation s is expressed in terms of the average $\overline{x}$ of the n available observations. This emphasizes how the process of calculating the average is at the very basis of the first, most elementary statistical steps, required to quantify even the most elementary quality of the available measurements. Therefore any error in the determination of the mean has the potential to invalidate the entire statistical analysis. To illustrate the potential impact of the issue let us analyse a case, for which the traditional heteroscedasticity assumption is not valid. In this simple, introductory example, we investigate the case that the measurements are generated by a Gaussian distribution of $\overline{x}$=3 and s=1. The data are considered affected by a Gaussian noise of zero mean but a varying standard deviation. In particular, the noise s increases almost linearly with the amplitude of the measurements; this is not an uncommon case in practice because in many instruments the measurement errors are a fixed percentage of the measured value. This situation is illustrated in Figure 1, which summarise a numerical experiment with 1000 data points.

The accuracy of the traditional estimates of location, mean, and mode is reported in Table 1, together with the values of the robust indicator introduced later in the paper (see Sections 3–5). The values obtained by application of our methodology, using the GDGM, are also shown. In Table 1, as for all the others reported either in the main text or in the Appendixes, the numerical values are the results obtained mediating over 1000 independent realisations. The details of the method proposed in this paper are given later; for the moment what should be retained is that the traditional statistical measures of location fare very badly for this kind of noise. Also the robust statistical indicators commit very serious overestimates. On the contrary, our approach of combining robust indicators with the GDGM reduces the inaccuracy in the estimate of location of even an order of magnitude.

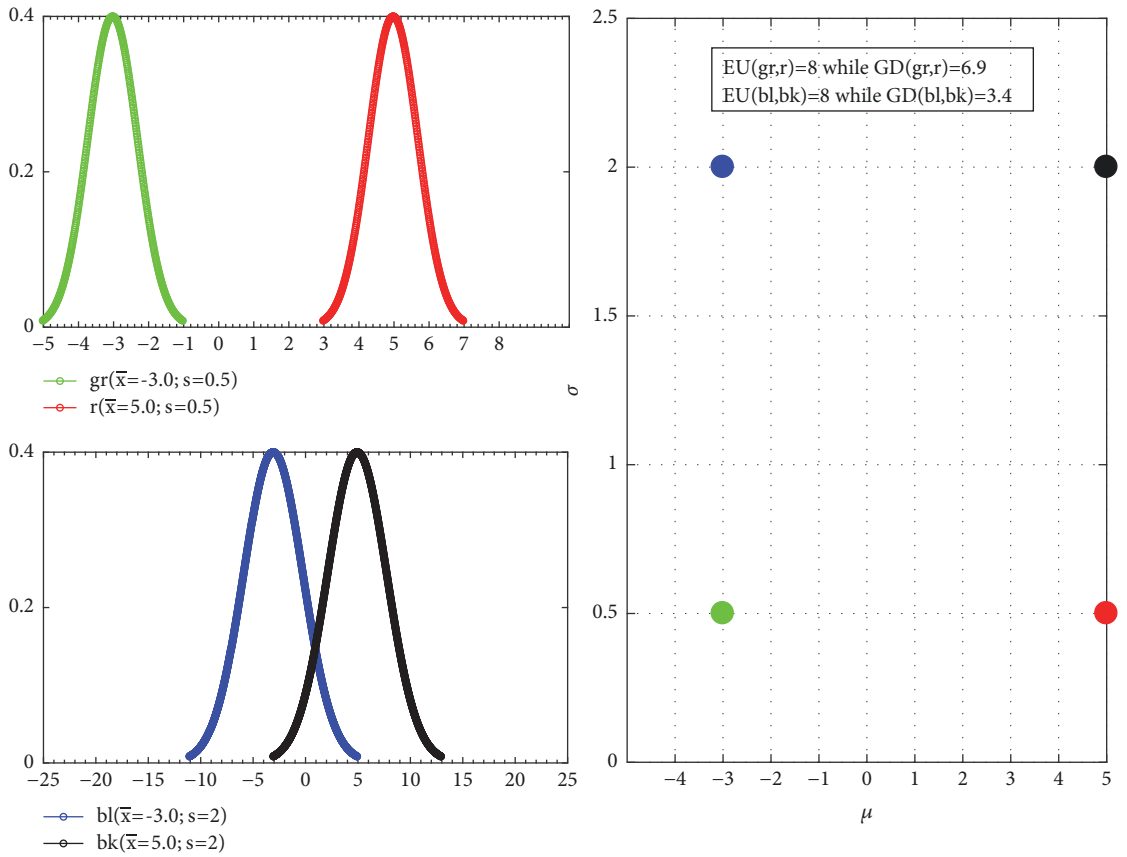

Figure 2: Examples to illustrate how the GDGM determines the distance between two Gaussians. The two couples of pdfs in the figure have the same mean but different s. The geodesic distance between the two with higher s is much smaller (see insert).

Table 1: Measures of location for the data of Figure 1. The ideal value to be obtained is 3. The acronym GD indicates the values obtained with the use of the Geodesic on the Gaussian Manifold (GDGM) proposed in the paper, which reduces the errors in the estimates even of an order of magnitude recovering almost the right value of 3.

	No Noise	Noise
Mode	2.975	4.728
Mean	3.000	4.664
GD_{Mean}	2.335	3.352
Trimmed Mean	2.999	4.687
$GD_{Trimmed}$	1.965	2.939
Wisorized Mean	3.000	4.680
GD_{Winsor}	2.122	3.088

3. Geodesic Distance on Gaussian Manifolds

As mentioned in the previous section, in the natural sciences the data available are typically the result of experimental measurements, which are affected by uncertainties referred to as noise. The sources of this uncertainty are normally several, independent and additive: as a consequence it is more than reasonable to assume that the pdf of the noise is normal. Each measurement can therefore be modelled as a probability density function of the Gaussian type, determined by its mean $\overline{x}$ and its standard deviation s:

$$p(x \mid \mu, \sigma) = \frac{1}{\sqrt{2\pi}\sigma} \exp\left[-\frac{(x-\mu)^2}{\sigma^2}\right] \quad (2)$$

The set of normal distributions can be seen as a two dimensional space, or better a two dimensional manifold, parameterised by $\overline{x}$ and s. Modelling measurements not as punctual values, but as Gaussian distributions, requires defining a distance between Gaussians. The most appropriate definition of distance between Gaussian distributions is the geodesic distance, on the probabilistic manifold containing the data, which is not a Euclidean but a Riemannian space. This geodesic distance on the Gaussian manifold can be calculated using the Fisher-Rao metric as it has been applied in Cannas et al. [9] and Murari et al. [10]. For two univariate Gaussian distributions $p_1(x \mid \mu_1, \sigma_1)$ and $p_2(x \mid \mu_2, \sigma_2)$, parameterised by their mean μ_i and standard deviations

σ_i $(i = 1, 2)$, the geodesic distance GD is given by

$$GD\left(p_1 \mid |p_2\right) = \sqrt{2}\ln\frac{1+\delta}{1-\delta} = 2\sqrt{2}\tanh^{-1}\delta,$$
$$where\ \delta = \left[\frac{\left(\mu_1-\mu_2\right)^2 + 2\left(\sigma_1-\sigma_2\right)^2}{\left(\mu_2-\mu_2\right)^2 + 2\left(\sigma_1+\sigma_2\right)^2}\right]^{1/2} \quad (3)$$

A pictorial view of the potential impact of the GDGM is provided in Figure 2, which shows the distance between two couples of Gaussian distributions having the same difference in means. The standard deviations of the two Gaussians in the bottom plot are much larger than the ones of the two Gaussians, whose distance is depicted in the top plot, using the Euclidean distance results in attributing the same distance to the two couples of normal distributions. On the contrary, according to the GDGM, the distance between the two Gaussians with a larger σ is much smaller, which makes intuitive sense since they overlap much more. As will be shown in detail in the next sections, the replacement of the Euclidean distance with the GDGM improves significantly all the robust estimators, reducing the effects of noise and outliers.

4. Nonnormal Distributions

To exemplify and prove the usefulness of the method proposed in this paper, a series of numerical tests has been performed, with probability density functions of families different from the Gaussian. To simulate realistic situations in the natural sciences, Gaussian noise of various amplitudes has been added to the data sampled from the nonnormal pdfs. The tests performed in the rest of the paper have been obtained from the pdfs belonging to the families: log-normal, exponential, contaminated χ^2 and the so called g-h pdf. The analysed distributions are defined in the rest of this section (more details are provided in Wilcox 2005 [11]):

The traditional log normal distribution corresponds to the pdf:

$$f_{\log Nor}\left(x \mid \mu, \sigma\right) = \frac{e^{-(\ln x-\mu)^2/2\sigma^2}}{x\sqrt{2\pi}\sigma} \quad with\ x > 0 \quad (4)$$

The pdf of the exponential distribution can be written as

$$f_{exp}\left(x \mid \lambda\right) = \frac{1}{\lambda}e^{-x/\lambda} \quad (5)$$

The contaminated χ^2 distribution $\chi^2_k(x)$ is the sum of two χ^2 distributions, the first sampled with probability 1- Ɛ, and the second with probability Ɛ. The $\chi^2_k(x)$ is defined as

$$\chi^2_k\left(x \mid k_1, k_2, \varepsilon\right) = (1-\varepsilon) \bullet \chi^2_{k1}\left(x \mid k_1, \varepsilon\right) + \varepsilon \bullet \chi^2_{k2}\left(x \mid k_2, \varepsilon\right) \quad with\ 0 \le \varepsilon \le 1 \quad (6)$$

In (6) k indicates the number of degrees of freedom of the distribution and $\chi^2_{ki}(x)$ is

$$\chi^2_k\left(x \mid k\right) = \frac{1}{2^{k/2}\Gamma\left(k/2\right)}x^{k/2-1}e^{-x/2} \quad with\ x > 0 \quad (7)$$

The g-h distribution is a family of pdfs parameterised by the two values g and h. It consists of a normal distribution $Z = \mathcal{N}(0, 1)$ modified by the parameters g and h, which determine its asymmetry and the relevance of the tail respectively. The pdf of the g-h distribution is

$$f_{gh}\left(x \mid g, h\right) = \frac{\exp\left(gZ\right)-1}{g}\exp\left(\frac{hZ^2}{2}\right) \quad (8)$$

If g = 0 then

$$f_{gh}\left(x \mid g, h\right) = Z\exp\left(\frac{hZ^2}{2}\right) \quad (9)$$

When both parameters are zero, the standard normal $\mathcal{N}(0, 1)$ is recovered.

5. The Approach of Robust Statistics and the GDGM

In this section the needs of a special treatment for pdfs with heavy tails are reviewed. The potential of the GDGM to address the issue of noise is introduced.

5.1. The Issues Presented by Non-Gaussian Pdfs. A typical case, discussed in detail to illustrate the main ideas behind the approach proposed in this paper, is the calculation of the sample mean. When the data are not sampled from a Gaussian distribution or are affected by a significant fraction of outliers, it is well known that a trimmed mean can produce a much better estimate of location as it is reported in Wilcox [11]. An example is the case of the log normal distribution shown in Figure 3.

This is the typical example of a nonsymmetric pdf, with significant asymmetric tails. Contrary to the case of the symmetric normal distribution, in the case of the log normal the mean does not correspond to the maximum value. Indeed, as can be appreciated by Figure 3, the mean value of the distribution is quite displaced to the right of the maximum. Therefore the mean value is no more representative of the most probable value to be expected once the log normal is sampled. As a consequence, if the measures of location are meant to determine the typical value of a quantity, as it is typically the case in the science of complexity, the traditional sample mean is not really representative. The median provides a much better estimate of central tendency for distributions with tails but it can provide quite wrong estimates in the case the data are indeed sampled from a normal distribution.

Various strategies can be adopted to alleviate this problem. In the work of Wilcox [11] they are referred to as robust measures of location. A very important family of these methods is based on some form of trimming of the available data. A trimmed mean or truncated mean consists of calculating the mean of the available data after discarding the high and low end parts of the samples (typically discarding an equal amount of both). The number of samples to be discarded is usually given as a percentage of the total number

Table 2: The estimates of location for different distributions with 20 points without noise. Respectively, we have lognormal distribution $\overline{x} = 2$ and $s = 1$ parameters; exponential distribution $\lambda = 2$ parameter; contaminated χ^2 $k_1 = 4, k_2 = 40$, and $\varepsilon = 0.9$ parameters; G-h distribution $g = 0.5$ and $h = 0.5$ parameters.

	Lognormal	Exponential	Contaminated χ^2	G-h
Mode	6,56209	0,99761	3,80171	0,30349
Mean	12.28140	1.99360	7.59350	0.70637
GD_{Mean}	10.77281	1.80658	6.24093	0.44912
Trimmed Mean	8.56378	1.56370	4.19754	0.07971
$GD_{Trimmed}$	8.30072	1.52316	4.07220	0.05915
Wisorized Mean	9.13209	1.65190	4.53569	0.12788
GD_{Winsor}	8.77492	1.59667	4.34010	0.09893

Table 3: In this table the values of location for a log-normal distribution of parameters $\overline{x} = 2$ and $s = 1$ and 30 % of Gaussian noise are reported. The level of noise is expressed as percentage of the mean of the distributions. In the columns we have the location values when the distributions are composed with 20, 50, 100, and 1000 points.

	20 points Location $\overline{x}$	50 points Location $\overline{x}$	100 points Location $\overline{x}$	1000 points Location $\overline{x}$
Mode	8,5394	6,5722	5,7292	3,75215
Mean	12.24879	12.2451	12.19511	12.20451
GD_{Mean}	10.78797	10.79425	10.75084	10.80813
Trimmed Mean	8.9453	8.9077	8.78285	8.75854
$GD_{Trimmed}$	8.68679	8.63359	8.48676	8.44375
Wisorized Mean	9.40048	9.43643	9.3558	9.36122
GD_{Winsor}	9.03414	9.00968	8.89143	8.86864

Table 4: Left: case of log normal distribution sampled 20 times and 30 % of Gaussian noise. Right: case of log normal distribution sampled 100 times and 30 % of Gaussian noise. The level of noise is expressed as percentage of the mean of the distributions. The parameters of the log normal are $\overline{x} = 2$ and $s = 1$.

Methods	Error Reduction $\overline{x}$ [%]	Methods	Error Reduction $\overline{x}$ [%]
GD_{Mean}	20.09	GD_{Mean}	18.73
$GD_{Trimmed}$	0.99	$GD_{Trimmed}$	0.54
GD_{Winsor}	5.14	GD_{Winsor}	5.62

Table 5: This table reports the values of scale for a log normal distribution of parameters $\overline{x} = 2$ and $s = 1$ and 30 % of Gaussian noise. The ideal value to obtain is 15.97. The level of noise is expressed as percentage of the mean of the distributions. In the columns we have the scale values when the distributions are composed with 20, 50, 100, and 1000 points.

	20 points Scale s	50 points Scale s	100 points Scale s	1000 points Scale s
Mean	14.59655	15.23205	15.68975	16.38328
GD_{Mean}	14.67788	15.30456	15.75851	16.44366
Trimmed Mean	1.53488	0.90977	0.64213	0.20385
$GD_{Trimmed}$	2.14418	1.28424	0.88579	0.27558
Winsorized Mean	5.63982	5.73328	5.74412	5.78392
GD_{Winsor}	5.67598	5.75673	5.76635	5.80524

Table 6: Relations to calculate the confidence intervals for the hypothesis tests.

	Confidence Intervals	
	Low Limit	Upper Limit
Classic	$(\mu_{clas,1} - \mu_{clas,2}) - \Delta$	$(\mu_{clas,1} - \mu_{clas,2}) + \Delta$
Trimmed	$(\mu_{trim,1} - \mu_{trim,2}) - \Delta_t$	$(\mu_{trim,1} - \mu_{trim,2}) + \Delta_t$
Winsorized	$(\mu_{wins,1} - \mu_{wins,2}) - \Delta_w$	$(\mu_{wins,1} - \mu_{wins,2}) + \Delta_w$

Table 7: The values of Type I errors for a log normal distribution of parameters $\overline{x} = 2$ and $s = 1$ and 30 % of Gaussian noise. The level of noise is expressed as percentage of the mean of the distributions. In the columns we have the percentage of improvement of the Type I errors values through the GDGM methods compared to conventional methods. The distributions are composed with 20, 50, 100, and 1000 points. The minus sign indicates an improvement with respect to the corresponding technique calculated without the GDGM.

	20 points Type I errors [%]	50 points Type I errors [%]	100 points Type I errors [%]	1000 points Type I errors [%]
GD_{Mean}	-56.0	-71.8	-67.6	-63.2
$GD_{Trimmed}$	2.24	-10.6	-4.3	-8.7
GD_{Winsor}	-12.1	-21.5	-16.1	-17.8

Table 8: The values of power for a log normal distribution of parameters $\overline{x} = 2$ and $s = 1$ and 30 % of Gaussian noise. The level of noise is expressed as percentage of the mean of the distributions. In the columns we have reported the values of the Power obtained with the GDGM methods compared to conventional methods. The distributions are composed with 20, 50, 100, and 1000 points.

	20 points Power	50 points Power	100 points Power	1000 points Power
Mean	0.015	0.024	0.023	0.025
GD_{Mean}	0.021	0.038	0.045	0.285
Trimmed Mean	0.164	0.236	0.307	0.885
$GD_{Trimmed}$	0.194	0.288	0.335	0.957
Winsorized Mean	0.159	0.204	0.256	0.722
GD_{Winsor}	0.182	0.278	0.351	0.957

Table 9: The estimates of location or the case of a lognormal distribution with heteroscedastic noise. The results have been obtained generating 1000 points.

	No Noise	Noise
Mode	2.576	2.731
Mean	3.250	3.248
GD_{Mean}	2.765	3.257
Trimmed Mean	3.052	3.158
$GD_{Trimmed}$	2.079	2.372
Winsorized Mean	3.100	3.216
GD_{Winsor}	2.249	2.646

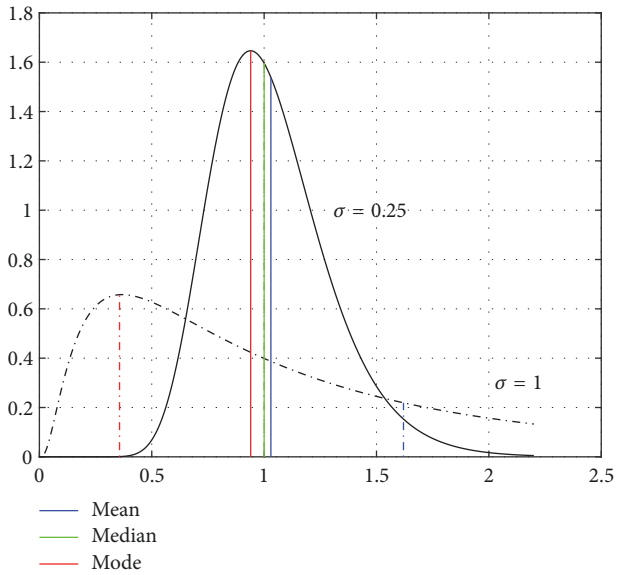

Figure 3: Log normal pdf. Comparison of mean, median, and mode of two log-normal distributions with different skewness.

Table 10: Log-normal distributions with 30% noise level.

	20 points Location $\overline{x}$	50 points Location $\overline{x}$	100 points Location $\overline{x}$	1000 points Location $\overline{x}$
Mode	8.5394	6.5722	5.7292	3.75215
Mean	12.24879	12.2451	12.19511	12.20451
GD_{Mean}	10.78797	10.79425	10.75084	10.80813
Trimmed Mean	8.9453	8.9077	8.78285	8.75854
$GD_{Trimmed}$	8.68679	8.63359	8.48676	8.44375
Winsorized Mean	9.40048	9.43643	9.3558	9.36122
GD_{Winsor}	9.03414	9.00968	8.89143	8.86864

Table 11: Log-normal distributions with 30% noise level.

20 points Scale s	50 points Scale s	100 points Scale s	1000 points Scale s
---	---	---	---
14.59655	15.23200	15.68975	16.38328
14.67788	15.30456	15.75851	16.44366
1.53488	0.90977	0.64213	0.20385
2.14418	1.28424	0.88579	0.27558
5.63982	5.73328	5.74412	5.78392
5.67598	5.75673	5.76635	5.80524

Table 12: Log-normal distributions with 30% noise level.

	20 points Type I errors	50 points Type I errors	100 points Type I errors	1000 points Type I errors
Mean	0.038	0.036	0.047	0.041
GD_{Mean}	0.009	0.018	0.016	0.014
Trimmed Mean	0.193	0.210	0.198	0.194
$GD_{Trimmed}$	0.179	0.187	0.180	0.167
Winsorized Mean	0.231	0.248	0.246	0.249
GD_{Winsor}	0.197	0.211	0.198	0.202

of samples. For most statistical applications, 5 to 25 percent of the ends are discarded; the 25% trimmed mean (when the lowest 25% and the highest 25% are discarded) is known as the interquartile mean. The trimmed mean is obviously more robust to the presence of outliers than the traditional mean. Similar considerations apply to the alternative methods to calculate robust measure of location, such as the winsorized mean discussed in the paper of Huber et al. (2009).

5.2. Application of the Geodesic Distance on Gaussian Manifolds to Measures of Location. The trimmed mean assumes that the data obtained are perfectly sampled from a distribution and they are not affected by noise. As mentioned, this is not realistic in the experimental investigations of complex systems, whose data are typically the results of complicated measurements always affected by a certain level of noise. The noise can often be modelled by a normal distribution of zero mean. The variance of the noise can often be determined experimentally but if that is not the case, the method proposed in this paper provides also a quite robust estimate of this important quantity (see Section 6.2).

To attack this second complication posed by the measurement noise, a good starting point is the observation that the mean can be considered the point having the minimum distance from the available data. This point can be calculated on the basis of the GDGM, which is an appropriate metric once the experimental values are affected by Gaussian noise. So instead of implicitly adopting the Euclidean metric to determine the trimmed and winsorized means, the more appropriate GDGM is used, which can properly take into account additive Gaussian noise.

The approach briefly described for the trimmed mean can be adopted for the other robust statistical techniques considered to determine the central tendency of pdfs. An appropriate metric, the Geodesic Distance on Gaussian Manifolds, is applied to the data already manipulated with the most appropriate robust statistical methods. So the robust statistical methods remedy the issue that the sampled distribution is not a Gaussian and the GDGM handles in a principled way the additional uncertainties due to the fact that the data is affected by noise. The details will be discussed in the next sections but, as far as the estimates of location

Table 13: Log-normal distributions with 30% noise level.

	20 points	50 points	100 points	1000 points
	Power	Power	Power	Power
Mean	0.015	0.017	0.014	0.018
GD_{Mean}	0.025	0.030	0.043	0.289
Trimmed Mean	0.183	0.210	0.300	0.888
$GD_{Trimmed}$	0.201	0.256	0.348	0.957
Winsorized Mean	0.163	0.192	0.256	0.722
GD_{Winsor}	0.184	0.261	0.367	0.968

Table 14: Log-normal with 20 points.

Methods	Reduction $\overline{x}$ dispersion [%]
GD_{Mean}	20.09
$GD_{Trimmed}$	0.99
GD_{Winsor}	5.14

Table 15: Log-normal with 50 points.

Methods	Reduction $\overline{x}$ dispersion [%]
GD_{Mean}	17.96
$GD_{Trimmed}$	-0.03
GD_{Winsor}	4.99

Table 16: Log-normal with 100 points.

Methods	Reduction $\overline{x}$ dispersion [%]
GD_{Mean}	18.73
$GD_{Trimmed}$	0.54
GD_{Winsor}	5.62

Table 17: Log-normal with 1000 points.

Methods	Reduction $\overline{x}$ dispersion [%]
GD_{Mean}	15.08
$GD_{Trimmed}$	1.38
GD_{Winsor}	6.62

are concerned, Tables 2 and 3 report a comparison between the traditional and robust estimators using the Euclidean distance and the GDGM for the case of data sampled from a log normal distribution. For the case with noise, the GDGM always improves the estimates of central tendency, by providing values closer to the mode compared to the robust statistics indicators. As already mentioned, all the results reported either in the main text or in Appendixes have been obtained by mediating over 1000 independent realisations.

6. Measures of Location

To show the potential of the proposed method, the GDGM has been applied first to the most common robust measures of location. In this section, it is assumed that the variance of the Gaussian noise has been already determined experimentally and it is known. In the next subsection an extension of the methodology is introduced to determine the variance of the noise directly from the data, without any a priori information.

6.1. Measures of Location in the Case the Variance of the Noise Is Known. The most common robust statistical measures of central tendency are the trimmed mean and the winsorized mean. The trimmed mean has already been introduced in the previous sections. The winsorized mean is a variant of the trimmed means, which involves the calculation of the mean after replacing given parts of the available samples, at the high and low end, with the most extreme remaining values. To summarise, the traditional mean, the trimmed and winsorized means are calculated according to the following formulas, in which $f(x_i)$ indicate the values sampled from the various pdfs.

The traditional mean is defined as

$$\mu = \frac{1}{N}\sum_{i=1}^{N} f\left(x_i\right) \tag{10}$$

where N is the number of available samples. The trimmed mean is defined as

$$\mu_t = \frac{1}{N}\sum_{i=g+1}^{N-g} f\left(x_i\right) \tag{11}$$

where g corresponds to the number of trimmed points. The winsorized mean is defined as

$$\mu_w = \frac{1}{N}\sum_{i=1}^{N} f_w\left(x_i\right) \tag{12}$$

where

$$f_w\left(x_i\right) = \begin{cases} f\left(x_{g+1}\right) & if\ f\left(x_i\right) \le f\left(x_{g+1}\right) \\ f\left(x_i\right) & if\ f\left(x_{g+1}\right) < f\left(x_i\right) < f\left(x_{N-g}\right) \\ f\left(x_{N-g}\right) & if\ f\left(x_i\right) \ge f\left(x_{N-g}\right) \end{cases} \tag{13}$$

It is worth mentioning that the results reported in the rest of the paper have been obtained for symmetric versions of trimming and winsorization but the proposed alternative

Table 18: Log-normal distributions with 50% noise level.

	20 points Location $\overline{x}$	50 points Location $\overline{x}$	100 points Location $\overline{x}$	1000 points Location $\overline{x}$
Mode	8.13208	6.55561	5.54906	3.66741
Mean	12.29718	12.31377	12.16425	12.18874
GD_{Mean}	10.99257	10.92512	10.84016	10.90433
Trimmed Mean	9.65059	9.37941	9.29027	9.24034
$GD_{Trimmed}$	8.67604	8.43508	8.32643	8.30944
Winsorized Mean	9.9673	9.80449	9.71431	9.67959
GD_{Winsor}	9.07352	8.92301	8.85649	8.83833

Table 19: Log-normal distributions with 50% noise level.

20 points Scale s	50 points Scale s	100 points Scale s	1000 points Scale s
---	---	---	---
14.94729	16.17283	16.17655	16.94800
15.02021	16.2375	16.23344	16.99725
1.85818	1.09043	0.7677	0.24331
2.60785	1.54737	1.0612	0.32813
6.5626	6.68409	6.65622	6.69046
6.72474	6.77077	6.72129	6.74397

Table 20: Log-normal distributions with 50% noise level.

	20 points Type I errors	50 points Type I errors	100 points Type I errors	1000 points Type I errors
Mean	0.022	0.037	0.025	0.038
GD_{Mean}	0.009	0.009	0.007	0.011
Trimmed Mean	0.135	0.153	0.159	0.168
$GD_{Trimmed}$	0.097	0.108	0.102	0.107
Winsorized Mean	0.156	0.196	0.199	0.193
GD_{Winsor}	0.098	0.122	0.133	0.130

geodesic distance could be applied equally well to asymmetric versions of these measures.

As already briefly discussed, to apply the GDGM, which is a distance, the mean is considered the point with the minimum distance to the available samples. To this end, the data used by the robust techniques, trimmed or winsorized, are used to calculate, with an iterative process, the value with the minimum GDGM. The value of the mean is scanned over a reasonable range using the traditional mean as the first guess. The value which minimises the mean calculated with (2) is then chosen. Of course the only precaution to take is that the scan must cover a sufficiently wide range to include this minimum, but such a condition is easy to implement. To perform the iteration, the expression for the GDGM is (3), which depends on two quantities μ and σ. As mentioned, the standard deviation of the noise is assumed known or can be found with the technique described in Section 6.2. For the sample mean μ, since the noise is assumed Gaussian, the measured value is taken as the most probable value and therefore μ is identified with the experimental measured value. A series of numerical tests and theoretical considerations support this choice as can be seen in Verdolaeege [12].

In more detail, indicating with $\overline{f(x)}$ either the traditional sample mean, the trimmed mean, or the winsorized mean (depending of the context) of the available data, sampled from the pdf $f(x)$, the iterative process consists of finding the p_{mean} in the expression $(1 + p_{mean})\bullet\overline{f(x)}$ which minimises the GDGM. In this last expression p_{mean} is the parameter scanned to obtain the measure of location $\overline{x}_{model}$ by minimising the distance to the available experimental points. As mentioned earlier, for the various parameters necessary to compute the GDGM, the following values are chosen:

$$s_{data} = p_{noise}\bullet\overline{f\,(x)} \tag{14}$$

$$\overline{x}_{model} = \left(1 + p_{mean}\right) \bullet \overline{f\,(x)} \tag{15}$$

$$s_{model} = \sqrt{\frac{\sum_{i=1}^{N}\left(f\,(x_i) - \left(1 + p_{mean}\right)\bullet\overline{f\,(x)}\right)^2}{N-1}} \tag{16}$$

Table 21: Log-normal distributions with 50% noise level.

	20 points	50 points	100 points	1000 points
	Power	Power	Power	Power
Mean	0.003	0.005	0.005	0.003
GD_{Mean}	0.011	0.015	0.016	0.093
Trimmed Mean	0.106	0.109	0.144	0.512
$GD_{Trimmed}$	0.038	0.026	0.044	0.310
Winsorized Mean	0.104	0.103	0.117	0.352
GD_{Winsor}	0.053	0.058	0.070	0.351

Table 22: Log-normal with 20 points.

Methods	Reduction $\overline{x}$ dispersion [%]
GD_{Mean}	14.28
$GD_{Trimmed}$	6.45
GD_{Winsor}	7.24

Table 23: Log-normal with 50 points.

Methods	Reduction $\overline{x}$ dispersion [%]
GD_{Mean}	17.54
$GD_{Trimmed}$	6.99
GD_{Winsor}	7.72

Table 24: Log-normal with 100 points.

Methods	Reduction $\overline{x}$ dispersion [%]
GD_{Mean}	15.78
$GD_{Trimmed}$	10.60
GD_{Winsor}	10.07

Table 25: Log-normal with 1000 points.

Methods	Reduction $\overline{x}$ dispersion [%]
GD_{Mean}	11.88
$GD_{Trimmed}$	10.00
GD_{Winsor}	8.75

In these relations, p_{noise} is the percentage of Gaussian noise added to the individual samples $f(x)$ and the subscript *model* indicates the type of mean (traditional, trimmed, or winsorized).

To prove the potential of the proposed method in solving realistic problems, a series of numerical tests have been performed. The data have been sampled from the pdfs reviewed in Section 4. Various levels of Gaussian noise have been added to the individual points. A series of realisations, up to 1000, have been generated for each case and the results reported in Tables 4–9 are the averages over these realisations. The results of the systematic tests for the measures of location and scale are reported in Appendix A. In the rest of this section only the example of sampling from a log normal pdf is provided. In order to condense the information, the percentage variation between the carious estimates is reported in the main text (all the details are in Appendix A). Therefore in Tables 4–9 quantities of the form (vertical bars indicate absolute values) are reported

$$\left[\frac{\sum_{i=1}^{1000}\left(\left|\left(\overline{x}_{GD,i}-\overline{x}_{robust,i}\right)\right|/\overline{x}_{robust,i}\right)}{\#realisations}\right]100 \tag{17}$$

where the estimates using the GDGM are compared to the ones of the various robust indicators. As mentioned in the previous sections, the robust techniques are meant to provide a better estimate of central density, compared to traditional techniques; in this context this means that they tend to give results closer to the mode of the distributions from which the data are sampled (with the term mode we indicate the value where the pdf presents the main peak). The estimators using the GDGM are considered to improve the measures of location if they provide values closer to the mode of the sampled pdf compared to the robust method using the Euclidean distance.

For the case of the log normal distribution, the results for 20 and 100 samples are reported in Table 4, where the percentage improvement with respect to the traditional robust indicators is reported.

From this table, it emerges very clearly that, even at a level of noise of 30%, which is typical of many applications, the improvement provided by the GDGM is significant. Indeed the quantities calculated with the help of the GDGM are closer to the peak of the log normal pdf compared to the results obtained with the trimmed and winsorized means. In Appendix A, the results of a series of systematic tests are reported, showing how the GDGM always improves the estimates of location, over a wide range of samples and noise levels. As can be seen in the Tables in Appendix A, the GDGM allows outperforming the various robust techniques also for a quite high number of points sampled from the distribution (in the order of thousands). Appendix A also shows how this performance is not limited to the case of the log normal distribution but is equally appreciable for all the other pdfs tested.

6.2. Measures of Location in the Case the Variance of the Noise Is Not Known. In the investigation of complex systems, it is possible that the level of Gaussian noise can not be precisely quantified. Typically some experimental evidence is available but sometimes the uncertainties on the level of additive noise can be substantial. Another advantage of the GDGM is that it allows determining the level of normal noise,

Table 26: Exponential distributions with 30% noise level.

	20 points Location $\overline{x}$	50 points Location $\overline{x}$	100 points Location $\overline{x}$	1000 points Location $\overline{x}$
Mode	1.08682	0.72509	0.55488	0.24546
Mean	2.00326	2.00368	2.00076	1.99978
GD_{Mean}	1.83384	1.82025	1.81152	1.80861
Trimmed Mean	1.64069	1.61470	1.59887	1.59382
$GD_{Trimmed}$	1.60141	1.56638	1.54532	1.53794
Winsorized Mean	1.71454	1.70998	1.70169	1.70036
GD_{Winsor}	1.65804	1.63565	1.61989	1.61463

Table 27: Exponential distributions with 30% noise level.

20 points Scale s	50 points Scale s	100 points Scale s	1000 points Scale s
---	---	---	---
2.00977	2.04677	2.06789	2.08265
2.01853	2.05554	2.07682	2.09144
0.30212	0.17907	0.12788	0.04047
0.40574	0.24667	0.17285	0.05368
1.05783	1.08824	1.10303	1.10650
1.06356	1.09219	1.10667	1.10989

in particular its sigma, directly from the data. This can be achieved by scanning the sigma of the noise s_{GDGM} in the GDGM and by repeating the procedure for the identification of the mean described in the previous subsection. In the scan, the estimated mean remains constant for values of the assumed s_{GDGM} lower than the actual sigma of the noise. The mean then starts decreasing drastically when the assume s_{GDGM} is higher than the actual sigma of the noise. The inflection point is a very good estimate of the actual sigma of the additive Gaussian noise.

The approach just described is illustrated graphically in Figure 4 for the case of the log normal distribution. Data have been sampled from the pdf and then additive normal noise of zero mean and a sigma of 20% of the mean has been added. The mean of the data has then been calculated with the GDGM for a wide range of s_{GDGM}. As can be seen from the Figure, the inflection point in the mean corresponds very well to the added level of noise.

The proposed procedure has been verified for all the pdfs used in the paper and it has typically provided a reasonable estimate of the noise sigma.

The capability to derive information about the level of noise affecting the available data is of course a significant added value of the proposed technique, which can have very significant practical applications in the experimental investigations of complex systems.

7. Measures of Scale

The robust statistical methods developed in the last decades allow improving not only the estimates of location but also those of scale. The scale measures tested in this paper are reported in the following (see [5]). As a reference the classic standard deviation is defined as

$$\sigma = \sqrt{\frac{\sum_{i=1}^{n} \left[f\left(x_i\right) - \mu \right]^2}{n-1}} \tag{18}$$

In the case the location is calculated with the trimmed mean, the standard deviation σ_t is defined as

$$\sigma_t = \sqrt{\frac{1}{n\left(n-1\right)\left(1-2\gamma\right)^2} \sum_{i=1}^{n} \left(f_t\left(x_i\right) - \mu_t \right)^2} \tag{19}$$

where n, γ, $f_t(x_i)$, and μ_t are the number of points sampled from the pdf, the percentage of trimming, the data of the trimmed, and the trimmed mean, respectively.

A similar definition applies to the standard deviation of the winsorized mean:

$$\sigma_w = \sqrt{\frac{1}{\left(n-1\right)} \sum_{i=1}^{n} \left(f_w\left(x_i\right) - \mu_w \right)^2} \tag{20}$$

To apply the GDGM to the standard deviations previously defined, the following formula has been applied:

$$\sigma_{GD} = \sqrt{\frac{\sum_{i=1}^{n} \left(f\left(x_i\right) - \left(1 + p_{mean}\right) \bullet \overline{f\left(x\right)} \right)^2}{n-1}} \tag{21}$$

where $\overline{f(x)}$ indicates either the traditional mean, the trimmed mean, or the winsorized mean of the available data.

The improvement in the determination of the scale using the GDGM is exemplified in Table 5 for the case of the log

Table 28: Exponential distributions with 30% noise level.

	20 points Type I errors	50 points Type I errors	100 points Type I errors	1000 points Type I errors
Mean	0.041	0.045	0.045	0.042
GD_{Mean}	0.032	0.027	0.029	0.018
Trimmed Mean	0.186	0.211	0.229	0.224
$GD_{Trimmed}$	0.183	0.215	0.219	0.221
Winsorized Mean	0.206	0.221	0.253	0.240
GD_{Winsor}	0.189	0.216	0.231	0.226

Table 29: Exponential distributions with 30% noise level.

	20 points Power	50 points Power	100 points Power	1000 points Power
Mean	0.041	0.048	0.050	0.046
GD_{Mean}	0.061	0.080	0.119	0.634
Trimmed Mean	0.292	0.434	0.589	0.999
$GD_{Trimmed}$	0.316	0.477	0.667	1.000
Winsorized Mean	0.262	0.351	0.454	0.982
GD_{Winsor}	0.287	0.420	0.597	0.998

Table 30: Exponential with 20 points.

Methods	Reduction $\bar{x}$ dispersion [%]
GD_{Mean}	5.80
$GD_{Trimmed}$	-0.71
GD_{Winsor}	2.55

Table 31: Exponential with 50 points.

Methods	Reduction $\bar{x}$ dispersion [%]
GD_{Mean}	5.00
$GD_{Trimmed}$	-0.26
GD_{Winsor}	2.14

Table 32: Exponential with 100 points.

Methods	Reduction $\bar{x}$ dispersion [%]
GD_{Mean}	7.64
$GD_{Trimmed}$	-0.16
GD_{Winsor}	3.60

Table 33: Exponential with 1000 points.

Methods	Reduction $\bar{x}$ dispersion [%]
GD_{Mean}	7.04
$GD_{Trimmed}$	-0.24
GD_{Winsor}	3.23

normal distribution. Again the impact on the other pdfs is reported in Appendixes. The results are very similar to the ones obtained by the other robust techniques, even if they are systematically slightly better. The advantages of the GDGM will become more evident in the case of hypothesis testing, described in the next section, where it will be shown how adopting the GDGM values of location and scale reduces significantly the Type I errors and improves the power.

8. Hypothesis Testing

In this section, the problems of computing confidence intervals and testing hypotheses are considered. The population variance is to be estimated from the sample variance and the standard deviation of the noise is considered known, either experimentally or by applying the method described in Section 6.2. The null hypothesis is as usual the one which assumes that the measure of location has a certain value: H_0: $\mu = \mu_0$. The alternative hypothesis is therefore $H_1 : \mu \neq \mu_0$. In the case of the classic significance tests, the null hypothesis is rejected at the confidence level $\alpha/2$ if

$$\begin{aligned} T &> t_{1-\alpha/2,n-1} \\ or\ T &< t_{\alpha/2,n-1} \\ H_1 &: \mu \neq \mu_0 \end{aligned} \tag{22}$$

where T is the student's T distribution and n the number of degrees of freedom. Robust statistical methods have been developed to test hypotheses when the usual assumptions of normal distribution of the sampled pdf and homoscedasticity are not verified. They are based on the robust estimators of location and scale introduced in the previous sections. An exhaustive treatment of these techniques can be found in Wilcox [11]. For the various robust indicators the null hypothesis can be rejected at the confidence level $\alpha/2$ if the conditions of the following inequalities are satisfied.

Table 34: Exponential distributions with 50% noise level.

	20 points Location $\bar{x}$	50 points Location $\bar{x}$	100 points Location $\bar{x}$	1000 points Location $\bar{x}$
Mode	1.06174	0.71622	0.56485	0.24778
Mean	1.99158	1.98960	2.00813	2.00242
GD_{Mean}	1.83644	1.82000	1.83880	1.82967
Trimmed Mean	1.69601	1.66348	1.67930	1.66705
$GD_{Trimmed}$	1.52821	1.49809	1.51042	1.50207
Winsorized Mean	1.75591	1.73586	1.75454	1.74685
GD_{Winsor}	1.59822	1.58391	1.60236	1.59234

Table 35: Exponential distributions with 50% noise level.

20 points Scale s	50 points Scale s	100 points Scale s	1000 points Scale s
---	---	---	---
2.12517	2.19360	2.22521	2.23517
2.13395	2.20117	2.23215	2.24189
0.33408	0.19687	0.14269	0.04497
0.46178	0.27742	0.19473	0.06013
1.15236	1.19450	1.21651	1.21824
1.18160	1.20810	1.22758	1.22814

In the case of the trimmed location estimate, according to the Yuen method described in Wilcox [5], the inequalities to evaluate are

$$T_{trim} = \frac{\mu_{trim,1} - \mu_{trim,2}}{\sigma_{wins,1-2}} > t_{1-\alpha/2,gdl}$$
$$or\ T_{trim} < t_{\alpha/2,gdl} \tag{23}$$
$$with\ gdl = \frac{(d_1 + d_2)^2}{d_1^2/(h_1 - 1) + d_2^2/(h_2 - 1)}$$

where

$$d_1 = \frac{(n_1 - 1)\,\sigma_{wins,1}^2}{h_1\,(h_1 - 1)};$$
$$d_2 = \frac{(n_2 - 1)\,\sigma_{wins,2}^2}{h_2\,(h_2 - 1)} \tag{24}$$
$$with\ h_i = n_i - 2g_i$$
$$\sigma_{wins,1-2} = \sqrt{d_1 + d_2}$$

In the case of the winsorized mean, the student test is

$$T_{wins} = \frac{\mu_{wins,1} - \mu_{wins,2}}{\sigma_{wins,1-2}} > t_{1-\alpha/2,gdl}$$
$$or\ T_{wins} < t_{\alpha/2,gdl} \tag{25}$$
$$with\ gdl = \frac{(d_1 + d_2)^2}{d_1^2/(h_1 - 1) + d_2^2/(h_2 - 1)}$$

where

$$d_1 = \frac{(n_1 - 1)\,\sigma_{wins,1}^2}{h_1\,(h_1 - 1)};$$
$$d_2 = \frac{(n_2 - 1)\,\sigma_{wins,2}^2}{h_2\,(h_2 - 1)} \tag{26}$$
$$with\ h_i = n_i - 1$$
$$\sigma_{wins,1-2} = \sqrt{d_1 + d_2}$$

The confidence intervals for these estimates can be derived from the following relations:

$$\Delta = t_{1-\alpha/2,gdl}\frac{\sigma_{clas,1-2}}{\sqrt{1/n_1 + 1/n_2}}$$
$$\Delta_{med} = t_{1-\alpha/2,gdl}\frac{\sigma_{med,1-2}}{\sqrt{1/n_1 + 1/n_2}} \tag{27}$$
$$\Delta_{trimmed} = t_{1-\alpha/2,gdl} \bullet \sigma_{wins,1-2}$$
$$\Delta_{winsor} = t_{1-\alpha/2,gdl} \bullet \sigma_{wins,1-2}$$

The extremes of the confidence intervals have been derived using the relations of Table 6. In the previous formulas and in Table 6, the subscript *clas* indicates the values calculated with the traditional methods and the Euclidean distance.

In order to verify the potential of the method proposed in this paper to help coping with Gaussian noise, all the previous tests have been calculated using also the estimates of location and scale obtained with the GDGM. Two main types of test have been performed. First, the data have been sampled by

Table 36: Exponential distributions with 50% noise level.

	20 points Type I errors	50 points Type I errors	100 points Type I errors	1000 points Type I errors
Mean	0.024	0.024	0.030	0.029
GD_{Mean}	0.018	0.017	0.013	0.016
Trimmed Mean	0.141	0.173	0.156	0.157
$GD_{Trimmed}$	0.111	0.122	0.105	0.106
Winsorized Mean	0.158	0.196	0.176	0.178
GD_{Winsor}	0.127	0.152	0.126	0.122

Table 37: Exponential distributions with 50% noise level.

	20 points Power	50 points Power	100 points Power	1000 points Power
Mean	0.026	0.029	0.038	0.026
GD_{Mean}	0.046	0.081	0.088	0.559
Trimmed Mean	0.256	0.329	0.471	0.991
$GD_{Trimmed}$	0.191	0.299	0.450	0.998
Winsorized Mean	0.237	0.292	0.371	0.931
GD_{Winsor}	0.205	0.310	0.467	0.997

Table 38: Exponential with 20 points.

Methods	Reduction $\overline{x}$ dispersion μ [%]
GD_{Mean}	4.25
$GD_{Trimmed}$	8.72
GD_{Winsor}	7.35

Table 39: Exponential with 50 points.

Methods	Reduction $\overline{x}$ dispersion [%]
GD_{Mean}	3.80
$GD_{Trimmed}$	11.22
GD_{Winsor}	7.27

Table 40: Exponential with 100 points.

Methods	Reduction $\overline{x}$ dispersion [%]
GD_{Mean}	5.44
$GD_{Trimmed}$	11.66
GD_{Winsor}	7.98

Table 41: Exponential with 1000 points.

Methods	Reduction $\overline{x}$ dispersion [%]
GD_{Mean}	5.06
$GD_{Trimmed}$	13.33
GD_{Winsor}	7.53

the same pdf and noise has been added. In this case, the objective is to verify the resilience of the various tests to Type I error, i.e., to the wrong rejection of the null hypothesis (see Table 7).

In the main body of the paper this analysis has been particularised for the log-normal distribution. Further examples are reported in Appendix A. Secondly, the data have been sampled from two different distributions before adding the noise. In this case, the objective consists of determining whether the GDGM can help in reducing Type II errors, i.e., the failure to reject a false null hypothesis (see Table 8). As an example, in the following the data have been sampled from a log normal and a normal distribution. This is one of the most difficult cases since one of the two pdfs is a Gaussian. The results of similar tests for the other pdfs are again reported in Appendix A.

Some representative results of the tests for the Type I errors are reported in Table 7, where a minus sign indicates the reduction of errors achieved when using the GDGM. The use of the GDGM improves significantly the situation by reducing the Type I errors even of 20% with respect to the robust statistics techniques.

The effect of the GDGM is even more significant on the power, as can be seen in Table 8, again for some representative tests. The increase in the Power with GDGM methods can indeed reach values of the order of 35% compared to conventional methods.

9. Nonnormal Distributions and Heteroscedasticity

This section of the paper is the meant to cover the combined effects of sampling from an asymmetric distribution in presence of heteroscedastic noise. As a reference case of particular importance, the log normal distribution is analysed in detail. The data are sampled from a log normal distribution. Gaussian noise has then been added to the sampled data. The noise has zero mean and a standard

Table 42: Contaminated χ^2 distributions with 30% noise level.

	20 points Location $\overline{x}$	50 points Location $\overline{x}$	100 points Location $\overline{x}$	1000 points Location $\overline{x}$
Mode	5.78549	3.95817	2.97873	2.79684
Mean	7.58377	7.54954	7.58573	7.59473
GD_{Mean}	6.22352	6.13670	6.11370	6.09931
Trimmed Mean	4.51128	4.40502	4.32975	4.31965
$GD_{Trimmed}$	4.37176	4.30535	4.22925	4.21665
Winsorized Mean	4.78413	4.61130	4.53624	4.52361
GD_{Winsor}	4.58346	4.45736	4.37613	4.36100

Table 43: Contaminated χ^2 distributions with 30% noise level.

20 points Scale s	50 points Scale s	100 points Scale s	1000 points Scale s
---	---	---	---
10.97391	11.29413	11.57125	11.68770
11.06586	11.3861	11.66667	11.78321
0.77077	0.43540	0.30710	0.09797
1.12487	0.61454	0.42045	0.13058
3.00377	2.75198	2.73383	2.73164
3.02638	2.7614	2.74088	2.73670

Table 44: Contaminated χ^2 distributions with 30% noise level.

	20 points Type I errors	50 points Type I errors	100 points Type I errors	1000 points Type I errors
Mean	0.035	0.040	0.048	0.038
GD_{Mean}	0.004	0.001	0.008	0.004
Trimmed Mean	0.130	0.148	0.172	0.169
$GD_{Trimmed}$	0.128	0.144	0.168	0.170
Winsorized Mean	0.202	0.214	0.230	0.236
GD_{Winsor}	0.134	0.166	0.190	0.179

Table 45: Contaminated χ^2 distributions with 30% noise level.

	20 points Power	50 points Power	100 points Power	1000 points Power
Mean	0.002	0.003	0.006	0.008
GD_{Mean}	0.008	0.044	0.087	0.930
Trimmed Mean	0.352	0.662	0.912	1.000
$GD_{Trimmed}$	0.391	0.686	0.923	1.000
Winsorized Mean	0.327	0.625	0.890	1.000
GD_{Winsor}	0.363	0.673	0.919	1.000

deviation equal to 50% of the value of the data. It is therefore a heteroscedastic noise quite common in practice, since often the uncertainties in the measurements are expressed as a percentage of their value. The effects of different types of noise are reported in Appendix B. Again the objective consists of estimating the mode, the most probable value of the data. The results of the various approaches are summarised in Table 9. From the table it is easily seen how the GDGM allows recovering values of central tendency much closer to the original distribution than the other indicators, even the robust ones. Such significant variations in the measures of location of course reverberate on the rest of the statistical quantities, from scale to hypothesis testing, again reducing significantly the errors committed by traditional robust indicators in the presence of Gaussian heteroscedastic noise.

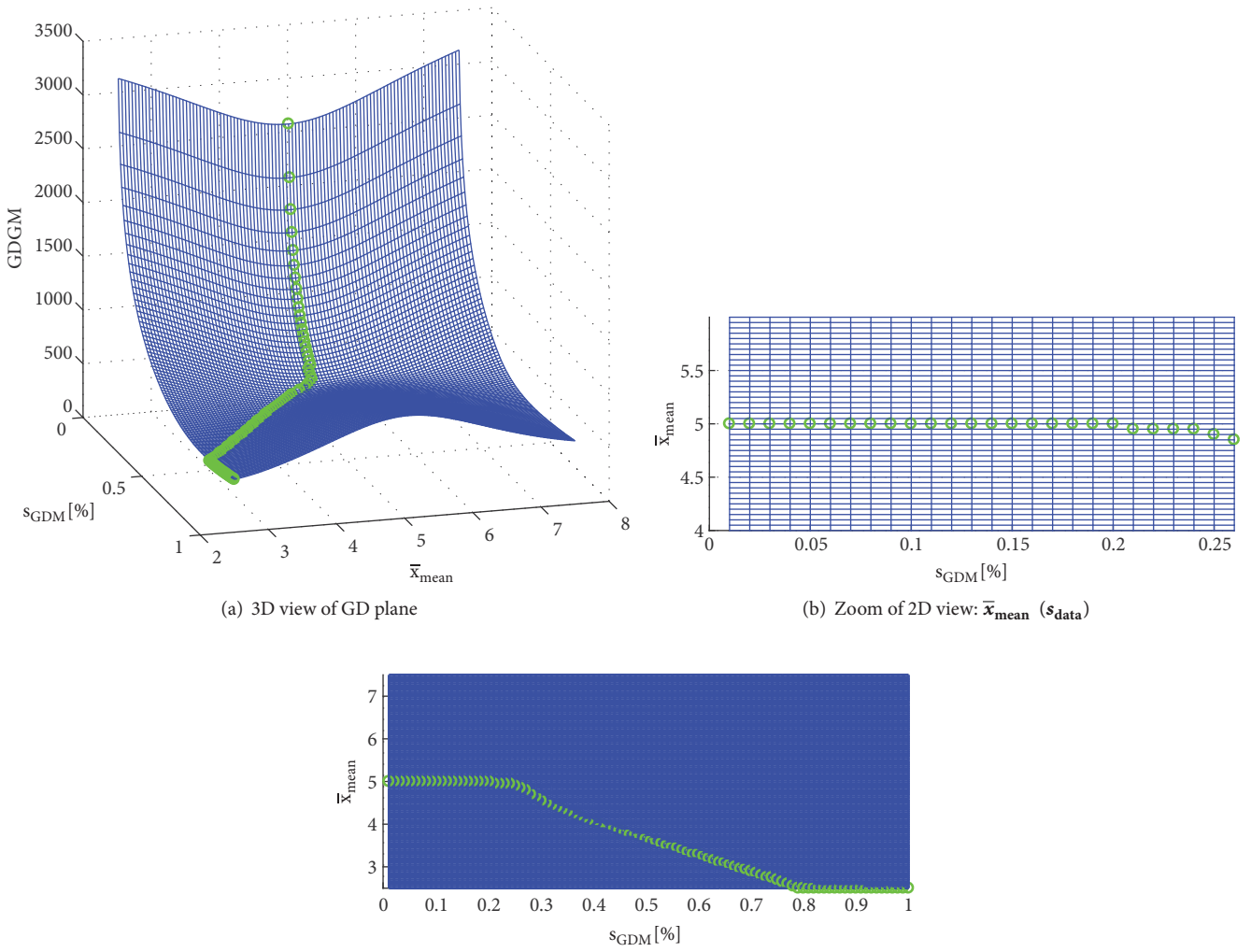

(a) 3D view of GD plane

(b) Zoom of 2D view: $\overline{\boldsymbol{x}}_{\mathbf{mean}}$ $(\boldsymbol{s}_{\mathbf{data}})$

(c) 2D view: $\overline{\boldsymbol{x}}_{\mathbf{mean}}$ $(\boldsymbol{s}_{\mathbf{data}})$

Figure 4: Pictorial description of the procedure to find the sigma of the additive Gaussian noise in the data. The plots correspond to the case of data sampled from a log normal distribution and an additive normal noise of 20% of the log-normal mean. On the left a 3D view of the scan in the sigma used to calculate the GDGM and indicated s_{GDGM}. On the right end side, the zoomed projections on the s_{GDGM} $\overline{x}_{mean}$ plane are reported. As can be seen, the inflection point in the $\overline{x}_{mean}$ corresponds exactly to the 20% of additive Gaussian noise.

Table 46: Contaminated χ^2 with 20 points.

Methods	Reduction $\overline{x}$ dispersion [%]
GD_{Mean}	24.94
$GD_{Trimmed}$	6.33
GD_{Winsor}	15.21

Table 47: Contaminated χ^2 with 50 points.

Methods	Reduction $\overline{x}$ dispersion [%]
GD_{Mean}	27.91
$GD_{Trimmed}$	0.65
GD_{Winsor}	10.76

Table 48: Contaminated χ^2 with 100 points.

Methods	Reduction $\overline{x}$ dispersion [%]
GD_{Mean}	28.79
$GD_{Trimmed}$	-0.397
GD_{Winsor}	7.094

Table 49: Contaminated χ^2 with 1000 points.

Methods	Reduction $\overline{x}$ dispersion [%]
GD_{Mean}	29.14
$GD_{Trimmed}$	-0.34
GD_{Winsor}	6.83

Table 50: Contaminated χ^2 distributions with 50% noise level.

	20 points Location $\overline{x}$	50 points Location $\overline{x}$	100 points Location $\overline{x}$	1000 points Location $\overline{x}$
Mode	5.75158	3.96113	2.99485	2.85649
Mean	7.56302	7.61410	7.62280	7.59842
GD_{Mean}	6.22725	6.17673	6.16274	6.11750
Trimmed Mean	4.86596	4.68968	4.65874	4.60903
$GD_{Trimmed}$	4.44994	4.28575	4.26848	4.24064
Winsorized Mean	5.13555	4.90040	4.85056	4.79522
GD_{Winsor}	4.67670	4.51967	4.49452	4.45354

Table 51: Contaminated χ^2 distributions with 50% noise level.

20 points Scale s	50 points Scale s	100 points Scale s	1000 points Scale s
---	---	---	---
11.30261	11.90185	12.01272	12.08214
11.39161	11.99292	12.10357	12.17283
1.00320	0.57917	0.40993	0.12959
1.47045	0.83018	0.56349	0.17282
3.79591	3.64577	3.57781	3.55555
3.88056	3.68090	3.60212	3.57244

Table 52: Contaminated χ^2 distributions with 50% noise level.

	20 points Type I errors	50 points Type I errors	100 points Type I errors	1000 points Type I errors
Mean	0.025	0.040	0.021	0.043
GD_{Mean}	0.003	0.001	0.000	0.001
Trimmed Mean	0.118	0.123	0.104	0.111
$GD_{Trimmed}$	0.079	0.085	0.068	0.073
Winsorized Mean	0.171	0.182	0.162	0.166
GD_{Winsor}	0.088	0.118	0.097	0.094

Table 53: Contaminated χ^2 distributions with 50% noise level.

	20 points Power	50 points Power	100 points Power	1000 points Power
Mean	0.003	0.004	0.001	0.004
GD_{Mean}	0.010	0.034	0.074	0.940
Trimmed Mean	0.329	0.566	0.812	1.000
$GD_{Trimmed}$	0.339	0.659	0.874	1.000
Winsorized Mean	0.316	0.535	0.787	1.000
GD_{Winsor}	0.335	0.617	0.839	1.000

Table 54: Contaminated χ^2 with 20 points.

Methods	Reduction $\overline{x}$ dispersion [%]
GD_{Mean}	22.14
$GD_{Trimmed}$	7.03
GD_{Winsor}	15.53

Table 55: Contaminated χ^2 with 50 points.

Methods	Reduction $\overline{x}$ dispersion [%]
GD_{Mean}	25.48
$GD_{Trimmed}$	7.20
GD_{Winsor}	12.13

Table 56: Contaminated χ^2 with 100 points.

Methods	Reduction $\overline{x}$ dispersion [%]
GD_{Mean}	26.55
$GD_{Trimmed}$	7.48
GD_{Winsor}	11.69

Table 57: Contaminated χ^2 with 1000 points.

Methods	Reduction $\overline{x}$ dispersion [%]
GD_{Mean}	27.16
$GD_{Trimmed}$	6.66
GD_{Winsor}	10.30

Table 58: G-h distributions with 30% noise level.

	20 points Location $\overline{x}$	50 points Location $\overline{x}$	100 points Location $\overline{x}$	1000 points Location $\overline{x}$
Mode	0.38020	0.31542	0.28250	-0.01744
Mean	0.72107	0.74738	0.77821	0.79727
GD_{Mean}	0.45726	0.46189	0.48348	0.52147
Trimmed Mean	0.10548	0.07130	0.07681	0.06771
$GD_{Trimmed}$	0.08557	0.05222	0.05795	0.04828
Winsorized Mean	0.15617	0.12161	0.13170	0.12392
GD_{Winsor}	0.12475	0.09072	0.09795	0.08498

Table 59: G-h distributions with 30% noise level.

20 points Scale s	50 points Scale s	100 points Scale s	1000 points Scale s
---	---	---	---
3.87104	4.69402	5.32664	7.73014
3.88735	4.70586	5.33644	7.73585
0.22745	0.12645	0.08848	0.02742
0.31618	0.18211	0.12396	0.03750
0.84574	0.82853	0.82003	0.80183
0.84784	0.82991	0.82116	0.80283

Table 60: G-h distributions with 30% noise level.

	20 points Type I errors	50 points Type I errors	100 points Type I errors	1000 points Type I errors
Mean	0.037	0.041	0.031	0.049
GD_{Mean}	0.008	0.004	0.001	0.003
Trimmed Mean	0.217	0.220	0.209	0.228
$GD_{Trimmed}$	0.214	0.207	0.187	0.185
Winsorized Mean	0.276	0.296	0.273	0.307
GD_{Winsor}	0.233	0.237	0.221	0.217

Table 61: G-h distributions with 30% noise level.

	20 points Power	50 points Power	100 points Power	1000 points Power
Mean	0.006	0.007	0.001	0.006
GD_{Mean}	0.008	0.013	0.019	0.116
Trimmed Mean	0.246	0.358	0.476	0.927
$GD_{Trimmed}$	0.269	0.430	0.538	0.943
Winsorized Mean	0.246	0.358	0.476	0.927
GD_{Winsor}	0.261	0.383	0.502	0.932

Table 62: G-h with 20 points.

Methods	Reduction $\overline{x}$ dispersion [%]
GD_{Mean}	39.60
$GD_{Trimmed}$	3.48
GD_{Winsor}	6.88

Table 63: G-h with 50 points.

Methods	Reduction $\overline{x}$ dispersion [%]
GD_{Mean}	43.90
$GD_{Trimmed}$	3.52
GD_{Winsor}	9.95

Table 64: G-h with 100 points.

Methods	Reduction $\overline{x}$ dispersion [%]
GD_{Mean}	42.65
$GD_{Trimmed}$	1.48
GD_{Winsor}	8.66

Table 65: G-h with 1000 points.

Methods	Reduction $\overline{x}$ dispersion [%]
GD_{Mean}	37.42
$GD_{Trimmed}$	9.27
GD_{Winsor}	11.90

10. Conclusions

In the science of complex systems, the data are often the output of delicate measurements and therefore are typically affected by Gaussian additive noise. Since the data are also not necessarily sampled from normal pdfs, it is important to develop tools which can handle both these problems. The Geodesic Distance on Gaussian Manifolds is a principled way to address the issue of Gaussian noise. In this paper, it has been shown how the GDGM can improve the estimates of robust statistical methods, ranging from the evaluation of location and scale to hypothesis testing. The improvements obtained with GDGM for the estimates of location and scale are not negligible for all the non-Gaussian distributions tested. In the case of hypothesis testing, the advantages provided by the GDGM are quite substantial; in particular the power is significantly improved since the Type II errors can be reduced typically of more than 30% for all the pdf tested. Moreover, since the GDGM is a distance on a Gaussian manifold, it does not introduce unacceptable errors if the data are sampled from a normal pdf. A specific development of the technique allows also estimating the level of noise associated with the measurements, when this information cannot be determined experimentally.

In terms of future developments, it is planned to investigate whether the GDGM can improve also other robust techniques, in particular those belonging to the class of the so called M-estimators, which are considered better performing than the ones based on trimming [Huber et al. (2009)]. First preliminary tests indicate that there is no reason to expect that the impact of the GDGM will be less positive for this class of estimators. It is therefore considered more urgent to apply the GDGM also to the methods of robust regression, to assess whether progress can be achieved also for this class of problems. Recently new regression methods, indicated collectively as symbolic regression, have allowed relaxing the constraints of linear regression and obtain formula in nonpower law form as in the works of Murari et al. [13, 14] and in the paper of Peluso et al. [15]. The use of the GDGM seems particularly promising also in this context as it has been shown in Murari et al. [16, 17]. The proposed methodology could be therefore profitably be used in the field of Thermonuclear Fusion to help in the development of more robust scenarios [18–20].

Appendix

A.

A.1. Log-Normal Distribution. See Tables 10–25.

A.2. Exponential Distribution. See Tables 26–41.

A.3. Contaminated χ^2 Distribution. See Tables 42–57.

A.4. Contaminated G-H Distribution. See Tables 58–73.

B.

B.1. Log-Normal Distribution with Asymmetric Noise (Positive). See Table 74.

B.2. Log-Normal Distribution with Asymmetric Noise (Negative). See Table 75.

B.3. Log-Normal Distribution with Heteroscedastic Noise. See Table 76.

B.4. Log-Normal Distribution with Step Noise (Type 1). See Table 77.

B.5. Log-Normal Distribution with Step Noise (Type 2). See Table 78.

B.6. Log-Normal Distribution with Step Noise (Type 3). See Table 79.

B.7. Log-Normal Distribution with Step Noise (Type 4). See Table 80.

Data Availability

In order to obtain the numerical dataset used to carry out the analysis reported in the manuscript, please contact the corresponding author Michele Lungaroni.

Table 66: G-h distributions with 50% noise level.

	20 points Location$\overline{\boldsymbol{x}}$	50 points Location $\overline{\boldsymbol{x}}$	100 points Location $\overline{\boldsymbol{x}}$	1000 points Location $\overline{\boldsymbol{x}}$
Mode	1.03893	0.36309	0.31981	0.05504
Mean	1.01079	0.77843	0.77888	0.78485
GD_{Mean}	0.61100	0.47946	0.47803	0.51055
Trimmed Mean	0.12524	0.09354	0.07864	0.07433
$GD_{Trimmed}$	0.10583	0.07508	0.05955	0.05389
Winsorized Mean	0.16985	0.13961	0.13018	0.12525
GD_{Winsor}	0.13458	0.10507	0.09164	0.08040

Table 67: G-h distributions with 50% noise level.

20 points Scale $\boldsymbol{s}$	50 points Scale $\boldsymbol{s}$	100 points Scale $\boldsymbol{s}$	1000 points Scale $\boldsymbol{s}$
---	---	---	---
4.97806	4.86858	5.39029	7.62799
5.00121	4.88114	5.40026	7.6337
0.27053	0.13910	0.09547	0.02946
0.37237	0.19648	0.13250	0.03990
0.98774	0.88558	0.86995	0.84722
0.99131	0.88741	0.87148	0.84853

Table 68: G-h distributions with 50% noise level.

	20 points Type I errors	50 points Type I errors	100 points Type I errors	1000 points Type I errors
Mean	0.031	0.032	0.031	0.039
GD_{Mean}	0.008	0.007	0.004	0.001
Trimmed Mean	0.188	0.183	0.191	0.230
$GD_{Trimmed}$	0.183	0.171	0.174	0.166
Winsorized Mean	0.231	0.235	0.261	0.289
GD_{Winsor}	0.198	0.175	0.188	0.179

Table 69: G-h distributions with 50% noise level.

	20 points Power	50 points Power	100 points Power	1000 points Power
Mean	0.003	0.004	0.005	0.006
GD_{Mean}	0.010	0.013	0.027	0.148
Trimmed Mean	0.233	0.357	0.528	0.939
$GD_{Trimmed}$	0.255	0.385	0.556	0.949
Winsorized Mean	0.217	0.328	0.479	0.926
GD_{Winsor}	0.236	0.353	0.532	0.942

Table 70: G-h with 20 points.

Methods	Reduction $\overline{\boldsymbol{x}}$ dispersion [%]
GD_{Mean}	47.85
$GD_{Trimmed}$	-0.88
GD_{Winsor}	-2.41

Table 71: G-h with 50 points.

Methods	Reduction $\overline{\boldsymbol{x}}$ dispersion [%]
GD_{Mean}	42.90
$GD_{Trimmed}$	-0.01
GD_{Winsor}	6.39

Table 72: G-h with 100 points.

Methods	Reduction $\overline{x}$ dispersion [%]
GD_{Mean}	44.90
$GD_{Trimmed}$	1.67
GD_{Winsor}	10.84

Table 73: G-h with 1000 points.

Methods	Reduction $\overline{x}$ dispersion [%]
GD_{Mean}	35.41
$GD_{Trimmed}$	7.96
GD_{Winsor}	15.53

Table 74: Log-normal distributions with asymmetric noise. The noise is composed of the sum of two Gaussians. The first Gaussian has zero mean and standard deviation equal to 10% of the maximum value of the data distribution $\overline{x}_1 = 0$, s_1 = 10% max(distribution); the second Gaussian has the mean equal $\overline{x}_2 = 2(s_1+s_2)$ and standard deviation s_2 = 20% max(distribution). The noise is composed of 1000 points; of these 80% of the points are sampled on the first Gaussian and the remaining on the second Gaussian. The noise has a positive mean because $\overline{x}_2 > 0$.

	No Noise	Noise
Mode	2.576	2.890
Mean	3.250	4.587
GD_{Mean}	2.765	4.101
Trimmed Mean	3.052	3.845
$GD_{Trimmed}$	2.079	2.950
Winsorized Mean	3.100	4.097
GD_{Winsor}	2.249	3.433

Table 75: Log-normal distributions with asymmetric noise. The noise is composed of the sum of two Gaussians. The first Gaussian has zero mean and standard deviation equal to 10% of the maximum value of the data distribution $\overline{x}_1 = 0$, s_1 = 10% max(distribution); the second Gaussian has the mean equal $\overline{x}_2 = -2(s_1+s_2)$ and standard deviation s_2 = 20% max(distribution). The noise is composed of 1000 points; of these 80% of the points are sampled on the first Gaussian and the remaining on the second Gaussian. The noise has a negative mean because $\overline{x}_2 < 0$.

	No Noise	Noise
Mode	2.576	2.731
Mean	3.250	3.248
GD_{Mean}	2.765	3.257
Trimmed Mean	3.052	3.158
$GD_{Trimmed}$	2.079	2.372
Winsorized Mean	3.100	3.216
GD_{Winsor}	2.249	2.646

Table 76: Log-normal distributions with heteroscedastic noise. The noise has zero mean and a standard deviation *s* equal to 50% of the value of the data. The noise is composed of 1000 points.

	No Noise	Noise
Mode	2.576	2.731
Mean	3.250	3.248
GD_{Mean}	2.765	3.257
Trimmed Mean	3.052	3.158
$GD_{Trimmed}$	2.079	2.372
Winsorized Mean	3.100	3.216
GD_{Winsor}	2.249	2.646

Table 77: Log-normal distributions with step noise (Type 1). The uniform noise is applied in the range from the minimum value to the maximum value of the distribution. The frequency of the samples decreases linearly, going to create a noise-shaped step. The noise is composed of 1000 points.

	No Noise	Noise
Mode	2.590	4.163
Mean	3.249	4.896
GD_{Mean}	2.765	3.869
Trimmed Mean	3.051	4.718
$GD_{Trimmed}$	2.078	3.112
Winsorized Mean	3.099	4.763
GD_{Winsor}	2.248	3.395

Table 78: Log-normal distributions with step noise (Type 2). The uniform noise is applied in the range from the minimum value to the maximum value of the distribution. The frequency of the samples increases linearly, going to create a noise-shaped step. The noise is composed of 1000 points.

	No Noise	Noise
Mode	2.590	6.197
Mean	3.249	6.376
GD_{Mean}	2.765	4.646
Trimmed Mean	3.051	6.307
$GD_{Trimmed}$	2.078	3.922
Winsorized Mean	3.099	6.319
GD_{Winsor}	2.248	4.126

Table 79: Log-normal distributions with step noise (Type 3). The uniform noise is applied in the range from the minus maximum value to the minimum value of the distribution. The frequency of the samples decreases linearly, going to create a noise-shaped step. The noise is composed of 1000 points.

	No Noise	Noise
Mode	2.590	-0.465
Mean	3.249	0.335
GD_{Mean}	3.120	0.245
Trimmed Mean	3.051	0.148
$GD_{Trimmed}$	2.539	0.126
Winsorized Mean	3.099	0.199
GD_{Winsor}	2.737	0.164

Table 80: Log-normal distributions with step noise (Type 4). The uniform noise is applied in the range from the minus maximum value to the minimum value of the distribution. The frequency of the samples increases linearly, going to create a noise-shaped step. The noise is composed of 1000 points.

	No Noise	Noise
Mode	2.589	2.023
Mean	3.249	2.054
GD_{Mean}	2.765	2.065
Trimmed Mean	3.051	2.020
$GD_{Trimmed}$	2.078	1.620
Winsorized Mean	3.099	2.019
GD_{Winsor}	2.248	1.799

Disclosure

The funders had no role in the design of the study; in the collection, analyses, or interpretation of data; in the writing of the manuscript; and in the decision to publish the results.

Conflicts of Interest

The authors declare no conflicts of interest.

References

[1] D. H. Freedman, *Wrong: Why Experts Keep Failing Us and How to Know When Not to Trust Them*, Little, Brown and Company, London, UK, 2010.

[2] J. P. A. Ioannidis, "Why most published research findings are false," *PLoS Medicine*, vol. 2, no. 8, article e124, 2005.

[3] S. S. Sawilowsky, "Nonparametric Tests of Interaction in Experimental Design," *Review of Educational Research*, vol. 60, no. 1, pp. 91–126, 1990.

[4] S. S. Sawilowsky and R. C. Blair, "A more realistic look at the robustness and Type II error properties of the t test to departures from population normality," *Psychological Bulletin*, vol. 111, no. 2, pp. 352–360, 1992.

[5] R. R. Wilcox, *Fundamentals of Modern Statistical Methods*, Springer, New York, NY, USA, 2001.

[6] R. R. Wilcox, *Applying Contemporary Statistical Techniques*, Academic Press, San Diego, CA, USA, 2003.

[7] P. J. Huber and E. M. Ronchetti, *Robust Statistics*, John Wiley & Sons, New York, NY, USA, 2nd edition, 2009.

[8] IEC-ISO., *Guide to the Expression of Uncertainty in Measurement*, 1992.

[9] B. Cannas, A. Fanni, A. Murari, A. Pau, and G. Sias, "Automatic disruption classification based on manifold learning for real-time applications on JET," *Nuclear Fusion*, vol. 53, no. 9, Article ID 093023, 2014.

[10] A. Murari, P. Boutot, J. Vega et al., "Clustering based on the geodesic distance on Gaussian manifolds for the automatic classification of disruptions," *Nuclear Fusion*, vol. 53, no. 3, Article ID 033006, 2013.

[11] R. Wilcox, *Introduction to Robust Estimation and Hypothesis Testing*, Academic Press, San Diego, Calif, USA, 2nd edition, 2005.

[12] G. Verdoolaege, "A New Robust Regression Method Based on Minimization of Geodesic Distances on a Probabilistic Manifold: Application to Power Laws," *Entropy*, vol. 17, no. 12, pp. 4602–4626, 2015.

[13] A. Murari, E. Peluso, M. Gelfusa, I. Lupelli, M. Lungaroni, and P. Gaudio, "Symbolic regression via genetic programming for data driven derivation of confinement scaling laws without any assumption on their mathematical form," *Plasma Physics and Controlled Fusion*, vol. 57, no. 1, Article ID 014008, 2014.

[14] A. Murari, E. Peluso, M. Lungaroni, M. Gelfusa, and P. Gaudio, "Application of symbolic regression to the derivation of scaling laws for tokamak energy confinement time in terms of dimensionless quantities," *Nuclear Fusion*, vol. 56, no. 2, Article ID 026005, 2015.

[15] E. Peluso, A. Murari, M. Gelfusa, and P. Gaudio, "A statistical method for model extraction and model selection applied to the temperature scaling of the L-H transition," *Plasma Physics and Controlled Fusion*, vol. 56, no. 11, Article ID 114001, 2014.

[16] A. Murari, E. Peluso, M. Gelfusa, I. Lupelli, and P. Gaudio, "A new approach to the formulation and validation of scaling expressions for plasma confinement in tokamaks," *Nuclear Fusion*, vol. 55, no. 7, Article ID 073009, 2015.

[17] A. Murari, E. Peluso, M. Gelfusa, M. Lungaroni, and P. Gaudio, "How to handle error bars in symbolic regression for data mining in scientific applications," *Statistical Learning and Data Sciences*, vol. 9047, pp. 347–355, 2015.

[18] J. Ongena, P. Monier-Garbet, W. Suttrop et al., "Towards the realization on JET of an integrated H-mode scenario for ITER," *Nuclear Fusion*, vol. 44, no. 1, pp. 124–133, 2004.

[19] M. E. Puiatti, M. Mattioli, G. Telesca et al., "Radiation pattern and impurity transport in argon seeded ELMy H-mode discharges in JET," *Plasma Physics and Controlled Fusion*, vol. 44, no. 9, pp. 1863–1878, 2002.

[20] F. Romanelli and R. Kamendje, "Overview of JET results," *Nuclear Fusion*, vol. 49, no. 10, p. 104006, 2009.

Hindawi
Complexity
Volume 2019, Article ID 5910625, 14 pages
https://doi.org/10.1155/2019/5910625

Research Article

Automatic Detection of Concrete Spalling Using Piecewise Linear Stochastic Gradient Descent Logistic Regression and Image Texture Analysis

Nhat-Duc Hoang,[1] **Quoc-Lam Nguyen**,[2] **and Xuan-Linh Tran**[1]

[1]*Faculty of Civil Engineering, Institute of Research and Development, Duy Tan University, P809 - 03 Quang Trung, Danang, Vietnam*
[2]*Faculty of Civil Engineering, Duy Tan University, P202 - 03 Quang Trung, Danang 550000, Vietnam*

Correspondence should be addressed to Xuan-Linh Tran; tranxuanlinh@dtu.edu.vn

Received 18 April 2019; Revised 10 June 2019; Accepted 26 June 2019; Published 16 July 2019

Guest Editor: Murari Andrea

Recognition of spalling on surface of concrete wall is crucial in building condition survey. Early detection of this form of defect can help to develop cost-effective rehabilitation methods for maintenance agencies. This study develops a method for automatic detection of spalled areas. The proposed approach includes image texture computation for image feature extraction and a piecewise linear stochastic gradient descent logistic regression (PL-SGDLR) used for pattern recognition. Image texture obtained from statistical properties of color channels, gray-level cooccurrence matrix, and gray-level run lengths is used as features to characterize surface condition of concrete wall. Based on these extracted features, PL-SGDLR is employed to categorize image samples into two classes of "nonspall" (negative class) and "spall" (positive class). Notably, PL-SGDLR is an extension of the standard logistic regression within which a linear decision surface is replaced by a piecewise linear one. This improvement can enhance the capability of logistic regression in dealing with spall detection as a complex pattern classification problem. Experiments with 1240 collected image samples show that PL-SGDLR can help to deliver a good detection accuracy (classification accuracy rate = 90.24%). To ease the model implementation, the PL-SGDLR program has been developed and compiled in MATLAB and Visual C# .NET. Thus, the proposed PL-SGDLR can be an effective tool for maintenance agencies during periodic survey of buildings.

1. Introduction

In the maintenance process of high-rise buildings, it is important to identify surface defects to ensure the serviceability of structures. The reason is that surface quality strongly affects the safety as well as esthetics of buildings. After buildings are delivered to clients, their conditions quickly deteriorate due to the combined influences of inclement weather conditions, occupants' activities, and structural aging [1]. The deterioration of buildings is usually reflected in forms of cracks and spalls. These forms of damage do not only bring about inconvenience to occupants but also degrade the structural integrity [2]. If periodic maintenance processes cannot detect and handle this damage timely, building's owners may suffer from financial losses due to degradation of asset value. Hence, correct detection of surface damage is a crucial task in building condition assessment.

Spalling (see Figure 1) happens when fragments of materials (e.g., concrete, mortar) are ejected from the surface structure because of impact or internal stress. Spalling occurs in concrete because of moisture incursion into structural elements. Spalls are commonly observed in various structural elements in buildings such as wall, beam, column, ceiling, and floor. Particularly for reinforced concrete structures, spalls are indicators of oxidation or corrosion of reinforcing steel [3–5]. Therefore, if this form of defect is unidentified and untreated during the building maintenance process, the problem of corroded reinforcements may quickly expand and significantly worsen the structural durability.

In Vietnam, periodic building maintenance is usually performed by human technicians. This practice is also common in other countries due to the fact that human inspection can help to obtain a high level of accuracy and directly

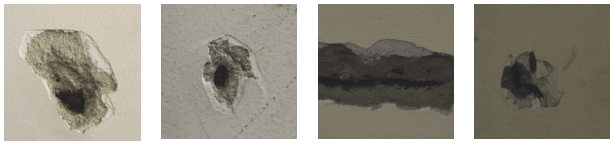

Figure 1: Spalls on concrete surface.

point out the problems underlying the detected defects [6]. Nevertheless, manual survey is notoriously known to be time consuming and labor intensive [3]. Moreover, the quality of building assessment is also strongly dependent on the skill, experience, and subjective judgment of human inspectors. This fact may lead to variability of building assessment results. In addition, the processes of data collection by means of measurement, data processing, and report are extremely time consuming for high-rise buildings having a huge number of structural elements needed to be surveyed periodically. Therefore, it is beneficial for maintenance agencies to be equipped with a more productive method of collecting and processing building condition data.

Among automated methods for building condition assessment, image processing based methods have been extensively used because of a quick advancement in the field and affordable cost of digital cameras [7–9]. Using image process techniques, regions of image samples suffering from spalling can be distinguished and isolated from healthy regions based on the features extracted from these regions. Essentially, spalling belongs to the category of area based defect. This means that using information of one pixel cannot be sufficient for spall detection. Hence, characteristics of an image region need to be extracted and analyzed for recognizing spall defect.

Nevertheless, recognition of area based defect on surface of structures is a challenging task. It is due to various difficulties including diversified textures of concrete surface, uneven illumination, irregular textures caused by stains, etc. Therefore, in recent years, a considerable number of research works have been dedicated to automatic detection of area based distress including spalling. Suwwanakarn et al. [10] proposed the employment of three circular filters to detect air pockets on the surfaces of concrete. Koch and Brilakis [11] put forward a pothole detection method which employs image thresholding, morphological thinning, elliptic regression, and texture extraction.

German et al. [4] extracted major properties of spalled regions on concrete columns for postearthquake safety assessment of buildings; this study involves the technique of image thresholding by means of a local entropy-based algorithm and a global adaptive thresholding approach. Subsequently, template matching and morphological operations can be performed to identify damaged regions [4]. A multispectral image analysis approach was presented by Valença et al. [12] to evaluate concrete damage and delineate the deteriorated zones in an automatic manner.

Kim et al. [13] established a framework to assess the dimensional and surface quality of precast concrete elements on the basis of BIM and 3D laser scanning. Paal et al. [14] present a computer vision based method for detecting building's columns and retrieving their properties used for damage recognition. A technique for localizing and quantifying spalling defects on concrete surfaces has been put forward by the employment of a terrestrial laser scanner [5]. Li et al. [15] investigate the feasibility of an integrated framework for the detection and measurement of potholes on the basis of 2D images and Ground Penetrating Radar data. Konishi et al. [16] detect void in subway tunnel lining using thermal image photographs and signal analyses. Dawood et al. [3] develop an integrated model based on image processing techniques and machine learning algorithms for spalling detection used in condition survey of subway networks; the image processing technique includes various methods of image smoothing, thresholding, histogram equalization, and filtering. Hoang [2] relied on steerable filters and machine learning for recognizing defects appearing on wall surface. Oliveira Santos et al. [17] and Santos et al. [18] put forward hyperspectral image processing models to detect cracking patterns both on clean and on concrete surface with biological stains. Recent research works [19–23] have pointed out an increasing trend of applying computer vision in structural health inspection.

Since the spalled areas and healthy ones have distinctive texture properties, texture of image samples can be computed and employed for spall recognition. Image texture expresses the spatial arrangement of color or intensities in an image sample [24]. Therefore, image texture computation methods such as statistical measurements of color channels (e.g., mean, standard deviation, skewness, etc.) [25], gray-level cooccurrence matrix [26], and gray-level run lengths [27] can be potentially applied for spall detection. Based on the image texture based features, machine learning approaches can be employed for classifying data instances into categories of spall (positive class) and nonspall (negative class). Nevertheless, few studies have investigated the efficiency of the aforementioned image texture computation in spall recognition. Moreover, it is evident that the combination of image processing and machine learning can potentially lead to effective solutions for structure health monitoring [28–34]. However, models that hybridize the strengths of image processing and machine learning based classifiers have rarely been employed for spall detection. Therefore, the current study is an attempt to fill these gaps in the literature.

Furthermore, the problem of spall detection can be formulated as a two-class pattern recognition; it is able to model the target output as a binary response variable with "nonspall" = 0 and "spall" = 1. Hence, logistic regression (LR), which is one of the models for binary data [35], can be employed for pattern classification. Logistic regression is a simple linear classifier yet effective machine learning model which is capable of delivering probabilistic prediction outcomes. The key procedure of a LR model is to define a linear classifier (in the form of a hyperplane) and an objective function (in the form of a log likelihood function); accordingly, gradient descent algorithm can be applied to adapt the model parameters [36]. The implementation of LR

is straightforward and its successful applications have been reported in various studies [37–39].

Nevertheless, one observable limitation of LR is that its employment of a linear classifier is expressed in the form of a hyperplane. To improve the capability of LR in dealing with nonlinear data, this study investigates the feasibility of replacing the conventional linear classifier used in LR by a piecewise linear model. This modification can lead to a higher degree of flexibility of model structure and potentially bring about a better predictive accuracy. In this study, a piecewise linear LR model, named PLLR, is developed for detecting spalled regions on surface of concrete wall structures. Additionally, a sequential algorithm described in the previous work of Hoang [40] and the stochastic gradient descent algorithm [41] are used to train the PLLR model. Data set including 1240 image samples has been collected to construct and verify the proposed method. The statistical descriptions of color channels, properties of the gray-level cooccurrence matrix, and properties of the gray-level run lengths are employed to compute the texture of image samples. In addition, based on the set of image texture based features, principal component analysis is employed for dimension reduction. The performance of the proposed PLLR is benchmarked with those of stochastic gradient descent LR and backpropagation artificial neural network.

The subsequent parts of the paper are organized as follows. The second section reviews the research methodology, followed by the third section that describes the collected image data set; the fourth section describes the structure of the proposed model used for automatic recognition of concrete wall spalling. The fifth section will report experimental results; several concluding remarks of this study are provided in the final section.

2. Research Methodology

2.1. Image Texture Computation. Due to the typical texture of concrete walls, two pixels having the same color/gray level can belong to both spalled and nonspalled areas. Thus, it is infeasible to detect spall in a pixel level because information of a single pixel is not sufficient for spall recognition. As stated earlier, since spalled and nonspalled concrete wall surface have distinctive features regarding color and roughness. Hence, information of texture of an image region can be helpful for identifying spalled wall sections. Accordingly, a large surveying image can be separated into a number of nonoverlapped image samples with a fixed size (e.g. 100x100 pixels). This division can also help to expedite the texture computation process. Based on such small image samples, image textures regarding statistical measurements of color channels [25], gray-level cooccurrence matrix [26], and gray-level run lengths [27] can be computed and used for data classification.

2.1.1. Statistical Properties of Color Channels. Since concrete surface background may contain irregular objects such as paints or stains caused by corroded steel reinforcements, information regarding the color of image samples can be helpful for the task of spall recognition. Let $P(I)$ represent the first-order histogram of an image sample S; $P(I)$ is computed as follows [25]:

$$P_c(I) = \frac{N_{I,c}}{W \times H} \tag{1}$$

where c is a color channel (either red or green or blue). $N_{I,c}$ denotes the number of pixels having color value of the channel $c = I$. H and W represent the two parameters of the image height and width.

Accordingly, the average (μ_c) and the standard deviation (σ_c) of color value can be computed in the following manner:

$$\mu_c = \sum_{i=0}^{NL-1} I_{i,c} \times P_c(I) \tag{2}$$

$$\sigma_c = \sqrt{\sum_{i=0}^{NL-1} (I_{i,c} - \mu_c)^2 \times P_c(I)} \tag{3}$$

where $I_{i,c} = 0, 1, 2, \ldots, 255$. $NL = 256$ is the number of discrete color values.

Moreover, the skewness (δ_c) and kurtosis (η_c) of discrete color values are calculated as follows:

$$\delta_c = \frac{\sum_{i=0}^{NL-1} (I_{i,c} - \mu_c)^3 \times P_c(I)}{\sigma^3} \tag{4}$$

$$\eta_c = \frac{\sum_{i=0}^{NL-1} (I_{i,c} - \mu_c)^4 \times P_c(I)}{\sigma^4} \tag{5}$$

The entropy (ρ_c) and range (Δ_c) of color intensity can be computed and characterize distinctive features of image samples. These ρ_c and Δ_c are calculated as follows:

$$\rho_c = -\sum_{i=0}^{NL-1} P_c(I) \times \log_2 (P_c(I)) \tag{6}$$

$$\Delta_c = \max(I_c) - \min(I_c) \tag{7}$$

2.1.2. Gray-Level Cooccurrence Matrix (GLCM). In computer vision field, gray-level cooccurrence matrix (GLCM) [26] is a commonly employed method for texture classification. A cooccurrence matrix provides information regarding the distribution of cooccurring pixel values at a given offset r [42]. After the cooccurrence matrix is computed, it is often normalized. Subsequently, a set of statistical measures can be computed from this normalized matrix. Furthermore, it is beneficial for texture classification to detect features of an image's region which are rotationally invariant. This is the reason why the cooccurrence matrix is usually computed at different regular angles (Δ) with certain value of offset r. The commonly used values of Δ are 0°, 45°, 90°, and 135° [42].

It is proper to note that a color image sample must be converted to a gray-scale image before the computation of its GLCM. Let $\delta = (r, \Delta)$ represent a relationship employed to compute a GLCM of an image. Thus, the joint probability of the pairs of color levels that occur at the two

locations dictated by the relationship δ can be calculated [42]. The information of this joint probability is provided in a cooccurrence matrix P_δ within which $P_\delta(i, j)$ denotes the probability of the two color levels of i and j occurring at the relationship δ [43].

The normalized cooccurrence matrix is computed as follows:

$$P_\delta^N(i,j) = \frac{P_\delta(i,j)}{S_P} \tag{8}$$

where P_δ^N represents the normalized GLCM and S_P is the total number of pixels.

With $r = 1$ and $\Delta = 0^\circ, 45^\circ, 90^\circ$, and 135°, we can establish four cooccurrence matrices. Based on these four matrices, the indices of angular second moment (AM), contrast (CO), correlation (CR), and entropy (ET) can be obtained and utilized for texture classification [44, 45]. These indices are calculated by the following equations [26]:

$$AM = \sum_{i=1}^{N_g}\sum_{j=1}^{N_g} P_\delta^N(i,j)^2 \tag{9}$$

where $N_g = 256$ denotes the number of color level values. Consider

$$CO = \sum_{k=0}^{N_g-1} k^2 \sum_{\substack{i=1\\|i-j|=k}}^{N_g}\sum_{j=1}^{N_g} P_\delta^N(i,j) \tag{10}$$

$$CR = \frac{\sum_{i=1}^{N_g}\sum_{j=1}^{N_g} i\times j\times P_\delta^N(i,j) - \mu_X\mu_Y}{\sigma_X\sigma_Y} \tag{11}$$

where μ_X, μ_Y, σ_X, and σ_Y represent the means and standard deviations of the marginal distribution associated with $P_\delta^N(i, j)$ [26].

2.1.3. Gray-Level Run Lengths (GLRL). First proposed by Galloway [27], texture analysis based on gray-level run lengths is an effective method in image processing. This method is based on the observation that relatively long gray-level runs occur more often in a coarse texture and a fine texture often includes short runs [46]. Based on previous experimental works, properties of gray-level run lengths can help construct useful features for texture classification tasks [47–50]. For an image sample and in a given direction, a run-length matrix $p(i\ j)$ is defined as the number of times that the image contains a run length j of gray level i *[27]*. Based on $p(i\ j)$, various texture features can be computed [46].

Let M and N denote the number of gray levels and the maximum run length, respectively. Moreover, let N_r be the total number of runs and let N_p be the number of pixels in the image. Given a set of directions $\{0^\circ, 45^\circ, 90^\circ, 135^\circ\}$, a run length matrix can be computed. Accordingly, based on each run length matrix, the Short Run Emphasis (SRE), Long Run Emphasis (LRE), Gray-Level Nonuniformity (GLN), Run Length Nonuniformity (RLN), and Run Percentage (RP) are defined as follows [27, 46]:

$$SRE = \frac{1}{N_r}\sum_{i=1}^{M}\sum_{j=1}^{N}\frac{p(i,j)}{j^2} \tag{12}$$

$$LRE = \frac{1}{N_r}\sum_{i=1}^{M}\sum_{j=1}^{N} p(i,j)\times j^2 \tag{13}$$

$$GLN = \frac{1}{N_r}\sum_{i=1}^{M}\left(\sum_{j=1}^{N} p(i,j)\right)^2 \tag{14}$$

$$RLN = \frac{1}{N_r}\sum_{j=1}^{N}\left(\sum_{i=1}^{M} p(i,j)\right)^2 \tag{15}$$

$$RP = \frac{N_r}{N_p} \tag{16}$$

In addition to the above five properties, Chu et al. [51] proposed the Low Gray-Level Run Emphasis (LGRE) and High Gray-Level Run Emphasis (HGRE) as follows:

$$LGRE = \frac{1}{N_r}\sum_{j=1}^{N}\sum_{i=1}^{M}\frac{p(i,j)}{i^2} \tag{17}$$

$$HGRE = \frac{1}{N_r}\sum_{j=1}^{N}\sum_{i=1}^{M} p(i,j)\times i^2 \tag{18}$$

Furthermore, the Short Run Low Gray-Level Emphasis (SRLGE), Short Run High Gray-Level Emphasis (SRHGE), Long Run Low Gray-Level Emphasis (LRLGE), and Long Run High Gray-Level Emphasis (LRHGE) have been proposed by Dasarathy and Holder [48] as follows:

$$SRLGE = \frac{1}{N_r}\sum_{j=1}^{N}\sum_{i=1}^{M}\frac{p(i,j)}{i^2\times j^2} \tag{19}$$

$$SRHGE = \frac{1}{N_r}\sum_{j=1}^{N}\sum_{i=1}^{M}\frac{p(i,j)\times i^2}{j^2} \tag{20}$$

$$LRLGE = \frac{1}{N_r}\sum_{j=1}^{N}\sum_{i=1}^{M}\frac{p(i,j)\times j^2}{i^2} \tag{21}$$

$$LRHGE = \frac{1}{N_r}\sum_{j=1}^{N}\sum_{i=1}^{M} p(i,j)\times i^2\times j^2 \tag{22}$$

2.2. Stochastic Gradient Descent Logistic Regression. It is noted that the task at hand is to construct a decision boundary that divides data instances into two class labels of nonspall and spall. Thus, the logistic regression (LR) model, which is a powerful pattern classifier, can be employed [52]. LR is selected to establish the spall detection model in this study because its learning phase is straightforward. Moreover, the LR model structure is easy to interpret. This machine learning

Procedure SGD
Create a training dataset
Randomly create θ
Defining *MaxEpoch* // the maximum number of epochs
Defining α // the learning rate parameter
For $ep = 1$ to *MaxEpoch*
  Shuffle samples in the training data set
  For $i = 1$ to M // M = number of data samples
    For $k = 0$ to D
      $\theta_k = \theta_k + \alpha \frac{\partial l(\theta_k)}{\partial(\theta_k)}$
    End For
  End For
End For
Return θ

Algorithm 1: Pseudo code of the Stochastic Gradient Descent (SGD) algorithm.

method has also been successfully applied in various recent applications [53–56].

Let y be the outcome of the model. $y = 1$ (the positive class) when an image sample is subject to spall and $y = 0$ (the negative class) when an image sample is free from spall. Let x be a vector of input features which are extracted from an image sample. Herein, $x_i = x_{i1}, x_{i2}, \ldots, x_{iD}$ where D denotes the number of the features used for classification. In addition, a vector of $\theta = \theta_0, \theta_1, \theta_2, \ldots, \theta_D$ represents adaptable parameters of a LR model.

$h_\theta(x_i)$ is used to express the probability of the positive class output of spall which is calculated as follows [35]:

$$h_\theta(x_i) = h_\theta(x_{i1}, x_{i2}, \ldots, x_{iD}) = \frac{1}{1 + \exp(-\eta_i)} = \frac{1}{1 + \exp(-\theta^T x_i)} \tag{23}$$

where $\eta_i = \theta_0 + \theta_1 x_{i1} + \theta_2 x_{i2} + \cdots + \theta_D x_{iD} = \theta^T x_i$.

Notably, $g(\eta_i) = 1/(1 + \exp(-\eta_i))$ is called the logistic function or the sigmoid function and its derivative is expressed in the following form [41]:

$$g'(\eta_i) = g(\eta_i) \times (1 - g(\eta_i)) \tag{24}$$

The probabilities of the positive and negative classes are given as follows:

$$P(y_i = 1 \mid x_i, \theta) = h_\theta(x_i) \tag{25}$$

$$P(y_i = 0 \mid x_i, \theta) = 1 - h_\theta(x_i) \tag{26}$$

Hence, the output probability can be computed in the following equation [41]:

$$P(y_i = 0 \mid x_i, \theta) = (h_\theta(x_i))^{y_i} (1 - h_\theta(x_i))^{1-y_i} \tag{27}$$

The likelihood of the LR model parameters can be expressed as follows [41]:

$$L(\theta) = \prod_{i=1}^{M} (h_\theta(x_i))^{y_i} (1 - h_\theta(x_i))^{1-y_i} \tag{28}$$

where M represents the number of data samples.

To identify the model parameter θ, the following log likelihood function is maximized:

$$l(\theta) = \log(L(\theta)) = \sum_{i=1}^{M} y_i \log(h_\theta(x_i)) + (1 - y_i)(1 - \log(h_\theta(x_i)) \tag{29}$$

The stochastic gradient descent (SGD) [36] can be employed to construct the LR model by adapting its adaptable parameters θ. Before the model construction phase, the original collected data sample should be divided into two sets: a training set and a testing set. The first set is employed to adapt the model parameters; the latter set is reserved for confirming the model generalization capability. The procedure of the SGD algorithm is described in Algorithm 1.

Within the SGD algorithm, the quantity $\partial l(\theta_k)/\partial(\theta_k)$ can be computed as follows:

$$\frac{\partial l(\theta_k)}{\partial(\theta_k)} = (y_i - h_\theta(x_i)) x_{i,k} \tag{30}$$

Thus, the update rule employed to determine the LR model parameter θ is expressed as follows:

$$\theta_k = \theta_k + \alpha (y_i - h_\theta(x_i)) x_{i,k} \tag{31}$$

where $x_{i,0} = 1$ with all i.

2.3. Piecewise Linear Model. As stated earlier, one limitation of the standard LR is that its decision is given in the form of a linear model which is essentially a hyperplane. This study aims at extending the capability of LR by employing a piecewise linear decision surface. The underlying concept is illustrated in Figure 2. Herein, a model $y(x)$ is used to separate the input space into two regions characterizing two data categories. Instead of using a linear decision surface, a piecewise linear one is employed to fit a subset of the input data x. The transition location from a certain subset to another one is termed a breakpoint or a knot [57].

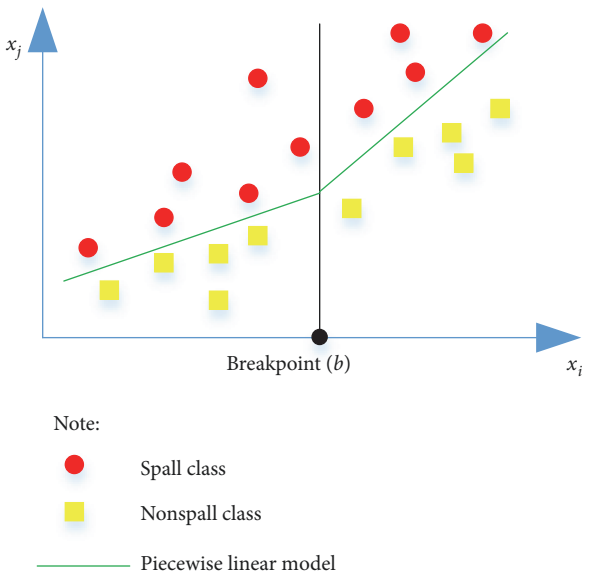

FIGURE 2: Piecewise linear model.

The breakpoints enhance the flexibility of the model by disintegrating the input space into subspaces in which each linear model can be used to fit the collected data [40].

Similar to the concept of a piecewise linear regression [58], the mathematical formulation of a piecewise linear model with one breakpoint is shown as follows:

$$y(x_i) = \begin{cases} \sum_{d=1}^{D+1} \theta_d x_{i,d} & if \ x_{i,d} \le b \\ \sum_{d=1}^{D+1} \theta_d x_{i,d} & if \ x_{i,d} > b \end{cases} \quad (32)$$

where x_i denotes the vector of the i^{th} predicting variable consisting of D elements. b represents the knot value. y denotes the model output.

The model establishment of the piecewise linear classification model requires the selection of the knots (b) and the model parameter (θ). In this study, the knot position is identified via a sequential algorithm described in the previous work of Hoang [40]. In addition, based on the collected data samples and the selected knots, the aforementioned SGD algorithm is used to train piecewise LR and reveal the set of θ that brings about the best fit to the data set at hand.

3. The Image Data Set

Since the logistic regression is a supervised machine learning algorithm, a data set consisting of 1240 pavement image samples with the ground truth label has been collected to construct the logistic regression based classification model. Herein, the numbers of image samples in the two categories of nonspalling and spalling are both 620. The digital images have been collected during survey trip of several high-rise buildings in Danang city (Vietnam). The employed camera is the Cannon EOS M10. The camera is positioned at a distance of about 1.5 meter from the concrete surface. Image samples of the two categories of nonspalling (label = 0) and spalling (label = 1) have been prepared for further analysis.

To expedite the speed of the feature extraction process, the size of image sample has been fixed to be 100x100 pixels. The collected image samples are demonstrated in Figure 3. It is worth noticing that the ground truth of image samples is assigned by human inspectors and the wall condition (either nonspalling or spalling) is determined at the image level. Moreover, an image is labeled as spalling if the spalling area occupies at least 50% of the entire image sample. To ensure the diversity of the image set, the class of nonspalling includes samples of intact concrete surface, cracks, and stains; the class of spalling also takes into account samples in which steel reinforcement is revealed.

4. The Proposed Piecewise Linear Stochastic Gradient Descent Logistic Regression Model for Wall Spall Detection

This section of the study describes the overall structure of the newly developed piecewise linear (PL) stochastic gradient descent logistic regression (SGDLR) model for wall spall detection. The proposed model, named PL-SGDLR, is a hybridization of image texture computation and data classification approach. The statistical measurements of color channels, GLCM, and GLRL are employed for computing the texture of each image sample. The PL-SGDLR uses the image texture as features for classifying data samples into the categories of nonspall and spall. The model structure is illustrated in Figure 4 which basically includes two modules: image texture based feature extraction and PL-SGDLR based data classification. The first module is developed in Visual C#.NET by the author; the second module is programmed in MATLAB. The graphical user interfaces of the two modules are demonstrated in Figure 5.

In the first module of feature extraction, image texture computing techniques including statistical analysis of color channels, GLCM, and GLRL are employed to extract features from image samples. This module has been developed by the author in Visual C# .NET (Framework 4.6.1). First, the group of features based on statistical properties of color images is computed. For each of the three color channels (red, green, and blue), six statistical indices of mean, standard deviation, skewness, kurtosis, entropy, and range are computed according to the aforementioned formulas. Thus, the total number of features extracted from these statistical measurements of an image sample is 6 x 3 = 18.

Second, the group of texture features extracted from four cooccurrence matrices corresponding to the directions of 0°, 45°, 90°, and 135° are obtained. Since each cooccurrence matrix yields four properties of the angular second moment, contrast, correlation, and entropy, the total number of features extracted from GLCMs is 4 x 4 = 16. Third, the feature group extracted from four GLRL matrices is calculated. The four GLRL matrices are constructed by considering the texture of pixels in the four directions of 0°, 45°, 90°, and 135°. For each GLRL matrix, the 11 properties of the Short Run Emphasis (SRE), Long Run Emphasis (LRE), Gray-Level

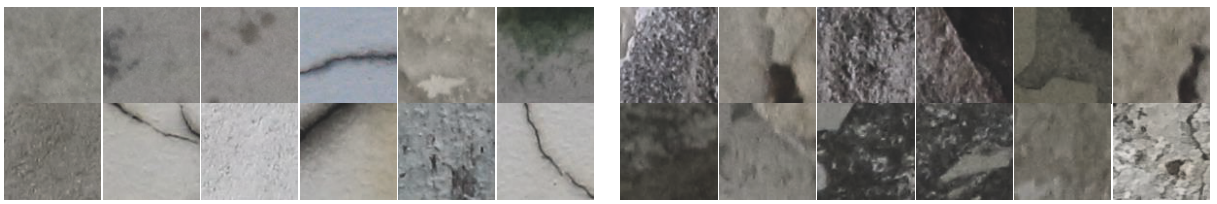

(a) (b)

Figure 3: The collected image samples: (a) nonspalling class and (b) spalling class.

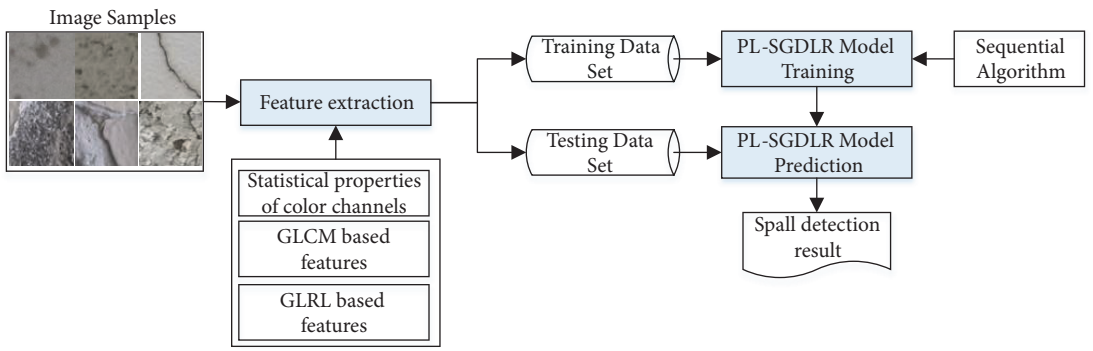

Figure 4: Structure of the proposed PL-SGDLR.

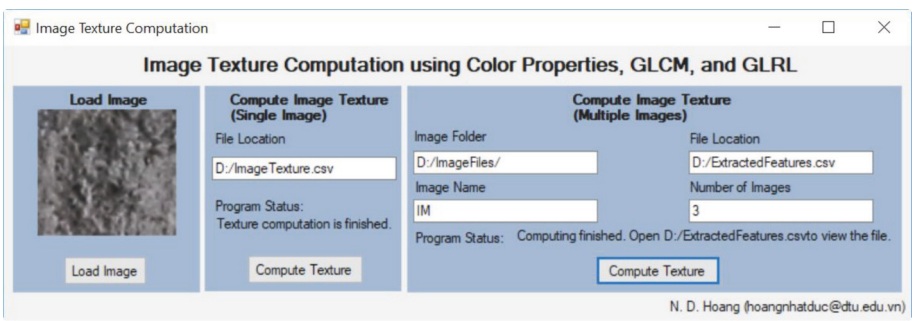

(a)

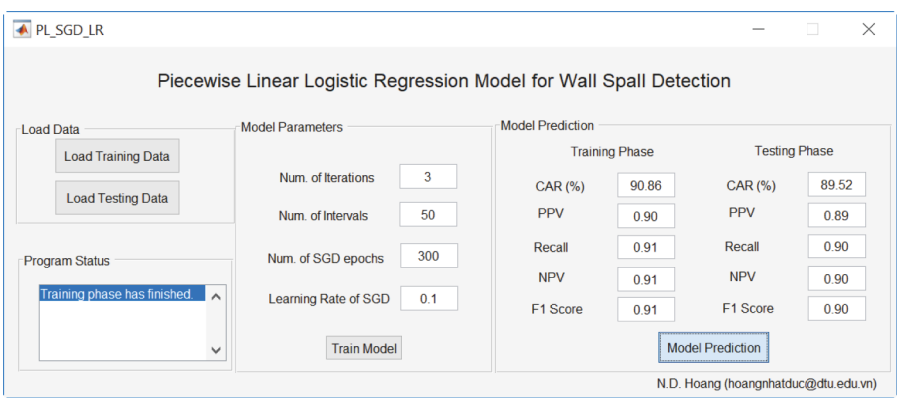

(b)

Figure 5: Graphical user interface (GUI) of the PL-SGDLR program. (a) Texture computation module and (b) data classification module.

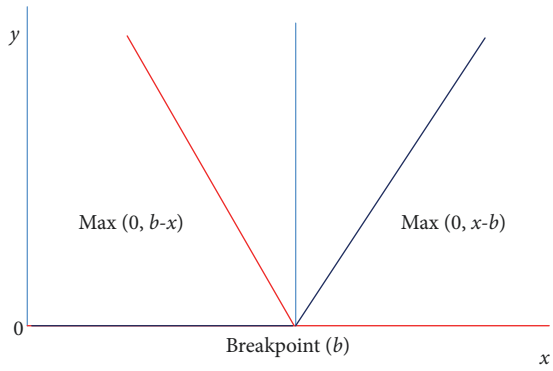

Figure 6: Concept of a hinge function.

Nonuniformity (GLN), Run Length Nonuniformity (RLN), Run Percentage (RP), Low Gray-Level Run Emphasis (LGRE), High Gray-Level Run Emphasis (HGRE), the Short Run Low Gray-Level Emphasis (SRLGE), Short Run High Gray-Level Emphasis (SRHGE), Long Run Low Gray-Level Emphasis (LRLGE), and Long Run High Gray-Level Emphasis (LRHGE) are calculated to represent an image texture. Hence, the total number of features extracted from GLRL matrices is 4 x 11 = 44.

Accordingly, each image sample is presented by a feature vector consisting of 18 + 16 + 44 = 78 elements. When the feature extraction module finishes, a numerical data set consisting of 1240 data samples and 78 input features is prepared for further analysis. This data set has two class outputs: 0 denoting nonspall (negative class) and 1 denoting spall (positive class). For standardizing the data ranges and facilitating the data modeling process, the extracted data set has been processed using Z-score data normalization [59]. Furthermore, the widely employed statistical procedure of principal component analysis (PCA) is employed for dimension reduction. PCA basically converts the input features of the original numerical data set into a set of linearly uncorrelated variables [60]. The processed data is then randomly separated into two sets: a training set (90%) and a testing set (10%). The first data set is used for model construction; the latter data set is reserved for model verification.

The training phase of a PL-SGDLR model relies on the concept of a hinge function [61] (see Figure 6). As can be seen from the figure, the output of a hinge function is zero for a certain part of its range. Therefore, this function is useful for dividing the data into separated regions; each of the regions can be satisfactorily fitted by a linear model. Using such a concept of hinge functions, a PL-SGDLR model having one predicting variable x and one breakpoint b is given as follows:

$$\begin{aligned} y = {} & \beta_o + \beta_{11} \max\left(0, \operatorname{sign}\left(x - b\right)\right) \\ & + \beta_{12} \max\left(0, \operatorname{sign}\left(b - x\right)\right) + \beta_{21} \max\left(0, x - b\right) \\ & + \beta_{22} \max\left(0, b - x\right) \end{aligned} \tag{33}$$

Hence, the output $y(x)$ according to different values of the explanatory variable x can be written as follows:

(i) If $x > b$ then $y = \beta_{11} + \beta_{21} \max(0, x - b)$.

(ii) If $x < b$ then $y = \beta_{12} + \beta_{22} \max(0, b - x)$.

(iii) If $x = b$ then $y = \beta_0$.

In essence, at two sides of a breakpoint b of the predicting variable x, two linear models are constructed. The terms β_0, β_{11}, β_{12}, β_{21}, and β_{22} are parameters of these two linear models. Without much difficulty, the model with one predicting variable and one breakpoint can be generalized to a model with many predicting variables and multiple breakpoints in the following manner:

$$y = \sum_{d=1}^{D} \sum_{v=1}^{V_d} LF_{d,v}\left(x_d\right) \tag{34}$$

where d is the index of predicting variables; D denotes the number of predicting variables; v represents the index of the hinge function of the d^{th} predicting variable; V_d denotes the number of hinge functions of the d^{th} predicting variable.

To identify the appropriate breakpoints for the predicting variables, the range of each input feature x_{d} is partitioned into N_{BP} equally spaced subranges as follows: $\min(x_d) < b_{d,1} < b_{d,2} < \cdots < \max(x_d)$. Accordingly, each variable x has $N_{BP} + 1$ candidates of knots. The model is then constructed sequentially by adding a suitable breakpoint for each input variable in each iteration. Procedure of the model construction phase is demonstrated in Algorithm 2.

In order to accept a breakpoint from a set of candidates, the following fitness function is proposed:

$$f_{Fitness} = \frac{PPV + NPV}{2} + \frac{\lambda}{SumBP + \omega} \tag{35}$$

where PPV and NPV are Positive Predictive Value and Negative Predictive Value, respectively. λ denotes a regularization parameter; $SumBP$ is the number of currently accepted breakpoints; $\omega = 1$ is a scalar simply used to ensure numerical stability.

These two quantities of PPV and NPV are computed as follows:

$$\text{Positive Predictive Value (PPV)} = \frac{TP}{TP + FP} \tag{36}$$

$$\text{Negative Predictive Value (NPV)} = \frac{TN}{TN + FN} \tag{37}$$

In (35), the first term $((PPV + NPV)/2)$ represents the model classification accuracy; the second term $(\lambda/(SumBP + \alpha))$ is used to quantify the model complexity. It is reasonable to obtain a model featuring a high value of classification accuracy with moderated complexity. It is because a model having a high degree of complexity tends to be overfitted. Moreover, the model complexity can be expressed in terms of the $SumBP$. Therefore, it is desirable to obtain a model with high value of both predictive values (PPV and NPV) and a low $SumBP$. The breakpoint acceptance criterion (BAC) calculates the fitness value to examine the benefit of accepting a knot candidate. If a candidate can help to increase the model's fitness value, it is allowed to enter the model structure. It is noted that in order to compute the classification accuracy the overall LR model is fitted by the SGD described in the previous section of the study.

Define the breakpoint acceptance criterion (BAC)
Define the maximum number of iterations *MaxIter*
Define the parameter N_{BP}
For $i = 1$ to*MaxIter*
  Initialize Model_Structure = []
  For $d = 1$ to D // D is the number of predicting variables
    Identify a breaking point for X_d based on BAC
    Update Model_Structure
    Identify Model_Parameter β using SGD algorithm
  End For
End For
Return Model_Structure and Model_Parameter

Algorithm 2: Pseudo code of the model training phase.

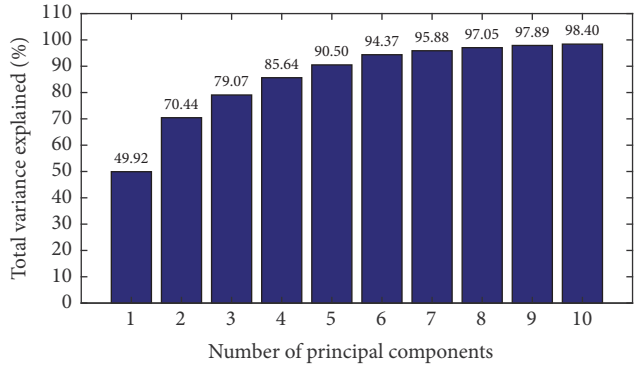

Figure 7: Total variance explained by principal components.

5. Experimental Result and Comparison

As mentioned in the previous section, the data set, which consists of 1240 samples and 78 input features, is employed to construct and validate the proposed PL-SGDLR approach. The original input data with the number of features = 78 has been preprocessed by PCA to eliminate linear correlation among its variables. The result of the PCA data transformation process is a new set of linearly uncorrelated variables; each new variable is a linear combination of the 78 original features representing texture of image samples.

Figure 7 reports the PCA result in the form of the total variance explained by principal components. Based on several trial runs, the threshold of total variance = 95% is used to select the suitable number of principal components. Accordingly, the number of principal components = 7 (corresponding to the total variance = 95.88%) is used. Additionally, the feature extraction process of the proposed PL-SGDLR model is demonstrated with an image sample of nonspall class (Figure 8(a)) and with an image sample of spall class (Figure 8(b)).

Based on the PCA result, the transformed data set including 7 input variables and the class label of either 0 (nonspall) or 1 (spall) has been divided into training and testing subsets. The former and the latter subsets consist of 90% and 10% of the collected data set, respectively. The first set is employed in the model construction phase; the second set is reserved for evaluating the model generalization capability when predicting spalls in novel image samples. Furthermore, because one time of model training and testing cannot well reveal the model generalization capability due to the randomness in data selection, this study has performed a random subsampling of the original data set. This random subsampling process contains 20 runs. In each run, 10% of the data is randomly drawn to form the testing set; the rest of the data is used for model training purpose.

As can be seen from the training process of PL-SGDLR, it is required to select the parameters of the number of training iterations (*MaxIter*), the number of training epochs (*MaxEpoch*), and N_{BP} which determines the number of knot candidates, learning rate (α) used in the SGD algorithm, and regularization parameter (λ) used in the training phase of PL-SGDLR. The suitable values of these hyperparameters of the model have been experimentally found as follows: *MaxIter* = 3, *MaxEpoch* = 300, $N_{BP} = 50$, learning rate (α) = 0.1, λ= 0.01.

In addition, besides the aforementioned PPV and NPV, Classification Accuracy Rate (CAR), Recall, and F1 score can also be employed to express the model spall detection result. These performance measurement indices are calculated as follows [62]:

$$\text{Classification Accuracy Rate: CAR} = \frac{TP + TN}{TP + TN + FP + FN} \times 100\% \quad (38)$$

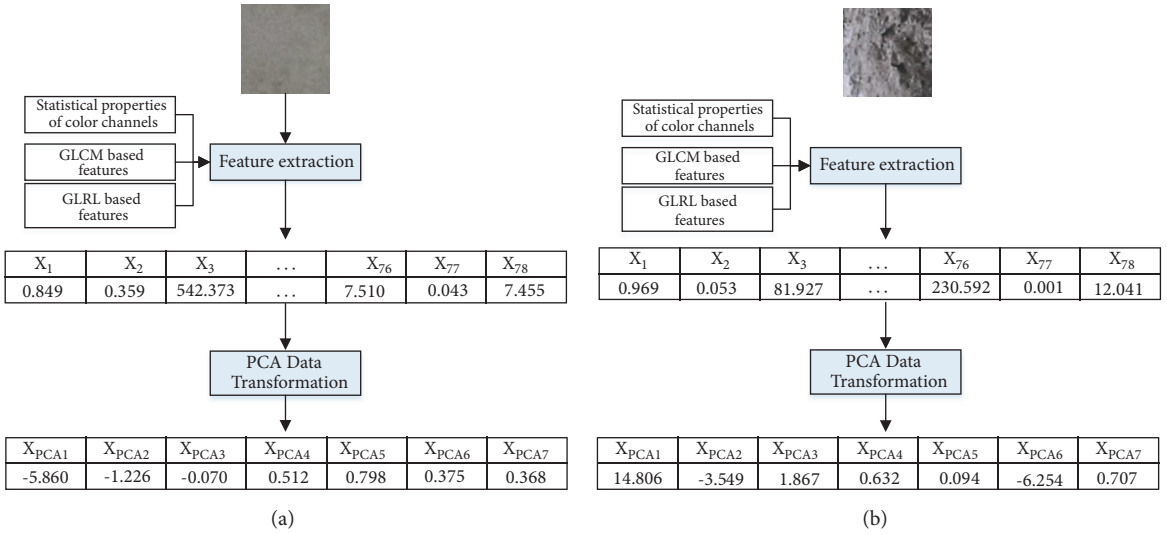

Figure 8: Illustration of the feature extraction process. (a) A nonspall sample and (b) a spall sample.

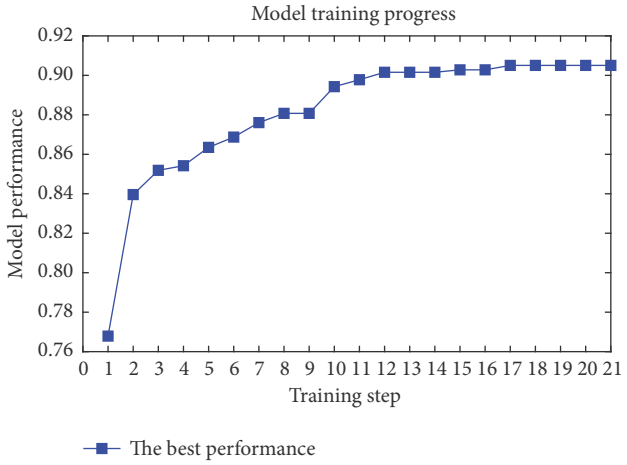

Figure 9: Illustration of the PL-SGDLR model's training progress.

$$\text{Recall} = \frac{TP}{TP + FN} \tag{39}$$

$$\text{F1 Score} = \frac{2TP}{2TP + FP + FN} \tag{40}$$

After the repeated data sampling with 20 independent runs, the average performance of the PL-SGDLR model used for predicting testing samples is reported as follows: CAR = 90.24%, PPV = 0.90, Recall = 0.91, NPV = 0.91, and F1 score = 0.90. A typical training phase of the proposed PL-SGDLR model is demonstrated in Figure 9. In this figure, the horizontal axis denotes the training step which is equal to the number of *MaxIter* multiplied by the number of input variables. Herein, *MaxIter* is 3 and the number of input variables is 7. The vertical axis represents the fitness function value described in (35).

As mentioned earlier, to guarantee the diversity of the image set and to better cope with the real-world circumstance, anomalies such as cracks and stains have been included in the image data set (see Figure 10). The category of spalling also contains image samples in which steel reinforcement is revealed. Image samples in which spalling and anomalies (such as crack and stains) coexist are also included in the image samples to train and verify the prediction model. Based on experimental results, the prediction model can predict the correct labels of the image samples containing anomalies.

In addition, to demonstrate the capability of the proposed PL-SGDLR model, the SGD-LR and the Levenberg-Marquardt Backpropagation Artificial Neural Network (LM-ANN) [63] are utilized as benchmark approaches. These two machine learning models are selected due to their successful applications reported in previous studies [37, 39, 64–66]. SGD-LR is programmed in MATLAB by the author. In addition, the LM-ANN model is constructed by the MATLAB's Statistics and Machine Learning Toolbox [67]. The SGD-LR is also trained with 300 epochs and the learning rate = 0.1. In addition, via several trial-and-error runs, the appropriate configuration of the BPANN model is as follows: the number of neurons = 7, the learning rate = 0.01, and the number of training epochs = 1000.

The performances of spall detection models obtained from the repeated data sampling with 20 runs are summarized in Table 1. As can be observed from the experimental outcomes, the proposed PL-SGDLR has obtained the best predictive performance (CAR = 90.24%, PPV = 0.90, Recall = 0.91, NPV = 0.91, and F1 score = 0.90), followed by LM-ANN (CAR = 88.83%, PPV = 0.88, Recall = 0.90, NPV = 0.90, and F1 score = 0.89) and SGD-LR (CAR = 84.40%, PPV = 0.84, Recall = 0.85, NPV = 0.85, and F1 score = 0.84). The box plots of spalling detection performance of the proposed PL-SGDLR as well as the benchmark models of LM-ANN and SGD-LR are shown in Figure 11. As shown in this figure, the

Table 1: Prediction Results Comparison.

Phase	Metrics	*SGD-LR*		*LM-ANN*		*PL-SGDLR*	
		Mean	Std.	Mean	Std.	Mean	Std.
Training	CAR (%)	86.42	0.40	90.68	1.46	91.07	0.72
	PPV	0.86	0.02	0.90	0.02	0.90	0.02
	Recall	0.87	0.02	0.91	0.01	0.93	0.02
	NPV	0.87	0.01	0.91	0.01	0.93	0.02
	F1 Score	0.86	0.00	0.91	0.01	0.91	0.01
Testing	CAR (%)	84.40	3.56	88.83	3.71	90.24	2.48
	PPV	0.84	0.05	0.88	0.04	0.90	0.04
	Recall	0.85	0.05	0.90	0.05	0.91	0.02
	NPV	0.85	0.04	0.90	0.04	0.91	0.02
	F1 Score	0.84	0.04	0.89	0.04	0.90	0.02

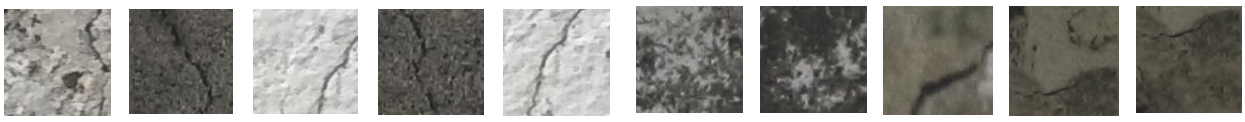

(a) (b)

Figure 10: Illustrations of image samples containing anomalies: (a) cracks and (b) stains.

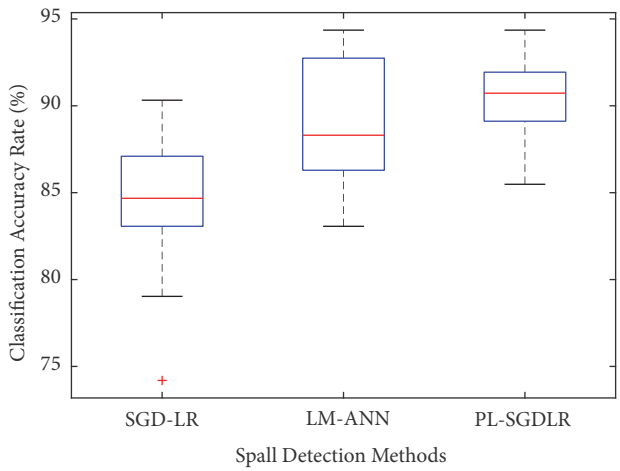

Figure 11: Box plots of classification performance.

median value of the CAR of the PL-SGDLR (90.72%) is also higher than those of the LM-ANN (84.68%) and SGD-LR (88.31%). Thus, it can be seen that the newly developed PL-SGDLR has outperformed the two benchmark methods in all of the employed performance measurement indices.

In addition, the Wilcoxon signed-rank test [68] is also employed in this section to investigate the statistical difference of each pair of spalling detection methods. Herein, the significance level of the test is set to be 0.05. By assessing the CAR values obtained from the repeated data sampling with 20 runs, the Wilcoxon signed-rank test shows that the spalling detection performance of the PL-SGDLR is statistically different from that of the SGD-LR with the p-values = 0.0001. Nevertheless, the statistical test regarding the performances of the PL-SGDLR and LM-ANN models has the p-values = 0.1971. Based on this result, it can be seen that the performance of the PL-SGDLR is highly competitive to that of the LM-ANN. However, since the CAR, PPV, Recall, NPV, and F1 Score of the PL-SGDLR are higher than those of LM-ANN, it is able to confirm that PL-SGDLR is a capable tool for detecting concrete wall spalls.

6. Conclusion

Detecting spalled areas in concrete wall structures is an important task in structural health monitoring. This study proposes a computer vision based model to replace the time-consuming manual method commonly used for periodic building survey. The proposed model is a hybridization of image texture analysis and machine learning approaches. Image texture computed by the statistical measurements of color channels, GLCM, and GLRL is employed as features to characterize the condition of concrete wall surface. Based on such extracted features, the PL-SGDLR is employed to classify image samples into two categories of nonspall and spall. An image data set consisting of 1240 samples has been collected to train and verify the PL-SGDLR model.

This study also extends the modeling capability of the standard LR model by employing a piecewise linear decision surface. A sequential procedure is proposed to iteratively construct the piecewise linear LR model. Experimental results point out that the newly developed model can help to achieve good spall detection accuracy with CAR = 90.24%. This result is better than those of LM-ANN (CAR = 88.83%) and LR (CAR = 84.40%). Since the performance of PL-SGDLR is better than that of LR, it is able to confirm that the utilization of a piecewise linear decision surface can help the LR to extend its nonlinear modeling capability. Accordingly, the proposed PL-SGDLR can be a potential

tool to assist maintenance agencies in the task of periodic survey. Future extensions of the current work may include the investigation into the effect of different spatial resolutions on the spalling detection results and the utilization of other advanced machine learning methods to enhance the prediction accuracy. Furthermore, the effect of different percentages of the spalling area on the model prediction outcome is also worth investigating.

Data Availability

The supplementary file provides the data set used in this study. The data set and the developed programs can be accessed via https://github.com/NhatDucHoang/PL_LR_WSD.

Conflicts of Interest

The authors declare that there are no conflicts of interest regarding the publication of this research work.

Acknowledgments

This research is financially supported by Duy Tan University.

Supplementary Materials

The supplementary file provides the data set used in this study. The first 78 columns of the data are texture based features extracted from image samples. The last column is the ground truth label of the data instance with 0 = "nonspall" and 1 = "spall." The data set and the developed programs can be accessed via https://github.com/NhatDucHoang/PL_LR_WSD. *(Supplementary Materials)*

References

[1] W. Zhang, Z. Zhang, D. Qi, and Y. Liu, "Automatic crack detection and classification method for subway tunnel safety monitoring," *Sensors*, vol. 14, no. 10, pp. 19307–19328, 2014.

[2] N. Hoang, "Image processing-based recognition of wall defects using machine learning approaches and steerable filters," *Computational Intelligence and Neuroscience*, vol. 2018, pp. 1–18, 2018.

[3] T. Dawood, Z. Zhu, and T. Zayed, "Machine vision-based model for spalling detection and quantification in subway networks," *Automation in Construction*, vol. 81, pp. 149–160, 2017.

[4] S. German, I. Brilakis, and R. Desroches, "Rapid entropy-based detection and properties measurement of concrete spalling with machine vision for post-earthquake safety assessments," *Advanced Engineering Informatics*, vol. 26, no. 4, pp. 846–858, 2012.

[5] M. Kim, H. Sohn, and C. Chang, "Localization and quantification of concrete spalling defects using terrestrial laser scanning," *Journal of Computing in Civil Engineering*, vol. 29, no. 6, Article ID 04014086, 2015.

[6] Y. Cha, W. Choi, G. Suh, S. Mahmoudkhani, and O. Büyüköztürk, "Autonomous structural visual inspection using region-based deep learning for detecting multiple damage types," *Computer-Aided Civil and Infrastructure Engineering*, vol. 33, no. 9, pp. 731–747, 2018.

[7] A. Mohan and S. Poobal, "Crack detection using image processing: a critical review and analysis," *Alexandria Engineering Journal*, 2017.

[8] Y.-S. Yang, C.-l. Wu, T. T. C. Hsu, H.-C. Yang, H.-J. Lu, and C.-C. Chang, "Image analysis method for crack distribution and width estimation for reinforced concrete structures," *Automation in Construction*, vol. 91, pp. 120–132, 2018.

[9] H. K. Jung and G. Park, "Rapid and non-invasive surface crack detection for pressed-panel products based on online image processing," *Structural Health and Monitoring*, 2019.

[10] S. Suwwanakarn, Z. Zhu, and I. Brilakis, "Automated air pockets detection for architectural concrete inspection," in *In Proceedings of the Construction Congress I, American Society of Civil Engineers*, Reston, VA, USA, 2007.

[11] C. Koch and I. Brilakis, "Pothole detection in asphalt pavement images," *Advanced Engineering Informatics*, vol. 25, no. 3, pp. 507–515, 2011.

[12] J. Valença, L. Gonçalves, and E. Júlio, "Damage assessment on concrete surfaces using multi-spectral image analysis," *Construction and Building Materials*, vol. 40, pp. 971–981, 2013.

[13] M.-K. Kim, J. C. P. Cheng, H. Sohn, and C.-C. Chang, "A framework for dimensional and surface quality assessment of precast concrete elements using BIM and 3D laser scanning," *Automation in Construction*, vol. 49, pp. 225–238, 2015.

[14] S. G. Paal, J. Jeon, I. Brilakis, and R. DesRoches, "Automated damage index estimation of reinforced concrete columns for post-earthquake evaluations," *Journal of Structural Engineering*, vol. 141, no. 9, Article ID 04014228, 2015.

[15] S. Li, C. Yuan, D. Liu, and H. Cai, "Integrated processing of image and GPR data for automated pothole detection," *Journal of Computing in Civil Engineering*, vol. 30, no. 6, Article ID 04016015, 2016.

[16] S. Konishi, K. Kawakami, and M. Taguchi, "Inspection method with infrared thermometry for detect void in subway tunnel lining," *Procedia Engineering*, vol. 165, pp. 474–483, 2016.

[17] B. Oliveira Santos, J. Valença, and E. Júlio, "Automatic mapping of cracking patterns on concrete surfaces with biological stains using hyper-spectral images processing," *Structural Control and Health Monitoring*, vol. 26, no. 3, Article ID e2320, 2019.

[18] B. O. Santos, J. Valença, and E. Júlio, "Detection of cracks on concrete surfaces by hyperspectral image processing," in *Proceedings of the Automated Visual Inspection and Machine Vision II*, vol. 10334, SPIE Optical Metrology, Germany.

[19] C. Liu, S. Shirowzhan, S. M. E. Sepasgozar, and A. Kaboli, "Evaluation of classical operators and fuzzy logic algorithms for edge detection of panels at exterior cladding of buildings," *Buildings*, vol. 9, no. 2, article 40, 2019.

[20] B. Wang, Y. Li, W. Zhao, Z. Zhang, Y. Zhang, and Z. Wang, "Effective crack damage detection using multilayer sparse feature representation and incremental extreme learning machine," *Applied Sciences*, vol. 9, no. 3, article 614, 2019.

[21] C. Koch, K. Georgieva, V. Kasireddy, B. Akinci, and P. Fieguth, "A review on computer vision based defect detection and condition assessment of concrete and asphalt civil infrastructure," *Advanced Engineering Informatics*, vol. 29, no. 2, pp. 196–210, 2015.

[22] X. W. Ye, C. Z. Dong, and T. Liu, "A review of machine vision-based structural health monitoring: methodologies and applications," *Journal of Sensors*, vol. 2016, Article ID 7103039, 10 pages, 2016.

[23] N.-D. Hoang, "Image processing based automatic recognition of asphalt pavement patch using a metaheuristic optimized machine learning approach," *Advanced Engineering Informatics*, vol. 40, pp. 110–120, 2019.

[24] L. G. Shapiro and G. C. Stockman, *Computer Vision*, Prentice Hall, Upper Saddle River, 2001.

[25] S. Theodoridis and K. Koutroumbas, *Pattern Recognition*, Academic Press, 2009.

[26] R. M. Haralick, K. Shanmugam, and I. Dinstein, "Textural features for image classification," *IEEE Transactions on Systems, Man, and Cybernetics*, vol. 3, no. 6, pp. 610–621, 1973.

[27] M. M. Galloway, "Texture analysis using gray level run lengths," *Computer Graphics and Image Processing*, vol. 4, no. 2, pp. 172–179, 1975.

[28] H. Kim, E. Ahn, M. Shin, and S. Sim, "Crack and noncrack classification from concrete surface images using machine learning," *Structural Health and Monitoring*, vol. 18, no. 3, pp. 725–738, 2018.

[29] S. Dorafshan, R. J. Thomas, and M. Maguire, "Comparison of deep convolutional neural networks and edge detectors for image-based crack detection in concrete," *Construction and Building Materials*, vol. 186, pp. 1031–1045, 2018.

[30] L. Li, L. Sun, G. Ning, and S. Tan, "Automatic pavement crack recognition based on bp neural network," *PROMET - Traffic&Transportation*, vol. 26, no. 1, pp. 11–22, 2014.

[31] G. K. Choudhary and S. Dey, "Crack detection in concrete surfaces using image processing, fuzzy logic, and neural networks," in *Proceedings of the IEEE Fifth International Conference on Advanced Computational Intelligence (ICACI '12)*, pp. 404–411, Nanjing, China, 2012.

[32] N. Hoang, Q. Nguyen, and D. Tien Bui, "Image processing–based classification of asphalt pavement cracks using support vector machine optimized by artificial bee colony," *Journal of Computing in Civil Engineering*, vol. 32, no. 5, Article ID 04018037, 2018.

[33] H. Hasni, A. H. Alavi, P. Jiao, and N. Lajnef, "Detection of fatigue cracking in steel bridge girders: A support vector machine approach," *Archives of Civil and Mechanical Engineering*, vol. 17, no. 3, pp. 609–622, 2017.

[34] S. Wang, S. Qiu, W. Wang, D. Xiao, and K. C. P. Wang, "Cracking classification using minimum rectangular cover–based support vector machine," *Journal of Computing in Civil Engineering*, vol. 31, no. 5, Article ID 04017027, 2017.

[35] A. Agresti, *An Introduction to Categorical Data Analysis*, Wiley Series in Probability and Statistics, John Wiley & Sons, Inc., Hoboken, NJ, USA, 2019.

[36] M. Gormley, "Lecture note, 10-701, introduction to machine learning," in *Logistic Regression*, Carnegie Mellon School of Computer Science, 2016, https://www.cs.cmu.edu/~mgormley/courses/10701-f16/slides/lecture5.pdf.

[37] M. Chang, M. Maguire, and Y. Sun, "Stochastic modeling of bridge deterioration using classification tree and logistic regression," *Journal of Infrastructure Systems*, vol. 25, no. 1, Article ID 04018041, 2019.

[38] L. Lombardo and P. M. Mai, "Presenting logistic regression-based landslide susceptibility results," *Engineering Geology*, vol. 244, pp. 14–24, 2018.

[39] H. Kim, T. Hong, and J. Kim, "Automatic ventilation control algorithm considering the indoor environmental quality factors and occupant ventilation behavior using a logistic regression model," *Building and Environment*, vol. 153, pp. 46–59, 2019.

[40] N.-D. Hoang, "Estimating punching shear capacity of steel fibre reinforced concrete slabs using sequential piecewise multiple linear regression and artificial neural network," *Measurement*, vol. 137, pp. 58–70, 2019.

[41] A. Ng, "Lecture notes," in *CS229 Machine Learning*, Stanford University, 2018, http://cs229.stanford.edu/notes/cs229-notes1.pdf.

[42] F. Tomita and S. Tsuji, *Computer Analysis of Visual Textures*, Springer Science+ Business Media, New York, NY, USA, 1990.

[43] M. Sonka, V. Hlavac, and R. Boyle, *Image processing, Analysis, and Machine Vision*, Cengage Learning, 2013.

[44] G. M. Hadjidemetriou, P. A. Vela, and S. E. Christodoulou, "Automated pavement patch detection and quantification using support vector machines," *Journal of Computing in Civil Engineering*, vol. 32, no. 1, Article ID 04017073, 2018.

[45] A. Jindal, N. Aggarwal, and S. Gupta, "An obstacle detection method for visually impaired persons by ground plane removal using speeded-up robust features and gray level co-occurrence matrix," *Pattern Recognition and Image Analysis*, vol. 28, no. 2, pp. 288–300, 2018.

[46] X. Tang, "Texture information in run-length matrices," *IEEE Transactions on Image Processing*, vol. 7, no. 11, pp. 1602–1609, 1998.

[47] J. S. Weszka, C. R. Dyer, and A. Rosenfeld, "Comparative study of texture measures for terrain classification," *IEEE Transactions on Systems, Man, and Cybernetics*, vol. 6, no. 4, pp. 269–285, 1976.

[48] B. V. Dasarathy and E. B. Holder, "Image characterizations based on joint gray level—run length distributions," *Pattern Recognition Letters*, vol. 12, no. 8, pp. 497–502, 1991.

[49] B. Abraham and M. S. Nair, "Computer-aided classification of prostate cancer grade groups from MRI images using texture features and stacked sparse autoencoder," *Computerized Medical Imaging and Graphics*, vol. 69, pp. 60–68, 2018.

[50] M. R. Mookiah, T. Baum, K. Mei et al., "Effect of radiation dose reduction on texture measures of trabecular bone microstructure: an in vitro study," *Journal of Bone and Mineral Metabolism*, vol. 36, no. 3, pp. 323–335, 2018.

[51] A. Chu, C. M. Sehgal, and J. F. Greenleaf, "Use of gray value distribution of run lengths for texture analysis," *Pattern Recognition Letters*, vol. 11, no. 6, pp. 415–419, 1990.

[52] W. W. Piegorsch, *Statistical Data Analytics: Foundations for Data Mining, Informatics, and Knowledge Discovery*, John Wiley & Sons, 2015.

[53] K. Kim, J. Kim, T.-Y. Kwak, and C.-K. Chung, "Logistic regression model for sinkhole susceptibility due to damaged sewer pipes," *Natural Hazards*, vol. 93, no. 2, pp. 765–785, 2018.

[54] T. K. Saha and S. Pal, "Exploring physical wetland vulnerability of Atreyee river basin in India and Bangladesh using logistic regression and fuzzy logic approaches," *Ecological Indicators*, vol. 98, pp. 251–265, 2019.

[55] H. C. Chan, C. C. Chang, P. A. Chen, and J. T. Lee, "Using multinomial logistic regression for prediction of soil depth in an area of complex topography in Taiwan," *Catena*, vol. 176, pp. 419–429, 2019.

[56] N. Hoang, "Automatic detection of asphalt pavement raveling using image texture based feature extraction and stochastic gradient descent logistic regression," *Automation in Construction*, vol. 105, Article ID 102843, 2019.

[57] S. E. Ryan and L. S. Porth, "A tutorial on the piecewise regression approach applied to bedload transport data," Gen

Tech Rep RMRS-GTR-189 Fort Collins, CO: US Department of Agriculture, Forest Service, Rocky Mountain Research Station, 2007.

[58] M. E. Greene, O. Rolfson, G. Garellick, M. Gordon, and S. Nemes, "Improved statistical analysis of pre- and post-treatment patient-reported outcome measures (PROMs): the applicability of piecewise linear regression splines," *Quality of Life Research*, vol. 24, no. 3, pp. 567–573, 2015.

[59] V. Nhu, N. Hoang, V. Duong, H. Vu, and D. Tien Bui, "A hybrid computational intelligence approach for predicting soil shear strength for urban housing construction: a case study at Vinhomes Imperia project, Hai Phong city (Vietnam)," *Engineering with Computers*, 2019.

[60] J. Shlens, "A Tutorial on Principal Component Analysis," https://arxiv.org/abs/1404.1100v1.

[61] L. Breiman, "Hinging hyperplanes for regression, classification, and function approximation," *IEEE Transactions on Information Theory*, vol. 39, no. 3, pp. 999–1013, 1993.

[62] A. Tharwat, "Classification assessment methods," *Applied Computing and Informatics*, 2018, https://doi.org/10.1016/j.aci.2018.08.003.

[63] M. Hagan and M. Menhaj, "Training feedforward networks with the marquardt algorithm," *IEEE Transactions on Neural Networks and Learning Systems*, vol. 5, no. 6, pp. 989–993, 1994.

[64] A. Nandi, A. Mandal, M. Wilson, and D. Smith, "Flood hazard mapping in Jamaica using principal component analysis and logistic regression," *Environmental Earth Sciences*, vol. 75, no. 6, article 465, 2016.

[65] C. Polykretis and C. Chalkias, "Comparison and evaluation of landslide susceptibility maps obtained from weight of evidence, logistic regression, and artificial neural network models," *Natural Hazards*, vol. 93, no. 1, pp. 249–274, 2018.

[66] P. Ngo, N. Hoang, B. Pradhan et al., "A novel hybrid swarm optimized multilayer neural network for spatial prediction of flash floods in tropical areas using sentinel-1 SAR imagery and geospatial data," *Sensors*, vol. 18, no. 11, article 3704, 2018.

[67] Matwork, *Statistics and Machine Learning Toolbox User's Guide*, Matwork Inc., 2017.

[68] S. Sidney, *Non-Parametric Statistics for the Behavioral Sciences*, McGraw-Hill, New York, NY, USA, 1988.

Hindawi
Complexity
Volume 2019, Article ID 9459038, 10 pages
https://doi.org/10.1155/2019/9459038

Review Article

Memory Property of Grey Accumulation Generation Sequence

Lifeng Wu, Xiaohui Gao, and Yan Chen

College of Economics and Management, Hebei University of Engineering, Handan 056038, China

Correspondence should be addressed to Yan Chen; 964129856@qq.com

Received 24 March 2019; Revised 16 May 2019; Accepted 10 June 2019; Published 1 July 2019

Guest Editor: Murari Andrea

The influence of grey accumulation generation operator on the memory of time sequence is discussed. Generalized Hurst exponent (GHE) approach is used to calculate the memory in three cases, namely, the M3-Competition data, the air quality index in Beijing, Xingtai, and Handan, and the power generating capacity, and car production index in Hebei province. The result indicates that one order accumulation generation operator (1-AGO) can weaken the volatility and strengthen the memory of time sequence. It also explains the reason that one-order accumulation can be used in grey prediction.

1. Introduction

Since the introduction of grey prediction theory, it is has been widely applied in many fields, such as Beijing's tertiary industry [1], natural gas demand in China [2], return flow of end-of-life vehicles [3], etc. Typically, a novel multivariable grey forecasting model was proposed to forecast the number of motor vehicles in Beijing [4]. By using a self-adapting intelligent grey model, the forecasting results were substantially improved [5]. A grey model, based on a data grouping approach, was used to predict quarterly hydropower production in China [6]. The nonlinear grey multivariable model was supposed to be potentially suitable for forecasting carbon emissions due to fossil energy consumption [7]. To explore the factors causing smog weather, the grey dynamic trend incidence model was developed [8]. The grey prediction model with a nonlinear optimized time response method was presented to forecast electricity consumption in China [9].

The AGO can change the process from grey to white. It also occupies an extremely important position in the grey system theory [10]. It can reveal the patterns (laws) in chaotic original data and smooth the irregularities in the raw data. Therefore, the AGO is an indispensable part of grey forecasting [11]. To enhance the prediction accuracy, many scholars have made significance contribution to the problem. Using the local sequence grey accumulation, the forecasting accuracy can be improved to some degree [12]. The seasonal rolling grey forecasting model with a cycle truncation AGO is a complement to grey prediction [13]. The fractional-order accumulation can reduce errors from the inverse AGO of the grey model [14]. However, no study has been conducted to determine whether the grey AGO can change the memory of time sequence. Because the Hurst exponent can represent the memory of time sequence, the GHE is utilized to estimate the memory in this paper. The influence of the AGO on the memory of time sequence is analyzed through a series of experimental cases.

The rest of this paper is organized as follows. The proposed calculation method is described in Section 2. The three experimental cases are detailed in Section 3. The comparison of first-order single variable grey forecasting model and other models is shown in Section 4. The conclusion is presented in Section 5.

2. Method

The GHE was presented to calculate the memory [15]. It is defined as

$$k_q(\tau) = \sum_{t=0}^{T-\tau} \frac{|X(t+\tau) - X(t)|^q}{T-\tau+1} \quad (1)$$

where T is the length of time sequence $X(t)$ and $k_q(\tau)$ is the statistic. Equation (1) can yield a series of values by changing

the value of τ. The relationship between $k_q(\tau)$ and τ can be described as follows:

$$k_q(\tau) \propto \tau^{qH(q)} \tag{2}$$

Thus, we can estimate the Hurst exponent of time sequence in (1)-(2) for $q = 2$. When $0 \le H < 0.5$, the time sequence reveals its antipersistence. In addition, the closer H to 0, the greater intensity of this antipersistence behavior [16]. When $H = 0.5$, the time sequence follows a random walk [17–22]. When $0.5 < H < 1$, the time sequence implies strong persistence. When $H = 1$, the tendency of future can be predicted by current state [23].

The process of estimation the Hurst exponent $H(2)$ is shown as follows.

Step 1. For positive time sequence $X = \{x^{(0)}(1), x^{(0)}(2), \cdots x^{(0)}(n)\}$, the one-order accumulation of the time sequence can be obtained by

$$X^{(1)}(t) = \sum_{j=1}^{t} x^{(0)}(j), \quad t = \{1, 2, \cdots n\} \tag{3}$$

Equation (3) is called the 1-AGO.

Step 2. Calculate a series of $K_2(\tau)$ by using the following:

$$k_2(\tau) = \sum_{t=0}^{T-\tau} \frac{\left|X^{(1)}(t+\tau) - X^{(1)}(t)\right|^2}{T-\tau+1}, \quad 3 \le \tau \le \frac{T}{2} \tag{4}$$

Step 3. According to the formula, we have

$$k_2(\tau) \propto \tau^{2H(2)} \tag{5}$$

The least-square method is utilized to estimate the Hurst exponent $H(2)$.

3. Experiments and Analysis

All the experiments in this study were conducted by using the software R i386 3.4.1. The Hurst exponent values and the corresponding analyses of three cases are described in detail below.

Case 1. The data are from the M3-Competition (N2831, N2832, and N2833) and are downloaded from the Internet site: https://cran.r-project.org/web/packages/Mcomp/. The one-order accumulation sequence is presented in Figure 1. The Hurst exponent value of three groups of data is given in Table 1. The memory of three groups of data is shown in Figure 2.

In Figure 1, the original data from N2831 to N2833 have different distribution and strong randomness. However, one-order accumulation sequence from N2831 to N2833 nearly distributes in a straight line; it implied that one-order accumulation sequence has substantial developing tendency and stronger regularity.

As shown in Table 1, the $H(2)$ values of the original sequence are less than 0.5; this indicated that the original time sequence reveals its antipersistence. In contrast, the $H(2)$ values of accumulation sequence are all larger than 0.90; it implied that the memory of time sequence can be strengthened and the randomness of the time sequence can be weakened by AGO.

Table 1: The Hurst exponent value of three groups of data.

	N2831	N2832	N2833
Original sequence	0.08	0.02	0.08
Accumulation sequence	0.99	0.94	0.98

It can be noted in Figure 2 that the accumulation sequence of time sequence is regularly distributed in a straight line. The $H(2)$ value of accumulation sequence is larger than that of the original time sequence.

Case 2. Beijing, Handan, and Xingtai are the three cities selected for comparison, where the air is seriously polluted. The air quality index (AQI) data are collected from http://www.zhb.gov.cn/. Since 2013, the air pollution has been noticed by citizens. The government has took urgent measures to control this situation. The result of $H(2)$ in the three cities is in Table 2. The AQI of Beijing, Handan, and Xingtai from 2014 to 2016 are given in Figure 3. The memory results of the three group data are plotted respectively in Figure 4.

It can be seen in Figure 3 that the AQI values in winter are higher than that of in the other seasons. In this situation, the AQI time sequence in Beijing, Handan, and Xingtai has fluctuated randomly. However, one-order accumulation of AQI has stronger regularity. It is possible to establish a suitable model.

As can be seen in Table 2, the $H(2)$ values of the original sequence are all close to 0; it implied that the original AQI time sequence have quite strong antipersistence and mutability. However, the $H(2)$ values of the accumulation sequence are all close to 1.0; it indicated that the accumulation AQI time sequence has higher regularity. Consequently, it can be more extensively applied for prediction in various fields.

It is observed in Figure 4 that the original AQI sequence is disperse randomly while the accumulation sequence is regularly distributed in a straight line; it revealed that the $H(2)$ value of the accumulation sequence is larger than that of the original time sequence.

Case 3. Hebei province is located in the North China Plain. Its power generating capacity and car production index are considered to analyze the memory. These data are collected from National Bureau of Statistics of China. The $H(2)$ values of the two industry indexes in Hebei province are listed in Table 3. The original value and one-order accumulation value of two indexes are presented in Figure 5. The memory results of two indexes in Hebei province are plotted in Figure 6.

It is implied that the tendency of both indexes are increasing slightly in Figure 5. Furthermore, one-order accumulation sequence of both indexes has strong regularity. It is clear that the trend of on- order accumulation sequence is more obvious than the original sequence.

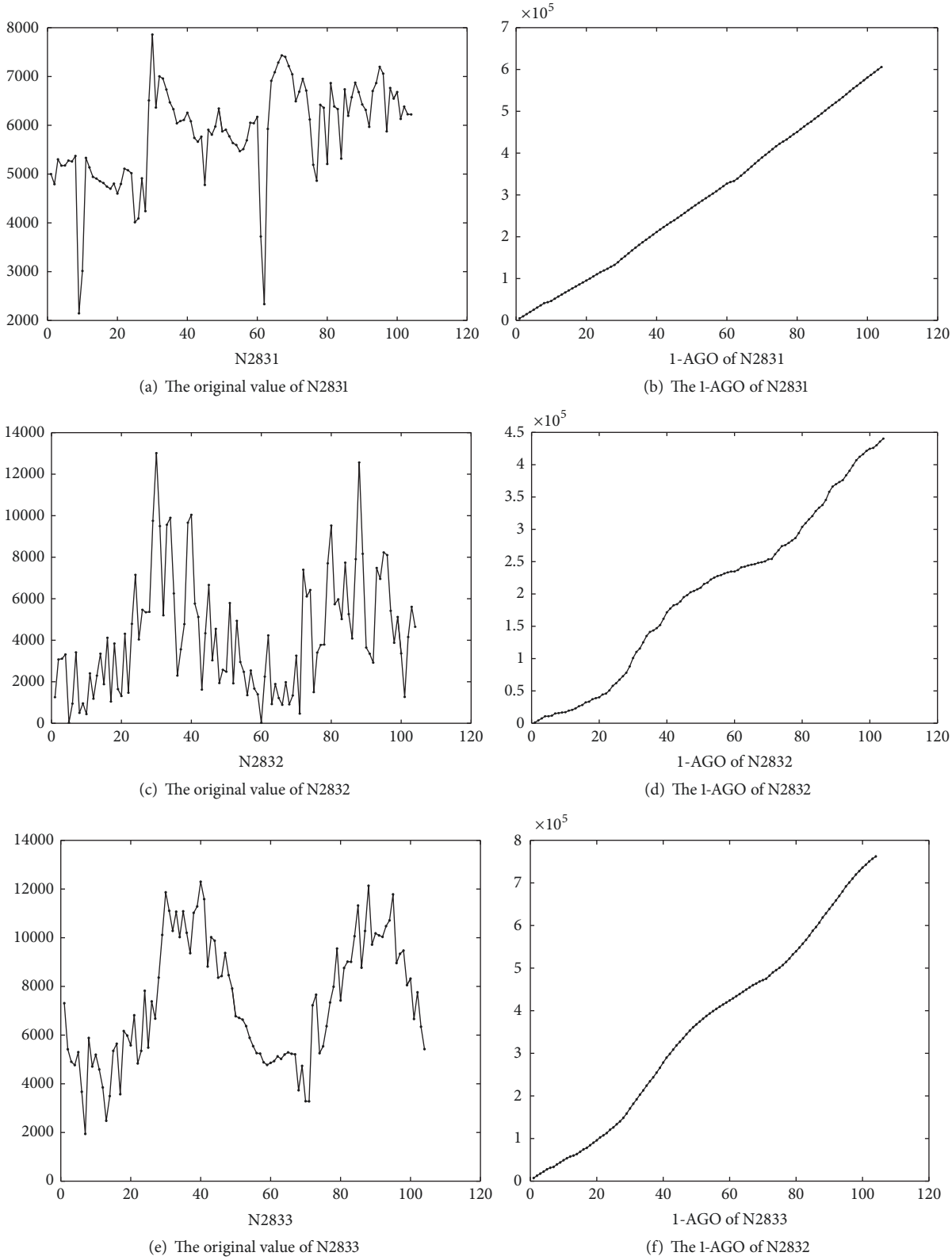

(a) The original value of N2831

(b) The 1-AGO of N2831

(c) The original value of N2832

(d) The 1-AGO of N2832

(e) The original value of N2833

(f) The 1-AGO of N2832

Figure 1: The original value and one order accumulation value of three groups data.

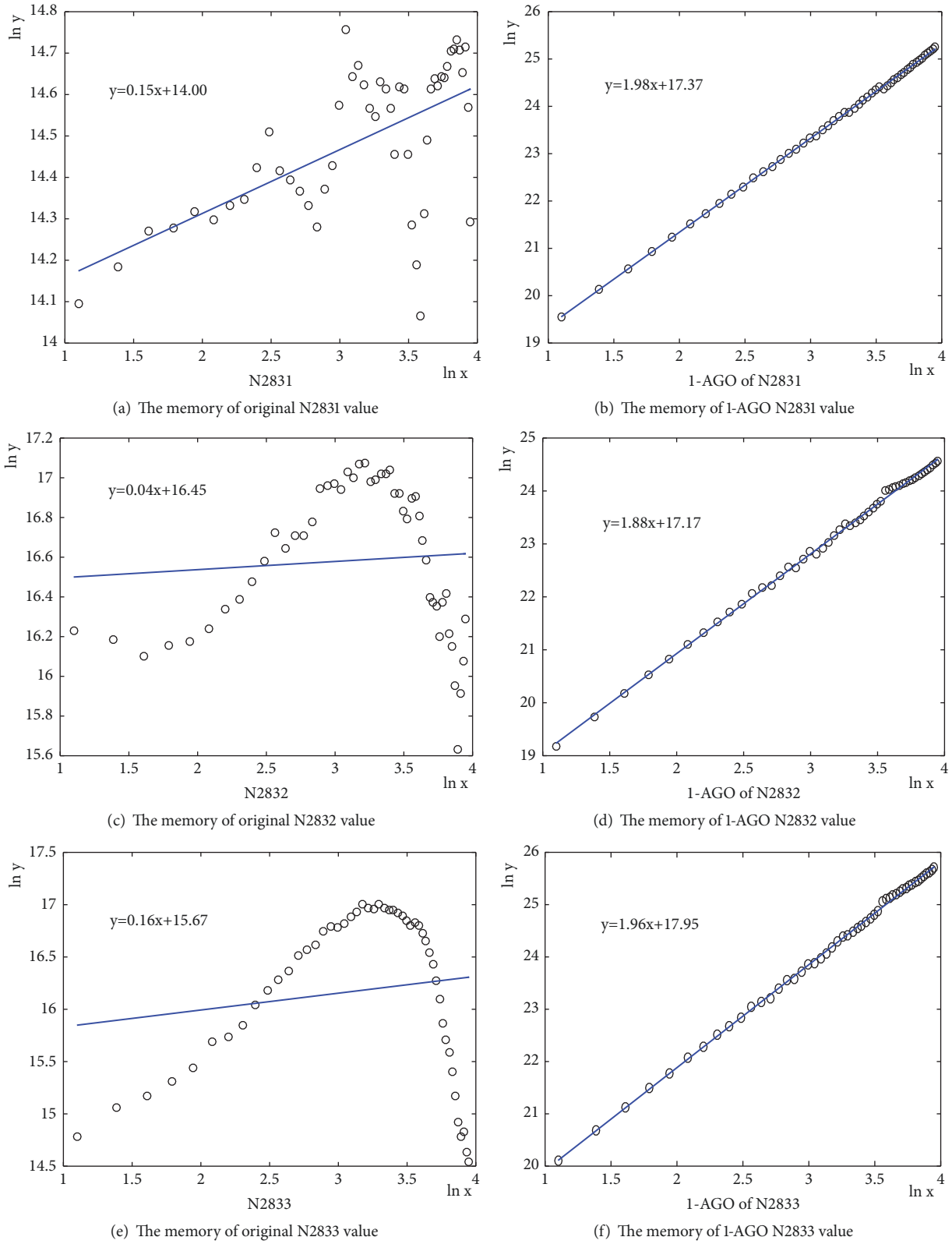

(a) The memory of original N2831 value

(b) The memory of 1-AGO N2831 value

(c) The memory of original N2832 value

(d) The memory of 1-AGO N2832 value

(e) The memory of original N2833 value

(f) The memory of 1-AGO N2833 value

Figure 2: The memory of original value and one-order accumulation value for three groups of data.

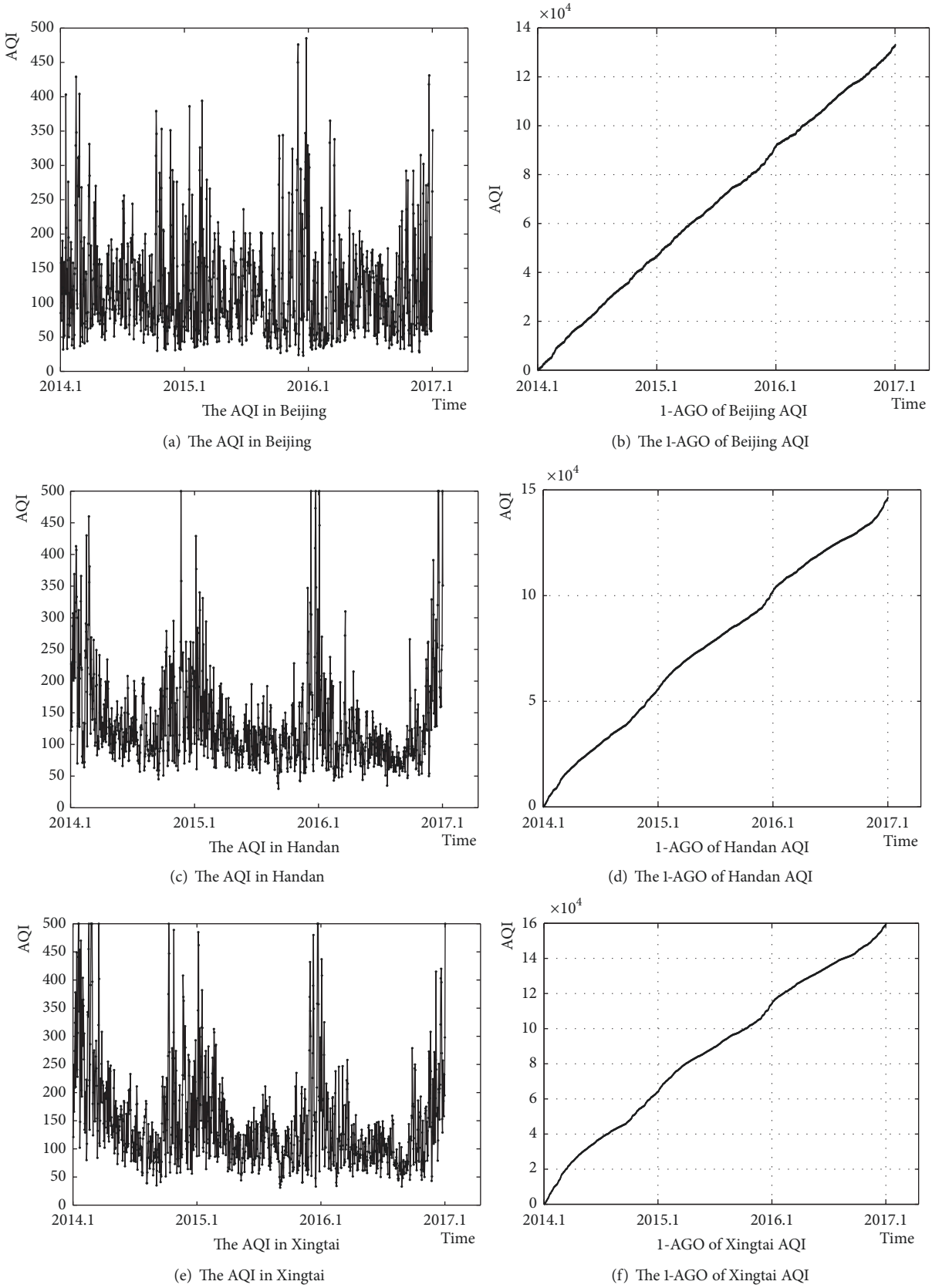

(a) The AQI in Beijing

(b) The 1-AGO of Beijing AQI

(c) The AQI in Handan

(d) The 1-AGO of Handan AQI

(e) The AQI in Xingtai

(f) The 1-AGO of Xingtai AQI

Figure 3: The original AQI value and one-order accumulation value of three cities.

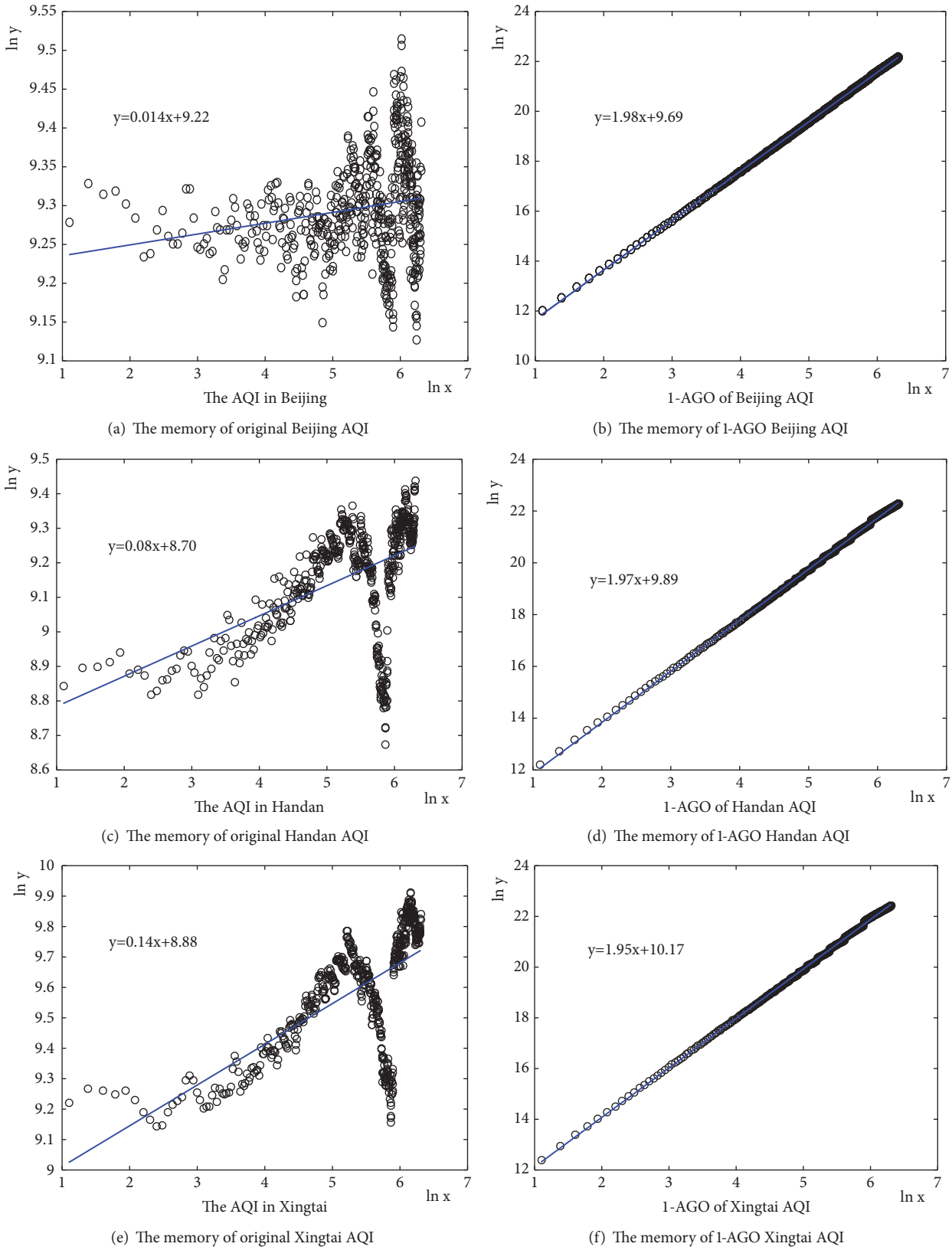

(a) The memory of original Beijing AQI

(b) The memory of 1-AGO Beijing AQI

(c) The memory of original Handan AQI

(d) The memory of 1-AGO Handan AQI

(e) The memory of original Xingtai AQI

(f) The memory of 1-AGO Xingtai AQI

Figure 4: The memory of original AQI value and one-order accumulation value of three cities.

Table 2: The AQI Hurst exponent value of three cities.

	Beijing	Handan	Xingtai
Original sequence	0.007	0.04	0.07
Accumulation sequence	0.99	0.99	0.98

Table 3: The Hurst exponent value of two indexes.

	Car production	Power generating capacity
Original sequence	0.20	0.34
Accumulation sequence	0.96	0.99

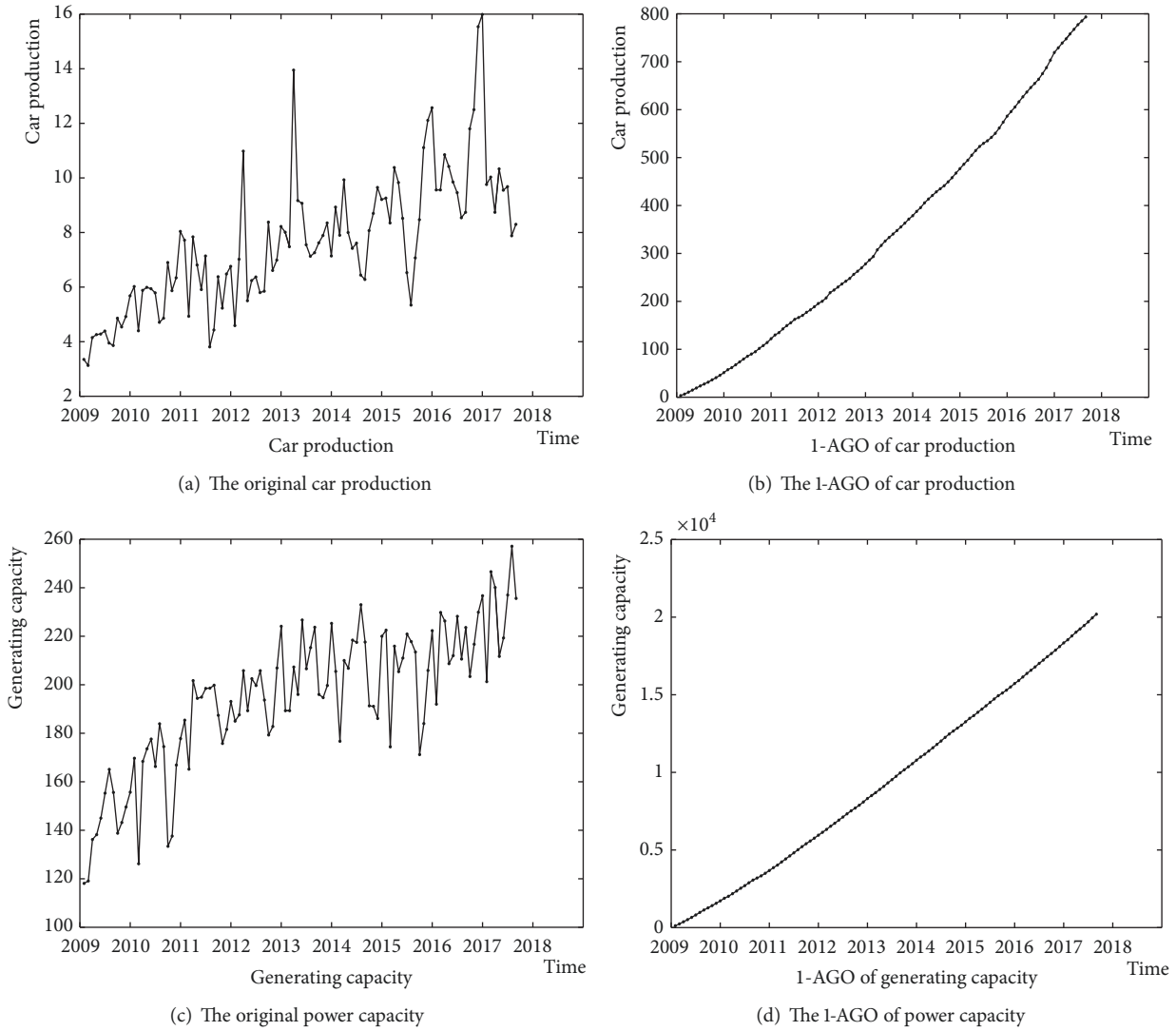

(a) The original car production

(b) The 1-AGO of car production

(c) The original power capacity

(d) The 1-AGO of power capacity

Figure 5: The original value and one order accumulation value for two indexes.

As seen in Table 3, the $H(2)$ values of the accumulation sequence are larger than those of the original time sequence for both indexes.

In Figure 6, it is noted that the points of the original value are scattered whereas those of the accumulation sequence are evenly distributed in a straight line. Therefore, the accumulation sequence yields superior persistence.

Actually, for the big size cases, the memory of sequence is enhanced by the 1-AGO. For the small size cases, the memory of sequence is also enhanced by the 1-AGO.

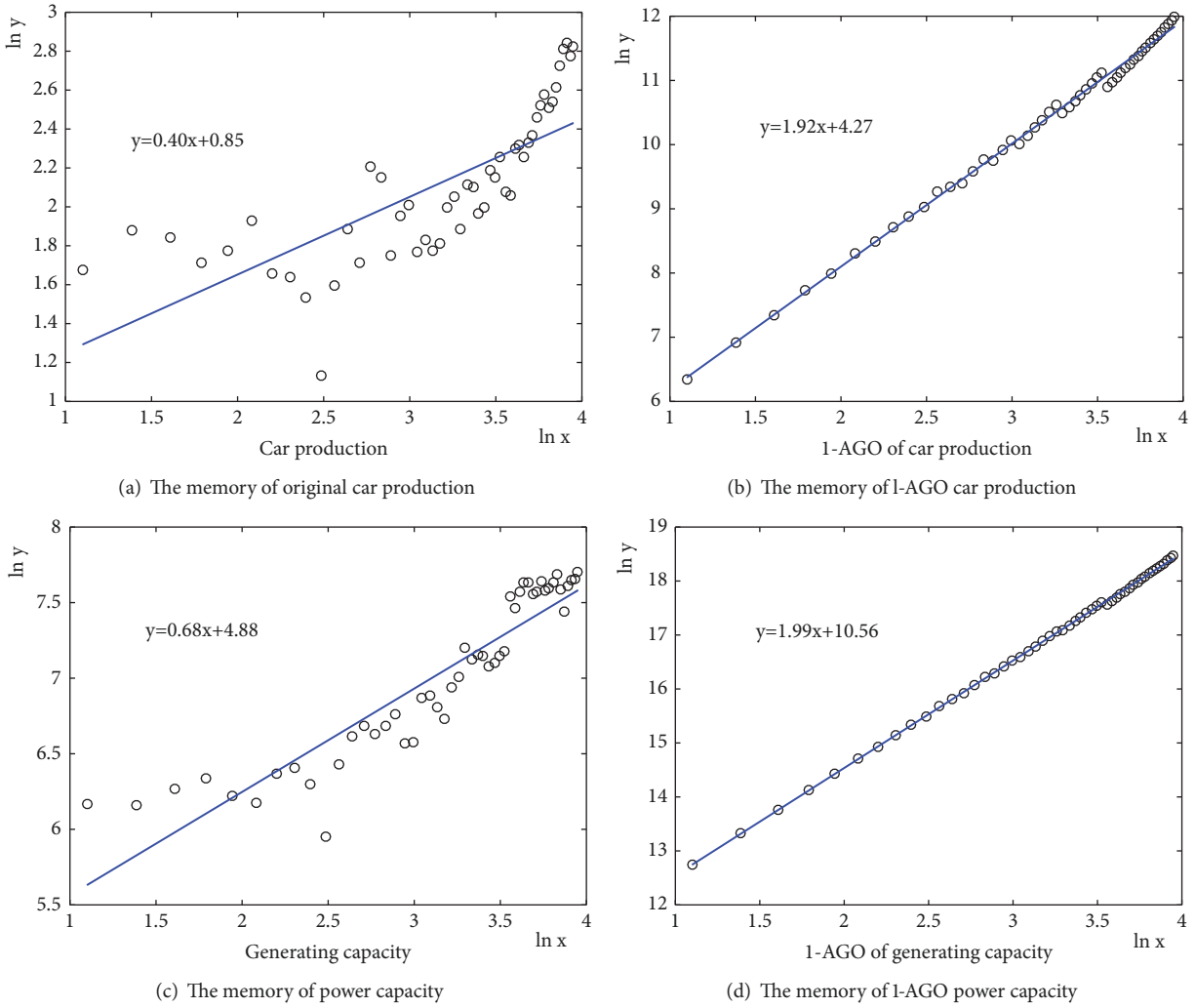

(a) The memory of original car production

(b) The memory of l-AGO car production

(c) The memory of power capacity

(d) The memory of l-AGO power capacity

Figure 6: The memory of original value and one-order accumulation value for two indexes.

4. Comparison of GM(1,1) Model and the Other Models

As the basis of the grey forecasting theory, GM(1,1) is the first-order single variable grey forecasting model, and it has been widely investigated and studied by many scholars in theoretical and practical fields [24]. The steps of GM(1,1) are shown in the following.

Step 1. An original positive sequence is $X^{(0)} = \{x^{(0)}(1), x^{(0)}(2), \cdots x^{(0)}(n)\}$. One-order accumulation sequence is $X^{(1)} = \{x^{(1)}(1), x^{(1)}(2), \cdots x^{(1)}(n)\}$.

Step 2. The GM(1,1) model is $x^{(0)}(k) + az^{(1)}(k) = b$, $z^{(1)}(k) = (1/2)(x^{(1)}(k) + x^{(1)}(k-1))$, $k = 2, 3, \cdots, n$.

Its whitenization equation is $dx^{(1)}/dt + ax^{(1)} = b$. a and b are coefficients. a is the developing coefficient, and b is the grey input. a and b are obtained by the least-squares method as follows:

$$\begin{bmatrix} \widehat{a} \\ \widehat{b} \end{bmatrix} = \left(B^T B\right)^{-1} B^T Y \tag{6}$$

where

$$Y = \begin{bmatrix} x^{(0)}(2) \\ x^{(0)}(3) \\ \vdots \\ x^{(0)}(n) \end{bmatrix}, \quad B = \begin{bmatrix} -z^{(1)}(2) & 1 \\ -z^{(1)}(3) & 1 \\ \vdots & \vdots \\ -z^{(1)}(n) & 1 \end{bmatrix}. \tag{7}$$

Step 3. The solution of $dx^{(1)}/dt + ax^{(1)} = b$ is $x^{(1)}(t+1) = (x^{(0)}(1) - b/a)e^{-at} + b/a$. According to $\widehat{x}^{(1)}(1) = x^{(0)}(1)$, $\widehat{x}^{(1)}(t+1)$ is obtained as $\widehat{x}^{(1)}(t+1) = (x^{(0)}(1) - \widehat{b}/\widehat{a})e^{-at} + \widehat{b}/\widehat{a}$.

Step 4. To obtain the predicted value of the data at time $(k+1)$, the forecasting sequence is $\widehat{X}^{(0)} =$

Table 4: The results for different models for M3C N1.

Data	GM(1,1)	Winter	ARAMRA	AUTO-ANN
5379.75	5506.72	5406.43	5553.26	5453.28
6158.68	6153.6	5875.96	6246.45	6003.49
6876.58	6876.48	6345.48	7026.18	6587.93
7851.91	7684.27	6815	7903.23	7206.76
8407.84	8586.96	7284.53	8889.77	7860.01
9156.01	9595.69	7754.05	9999.45	8547.55
MAPE	1.92	9.11	3.74	4.91

$\{\hat{x}^{(0)}(1), \hat{x}^{(0)}(2), \cdots, \hat{x}^{(0)}(n)\}$ and the inverse accumulating generation operation $\hat{x}^{(0)}(k+1) = \hat{x}^{(1)}(k+1) - \hat{x}^{(1)}(k)$ is applied as follows: $\hat{x}^{(0)}(t+1) = (x^{(0)}(1) - \hat{b}/\hat{a})(1 - e^{a})e^{-at}$.

GM(1,1) is one of the most common methods used for studying data sets characterized by small size. The above cases have big size; GM(1,1) is not the better model for above cases. Therefore, the series N1 (sample size is 14) from the M3 forecasting competition is selected as the evaluation data. The data is downloaded from the Internet site: http://www.insead.fr/facultyresearch/forecasting.

The memory of accumulation sequence is evaluated by comparing the traditional GM(1,1) model with the other models in this section. Therefore, mean absolute percentage error (MAPE = $100\%(1/n)\sum_{k=1}^{n} |(x^{(0)}(k) - \hat{x}^{(0)}(k))/x^{(0)}(k)|$) compares the actual values with the forecasting values. The last 6 observations are used to evaluate their accuracy. The forecasting results of the series N1 are listed in Table 4 and are plotted in Figure 7.

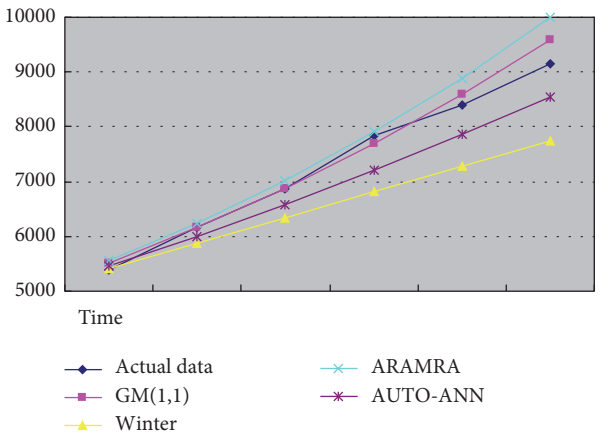

Figure 7: The predicted and true values for M3C N1.

Winter model, ARAMRA, and AUTO-ANN are the most common methods used for studying data sets characterized by small size. In Table 4, it indicated that the MAPE of GM(1,1) are smaller than that of other models. We can say that the GM(1,1) model is better than the others. The original time sequence always shows strong antipersistent behavior. It is difficult to dig out the information in the sequence. The AGO can strengthen the memory of the time sequence. Therefore, it plays a pivotal role to establish model. With the application of AGO in GM(1,1) model, the case imply that GM(1,1) model has higher forecasting performance.

5. Conclusion

For a time sequence, the current state is the result of a series of interrelated events. The development state has a long-term (short-term) memory. In general, the Hurst exponent of original time sequence is less than or close to 0.5. In this situation, the time sequence always shows stronger antipersistent behavior; it means that the time sequence follows a random walk with mutability or volatility. As can be seen from the experimental cases, the Hurst exponent of one-order accumulation sequence was very close to 1, the randomness of the time sequence was significantly weakened and the regularity was strengthened. By the 1-AGO, the memory of sequence is enhanced and the accumulation sequence yields superior persistence. The future trend can be predicted based on the present state.

It is worthwhile to use 1-AGO in grey prediction. On one hand, the randomness of the original sequence is weakened by 1-AGO. On the other hand, grey accumulation generation sequence can provide additional information for modeling and enable the data to construction a more appropriate model. Because the Hurst exponent of one order accumulation sequence was very close to the maximum (i.e., 1), for the grey forecasting model, the accumulation-order number cannot be more than 1 in practical applications.

Three cases are discussed to demonstrate the memory of grey AGO. In the future, more cases are needed to be discussed to demonstrate the memory. All values in this paper are positive, so the accumulation frequency is always increasing. In this case, the Hurst Exponent is close to 1. Of course, this property may change when the original time sequence contains negative values. In the future, more cases with negative values are needed to be discussed.

Conflicts of Interest

All authors declare that they have no conflicts of interest.

Acknowledgments

The relevant researches in this paper are supported by the National Natural Science Foundation of China (Nos.

71871084, 71401051), the Excellent Young Scientist Foundation of Hebei Education Department (No. SLRC2019001), and the project of high-level talent in Hebei province.

References

[1] Q. Wang, L. Liu, S. Wang, J.-Z. Wang, and M. Liu, "Predicting Beijing's tertiary industry with an improved grey model," *Applied Soft Computing*, vol. 57, pp. 482–494, 2017.

[2] F. Shaikh, Q. Ji, P. H. Shaikh, N. H. Mirjat, and M. A. Uqaili, "Forecasting China's natural gas demand based on optimised nonlinear grey models," *Energy*, vol. 140, pp. 941–951, 2017.

[3] S. Ene and N. Öztürk, "Grey modelling based forecasting system for return flow of end-of-life vehicles," *Technological Forecasting & Social Change*, vol. 115, pp. 155–166, 2017.

[4] B. Zeng, C. Luo, C. Li, and S. Liu, "A novel multi-variable grey forecasting model and its application in forecasting the amount of motor vehicles in Beijing," *Computers & Industrial Engineering*, vol. 101, pp. 479–489, 2016.

[5] B. Zeng and C. Li, "Forecasting the natural gas demand in China using a self-adapting intelligent grey model," *Energy*, vol. 112, pp. 810–825, 2016.

[6] Z.-X. Wang, Q. Li, and L.-L. Pei, "Grey forecasting method of quarterly hydropower production in China based on a data grouping approach," *Applied Mathematical Modelling*, vol. 51, pp. 302–316, 2017.

[7] Z.-X. Wang and D.-J. Ye, "Forecasting Chinese carbon emissions from fossil energy consumption using non-linear grey multivariable models," *Journal of Cleaner Production*, vol. 142, pp. 600–612, 2017.

[8] J. Wang, K. W. Hipel, and Y. Dang, "An improved grey dynamic trend incidence model with application to factors causing smog weather," *Expert Systems with Applications*, vol. 87, pp. 240–251, 2017.

[9] N. Xu, Y. Dang, and Y. Gong, "Novel grey prediction model with nonlinear optimized time response method for forecasting of electricity consumption in China," *Energy*, vol. 118, pp. 473–480, 2017.

[10] L. Wu, S. Liu, D. Chen, L. Yao, and W. Cui, "Using gray model with fractional order accumulation to predict gas emission," *Natural Hazards*, vol. 71, no. 3, pp. 2231–2236, 2014.

[11] C.-J. Chang, J.-Y. Lin, and P. Jin, "A grey modeling procedure based on the data smoothing index for short-term manufacturing demand forecast," *Computational and Mathematical Organization Theory*, vol. 23, no. 3, pp. 409–422, 2017.

[12] K. L. Wen, *Grey prediction theory and application*, Open Tech Company, Taipei, Taiwan, 2002.

[13] X. Xiao, J. Yang, S. Mao, and J. Wen, "An improved seasonal rolling grey forecasting model using a cycle truncation accumulated generating operation for traffic flow," *Applied Mathematical Modelling*, vol. 51, pp. 386–404, 2017.

[14] L. Wu, S. Liu, L. Yao, R. Xu, and X. Lei, "Using fractional order accumulation to reduce errors from inverse accumulated generating operator of grey model," *Soft Computing*, vol. 19, no. 2, pp. 483–488, 2014.

[15] T. Di Matteo, T. Aste, and M. M. Dacorogna, "Scaling behaviors in differently developed markets," *Physica A: Statistical Mechanics and its Applications*, vol. 324, no. 1-2, pp. 183–188, 2003.

[16] J. P. Ramos-Requena, J. E. Trinidad-Segovia, and M. A. Sánchez-Granero, "Introducing Hurst exponent in pair trading," *Physica A: Statistical Mechanics and its Applications*, vol. 488, pp. 39–45, 2017.

[17] L. Salim and S. Amir, "Accurate classification of seizure and seizure-free intervals of intracranial EEG signals from epileptic patients," *IEEE Transactions on Instrumentation*, vol. 68, no. 3, pp. 791–796, 2019.

[18] S. Lahmiri, "An accurate system to distinguish between normal and abnormal electroencephalogram records with epileptic seizure free intervals," *Biomedical Signal Processing and Control*, vol. 40, pp. 312–317, 2018.

[19] L. Salim, "Glioma detection based on multi-fractal features of segmented brain MRI by particle swarm optimization techniques," *Biomedical Signal Processing and Control*, vol. 31, pp. 148–155, 2017.

[20] T. Blachowicz, A. Ehrmann, and K. Domino, "Statistical analysis of digital images of periodic fibrous structures using generalized Hurst exponent distributions," *Physica A: Statistical Mechanics and its Applications*, vol. 452, pp. 167–177, 2016.

[21] M. Ausloos, "Generalized Hurst exponent and multifractal function of original and translated texts mapped into frequency and length time series," *Physical Review E: Statistical, Nonlinear, and Soft Matter Physics*, vol. 86, no. 3, Article ID 031108, 2012.

[22] C. Dou, X. Wei, and J. Lin, "Fault diagnosis of gearboxes using nonlinearity and determinism by generalized hurst exponents of shuffle and surrogate data," *Entropy*, vol. 20, no. 5, p. 364, 2018.

[23] W. Wang, *Long Memory Characteristics And Prediction of Financial Time Series*, Nankai University Press, 2018.

[24] B. Zeng, H. Duan, and Y. Zhou, "A new multivariable grey prediction model with structure compatibility," *Applied Mathematical Modelling: Simulation and Computation for Engineering and Environmental Systems*, vol. 75, pp. 385–397, 2019.